Lecture Notes in Electrical Engineering 176

David Jin
Sally Lin
Editors

Advances in Mechanical and Electronic Engineering

Volume 1

Springer

For further volumes:
http://www.springer.com/series/7818

David Jin and Sally Lin (Eds.)

Advances in Mechanical and Electronic Engineering

Volume 1

Editors
David Jin
Wuhan Section of ISER Association
Wuhan
China

Sally Lin
Wuhan Section of ISER Association
Wuhan
China

ISSN 1876-1100
ISBN 978-3-642-31506-0
DOI 10.1007/978-3-642-31507-7
Springer Heidelberg New York Dordrecht London

e-ISSN 1876-1119
e-ISBN 978-3-642-31507-7

Library of Congress Control Number: 2012940780

Printed on acid-free paper

Springer is part of Springer Science+Business Media (www.springer.com)

Preface

In the proceeding of Volume 1 of ICMEE2012, you can learn much more knowledge about Mechanical Engineering and Automation; Vehicle Engineering and Technology all around the world. The main role of the proceeding is to be used as an exchange pillar for researchers who are working in the mentioned field. In order to meet high standard of Springer, the organization committee has made their efforts to do the following things. Firstly, poor quality paper has been refused after reviewing course by anonymous referee experts. Secondly, periodically review meetings have been held around the reviewers about five times for exchanging reviewing suggestions. Finally, the conference organization had several preliminary sessions before the conference. Through efforts of different people and departments, the conference will be successful and fruitful.

During the organization course, we have got help from different people, different departments, different institutions. Here, we would like to show our first sincere thanks to publishers of Springer, LNEE series for their kind and enthusiastic help and best support for our conference.

In a word, it is the different team efforts that they make our conference be successful on June 23–24, 2012, Hefei, China. We hope that all of participants can give us good suggestions to improve our working efficiency and service in the future. And we also hope to get your supporting all the way. Next year, In 2013, we look forward to seeing all of you at ICMEE2013.

April 2012 ICMEE2012 Committee

Committee

Honor Chairs

Prof. Chen Bin	Beijing Normal University, China
Prof. Hu Chen	Peking University, China
Chunhua Tan	Beijing Normal University, China
Helen Zhang	University of Munich, China

Program Committee Chairs

Xiong Huang	International Science & Education Researcher Association, China
LiDing	International Science & Education Researcher Association, China
Zhihua Xu	International Science & Education Researcher Association, China

Organizing Chair

ZongMing Tu	Beijing Gireida Education Co.Ltd, China
Jijun Wang	Beijing Spon Technology Research Institution, China
Quanxiang	Beijing Prophet Science and Education Research Center, China

Publication Chair

Song Lin	International Science & Education Researcher Association, China
Xionghuang	International Science & Education Researcher Association, China

International Committees

Sally Wang	Beijing Normal University, China
LiLi	Dongguan University of Technology, China
BingXiao	Anhui University, China
Z.L. Wang	Wuhan University, China
Moon Seho	Hoseo University, Korea
Kongel Arearak	Suranaree University of Technology, Thailand
Zhihua Xu	International Science & Education Researcher Association, China

Co-sponsored by

International Science & Education Researcher Association, China
VIP Information Conference Center, China
Beijing Gireda Research Center, China

Reviewers of ICMEE2012

Z.P. Lv	Huazhong University of Science and Technology
Q. Huang	Huazhong University of Science and Technology
Helen Li	Yangtze University
Sara He	Wuhan Textile University
Jack Ma	Wuhan Textile University
George Liu	Huaxia College Wuhan Polytechnic University
Hanley Wang	Wuchang University of Technology
Diana Yu	Huazhong University of Science and Technology
Anna Tian	Wuchang University of Technology
Fitch Chen	Zhongshan University
David Bai	Nanjing University of Technology
Y. Li	South China Normal University
Harry Song	Guangzhou Univeristy
Lida Cai	Jinan University
Kelly Huang	Jinan University
Zelle Guo	Guangzhou Medical College
Gelen Huang	Guangzhou University
David Miao	Tongji University
Charles Wei	Nanjing University of Technology
Carl Wu	Jiangsu University of Science and Technology
Senon Gao	Jiangsu University of Science and Technology
X.H Zhan	Nanjing University of Aeronautics
Tab Li	Dalian University of Technology (City College)
J.G Cao	Beijing University of Science and Technology
Gabriel Liu	Southwest University
Garry Li	Zhengzhou University
Aaron Ma	North China Electric Power University
Torry Yu	Shenyang Polytechnic University
Navy Hu	Qingdao University of Science and Technology
Jacob Shen	Hebei University of Engineering

Contents

Section One: Mechanical Engineering and Automation

Improvement of Lapping Machine Slurry Supplying System

Lihui Jin, Yutian Wang, Guorui Wang, and Chungeng Yang

Tianjin Huanou Semiconductor Material and Technology Co., Ltd Tianjin, 300384, China
Jinlihui@gmail.com

Abstract. Wafer lapping process affects product quality and competitiveness. Improving existing wafer lapping equipment, adding a automatically tuning system of slurry flow rate, wafer surface quality is improved, defective goods are decreased, and cost is saved.

Keywords: lapping machine, automatically, tuning system of slurry flow rate.

1 Introduction

Slurry plays a very important role in the lapping process of semiconductor wafer, crystal and all kinds of Rigid-fragile materials. For wafer surface, when slurry flow rate is increased, the ability of impurities removal is enhanced, wafer laps more sufficiently, wafer surface quality is better. But too high slurry flow rate will increase material cost and reduce product competitiveness.

With the high speed development of semiconductor industrial, the demand of material surface quality such as wafer becomes more and more critical. So far the best way to improve surface quality is to increase slurry flow rate during the fine lapping. Existing equipment applies manual control of slurry flow rate, but it can't meet product acquirement. So the automatically tuning system of slurry flow rate is more and more attractive for lapping machine.

2 Improvement Plan

Background: Wafer lapping process consists of two sub-processes ----coarse lapping and fine lapping. Coarse lapping utilizes slurry to remove affected layer from slice process. Fine lapping improves surface quality by the way of increasing slurry flow rate. For existing lapping machine, operator manually adjusts slurry system to change flow rate to accomplish coarse and fine lapping, but this method depends on experience of operator, and operator couldn't exactly control flow rate and time, so that wafer surface quality after lapping is unstable.

Method: After improvement, new slurry system can automatically adjust flow rate according to the two sub-processes. New system hardware consists of automatic level

D. Jin and S. Lin (Eds.): Advances in Mechanical and Electronic Engineering, LNEE 176, pp. 1–4.
springerlink.com

control (ALC), programmable logic controller (PLC), touch panel and rotate speed control unit of peristaltic pump. ALC consists of industrial-computer, thickness meter and measurement probe. Measurement probe measures wafer thickness and compare with target thickness to generate Transistor-Transistor Logic (TTL) signal. PLC consists of digital input and relay output. Digital inputs receive TTL signal from ALC, PLC calculates and controls output signals.

Fig 1 shows main control unit of the new slurry system.

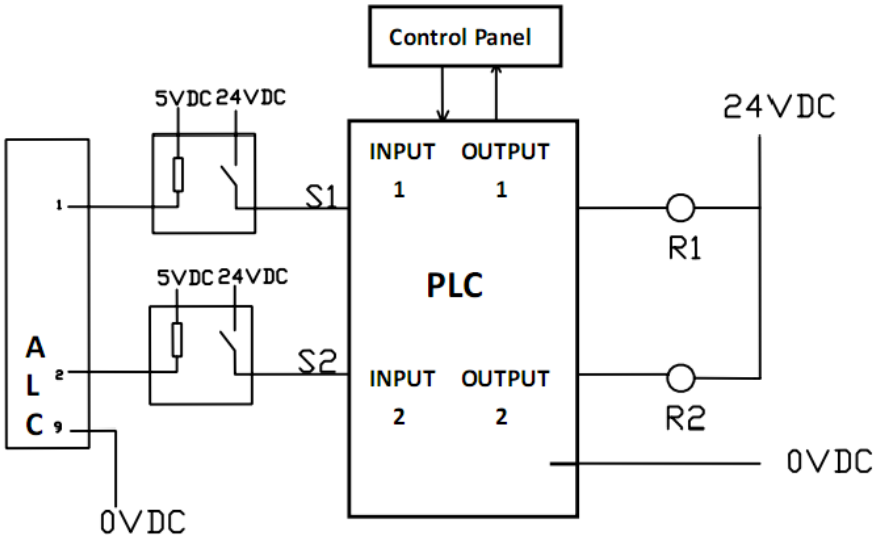

Fig. 1. New slurry system main control circuit

Two outputs of PLC connect to relay R1, R2; ALC's output signal S1, S2 connect to input 1, 2 of PLC respectively.

Fig 2 shows the peristaltic pump's control diagram of new slurry system.

Auxiliary normally open (NO) contact R1NO connects auxiliary normally closed (NC) contact R2NC, potentiometer T1 and analog input of peristaltic pump;

Auxiliary NO contact R2NO connects auxiliary NC contact R1NC, potentiometer T2 and analog input of peristaltic pump.

Peristaltic pump unit consists of pump rotation direction control switch and analog input which control rotation speed.

Used touch panel as man machine interface. RS 232 Communication is between touch panel and PLC. Fig3 shows the flow rate control interface of touch panel. There are two rotation speed selected buttons of peristaltic pump, which are Pump speed 1 and Pump speed 2.

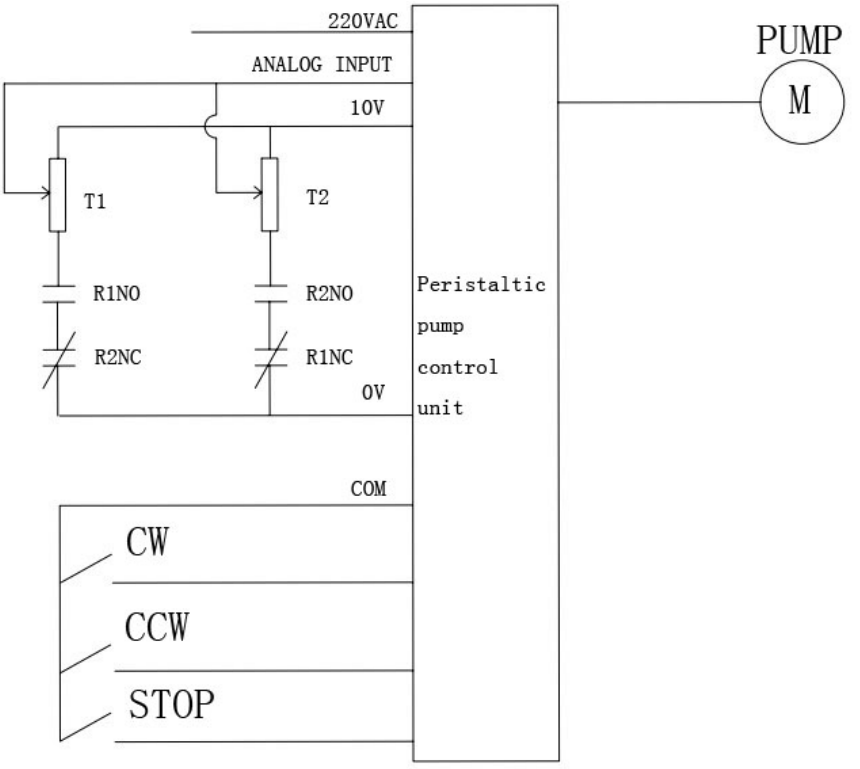

Fig. 2. Control diagram of peristaltic pump

Fig. 3. Main machine interface

Fig. 3. *(continued)*

3 Process Procedure after Improvement

(1) Setting the thickness signal of ALC to trigger auxiliary relay R1 and R2, rotation speed of peristaltic pump could be automatically adjusted.

(2) When button "Pump speed 1" is pressed, PLC outputs. The relay R1 is energized by PLC output 1. Circuit of pump speed control 1 is connected and speed control 2 is disconnected. It is to determine rotation speed 1 of pump by adjusting potentiometer T1.

(3) When button "Pump speed 2" is pressed, PLC outputs. The relay R2 is energized by PLC output 2. Circuit of pump speed control 2 is connected and speed control 1 is disconnected. It is to determine rotation speed 2 of pump by adjusting potentiometer T2.

(4) The signal which is generated by ALC controls relay R1 and R2's on or off. When wafer's thickness value measured by ALC doesn't reach target value, R1 is energized and R2 is not energized, pump is running by speed 1. Circuit of pump speed control 2 disconnects. When thickness value measured by ALC reach target value, R2 is energized and R1 is not energized, peristaltic pump changes to speed 2, Lapping machine gets into fine lapping. When thickness value reaches target value, ALC generates TTL signal S2 and PLC receives it. Equipment stops, lapping process finishes.

4 Conclusion

After installing automatically tuning system of slurry flow rate, coarse lapping and fine lapping are distinguished by ALC signal. Slurry flow rate is automatically adjusted during different lapping process to improve surface quality and reduce slurry consumption, surface quality of wafer improves greatly, product qualified rate is increased from 96.5% to 99 %, and slurry consumption per wafer is reduced 8%.

The SMA Miniature Obstacle-Navigation Mobile Robot System Control

Xuepeng Liu and Dongmei Zhao

Zhongshan Polytechnic, P.R. China
aliuxuepeng1026@yahoo.com.cn, bzdmeihn@163.com

Abstract. The obstacle-navigation mechanism of SMA Miniature the obstacle-navigation mobile robot is introduced. The movement model of the obstacle-navigation mobile robot is studied. According to model of SMA, the SMA robot is controlled using PWM heating method. The movement of the obstacle-navigation mobile robot is simulated, and the simulation animation figures are supplied.

Keywords: The SMA driver, PWM heating mode, simulation animation, obstacle-navigation.

1 Introduction

Miniature robot in the industry, national defense, medical science, biological engineering, aerospace and other fields have a wide range of applications. In industry, robot can be used for integrated circuit manufacturing, processing, etc. In medical science it can be used for a surgery, organs, and blood tests. In biological engineering, can in cell level of genetic operations.

At present, the robot to miniaturization, intelligent and integrated the direction of development, intelligent robot system to hot spot. Miniature robot system is developed, the first to solve the problem of drive, the driver of the robot is to meet the size is small, heavy work than high, can accurate control requirements.

Shape memory alloy (SMA) because of its power to weight than the big, sensors and actuators for collection etc, and is an ideal material for enhanced function. The obstacles of SMA micro-module will shape memory alloy this intelligent materials and micro-motor technology, and the combination of increased the obstacles function. So not only its functions were enhanced, miniature robot is more adaptive capacity, can complete many tasks, and is consistent with the size of the robot don't add much requirements. The robots need to increase after the function is of high intelligence level, so as to give full play to the advantages of its versatile.

Mobile robot obstacle-avoidance problem is always the researchers focus on one of the topics. Ordinary mobile robot meet obstacles in commonly there are two solutions: one is by many intelligent sensor detection, provide the environment information to the robot navigation system, control of the robot diverted obstacle avoidance; Another way is through the sensor detection, obtain the geometry of the obstacles shape, size, directly across the smaller obstacles. This way don't need

D. Jin and S. Lin (Eds.): Advances in Mechanical and Electronic Engineering, LNEE 176, pp. 5–8.
springerlink.com

navigation system to do complex obstacle avoidance path planning, can greatly improve the efficiency, but it need to move robots have special properties, the negotiation of sensor system also have higher requirements. In a small mobile robot obstacle-avoidance problem study, for diverted obstacle avoidance way, have a lot of success to the researchers to try, but limited to mechanical processing, control, test method and other reasons, the obstacles to direct, the work less. The obstacles of SMA small small-sized mobile robot using new functional materials, shape memory alloy (SMA), realized the rules of a low cross obstacle or gully function. Due to its own characteristics of SMA components, the disabled institutions, simple in structure, fast response, doing work ability and application in miniature robot drive are relatively suitable.

2 The Obstacle-Navigation Mobile Robot

The original structure of the obstacle SMA miniature mobile robot includes two parts: double function of driving type of the obstacles and the main body part function.

The obstacles of SMA small small-sized mobile robot obstacle-navigation function to realize the essence of SMA components is action, robot, complete functions, deformation switch after the obstacles again by SMA element action, return to its original shape. The robot the whole the negotiation process is divided into four steps:

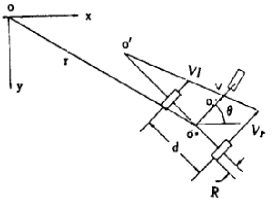

Fig. 1. Movement model

1, when the robot in the ground to walk in the round, robot active motor drive forward movement, but also under complete back, left turn, turn right such action.

2, when the robot obstacle, near the edge, before and after skateboard in the driving of SMA component protruding from the rotation, and drive down, will assist a robot main body wheel carried from the ground, robot obstacle-navigation switch to the working condition.

3, robot in auxiliary motor drive forward movement under the action of the main body, will give obstacles.

4, before and after the board of SMA components in under the action of the obstacles to take back the state before, it causes a lift, auxiliary rotary wheel on the ground will be the main body, the switch back to the ground robot operation.

3 The Movement Model of the Obstacle-Navigation Mobile Robot

Double independent drive structure is made up of two driving wheel speed difference to realize the turn. Turn control of the wheel speed by omega on both sides of the decision. The model is shown in fig.1 O turn for the instantaneous. Choose drive shaft

center O * for robot ontology reference point, is the main body of the speed, angular velocity are:

$$v = \frac{dr}{dt} = \frac{v_L + v_R}{2} = \frac{R(\omega_L + \omega_R)}{2}$$

$$\omega = \frac{d\theta}{dt} = \frac{v_L - v_R}{d} = \frac{R(\omega_L - \omega_R)}{d}$$

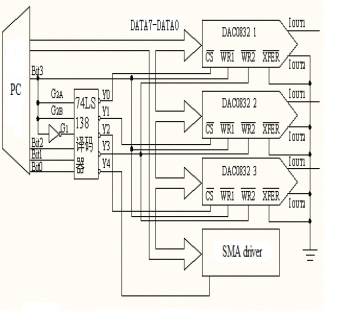

Fig. 2. Control circuit

Currently USES the dc servo driver and micro-motor armature voltage speed method. The armature voltage controlled by a computer system to adjust, can achieve high precision and strong anti-interference ability. The computer control circuit by the computer interface circuit, D/A transformation circuit, power amplifier circuit component in fig.2.

4 The SMA of Components of the Control Model

The SMA components in pulse voltage heating function, its temperature change is divided into six stages, temperature and change rules are not all the same

$$t_1 = -T_1 \ \ln(1 + \frac{\theta_0 - A_s}{E \cdot B})$$

$$t_2 = -T_2 \ \ln(1 + \frac{A_s - A_f}{E \cdot B + \theta_0 - A_s})$$

$$t_3 = -T_1 \ \ln(1 + \frac{A_f - \theta_M}{E \cdot B + \theta_0 - A_f})$$

$$t_4 = -T_1 \ \ln(1 + \frac{\theta_M - M_s}{\theta_0 - \theta_M})$$

$$t_5 = -T_5 \ \ln(1 + \frac{M_s - M_f}{\theta_0 - M_s})$$

$$t_6 = -T_1 \ \ln(1 + \frac{M_f - \theta_L}{\theta_0 - M_f})$$

5 The Simulation of Obstacle-Navigation Mobile Robot

The following are the simulation animation figures

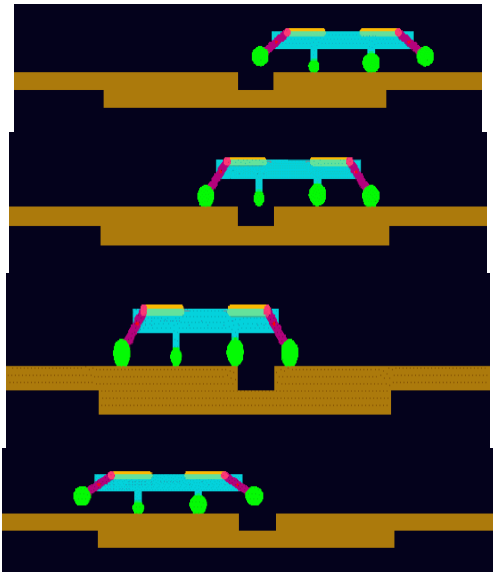

Fig. 3. Simulation

References

[1] Song, Y., Guo, W.: Micro Operation System Based on Miniature Mobile Robot. Chinese Journal of Mechanical Engineering 43(2) (2007)
[2] Luan, X.-H., Zheng, L.-P.: A 3DOF Miniature Robot System Based on Inertia Impact Drive Principle. Machinery & Electronics (11) (2007)
[3] Yujun, Y.: Cooperation Learning for Autonomous Micro-mobile Robot. Computer Engineering 29(10) (2003)
[4] Sun, L.-N., Zhong, M.: Mobile miniature self-reconfigurable robot based on embedded vision. Optics and Precision Engineering 17(12) (2009)

Research on Frequent Flyer Churn Early Warning in Civil Aviation Based on Predictive Value

LiFeng Wei[1,2], JianWei Ji[1], and BingMei Zhao[2]

[1] Collage of Information and Electrical Engineering, Shenyang Agricultural University, Shenyang 110016, China
[2] School of Economic & management, Shenyang Aerospace University, Shenyang 110136, China
{lfwei,zbmhh}@126.com, jianweiji7879@hotmail

Abstract. Frequent flyer is important part of gain in airline and airport, the struggle for which becomes increasingly prominent today. The frequent flyer churn will cause problems of increasing marketing costs and decreasing profits for civil aviation. After construction of passenger flying record data mining model, a kind of airline frequent flyer churn early warning model based on predictive value method was presented. The early warning data collection and cleaning system was also built to catch spending data of passengers to achieve the target of capture early warning passengers and reduce frequent flyer churn rate, so as to retain flyers to high-end under limited investment of resources.

Keywords: airline, frequent flyer, churn, early warning, predictive value.

1 Introduction

With the opening of China civil aviation, foreign airlines and domestic private airlines enter the domestic aviation market. These potential competitors bring heavy pressure on domestic airlines. Therefore, the airline will consider how to provide various services and preferential actions to attract travelers and how to expand consumer groups to gain more profit. Found from researches on traveler constitutes, we know that part of a small number of public service, business travelers often take flight, which occupies a high proportion in the airline transportation revenue. Such part of travelers is called frequent flyers [1-3]. The frequent flyer can improve proportion of high-end travelers in flight, and then to reduce pressure from cheap tickers, so that the airline can jump from cycle of vicious competition on prices. As same as other industries, the frequent flyer of airline also may be lost due to rivals and threat of substitute produces. They may select other airlines or other modes of transportation. Therefore, each airline has established their own customer relationship management system, so as to maintain quality of customer service level while reduce operating cost as much as possible, and the limited customer service resources for high-value customers [4, 5]. However, in the airline customer relationship management, the frequent flyer churn prediction has always been a weak point. From the view of traveler, the frequent flyer churn is a selection on rational consuming. Its occurrence has very clear causal relationship, which is always reflected in past flying record of frequent flyers. Some scholars determine whether the customer has churned with data

D. Jin and S. Lin (Eds.): Advances in Mechanical and Electronic Engineering, LNEE 176, pp. 9–14.
springerlink.com

mining technology, which is similar to subscriber churn early warning in telecommunication industry. For example, Mozer *et al* predicted customer churn probability in the next period of time with Logistic regression, decision tree and artificial neural network.

To address above problems, the paper determines predictive target of model based on screening prediction field with predictive value. The factors of predictive target, time span and others of model were determined. The frequent flyer churn early warning model as well as early warning data collection and cleaning system were established to periodically collect various traffic data of frequent flyer and access to early warning traveler and reduce churn rate of frequent flyer. The paper is organized as follows: section 2 gives early warning model structure based on data mining; section 3 introduces specific algorithm and early warning process; section 4 performs detail data analysis and section 5 concludes our work.

2 Research on Model

2.1 Model Structure

According to data mining on abroad record of frequent flyer, we presented a three-layer data mining model as shown in Fig. 1. The background is database system; forward provides experimental result and middle layer is for data processing.

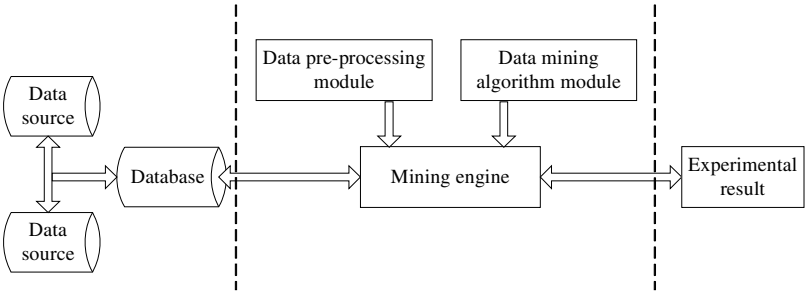

Fig. 1. Three-layer data mining model

2.2 Data Selection

In order to gain maximum return on investment, the data source in Fig. 1 was adjusted to frequent flyer. This part of travelers is made up of several parts:

(1) Standard frequent flyer. The number of 10,000km/line in continuous three months is greater than or equal to 1/6.
(2) VIP customers.
(3) The travelers whose number of 10,000km/line in continuous three months is greater than or equal to 1/6 are reserve forces of frequent flyers.

This data mainly comes from database in customer relationship management and that from investigation by relationship departments.

2.3 Data Pre-processing

In the real world, the database is vulnerable to interference from noise data, vacancy data and inconsistent data. These data may influence and even change results of data mining, resulting in invalid or wrong decisions. In addition, data mining is based on large amounts of data. Vacancy or inconsistent data often affect the efficiency of mining. Before data mining, the data preprocessing technology should be utilized to improve accuracy and performance of data mining model [6]. The data preprocessing method in the paper mainly includes data cleaning, data integration and data transformation.

The data and investigation result from relational database are merged into original mining data. Not all data meet the specifications. Only the records meet condition can be inputted into model, so the original mining data should be processed. The data to be cleaned includes vacant value or abnormal value and that are not frequent flyers. The existence of these data will affect efficiency and results of data mining process, so we should delete the data. After data cleaning, the data should be unified for the inconsistency of data format. After data cleaning and integration, the noise is eliminated and there is no inconsistent data, but there are still large amount of duplicate records. As the data seems chaotic and there is no worry, we need to perform data transformation to change data into appropriate mining model. With the method of clustering, the data is summarized [7].

2.4 Time Span Model

To obtain between frequent flyer retain effect, add transition period before prediction period. Smaller transition period means better model performance. However, the transition period also represents planning and implementation duration of activity. Longer transition means the marketers have more time to design effective frequent flyer remain activities. In the prediction of traveler churn, the marketers need at least one month for preparatory work. The model postpone prediction period to extend preparation time. In case of retain method and preferential conditions, the frequent flyer have not churned [8]. Meanwhile, The observation period was extent to 4 months to increase accumulative quality of prediction data, as shown in Fig. 2.

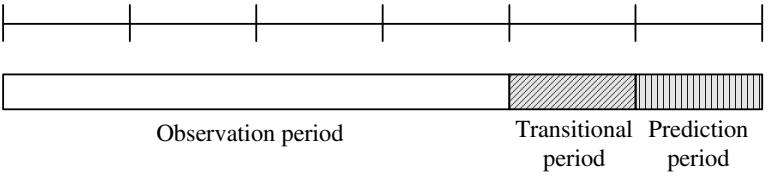

Fig. 2. Time-span model

The churn of frequent flyer can be divided into two types of hard loss and soft loss. The hard loss id churn in true meaning, but most travelers still take flight of this airline in the transition period, so we can take appropriate retention measures. Although the traveler has VIP card, they take small number of flight in the observation period.

3 Algorithm and Process Design

3.1 Algorithm Design

The specific steps of algorithm are as following:

Step 1: Set object set as U (i=1 to m); condition attribute set C (j= 1 to n) and decision attribute set as D.

Step 2: Determines membership function and linguistic variable value of each conditional attribute.

Step 3: For i=1 to m, the conditional attribute of object can be changed into the format:

$$A_j = F_{j1}^i / R_{j1} + F_{j2}^i / R_{j2} + \cdots + F_{jl}^i / R_{jl} . \tag{1}$$

Where, F_{jl}^i is object attribute value and R_{jl} is conditional attribute. Based on time span model, the R here takes 4 and A is mean under same condition.

Step 4: Compute each sub-predictive value $y_i^{'}$, where $y_i^{'} = F_{jl}^i - F_{jl}^i / A_j$.

Step 5: The y' is change amplitude of this index related to its own value in continuous two months. Then, the data is discretized and the boundary value is given in accordance with experiences.

Step 6: The linear method is used for analyzing response variable y and predictive variable $x_i (1 < i < n)$. It is simple linear form and is modeling of x_i on y, namely:

$$Y = W_0 + W_1 X_1 + W_2 X_2 + \cdots + W_i X_i . \tag{2}$$

Step 7: Obtain decision table and analyze the trend.

3.2 Process Design

Organize the data from 4 observation months into wide table data, using two strategies:

(a) As to state variable as flight number and purchase amount, take the data of last observation month.

(b) As to data as flight miles and investment rate of return: different traveler has different performance on some index. The mean of value in 4 observation months can represent value of users on this index recently. The churn of frequent flyer should be a trend in time sequence. Each traffic data inside it also has its own trend. Therefore, the trend of index can better reflect churn trend of travelers.

Set 4 observation values of some index as flight number as x_1, x_2, x_3 and x_4; the mean as M, so it should has 3 sub-predictive values. Discretize y_i as following:

$$y_i \in \begin{cases} 0(y_i^{'} < -0.2) \\ 1(-0.2 < y_i^{'} < 0.2) \\ 2(y_i^{'} > 0.2) \end{cases} . \tag{3}$$

Set 0.2 as threshold; 0 as downward trend and 2 as upward trend. The prediction value of 4 month is defined as:

$$y = y_1 + 3 \times y_2 + 9 \times y_3 \quad y \in [0,26]. \tag{4}$$

The determination of weight coefficient mainly bases on the following two considerations: the sub-predictive value y_i closet to observation has greater impact on overall predictive value. The mode of each sub-predictive value is 3, so the coefficient of single sub-trend is 1, 3 and 9 respectively.

Each prediction value y represents a trend, such as 25=1+3×2+9×2 indicates (unchanged, up, up). Finally, according to data in the predictive month, we can determine the predictive target of each record can be used as target value of model training.

4 Experimental Result

To ensure data in various churn state has considerable sample into model, in case of samples training, randomly select travelers to some extent from each class. The sampling data after processing is shown in Table 1.

Table 1. Sampling data

Predicted state	Overall number	Sampling number	Sampling proportion/%
0	134923	9463	7.01
1	543	291	53.59
2	93	49	52.69
3	7998	3946	49.34
4	616	305	49.51

Run the model, the confusion matrix to verify model is shown in Table 2.

Table 2. Confusion matrix

	0 prediction	1 prediction	2 prediction	3 prediction	All
0	5964	1683	1276	965	9888
1	800	1538	409	300	3047
2	1136	603	1505	705	3949
3	436	227	384	1057	2104
All	8336	4051	3574	3027	18988

The recall and precision are shown in Table 3.

Table 3. Recall and precision

	0 (prediction)	1 (prediction)	All
0	7498	1942	9440
1	1616	3243	4859
All	9114	5185	14299

The recall is 3243/5185=62.5% and precision is 3243/4859=66.7%.

5 Conclusion

To address the frequent flyer churn problem in civil aviation, the paper determined data source, time span and predictive target of early warning model combining with experiences on the basis of large amount of data. According to exploration, the model division was determined and data collection flow was also established. Based on the proposed data integration method of prediction value, the model indexes as recall and precision were given, which can provide assurance to future customer relationship management.

References

1. Tzokas, N., Sarge, M.: Building relationship platforms in consumer markets: A value chain approach. Journal of Strategic Marketing 5, 100–125 (1997)
2. Walter, A., Ritter, T., Gemunden, H.G.: Value creation in buyer-seller relationships. Industrial Marketing Management 7, 365–377 (2001)
3. Zikmund, W.G., McLeod, R., Gilbert, F.W.: Customer Relationship Management: Integrating Marketing Strategy and Information Technology, pp. 206–218. Wiley (2002)
4. Berry, L., Parasuraman, A.: Marketing Service: Competing through Quality, pp. 203–257. The Free Press (1991)
5. Schimittlein, D.C., Robert, A.P.: Customer base analysis: an industrial purchase process application. Marketing Science 13, 41–67 (1994)
6. Bitner, M.J., Stephen, W., Meuter, M.L.: Technology Infusion in Service Encounters. Journal of Academy of Marketing Science 28, 138–149 (2000)
7. Eugene, W., Anderson, C.: Foundations of the American Customer Satisfaction Index. Total Quality Management 11, 869–882 (2000)
8. Johnson, D., Grayson, K.: Cognitive and affective trust in service relationships. Journal of Business Research 58, 500–507 (2005)

The Design Analysis Based on Numerical Control Lathe Manipulator Dummy Prototype Engine

Hongpu Liu and Jianjun Ma

Henan Polytechnic Institute, Nanyang Henan, China
liuhongp@tom.com

Abstract. This article studied establishment flow concerning the numerical control lathe manipulator dummy specimen, the construction dummy specimen model, the applied analysis software has analyzed the manipulator stress and the collision to carry on mechanics analysis, has realized manipulator's dummy specimen platform through ADAMS, and realized the optimization to manipulator.

Keywords: Manipulator, Dummy specimen, Analysis, ADAMS, Model.

1 Establish Manipulator Dummy Specimen

1.1 The Establishment Flow of the Manipulator Dummy Specimen

(1) Construction model, the modeling contains three parts of work:①Foundation components: there are two ways to found each kind of simple movement Yuan components through the ADAMS/Wiew components storehouse;Introduces the complex CAD model with ADAMS/Exchange.② Model infliction restraint and movement;③The model exerts each kind of load.

(2) Test model.Definition survey, carries on the preliminary simulation to the model, through simulation result examination model in each components, binding force is whether correct.

(3) Verification model.Lead in the actual experiment test data, carries on the comparison with the hypothesized simulation result.

(4) Model refinement.After determining the model basic movement through the preliminary simulation, might join a more complex unit in the model, joined the friction in the pair of element, with the linear equation or the general equation definition control system, joined the flexible bridge piece and so on, caused the model and the real system is more approximate.

(5) Optimized model.Carry on the parameter analysis to the model, the optimized design.

(6) Custom-made the user's environment.The user may custom-made the menu, the dialog box, or cause many repetition work to carry on automatically using macro.

1.2 Constructs the Dummy Specimen Model

The step to construct manipulator dummy specimen as follows:

(1) CAD model which constructs in Pro/e, inspects each components unit whether unifies, the assembly rank only should have the level.

D. Jin and S. Lin (Eds.): Advances in Mechanical and Electronic Engineering, LNEE 176, pp. 15–20.
springerlink.com

(2) Leading in ADAMS2005 through MECHPro2005.
(3) Increase the restraint in ADAMS2005.
(4) Simulation the stress of fingernail clamp work piece, increase load.
(5) Increase actuation, utilizes the STEP function, according to work flow, establishment actuation.
(6) Selects the solution, establishes the solution step, solution.

1.3 Solved Question Which Constructs the Dummy Specimen

(1) Edition question. The reason: Pro/e and ADAMS use ADAMS2005+MECHPro2005+ Pro/E Wildfire3.0 to carry on design alternately.Finally: The Pro 3.0 construction model models need use 2.0 to open and to induct the ADAMS solution: duplicates readnewermodels.dil to /i486_nt/obj which is wildfire2's setup.

(2) Unit and restraint question.Unit: mmks, if uses other systems of units to be able to cause MECHPro2005 to be unable to induct the ADAMS2005.Restraint: In order to causes all components in ADAMS all to become single Part, assembles the level in pro/e only then the level, otherwise also can cause MECHPro2005 to induct not successfully.

(3) The function of step.Step function form is: step (x, x0, h0, x1, hl).STEP5's curve is smoother than the STEP, the light is suitable, as shown in Figure 1 is the STEP function application example.

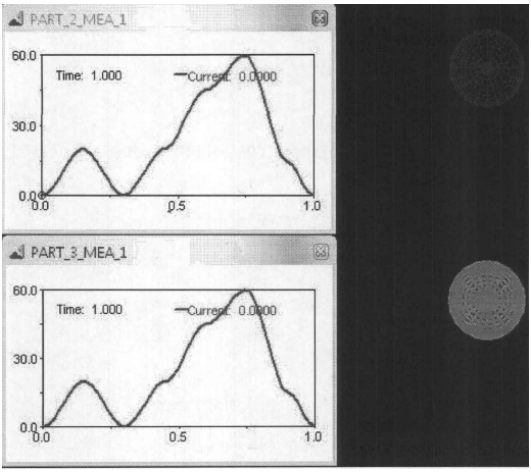

Fig. 1. STEP function's application example

2 The Analyze of Manipulator's Paw Collision

2.1 Constructs the Dummy Specimen Model

(1) When the definition materials behavior guaranteed has used the coordinated unit. the wrong unit not only decide the material response, moreover influence material contact rigidity.

(2) Choose the most appropriate material model from the model given, if cannot determine some Part's physics responds whether should contain some special characteristic, defines one kind to contain all possible characteristics material model is always the best.

(3) The initial contact does not allow between two contact faces, guarantees the model has not overlapped in the definition contact place. Always uses the real materials behavior and the shell thickness value, the contact face materials behavior and the geometry shape are used to decide the rigidity.

(4) Avoid the simple point load, they may cause the hourglass pattern easily. Since the hour glass unit can pass to the hour glass pattern of the neighboring unit, should avoid the application point load as far as possible.

(5) Does not permit on the restraint rigid body the node, all restraints must add in the rigid body center of mass (through the order that EnMp, RloID).

2.2 The Flow of Collision Analyzes

(1) CAD modeling, removes the nonessential characteristic;
(2) Grid division, definition material attribute, unit attribute;
(3) Found the rigid wall. The rigid wall mainly applies contact between the rigid body and the elastomer. In the very many contact question, a side of contacts all may simplify rigid body, like hit simulation between the automobile and the wall surface, the wall may process as the rigid body. The rigid wall definition mainly has two ways, uses key words *RIGIDWALL_GEOMETRIC_option and *RIGIDWALL_PLANAR_option separately in HYPERMESH defines;
(4) Definition initial velocity, edition solution parameter;
(5) Moves the LS_DYNA to solve and analyze;
(6) Process the examination result, as shown in Figure 2.

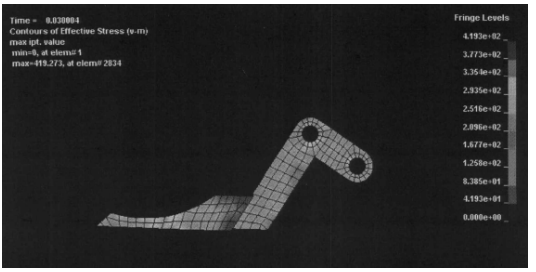

Fig. 2. Manipulator paw collision equivalent stress cloud chart

3 The Manipulator Designs and Analyzes

3.1 Manipulator Parameter Computation and the Analysis

Establish space joint connecting rod coordinate system, chooses the independent generalized coordinates to express relative motion between the rigid body. Takes the

big arm joint center of rotation as operation three-dimensional coordinate system zero point O, the connecting rod coordinate system which establishment as shown in Figure 3.

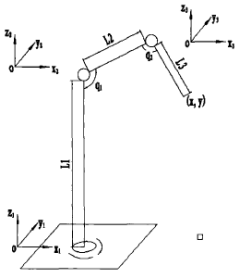

Fig. 3. Manipulator connecting rod coordinate system

3.2 The Manipulator Organization Optimization

Non-linearity restraint optimization question is optimized question that the objective function as the decision variable nonlinear function as well as the constraint condition for the decision variable equality or the inequality constitution. Considers the adjustable support determination angle restraint question. The adjustable support mainly is uses in connecting forearm and the arm, plays role which the support locates; Through the adjustment adjustable support length, in the adjustment between the arm and the forearm included angle, and determined the fingernail needs to install the angle. Because the different engine bed, the different work piece, the different orbital position, need the included angle is dissimilar; Through adjustable support, may increase manipulator's general performance greatly. The manipulator optimizes the process to be as follows:

(1) Carries on the three dimensional modeling using the CAD software;
(2) Establishment finite element model. Because the Optistruct optimization techniques is established based on the finite element analysis, therefore must establish this parameter flower the finite element model first before the optimization. Uses around the highly effective finite element processor HyperMesh to establish each kind of complex model's finite element model generally. Need carries on simplification processing to the geometry model, for instance nonessential bevel edge, immaterial eyelet and so on.
(3) Division grid, definition material and geometry characteristic;
(4) Infliction load and boundary condition;
(5) Establishment optimization parameter. Mainly is to define the design space of the topology optimization, defines its corresponding, the optimized restraint and the objective function;
(6) Carries on the solve of iteration, the examination density result and corresponding appropriate is surface chart like chart 4 and shown in Figure5.

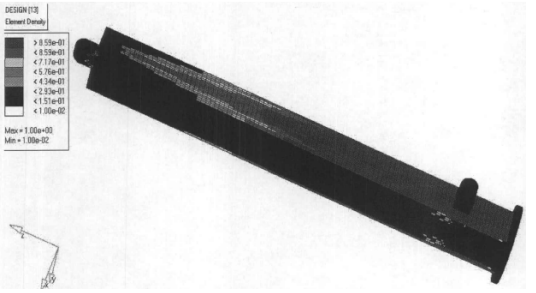

Fig. 4. Drawing of the density schematic after the manipulator foundation optimizes

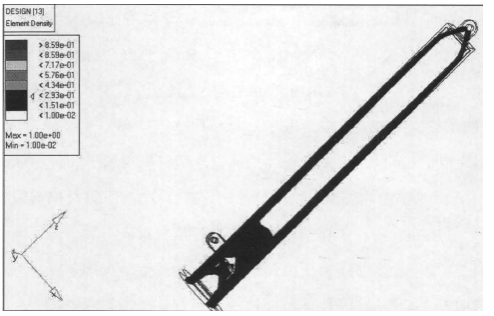

Fig. 5. The drawing of the density to be bigger than 0.2 schematic after the manipulator foundation optimizes

4 Conclusion

Clamps the scene using the CAD tool construction three-dimensional model and the build attire, has studied the dummy specimen technology and clamps manipulator's application in the attire. Realized the clamp manipulator's dummy specimen platform through ADAMS. Clamps the manipulator's structure reasonable, may utilize the appropriate analysis software to carry on mechanics analysis to manipulator, to realize optimization analysis of the manipulator.

References

1. Pingan, D.: Processing method of Structure finite element analysis shape. Machinery and Electronic (1), 26–27 (2000)
2. Chen, Z., Shi, X.: Three dimensional entity modeling and finite element analysis's relations. Electronic Mechanical Engineering 18(3), 21–22 (2002)
3. Chen, J.O., Cai, G.: The computer assistance project analyzes the ANsYS operating guide, 1st edn., pp. 135–156. Chinese Railroad Publishing company (2001)

4. Bobrow, J.E., Mcdonell, B.W.: Modeling identification and control of Pneulnatically actoated robot. In: Proceedings of the 1997 IEEE International Conference on Robotics and Automation, ICRA, Partl(of4), Albuquerque, April 20-25, pp. 124–127. IEEE, Plscataway (1997)
5. Zhang, Q.: The new numerical control engine bed attire clamps the manipulator design and the analysis, pp. 22–56. Jiangsu University (2010)
6. Zheng, H.T., Cai, Z., Peng, X.: Dummy specimen multi-disciplinary design optimization question modeling research group. Journal of System Simulation, 25–67 (2006)
7. Zhang, J.: General finite element procedure ANSYs in large-scale, complex building work applied research, pp. 25–50. Tongji University library (2001)
8. Fan, C.: The bear is bright, Zhou Mingfei. Dummy specimen software MSC. ADAMS application and enhancement, pp. 36–89. Mechanical industry publishing house (2006)
9. Zheng, J.: The .ADAMS- dummy specimen technology crosses the threshold with the enhancement, pp. 24–80. Mechanical industry publishing house (2002)
10. Zhou, C., Xiu, Zhang, J.: Project finite element and optimized analysis application example course, pp. 2–26. Scientific publishing house (2005)

6-DOF Robot Kinematics Analysis and PTP Motion Control Study Based on Matlab

Zhichao Zhao and Shengqi Sun

College of Information Engineering, Shenyang University, Shenyang 110044, China
sunshengqi@sina.com, 469986077@qq.com

Abstract. This paper takes a 6-DOF robot as research object to deal with the related problems such as kinematics and PTP motion control of the robot. A comprehensive consideration is also given in the research in terms of establishment of robot coordinate system, the coordinate transformation of D-H parameter, as well as the inverse problem solving of kinematics. Using Matlab tools to implement both the forward and inverse kinematic solutions for robot, the research performed modeling of the robot and PTP motion control simulation and achieved the accurate control for robot end effecter. In the research the method of parabola transition linear interpolation is applied to realize PTP motion control, resulting in greater smoothness of the joint's trajectory and convenience for speed and acceleration implementation for engineering practice.

Keywords: Robot, Kinematics, PTP motion control, parabolic transition interpolation.

1 Introduction

More and more people made research work on the robot kinematics and PTP motion control for 6-DOF robot. The kinematics is an important branch of robot technology, which is the basis for the control of the motion. Inverse kinematic solution is the key to realize the PTP motion control. Due to the motion analysis and movement simulation generally involving complicated mathematics. The paper uses MATLAB tools to complete the inverse kinematic solution of robot, and builds robot model to PTP movement control simulation. The method parabolic transition linear interpolation is applied to solve the problem of robot's PTP motion control, and also the paper compared the two group curve of motion trajectory and velocity, acceleration and concluded.

2 The Kinematics Simulation Model and Algorithm

2.1 The Mathematical Model of the Kinematics Analysis

6-DOF robot's arm can operate as a type of sports chain, consisting of connecting a series of connecting rods through the rotating joint, and the relative rotation of joints

D. Jin and S. Lin (Eds.): Advances in Mechanical and Electronic Engineering, LNEE 176, pp. 21–26.
springerlink.com

cause the movement of connecting rod. 6-DOF connecting rod coordinate system as shown in figure1.Use the link between homogeneous transformation matrixes (A_i) established the robot's kinematics equations (T).

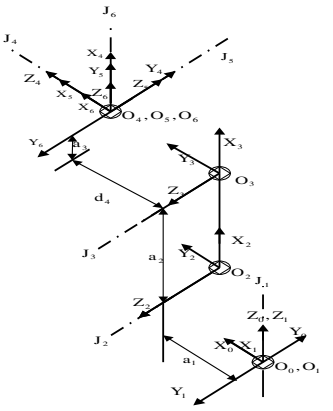

Fig. 1. 6-DOF of robot's connecting rod coordinate system

$$T = A_1 A_2 A_3 A_4 A_5 A_6 \tag{1}$$

$$\begin{aligned} A_i &= Trans(a_{i-1},0,0)Rot(X_{i-1},\alpha_{i-1})Trans(0,0,d_i)Rot(Z_i,\theta_i) \\ &= \begin{bmatrix} c\theta_i & -s\theta_i & 0 & a_{i-1} \\ s\theta_i c\alpha_{i-1} & c\theta_i c\alpha_{i-1} & -s\alpha_{i-1} & -d_i s\alpha_{i-1} \\ s\theta_i s\alpha_{i-1} & c\theta_i s\alpha_{i-1} & c\alpha_{i-1} & d_i c\alpha_{i-1} \\ 0 & 0 & 0 & 1 \end{bmatrix} \end{aligned} \tag{2}$$

In equation (2) : c representative cos functions; s representative sin function.

2.2 Positive Kinematics Issues

The positive kinematics issues are based on the robot's displacement of each joint and parameters of structure to obtain the every connecting rod's position and posture relative to base coordinate system. We can find out the N connecting rod's base coordinate transformation matrix (T_n) relative to base coordinate system.

$$T_n = A_1 A_2 A_3 A_4 A_5 A_6 = \begin{bmatrix} R_n & P_n \\ 0 & 1 \end{bmatrix} \tag{3}$$

In equation (3): R_n is n coordinate system for x, y, z axis's orientation cosine vector relative to base coordinate system; P_n is n coordinate system's origin's position vector of relative to the base coordinate system. If a point relative to the n coordinate system is S_n, is that the base coordinate system of relative position vector.

$$S_0^n = T_n S_n \tag{4}$$

So, robot kinematics issue is boiled down to the problem of homogeneous transformation matrix T_n.

2.3 Inverse Kinematics Issues

The problem of inverse kinematic is known as the position and posture of end effectors moved to the location of specified, work out joint variables of every connecting rod. For the solving method of 6-DOF robot's inverse kinematic problem is multiply A's matrix inverse on left of the movement equation T at both ends , and make the corresponding elements of the equal matrix on both ends are equal, can get the joint variables[2].

$$^{i-1}T_6 = A_i A_{i+1} .... ^5A_6 \tag{5}$$

3 Trajectory Planning and Movement Simulation

Robot's PTP movement problem is mainly the problem of inverse kinematic solution, defined as the posture of the robot's end device, using the method of robot's inverse kinematic solution to solve the angle of every joint's moved from the initial point to the end point, realizing the robot's PTP movement.

3.1 Construction of Robot's Model

The D-H parameters of 6-DOF robot are used to build robot's model with the help of Matlab-robotics toolbox[3].

Table 1. D-H parameters of 6-DOF robot

Joint(i)	θ_i /(°)	α_{i-1} /(°)	a_{i-1} / mm	d_i / mm	Range(o)
1	0	0	0	0	170~170
2	-90	-90	150	0	105~175
3	0	0	570	0	235~85
4	0	-90	150	650	180~180
5	0	90	0	0	40~220
6	0	-90	0	0	360~360

Through the execution of the program we can get the results of robot model and the slider controller. We can change the parameter variable of joint through driving each joint of the corresponding scroll bar instantly, and then the situation reflected in model can be changed intuitively.

3.2 Motion Simulation

In fact, PTP movement issue is an inverse kinematic solution; we can use the above mentioned and defined specific 'Robot' to realize the Robot's movements from initial pose *qA* to terminate pose *qB*. The motion to *qB* point of robot's 3D image as shown in figure2, and the joint's curve of position, velocity, and acceleration in the process of movement as shown in figure3.

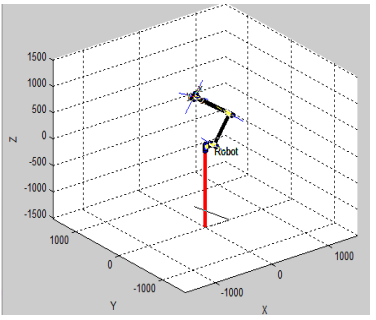

Fig. 2. The motion to point B of robot's 3D map

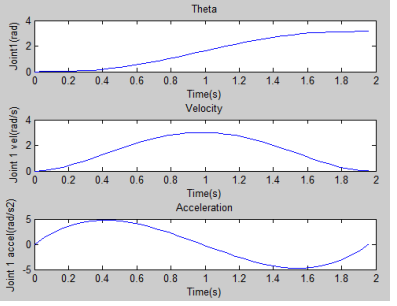

Fig. 3. Movement process of robot joint's position, speed and acceleration

Each joint of the corresponding graph shows that the change of joint's position, velocity, and acceleration in movement process is smooth, reduced the robot's vibration and impact effectively.

3.3 Parabolic Transition Linear Interpolation

The method of parabolic transition's linear interpolation includes the use of linear interpolation between period, and also parabolic transition at both ends. As shown in figure 4.

The need for solve is a transition point position of parabola and linear, and its path track of joint see formula (6):

$$q(t)=\begin{cases} q_0+\frac{1}{2}\ddot{q}t^2, & 0\le t<t_b \\ q_b+\ddot{q}t_b(t-t_b), & t_b\le t\le t_f-t_b \\ q_f+\frac{1}{2}\ddot{q}(t_f-t)^2, & t_f-t_b<t\le t_f \end{cases} \tag{6}$$

To one rotary joint, when $t_0=0$, $t_f=1s$, $q_0=0$, $q_f=\pi/4$, $\dot{q}_0=\dot{q}_f=0$, $\ddot{q}=4.5rad/s^2$, The move trajectory of parabolic transition linear interpolation as shown in figure 5.

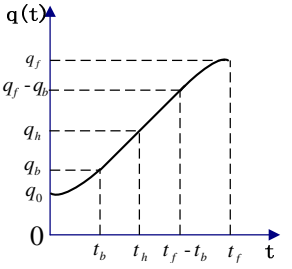

Fig. 4. Parabolic transition's linear interpolation

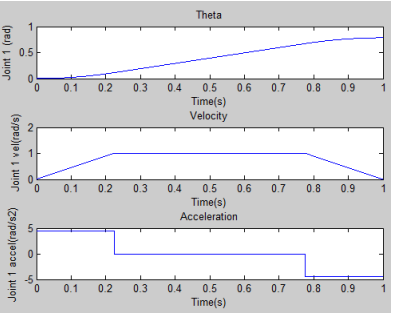

Fig. 5. Joint's position, speed and acceleration of parabolic transition linear interpolation

We can find that the moving trajectory of parabolic transition linear interpolation is smoother, and both the speed and acceleration are easy to be realized from the speed and acceleration of path curve in figure 5. Speed curve is a trapezoidal curve, consists of three stages of acceleration, constant speed and slows down, and three stages are all linear.

4 Conclusion

With the MATLAB tools we can conduct simulation modeling of robot, which realizes the robot's PTP smooth movement, and we can use the slider interface to arbitrarily control of the robot joints change, which visually express that the position and pose of the whole movement process, the information improves the spatial trajectory planning maneuverability and visibility. With help of matlab we can draw robot joint's curve of position, velocity, acceleration and robot joint's curve of position, velocity, and acceleration with parabolic transition linear interpolation. Contrasted with the two curves, we found that the trajectory of parabolic transition into linear movement was smooth, and speed curve consists of accelerating, constant speed, slow and the three stages constitute a trapezoid curve, the acceleration of three horizontal structures, this control strategy in engineering is easier to implement, and also make robots point-to-point trajectory easier to control. This method can also be applied to path tracking trajectory planning.

References

1. Craig, J.J.: Introduction to Robotics, pp. 14–99. Mechanical industry press, M. Bei Jing (2006)
2. Li, Q., Liu, J.: 6-DOF industrial robot kinematics analysis and simulation. J. Mechanical and Electrical Engineering Technology 11, 56–60 (2008)
3. Corke, P.: A Robotics Toolbox for MATLAB. J. IEEE Robotics and Automation Magazine 1, 24–32 (1996)
4. Xie, B., Cai, Z.: Robotics simulation experiment teaching based on MATLAB Robotics Toolbox. J. Computer Education 19, 19–22 (2010)
5. Sun, Z.: Robot system simulation and application. J. System Simulation Academic Journal 3, 23–29 (1995)
6. Tan, M., Xu, D., Hou, Z., et al.: Advanced robot control, pp. 90–107. Higher education press, M. Beijing (2007)
7. Wang, H., Gu, Z., Liu, B.: A kind of mobile robot movement control methods study. J. The Modern Electronic Technology 22 (2007)
8. Zeng, J., Lin, Y., Liao, X.: 6R type spraying robot's kinematics analysis and simulation. J. Mechanical Design and Manufacturing 6 (2010)

Real-Time Motion Estimation of Mobile Robots Based on Electronic Images

Xiaoming Dong* and Benyue Su

School of Computer & Information, Anqing Teachers College
Linghu South road 128, Anqing, anhui province, China
Xiaoming.dong@ ia.ac.cn, bysu@aqtc.edu.cn

Abstract. A new method based on multi-cues fusion of electronic images is proposed to achieve the task of robots estimation in this paper. The method has a premise that the robot is moving on locally planar ground, which is reasonable in indoor environments. To meet the acquirement of real-time and accurateness, the proposed method integrates KLT and SIFT features of electronic digital images to achieve mobile robots speed estimation effectively and accurately. Experiments show the effectiveness and robustness of this method in various environments.

Keywords: Mobile robot, multi-cues fusion, Visual odometry.

1 Introduction

Mobile robots self-localization and position tracking is one of the most important tasks in various applications. A common way to implement this task is so called dead-recking, which estimates the speed and direction of mobile robots according to inertial sensors. This method is difficult to resolve the problem of robot's wheel slipping, so the accumulated errors impact the estimation accuracy greatly [1-4]. GPS is another commonly used technique to resolve this problem. However, GPS can't be used in some conditions such as indoor environments, and it cannot achieve the high accuracy required by various applications. Visual sensor based on electronic digital images has long been used to estimate the ego-motion of mobile robots. The technical is so called visual odometry and it is a promising technique for the mobile robots to estimate its ego-motion. Extensive research has been done to make use of visual odometry in practice, Several methods have been proposed based on monocular image sequences or stereo image sequences; however, there are still many difficulties in estimating the robots motion effectively because of the inaccurate feature matching and outliers between electronic images. The aim of this paper is to develop a method that utilizing multi-cues fusion to improve the effect of visual odometry. For the object of the real-time and accurate estimation, the proposed method is applied to the indoor environment, which assumes that the robot is travelling in flat floor.

* This work is supported by the natural science project of Anhui Provincial Education Department under Grant No.KJ2012B090, KJ2009A123 and KJ2011B086.

D. Jin and S. Lin (Eds.): Advances in Mechanical and Electronic Engineering, LNEE 176, pp. 27–31.
springerlink.com

The paper is organized as follows. In section 2, we analysis the way of the features selection and multi-cues fusion; outlier occlusion and motion estimation is discussed in Section 3, the method is verified in experiments. The conclusions are given in section 4.

2 Feature Fuse and Motion Estimation

The primary idea in visual odometry is to implement the motion estimation based on the feature correspondence between digital images. So the feature selection is the key problem. Based on the compares of the different features [5-10], we found that KLT and SIFT is more prominent than other features. KLT is quick to be obtained but it is easy to be impacted by light and angle change, meanwhile, SIFT can present a satisfactory result but the computation and feature matching is high time consuming. So the fuse of KLT and SIFT to implement the visual odometry is a good solution, the following part give the detailed description of the KLT and SIFT and feature fuse respectively.

Two steps are applied to reject outliers. Firstly, an initial estimate of the homography matrix H is obtained by the RANSAC algorithm, secondly escaping the unmatched features according to the homography matrix H. the process to resolve the homography matrix according to the correspondent features is described as follows:

Assumed the correspondent features are $P_i(x_i, y_i)(i = 1, ..., 5)$, and then we can compute $\mathbf{H}$ as follows.

P_i And V_i satisfy:

$$k\begin{bmatrix} u_i \\ v_i \\ 1 \end{bmatrix} = \mathbf{H}\bullet\begin{bmatrix} x_i \\ y_i \\ 1 \end{bmatrix}, \quad \mathbf{H} = \begin{bmatrix} m_1 & m_2 & m_3 \\ m_4 & m_5 & m_6 \\ m_7 & m_8 & m_9 \end{bmatrix} \tag{1}$$

Eliminating k from (1), we can get two equations. Combine these two equations, we get:

$$\mathbf{K}\bullet\mathbf{M} = m_9 \bullet \mathbf{U} \tag{2}$$

Where $\mathbf{K}$, $\mathbf{M}$ and $\mathbf{U}$ are defined as follows $(i = 1, ..., 5)$:

$$\mathbf{K} = \begin{bmatrix} x_i & y_i & 1 & 0 & 0 & 0 & -x_i u_i & -y_i u_i \\ 0 & 0 & 0 & x_i & y_i & 1 & -x_i v_i & -y_i v_i \\ & & & & \cdots & & & \\ & & & & \cdots & & & \end{bmatrix} \tag{3}$$

$$\mathbf{M} = (\mathbf{K}^T\mathbf{K})^{-1}\mathbf{K}^T\mathbf{U} \tag{4}$$

Fig. 1 shows the correspondences of the vertices in a book, we compute the homography matrix of the correspondent feature and project the vertices in the last frame to the current frame. The result shows that the vertices between two frames are very clear, the result is satisfactory.

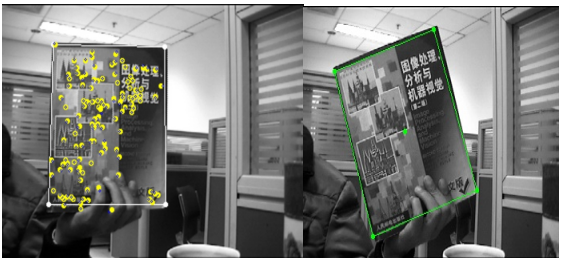

Fig. 1. The correspondence between the vertices according to the homography matrix

When the two images are consecutive, the relative motion will be very small; we can obtain the motion speed according to the correspondences of the features in images. Based on the assumption of the planar ground [10-13], we can calculate the world coordinate according to the coordinate in the image according to equ (5) :

$$s\begin{bmatrix} X \\ Y \\ 1 \end{bmatrix} = \mathbf{m}^{-1}\begin{bmatrix} u \\ v \\ 1 \end{bmatrix} \tag{5}$$

The process can be concluded as follows:

1) Capturing the current frame of the video and rectifying it to remove the distortion.
2) Finding the correspondent features in the current frame according to the features in the last frame
3) Computing the correspondent world coordinate of the feature point in the image
4) Inferring the motion parameter according to distance of the world coordinate correspondent to the two images.
5) Capturing the next frame and repeat this process

3 Experiments and Analysis

Various experiments have been carried out in the robot shown in the left of fig 2. The camera is precisely calibrated beforehand and is mounted on the center of the robot fixedly. Actually, the camera motion does not equal to the robot motion as the camera is not placed at the robot's center of rotation. The calibration parameter is shown in table 1. Assumed that camera is not subject to large vibrations when the robot moves on the ground.

Table 1. Intrinsic Camera Parameters

		Left camera	Right camera
The number of image		14	14
kx	result	569.27172	567.35791
	variance	2.54858	2.18107
ky	result	567.21057	568.58273
	variance	2.66821	2.97379
u0	result	230.77377	231.12314
	variance	2.22473	2.86419
v0	result	182.17209	178.77224
	variance	2.26684	2.37972

The experiment shows that the measured angle rotation is 83.6° based on our visual odometry but the real rotation angle is about 90°, the visual odometry is computed based on 200 frames in this experiment. It is worth mentioning, since the measured angles and distances are processed by hand, so the errors due to human inaccuracy are also considered. However, the precision of the proposed method is satisfactory for the estimation of robots moving speed.

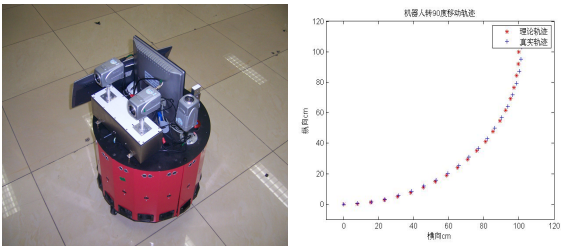

Fig. 2. The left of the figure is the robot and the right of figure is the the measurement of the rotation angle based on visual odometry

4 Conclusions and Future Work

In the problem of the mobile robots speed estimation, Traditional sensor based on inertial sensors is easy to be impacted by the wheel slipping, so the accumulated error is difficult to be resolved. Meanwhile, Vision sensor has advantages that it can

provide larger amount of information and can't be affected by the wheel slipping. In this paper, a visual odometry method utilizing multi-cues fusion of electronic images is proposed to estimate the robot motion. The experiment shows that it can achieve more accurate result than traditional odometry.

Visual odometry has its shortcoming because the features extracted by the electronic digital image could be affected by the environment, so the robustness in complex environment may not be satisfactory. Future work will consider more about the robustness of the Visual odometry and a possible way to resolve this problem maybe the combination of the traditional sensor and the Visual odometry. Some filter algorithm based on probabilistic would be applied to it and that is the promising direction of the research.

References

1. Levin, A., Szeliski, R.: Visual odometry and map correlation. In: CVPR 2004, vol. 1, pp. 611–618 (2004)
2. Nistér, D., Naroditsky, O., Bergen, J.: Visual odometry for ground vehicle applications. Journal of Field Robotics 23(1), 3–20 (2006)
3. Helmick, D.M., Chang, Y., Roumeliotis, S.I., Clouse, D., Matthies, L.: Path Following using Visual Odometry for a Mars Rover in High-Slip Environments. In: Proc. 2004 IEEE Aerospace Conference, Big Sky, MT, March 6-13 (2004)
4. Olson, C.F., Matthies, L.H., Schoppers, M., Rover, M.W.: Navigation using stereo ego-motion. Maimone in Robotics and Autonomous Systems 43(4), 215–229 (2003)
5. Cumani, A., Guiducci, A.: Comparison of feature detectors for rover navigation. Mathematical Modelling and Applied Computing (1) (2010)
6. Ascani, A., Frontoni, E., Mancini, A.: Feature group matching for appearance-based localization. In: IROS (2008)
7. Shi, J., Tomasi, C.: Good features to track. In: IEEE Computer Society Conf. on Computer Vision and Pattern Recognition, Seattle, Washington, USA, pp. 593–600 (June 1994)
8. Campbell, J., Sukthankar, R., Nourbakhsh, I.: Techniques for Evaluating Optical Flow in Extreme Terrain. In: Proceedings of IROS (2004)
9. Birchfield, S.: KLT: Kanade-Lucas-Tomasi feature tracker (August 2007), `http://www.ces.clemson.edu/stb/klt/installation.html`
10. Lowe, D.G.: Distinctive image features from scale invariant keypoints. International Journal of Computer Vision 60(2), 91–110 (2004)
11. Torr, P.H.S., Fitzgibbon, A., Zisserman, A.: The Problem of Degeneracy in Structure and Motion Recovery from Uncalibrated Image Sequences. International Journal of Computer Vision 32(1), 27–45 (1999)
12. Azarbayejani, A., Pentland, A.P.: Recursive estimation of motion, structure, and focal length. IEEE Transactions on Pattern Analysis and Machine Intelligence 17(6), 562–575 (1995)
13. Alon, J., Sclaroff, S.: Recursive estimation of motion and planar structure. In: IEEE Computer Vision and Pattern Recognition, pages II, pp. 550–556 (2000)

Visual Modeling Method and Analysis of Geometric Characteristic for Triangular Helical Structure in Mechanical Engineering

Jing Song, Guohua Cao, Yongguang Cao, and Ronghua Wu

School of Mechatronic and Engineering, China University of Mining and Technology, 221116 Xuzhou, China
songjing2008long@163.com

Abstract. Triangular helix structure gets general application in the field of mechanical engineering and it has a great meaning to study it. In this paper, modeling method and geometric characteristics of triangular helix structure are investigated, and parameter equations of central trajectories are deduced based on the structure analysis of the straight triangle structure. 3D model of triangular helix structure is depicted by the Pro/E Wildfire software. And by comparison of geometric characteristics from round and triangular helix structures, geometric characteristics of twisting angle, curvature and torsion for single helical structure are analyzed. This paper lays a foundation for further research on triangular helix structure in mechanical engineering.

Keywords: Triangular helix structure, Visual Modeling Method, 3D model, Geometric characteristic.

1 Introduction

Triangular helical structures of mechanical engineering such as ropes or cables were widely used in the fields of mine, bridge, power and communication. And these structures are important to guarantee the safety and reliability of above fields. Triangular helical structures have advantages in larger contact area, better wear resistance and higher breaking force compared with the round structure [1]. For the above reasons, modeling and analysis of geometry features for triangular helical structure are necessary to investigate. But due to complexity of triangular helical structure, it has not been widely investigated. On the contrary, the round helical structure had been widely studied by a lot of scholars: Xia et al obtained modeling method for the round structure [2]; Hobbs et al investigated curvature and relative motion characters of helical units close to head sheave [3-4]; Wang et al analyzed characteristics of curvature and torsion for double helical unites [5]; Cao et al studied geometry features of double helical unites under the load [6]. In this paper, parameter equations of central trajectories were deduced based on the structure analysis of the structure. Solid model was depicted by the Pro/E Wildfire software, and geometric characteristics of triangular helix structure were investigated. This research lays a foundation for investigating the characteristics of geometrics and

D. Jin and S. Lin (Eds.): Advances in Mechanical and Electronic Engineering, LNEE 176, pp. 33–40.
springerlink.com

mechanics of triangular structure under load or temperature effect which are very useful in mechanical engineering.

2 Visual Modeling for Triangular Helical Structure

2.1 Geometric Parameters of Structure Core

In mechanical engineering, the kinds of core of triangular helix structure mainly includes 1×3, 1×6 and 3×2+3 etc. And in this paper, the 12+9+1×6 single helical triangle structure was taken as research object which was parallel laid structure. δ_0 and δ_i are respectively diameters of the central and ith layer; t is the lay pitch of the structure. The coordinates of pointes A_0, B_0 and C_0 in Fig. 1 could be defined as $(\bar{x}_1, \bar{y}_1)$, $(\bar{x}_2, \bar{y}_2)$ and $(\bar{x}_3, \bar{y}_3)$.

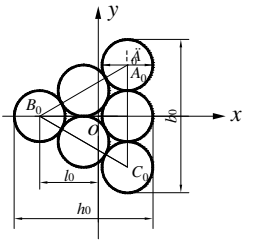

Fig. 1. Section of struture core

According to literature [7], scalars of l_0, b_0 and h_0 could be expressed as

$$l_0 = 1.155\delta_0, b_0 = 3\delta_0, h_0 = 2.732\delta_0, \tag{1}$$

where l_0, b_0 and h_0 are respectively component's eccentricity on the sharp edge, width and length of strand core.

2.2 Structure Analysis of the Helical Structure

Initial Angles of Arc or Straight Segments' Endpoints. As Fig. 2 showed that central trajectories of both internal and external of the helical structure were composed of 3 arc and 3 straight segments, where J_i and K_i are respectively any points on arc segment $\overset{\frown}{A_iB_i}$ and line A_iF_i of ith layer. Central angle of arc segment was 120°and arc center was the component's center on the sharp edge of the structure core. Scalars r_i and d_i are respectively arc radius and the distance between origin o and straight segment for ith layer, which could be deduced easily.

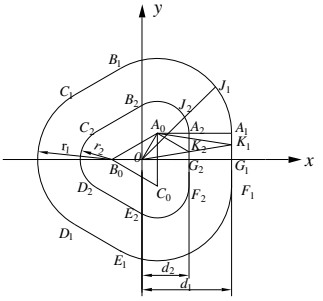

Fig. 2. Central trajectories of section of straight triangle structure

According to Fig. 2, the initial angle of endpoint A_i on the line A_iF_i could be derived as

$$\angle A_iOG_i = \arctan\left(A_iG_i/OG_i\right) = \arctan\left(\delta_0/d_i\right). \tag{2}$$

According to Eq. 2, initial angles of $\angle B_iOG_i$, $\angle C_iOG_i$, $\angle D_iOG_i$, $\angle E_iOG_i$ and $\angle F_iOG_i$ could be respectively expressed as $2\pi/3-\angle A_iOG_i$, $2\pi/3+\angle A_iOG_i$, $4\pi/3-\angle A_iOG_i$, $4\pi/3+\angle A_iOG_i$ and $2\pi-\angle A_iOG_i$.

Parameter Equations of Central Trajectories. Because helical structure was parallel laid and moved at a constant speed on z-axis during twisted, parameter equation of the structure along z-axis could be expressed as

$$z=t\theta/2\pi, \tag{3}$$

where θ is the rotation angle of component in the *xoy* plane.

In the Fig. 2, line A_iF_i's parameter equation could be deduced as

$$\begin{cases} x_i=OK_i\cos\theta=d_i\left(2k\pi\le\theta<\angle A_iOG_i+2k\pi,\angle F_iOG_i+2k\pi\le\theta\le2\pi+2k\pi\right) \\ y_i=OK_i\sin\theta=d_i\tan\theta\left(2k\pi\le\theta<\angle A_iOG_i+2k\pi,\angle F_iOG_i+2k\pi\le\theta\le2\pi+2k\pi\right) \end{cases}. \tag{4}$$

In the triangle ΔA_iOK_i and $\Delta A_iA_0K_i$, based on sine theorem, the angle $\angle K_iA_0A_i$ could be derived as $\angle K_iA_0A_i=\theta-\arcsin\left[l_0\sin(\pi/3-\theta)/r_i\right]$. And so parameter equation of arc $\overset{\frown}{A_iB_i}$ could be deduced as

$$\begin{cases} x_i=\overline{x}_1+r_i\cos\left\{\theta-\arcsin\left[l_0\sin(\pi/3-\theta)/r_i\right]\right\}\left(\angle A_iOG_i+2k\pi\le\theta<\angle B_iOG_i+2k\pi\right) \\ y_i=\overline{y}_1+r_i\sin\left\{\theta-\arcsin\left[l_0\sin(\pi/3-\theta)/r_i\right]\right\}\left(\angle A_iOG_i+2k\pi\le\theta<\angle B_iOG_i+2k\pi\right) \end{cases}. \tag{5}$$

According to solution methods of Eq. 4 and Eq. 5, parameter equations of remaining arc and straight segments could be expressed as follows

$$x_i=\begin{cases} d_i\cos\theta/\cos(2\pi/3-\theta)\left(\angle B_iOG_i+2k\pi\le\theta<\angle C_iOG_i+2k\pi\right)\\ \bar{x}_2+r_i\cos\left\{\theta-\arcsin\left[l_0\sin(\pi-\theta)/r_i\right]\right\}\left(\angle C_iOG_i+2k\pi\le\theta<\angle D_iOG_i+2k\pi\right)\\ d_i\cos\theta/\cos(4\pi/3-\theta)\left(\angle D_iOG_i+2k\pi\le\theta<\angle E_iOG_i+2k\pi\right)\\ \bar{x}_3+r_i\cos\left\{\theta-\arcsin\left[l_0\sin(5\pi/3-\theta)/r_i\right]\right\}\left(\angle E_iOG_i+2k\pi\le\theta<\angle F_iOG_i+2k\pi\right)\end{cases}, \quad (6)$$

$$y_i=\begin{cases} d_i\sin\theta/\cos(2\pi/3-\theta)\left(\angle B_iOG_i+2k\pi\le\theta<\angle C_iOG_i+2k\pi\right)\\ \bar{y}_2+r_i\sin\left\{\theta-\arcsin\left[l_0\sin(\pi-\theta)/r_i\right]\right\}\left(\angle C_iOG_i+2k\pi\le\theta<\angle D_iOG_i+2k\pi\right)\\ d_i\sin\theta/\cos(4\pi/3-\theta)\left(\angle D_iOG_i+2k\pi\le\theta<\angle E_iOG_i+2k\pi\right)\\ \bar{y}_3+r_i\sin\left\{\theta-\arcsin\left[l_0\sin(5\pi/3-\theta)/r_i\right]\right\}\left(\angle E_iOG_i+2k\pi\le\theta<\angle F_iOG_i+2k\pi\right)\end{cases}. \quad (7)$$

Initial Angle of Component. In *1*th layer, initial angles of 2_1, 4_1, 6_1, 8_1, $10_1$and 12_1 components were respectively π/3, 2π/3, π, 4π/3, 5π/3, and 0.

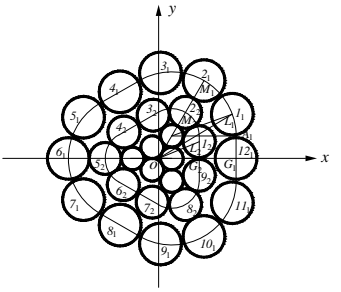

Fig. 3. Section of straight triangle structure

According to literature [7], the gap between components of *i*th layer was $0.03\delta_i$. Taking 1_1 and 12_1 components as examples, the length of arc $\widehat{L_1A_1}$ was $r_1\sin\varphi=1.03\delta_1-\delta_0$, where φ is central angle of arc $\widehat{L_1A_1}$, so we could get $\varphi=\arcsin\left[(1.03\delta_1-\delta_0)/r_1\right]$.

The central coordinate value of component 1_1 which could be obtained using the expression of φ angle was defined as (x_1', y_1'), therefore, the initial angle of component $1_1$was expressed as

$$\angle L_1OG_1=\arctan\left(x_1'/y_1'\right). \quad (8)$$

Using equation $\angle M_1OL_1 = \pi/3 - \angle L_1OG_1$, initial angles of 3_1, 5_1, 7_1, $9_1$and 11_1components were respectively $\pi/3 + \angle M_1OL_1$, $\pi - \angle M_1OL_1$, $\pi + \angle M_1OL_1$, $5\pi/3 - \angle M_1OL_1$ and $5\pi/3 + \angle M_1OL_1$.

According to Fig. 3, initial angles of 2_2, 5_2 and 8_2 components were respectively $\pi/3$, π and $5\pi/3$. And the initial angle of component 1 could be expressed as

$$\angle L_2OG_2 = \arctan\left(L_2G_2/OG_2\right) = 1.03\delta_2/\left(2d_2\right). \tag{9}$$

Based on expression $\angle M_2OL_2 = \pi/3 - \angle L_2OG_2$, initial angles of 3_2, 4_2 ,6_2, 7_2 and 9_2components were respectively $\pi/3 + \angle M_2OL_2$, $\pi - \angle M_2OL_2$, $\pi + \angle M_2OL_2$, $5\pi/3 - \angle M_2OL_2$ and $5\pi/3 + \angle M_2OL_2$.

2.3 Visual Modeling of the Helical Structure

Parameters of the Triangular Helical Structure. According to literature [7], the diameters ratio of δ, δ_1 and δ_0 was $1:0.767:0.543$, and t was the lay pitch of the structure. In this paper, values of δ_0, δ_2, δ_1 and t were respectively 1.6mm, 2.258mm, 2.944mm and 73mm. According to the above analysis, IBL files containing coordinates of all components could be generated in the MATLAB software.

3D Structure Modeling. The 3D model of the helical structure could be depicted by the Pro/E Wildfire software as the following mainly processes: 1. building a new PRT file; 2. clicking “insert a spline ”, and then selecting “from the file ”; 3. introducing into IBL file and then a new spatial spline built in the window; 4. generating solid mold by the means of “variable section sweep”.

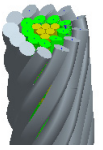

Fig. 4. 3D model of triangular helical structure

3 Analysis of Geometry Characteristics

According to basic theory of mechanical engineering, geometry characteristics are related to mechanical characteristics, so it’s important to investigate geometry characteristics. Through the comparison of the triangular and equivalent round structure, definite geometry characteristics of the triangular structure could be got. Equivalent dimensions of r_1 and r_2 are 6.058mm and 3.457mm, where r_i is the trajectory radius of ith layer in xoy plane for equivalent round structure.

3.1 Characteristic Analysis of Twisting Angle

According to definition of twisting angle, the expression of it could be deduced as

$$\beta = \arctan\left(\sqrt{\dot{x}^2 + \dot{y}^2}\,/\,\dot{z}\right). \tag{10}$$

The twisting angle influenced by rotational angle increment are shown in Fig.5, in which β_i is the twisting angle of ith layer.

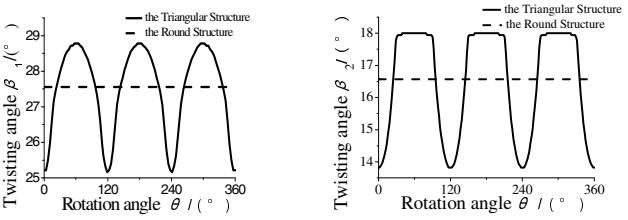

(a) (b)

Fig. 5. Twisting angles of round and straight triangular structures

According to Fig. 5, twisting angle of inside and outside of triangular helix structure varied with rotation angles of 120 degree periodically, while it was constant value for round strand; the outside twisting angle of triangular helix strand was greater than the inside, and so round strand.

3.2 Characteristic Analysis of Curvature and Torsion

According to literature [6], formulas of curvature and torsion at unload could be respectively expressed as

$$\kappa = \{(\dot{x}\ddot{y} - \ddot{x}\dot{y})^2 + (\dot{y}\ddot{z} - \ddot{y}\dot{z})^2 + (\dot{z}\ddot{x} - \ddot{z}\dot{x})^2\}^{1/2} / (\dot{x}^2 + \dot{y}^2 + \dot{z}^2)^{3/2}, \tag{11}$$

$$\tau = \begin{vmatrix} \dot{x} & \dot{y} & \dot{z} \\ \ddot{x} & \ddot{y} & \ddot{z} \\ \dddot{x} & \dddot{y} & \dddot{z} \end{vmatrix} \Big/ \left[(\dot{x}\ddot{y} - \ddot{x}\dot{y})^2 + (\dot{y}\ddot{z} - \ddot{y}\dot{z})^2 + (\dot{z}\ddot{x} - \ddot{z}\dot{x})^2\right], \tag{12}$$

where k and τ are respectively curvature and torsion.

Based on Eq. 11 and Eq. 12, curvature and torsion of round or triangular structure was respectively showed in Figure.6 and Figure.7, in which k_i and τ_i are the curvature and torsion of ith layer respectively.

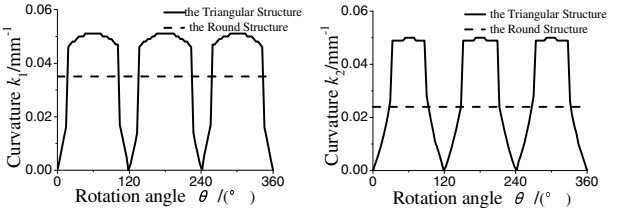

(a) (b)

Fig. 6. Curvature of round and straight triangular structures

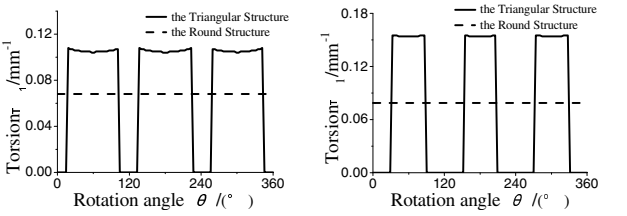

(a) (b)

Fig. 7. Torsion of round and straight triangular structures

According to Fig. 6, curvature of inside or outside of triangular helix structure varied with rotation angles of 120 degree periodically and it was greater on arc segments than on the straight, while constant value for round structure.

According to Fig. 7, torsion of inside or outside of triangular helix structure varied with rotation angles of 120 degree periodically, especially approach to zero on arc segments for non-distorted; but it was constant value for round structure.

4 Conclusions

In this paper, the triangular helical structure which is a kind of important mechanical equipment in mechanical engineering is systematically investigated. Based on the above analysis, some conclusions are obtained and summarized as follows:

1. Based on the structure analysis of the single helix triangular structure, a theoretic model of the triangular helical structure is proposed to investigate parameter equations of central trajectories. According to IBL files of components generated by the MATLAB software, the visual 3D model of the triangular helical structure is depicted by the Pro/E Wildfire software.

2. For further evaluating the geometrical characteristics, the round model of the single helical structure is established by comparison. The results indicate that: twisting angle, curvature and torsion of triangle structure vary with rotation angles of 120 degree periodically, while constant values for the round; twisting angle of external

layer is greater than the internal both for the triangular and round structures; curvature and torsion of arc segments are greater than straight line segments, while torsion of straight line segments is approximate zero.

3. Visual 3D model and geometrical characteristics are investigated, which are useful to compile a general program for designing complicated helical structures and investigate the characteristics of geometrics and mechanics of triangular structure under load or temperature effect in future. And this paper promotes the development of basic theory of mechanical engineering.

Acknowledgments. This research is sponsored by the "National Science Foundation for Young Scientists of China" (51005233), the "Technology Research Directional Plan Project for Technology Research of China National Coal Association"(MTKJ2011-299).

References

1. Wen, L., Guo, Z.L., Liu, X.T.: Development of Triangle Strand Wire Rope for Main Cable of Cable Crane. Steel Wire Products 32(6), 5–6 (2006)
2. Xia, Q.P., Shi, D.W.: Modeling of the Wire Rope Based on MATLAB and Pro/E. Mechanical Engineer (9), 69–70 (2010)
3. Hobbs, R.E., Nabijou, S.: Changes in Wire Curvature As a Wire Rope Is Bent over a Sheave. Journal of Strain Analysis for Engineering Design 30(4), 271–281 (1995)
4. Nabijou, S., Hobbs, R.E.: Relative Movements within Wire Ropes Bent over Sheaves. Journal of Strain Analysis for Engineering Design 30(2), 155–165 (1995)
5. Wang, R.C., Mckewan, W.M.: A Model for the Structure of Round-Strand Wire Ropes. OIPEEC Bulletin (81), 15–42 (2001)
6. Cao, G.H., Zhu, Z.C., Peng, W.H., Chen, G.A.: Variations of Curvature, Torsion and Stress of Double Helix Wire in 6×7+IWS Wire. Journal of Mechanical Strength 31(3), 491–496 (2009)
7. Pan, Z.Y., Qiu, H.M.: Production Technology of Steel Wire Rope. Hunan University's Publishing House, China (2008)

Particle Mechanical Vibration Analysis on the Basis of Matlab

Ming Hu and Suiyuan Li

Jiaozuo Teachers College, Henan Province 454000, China
zcactus03@126.com

Abstract. By adopting the means of Matlab digital analogy, this article has analyzed the synthesis of particle mechanical vibrating under single-degree-of-freedom system, and researched the new analysis method of mechanical engineering. Through the study, some problems have been found, which will be helpful for mechanical engineering in the future.

Keywords: Matlab, particle dynamics, mechanical engineering.

1 Introduction

Computer numerical simulation research method has become a significant research means after experimental study and theoretical analysis, it is widely applied in physics and mechanical engineering application. MATLAB software has strong computing and mapping functions as an important tool for scientific and technical personnel to undertake scientific research and mechanical engineering calculation. Applying this software to experimental data processing can reduce computing workload and obtain accurate fitting curve. Matlab has become the most popular software tool in mechanical engineering, it can be used for the solution of specific discipline. Matlab is characterized by extensibility, easiness to learn and use, high efficiency;

2 Simulation of Mechanical Vibration Synthesis by Means of Matlab

Start from the easiest condition: simple harmonic vibration, a particle of straight-line vibration, if its equilibrium position is taken, and its movement track goes along x axis, then x, the displacement of the particle away from the equilibrium position, changes as the time *t* changes, following cosine function or sine function, this kind of straight-line vibration is considered simple harmonic vibration, whose dynamical equation is:

$$\ddot{x} + \omega^2 \dot{x} = 0 \tag{1}$$

By solving this equation, the following kinematical equation is developed:

$$x = A\cos(\omega t + \phi) \tag{2}$$

In actual question, sometimes a particle can simultaneously join more than two vibration, which is the problem to be solved for vibration synthesis. Next let's study the

D. Jin and S. Lin (Eds.): Advances in Mechanical and Electronic Engineering, LNEE 176, pp. 41–44.
springerlink.com

synthesis of two simple harmonic vibration with the same frequency along the same line, we assume the both of the two phase are 0.

Writing following m file with Matlab:

```
t=0:0.01:10; a1=1;w1=20; a2=1;w2=20;
x1=a1*sin(w1*t); x2=a2*sin(w2*t);
x=x1+x2;
subplot(3,1,1),plot(t,x1);axis([0 10 -1.2 1.2]);
subplot(3,1,2),plot(t,x2);axis([0 10 -1.2 1.2]);
subplot(3,1,3),plot(t,x);axis([0 10 -2.4 2.4]);
```

The result will be shown In Fig 1. after operation:

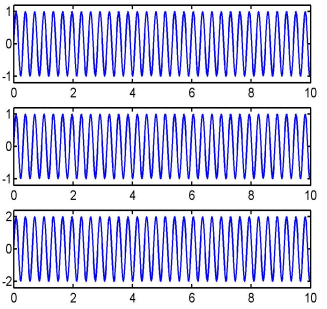

Fig. 1. The synthesis of two simple harmonic vibration with the same frequency along the same line

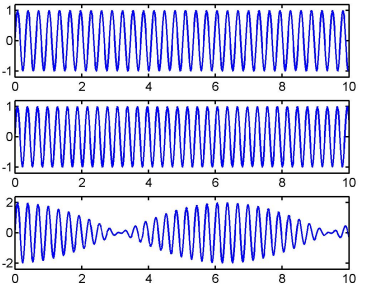

Fig. 2. The synthesis of two simple harmonic vibration with different frequency along the same line

Conclusion: two simple harmonic vibration with the same direction and frequency are still one simple harmonic vibration with the same frequency after synthesis. But amplitude of vibration will stack on the same point.

If w2=20 in the above m file is changed into w2=21, that is to say the two simple harmonic vibration have different frequency and the following results can be developed.

Conclusion: two simple harmonic vibration with the same direction but different frequency will form "beat frequency"(Fig.2) which is "beat frequency" phenomenon.

3 Simulation of Forced Mechanical Vibration by Means of Matlab

In a system with spring, particle and damper, if there is periodic external force acting on the particle, then this kind of particle vibration is called forced vibration, the kinematics differential equation of which is as follows:

$$\ddot{x} + 2\beta\dot{x} + \omega_0^2 x = f_0 \cos(\omega t) \tag{3}$$

Where β is the damper coefficient, ω0 is the intrinsic frequency of the vibration system, ω is the circular frequency of the driving force, f0 is the amplitude of the driving force. Assuming x(1)=x, x(2)=dx/dt, the above equation can be rewritten as:

$$\dot{x}(1) = x(2) \tag{4}$$

Changing the value of ω can study resonance phenomenon. Assuming f=0, then damper vibration appears. Taking a full consideration, then forced vibration appears, applying Matlab to the solution of this differential equation for the study of relationship between displacement and time. Here we use ode45 in Matlab to solve this differential equation, for which, function vbfun.m should be established at first for the purpose of function ode45, if needed, then the function of vbfun.m written is as follows:

```
function xx=fun(t,x,flag,b,w0,f0,w)
xx=[x(2);f0*cos(w*t)-2*b*x(2)-x(1)*w0^2];
```

The following main program is the range of t from 0 to 20, when f=0, it is damper vibration. And if vibration starts from the point t=0, the particle displacement is the largest, assuming A=1, the response of vibration against the driving force is:

```
clear,clc
b=0.2;w0=3;f0=0;w=10;
[t,x]=ode45('fun',[0:0.1:20],[1,0],[ ],b,w0,f0,w);
subplot(3,1,1);
plot(t,x(:,1),'b')
axis([0 20 -1.2 1.2]);
```

The operation result is as shown in upper diagram in Fig. 3.

If driving force is added, as f0=10 in the set main program, other conditions remain the same, then it is forced vibration presented, shown as the middle diagram in Fig. 3, a thorough analysis of figure 2 clearly finds out the difference of damper vibration and forced vibration, if time is sufficient enough, and the amplitude of damper vibration approaches 0, while forced vibration turns into another kind of vibration, this must be related to the vibration of periodic driving force.

If f0 is not 0, for example f0=4 and in the meanwhile w in the main program is 3, which means the driving force frequency share the same value with the frequency of the original vibration, then resonance will appear, shown as lower diagram in Fig. 3, where amplitude increases infinitely.

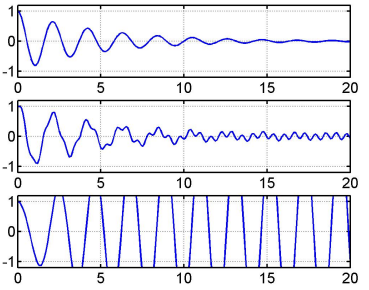

Fig. 3. Diagram of damper vibration (above), forced vibration (middle) and resonance (lower) as t changes from 0 to 20

What we studied is the displacement response of vibration, by the same means, speed response can be worked out. When frequency of periodic external force approaches the intrinsic frequency of the system, amplitude of the forced vibration reaches its maximum, leading to resonance phenomenon, which we call amplitude resonance or displacement resonance. The above solution fully explains the convenience and high-efficiency of the Matlab.

4 Conclusion and Prospects

Concluded from the above two experiments, Matlab has great advantage in mechanical engineering in terms of simulation, it can save a lot the time for computing with high accuracy in the meantime, as the indispensable tool in this field, marlab is widely used in other aspects of mechanical engineering. for example, in the field of mechanical engineering design where people establish mould for object of the study and by means of computer program, operation process of the system and the computing result are realized, they search for the electronic engineering , the electronic technology and other fields.

References

1. Zhang, Z.: Proficient in MATLABS 5.3, pp. 244–263. Beihang University Press, Beijing (2000)
2. Yang, G.: Mordern Physic Experiment, pp. 22–26. Zhejiang University Press, Hangzhou (1997)
3. Gao, J.: The Computer Simulation of the Coherent Optics System. Chinese Journal of Lasers 24(10), 957–960

The Impact of Organizational Slack on the Performance of Mechanical Manufacturing Firms

Heping Zhong

School of Economics and Management, Xuchang University, China
Hepingz2004@163.com

Abstract. Although organizational slack research posits various relationships between a firm's slack and performance, findings to date have been ambiguous. In order to provide insight into this relationship, This paper studies the impact of organizational slack on the performance of mechanical manufacturing firms by using empirical analysis based on the data get from 89 firms in Henan Province. The result shows that organizational slack is positively related to the performance of mechanical manufacturing firms. Thus keeping more slack is more conducive to promoting performance in mechanical manufacturing firms. In addition, the analysis also finds that there is the nonlinear relationship between organizational slack and performance, but this relationship is not significant. Overall, results highlight the importance of additional research into intervening factors impacting the slack–performance relationship.

Keywords: mechanical manufacturing firm; organizational slack, performance, mechanical manufacturing industry, linear relationship model, software application, empirical analysis.

1 Introduction

Organizational slack is potentially utilizable resources that can be diverted or redeployed for the achievement of organization goals [1]. At present, more and more scholars focus on the relationship between organizational slack and performance. However, the existing literature provides no compelling answers regarding whether slack resources facilitates or inhibits performance [2]. What is the relationship between organizational slack and performance? Based on prior findings, the slack-performance relationship is generally conceptualized as linear, nonlinear relationship [1-4]. The current literature has not reconciled these perspectives, and the issue regarding the influence of organizational slack on performance remains an interesting but not fully explored issue [2].

Such ambiguity can arise from many sources including random variation due to differing sample sizes across studies (i.e., ''sampling error''), inconsistent variable measurement [3] and different sample. Thus, in order to provide insight into this relationship, this study employed a empirical analysis based on 89 mechanical manufacturing firms in Henan Province to examine extant research results. Specifically,

D. Jin and S. Lin (Eds.): Advances in Mechanical and Electronic Engineering, LNEE 176, pp. 45–50.
springerlink.com

I focus on firms of a industry in China, based on survey data, to investigate whether organizational slack contributes toward or inhibits firm performance.

2 Theory and Hypothesis

Organizational Slack has been argued to have a positive impact on performance for several reasons. Firstly, organizational slack provides firms with sufficient resources to capitalize on external opportunities permitting them to enjoy continuous growth except where managerial capabilities are inadequate [2]. Secondly, organizational slack also enables firms to conduct additional experimentation, thus enhancing innovation and risk-taking. Essentially, organizational slack provides firms with more options for developing strategic behaviors to create competitive advantages [2]. Thirdly, organizational slack can become a resource for conflict resolution. The upshot is that, with sufficient slack, there can be a solution for every problem [4,5]. Accordingly, it can be argued that the more likely it is that organizational slack is used by managers to improve performance in mechanical manufacturing firms. This leads to the first hypothesis.

Hypothesis1: In mechanical manufacturing firms, organizational slack is positively related to performance.

On the other hand, organizational slack has been argued to have negative impacts on firm performance. Daniel et al. (2004) suggest that idle resources, like idle hands, invite inefficiency demons. This "slack as inefficiency" perspective posits that slack can encourage satisficing, politics, or self-serving managerial behaviors that hurt performance [3]. From an agency theory perspective, managers inherently have a set of goals, such as the pursuit of power, prestige, money, and job security, that are not always aligned with those of principals, managers may use organizational slack to engage in excessive diversification, empire-building, and on-the-job shirking [4,5]. As a result, in mechanical manufacturing firms, organizational slack may become a source of agency problems, which breed inefficiency [5]. This leads to the second hypothesis.

Hypothesis2: In mechanical manufacturing firms, organizational slack is negatively related to performance.

Rather than weigh in on one side of the debate for or against the performance-enhancing benefits of organizational slack, a reconciliation of these perspectives has been proposed. Some researchers find merit in both perspectives, arguing that slack improves performance within, but hurts it beyond, a given range [6]. The resulting curvilinear relationship suggests that, ideally, firms should have surplus resources sufficient to address unforeseen threats or opportunities but limited enough to prevent managers' irresponsible behavior [3]. Therefore, in mechanical manufacturing firms, it can be argued that organizational slack beyond a certain level may reduce firm performance, that is to say, the relationship between organizational slack and performance is curvilinear, generally positive but falling off beyond a certain level. This leads to the third hypothesis.

Hypothesis3: In mechanical manufacturing firms, the relationship between organizational slack and performance is inverse U-shaped.

3 Methods

3.1 Sample

The sample was drawn from mechanical manufacturing firms in Henan province by questionnaire. I selected 89 firms according to convenience. The questionnaire was accomplished by intermediate and senior managers. Descriptors of the sample are summarized in Table 1 to Table 3.

Table 1. The distributing of respondents' job

Respondent post	Number	Percentage (%)
Intermediate manager	35	39.3
Senior manager	19	21.3
General manager	12	13.5
President	5	5.6
Other	18	20.3

Table 2. The distributing of firm ownership of respondents

Firm ownership	Number	Percentage (%)
State-owned firm	19	21.3
Private-owned firm	58	65.2
Foreign capital-owned	8	9.0
Other firm	4	4.5

Table 3. The distributing of firm size of respondents

Firm size	Number	Percentage (%)
Oversize firm	3	3.4
Big firm	18	20.2
Middle firm	40	44.9
Small firm	28	31.4

3.2 Variables Measure

Firm performance: Based on the previous literature[5,7], firm performance is measured by: (1) sales growth; (2) asset-profit ratio; (3) increase of market share; and (4) net profit. In the questionnaires the answers were measured on 5-point Likert scale, using the scale from 1, strongly draggle, to 5, strongly keep ahead. The Cronbach's coefficient alpha for this scale is 0.875; the total variance explained is 73.043%.

Organizational slack: Following previous studies[5,8,9], organizational slack is measured by the following three items: (1) The resource sharing level of various departments within the firm is very high; (2) New uses of existing resources in a firm are often found; (3) Some new resources or new mix of existing resources in a firm are often found. In the questionnaires the answers were measured on 5-point Likert scale, using the scale from 1, strongly disagree, to 5, strongly agree. The Cronbach's coefficient alpha for this scale is 0.734; the total variance explained is 65.366%.

Control variable: Like prior studies, this study adopts total capital to measure the size of a firm, and take it as a control variable. The firm size is measured by logarithm of the total capital.

3.3 Results

I test my model with the statistical software SPSS 13.0 and use exploratory factor analysis to test every index. In order to test the hypothesis all above, the paper uses once, twice, thrice regression equation model including independent variable to process hypothesis testing [10]. The regression equation model is as follow: $performance = \beta_0 + \beta_1 size + \beta_2 \mathrm{var} + \beta_3 \mathrm{var}^2 + \beta_3 \mathrm{var}^3 + \varepsilon$ I use the method of stepwise regression, the result of hypothesis testing shows as Table 4 to Table 6.

Table 4. Model factor loading of the elements and Cronbach's α

Elements discribing indicators (N=89)	**Factor loading**
Firm performance (Cronbach's α = 0.875)	
V1 Sales growth	0.878
V2 Asset profit ratio	0.876
V3 Increase of market share	0.861
V4 Net profit	0.801
Organizational slack (Cronbach's α = 0.734)	
V5 The resource sharing level of various departments within the firm is very high	0.722
V6 New uses of existing resources in a firm are often found	0.868
V7 Some new resources or new mix of existing resources in a firm are often found	0.829

Table 5. Means, standard deviations and correlations

variables	**mean**	**s.d.**	1	2
1 Firm size	8.4349	2.29993		
2 Organizational slack	4.0978	1.11747	-0.044	
3 Firm performance	3.9053	0.84027	0.385***	0.290**

*** p <0.001 ** p <0.01 * p <0.05 ^{+}p <0.10.

Table 6. Regression model of organizational slack and firm performance

variables	Model 1	Model 2	Model 3	Model 4
Constant	2.674***	1.744***	1.391	3.480
Firm size	0.143***	0.144***	0.144***	0.145***
Organizational slack		0.223**	0.400	-1.282
Organizational slack ^{2}			-0.020	0.403
Organizational slack ^{3}				-0.034
F	13.406***	11.966***	7.921***	5.981***
R^2	0.148	0.239	0.241	0.244
Adjusted R^2	0.137	0.219	0.210	0.203

*** p <0.001 ** p <0.01 * p <0.05 ^+p <0.10.

The result of exploratory factor analysis from table 4 indicates that factor loading and Cronbach's alpha are more than 0.70, every index is in accordance with requirement of hypothesis testing. Goodness-of-Fit test and significance test from table 6 indicate that model 2 is better than model 3 and model 4. Meanwhile, collinearity and heteroscedasticity test indicate that there is no multicollinearity problems and heteroscedasticity issues (relevant test data are ignored). Therefore, hypothesis 1 is supported by these testing. Regression curve as Fig. 1 (control variable is ignored).

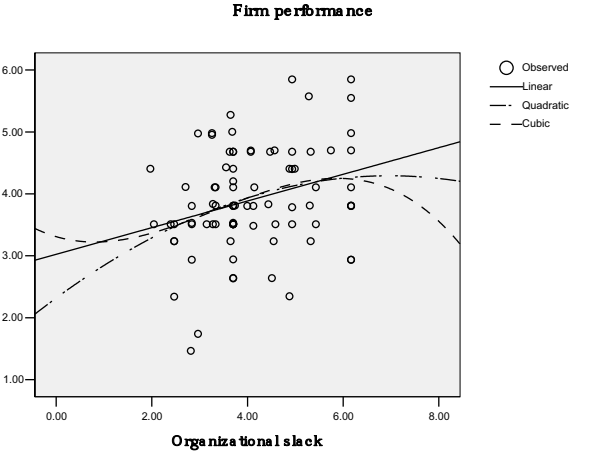

Fig. 1. Regression curve

4 Conclusions

In this study, my contributions focus on examining the relationship between organizational slack and the performance of mechanical manufacturing firms from Henan Province in China. The result shows that organizational slack is positively related to the performance

of mechanical manufacturing firms. Thus, in mechanical manufacturing firms, keeping more slack is more conducive to promoting performance.

Because of data limitations, this paper only studies mechanical manufacturing firms in Henan Province, the universality of its conclusions shall be tested by the mechanical manufacturing firms of other regions in future. Of course, other environment variables, such as firm age, competition, and so on, may have an impact on the relationship between organizational slack and the performance of mechanical manufacturing firms, which provides opportunity for future research efforts.

Acknowledgments. This paper is supported by the Humanities and Social Science Research Project of the Ministry of Education of China (Grant No.12YJA630198), the Government Decision-making Research Project of Henan Province of China (Grant No.2011B726). Thanks for the guidance of Qing-Hua Xia of Wuhan University.

References

1. George, G.: Slack resources and the performance of privately held firms. Academy of Management Journal 48(4), 661–676 (2005)
2. Chiu, Y.-C., Liaw, Y.-C.: Organizational slack: is more or less better? Journal of Organizational Change Management 22(3), 321–342 (2009)
3. Daniel, F., et al.: Slack resources and firm performance: a meta-analysis. Journal of Business Research 57, 565–574 (2004)
4. Tan, J., Peng, M.W.: Organizational Slack and Firm Performance During Economic Transitions: Two Studies from an Emerging Economy. Strategy Management Journal 24(13), 1249–1263 (2003)
5. Zhong, H.: The Impact of Organizational Slack on the Performance of Material Production and Processing Firms. Advanced Materials Research 204-210, 1655–1658 (2011)
6. Bourgeois, L.: On the measurement of organizational slack. Acad. Manage. Rev. 6, 29–39 (1981)
7. Zhong, H.: The Relationship between Slack Resources and Performance: an empirical study from China. International Journal of Modern Education and Computer Science 3(1), 1–8 (2011)
8. Fang, R.S., Wang, C.L.: On the Relationship Between Types of Decision-making and Organizational Slack. R&D Management 20(5), 47–51 (2008) (in Chinese)
9. Zhong, H.: The Impact of Organizational Slack on Technological Innovation: Evidence from Henan Province in China. In: The 4th International Conference on Management and Service Science (2010)
10. Zhong, H., Fang, R., Li, X., Sun, L., Sun, X.: Human Resource Slack and Technological Innovation: Evidence from Henan Province in China. In: 2008 IEEE International Conference on Engineering, Services and Knowledge Management. IEEE (2008)

Fault Diagnosis of Electronic Ignition System of Automobile Engine Based on Wavelet Transform

ZhiGang Han, XiaoYan Liu, and ShuXia Jiang

Central-South University of Forestry and Technology, 498 Shaoshan south road, Changsha, 410004, China
gzhzg@163.com

Abstract. This paper aims to analyze the fault of engine electronic ignition system by ignition voltage signal waveform. When the fault information of time domain waveform is not obvious to be recognized, the wavelet transform and Fourier transform can be used to transform the original ignition secondary waveform of the engine into frequency domain waveform and power spectral density, in which obvious fault waveform can be observed. The results show that the frequency domain waveform analysis provides an effective supplement for the time domain waveform analysis and effectively improves the accuracy of the automotive fault diagnosis.

Keywords: engine, electronic ignition system, wavelet transform, frequency domain, fault diagnosis.

1 Introduction

The modern automobile is a mechanical and electrical integration products. With the development of automobile industry, the application of microcomputer -controlled ignition system, electronic control fuel injection system, anti-brake system, automatic transmission and other structures on the car is very popular. As to the advance of automotive technology, traditional artificial diagnosis can no longer meet the needs of modern auto diagnostic service. Since 1960, a number of countries began using the oscilloscope on fault diagnosis, and wave testing has become one of the important means of modern auto diagnosis.

Five kinds of determined engine electronic signals are based on amplitude, frequency, shape, pulse width, and array [1]. Generally, engine ignition waveform is used to observe, compare, and analyze the waveform shapes, amplitude and pulse width in time domain by collecting primary and secondary ignition voltage waveforms in real time, then the working condition and the cause of the fault of electronic ignition component such as ignition coils, spark plugs and signal generator be detected[2]. When the waveform comparison is not very obvious, it is hard to accurately judge the fault. This paper analyze the waveform fault from the perspective of the frequency domain by way of wavelet decomposition and reconstruction, and the establishment of the power spectrum of the secondary ignition voltage waveform, thus improve the accuracy of fault diagnosis on engine.

D. Jin and S. Lin (Eds.): Advances in Mechanical and Electronic Engineering, LNEE 176, pp. 51–55.
springerlink.com

2 Data Sources and Methods

2.1 Data Sources

Waveform data be collected from the SPX engine analyzer and the engine of Toyota Previa.

2.2 Analysis method

The wavelet transform specially applies to the decomposition from non-steady state of signal into different frequency components. The most prominent advantage of wavelet transform is to give out the information of signals in the time domain and frequency domain[3,4]. The basis function of wavelet transform is a generating function $\psi(t)$ with compact support, and a wavelet sequence appears by dilation and translation of the generating function $\psi(t)$.

$$\psi_{a,b}(t) = |a|^{-\frac{1}{2}} \psi\left(\frac{t-b}{a}\right) \qquad a, b \in R, a \neq 0 \tag{1}$$

a - scale factor b - translate factor

the continuous wavelet transform for an arbitrary function $f(t) \in L2(R)$:

$$W_f(a,b) = \frac{1}{\sqrt{a}} \int_R f(t) \psi * (\frac{t-b}{a}) dt, \quad a > 0 \tag{2}$$

This paper adopts the discrete wavelet transform, this method not only provides enough information for decomposition and synthesis of the original signal, but also significantly saves calculation time [5].

Power spectral density (PSD) is the power carried by per unit frequency waves which is the result as spectral density of random signals wave is multiplied by an appropriate coefficient.

$$P_n(f) = \frac{1}{N\Delta t} X_n^{\ 2} \tag{3}$$

N -the number of sampling points (must be 2^n); Δt -sampling interval; x_n -Fourier component

Because the secondary ignition waveform data obtained from the engine analyzer is not evenly spaced, data processing should be taken before the data analysis. First, the map with the original waveform be drawn with MATLAB and use an interpolation method to redraw. Then, the wavelet transform be made on waveform data and obtain the waveforms decomposition in time domain and frequency domain. Finally, fast Fourier transform be used to obtain the power spectrum, and we can judge the faults from a multiple angles.

3 Results and Analysis

3.1 Data Process and Waveform Redraw

Take the secondary ignition waveform of the first cylinder as an example (Fig.1). Through the comparison of the original waveform and the redrawn waveform, the error of redrawing the waveform by using an interpolation method is very small, the way does not affect the results of the latter wavelet analysis.

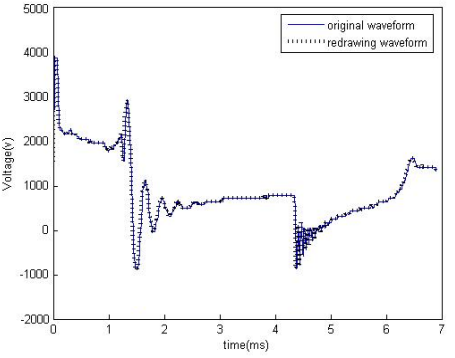

Fig. 1. The redrawing waveform of the 1st cylinder

3.2 Wavelet Decomposition and Analysis

Fetch the first cylinder normal waveform data and abnormal waveform data, and draw the map with MATLAB (Fig.2). The difference between the fault and the normal waveform can be observed, but it is not obvious, will affect the fault diagnosis. Due to it is difficult to accurately diagnose where the fault is only on the basis of the time domain waveform, the diagnosis can be taken through frequency analysis.

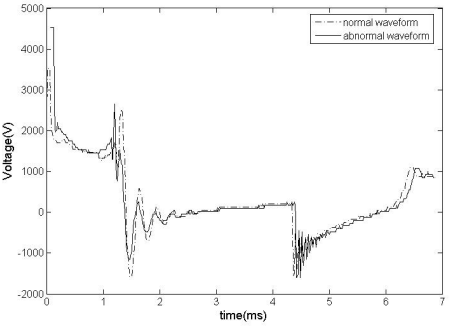

Fig. 2. Normal waveform and abnormal waveform

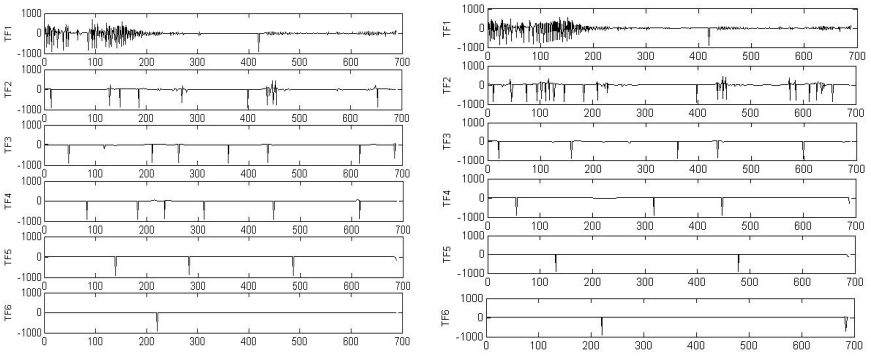

(a)normal decomposition signal (b) abnormal decomposition signal

Fig. 3. Decomposition signal in frequency domain of normal waveform and abnormal waveform

This paper takes the Daubechies wavelet functions as mother wave of wavelet transforms, makes wavelet decomposition of 2 sets of data, the time domain waveform and frequency domain waveform can be decomposed separately. Due to the little difference between the normal and abnormal waveform after time domain decomposition, analysis is needless here. The initial waveform of the normal waveform and abnormal waveform are decomposed to 6 layer waveforms as TF1~TF6, which x-coordinate is frequency, y-coordinate is amplitude (Fig.3). In Figure 3, a certain difference can be shown in the TF2, and there are more cluttering waves of the abnormal waveform near 100Hz and 600 Hz. In order to clearly observe and verify the difference between the normal and abnormal waveform in frequency domain, power spectrum can be used for further analysis.

3.3 Power Spectrum Analysis

Compared to the normal and abnormal secondary ignition waveform of the first cylinder, some difference of spark line between normal and abnormal waveform in time domain part was found. Calculate the power spectral density and draw the map of the power spectrum, which x-coordinate is frequency, y-coordinate is the square of the amplitude of each harmonic component. In order to better compare the normal and fault spectrum, the normal and abnormal map of the first cylinder be local enlarged (Fig. 4).

Figure 4 shows that near the frequency range (120,140 Hz) and (590,610 Hz), there is a big difference between the normal and abnormal power spectrum of the first cylinder, it should be due to the fact that the fault is caused by two frequency-related clutter, such as carbon deposition on plug or abnormal ignition. Consequently, it is concluded that at the time of fault diagnosis of engine single cylinder, if there are a number of differences between the normal and abnormal ignition waveforms in time domain of the same cylinder, but these differences are not very obvious, we could compare the frequency spectrum, and the results will be more reliable.

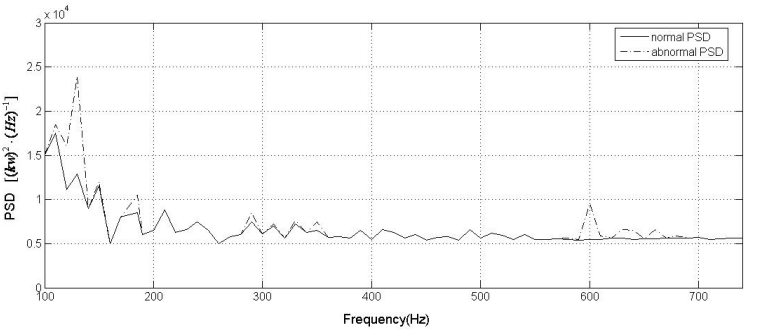

Fig. 4. Selective enlargement of normal and the abnormal ignition secondary PSD of the 1st cylinder

4 Conclusion

Traditional fault waveform analysis of engine electronic ignition system is compare the similarities and differences of waveforms in various regions of each cylinder in time domain. When the difference is not very obvious, it is difficult to determine if there is a fault. This paper gets ignition voltage signal changes at different frequencies by the way of the wavelet transform method. Combined with time domain waveform and frequency domain waveform, it is make more accurate judgment and analysis of fault. The method can also be used for the detection of engine fuel injector waveform and noise waveform, helpful to improve engine fault diagnosis accuracy.

Acknowledgment. This work was carried out at the Youth Fund of Central-South University of Forestry and Technology "The experimental vehicle modification of transportation Specialty, 101-0813".

References

[1] Jun, Z.: Circuit Waveform Analysis of Electronically Controlled Engine, pp. 4–8. Mechanical Industry Press, Beijing (2003)
[2] Jiang, C.H.: Vehicle Detection and Diagnosis. Mechanical Industry Press, Beijing (November 2007)
[3] Tai, C.J.: Wavelet Analysis Introduction. Xi'an Jiaotong University Press, Xi'an (1995)
[4] Mallat, S.G.: A Wavelet Tour of Signal Processing. Academic Press, San Diego (1998)
[5] Yu, D.: Fault Detection of Automobile Rear Drive Assembly by Using Wavelet Decomposition. Journal of Vibration, Measurement &Diagnosis 3(29) (2009)

Research on the Jet Influence on the Mechanical Launcher of Various Ignition Height

WeiDong He[1,2], Yi Jiang[1], and YanLi Ma[2]

[1] School of Aerospace Engineering, Beijing Institute of Technology, Beijing 100081, China
[2] The Third Institute of China Aerospace Science and Technology Corporation 8359, Beijing 10089, China
yanli8509@163.com

Abstract. In order to research the different ignition height of the gas jet on the mechanical ejection launcher, the finite volume method was used, a fully structured grid was used to solve the three-dimensional N-S equations, the quasi-steady in the ignition on the nozzle height of 15m, 30m, 35m and 40m conditions were calculated to obtain the different ignition height under deck hatch, as well as temperature and pressure load distribution launchers. The result provides a mechanical reference for the launcher firing height.

Keywords: rocket plume, ignition height, launching mechanical equipment, numerical simulation.

1 Introduction

The nozzle firing height is too low, then, the gas jet may ablation launch platform for the ejection-launched missile launchers. The ignition height is too high, the ejection force is larger. The ignition height is a key factor in decision to ejection launch process[1]. The height of the launcher so different ignition study is necessary [2].

In this paper, the ignition is on the nozzle height of 15m, 30m, 35m and 40m conditions were calculated, the temperature and pressure load distribution on the deck, hatch as well as launchers was accessed, and the calculation results analysis provides a reference for the hair ignition height selection.

2 The Theoretical Basis

2.1 Control Equations[3]

Continuum equations:

$$\frac{\partial \rho}{\partial t} + \nabla \cdot (\rho \vec{u}) = 0 . \tag{1}$$

Where ρ : flow density

$\vec{u}$: flow velocity vector

D. Jin and S. Lin (Eds.): Advances in Mechanical and Electronic Engineering, LNEE 176, pp. 57–63.
springerlink.com

Momentum equations:

$$\frac{\partial}{\partial t}(\rho u_i)+\frac{\partial}{\partial x_j}(\rho u_i u_j)=-\frac{\partial p}{\partial x_i}+\frac{\partial \tau_{ij}}{\partial x_j}. \tag{2}$$

Where u_i, u_j :the i and j weight flow velocity, p :the flow pressure, x_i, x_j :i, j direction coordinate, τ_{ij} : the stress tensor. Its expression is:

$$\tau_{ij}=[\mu(\frac{\partial u_i}{\partial x_j}+\frac{\partial u_j}{\partial x_i})]-\frac{2}{3}\mu\frac{\partial u_l}{\partial x_l}\delta_{ij}. \tag{3}$$

Energy equations:

$$\frac{\partial}{\partial t}(\rho H)+\frac{\partial}{\partial x_j}(\rho u_j H)=\frac{\partial p}{\partial t}+\frac{\partial}{\partial x_j}(u_i\tau_{ij}-q_j)\cdot \tag{4}$$

Where H :total enthalpy $H=h+\frac{1}{2}u_i^2$, where $h=C_pT$, C_p is stated specific heat, T is static temperature, q_j is heat flux $q_j=-\frac{\partial T}{\partial x_j}$.

2.2 Turbulence Equations

The standard k-ε model [4] [5] equation was used. The transportation equation of the turbulence kinetic energy k is

$$\frac{\partial}{\partial t}(\rho k)+\frac{\partial}{\partial x_i}(\rho k u_i)=\frac{\partial}{\partial x_i}[(\mu+\frac{\mu_t}{\sigma_k})\frac{\partial k}{\partial x_j}]+G_k+G_b-\rho\varepsilon-Y_M+S_k\cdot \tag{5}$$

The equation of the dissipation rate of the turbulence kinetic energy is

$$\frac{\partial}{\partial t}(\rho\varepsilon)+\frac{\partial}{\partial x_i}(\rho\varepsilon u_i)=\frac{\partial}{\partial x_j}\left((\mu+\frac{\mu_t}{\sigma_\varepsilon})\frac{\partial\varepsilon}{\partial x_j}\right)+C_{1\varepsilon}\frac{\varepsilon}{k}(G_k+C_{3\varepsilon}G_b)-C_{2\varepsilon}\rho\frac{\varepsilon^2}{k}+S_\varepsilon$$

$$\mu_t=\rho C_\mu\frac{k^2}{\varepsilon}. \tag{6}$$

3 Calculated Conditions

3.1 Calculated Model

The computational simulation of nozzle firing at a distance of deck height of 15m, 30m, 35m and 40m are several conditions gas jet generating device. The fully structured grids were used, and a total of one million grids, the Figure 1 show the calculation model [6].

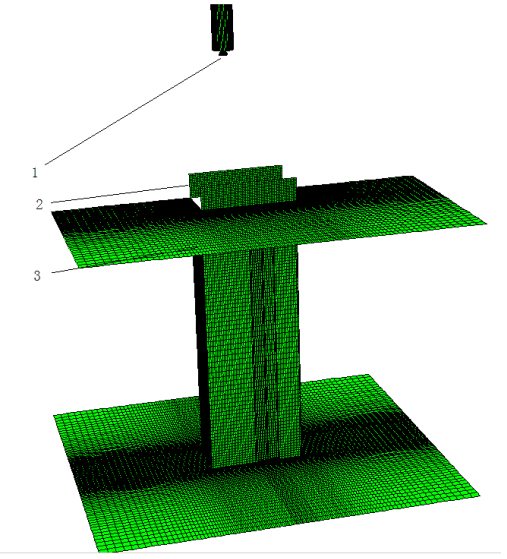

Fig. 1. Ignition height of 15m

3.2 Boundary Conditions

The pressure inlet boundary condition was used in the nozzle exit. Deck, engine surface, launch the box wall and hatch at the solid wall with the wall boundary conditions, the boundary of the object surface with no slip wall and adiabatic wall boundary conditions, the near-wall turbulence calculated using the standard wall function method [7].

4 Different Ignition Height of Jet Launcher

4.1 Analysis of Simulation Results for Different Operating Conditions

Shown in Figure 2, a high degree of symmetry plane under the velocity distribution was obtained at 15m, 30m, 35m and 40m ignition height. The figure shows, the core area within a height of 15m when the ignition in the gas jet, deck, deck temperature is higher. The deck and the launch tube away from the jet core area, low surface temperature at 30m. The impact and temperature reduce with the ignition of the increasing.

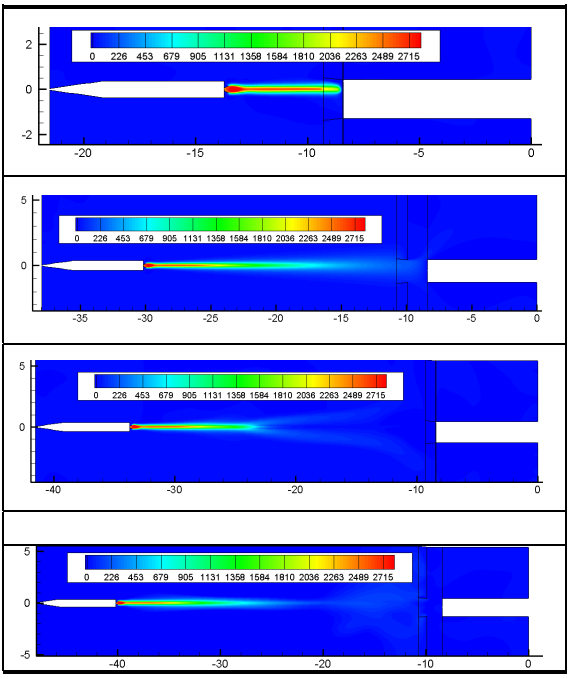

Fig. 2. 15m, 30 m, 35m and 40m ignition under a high degree of symmetry surface velocity distribution

4.2 The Simulation Data Statistics

Figure 3 shows the schematic for the covers are in place.

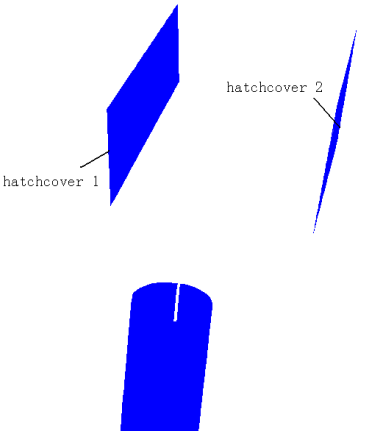

Fig. 3. Hatch position description (the hatch label launch tube ipsilateral to 1, with different side of the launch tube hatch label 2)

Table 1 shows the hatch 1 in all directions by the force. Hatch a force can be seen that with the increase of ignition distance, hatch a force in the x direction along the positive direction and gradually increase, and then becomes negative.

Table 1. Hatch covers 1 each direction of force

L(m)	X	Y	Z
15	373	-5230	11
20	986	-11104	34
25	1481	-15363	43
30	-165	1635	0
35	-305	2904	1
40	486	-4087	1

Table 2 shows the hatch 2 in all directions by the force. The force first increase and then decrease with the increase of ignition distance at X direction. Y the force is first increased and then decreased, this may be because the 15m position when the ignition, the hatch covers basic subject only to the impact of the gas core area, the smaller the role. With the ignition distance increases, the hatch is located in the jet boundary area, the border area led to an expansion cylinder cover the scope, and thus the force. With the further increase of the ignition distance, the hatch away from the jet boundary area, the force decreases.

Table 2. Hatch covers 2 each direction of force

L(m)	X	Y	Z
15	408	6108	100
20	1200	12741	74
25	2511	23424	38
30	168	1643	-1
35	345	3321	-2
40	-194	-3478	2

Table 3 shows the launch tube to cover all directions of force. Can be seen that the force covered by the launch tube launcher cover x to the power of the basic trend is to decrease with increasing distance.

Table 3. Launching tubes all direction of force by the cover

L(m)	X	Y	Z
15	65398	-410	78
20	67032	-337	96
25	66221	-216	98
30	3767	6	-3
35	3140	1	0
40	1678	-9	6

Table 4 shows the maximum temperature of various parts. Various parts of the temperature distribution can be seen as the maximum temperature of various parts of the ignition distance increases gradually decreases, which is mainly caused due to the impact effect of the gas flow is reduced

Table 4. Each part of the maximum temperature(K)

L(m)	Deck	Hatchcover	launcher	box
15	1480	1850	363	934
20	1070	1170	595	781
25	682	699	597	599
30	376	382	365	371
35	363	355	339	343
40	380	360	333	412

Table 5 shows the maximum pressure of various parts. Various parts of the maximum pressure can be seen, the pressure from all parts of the small, the maximum pressure in various parts of the trend decreases with the increase of ignition distance, which is mainly caused due to the impact effect of the gas flow is reduced .

Table 5. Each part of the maximum pressure(10E5Pa)

L(m)	Deck	Hatchcover	launcher	box
15	1.14	1.91	1.06	1.01
20	1.1	1.64	1.16	1.07
25	1.08	1.42	1.1	1.02
30	1.03	1.03	1.02	1.04
35	1.03	1.03	1.02	1.03
40	1.05	1.04	1.02	1.03

5 Conclusions

1. With the ignition distance increases, the maximum temperature of all parts is reduced, this is mainly because the distance between transmitter and gas increases caused. The result provides a mechanical reference for the launcher firing height.

2.With the increase of ignition distance, the force of all parts of the basic first increases and then decreases, mainly due to the special structure of the gas jet. Beginning to launch the device is located outside the jet core area by the smaller role. With the ignition distance increases, the transmitter is located in the jet boundary area, the proliferation of border zone launcher force increased, with the further increase of the ignition distance, the transmitter is located outside the jet boundary area, by the force decreases.

References

1. Yuan, Z.-F.: The rockets catapulted ballistics missile within, the publishing company of the Beijing institute of the technology (1987)
2. Zhao, C.-Q., Jiang, Y.: The Dynamics of The Jet Flow. The publishing company of the Beijing institute of the technology (1995)
3. Armsfield, S., Street, R.: The fractional-step method for the Navier-Stokes equations on staggered grids: accuracy of three variations. Journal of Computational Physics 153, 660–665 (1999)
4. Miao, R.-S., Ju, X.-M.: Gas Dynamics for Rocket. National Defense Industry (1993)
5. Wang, F.-J.: The computational fluid dynamic. The publishing company of the Tsinghua University (2001)
6. Li, J., Cao, C.-Y., Xu, Q.: Numerical simulation the form and development of rocket gas near flow field. Journal of Propulsion Technology 24(5), 410–413 (2003)
7. Fu, D.-B., Liu, Q., Chen, J.-W.: Numerical Simulation on Missile Launching Procedure. Journal of Ballistics 16(3), 11–15 (2004)

Optimization Design for Launch Box Based on the Effect of the Shock Wave

ShaoZhen Yu, Yi Jiang, Jia Deng, BoWei Liu, and GangLian Zhao

Department of Aerospace Engineering, Beijing Institute of Technology, Beijing, China, 100081
bitysz@bit.edu.cn

Abstract. The article is based on the numerical simulation of the shock wave which caused by the jet flow in the launch box. For this kind of launch box, the two lips are opening when the missile is launching. By comparing the force on the four walls of the box and the two guides in which, we can get the parameters of the jet flow. Besides, the thermal effects and erosion effects are very important factors for the mechanical engineering, so the contours of temperature and pressure on different parts of the box are given to analysis the spreading process of the shock wave. The Standard κ–ε turbulence model is used. The conclusion is helpful for protecting the launch box when the missile is launched and improving the design scheme for the next generation.

Keywords: jet flow, shock wave, numerical simulation, launch box.

1 Introduction

When the missile is preparing for launch, the two lips of the launch box are opened by the launcher, and then the missile is fired and moved along with the guide by the force of the thrust itself. However, the space in the box is relatively small for the exhaust of the jet flow. Which lead to congestion. The shock wave begins to form and effect the box. The high temperature and pressure gas will produce thermal effects and erosion effects. Even destroy the protection layer in very short time and the resin layer of the box will be flushed. Also the high temperature can be one of the factors which cannot be ignored for the arrangement of the cable and the electronic components on the box. And thus lead to launching accident we would not want to see.

The process of missile launching for the launching mode we mentioned as the two lips are opening before the missile firing was simulated. The simulation is based on one of the missile works in lower pressure. The force on the walls and the erosions effects were analyzed. The flow field and the movement of the missile were computed coupled. The transfer law of the disturbing wave inside the box and the distribution of pressure and temperature were obtained. The analysis of the calculation results provided some references on the optimization design for launching equipment.

2 Calculation Theory and Model

2.1 Control Equations for Jet Flow[1]

Continuum equations:

$$\frac{\partial \rho}{\partial t} + \nabla \cdot (\rho \vec{u}) = 0 \tag{1}$$

D. Jin and S. Lin (Eds.): Advances in Mechanical and Electronic Engineering, LNEE 176, pp. 65–70.
springerlink.com

Where ρ is flow density , $\vec{u}$ is flow velocity vector.

Momentum equations:

$$\frac{\partial}{\partial t}(\rho u_i)+\frac{\partial}{\partial x_j}(\rho u_i u_j)=-\frac{\partial p}{\partial x_i}+\frac{\partial \tau_{ij}}{\partial x_j} \tag{2}$$

Where u_i, u_j: the i and j weight flow velocity; p: the flow pressure; x_i, x_j: i,j direction coordinate; τ_{ij}: the stress tensor. Its expression is:

$$\tau_{ij}=[\mu(\frac{\partial u_i}{\partial x_j}+\frac{\partial u_j}{\partial x_i})]-\frac{2}{3}\mu\frac{\partial u_l}{\partial x_l}\delta_{ij} \tag{3}$$

Energy equations:

$$\frac{\partial}{\partial t}(\rho H)+\frac{\partial}{\partial x_j}(\rho u_j H)=\frac{\partial p}{\partial t}+\frac{\partial}{\partial x_j}(u_i\tau_{ij}-q_j) \tag{4}$$

Where H : total enthalpy $H=h+u_i^2/2$, where $h=C_pT$, C_p is stated specific heat, T is static temperature ; q_j is heat flux $q_j=-\partial T/\partial x_j$

Turbulence Equations

The standard k-ε model[4] equation was used. The transportation equation of the turbulence kinetic energy k is

$$\frac{\partial}{\partial t}(\rho k)+\frac{\partial}{\partial x_i}(\rho k u_i)=\frac{\partial}{\partial x_i}[(\mu+\frac{\mu_t}{\sigma_k})\frac{\partial k}{\partial x_j}]+G_k+G_b-\rho\varepsilon-Y_M+S_k \tag{5}$$

The equation of the dissipation rate of the turbulence kinetic energy is:

$$\frac{\partial}{\partial t}(\rho\varepsilon)+\frac{\partial}{\partial x_i}(\rho\varepsilon u_i)=\frac{\partial}{\partial x_j}\left((\mu+\frac{\mu_t}{\sigma_\varepsilon})\frac{\partial\varepsilon}{\partial x_j}\right)+C_{1\varepsilon}\frac{\varepsilon}{k}(G_k+C_{3\varepsilon}G_b)-C_{2\varepsilon}\rho\frac{\varepsilon^2}{k}+S_\varepsilon$$

$$\mu_t=\rho C_\mu\frac{k^2}{\varepsilon} \tag{6}$$

2.2 Model and Calculation Conditions

The model is shown as Fig.1: The missile, the front guide and the back guide, the launch box are the parts of the model. The missile moved along the guide and leaves

them at the same time. The entire computational domain using fully structured grid with a total of 0.8 million, and the trajectory of the missile was given by engineering test. the launch mode is inclined.

Monitor points: based on the law of the shock wave, we set the center on the top wall of the launch box as the monitor points, from which we will monitor the ratio of static pressure and temperature changed with the spread of the shock wave.

Boundary conditions: For the calculation, the total pressure was set at the time when the engine ignition pressure is stable. The total combustion chamber pressure of 9.4 MPa, and the total temperature is 3600 K. the jet flow in the box is near-field, the ratio of static pressure is 1.2, which meets the characteristics of under-expanded. The difference of the speed at the nozzle is very small, also because of the large Re and Fτ, the influence caused by gravity and viscosity can be ignored. The pressure of the environment is 0.01MPa. The wall boundary used the stationary and insulated conditions, and the standard wall function was used to handle the near wall turbulence calculation. The convergence condition is set as 10^{-3}.

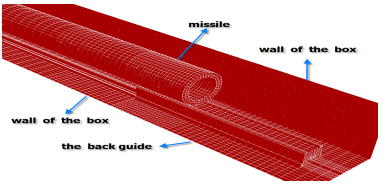

Fig. 1. Computational model

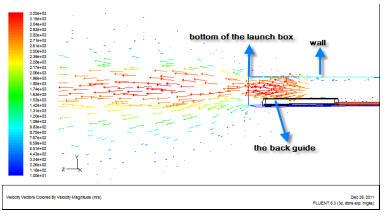

Fig. 2. Velocity vectors on the central plate of nozzle

3 Results and Discussion

Fig. 2 is velocity vectors on the central plate of the nozzle when the missile begins to move and the pressure in the jet reached stable. From the figure we can get that the expanding of the jet flow is violent and the gas was congested in the launch box at the very beginning. Besides the suction phenomenon appeared that gas outside was sucked into the box.

Fig.3 is the curve shows the ratio of static pressure at the monitor point changed with the spread of the shock wave, when the missile moved to the middle of the box, the influence caused by the shock wave reached peak. After that with the weakening of the shock wave, the pressure begins to decay. From the curves of temperature changed at the monitor point shown in Fig.4 we can also get the similar conclusion.

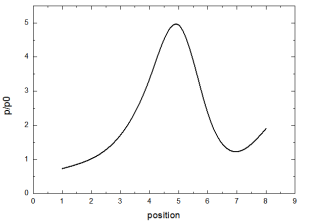

Fig. 3. The ratio of static pressure on the monitoring point changed with missile position

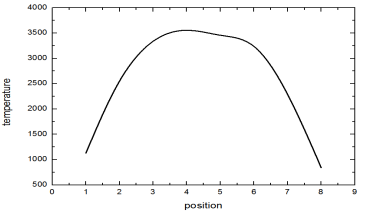

Fig. 4. Temperature on the monitoring point changed with the missile position

Fig.5 is the curves of the force on the guide, from the figure we can get that when the missile moved at the center position (5m around shown as the x axis)of the launch box ,the force on the back guide reached the peak value, it's also the time that the box was the most affected state by the shock wave. The smaller figure in Fig. 5 is the fore on the front guide ,compared with the back one, the force is very small but increased with the missile's movement.

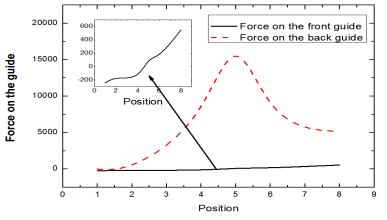

Fig. 5. Force changed on the guides with the missile position

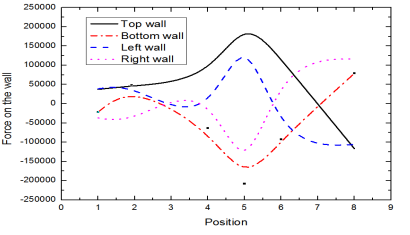

Fig. 6. Force on the wall changed with the missile position

Fig.6 shows the force acted on the four walls of the box, it had the similar regularity. From which we can also get that the shock wave decayed with its spread.

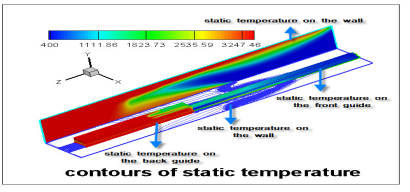

Fig. 7. Contours of temperature for the guides,the walls of the launch box(1m)

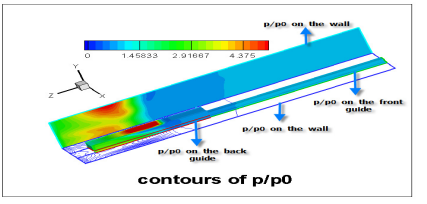

Fig. 8. Contours of p/p0 for the guides,the walls of the launch box(1m)

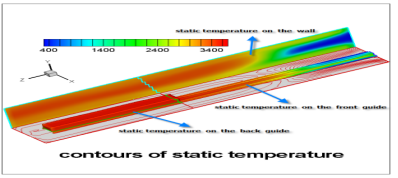

Fig. 9. Contours of temperature for the guides,the wall of the launch box(5m)

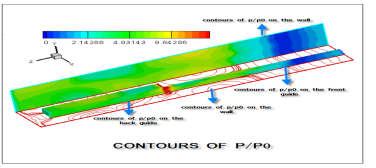

Fig. 10. Contours of p/p0 for the guides,the wall of the launch box(5m)

Fig.7 to Fig.10 shows the contours of the guides, the walls of the launch box, From Fig.7 and Fig .9 we can get that the back guide was seriously affected by the jet flow, the temperature is closed to the jet flow. From the contours of p/p0,as shown in Fig.8 and Fig.10, we can get that at the four corners of the box ,the pressure is higher than the middle part.

4 Conclusion

(1) The force acted on the launch box by the shock wave is increased with the movement of the missile before the missile moved to the middle part. Then it decreased till the missile flied out of the box. so we should use high impact materials on the back and the shortest length as possible to reduce the force.

(2) The shock wave decayed with the spread along the launch box, but for this kind of launching mode, the influence caused by the shock wave will interfere with the launching and the flying trajectory when the missile is launched.

(3) For the two guides in the box, the back guide was effected by the thermal effects and erosion effects would last till the missile flied out of the box. However, the front guide has less affected. So for the back guide design, corrosion resistance and high temperature anti-oxidation ability of alloy should be used.

(4) For the walls of the box, the pressure at the corner is much larger than the middle part. And in the lower pressure environment, the airflow was entrainment into the gap between the box and the missile, which would produce a negative pressure lead to the force acted on the box increased largely. So the double-decker which for the outside tube is square and the inner is circular may be take into consideration.

References

1. Zhao, C.-Q., Jiang, Y.: The Dynamics of The Jet Flow. The publishing company of the Beijing institute of the technology (in press)
2. Wang, F.-J.: The computational fluid dynamic. The publishing company of the Tsinghua University (in press)
3. Jiany, Y., Geng, F., Zhang, Q.: Numerical Calculation & Experiments for the Opening Process of Missile Launcher's Cover. Journal of Ballistics 20(3), 33–35 (2008)

4. Miao, R.-S., Ju, X.-M.: Gas Dynamics for Rocket. National Defense Industry (in press)
5. Fu, D.-B., Liu, Q., Chen, J.-W.: Numerical Simulation on Missile Launching Procedure. Journal of Ballistics 16(3), 11–15 (2004)
6. Li, X.: Characteristic Analysis of Missile Combustion-Gas in a Launching-Container (Launching-Tube)—Hot Experiment Study. Journal of Astronautics

Cracked-Shell Detection of Preserved Eggs Based on Acoustic Response and Bayes Theory in Mechanical Engineering

Zhihui Zhu, Lanlan Wu, Lirong Xiong, Daodong Hu, and Youxian Wen

College of Engineering, Huazhong Agricultural University, Wuhan, Hubei 430070, China
zzhlsx@sohu.com

Abstract. The cracked-shell detection of preserved eggs based on acoustic response and bayes theory in mechanical engineering was implemented. The acoustic response signals were captured and analyzed based on power spectrum and five parameters (the area of the power spectrum, the amplitude of resonance peak, the formant frequency, the average amplitude of resonance peak, the range of amplitude of resonance peak) were extracted as characteristic parameters. The discriminative models were established by bayes theory. The testing result shows that the method is capable of the cracked-shell detection of preserved eggs with best classification accuracy was 87.5%.

Keywords: Preserved egg, cracked-shell, detection, acoustic response, bayes, mechanical engineering.

1 Introduction

Preserved egg is a kind of the egg which has particular flavor and rich nutrition. The cracked-shell of preserved egg has a serious effect on the quality of it, and therefore during the process of its manufacturing, the examination and elimination of broken eggs are the key procedures. At the present, we mainly adopt artificial examination which means mass manpower; low production efficiency and can not match the requirement of the manufacturing. Many researches on eggshell crack detection of fresh eggs by machine visions [1-3] , acoustic response [4-8] was reported in recent year. Few reports focused on nondestructive testing of preserved egg. Compared to the fresh egg, the contents of preserved egg are black coagulation status which is difficult to detect by the reflection light and the transmission light; and the stains on the surface are deep which it will cause errors of detection based on machine vision. Taken together, acoustic response was used to detect cracked preserved egg. Power spectrum of normal preserved egg and cracked preserved egg was comparatively analyzed to determine character parameters. The discriminant model was established by Bayes theory.

2 Materials and Methods

2.1 Testing Material

One hundred intact preserved eggs were supplied by Hubei Shendan Health Food CO., LTD. in China. These preserved eggs were numbered. We randomly chose, 60

D. Jin and S. Lin (Eds.): Advances in Mechanical and Electronic Engineering, LNEE 176, pp. 71–77.
springerlink.com

preserved eggs were used to build the model and the remaining 40 eggs were put aside for testing set. The 100 intact eggs were cracked by man-made knocking to be regards as the cracked eggs.

2.2 Testing System

The hardware device of the testing system was composed of the knocking equipment, the audio response acquisition equipment and the computer processing (shown in Fig.1). The knocking equipment was consisted of epoxy impacted head, a proximity switch and a buffer device [9]. The audio response acquisition equipment was composed of a mini microphone and a PCI128 digital sound card. The acoustic impulse signal was collected to be conducted by the computer.

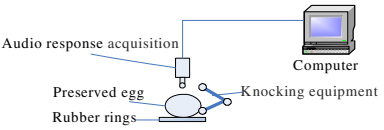

Fig. 1. Cracked detection system

2.3 Testing Method

The preserved eggs were knocked uniformly and moderately at the big end, the middle end and the small end respectively. The sampling frequency was 24000 Hz. The 128 points of the each sound signals were recorded respectively. Then the eggshell of the each normal preserved egg was cracked by man-made knocking. Similarly, the sound signal of the cracked eggshell was collected by the former knocking testing. The sound signal data were processed by filter and presented further for the power spectrum analysis. By comparing power spectrum profiles of normal eggs and cracked eggs, the characteristic parameters were extracted for eggshell crack detection.

2.4 Characteristic Parameters Extraction

The power spectrum of the normal preserved egg and cracked preserved egg was shown in the Fig.2 and Fig.3. It was found that there were many differences in the average area of power spectrum, the amplitude of resonance peak and the formant frequency. According to preliminary research results of Research Group [10], the three parameters were taken as the characteristic parameter. They were expressed as following:

Area of the power spectrum (Area):

$$Area = \sum_{i=0}^{k} P_i \tag{1}$$

Where P_i: amplitude of power spectrum at its frequency; i: number of egg signal frequency (i=0,1,2,...,k).

The amplitude of resonance peak ($P_{i.max}$):

$$P_{i.max} = max \ P_i \tag{2}$$

Where $P_{i.max}$: the maximum amplitude of power spectrum at its frequency; i: number of egg signal frequency (i=0,1,2,...,k)

The formant frequency (Fres):

$$Fres = F\left(P_{i.max}\right) \tag{3}$$

The three characteristic parameters could be obtained respectively from MATLAB function library when the eggshell was knocked at the big end, the middle end and the small end every time. Thus, the average and range of three times characteristic parameters were taken as the characteristic variables as followings:

(1) the average area of the power spectrum (x_1):

$$x_1 = \frac{1}{3}\sum_{i=1}^{3}\left(Area\right)_i \tag{4}$$

Where i: number of impacts, i=1,2,3

(2) the range of the power spectrum area (x_2):

$$x_2 = max\left[\left(Area\right)_i\right] - min\left[\left(Area\right)_i\right] \tag{5}$$

(3) the average amplitude of resonance peak (x_3):

$$x_3 = \frac{1}{3}\sum_{i=1}^{3}P_{i.max} \tag{6}$$

(4) the range of amplitude of resonance peak (x_4):

$$x_4 = max\left(P_{i.max}\right) - min\left(P_{i.max}\right) \tag{7}$$

(5) the average value of the formant frequency (x_5):

$$x_5 = \frac{1}{3}\sum_{i=1}^{3}\left(Fres\right)_i \tag{8}$$

(6) the range of the formant frequency (x_6):

$$x_6 = max\left[\left(Fres\right)_i\right] - min\left[\left(Fres\right)_i\right] \tag{9}$$

The variables $x_1, x_2, x_3, x_4, x_5, x_6$ were regarded as the candidates characteristic variables for the identification between the normal preserved eggs and the cracked preserved eggs. The sixty normal preserved eggs and sixty cracked preserved eggs were analyzed with the six variables in order to choose characteristic variables with sizeable difference.

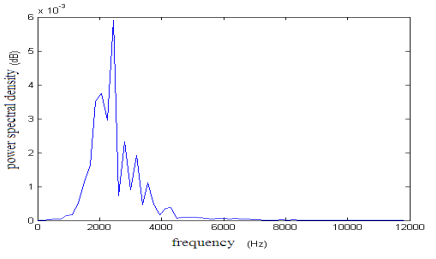

Fig. 2. The power spectral density ofan intact egg

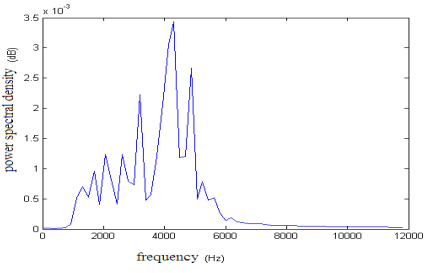

Fig. 3. The power spectral density of a cracked egg

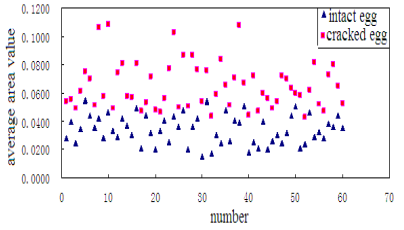

Fig. 4. Comparison of the power spectral average area value

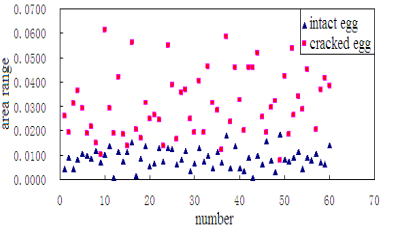

Fig. 5. Comparison of the power spectral area range

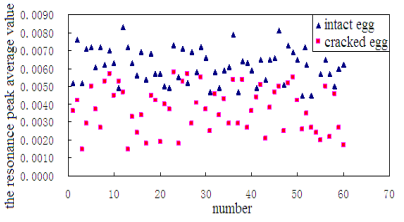

Fig. 6. Comparison of the resonance peak average value

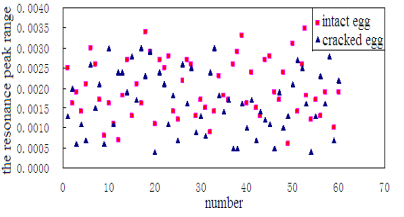

Fig. 7. Comparison of the resonance peak range

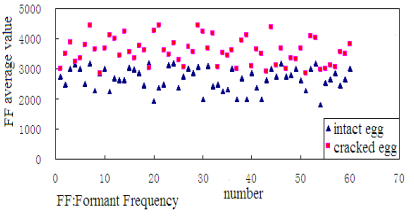

Fig. 8. Comparison of the formant frequency average value

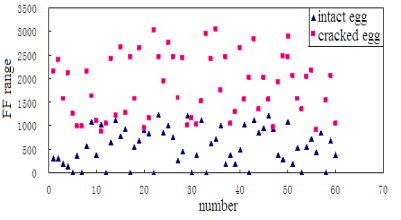

Fig. 9. Comparison of the formant frequency range

From Fig.4, 5, 6, 8, 9, there was obvious difference between the normal preserved eggs and the cracked preserved eggs. From Fig.7, there was no significant difference in the resonance peak range between the normal preserved eggs and the cracked preserved eggs. Therefore, according to above analysis, the parameters including the average area of the power spectrum (x_1), the range of the power spectrum area (x_2), the average amplitude of resonance peak (x_3), the average value of the formant frequency (x_5), and the range of the formant frequency (x_6) were chose as characteristic parameters for establishing the discrimination model; and the resonance peak range (x_4) was not chose as the characteristic variable.

2.5 Discriminant Modeling

Supposing each sample indexed by n parameters $x_1, x_2, x_3, ..., x_n$, belongs to one of K classes $G_1, G_2, G_3, ..., G_K$, using Bayes discriminant rule to distinguish to which class a given random sample denoted $X = (x_1, x_2, x_3, ..., x_n)$ belongs, the discrimination error will be minimized. Bayes discriminant rule was explained as following:

Supposing the probability densities of the sample X of $G_1, G_2, G_3, ..., G_K$ are $f_1(x), f_2(x), f_3(x), ..., f_K(x)$ respectively and the prior probability of X belonging to one of K categories G_i is P_i and the conditional probability for the occurrence of X given that G_i has occurred is $P(X \mid i)$. According to the method of total probability calculation, the total probability of X occurrence is:

$$P(X) = \sum_i P_i \cdot P(X \mid i) \tag{10}$$

According to Bayes formula, the posterior probability of belonging to one of K categories G_h is

$$P(h \mid X) = \frac{P_h \cdot P(X \mid h)}{\sum_i P_i \cdot P(X \mid i)} = \frac{P_h \cdot f_h(x)}{\sum_i P_i \cdot f_i(x)} \tag{11}$$

The denominator in the above formula is fixed, so the larger the numerator, the greater the probability $P(h \mid X)$. Suppose:

$$\eta_h(X) = P_h \cdot f_h(x) \tag{12}$$

After calculating $\eta_h(X)$ one by one, it will be decided whether X belongs to G_h according to the following formula:

$$\eta_{h^*}(X) = \max_h \eta_h(X) \tag{13}$$

3 Results and Discussion

The samples used in the experiment were consisted of 200 preserved eggs, including 100 normal preserved eggs and 100 cracked preserved eggs. 60% of the samples to build discrimination function (60 normal preserved eggs and 60 cracked preserved eggs) and the remaining 40% was put aside for testing set. According to above analysis, The five characteristic parameters including the average area value of the power spectrum (x_1), the power spectral area range (x_2), the resonance peak average value (x_3), the formant frequency average value (x_5), the formant frequency range (x_6) were chose as the variables of the distinguishing model. The discriminative model was established as following by the software SAS:

The distinguishing model of normal preserved eggs was as following:

$$G_0 = -45.77363 + 124.8584x_1 + 256.0067x_2 + 4890x_3 + 0.01894x_5 + + 0.0073x_6 \tag{14}$$

The distinguishing model of cracked preserved eggs was as following:

$$G_1 = -85.0123 + 288.33656x_1 + 4162933x_2 + 2923x_3 + 0.02831x_5 + 0.01423x_6 \quad (15)$$

The test of differentiating effect for multiple of the distinguishing model was shown in the Table.1. From Table.1, it was remarkable by F tests. In addition, distribution for statistics χ^2 inspection was carried out, n=120, p=5, k=2, λ=0.1141 $p \cdot (k-1) = 5$, $\chi^2 = -\left[(n-1) - \frac{1}{2}(p+k)\right] \ln \lambda = 250.7358$, and the threshold value $\chi^2_{0.01}(5) = 15.1$, $\chi^2 > \chi^2_{0.01}(5)$ .Therefore, the result of distinguishing function shows highly significant.

Table 1. Statistics of Wilks, Lambda

Statistics	DF of parameters	DF of observed value	F Value	Pr>F
Wilks' Lambda	5	114	177.06	<0.0001

DF:degree of freedom.

To test the result of the distinguishing models, 40 normal preserved eggs and 40 cracked preserved eggs were used for testing. The detection accuracy of the normal preserved model and the cracked preserved model were 90% and 85% respectively. The overall accuracy was 87.5%. The test found that the result was affected by the size of the preserved egg, crack size of the egg shell and the range between the crack and knocked location. If we add the number and the location of the knocking, it may reduce the error by knocking at nonsensitivity of the crack.

4 Conclusion

In this study, acoustic response techniques was used for eggshell cracks detection of preserved eggs. The power spectrum analysis was adopted for the acoustical signals. The results show that there are big differences in the average area of the power spectrum, the average amplitude of resonance peak and the formant frequency between the normal preserved eggs and the cracked preserved eggs. Therefore, The five characteristic parameters including the average area value of the power spectrum (x_1) ,the power spectral area range (x_2) , the resonance peak average value (x_3), the formant frequency average value (x_5), the formant frequency range (x_6) were chose as the variables of the distinguishing model. The discriminative model was established based on the Bayes theorem. The results of differentiating effect for multiple of the distinguishing model show that the model is effective.

Acknowledgments. This work was supported by the Fundamental Research Funds for the Central Universities (Grant No. 2010QC008). The authors would like to thank the reviewers of this paper for their constructive comments and advice, which greatly helped us to improve the quality of the paper.

References

1. Goodrum, J.W., Elster, R.T.: Machine vision for crack detection in rotation eggs. Trans. ASAE 35, 1323–1328 (1992)
2. Pan, L.Q., Tu, K., Su, Z.P.: Crack detection in eggs using computer vision and BP neural network. Trans. CSAE 23, 154–158 (2007)
3. Lawrence, K.C., Yoon, S.C., Jones, D.R., Heitschmidt, G.W., Park, B., Windham, W.R.: Modified pressure system for imaging egg cracks. Trans. ASABE 52, 983–990 (2009)
4. De Ketelaere, B., Coucke, P., De Baerdemaeker, J.: Eggshell Crack Detection based on Acoustic Resonance Frequency Analysis. J. Agric. Eng. Res. 76(2), 157–163 (2000)
5. Coucke, P., De Ketelaere, B., De Baerdemaeker, J.: Experimental analysis of the dynamic, mechanical behaviour of a chicken egg. J. Sound Vib. 266, 711–721 (2003)
6. Cho, H.K., Choi, W.K., Paek, J.H.: Detection of surface cracks in shell eggs by acoustic impulse method. Trans. ASAE 43(6), 1921–1926 (2000)
7. Bamelis, F.R., De Ketelaere, B., Mertens, K., Kemps, B.J., Decuypere, E.M., De Baerdemaeker, J.G.: Measuring the conductance of eggshells using the acoustic resonance technique and optical transmission spectra. Comput. Electron. Agric. 62, 35–40 (2008)
8. Lin, H., Zhao, J.W., Chen, Q.S., Cai, J.R., Zhou, P.: Eggshell crack detection based on acoustic response and support vector data description algorithm. Eur. Food Res. Technol. 230, 95–100 (2009)
9. Wang, S.C., Ren, Y.L., Chen, H., Xiong, L.R., Wen, Y.X.: Detection of cracked-shell eggs using acoustic signal and fuzzy recognition. Trans. CSAE 20(7), 130–133 (2004)
10. Zhou, P., Liu, L.Y., Wen, Y.X.: Nondestructive testing of cracked-shell duck-eggs based on support vector machine. Trans. CSAM 39(1), 195–200 (2008)

The Clustering NIGA for Solving the Nesting Problem in the Hull Construction Automatic Nesting System

Ying Mei

Computer and Information Engineering Department
Guangzhou Maritime High College
Guangzhou, 510725, China
yzsmcg@sina.com

Abstract. For improving the nesting efficiency, the clustering idea and algorithm are introduced and the effective characteristics of matching nesting-graphics are extracted and analyzed. The paper discusses the irregular parts nesting problem based on an improved immune genetic algorithm, and a NIGA based on crowing mechanism is proposed. GA, an improved immune genetic algorithm, and NIGA are applied to practical experiments respectively to solve the nesting problem and optimize the results, and we compare the results. In solving the large-scale nesting problem, the application of immunity operator and niche genetic algorithm based on crowing mechanism improves the global optimization performance and velocity of convergence. The improved algorithms based on the clustering idea are effective and feasibility for solving the hull construction automatic nesting problem.

Keywords: nesting optimization, clustering idea, niche skill.

1 Introduction

The optimized solution of 2D nesting problem (the nesting problem of the large-scale regular nesting-graphics and irregular graphics) is based on the stochastic algorithm, and in particular, with the increasing of dimensions of regular nesting-graphics and irregular graphics, the complexity of computation increases rapidly. How to increase the time of nesting and improve the utilization ratio of materials is the focus and we try to find an appropriate balance point between them as the final choice.

The study is to find a fast convergent stochastic algorithm (the heuristic algorithm). We use an improved niche immune genetic algorithm (NIGA) to avoid the shortcoming of prematurity convergence of genetic algorithm, and use it to solve the irregular graphics nesting problem in the hull construction automatic nesting system.

In the study of the nesting optimized algorithm of the hull building automatic nesting system, we find that the same type graphics can be contact in nesting. So we practice clustering analysis for irregular graphics at first. Effective data features of matching nesting-graphics are extracted and analyzed: the area, the coverage rate of enveloping rectangles (the coverage rate of enveloping circle) and the approximately ratio of long axes and short axes are brought out to make sure that the characteristics

D. Jin and S. Lin (Eds.): Advances in Mechanical and Electronic Engineering, LNEE 176, pp. 79–84.
springerlink.com

of nesting-graphics are extracted effectively. And the paper designs the clustering algorithm that adapt to nesting of matching-graphics. After clustering, we use an improved niche immune GA for solving the nesting problem.

2 Extraction of the Characteristics of the Nesting Graphics

Definition 1: The minimum enveloping rectangle. The set of enveloping rectangle area is:

$$S_{exre} = \{l_i \times w_i \,|\, (l_i, w_i) \in V_{exre}\}, i = 1, 2, ... |V_{exre}|$$

So the minimum enveloping rectangle area is:

$$S_{\min exre} = \min\{S_{exrei} = l_i \times w_i \,|\, (l_i, w_i) \in V_{exre}\}$$

And the minimum enveloping rectangle is:

$$(l_{\min s}, w_{\min s}) = \arg_i (S_{\min exre}), i = 1, 2, ..., 180^\circ / k^\circ$$

$$(l_{\min s}, w_{\min s}) = \arg_j (\min\{S_{exrej} = l_j \times w_j \,|\, (l_j, w_j) \in V_{mexre}\}), i = 1, 2, ..., |V_{mexre}|$$

Here, $|V_{mexre}|$ means the number of the bitmap's matching enveloping rectangle set.

Definition 2: The coverage rate of enveloping rectangles. The value of ratio between the bitmap area S_{raw} and the bitmap minimum enveloping rectangle area $S_{\min exre}$ is defined as the coverage rate of enveloping rectangle area. $\rho = S_{raw} / S_{\min exre}$. Obviously, $o < \rho \le 1$.

Definition 3: the approximately ratio of long axes and short axes.
$\lambda = l_{\min s} / w_{\min s}$. Obviously, $\lambda \ge 1$.

The clustering characteristics of the nesting graphics are the area, the coverage rate of enveloping rectangles and the approximately ratio of long axes and short axes. The area reflects the size of the graphics; the coverage rate of enveloping rectangles reflects the regular degree of the graphics and the cavity existence probability; the approximately ratio of long axes and short axes shows that the graphics is likely the square or the strip. The three characteristics are the strong characteristics for clustering.

3 The Clustering Algorithm for Nesting of Matching-Graphics

With the analysis of the nesting problem, we introduce the subtractive clustering. For getting the proper clustering center and ensuring the meaningful and practical clustering results, the parameters in the subtractive clustering is modified correspondingly.

We want to get the graphics clustering results with strong similarity in nesting graphics clustering. Namely, the area, the coverage rate of enveloping rectangles (the coverage rate of enveloping circle) and the approximately ratio of long axes and short axes are similar for the clustering results. So, the choice when we use the subtractive clustering in MATLAB fuzzy toolbox is as the following:

The small clustering influence scope: The radius is 0.3;
To ensure enough clustering center: accept Ratio is 0.5, reject Ratio is 0.
The subtractive software package in MATLAB toolbox only finds the clustering center. We calculate the minimal distance from each point to the clustering center and get the category $C(x_j)$. The c clustering points are $w_i, i = 1,2,...,c$,

$$c(x_j) = \arg_c(\min\{\|x_j - w_i\|^2, i = 1,2,...,c\})$$

The application of clustering results in the paper is as the following:
The initial solution of the NIGA doesn't generate randomly (or the big graphics don't pack first.). One of the results uses the method that the graphics of the same category are nested together.

4 The Irregular Graphics Nesting Algorithm Based on the NIGA

4.1 Problem Description

The goal of 2D nesting cutting problem is to put more parts without overlaps in the given sheets and get the maximal utilization of materials. They are all NP-hard problems.

The goal is to put more parts ($\{p_1, p_2, ..., p_t\}, 1 \le t \le n, n$ is the number of nesting parts) without overlaps in the given rectangle sheets (L_S, W_s) and get the maximal utilization of materials. t is the number of actually nesting parts; the goal is to maximize the utilization ratio of materials, and the residual materials can be reused. So, the goal of solution is

$$Object = \max\{\sum_{j=1}^{t} S_{pi} / W_u * L_u\}, 0 < W_u \le W_s, 0 < L_u \le L_s$$

Here W_u, L_u is the maximum width and length that the nesting parts occupy the nesting area from the left-bottom point of the nesting area.

4.2 Coding, Fitness Function and Nesting Principle

We use the decimal system coding. One nesting graphics is called one integer series I_1, $I_1 = \{p_{11}, p_{12,\cdots,} p_{1n}\}$, which is composed by the parts serial number. Each integer represents one irregular graphics, and the positive integers represent that the parts is not rotated. The negative integer represent that the parts is 90 degree rotation.

The fitness function is as the following:

$$Fitness(I_i) = Object = \max\{\sum_{j=1}^{t} S_{pi} / W_u * L_u\},$$

$$0 < W_u \le W_s, 0 < L_u \le L_s$$

Here, I_i means the coding of the individual i.

We use bottom-left principle as the nesting principle: the nesting parts' position $(x, y) = \arg\{\min\{L_i\}\}$ or $\min\{W_i, when \arg\{\min\{L_i\}\}\}$ is not unique. Here, (x, y) is the top left coordinate. L_i and W_i is the occupied material's maximal length and width after nesting i parts.

4.3 Problem Solving

The selection operator: the selecting operation introduces the similarity operator and the concentration operator, and it uses the conception of information entropy. It's as the following:

$$A_{apI_1I_2} = \sum_{j=1}^{n} W_j V_j$$

$$V_j = \{1, p_{1j} = p_{2j}; 0, p_{1j} \ne p_{2j}\}$$

Here, W_j is the weight when we form the similarity operator, and it means the number on the j position is the same. If the times are h that the number on the front corresponding positions is continuously same, the weight of the similarity is $h+1$. The original selecting operation in proportion is changed into the following selection rate:

$$S_{I_i} = \frac{fitness(I_i)\prod_{t=1}^{m}(1 - A'_{I_iI_t})}{c_{I_i}\sum_{j=1}^{m} fitness(I_j)}$$

Here, $A'_{I_iI_t} = \{A_{I_iI_t}, A'_{I_iI_t} \ge A_{g2}; 0, A'_{I_iI_t} < A_{g2}\}$, and A_{g2} is the given threshold. According to the irregular graphics nesting problem, we need to have an accurate similarity definition. We can consider the different rotation angle or turnover mark when we get the individual similarity. For example:

I_1

1	25	1	2	25	1	3	15	1	4	25	0	5	80	1

I_2

1	25	1	2	25	1	3	15	1	4	25	0	5	80	1

I_3

1	25	0	2	25	1	3	25	0	4	25	1	5	80	1

In anterior simplified discussion, $A_{apI_1I_2} = A_{apI_1I_3} = 15$. Here, $\gamma_i = 1$. And we have the modified definition: if the corresponding parts' position coding number is the same but the rotation angle or turnover isn't the same, the similarity operator need to subtract 0.6(reference value). At this time, $A_{apI_1I_2} = 15, A_{apI_1I_3} = 13.8$. It can show that the modified similarity definition embodies the similarity degree between the individuals.

In solving the irregular graphics nesting problem, we comprehensively consider the fitness degree and similarity degree to decide which individual can be chosen. The paper reserves the anterior m/3 with the high fitness value and the anterior m-m/3 with the low concentration value for the individual selection.

The improved Niche Immune GA:

We also consider using the niche technology based on the crowing mechanism in the improved immune genetic algorithm for optimal selection. The algorithm is as the following: (1) To generate N initial antibody to form the initial population, and get every individual's similarity and fitness. Then preserve the first N / CF (in the paper, $CF = 3$) individuals with high fitness and preserve the first $N - N / CF(N < M)$ individuals with low similarity for implementing the individual selection and forming the antibody population. (2) GA evolves the antibody population. Selection operation, calculate the individual I_i selection rate according to the fitness and similarity; crossover operation; mutation operation. (3) The niche technique selection operation. (4) Termination criterion. If it doesn't meet the terminal conditions, the first N individuals in step (3) are regarded as the new next generation population and go to the step (2) for further operation; if it satisfies the termination, we'll get the optimal result. The algorithm ends.

5 Testing

5.1 The Example Description and the Results Comparison

The irregular parts nesting example:

For a group of irregular graphics, the clustering idea is applied first. We use GA, the improved immune GA and the improved niche immune GA for the nesting problem, the results is as the following graphics:

Here, m=13, the convergence generation of GA and advanced GA is 87 and 78, the material utilization ratio is 79.8%.

5.2 The Analysis of the Experiment Results

We practice clustering analysis for irregular graphics at first. When we respectively use the GA, the improved Niche Immune GA, the latter can fast skip from local optimization. When the population size is larger, the latter algorithm has better global optimization and the convergence rate.

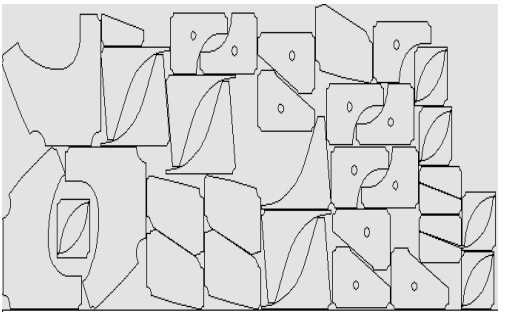

Fig. 1. Example of results of irregular graphics nesting

6 Conclusion

The clustering idea and algorithm for improving the nesting efficiency are introduced in the paper, and effective characteristics of matching nesting-graphics are extracted and analyzed. For solving the irregular parts nesting problem in the hull building automatic nesting system, the paper introduces an improved immune GA and the niche technology. By comparisons of more experiments, in the large-scale irregular parts nesting process, the NIGA can find satisfied nesting results fast and stably, and at the same time we can improve the efficiency of the material cutting to a certain degree.

References

1. Song, Y.-N.: Study of Algorithm of Graphic-Matching, Control of Nesting and Contacting in Two-Dimensional Nesting System. South China University of Technology, Guangzhou (2004)
2. Si, W., Ju, C.: Optimal Layout of Silicon Steel Sheet Based on Niche Immune Genetic Algorithm. Computer Engineer 5, 181–183 (2008)
3. Zhang, Z.-Z., Zhang, W.-Y.: A Novel Niche Genetic Algorithm of Accurate Optimization Performance. Computer Applications 8, 1903–1905 (2005)
4. Shi, J.-Y., Feng, M.-G.: Niche Genetic Algorithm for Two Dimensional Irregular Parts Optimal Layout. Journal of Engineer Design 4, 171–174 (2007)
5. Jiang, X.-B., Lv, X.-Q., Liu, C.-C.: Improved Genetic Algorithm for Nesting Problem of Rectangles. Computer Engineering and Applications 44(22), 244–248 (2008)

The Research on Secondary Development of Parametric System of Cylindrical Gear Reducer Based on Pro/E

Rongzheng Xu

Henan Polytechnic Institute, Nanyang Henan, China
Hygy2011@126.com

Abstract. This paper constructed the shaft parts in the middle of cylindrical gear reducer and three-dimensional model of components by using Pro/E, compile the corresponding application program of Pro/TOOLKI to access the design results of parametric system and other relevant code, finally realized virtual design and assembly of shaft parts and components, and add user interface, such as custom menu and menu item and dialog etc., according to the user's choose, displayed the corresponding parts or component model.

Keywords: cylindrical gear reduce, Parameter, Pro/E, secondary development, code, data.

1 The Basic Principle of Parametric Program Designation

The basic principle of parametric program designation make by three-dimensional model and process control with combined method.Three-dimensional model is not created by the program, but is generated by interactive way.According to the requirements of design further, then established a set of design parameters who can control the shape and size of 3d model fully on the basis of the parts of three-dimensional model which have been created on.Parametric programs make programming for design parameters of this parts, and derived new 3d model by modifying design parameters.The realization shown in Figure 1:

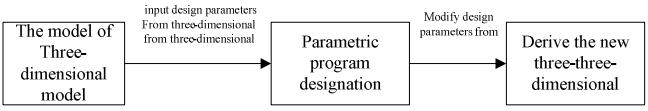

Fig. 1. The implementation process of the parametric design based on the three-dimensional models

The model of three-dimensional model which established by man-computer in Pro/E is the same as the usual three-dimensional model, but must pay attention to the following.

D. Jin and S. Lin (Eds.): Advances in Mechanical and Electronic Engineering, LNEE 176, pp. 85–90.
springerlink.com

1.1 Realized the Whole Constraint of Geometrical Figure by Using These Relations

Such as dimensions and applying tangent, a fixed point, concentric and co-line, vertical and symmetry etc., when we have the feature modeling for the model of three-dimensional model.

1.2 Setting Design Parameters of Control Model Correctly

Design parameters can be divided into two categories:one is that the independent parameters are independent of the others, mainly used to control the relationship between geometry and topology of three-dimensional model;the other is that the non-independent parameters are related to the others, can be used the independent parameters as variable.In fact, parametric program designation uses the first one, for the second can not set parameter, but with equation directly.

1.3 Establishing the Relationship between Design Parameters and the Size of Three-Dimensional Model

When creat sketches, materials and other modified characteristics in Pro/E, the system will be named for constraint parameters automaticcally with default symbol, such as d0, d1, d2, ... the value controls the relationship between geometry and topology of three-dimensional model, is not concerned in the parameters which established by users. the design parameters which established by users enable to control three-dimensional model, so that must be assocoated.There are two methods:

(1)In creating and modifying the characteristics need to input value, input parameter name directly.Such as marked on the sketches or modify the size value, with parameter name instead of specific values.

(2) Creat a new relationship by using the fuctions of relations of Pro/E, make Pro/E system which create constraint parameter name automatically associated with design parameters.

2 Part of Code of the Model of High-Speed Larger Gears Regeneration

2.1 Write the Source Code

After adding the project settings, program framework design and initial function and end function, we can develop program which provided all the classes and functions by VC. If want to use Pro/TOOLKIT function in programming process, calls directly through adding corresponding header file.The main part of the application is composed of user-defined function, can calls directly in user_initialize () function, or calls through menu items in user_initialize () function definited.The former will be direct called when loading initialization of application, the latter will be called through choosing user program to add menu item in Pro/e system.The second method is the same as menu commands in Pro/e system itself, is the main operating ways for synchronous

Pro/TOOLKIT application.Set the developing environment under VC, compile the connection with Pro/TOOLKIT library function and VC class library, generate solutions.

2.2 Code Generation

Using Pro/TOOLKIT secondary development program can realize automatic regeneration for three-dimensional model which have been designed.Part of code of the model of high-speed stage gears regeneration, as follows:

……

```
status=ProMdlLoad(PartName, PRO_MDL_UNUSED, PRO_B_FALSE, &solid_mdl);

ProMdlCurrentGet(&solid_mdl);
status=ProMdlToModelitem(solid_mdl, &modelitem);
ParamUpdate(highModule, "mn", modelitem);
```

……

Among them ParamUpdate () function is user-defined parameters transfer function.The results of three-dimensional regenerating model of high-speed stage gears, shown in figure 2.

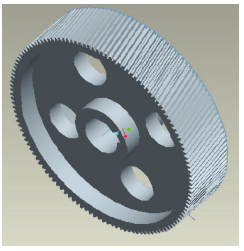

Fig. 2. The three-dimensional regeneration model of the high-speed stage gear

3 System Data Files

3.1 Programmed Graph

In engineering design, often encounter some chart for search coefficient or parameters, some are given in the form of curve.Programmed graph has the the following kinds of processing methods:

(1) Some chart would have been some precise formula, in order to facilitate manual design, then made the form for design check, for this kind of chart will strive to find the original theory calculation formula or empirical formula, compiled into application.

(2) The chart will be processed by simplified method.For example, calculate dynamic load coefficient Kv by using the coefficient, determinate that:

The simplified method Kv based on experience data, main consideration is gear manufacturing precision and the influence of line.According to experience, in the curve range of chart without considering the resonant.This method is especially suitable for Kv value which lack of details at the preliminary design stage.

3.2 Data Files Use

Data files use a text files who generated by "second cylindrical gear reducer parametric system", in the compile and run Pro/TOOLKIT, application .dll is generated, and after registered in [tools] / [auxiliary application program] of Pro/e, driving the model of three-dimensional model which established in Pro/e by using new design parameter, then generate shaft parts of three-dimensional model and component model after the design, the object which produced by each text file is instantiated through CStdioFile in c + +, realizing flow operation in different processes through the object is called corresponding function CStdioFile, such as Open (), Close (), WriteString () and ReadString () and etc.. For example, the size parameters of high-speed stage gear which designed from design system is transmitted to Pro/e to achieve its parametric model rebirth automatically, the process as follows:

The output code in"Secondary cylindrical gear reducer parametric system"is:

```
CString str=_T("E:\\GearReducer\\protk\\HighGear.txt");
CStdioFile highGearFile;
highGearFile.Open(str, CFile::modeCreat|CFile::modeWrite|CFile::typeText);
CString strtp;
strtp.Format(_T("%lf\n"), (double)m_iHighGearNum);
highGearFile.WriteString(strtp);
……
highGearFile.Close();
```

The code of design parameters which acessed from Pro/TOOLKIT application are:

```
CString str=_T("E:\\GearReducer\\protk\\HighGear.txt");
CStdioFile highGearFile;
highGearFile.Open(str, CFile::modeRead|CFile::typeText);
CString strtp;
highGearFile.ReadString(strtp);
double highGearNum=atof(strtp);
……
highGearFile.Close();
```

4 Pro/TOOLKITF Secondary Development Program

The design calculation of cylindrical gear reducer is a very typical process in the mechanical design, include calculation, experienced rules, deal with a large number, charts, and many back process, after careful analysis and summarized, we can found that it has obvious stages, can be expressed a series of chain sequence of design task.

In the application, add MFC ODBC, as follows:

(1) Open standard framework header files "StdAfx. J h", and add quote for"afxdb. J h" after the last #include:“#include<afxdb.h>//ODBC DataBase classes”.

(2) Under VC, with guide to add a new class drived from CRecordSet. the "Datasource"are"ODBC", and choose the data source who has been registered, “GearReducerDSN”, then choose a table of database which operated by records.

(3) Add the class statement of new drived recordset in header file which needed to use recordset, in a source document contains the header files of new derived recordset.

(4) In application added class object CDataBase, established connection with the data source, to construct derived class object CRecordset, call Open() member function, and after estabilishing recordset, can make various operations for data source.

After the registration file of secondary development application is registered and run in Pro/E, the shaft component assembly model which desiged by parametric system automatically generate as shown in figure 3, figure 4, and in the menu for Pro/E system, appears[shaft parts and components]menu of the secondary development program.

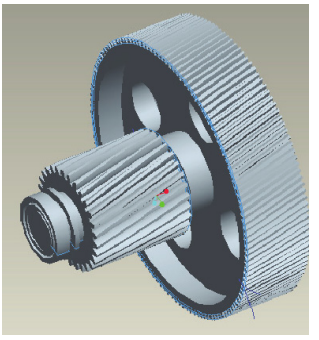

Fig. 3. The virtual assembly of the middle shaft components of the two-stage gear reducer-elical

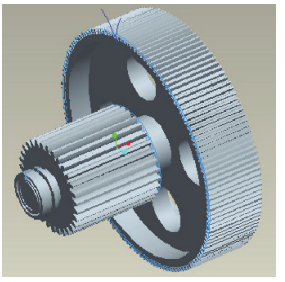

Fig. 4. The virtual assembly of the middle shaft components of the two-stage gear reducer—spur gear in gear type

5 Conclusion

Parametric modeling and secondary development technology, according to its characteristics of cylindrical gears reducer, under VC++ integrated development

environment, with Pro/TOOLKIT secondary development tools, to achieve conventional and reliability design for high and low-speed gear transmission of two-stage gear reducer-helical, and the virtual design of the middle shaft parts and the virtual assembly of the middle shaft components, and designed easy and convenient visual interface, which greatly improve the design efficiency, product quality and reliability, has a strong practical significance.

References

1. Wu, L., Chen, B.: Secondary development technique foundation of Pro/e. Electronic industry press (July 2006)
2. Charles, W.E.: Introduction to Reliability and Maintainability Engineering. Tsinghua university press (June 2008)
3. Min, L.: The CAD of the Gear Transmission System, vol. 2, pp. 2–6. Northeastern University (2003)
4. Song, L.: Two-stage gear reducer parametric CAD system, vol. 7, pp. 50–70. Taiyuan University of Science and Technology (2009)
5. Chen, S.: A 3D CAD System of involute planet gear reducer with parametric driving based on Pro/E, vol. 12, pp. 9–10. Dalian Jiaotong University, Dalian (2005)
6. Ge, X.: Initial reaearch on calculation method for gear dynamic load coefficient. Journal of Huainan Vocational & Technical College 3, 53–61 (2002)
7. Mort, R.L.: Machine Elements in Mechanical Design. 3, vol. 1, pp. 318–405. Mechanical industry press, Beijing (2004)
8. Shigley, J.E., Mischke, C.R., Budynas, R.G.: Mechanical Engineering Design. 7, vol. 4, pp. 280–337. Higher education press (2007)

Dual Optical Fiber Temperature Sensor Application in Mechanical Engineering

Yongzhe Yue[1], Zhanmin Zhao[2], and Ran Li[3]

[1] Institute of Information Science and Engineering,
Hebei University of Science and Technology
[2] Shi Jia Zhuang University of Economics
[3] Shi Jia Zhuang Information Engineering Vocational College

Abstract. This paper is based on the optical fiber temperature sensor.By studying temperature measurement of dual optical fiber with high precision, measurement method and data acquisition circuit are attained. It also studies how to design temperature monitoring in mechanical engineering, thus achieving good measurement results.

Keywords: temperature measurement of optical Fiber, Distributed, Double optical fiber, block diagram.

1 Introduction

In recent years, the sensor is being developed in the sensitive, accurate, adaptable, small and exquisite and intelligent direction. In this course, the optical fiber sensor as a new member of sensor family, is favored extremely. The sensing technology of optical fiber was developed rapidly with the development of optical fiber communication technology in the seventies of the 20th century, regarding light wave as carrier, optical fiber medium, aesthesia and transmit external world measure into new-type sensing technology of signal.

The light wave as the signal carrier and the optical fiber as the propagating media, have many unique advantages, other carriers and media are difficult to compare. The light wave does not produce interfering electromagnetically; it is not interfered electromagnetically, easy to be received by various kinds of devices, can conveniently change between electricity and light and is apt to match with the modern electronic device and computer of high development. Compared with traditional temperature sensor, the sensing component of the distributed optical fiber temperature sensor measuring system --optical fiber, regarding silica as main raw material, is very thin, soft and low loss, therefore has lots of intrinsic properties and essential security such as insulating electricity, ability of bearing the corrosives , geometry structure mutability , bandwidth of signal transmission transmits and low loss during the information transmission at a long distance. And the optical fiber works with bandwidth and dynamic heavy range. It is a fine transmission line with low loss that is suitable for telemeter measurement remote control. The optical fiber oneself is not only the function component of the temperature sensing, but also the information transmission pass way.

D. Jin and S. Lin (Eds.): Advances in Mechanical and Electronic Engineering, LNEE 176, pp. 91–94.
springerlink.com

This is incomparable to traditional sensor. Therefore, as soon as it comes out, the sensing technology of optic fiber is paid more attention. The range of its application is very extensive. It can be used in many fields, such as metallurgy, chemical industry, electricity , building materials ,etc to solve many problems of great electromagnetic interference and environment measurement and control in abominable occasions.

Because the manufacturing technology of optical fiber has been already comparatively ripe at present. Realization of making two optical fibers in the same protection membrane becomes very easy. Thus two optical fibers can experience the same environment to achieve the purpose of gathering a lot of measurement value at the same time. The measurement principle of one pair of optical fibers is as follows:

Two different optical fibers have been adopted as measuring sensor in the system of temperature measurement. At the time of measurement, two optical fibers carry on measurement at the same time with the light of different intensity or different frequency under control of the computer. The data of two optical fibers can change through AD converter at the same time and pass to the computer through PCI interface. In this way, the computer receives two groups of amount D_1 and D_2 and receives two pieces of temperature value through calculating namely T_1 and T_2. Two groups of data coming from AD converter can be dealt with to get D3, namely $D_3 = D_1 - D_2$. Thus we can find a corresponding temperature value to D_3, namely T_3. In this way, final temperature can be got according to the weights of T_1, T_2, T_3. The relation between amount and temperature is as Fig. 1 shows.

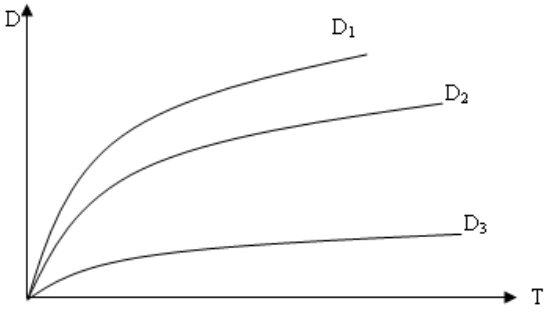

Fig. 1. The curve of data and temperature

2 Structure of Double Optical Fiber Temperature Measurement

Fig.2 shows the structure of double optical fibers temperature measurement. Because the two working courses of optical fiber are totally the same, one cause can be explained thoroughly.

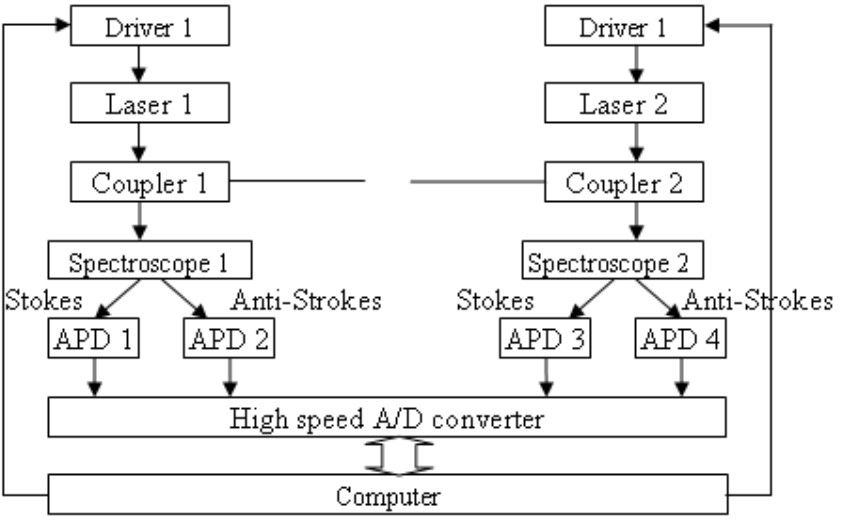

Fig. 2. Block diagram of distributed optical fiber temperature sensor

The systematic mechanism of temperature sensing of optical fiber is as follows: The computer controls and sends out the cycle electric signal of the pulse, the pulse of starting the semiconductor laser instrument (LD) drives the work of the power , driving the light source LD work of the semiconductor. The mere power of the pulse that LD sends out reaches the sensing optical fiber through directional coupler coupling. The sensing optical fiber places oneself in the midst of temperature field at the same time. Light pulse of spreading in the sensing optical fiber propagates scattered light caused on each point position in the course Stokes of the scattered light one of (Strokes and Anti-Strokes of Ramon) in undergoing back to scattering part. Through optical waves we can get the scattered light after strain and lose the auspicious profit with relatively strong energy, isolating anti-Strokes lighting loading with temperature information and Strokes light for reference. They are separately changed by photoelectric receiver APD, after enlarging leadingly and mainly enlarging received and changed by A/D converter at a high speed. The computer sends out the pulse to start the driving source of LD, starting digital signal deal at the same time(Digital Multi-Points Signal Averager, Store, Linear Accumulation of Cycle Signal). Then computer sends out the pulse again. Repeat above-mentioned course M times to realize the average figure, the noise suppression and SNR improvement. The distributed temperature measurement of examining temperature field can be finished by the corresponding relation of the signal and temperature, coordination in the show and operation of software.

The system consists of the optical part (including the power of pulse driving, directional coupler of optical fiber, sensing optical fiber, optical dividing devices, photoelectricity measurement), signal gathering and dealing part (including signal amplification, data gathering and transmit, digital multi-points signal averager) ,etc. Each part has its special request. Taking all the factors which could influence the temperature

sensibility into consideration, choose the best working wave length.Generally use avalanche photodiode APD (Avalanche Photodiode) as the component of the photoelectricity measurement to finish the faint Ramon's Anti-strokes and Strokes. Coming from the sensing optical fiber into electric signal.

3 Error Analysis of System

According to the law of error and their influence degree of the result, the error can divide into systematic error, random error and thick error, etc. Certain law appears in the systematic error, when really knowing the law of its influence factors, people can control or revise these errors. Therefore systematic error can be dispelled in measurement. The random error is caused by many unknown or small factors.

Under the measurement of equal-weighted, if the same parameter could be measured many times, the arithmetic mean of the random error will approach zero gradually.

The systematic error, like the multistage faint signal amplifier, causes small error brought by temperature drifts and AD to change the tiny error; the structure parameter of the optical fiber varies with temperature; the bending, shaking of optical fiber causes the small error and coupling error of optical fiber; the luminous intensity of the light source is unstable and the photoelectricity devices drift. All these could cause error. Though we can't totally dispel their influence, has already brought them down to the minimum limit. Concerning the gathering and dealing of the very faint signals, the system could be easily affected by external environment, for example vibration, etc. The experiment shows that the optical fiber and coupling place of optical fiber are extremely apt to produce the error influenced by external environment, the measurement accuracy and stability of the whole system could be affected greatly.

4 Summary

The optical fiber sensor has been widely used at present. Its development prospect is good. Besides temperature measurement, pressure, displacement, acceleration, etc. can be measured in this way. Furthermore, it is difficult to be interfered by the electromagnetic wave, it can be widely used in such fields as electricity transmit, oil exploitation ,etc. The results are all very good.

References

1. Chang, C., Li, Z., Zhou, Y.: Design of distributed temperature sensor system using raman back-scattering base engineering methodology. ACTA Photonica Sinica 30(1), 50–53 (2001)
2. Tanankam, Hotatek: Application of correlation-based continuous-wave technique for fiber Brillouin sensing to measurement of strain distribution on a small size material. IEEE Photon Technol. Lett. 14(5), 675–677 (2002)
3. Liu, R., Shi, J.: The Optical Fiber sensor and Application. China Machine Press, Beijing

Research on Production Agent Modeling of Ship-Repair Based on MAS

Li He[1,2], Xuewen Huang[2], and Xiaobing Liu[2]

[1] School of Mechanical Engineering, Shenyang Ligong University, Shenyang 110159, China
[2] CIMS Center, Dalian University of Technology, Dalian,116024, China
hl0404@163.com

Abstract. Firstly, the concept of Multi-Agent System (MAS) was described. Aiming at the current situation of ship-repair enterprises, the production Agent (PA) modeling of ship-repair enterprises was introduced, which is built on MAS. It includes three agents, Task Agent (TA), Resource Agent (RA) and Outer worker Agent (WA). It has been found that this modeling can improve the production efficiency and shorten the time of delivery.

Keywords: Production Agent, MAS, Modeling, Ship-repair.

1 Multi-Agent System Structure

Agent is a new computing model in the artificial intelligence field and can continually perceive the change outside and itself, and also can give a corresponding action by itself. Agent can perceive the environment via sensors and act on the environment via effectors. And can communicate and cooperate with each other and complete complicated tasks. Along with the development of computer network and communication, the technology about agent is not only a hotspot in artificial intelligence but in information technology, manufacture technology and some other fields. [1],[2]

A complex system maybe includes one or more interactional agent systems. This system is named Multi-Agent System (MAS). MAS denotes that one complex problem can be solved via cooperation, harmonization and negotiation of two or more agents together. MAS is considered as the key technique to lower production cost, realize decentralized production and self-adaption, and resolve complicated process. And it is also a new methodology, which runs through each modern advanced manufacturing field, from the dynamic alliance, distributed intelligent manufacture system, enterprises integration, Enterprise Resource Planning (ERP) to field control. [3]

There are three steps during developing MAS system. First, modeling the agent; and then internally structuring agent; and at last integrating agents and forming MAS. See Fig.1.

D. Jin and S. Lin (Eds.): Advances in Mechanical and Electronic Engineering, LNEE 176, pp. 95–100.
springerlink.com

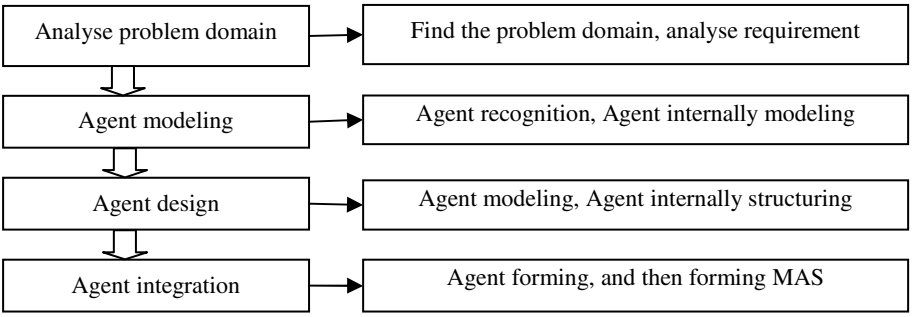

Fig. 1. Exploitative Truss of MAS

2 Current Situation

Ship is the important ocean resource in the future. Each country in the world develops the ship maintenance industry while develop the shipbuilding industry. In recent years, the ship maintenance center has been transferred rapidly to newly shipbuilding countries such as China and the four important ship maintenance centers in the world are Singapore, China, the Middle East and Western Europe. The ship-repair enterprises belong to a special industry which concentrates management, production, technology and service. The process of ship-repair has highly complexity because of the constantly changed task and different ship type and the short repair period. In general, the ship-repair belongs to individual production and includes numerous projects. It is difficult to plan for ship-repair enterprises.[4] With the development of computer technology, more and more ship-repair enterprises adopt high-tec to realize the integration of data stream, business flow and fund flow.

3 The Modeling of PA Based on MAS

The function of PA is planning the resources, which includes equipment, workers and production schedule. PA was built based on MAS, which includes Task Agent (TA), Resource Agent (RA) and Outer worker Agent (WA). Each agent defines its own rule according to its own task and characteristic and then put it in rule database which was packaged in agents. PA implements general scheduling and harmonizes the conflict between RA, WA and TA. PA can get the tasks and available resources according to the engineering order, and disassembles the engineering task received by repairing order into work order and then transmits it to TA, RA and WA. At the same time, PA records the information to the task table. The system inquires the unoccupied equipments via RA and available workers via WA. And then assign the task to suitable equipment and workers. Each TA, RA and WA register with registration form afforded during initialization.

In this paper, TA, RA and WA ensure the distribution of each task on each resource according to the inviting public bidding-bidding mechanism of CNP.[5] TA receives the information of unoccupied equipments and available workers from RA and WA after RA and WA evaluates throughput itself according by the task from PA. PA determines the equipment winning the bidding by the biding information, and sends the winning bidding information to TA and RA, and thus the whole inviting public bidding-bidding process can be completed. See Fig.2.

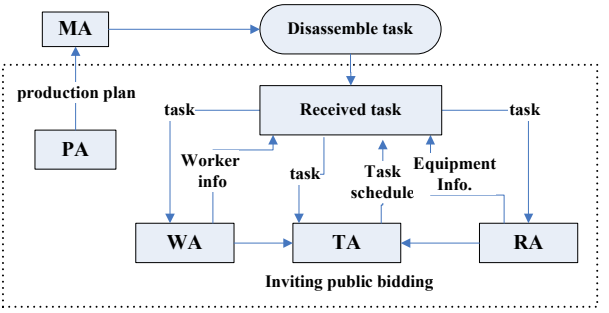

Fig. 2. The relationship of PA and MA

PA can get the information about tasks and available resources according to the registration form (see Table 1).

Table 1. Table of Registration

Machine-id	Machine-type	Worker-no	Registration-time	Note
1001001	1	16	11-08-10	
1001002	1	31	11-09-19	
1001003	2	04	11-12-16	
1001004	2	13	11-12-25	

Decompose the task received by contract information to form task information for TA and MA records it to the task table (see Table 2).

Table 2. Table of Plan

Plan-id	Plan -name	Due-date	Note
1000001	A	12-1-12	

PA collects bidding value of each RA and forms bidding table. Then, confirms the winning RA according to the bidding value and affords the machining contract made by contract table and the winning RA. The RA will be droved to machine workpiece (see Table 3 and Table 4).

Table 3. Table of Biding

Machine-id	Bid-number	Bid-value
1001001	1	1234
1001002	1	1324
1001003	1	1342
1001004	1	1432

Table 4. Table of Pact

Plan-id	Machine-id	Bid-number	Bid-value
1000001	1001001	1	1234

WA assigns the workers for suitable work. When there is not enough workers for the task, WA will hire new workers or brigade.

The modeling of PA sees Fig. 4.

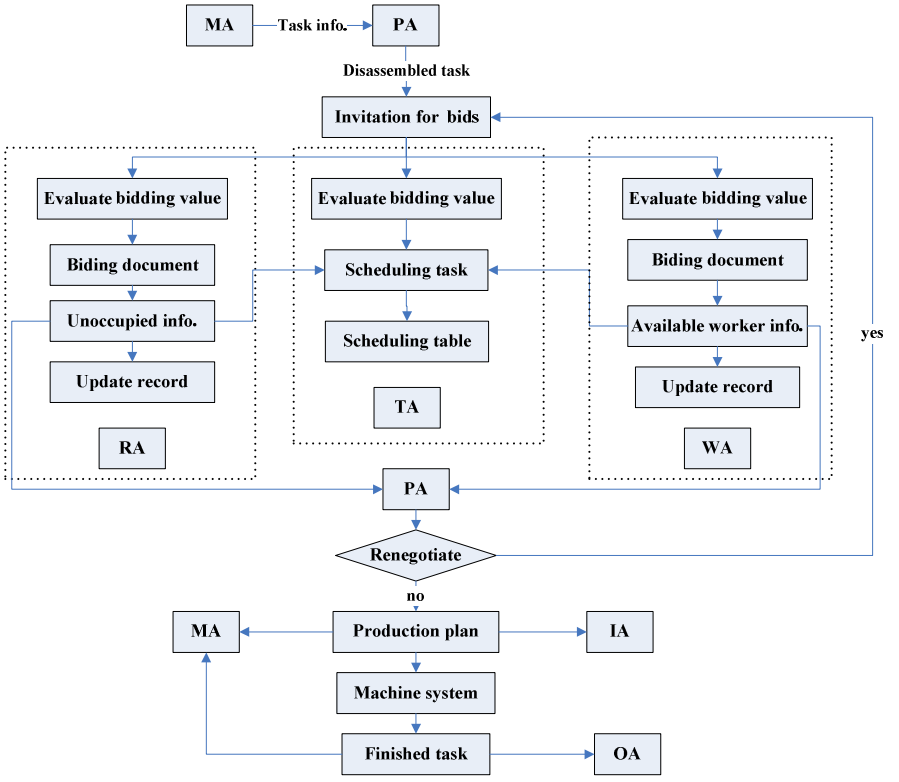

Fig. 4. The modeling of PA based on MAS

The structure of PA is the following:

<Production Agent>::=<information management><task management><resource management ><outer worker management>
<information management >::=<received information >< registered task><canceled task><registered resource>< canceled resource>
< Task management >::=< received task >< published task >< task condition >< new task >< urgent task >
<resource management>::=<resource name><resource number><resource condition><update resource>
< outer worker management >::=< brigade ><assigned task><unoccupied><needed><work type >< quality >< reward ><punishment>< remarks >
< feedback information >::=< task condition >< resource condition >< finished task >
< finished task >::=< machining quality >< machining time >< machining cost >
<record>::=<task number><task name><task content>< resource number and name>

(1) *RA*. It is built on client. After registration, RA begins to wait for inviting public bidding. When RA receives inviting public bidding document, it will evaluate the task according to production state and ability. Then computes a feasible bidding value and fills in the bidding document and sends it to PA (See Fig.5).

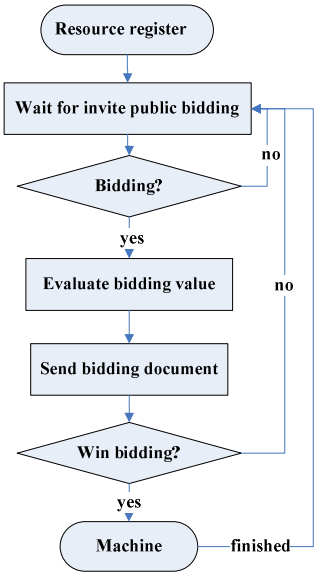

Fig. 5. Flow chart of RA

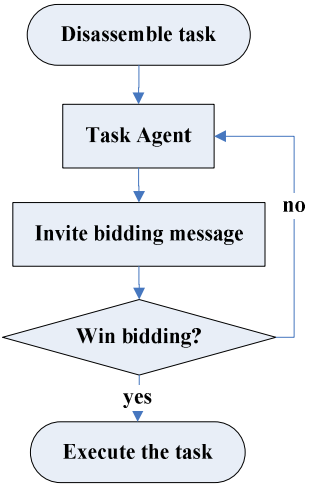

Fig. 6. Flow chart of TA

When RA receives the winning bidding message, the task will be scheduled on corresponding machine. After finish the task, RA will waiting for the next bidding. Also RA monitors and controls the machining process real time. If the normal state are changed, for example there are something wrong with certain machine or add new machines, RA immediately reports it to PA and PA will reschedule. The dynamic scheduling is finished.

(2) *TA*. TA answers for executing the whole production plan. It creates automatically and will be vanished automatically after finished one task. It can finish the distribution and execution of the plan via negotiation of each client and server. An incepting buffer and a sending buffer are packaged in each agent for communicating to other agents. The working flow sees Fig.6.

3) *WA*. There is a characteristic in the labour force management in almost all the ship-repair enterprises. Most workers are out workers. That is to say, they belong to certain engineering brigade. When the repairing task are so much or so urgent or some other condition that the existing hired workers can not be competent for the repairing work, the production management department will hire extra engineering brigade. WA is responsible for managing the engineering brigades and its workers. Instantaneously record the engineering brigade and its workers' information, contact NO, telephone number, the starting and ending time, amount of work, working hours, reward, punishment, specialties, and its equipments and so on.

5 Conclusion

The production modeling of ship-repair enterprises based on MAS can realized the information transmission and share instantly. TA, RA and WA can work in parallel and communicate and collaborate with each other. They complete each task according to the inviting public bidding-bidding mechanism of CNP. It has been found that this modeling can improve the production efficiency and shorten the time of delivery.

References

1. Qiu, X.L., Yi, H., Wu, X.Y., et al.: Apply Principal-Agent to actualize the Agile Manufacturing. J. Manufacturing Automation 22, 1–3 (2000)
2. Usher, J.M., Wang, Y.-C.: A Negotiation between Intelligent Agents for Manufacturing Control. In: 4th International Engineering Design and Automation Conference, pp. 511–519. IEEE Press, New York (2000)
3. Huang, Y.Q.: Research on the Agent and Feature Technology Based Distributed CAPP and Its Application in the Manufacturing of Hydraulic Press Machine, Ph.D. dissertation, Tianjin University, China (2002)
4. Sun, T., Li, J., Zhu, G.: Research and Design of ERP System in Dockyard. J. Transportation Science & Technology (2), 67–69 (2003)
5. Smith, R.G.: The contract net protocol: High-level communication and control in a distributed problem solver. IEEE Trans. on Computers (12), 1104–1113 (1999)

Q Parameterized Stabilizing Controller for Piecewise Linear Systems

Zhizheng Wu and Lu Wang

Department of Precision Mechanical Engineering, Shanghai University,
#149 Yanchang Road, Shanghai, China, 200072
zhizhengwu@shu.edu.cn

Abstract. This paper is considered to design a stabilizing switched controller for piecewise linear systems. The design of the proposed controllers involves a set of observer-based Q-parameterized stabilizing controllers for the switched systems and the stability of the resulting closed loop switched system with the Q-parameterized controllers is analyzed.

Keywords: Q-parameterized, stabilizing, piecewise linear systems.

1 Introduction

Recently, switched control systems have been attracting much attention in the control community since they present problems that are not only academically challenging, but also of practical importance. Switched systems are hybrid systems that combine various types of dynamic behavior, including continuous-time dynamics, discrete-time dynamics, switching and state variable jumps [1]. Among the large variety of problems encountered in practice, one can study the existence of switching rules that ensure stability of the switched system [2,3]. One can also assume that the switching sequence is not known a priori and look for stability results under arbitrary switching sequences [4,5]. Another important class of stability studies involve a finite number of piecewise linear systems together with a set of predefined switching rules [6,7]. Most of the literature on switched systems focuses the stability analysis for such systems. In practice, in additional to stability requirements, there is a need to find controllers that would achieve regulation or other optimal control performance against reference or disturbance signals. In this paper, a set of Q -parameterized all stabilizing controller design approach is presented for switched systems, based on which different control constraints can be easily added for achieving desired control objectives, i.e. exact regulation or optimal noise cancellation [8,9].

2 Parameterization of a Set of Stabilizing Controllers

Consider a piecewise linear system given by sets of state-space equations:

$$\sum_r : \begin{cases} \dot{x} = A_r x + B_r u, \quad x(0) = x_0 \\ y = C_r x, \end{cases} \tag{1}$$

D. Jin and S. Lin (Eds.): Advances in Mechanical and Electronic Engineering, LNEE 176, pp. 101–106.
springerlink.com

where $x \in \mathbb{R}^n$ is the state vector, $u \in \mathbb{R}^m$ is the control input, $y \in \mathbb{R}^s$ is the measurement signal to be fed to the controller and $r \in \{1, \ldots, i\}$. The system Σ_r is supposed to switch arbitrary or under predefined switching rules.

The controller design approach presented in this paper relies on the construction of a Q-parameterized set of output feedback stabilizing controllers for the switched system. Consider the following observer-based state feedback controller for the switched system:

$$\Sigma_r^o : \begin{cases} \dot{\hat{x}} = A_r \hat{x} + B_r u + L_r (\hat{y} - y), & \hat{x}(0) = \hat{x}_0, \\ u = K_r \hat{x}, \end{cases} \tag{2}$$

where $\hat{x}$ is an estimate of the plant state vector x and $\hat{y} = C_r \hat{x}$ is an estimate of the plant output y. The state feedback gains K_r, and the observer gains L_r, are assumed to switch arbitrary or according to a rule. Moreover, it is assumed that there are no impulsive changes in the controller states at the switching times. The construction of a Q-parameterized set of stabilizing controllers for the switched system (1) proceeds along the same lines as in the case of linear time-invariant systems [10]. Each controller is expressed as a linear fractional transformation involving a fixed system J_r and a proper asymptotically stable system Q_r that could be chosen as desired. The state space representation of the system J_r is given by:

$$J_r : \begin{cases} \dot{\hat{x}} = (A_r + L_r C_r + B_r K_r)\hat{x} - L_r y + B_r y_Q, & \hat{x}(0) = \hat{x}_0, \\ u = K_r \hat{x} + y_Q, \\ y - \hat{y} = y - C_r \hat{x}. \end{cases} \tag{3}$$

The Q_r parameter is given by:

$$Q_r : \begin{cases} \dot{x}_Q = A_Q x_Q + B_Q (y - \hat{y}), & x_Q(0) = x_Q^0, \\ y_Q = C_{Q_r} x_Q, \end{cases} \tag{4}$$

where $x_Q \in R^{n_q}$. In particular, throughout the rest of the paper, the Q_r parameter is such that A_Q is a fixed stability matrix, B_Q is a fixed matrix, and the matrix C_{Q_r} changes with $r \in \{1, \ldots, i\}$.

Let $\tilde{x} = \hat{x} - x$ denote the state estimation error and $\chi = \begin{bmatrix} x^T & x_Q^T & \tilde{x}^T \end{bmatrix}^T_{1 \times N}$ denote the state vector for the resulting closed loop system with $N = 2n + n_q$. The resulting closed loop system is given by the following state space representation:

$$\begin{bmatrix} \dot{x} \\ \dot{x}_Q \\ \dot{\tilde{x}} \end{bmatrix} = \begin{bmatrix} A_r + B_r K_r & B_r C_{Q_r} & B_r K_r \\ 0 & A_Q & -B_Q C_r \\ 0 & 0 & A_r + L_r C_r \end{bmatrix} \begin{bmatrix} x \\ x_Q \\ \tilde{x} \end{bmatrix}. \tag{5}$$

3 Stability of the Q-Parameterized Switched Closed Loop System

Consider now the three switched subsystems given by the following state equations:

$$\dot{x} = \left(A_r + B_r K_r \right) x, \tag{6}$$

$$\dot{\tilde{x}} = \left(A_r + L_r C_r \right) \tilde{x}, \tag{7}$$

$$\dot{x}_Q = A_Q x_Q. \tag{8}$$

Then, the internal stability of the switched closed loop system (5) is given by the following result.

Theorem 1: If the nominal switched systems (6) and (7) are each asymptotically stable under arbitrary switching and A_Q is a stability matrix, then the switched system (5) is also asymptotically stable under arbitrary switching. ❑

Proof: In the following, assume the initial time $t_0 = 0$. If the switched system (7) is asymptotically stable, then according to the definition and theorem 1, we have:

$$\left\| \tilde{x}(t) \right\| = \left\| \tilde{\phi}(t, t_0, \tilde{x}(0)) \tilde{x}(0) \right\| \le \tilde{c} \left\| \tilde{x}(0) \right\| e^{-\tilde{\lambda} t}, \tag{9}$$

for some $\tilde{c}, \tilde{\lambda} > 0$, where $\tilde{\phi}(t, t_0, \tilde{x}(0))$ is the state transition matrix of the switched system (7). Then, in (9), we have $\tilde{x} \to 0$ as $t \to \infty$ for any $\tilde{x}(0)$. Therefore, for the state variable $\tilde{x}$ in (5), we obtain

$$\lim_{t \to \infty} \tilde{x}(t) = 0, \ \ \forall \ \tilde{x}(0) \in \mathbb{R}^n. \tag{10}$$

Similarly, if the switched system (8) is asymptotically stable, then we have that:

$$\left\| x_Q(t) \right\| = \left\| \phi_Q(t, t_0, x_Q(0)) x_Q(0) \right\| \le c_Q \left\| x_Q(0) \right\| e^{-\lambda_Q t},$$

for some $c_Q, \lambda_Q > 0$, and where $\phi_Q(t, t_0, x_Q(0))$ is the state transition matrix for the switched system (8). The response of the state variable of x_Q in (5) is then given by:

$$x_Q(t) = \phi_Q(t, t_0, x_Q(0))x_Q(0) - \int_{t_0}^{t} \phi_Q(t, \xi, x_Q(0))B_Q C_r^y \tilde{x}(\xi)d\xi .$$

It follows that

$$\|x_Q(t)\| \le \|\phi_Q(t, t_0, x_Q(0))x_Q(0)\| + \left\|\int_{t_0}^{t} \phi_Q(t, \xi, x_Q(0))B_Q C_r^y \tilde{x}(\xi)d\xi\right\|$$

$$\Rightarrow \|x_Q(t)\| \le c_Q \|x_Q(0)\| e^{-\lambda_Q t} + \int_0^t c_Q e^{-\lambda_Q (t-\xi)} \left\|B_Q C_r^y\right\|_{\max} \tilde{c} \|\tilde{x}(0)\| e^{-\tilde{\lambda}\xi} d\xi$$

$$\Rightarrow \|x_Q(t)\| \le c_Q \|x_Q(0)\| e^{-\lambda_Q t} + c_Q \tilde{c} \left\|B_Q C_r^y\right\|_{\max} \|\tilde{x}(0)\| \int_{t_0}^{t} e^{-\lambda_Q (t-\xi)} e^{-\tilde{\lambda}\xi} d\xi$$

$$\Rightarrow \|x_Q(t)\| \le \left[c_Q \|x_Q(0)\| + \frac{c_Q \tilde{c} \left\|B_Q C_r^y\right\|_{\max} \|\tilde{x}(0)\| (1 + e^{(\lambda_Q - \tilde{\lambda})t_0})}{|\lambda_Q - \tilde{\lambda}|} \right] e^{-\lambda_m t}$$

where $\lambda_m = \min(\lambda_Q, \tilde{\lambda})$. Therefore, for the state variable x_Q in (5), we have

$$\lim_{t \to \infty} x_Q = 0 , \quad \forall\, x_Q(0) \in \mathbb{R}^{n_Q} . \tag{11}$$

Similarly, if the switched system (6) is asymptotically stable, then

$$\|x(t)\| = \|\phi(t, t_0, x(0))x_n(0)\| \le c \|x(0)\| e^{-\lambda t} ,$$

for some $c, \lambda > 0$, where $\phi(t, t_0, x_n(0))$ is the state transition matrix for the switched system (6). The response of the state variable of x in (5) is given by:

$$x(t) = \phi(t, t_0, x_0) + \int_{t_0}^{t} \phi(t, \xi, x_0)B_r C_r^Q x_Q(\xi)d\xi + \int_{t_0}^{t} \phi(t, \xi, x_0)B_r K_r \tilde{x}(\xi)d\xi$$

Let $c_m = c_Q \|x_Q(0)\| + \dfrac{c_Q \tilde{c} \left\|B_Q C_r^y\right\|_{\max} \|\tilde{x}(0)\| (1 + e^{(\lambda_Q - \tilde{\lambda})t_0})}{|\lambda_Q - \tilde{\lambda}|}$. Then we obtain:

$$\|x(t)\| \le \|\phi(t, t_0, x_0)\| + \left\|\int_{t_0}^{t} \phi(t, \xi, x_0)B_r C_r^Q x_Q(\xi)d\xi\right\| + \left\|\int_{t_0}^{t} \phi(t, \xi, x_0)B_r K_r \tilde{x}(\xi)d\xi\right\|$$

$$\Rightarrow \|x(t)\| \le c\|x(0)\| e^{-\lambda t} + \int_0^t c e^{-\lambda(t-\xi)} \left\|B_r C_r^Q\right\|_{\max} c_m e^{-\lambda_m \xi} d\xi + \int_0^t c e^{-\lambda(t-\xi)} \left\|B_r K_r\right\| \tilde{c} e^{-\tilde{\lambda}\xi} \|\tilde{x}(0)\| d\xi$$

$$\Rightarrow \|x(t)\| \le c\|x(0)\| e^{-\lambda t} + c c_m \left\|B_r C_r^Q\right\|_{\max} \int_0^t e^{-\lambda(t-\xi)} e^{-\lambda_m \xi} d\xi + c\tilde{c} \left\|B_r K_r\right\| \|\tilde{x}(0)\| \int_0^t e^{-\lambda(t-\xi)} e^{-\tilde{\lambda}\xi} d\xi$$

$$\Rightarrow \|x(t)\| \le \left[c\|x(0)\| + \frac{c c_m \left\|B_r C_r^Q\right\|_{\max} (1 + e^{(\lambda - \lambda_m)t_0})}{|\lambda - \lambda_m|} + \frac{c\tilde{c} \left\|B_r K_r\right\| \|\tilde{x}(0)\| (1 + e^{(\lambda - \tilde{\lambda})t_0})}{|\lambda - \tilde{\lambda}|} \right] e^{-\lambda_n t} \tag{12}$$

where λ_n is the minimum value of λ, λ_Q and $\tilde{\lambda}$. It is easy to see that $x \to 0$ as $t \to \infty$ for any $x(0)$ in (12). Therefore, for the state variable x in (5), we have

$$\lim_{t\to\infty} x(t) = 0\,,\ \forall\, x(0) \in \mathbb{R}^n\,. \tag{13}$$

Then based on equalities (10), (11) and (13), it shows that the switched system (5) is asymptotically stable. ❑

Based on Theorem 1, a parameterized set of stabilizing controllers can be designed by separately designing the individual switched systems (6), (7) and the system (8). For example, using the following Lemma, the gains K_r and L_r, can be chosen to make the switched systems (6) and (7) asymptotically stable.

Lemma 1: The origin is an asymptotically stable equilibrium point for the switched systems (6) and (7) under arbitrary switching if there exist matrices $P_K = P_K^T > 0$, $P_L = P_L^T > 0$ and matrices K_r, L_r, such that:

$$\left(A_r + B_r K_r\right)^T P_K + P_K \left(A_r + B_r K_r\right) < 0, \quad r \in \{1,\ldots,i\},$$
$$\left(A_r + L_r C_r\right)^T P_L + P_L \left(A_r + L_r C_r\right) < 0, \quad r \in \{1,\ldots,i\}.$$

Acknowledgment. This work was supported by the National Natural Science Foundation of China (51075254), the Shanghai Pujiang Program (11PJ1404000), the Innovation Program of Shanghai Municipal Education Commission (11YZ16) and the 211 Leading Academic Discipline Project of Shanghai University (A004-1-yi-1002).

References

1. Lin, H., Antsaklis, P.J.: Stability and Stabilizability of Switched Linear Systems: A Survey of Recent Results. IEEE Transactions on Automatic Control 54(2), 308–322 (2009)
2. Sun, Z.: A Note on Marginal Stability of Switched Systems. IEEE Transactions on Automatic Control 53(2), 625–631 (2009)
3. Guan, Z., Hill, D., Shen, X.: On Hybrid Impulsive and Switching Systems and Application to Nonlinear Control. IEEE Transactions on Automatic Control 50(7), 1058–1062 (2005)
4. Shorten, R., Narendra, K.S., Mason, O.: A Result on Commom Quadratic Lyapunov Functions. IEEE Transactions on Automatic Control 48(1), 110–113 (2003)
5. Cheng, D., Guo, L., Lin, Y., Wang, Y.: Stabilization of Switched Linear Systems. IEEE Transactions on Automatic Control 50(5), 661–666 (2005)
6. Goncalves, J.M., Megretski, A., Dahleh, M.A.: Glogal Analysis of Piecewise Linear Systems Using Impact Maps and Surface Lyapunov Functions. IEEE Transactions on Automatic Control 48(12), 2089–2106 (2003)
7. Johansson, M., Rantzer, A.: Computation of Piecewise Quadratic Lyapunov Functions for Hybrid Systems. IEEE Transactions on Automatic Control 43(4), 555–559 (1998)

8. Wu, Z., Ben Amara, F.: Flying Height Control for a 2-DOF Tripad Slider in Hard Disk Drives with Switched Regulators. In: ASME International Mechanical Engineering Congress and Exposition, Orlando, Florida, November 5 - 11 (2005)
9. Boettcher, U., Li, H., de Callafon, R.A., Talke, F.E.: Dynamic Flying Height Adjustment in Hard Disk Drives through Feedforward Control. IEEE Transactions on Magnetics 47(7), 1823–1829 (2011)
10. Zhou, K., Doyle, J.C., Glover, K.: Robust and Optimal Control. Prentice-Hall (1996)

Analysis of Piston Pneumatic Motor Work Process

Zhiping Guo[1], Yanzheng Lu[1], Haizhong Hao, Yanfei Wang, Guanfu Li, and Wei Guo

[1] College Of Mechanical Engineering, Inner Mongolia University of Technology, Inner Mongolia, 010051, China
yuqilu86@163.com

Abstract. Pneumatic motor is the device that makes the pressure of compressed air into the mechanical movement. For the pneumatic motor which have the same positive and negative performance, it's specific work process may be divided into seven processes, include intake, power of expanding compressed gas, the main exhaust, residual gas compression, vice exhaust, the more than gas compression, and the more than gas expansion. But intake and the power of expanding compressed gas is the key influence of motor performance.

Keywords: Crankshaft Connecting Rod, Gas Phase, Power, Gas Consumption.

1 Introduction

Pneumatic motor provide the power source for the pneumatic manned winch, it uses compressed air as medium. Pneumatic motor has good explosion-proof performance, not affected by high temperature and vibration; With long-term work, and smaller temperature; Wide power and speed range , and high starting torque and bring in launched; Simple structure, manipulation convenient, easy maintenance, low cost are advantages. Shandong Tai'an the OS to our drilling equipment Co., LTD JQH type of pneumatic winch, for example, the piston to the working process of the pneumatic motor do simple analysis.

1.1 Instructions of Pneumatic Motor with Gas

It is shown in fig1 that the angle of the air valve with the gas distribution window's the section. It is the central angle that the inlet of valve sets opposite, it is the rotation angle that is from starting intake to exhaust. The air valve of JQH belong to symmetrical expansion type (exhaust process has compressed). The pneumatic motor have the same positive and negative performance, inflation angle and compression angle are uniform.

Pneumatic motor with gas phase of JQH type pneumatic winch was shown in Fig. 2, turned 6 °on the crankshaft piston check point , intake valve open, cylinder started charging, In the distance the piston 66 when valve closed, and complete the inflatable process. In the next 39 ° trip, cylinder is sealed. It is process that cylinder gas expanded, then the key door of exhaust opened, and started the first exhaust, the crankshaft trip of this process is 54 °. When the first exhaust ended, cylinder is in a state of seal. In the trip of 39 °, the gas in the cylinder is compressed to do negative work. And then the vice-exhaust valve open and exhaust. With the 6° at TDC, vice-exhaust valve closed, finish the second exhaust. The crankshaft continues to rotate, and get ready for the next cycle.

D. Jin and S. Lin (Eds.): Advances in Mechanical and Electronic Engineering, LNEE 176, pp. 107–112.
springerlink.com

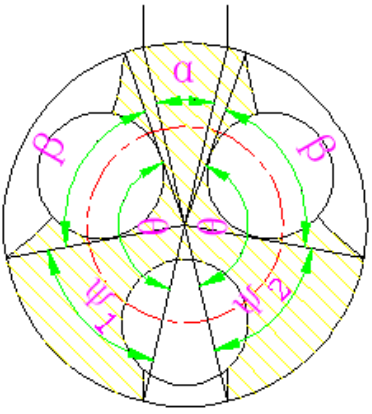

Fig. 1. Distribution valve

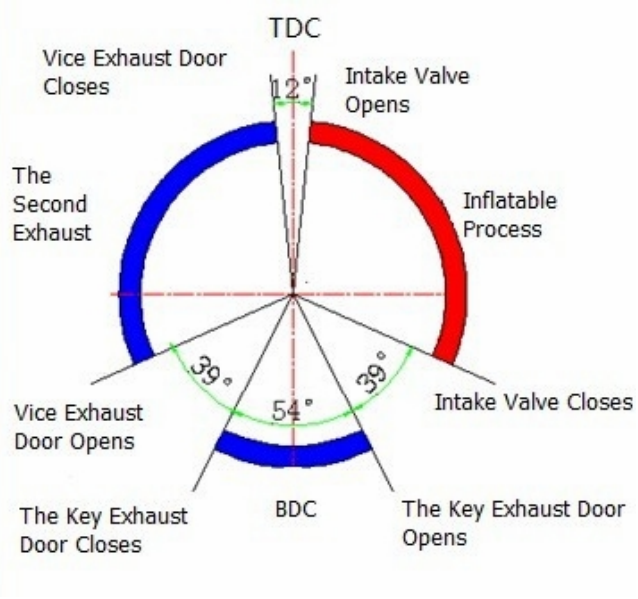

Fig. 2. Phase of distributing gas

2 Analysis of the Motor Work Process

In order to facilitate research and not lose the essence of the problem, it is assumed that compressed air to pneumatic motor of the piston doing work process meet the following a few ideal situations:

The inlet pressure in the process remains unchanged.

The expansion and the compression of the gas in the cylinder is changeable. In the expansion or compression process, changeable process index remains unchanged.

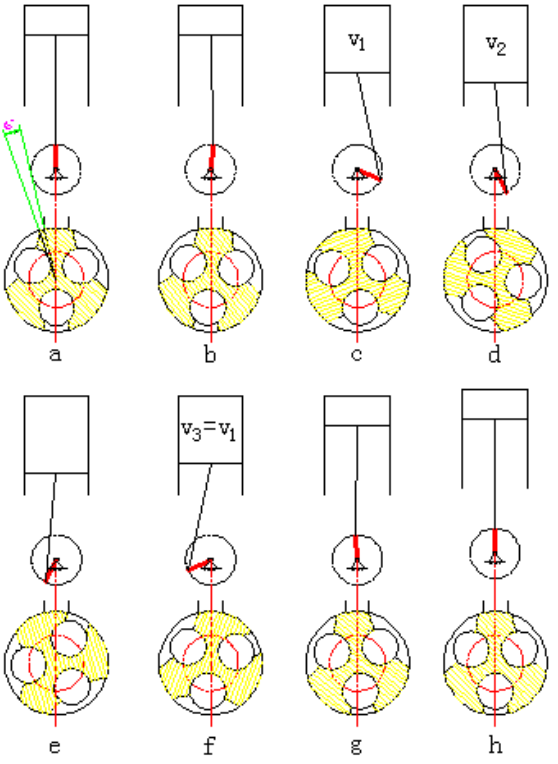

Fig. 3. The movement of pneumatic motor

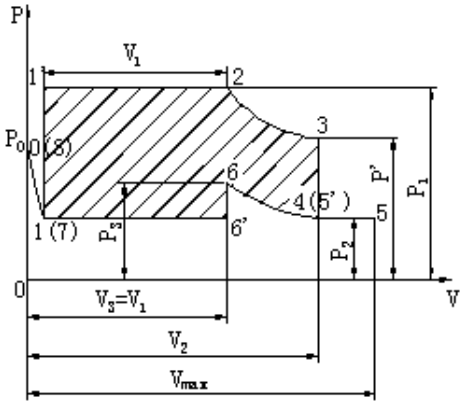

Fig. 4. Indicator diagram

There is no friction loss, eddy current and leakage when gas flow in pneumatic motor.

More volume gap is not considered.

In Fig. 3a, the piston is in the TDC, but inlet window of valve cover and inlet valve core also differs 6 °, so at this moment, there is no intake. With the rotation of the crank, cylinder is a gas more than the expansion of the process, in the Fig. 4with curve segment 0-1 shown.

In Fig. 3 b the shown, at this time, the pressure of the inlet is P_2. Figure 3 c position said inlet ending. Figure 3 b to figure 3 c is the process of the intake process, in the damping-displacement figure 4 with level line 1, 2 said. Compressed air do work to piston is $L_1 = P_1V_1$.

Figure 3 d is about to begin to exhaust. The process of Figure 3 c to figure 3 d is compressed air expanding power. In this process, the pressure drop from P_2 by gradually to $P^{'}$. In the damping-displacement with curve 2-3 describes the process. In the process gas piston do work as theory.

Figure 3 e position said the first exhaust ending. Figure 3 d to figure 3 e shows the process of the first Lord exhaust, when exhaust passage connects stoma, the pressure drop to quickly. In this process the power of gas to piston offset the power of piston to gas each other. In the damping-displacement figure with the line of level 4-5-5 shown.

Figure 3 f said the end of excess gas in the cylinder is compressed, it is about to begin the next exhaust. The process of the figure 3 e to figure 3 f is the compression process, when the end of the first exhaust, the excess gas in the cylinder is compressed due to the piston upward, the pressure rise gradually from P_2 to P_3. With the line of level 5'-6 shown in the damping-displacement figure, the gas does negative work on the piston in this process, its value is $L_3 = -\int_{V_3}^{V_2} PdV$.

Figure 3 g said the end of the second exhaust, the figure 3 f to figure 3 g shows the process of exhaust, exhaust pressure is P_2 (just above the atmospheric pressure), this process in the damping-displacement map with horizontal line 6, 7 shown, The gas does negative work on the piston as theory in this process, its value is $L_4 = -P_2V_3$.

Figure 3 g to figure 3 h show the process of excess gas compressed, in the damping-displacement map with curve segment 7-8 shown. Figure 3 h shows the position that the piston come back to the dead spot, namely completed a work cycle, and is about to enter the next work cycle.

To sum up, a theoretical cycle of the pneumatic motor includes inflation of excess gas, intake, gas expansion, compression, exhaust and compression of excess gas. In a theoretical cycle, compressed air made the total power of the theory to a piston is namely

$$L = P_1V_1 + \int_{V_1}^{V_2} PdV - \int_{V_3}^{V_2} PdV - P_2V_3$$

$$= P_1V_1 + \frac{1}{n-1}\left(P_1V_1 - P^{'}V_2\right) - \frac{1}{n-1}\left(P_3V_1 - P_2V_2\right) - P_2V_1$$

Assume the expansion ratio of compressed air doing expanding power in cylinders is

$$\varepsilon = \frac{V_2}{V_1}$$

$$P_1 V_1^n = P' V_2^n, \quad P_2 V_2^n = P_3 V_1^n$$

$$P' = P_1 \left(\frac{V_1}{V_2} \right)^n = P_1 \frac{1}{\varepsilon^n}$$

$$P_3 = P_2 \left(\frac{V_2}{V_1} \right)^n = P_2 \varepsilon^n$$

$$L = V_2 \left\{ \frac{1}{\varepsilon}(P_1 - P_2) + \frac{1}{n-1} \times \left[P_1 \left(\frac{1}{\varepsilon} - \frac{1}{\varepsilon^n} \right) + P_2 \left(1 - \varepsilon^{n-1} \right) \right] \right\}$$

P_1, P_2 were the absolute pressure of intake and exhaust Pa

V_2 cylinder volume of inflation ending m^3

n changeable process index namely n=1.25～1.3

ε expansion ratio

The theoretical power of JQH type pneumatic winch's motor is N (W)

$$N = \frac{LZn'}{60}$$

Among Z- Number of cylinders

n' - rotate speed

Motor gas consumption M (m^3 / min)

$$M = ZV_1 n' \frac{P_1}{T_1} \times 293$$

Among Z- Number of cylinders (Generally take 3-6)

V_1 -Intake volume

n' - rotate speed. r / min

P_1 -The inlet pressure. kg / cm^2

T_1 - absolute temperature of intake. K

Considering the leakage, excess volume and throttling pressure drop, the actual gas consumption is M_e.

$$M_e = \mu_1 \mu_2 M \quad (m^3 / \min)$$

Among μ_1 Leakage and clearance volume impact factor. Generally take 1.2-1.6

μ_2 throttling pressure drop

So $M_e =$ (0.84～1.28) M $(m^3 / \min)$

3 Conclution

In the certain circumstances of inlet and outlet pressure, the factor which affect the air motor power is V_2 , namely the volume of compressed gas expansion ending; the factor which affect air consumption is V_1, namely the volume of intake ending. When the size of air motor crankshaft, connecting rod, cylinder is constant, he structure of valve decide V_1 and V_2. Therefore, it is an important way that the angle is designed to improve performance of pneumatic motor.

References

1. Xi'an Jiaotong University, Department of internal combustion engines. Combustion theory. China Agricultural Machinery Press
2. Zhang, S., Zheng, Y., Zhang, Z.: Radial piston air motor design and calculation of main parameters. Manipulators Pneumatic Tools (February 1979)
3. Zhang, S.: An effective way to improve the efficiency of air motors. Manipulators Pneumatic Tools (January 1995)
4. Cui, P.: Piston air motor design problems. Construction Machinery (August 1981)

The Application of Energy Feedback Device in Port Crane Control System

Qi Liu

Wuhan University of Technology, Wuhan, China
936430013@qq.com

Abstract. Basing on the load characteristics of the crane, the energy feedback device is used in the vary-frequency control system in the port crane using the regeneration energy resulted by each operation cycle of the port crane to conserve energy and reduce cost. The economic efficiency of the port is increased greatly.

Keywords: crane, vary-frequency converter, energy feedback1 Introduction.

1 Introduction

With the rapid development of economic, energy conservation and environmental protection become the trend of port crane. Due to the special job conditions, port crane has large energy saving potential. The effective appliance and utilization of renewable energy is the focus of attention and research all the times. Considering the load characteristics of port cranes, combined with energy feedback devices to recover large amounts of renewable energy in the process of degradation and brake of the declining of hoisting mechanism, you can take full advantage of variable frequency speed-adjusting technology to realize energy saving and consumption reducing.

2 Load Characteristics and Mechanical Properties of the Port Cranes

Crane load is mainly potential energy load which requires motor with asymmetric features and can be divided into resistance load and dynamic load according to different job conditions. When upgrading or falling with empty hook, motor with electric state outputs power by overcoming resistance, this is resistance load. When weights fall, due to weight's power under its own gravity, motor with regenerative braking state absorbs energy, this is the dynamic load. According to different conditions of hoisting mechanism, we analyze mechanical characteristics of vary-frequency on motor below:

(1) When weights are lifting up, the direction of motor rotates and torque caused by the armature current are the same, that's to say motor is controlled by a positive torque effect, mechanical characteristics is in the first quadrant, as shown in Fig.1,curves ①.

D. Jin and S. Lin (Eds.): Advances in Mechanical and Electronic Engineering, LNEE 176, pp. 113–117.
springerlink.com

When motor slows down by reducing the frequency, the mechanical characteristics switch to curve②the moment frequency changes, the working point jumps from A to A ' and enters into the second quadrant, speed for short periods after falling back gets into the first quadrant to point B with stability.

(2) When empty hook are falling which is achieved by the motor running reversely. Motor's torque and speed is negative at this time, so the mechanical characteristic curves are in the third quadrant. Shown in Fig.2, curves ③.

When motor slows down by reducing the frequency, the mechanical characteristics switch to curve④ the moment frequency changes, the working point jumps from C to C ' and enters the forth quadrant, speed for short periods after falling back gets into the third quadrant to point D with stability.

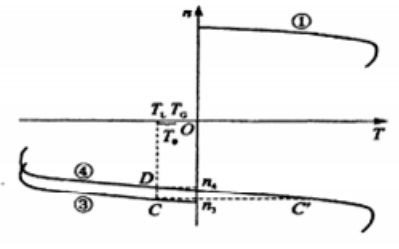

Fig. 1. The working condition on weights lifting

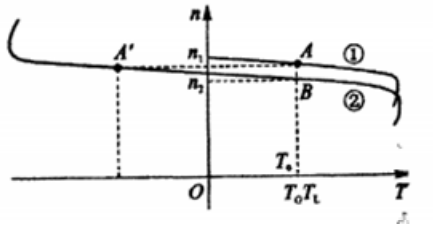

Fig. 2. The working condition on empty hook falling

(3) Weight falls under its own gravity when overloads fall, the direction of the motor rotates is reversed, but its direction of the torque and rotation are opposite. Its mechanical properties is shown in Fig.3 curve ⑤, working point E, speeds of n5. Motor effect is to prevent weight accelerating because of the acceleration of gravity to achieve falling in a constant speed. In this case, the friction torque will impede the weight down, so when weights fall, the load torque is smaller than the weights rise.

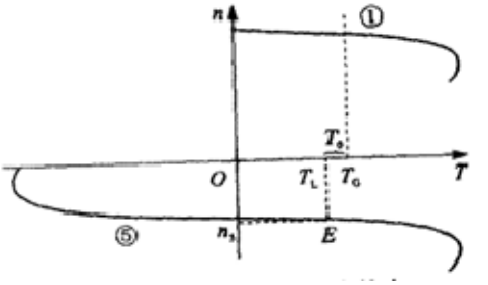

Fig. 3. The working condition on overloads falling

Another feature is that there has a large number of potential energy load aspects of power need to be released in decentralization, the load requirements of regenerative braking capacity is the maximum load. In the process of falling, all potential energy

of the weight will be released, with the exception of a small amount of energy losing in the internal and external of the motor and inverter, most of the potential energy will feedback to the DC bus converter. If the upgrading and decentralization are frequent, the total energy per unit of time feedbacked is substantial.

3 Energy Feedback Device in Vary-Frequency System

Traditional PWM inverter can't make renewable energy feedback to three - phase power supply, so all energy motor absorbed from inverters are stored in the capacitor energy storage, eventually bus voltage increases. Then you need to take necessary measures to release energy, reduce the voltage.

The vary-frequency system in port crane mainly uses the way that shares a common DC bus and energy conversion is done on it. Usually there are two ways to release the energy feedbacked from loads: one is the energy-consuming way, that is, connecting power braking resistor on the DC bus, when the feedback energy on motor side transfers into electricity by frequency converter which reflects increase in bus voltage on the DC bus when braking unit module used to control the braking resistor is connected to the DC bus with brake resistance. Because the resistance of braking resistance is very small, a discharge process can be completed within a very short time, transfers electrical energy into heat energy consumed on the braking resistor.

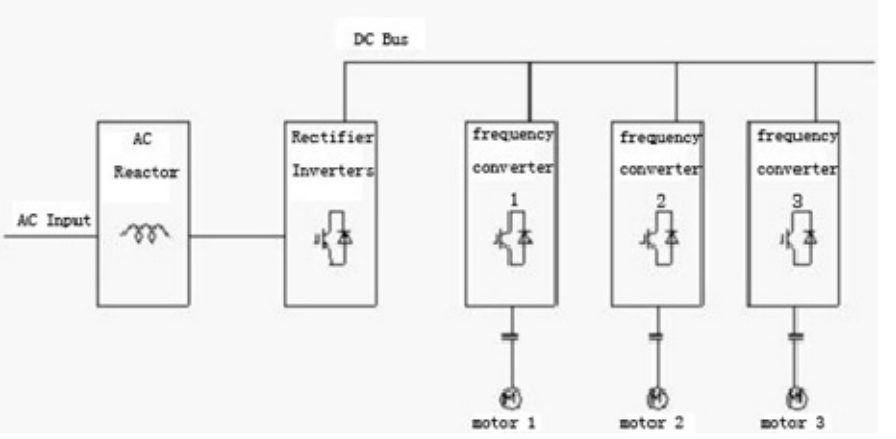

Fig. 4. AC main circuit composition

Another way is feedback, firstly energy stored on the DC bus can be consumed by other inverters on the same bus as the power, if it can't be consumed out, energy on DC Bus bar can be transfered to alternate which is same to the power grid with the same amplitude, frequency, phase that feedbacks to the main transformer side through the energy feedback devices. It is firstly consumed and used by other feedback devices and the hanging mechanism of auxiliary transformer. If it also can't be consumed out, it can be consumed by adjacent quayside on AC power grid. Finally the remaining energy really feedback to power grid, With respect to the energy in this

way, the biggest advantage is not only energy-saving and do not require power compensation devices and harmonic suppression device, but also reduces requirements for installation. This is the standard configuration between port side bridges and large - tonnage Crane drive system.

4 The Energy Feedback Device

The energy feedback device shown in Fig.5 cooperated with inverter has currently been applied into 25T and 40T door machines with more than hundred sets of application in Tianjin Port; Huanghua port; Qingdao investment port; Shenzhen Shekou port and so on, especially in 40T door machine. Its basic principles are as follows:

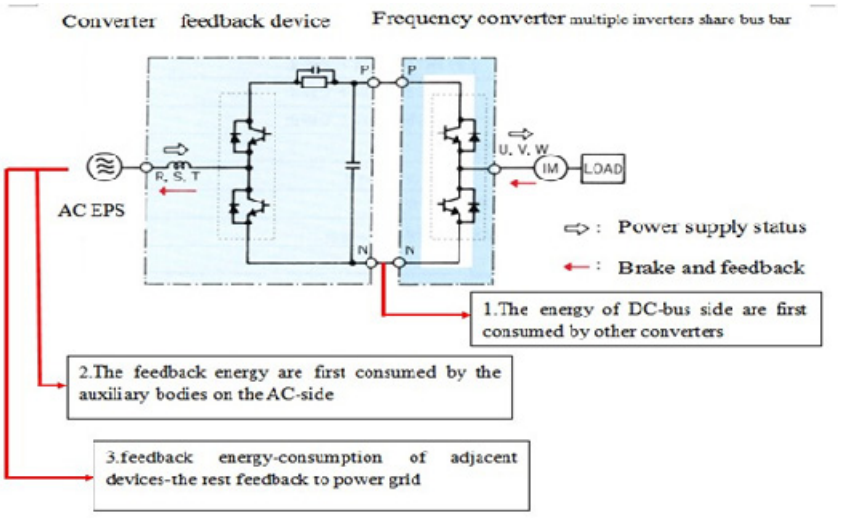

Fig. 5. Energy feedback device

(1) When the motor is in motor operation(such as lifting), energy by POWER=＞CONVERTER=＞INVERTER=＞MOTOR, electric current and voltage have the same phase. At this moment, CONVERTER needs to use the PWM pulse width modulation technique to modulate current, voltage to sine wave which the phase angle are close to 0 degrees to ensure the power factor of 0.95 and more and the harmonic components under 5 percent.

(2) When the motor is in power state(such as declining), power by MOTER=＞INVERTER=＞CONVERTER=＞POWER, electric current and voltage have the opposite phase. At this moment, CONVERTER also needs to use the PWM pulse width modulation technique to modulate current, voltage to sine wave which the phase angle are close to 180 degrees to ensure the power factor of 0.95 and more and the harmonic components under 5 percent.

In short, the operating principle of the CONVERTER is to use high switching frequency of IGBT power devices and PWM pulse width modulation technique to modulate the input and output current, voltage wave to standard sine wave to ensure minimum harmonic components and maximum power factor and make the extra energy feedback to power supply side in power state.

From the above analysis, we can see the energy feedback devices have the following properties: it can feedback energy by power feedback function, save the energy consumption to achieve the maximum braking capacity of inverter driving; By the PWM control on sine wave, it produces the perfect sine wave currents, greatly reduces higher harmonic current waveform; By power rate 1 (phase voltage and current phase of the power supply are in same control ways)and PWM, load size and power capacity can be 1:1, so the cost of the power supply cable, electrical power equipment such as electricity machine are significantly reduced.

5 Summary

With the development of our economy, the tonnage and the running mechanism speed of port machinery are increasing, there are a lot of energy recycling issues in the process of loading and unloading of the goods. Using vary-frequency technology, recycling energy will feedback to AC power. It can achieve the goal of energy saving. Consumption reducing and feedback device is the key to the total system. The energy feedback device is to make the load inertia energy feedback to the power grid, and have small energy feedback units with regeneration and braking function. By combination use with frequency converter, it can play a preeminent energy - saving effect in crane load uses in the opposite direction. It is widely used in port just because of its high performance.

References

1. Li, F.: Discussion on load generation and ways on vary-frequency brake. Electrical Applications (July 2003)
2. Zhang, C., Du, C., Li, K.: The regenerative braking and feedback technology on vary-frequency drive asynchronous motor. Journal of Motor and Control (April 2006)
3. Cheng, G.: Technology and application of PWM inverter. China electric power press, Beijing (2007)
4. Wang, R., Fang, Y., Xing, Y.: Research on three-phase high power factor in PMW converter reversible operation. Journal of Electrical Engineering Technology (August 2007)

The FEA Contact Analysis of High Pressure Packers

Zhiping Guo[1], Yanfei Wang[1], Qing'an Li[1], Guanfu Li[1], Wei Guo[1], Yanzheng Lu[1], and Haizhong Hao

[1] College of Mechanical Engineering, Inner Mongolia University of Technology, Inner Mongolia, 010051, China
wangfeipc@qq.com

Abstract. At present, the high pressure packer was researchers mainly in structure. Through the finite element ANSYS analysis can improve the packers' structure to enhance packer ability of working pressure. At the finite element ANSYS analysis, great impact on the contact pair of parameter and friction coefficient setting, set not properly, the results and actually have very big difference. The analysis of this problem of the domestic and foreign many is insufficient, the author will analysis is the relationship between contact pair of parameter and the friction coefficient with the contact stress, find out the parameters fit with the actual. The paper according to packer-type is FGQ-C 9-5/8 "x 7" proceed packer rubber barrel and casing wall of the stress analysis using ANSYS software, the FKN and FTOLN parameters have been changed, it is concluded that the appropriate parameters through the contrast analysis, the calculation results complied with engineering practice.

Keywords: Finite-element analysis, Contact analysis, FKN, FTOLN.

1 Introduction

High pressure packer of the main seal components is rubber barrel, it is a super elastic rubber material. Rubber barrel will produce geometry nonlinear large deformation in the work, and rubber material constitutive relation is nonlinear, another rubber barrel and casing wall contact process is a state of nonlinear contact problem. Therefore, the packer rubber barrel working process is a both geometry, materials and state triple nonlinear problem. This brought great difficulties for rubber material components of the theoretical analysis and calculation.

The finite element ANSYS analysis software can be very good deal with this type of nonlinear problems. When the packer carry axial load, the rubber barrel will have large deformation in the radial, between rubber barrel and casing form contact pressure, for this reason seal up annular space between the center pipe and casing pipe. Contact pressure between rubber barrel and casing is rubber barrel load bearing work pressure necessary condition. Therefore, research the relationship of working load and maximum contact stress has an important significance.

2 The Stress Analysis Based on ANSYS

2.1 ANSYS Contact Analysis

Contact problem is a highly nonlinear problem that requires a lot of computing resources. Contact problem have two large difficulties: the first of, before solve

D. Jin and S. Lin (Eds.): Advances in Mechanical and Electronic Engineering, LNEE 176, pp. 119–124.
springerlink.com

problems, you don't know the contact area, surface is contact or separate is unknown, and suddenly change, this with load, material, the boundary conditions and other factors determine; The second, most of the contact problem need to calculate the friction, there are several kinds of friction and model for you to choose in the ANSYS, they are all of the nonlinear, that the convergence are difficult.

When it involves to contact of rigid body and soft body, "target" face always rigid, "contact" face always soft surface, the two sides taken together is called the "contact pair", use of Targe170, Conta173 and Conta174 to define the 3-d contact. The system recognized "contact pair" by same real constant.

ANSYS defined through FKN definition method to contact stiffness factor; FTOLN defined the penetration of the largest range. Generally, real constant FKN of default value in 0.01-0.1. Real constant FTLON the default value of 0.1, that can change this value, but if this value is too little may cause too much iteration number and not to convergence.

2.2 Preprocessing

The structure models direct establish in ANSYS by simplification. Rubber barrel select HYPER158 hyper elastic element and the other of the component selection Solid 185 solid element. All parts material and characteristic parameters such as table 1.

Table 1. Material attribute of components

Items / Parts	Materials	Young's modulus/GPa	Poisson's ratio
Rubber barrel	Rubber-40	17.33	0.49
Cone, Central pipe, Casing pipe	35CrMo	206	0.3
Expansion sleeve	2Cr13	214	0.3

After the mesh for every sealing device parts, on the casing, and expand sleeve bottom all constraint, on the top of cone bear on displacement load 147 mm.

2.3 The Stress of Casing Wall

For the figure 1, it is known that in the default Values of the parameters of the setting FKN = 0.1, FTOLN = 0.1, the calculation results of the maximum equivalent stress for 600 MPa, this time the stress for the inner surface of the casing is 77.2 MPa, to meet the requirements of the seal stress for not less than 70 MPa. Analysis results show that the structure can meet requirements, and has a larger space for the analysis.

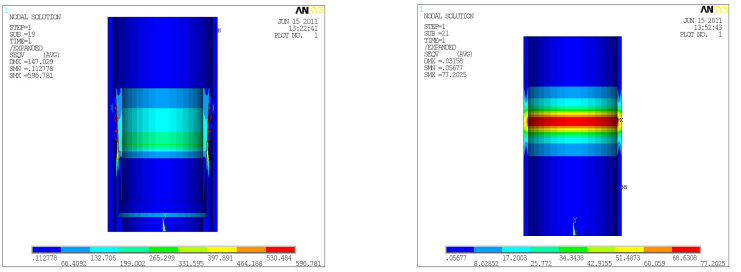

Fig. 1. Program default parameters an inferior effect force cloud pictures

3 Real Constant FKN for Casing Wall Stress of the Effect

Under the other parameters invariable, change the value of the real constant FKN. Generally, real constant FKN is 0.01-0.1, so for segmentation and analysis calculation. The calculated results integration is shown the table 2:

Table 2. Calculation results table

Real constant FKN	The casing pipe maximum stress/MPa	Real constant FKN	The casing pipe maximum stress /MPa
0.04	40.4	0.09	72.9
0.05	57.1	0.1	77.2
0.06	61	0.11	91.8
0.07	71.1	0.12	99.1
0.08	71.9	0.13	106.5

From the table 2 can see, under the other parameters invariable, FKN = 0.04, casing wall of the maximum stress for 40.4 MPa; FKN = 0.13, the biggest stress for casing wall 106.5 MPa, FKN value on the casing wall stress influence of the more obvious. Along with the increase FKN of value, casing wall of the stress with increase, through the Figure 2 can see some more intuitive.

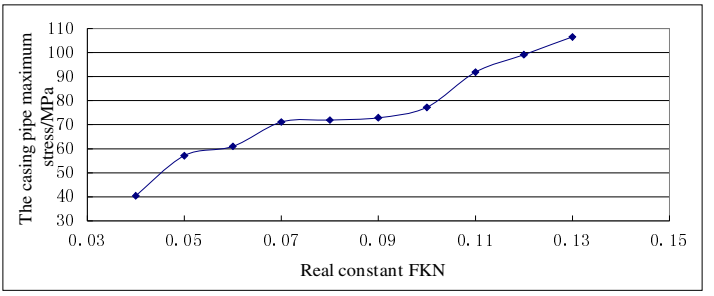

Fig. 2. Different FKN value casing wall equivalent stress fitting curve

Can be seen from above, the value of FKN and the biggest stress is nonlinear relation. When FKN in 0.07-0.09, casing wall stress change quite gentle, suitable for practical problems, this time the results of calculation is accurate. The corresponding to different FKN value, the casing wall should be tried to as shown in figure 3.

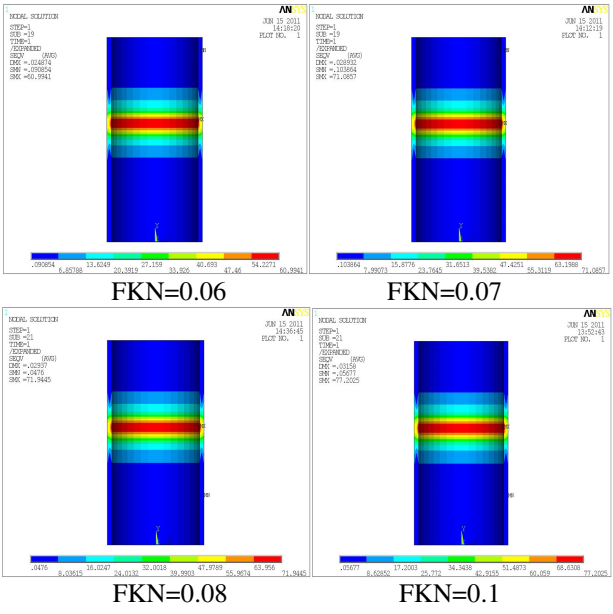

Fig. 3. Different FKN value casing wall equivalent stress cloud pictures

4 Real Constant FTOLN for Casing Wall Stress of the Effect

Real constant FTOLN is the largest penetration defined contact boundaries, under the other parameters invariable, FKN=0.08, change the value of the FTOLN real constant. Because real constant FTOLN value default for 0.1, so it should be increase and decrease, analysis and calculation of the casing wall of stress state, the effects of the integration of calculating results are shown table 3:

Table 3. Calculation results table

Real constant FTOLN	The casing pipe maximum stress /MPa	Real constant FTOLN	The casing pipe maximum stress /MPa
0.05	106.4	0.1	71.9
0.06	96.1	0.11	70.7
0.07	92.9	0.12	66.9
0.08	86.3	0.13	55.2
0.09	75.8	0.14	42.1

From the table 3 can see, under the other parameters invariable, FTOLN = 0.05, the biggest stress for casing wall 106.4 MPa; FTOLN = 0.14, the biggest stress for casing wall 42.1 MPa, FTOLN value on the casing wall stress influence of the more obvious. Along with the increase of FTOLN value, casing wall of the stress with increase, through the Figure 4 can see some more intuitive.

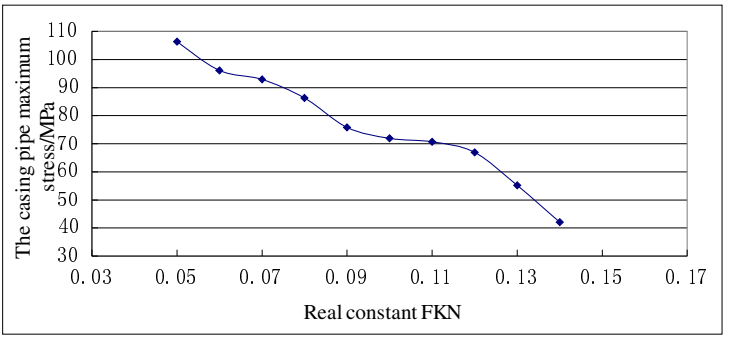

Fig. 4. Different FTOLN value casing wall equivalent stress fitting curve

The above can see, FTOLN value and the maximum stress is nonlinear relation, When FTOLN value in 0.1-0.11, casing wall stress change quite gentle, suitable for practical problems, this time the results of calculation is accurate.

The corresponding to different FTOLN value, the casing wall should be tried to as shown in figure 5.

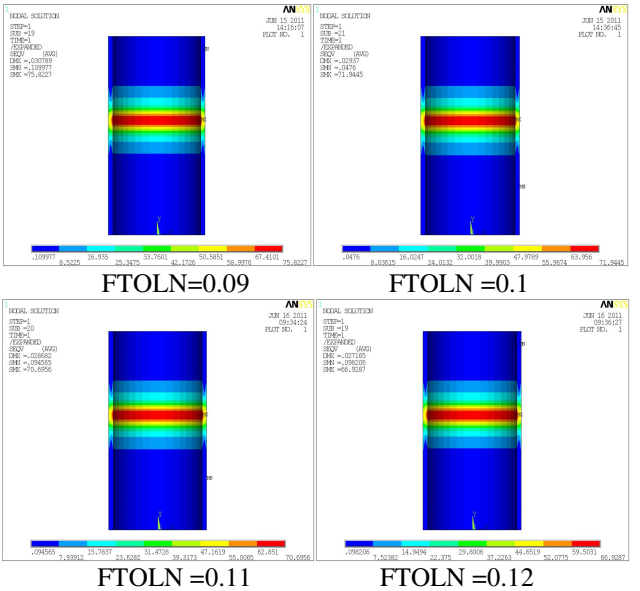

Fig. 5. Different FTOLN value casing wall equivalent stress cloud pictures

5 Conclusion

The FKN value and casing maximum stress is direct proportion relationship, increase FKN value, casing wall of the biggest stress increase. FKN value is between 0.07 and 0.09, casing wall stress change quite gentle, suitable for practical problems, so FKN value should be in 0.07-0.09.

The FTOLN value and casing maximum stress is direct proportion relationship, increase the FTOLN values, the biggest stress casing wall with increased. FTOLN value is between 0.1 and 0.11, casing wall stress change quite gentle, suitable for practical problems, so FTOLN value should be in 0.1-0.11.

References

1. Liu, Y.: Packer rubber barrel performance finite element analysis and the structure improvement. Southwest Petroleum university (April 2006) (in China)
2. Du, C., et al.: Rubber barrel stress the numerical simulation and structure optimization research of packer (March 2008)
3. Zhan, J.: Packer the system between simulation research work behavior. Southwest Petroleum university (October 2005) (in China)
4. Lian, Z.: The packer working process by the finite element analysis. Petroleum Machinery (2007) (in China)
5. Yang, X.: Hydraulic the packer of rubber barrel between the numerical analysis process. The University of Petroleum Journal (2003) (in China)

Discussion on a Calculating Method for Anti-overlapping Winding Number in Textile Mechanical Engineering

Wenyuan Chen[1,2], Chongchang Yang[1,2], Xuehui Gan[1,2], and Bingbing Chen[1]

[1] Engineering Research Center of Advanced Textile Machinery, Ministry of Education, Shanghai, P.R. China
[2] College of Mechanical Engineering, Donghua University, Shanghai, P.R. China

Abstract. Filament overlapped has great impacted to roll-forming when winding in the process of high-speed spinning. This paper puts forward a new calculation method for anti-overlapping wind number: that is, get the anti-overlapping winding number from rectification overlapping winding number, then filter it and use mechanical engineering experiment to get a group of effective and ideal anti-overlapping winding number. It provides the theoretical foundation for designing the anti-overlapping mechanism and electromechanical control method.

Keyword: winding, anti-overlapping, winding number.

1 Introduction

Winder is the key unit of the chemical fiber production equipment and the filament production requires the winder roll forming stable, large capacity, yarn evenly distributed, density consistent; uniform tension, no wrinkling and bulging side; easy unwinding, no mutual entanglement as well as no edge collapse and unseating.

There are three hazards when the filament was overlapped:

1) Filament overlapping will cause the roll density unevenly, the surface out of flatness and susceptible to scratches in the silk layer dense areas;
2) Winding head vibration increase, harsh voice, and the tension of filament would fluctuate unevenly while unwind.
3) Easy tangled, wool yarn produced ,broken ends, etc which will affect the production of the next process directly

According to the spinning mechanical engineering practical experience and theory shows that filament overlapping has a direct relationship to whether the winding number selected properly or not. The mainstream electromechanical control method of anti-overlapping both at home and abroad tend to be a clear ideas: that is divided the process of full volume winding into sections from small to large by volume package diameter, with adopting the appropriate anti-overlapping winding number in sub-paragraphs diameter to achieve precision winding. It is not difficult to know that it

D. Jin and S. Lin (Eds.): Advances in Mechanical and Electronic Engineering, LNEE 176, pp. 125–130.
springerlink.com

is the constant helical angle winding method from the whole winding process while each subparagraphs diameter is precision [1] wind which has been proved to be an ideal winding way and solve the problems.

How to select the appropriate anti-overlap winding number quickly and efficiently in boundless winding number during the winding process while also allowing the trend of winding number correspond with characteristics the changes of winding number in constant helical angle winding will be explored in this paper.

2 Anti-overlapping Winding Number Derivate

2.1 The Accurate Definition of Anti-overlapping Winding Number

Winding number can be divided into overlapping winding number and anti-overlapping winding number according to whether wind overlapped or not. To describe the relationship between winding number and filament overlap [2-5] more facilitate, the winding number will disassembled as follow:

$$i=i_0+i_x \tag{1}$$

i_0 is integer part of the winding number i, i_x is decimal part of winding number i.

According to analysis method for winding number in literature [5] we will find the filament would finally return to starting point with the winding number must be expressed in decimal form during production. Therefore, it is far-fetched to define anti-overlap if only according to filament return to the starting point or not.

Here is the accurate definition of the anti-overlapping winding number:

Assuming winding with the winding number i_k, filament start from a starting point at end face, traverse guide mechanism go through m_k times reciprocating motion. When the return back point of filament end face coincided with the assumed starting point, then it can be said that this winding time was a corresponding winding cycle time T_k at the winding number i_k. The reciprocating frequency m within one minute was as followed:

$$m = v \cdot sin\alpha /(2H) \tag{2}$$

m is the reciprocating number per minute (number/min); v is winding speed (m/min); α is winding Angle; H is winding distance (m)

The winding cycle T_k corresponding to the winding number was as followed:

$$T_k = m_k / m \tag{3}$$

T_k- The winding cycle corresponding to the winding number (min);
m_k-The reciprocating times of traverse guide mechanism for filament return back to the starting point;

If the silk layer $2m_k$ was thick enough in the winding cycle T_k and met the type as followed;

$$2m_k \geq M_k \tag{4}$$

M_k is the least silk layers which does not produce silk overlapping;

Filament spread out evenly in two spiral direction of winder axial, and the surface of winder axial not bumpy. It called that the winding number i_k achieved the result of anti-overlap in winding. The winding number i_k is the anti-overlapping winding number.

In conclusion, the anti-overlapping winding number is the special overlapping winding number. So the study of anti-overlapping winding number began from the overlapping winding number.

2.2 The Amendment for Winding Number

Here express the winding decimal in the form of mixed fraction:

$$\mathrm{i} = i_0 + \mathrm{Q} / \mathrm{N} \tag{5}$$

i-winding number; i_0-winding integer; Q-molecules of the decimal Winding simplest proper fraction, Q = 1,2… (n-2); *N*-denominator of the decimal Winding simplest proper fraction ($Q<N$, and Q / N is the simplest proper fraction).

As shown in Figure 1, O_1, O_2…O_n are the turn back point at the end face which a certain winding number *i* corresponds to, turn back point number is n-1. S is the spacing in circumferential direction of adjacent retrace point at the end face during one winding cycle (its size decided by winding diameter D_k and winding number *i*), Z is the spacing in circumferential direction of initial point within adjacent cycle also known as the starting point of the adjacent winding cycle offset spacing in circumferential direction. Known by formula 5, *i* corresponds to the denominator N = n-1, *i* corresponds to the silk layers in one winding cycle are 2(n-1).

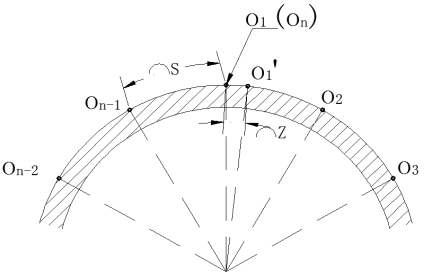

Fig. 1. The filament winding spacing S and Anti-overlap offset distance Z

If the filament start from the O_1 point, after a reciprocating stroke, silk retrace point offset a short arc length Z (offset more or less will be ok, the icon shown more than offset Z) than the original O_2, continue winding and the follow-up of yarn retrace point

compared to the retrace point which overlap of the winding number corresponding to all will offset a short distance Z, thus avoid winding overlap after the n-1 reciprocating stroke. After a winding cycle, O_1' as a starting point for the next winding cycle, the next winding cycle winding starting point of $0_1''$ relative points $0_n'$ ($0_1'$) will offset a period of arc length Z. It is achieved the extension of the winding cycles, filament spread evenly and prevent filament overlapped. So long as the arc length Z and the value of denominator in winding number N selected properly, anti-overlapping would be achieved.

So overlapping winding number amends as follows:

$$i_s = i_c \pm \Delta \tag{6}$$

$$\Delta = Z / (\pi \cdot D_k) \tag{7}$$

i_s- rectification winding number; i_c-overlapping winding number; Z-default silk offset distance; D_k -roll diameter.

According to the above equation, the anti-overlapping winding number can be achieved by overlapping winding number of the amendments, but it does not mean the overlapping winding number to be amended will certainly be able to prevent overlapping, but also need analysis and validation it's reasonable. The process of Specific calculation for winding number is as follows:

1) According to the bobbin diameter D_0, stroke H, winding number α to calculate the initial winding number i_0, determine the numerator Q, denominator N by the fractional part of the winding number, thus identifying the first overlapping winding number: $i_c(1)$=P(1)+Q(1)/N(1).

2) The relationship of the winding number would be decreased gradually as the roll diameter increasing in constant helical angle winding, Q(j) decreased with the step length 1 and the subsequent winding number ic(j) are as followed:

P(1)+(Q(1)-1)/N(1), P(1)+(Q(1)-2)/N(1), …, P(1)+1/N(1);
P(1)-1+(Q(2)-1)/N(2), P(1)-1+(Q(2)-2)/N(2), …, P(1)-1+1/N(2);…

Default Z distance between starting point of two adjacent winding cycle in circumferential direction, and amendment each overlap sequence derivates according with the formula (6) and (7), the anti-overlapping winding number sequence:

$$i_s(j) = i_c(j) \pm Z / (\pi \cdot D_k) \tag{8}$$

Overlapping winding number after initial derivate, we can delete some winding number directly which can be find out easily that do not have the anti-overlap[6]. If the rest of the winding number have longer winding cycle than the original overlap winding number and to eliminate the symptoms of overlap completely or not also need experiment to analysis and verify the anti-overlap effect.

3 Section of Mechanical Engineering Experimental

Experimental equipment: JWA1680 winding head and the supporting melting spinning platform, German testo476 stroboscope.

Experimental Procedure:

Step 1: Set the starting point of the adjacent winding cycle offset distance Z and the value of denominator N in winding number, using the winding number of projection methodology described above, substitute it with JWA1680 winding head spinning process parameter and filtered by using simulation program written in MATLAB to get a group of anti-overlap winding number sequence i_j

Step 2: According to the basic principles and formula of winding to calculate the roll diameter range $[D_j, D_j+1]$ of each winding number i_j corresponding to and establish i_j-D_j form.

Step 3: With the help of stroboscope and camera we can shoot to the surface of roll forming situation as it is shown in Figure 2 and Figure 3 is winding overlapped and precision winding photos.

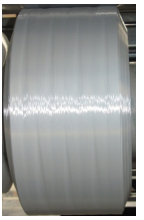

Fig. 2. Winding overlapped

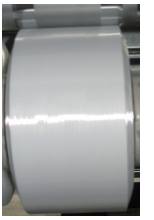

Fig. 3. Precision winding

Step 4: Observe constantly in experiments, track the draw texturing, and a group of ideal anti-overlap winding number sequence will be obtained ultimately by amending offset distance Z of the adjacent winding cycle starting point and the denominator N in the winding number, then filtered anti-overlap winding number and optimize the inappropriate winding number. Figure 4 show the changed sequences of winding number by the roll diameter increases gradually.

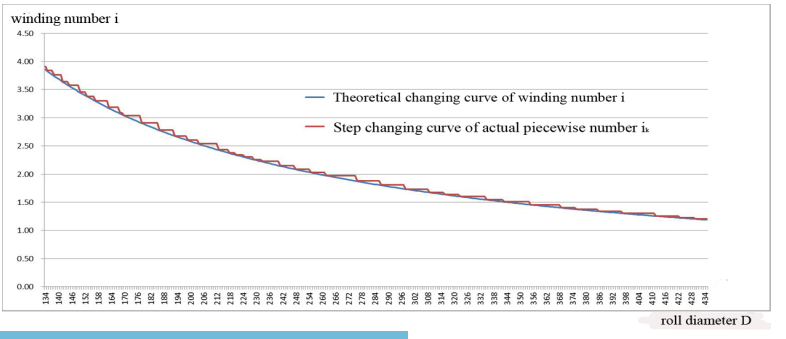

Fig. 4. Changing anti-overlap winding number sequence i as roll diameter D

After adjusting for several times, the problem of winding overlapping improved effectively and the roll surface forms good in each diameter section. The symptoms of broken ends was disappeared which was caused by winding overlap in the next process of draw texturing and reached the ideal anti-overlap effect.

4 Conclusion

(1) As based on the existing research, the influence of winding overlapping made by Winding decimal was analyzed and the clear definition of anti-overlap winding number and overlap winding number were confirmed.Any winding number will cause the filament return back to the winding starting point ultimately, while the difference between anti-overlapping winding number and overlapping winding number showed as follow: the anti-overlapping winding number make article silk uniform winding and does not appear uneven roll in the corresponding a winding cycle.

(2) A derivation method of winding number based on preventing stack mechanism was proposed, and issues in its process need to be attention. The principle of this calculation method was selected the appropriate offset distance Z in the starting point of the adjacent winding cycle as well as the denominator N in winding number, then fixed the overlapping winding number available to get a set of winding number amendments.

(3) Make use of the stroboscope to keep track of roll surface formation, then further screening, fix the winding number and put it inJWA1680 to check by mechanical engineer experiment, and finally get group of more ideal and effective anti-overlap winding number.

Acknowledgments. Fund name: The Fundamental Research Funds for the Central Universities of Donghua University (additional).

References

1. Wei, J., Kuang, J., Chen, S., Chen, Z.: Research on Winding System for High Speed Winders. J. Synthetic Fiber in China 08, 6–41 (2006)
2. Hu, Q., Xu, L.: The Anti-ribboning Analysis and Design on Precision Winding. Journal of Donghua University (Natural Science) 13(01), 9–17 (1987)
3. Jaksic, D.: The Method of Precision Winding of Textile Yarn into Packages by Frequently Changing the Wind Ratio within One Winding Cycle. EP 1930273 (2008)
4. Yu, J.: Discussion on Preventing Silk-loop Overlapping. Journal of Textile Research 09, 84–85 (2006)
5. Wei, D.: Chemical Fiber Mechanical Design Principle, pp. 165–230. Textile Industry Press, Beijing (1984)
6. Yu, J.: Best Fraction for Anti-ribbon and Analysis of Anti-ribbon of Cop Winders. Journal of Suzhou Institute of Silk Textile Technology 02, 1–6 (1993)

Dynamic Modeling and Simulation of Five-Cylinder Forging Machine

DaPeng Zhang[1,2], BaoHua Cheng[1], ChangBin Li[1], and AiGuo Wu[1]

[1] School of Electrical Engineer and Automation, Tianjin University, 300072, Tianjin, China
[2] Tianjin Key Laboratory of Process Measurement and Control, 300072, Tianjin, China
Zdp1995@163.com

Abstract. The five-cylinder structure is a representative framework in heavy forging machine. The forging machine is divided to a hydraulic working connection and a mechanical slide block to model. In working connection the model is built on the analysis of proportional servo valve, hydraulic cylinder and oil flow continuity. In mechanical slide block the model is built on the analysis of stress and moment from five cylinders to slide block according to the force balance equation and the moment balance equation. The model expresses the relation of proportional servo valve's opening and slide block's displacement. The simulation shows this model has a good tendency and steady-state accuracy with an actual forging machine.

Keywords: forging machine, model, five-cylinder.

1 Introduction

Many important forge pieces of national defense, aerial and astronavigation are made only by a forging machine. The forging machine which depends on the hydraulic cylinder is one of vital equipments in the manufacturing industry. A single cylinder only yields the pressure of 25-32MPa with the limit of current technology. So the heavy forging machine must be cooperated by several hydraulic cylinders in order to yield over kilotons pressure. The five-cylinder structure which is one of representative framework in heavy forging machines has a good characteristic of safety and is widely applied. But when it is working many technical parameters cannot reach the design criteria since the interaction of variables such as pressure, oil flow, slide block motion, velocity and so on. This cause the forging piece product must be further processed by cutting. Thus a lot of valuable raw materials have been wasted.

A good performance of forging machine can reduce the wastes. A way to improve the forging machine's performance is in time adjusting the correlated variables which keeps all parameters in the range of permission and lets the machine always work in a good state. Some researchers have proposed many approaches to control the forging machine [1-8]. These approaches have a same drawback of dependence on the experiences in some extent and it is difficult for them to further improve the performance since a forging machine which is a complexity of hydraumatic, mechanism and electricity is too complex to be hold only by experiences. So the model of forging machine must be built. The arguments in paper are listed in table 1 for conveniency.

D. Jin and S. Lin (Eds.): Advances in Mechanical and Electronic Engineering, LNEE 176, pp. 131–137.
springerlink.com

Table 1. The arguments

Variables	meaning	Variables	meaning
q_i	the oil flow(ith branch)	F_f	load force
A_i	The power acting point	x_i	the displacement of A_i
S	the plunger's sectional area of exporting cavity of hydraulic cylinder	F_i	the force from ith hydraulic actuating cylinders to slide block
x_a	the displacement at the centre of slide block	B	the viscosity damping coefficient
J_y , J_x	the rotational inertia of slide block rotating with axis y and axis x	α β	a included angle between l and axis x, between F_2 to axis x in plane xy
a , b $2h$	the length, width and height of slide block	m	the mass of plunger and slide block
p_i v_i	the oil pressure, the moving speed of plunger	φ_x φ_y	the projection of plane xy on plane xz and plane yz
ω_n ξ K_q	the inherent frequency, the damping rate, the flow gain of propositional servo valve	d	the distance from the acting point to the centre of slide block upper surface

2 The Working Connection Model

The working connection of five-cylinder forging machine is in figure 1.

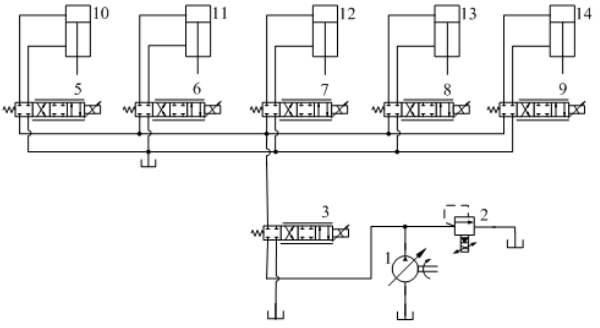

Fig. 1. The schematic diagram of working connection of five-cylinder forging machine

The system consists of an oil tank (no labeled), a constant rate pump (labeled 1), six proportional servo valves (labeled 3,5,6,7,8,9), five hydraulic actuating cylinders (labeled 10,11,12,13,14) and pipes (no labeled). An oil tank is used to store the oil. A constant rate pump is used to force the oil to flow from the oil tank to pipelines. In six

proportional servo valves one in main pipe (labeled 3) is used to control the total oil flow and five in branch pipes are used to control the oil flow into hydraulic actuating cylinder. Each of hydraulic actuating cylinders is divided to an upper cavity and a lower cavity and both cavities are insulative. The pressure oil goes into the upper cavity of cylinder and products the working pressure. So a slide block is driven down by this pressure and the slide block's velocity is controlled by adjusting the opening of proportional servo valves.

The proportional servo valve is modeled as

$$\frac{1}{\omega_n^2}\frac{d^2 q_i}{dt^2}+\frac{2\xi}{\omega_n}\frac{dq_i}{dt}+q_i=K_q\cdot A_s \tag{1}$$

The hydraulic actuating cylinder is modeled as

$$p_i S=m\frac{dv_i}{dt}+Bv_i+F_f \tag{2}$$

Further the model of all hydraulic actuating cylinder controlled by a corresponding proportional servo valve is gained.

The oil flow continuity is modeled as

$$q_s=\sum_{i=1}^{5} q_i \tag{3}$$

3 The Slide Block Model

Five hydraulic actuating cylinders work together to accomplish the balance of a slide block. The stress of slide block is in figure 2.

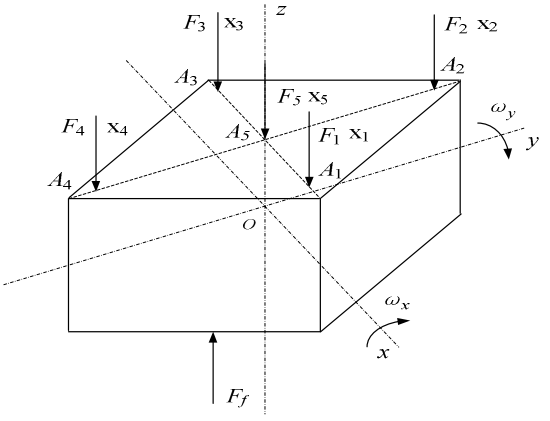

Fig. 2. The simplified force diagram of slide block

Suppose: 1) a dispersive load force is equivalent to a concentrate force; 2) the elasticity and plastic deformation of slide block are ignored. The displacement of acting point of slide block is made up of both offset caused by non-uniform force and shift caused by overcoming the load force.

3.1 The Offset Caused by Rotation

According to the moment balance equation we gain

$$\begin{aligned} J_y \frac{d\omega_y}{dt} &= F_1\left(\mathrm{d}\cos\varphi_y + \mathrm{h}\sin\varphi_y\right) + F_2\cos\beta(d\cos\varphi_x + h\sin\varphi_x) \\ &+ F_m \mathrm{h}\sin\varphi_y - F_3\left(\mathrm{d}\cos\varphi_y - \mathrm{h}\sin\varphi_y\right) - F_4\cos\beta \\ &(d\cos\varphi_x - h\sin\varphi_x) - F_f\left(l\cos\alpha\cos\varphi_y - \mathrm{h}\sin\varphi_y\right) \end{aligned} \tag{4}$$

The offset Δx_{ω_y} caused by rotational speed ω_y is

$$\Delta x_{\omega_y} = [\mathrm{d}\sin(\varphi_y + \Delta\varphi_y) - \mathrm{d}\sin\varphi_y] - [\mathrm{h}\cos(\varphi_y + \Delta\varphi_y) - \mathrm{h}\cos\varphi_y] \tag{5}$$

So

$$\begin{aligned} \frac{dx_{\omega_y}}{dt} &= \lim_{t\to 0}\Delta x_{\omega y} = \lim_{t\to 0}\frac{[\mathrm{d}\sin(\varphi_y + \Delta\varphi_y) - \mathrm{d}\sin\varphi_y] - [\mathrm{h}\cos(\varphi_y + \Delta\varphi_y) - \mathrm{h}\cos\varphi_y]}{t} \\ &= d\cos\varphi_y + h\sin\varphi_y \end{aligned} \tag{6}$$

Similarly we gain the derivation of offset Δy_{ω_x} caused by rotational speed ω_x

$$\begin{aligned} \frac{dy_{\omega_x}}{dt} &= \lim_{t\to 0}\Delta y_{\omega_x} = \lim_{t\to 0}\frac{[\mathrm{d}\cos\beta\sin(\varphi_x + \Delta\varphi_x) - \mathrm{d}\cos\beta\sin\varphi_x] - [\mathrm{h}\cos\beta\cos(\varphi_x + \Delta\varphi_x) - \mathrm{h}\cos\beta\cos\varphi_x]}{t} \\ &= d\cos\beta\cos\varphi_x + h\cos\beta\sin\varphi_x \end{aligned} \tag{7}$$

The total offset Δx_{xy} caused by both ω_x and ω_y is

$$\begin{aligned} \frac{dx_{xy}}{dt} &= \frac{\partial x_{xy}}{\partial x_{\omega_x}}\frac{dx_{\omega_x}}{dt} + \frac{\partial x_{xy}}{\partial y_{\omega_y}}\frac{dy_{\omega_y}}{dt} = \frac{y}{\sqrt{x^2+y^2}}\frac{dx_{\omega_x}}{dt} + \frac{x}{\sqrt{x^2+y^2}}\frac{dy_{\omega_y}}{dt} \\ &= \frac{d\cos\beta\sin\varphi_x}{\sqrt{(d\cos\beta\sin\varphi_x)^2 + (d\sin\beta\sin\varphi_y)^2}}(d\cos\beta\cos\varphi_x + h\cos\beta\sin\varphi_x) \\ &+ \frac{d\sin\beta\sin\varphi_y}{\sqrt{(d\cos\beta\sin\varphi_x)^2 + (d\sin\beta\sin\varphi_y)^2}}(d\cos\varphi_y + h\sin\varphi_y) \\ &= \frac{d\cos\beta\cos\varphi_x + h\cos\beta\sin\varphi_x + d\cos\varphi_y + h\sin\varphi_y}{\sqrt{(\cos\beta\sin\varphi_x)^2 + (\sin\beta\sin\varphi_y)^2}} \end{aligned} \tag{8}$$

3.2 The Downward Shift

According to the force balance equation we gain

$$m\frac{d^2x_a}{dt^2} = F_1 + F_2 + F_3 + F_4 + F_5 - F_f \tag{9}$$

Let $z_6 = \frac{dx_a}{dt}$, so

$$\begin{cases} \frac{dx_a}{dt} = z_6 \\ \frac{dz_6}{dt} = \frac{1}{m}(F_1 + F_2 + F_3 + F_4 + F_5 - F_f) \end{cases} \tag{10}$$

3.3 The Displacement of Offset and Shift Together

The displacement x_1, x_2, x_3, x_4 respective at A_1, A_2, A_3 and A_4 is as follows.

$$\frac{dx_1}{dt} = \frac{d(x_a + x_{\omega y})}{dt} = \frac{dx_a}{dt} + \frac{dx_{\omega y}}{dt} = z_6 + d\cos\beta\cos\varphi_x + h\cos\beta\sin\varphi_x$$
$$= z_6 + d\cos\beta\frac{\sqrt{a^2+b^2}}{\sqrt{a^2+b^2+(x_1-x_3)^2}} + h\cos\beta\frac{x_1-x_3}{\sqrt{a^2+b^2+(x_1-x_3)^2}} \tag{11}$$

$$\frac{dx_3}{dt} = \frac{d(x_a - x_{\omega y})}{dt} = \frac{dx_a}{dt} - \frac{dx_{\omega y}}{dt} = z_6 - d\cos\beta\cos\varphi_x + h\cos\beta\sin\varphi_x$$
$$= z_6 - d\cos\beta\frac{\sqrt{a^2+b^2}}{\sqrt{a^2+b^2+(x_1-x_3)^2}} - h\cos\beta\frac{x_1-x_3}{\sqrt{a^2+b^2+(x_1-x_3)^2}} \tag{12}$$

$$\frac{dx_2}{dt} = \frac{d(x_a + x_{xy})}{dt} = \frac{dx_a}{dt} + \frac{dx_{xy}}{dt} = z_6 + \frac{d\cos\beta\cos\varphi_x + h\cos\beta\sin\varphi_x + d\cos\varphi_y + h\sin\varphi_y}{\sqrt{(\cos\beta\sin\varphi_x)^2 + (\sin\beta\sin\varphi_y)^2}} = z_6 +$$
$$\frac{d\cos\beta\frac{\sqrt{a^2+b^2}}{\sqrt{a^2+b^2+(x_1-x_3)^2}} + h\cos\beta\frac{x_1-x_3}{\sqrt{a^2+b^2+(x_1-x_3)^2}} + d\frac{\sqrt{a^2+b^2}\sin\beta}{\sqrt{(a^2+b^2)\sin^2\beta+(x_2-x_4)^2}} + h\frac{x_2-x_4}{\sqrt{(a^2+b^2)\sin^2\beta+(x_2-x_4)^2}}}{\sqrt{(\cos\beta\frac{x_1-x_3}{\sqrt{a^2+b^2+(x_1-x_3)^2}})^2 + (\sin\beta\frac{x_2-x_4}{\sqrt{(a^2+b^2)\sin^2\beta+(x_2-x_4)^2}})^2}} \tag{13}$$

$$\frac{dx_4}{dt} = \frac{d(x_a - x_{xy})}{dt} = \frac{dx_a}{dt} - \frac{dx_{xy}}{dt} = z_6 - \frac{d\cos\beta\cos\varphi_x + h\cos\beta\sin\varphi_x - d\cos\varphi_y - h\sin\varphi_y}{\sqrt{(\cos\beta\sin\varphi_x)^2 + (\sin\beta\sin\varphi_y)^2}} \tag{14}$$

4 Test and Verify

There are 31 state variables (including 6 middle state variables), 5 control variables and 27 parameters. An actual 100MN forging machine is used to test. The speed and

balance of slide block are controlled by adjusting the opening of propositional servo valve and the 27 parameters obtained from drawing paper. The simulation is made by MATLAB 7.0 according to the proposed model and many results are obtained. Due to limited space only one case appears here.

Case: The velocity of simulation and of measure of slide block at the centre are in figure 3 when the right-front servo valve is from close to open in case of other propositional servo valves' openings keep fixed.

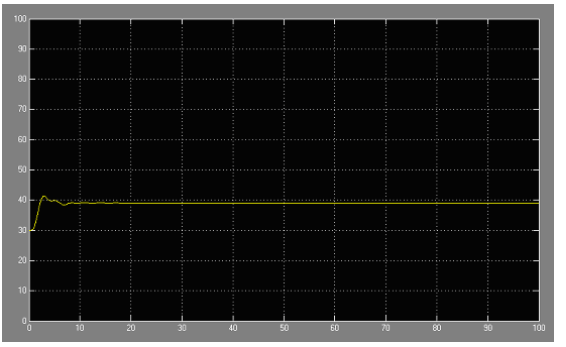

Fig. 3. The simulation of velocity at slide block centre

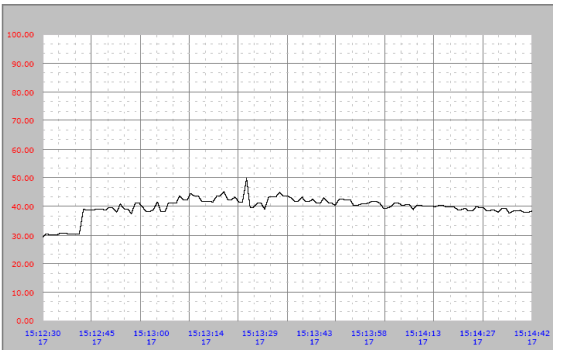

Fig. 4. The measure of velocity at slide block centre

It is seen from figure 3 that in simulation the speed of slide block center makes a jump from original 30μm/s to 39μm/s when the opening of right front servo valve is from close to open which means to generate a step driver. The transient time is about 8 seconds and a small overshoot is generated. While at the same condition the speed of slide block center in measure also makes a jump from 30μm/s to 39μm/s in 4 seconds and keeps about 39μm/s finally. Though the speed has a small fluctuation there is no overshoot which once appeared in simulation. It is a reason that the damp coefficient of real hydraulic system is bigger and the transient process finishes in a

period. The similarities appear in other cases. There are a few differences of transient time between simulation and measure since the damp coefficient of real hydraulic system is bigger. But the whole tendency of simulation consists to that of measure and there is a few steady-state errors.

5 Conclusions

Building a dynamic model will benefit to disclose the relations of important variables in forging machine. It also supplies a theoretical foundation for further advanced control on forging machine. This paper builds a dynamic model of five-cylinder forging machine based on the analysis of the components characters and the stress of slide block. The simulation shows this model has a good consistence in tendency and has a high accuracy in steady state.

Acknowledgement. This work is supported by Young Fertilizer Foundation of Tianjin University (TJU-YFF-08B77).

References

1. Chen, B., Huang, S., Gao, J., et al.: Control Strategy for Free Forging Hydraulic Press. Chinese Journal of Mechanical Engineering 44, 304–307, 312 (2008)
2. Li, X., Zhou, E., Lin, J., et al.: Research on Hydraulic Synchronization Control of Four-cylinder Systems. Machine Tool & Hydraulics 38, 28–30 (2010)
3. Tan, J., Huang, C., Liu, B., et al.: Control strategy of hydraulic operation control system under the transient load in giant hydraulic press. Chinese Journal of Mechanical Engineering 44, 272–276 (2008)
4. Yao, J., Kong, X., He, L., et al.: The Hydraulic Control System of 22 MN Fast Forging Press. Machine Tool & Hydraulics 38, 24–27 (2010)
5. Zhang, D., Zhai, W., Wu, A., et al.: Decoupling control of forging machine based on PID neural network. In: Proceedings of the World Congress on Intelligent Control and Automation, pp. 1857–1862. Institute of Electrical and Electronics Engineers Inc., Piscataway (2010)
6. Chunyan, D., Aiguo, W., Aihong, Z.: The application of single neuron adaptive PID method to the speed control of isothermal forging processes. In: Proceedings of the World Congress on Intelligent Control and Automation, pp. 8519–8522. Institute of Electrical and Electronics Engineers Inc., Piscataway (2006)
7. Hu, J., Yin, J.: Knowledge discovery and management from numerical simulation and its application to robust optimization of extrusion-forging processing. Key Engineering Materials 340, 659–664 (2007)
8. Yu, D., Li, Z., Shiyu, Z.: Phase I analysis for monitoring nonlinear profiles in manufacturing processes. Journal of Quality Technology 38, 199–216 (2006)

Genetic Algorithm Combined with Simulation for Job Shop Scheduling Problem in Mechanical Engineering

Hua Yu and Lei Wang

School of Mechanical and Automotive Engineering, Anhui Polytechnic University, Wuhu, 241000
ahyuhua@126.com

Abstract. In this paper, we describe a simulation combined with genetic algorithm for job shop scheduling problems in mechanical manufacturing and engineering. In first phase of the scheduling and real-time control system, optimization algorithms for scheduling will reduce drastically the computational burden on simulation, while in second phase, simulation can provide a problem free execution of the predictive plans and can be used to check the validity of the schedule, and most importantly, to improve or fine tune the schedule in mechanical manufacturing area. Therefore combination with genetic algorithm and optimization algorithm for job shop scheduling has significance for guiding the practical mechanical manufacturing.

Keywords: Job shop scheduling, Genetic algorithm, ExtendSim, Modeling and simulation, Mechanical manufacturing.

1 Introduction

Job-shop scheduling problem (JSP), which is among the hardest combinatorial optimization problems [1], is a branch of production scheduling. It is well known that this problem is NP-hard [2]. Many real scheduling problems in the manufacturing engineering are quite complex and very difficult to be solved by conventional optimization techniques. Usually, these difficult-to-solve problems are characterized as combinatorial optimization problems subject to highly complex constraints.

In recent years, there are many optimization methods such as branch-and bound method [3], heuristic method [4], and stochastic search methods [5-7] to solve JSP have been widely studied. However, in order to simulate the practical production well, the optimization result needs to be combined with simulation methods. Simulation is widely used in the world and therefore it is very familiar [8]. The most important reasons and advantages of simulation methodology for modeling manufacturing engineering are illustrated in [9, 10].

In this paper, we describe a simulation combined with genetic algorithm for job shop scheduling problems in mechanical manufacturing. In first phase of the scheduling and real-time control system, optimization algorithms for scheduling will reduce drastically the computational burden on simulation, while in second phase, simulation can provide a problem free execution of the predictive plans and can be

D. Jin and S. Lin (Eds.): Advances in Mechanical and Electronic Engineering, LNEE 176, pp. 139–144.
springerlink.com

used to check the validity of the schedule, and most importantly, to improve or fine tune the schedule. Therefore combination with genetic algorithm and optimization algorithm for job shop scheduling has significance for guiding the practical mechanical manufacturing.

2 Job-Shop Scheduling Model

In general, JSP is described as follows: There are n different jobs and m different machines to be scheduled. Each job is composed of a set of operation and the operation order on machines is prespecified. The required machine and the fixed processing time characterize each operation. There are several constraints on jobs and machines:

(1) A job does not visit the same machine twice.
(2) There are no precedence constraints among the operations of different jobs.
(3) Operations cannot be interrupted.
(4) Each machine can process only one job at a time.
(5) Neither release times nor due dates are specified.

The problem is to determine the operation sequences on the machines in order to minimize the makespan-that is, the time required to complete all jobs, namely:

$$\min f(x)=\max(c_{ik}) \tag{1}$$

where c_{ik} denotes the finishing time of job i(i=1,2,…,n) on machine k(k=1,2,…,m).

3 GA for Job-Shop Scheduling Problem

Genetic algorithm (GA) is stochastic search technique based on analogy to Darwinian natural selection. Individuals who fit the environment best should have a better chance to propagate their offspring. By the same reason, solutions that have the best "fitness" should receive higher probability to search their "neighbors". The main advantage of GA lies in its powerful implicit parallelism. In Holland's theory, a GA implicitly evaluates a number of patterns larger than population size without additional computational time and memory. The main procedures of a GA for JSP are as follows:

3.1 Chromosome Representation

A chromosome has gene information for solving the problem in GA. The permutation encoding [11] is widely used to solve the scheduling problem easily, because this coding method can create an active schedule at every time. The chromosome shows the order of job-number. If the number of jobs is n and the number of machines is m, the chromosome consists of n×m genes. Each job will appear m times exactly; it shall be depending on an order relation. Thus, each chromosome represents a feasible solution.

3.2 Fitness Function Decision

In this paper, the reciprocal of the maximal makespan is selected as the fitness function, and then the fitness of each chromosome can be calculated according to Eq.(2).

$$g(x) = 1/f(x) \tag{2}$$

3.3 Selection

The best solution should be considered in subsequent generations. At a minimum, the single best solution from the parent generation needs to be copied to the next generation thus ensuring the best score of the next generation is at least as good as the prior generation. Here the selection probability R is adopted according to Eq.(3).

$$R = \frac{g_i}{\sum g_i} \tag{3}$$

where, g_i is individual fitness, $\sum g_i$ is the sum of the individual fitness.

If the number of population is N, then the number of each chromosome for the next generation is given as follows.

$$N_i = R \cdot N = \frac{g_i}{\sum g_i} \cdot N \tag{4}$$

3.4 Crossover and Mutation

Order Crossover (ODX) is used in the HGA since Brizuela et al. [12] reported good results for GA with ODX in JSP problems. The procedures of ODX can be referred to [13]:

The mutation operator is called simple exchange mutation which selects two genes from a chromosome at random and then exchanges their positions.

3.5 Offspring Generation

The offspring generation is obtained by the processes of crossover and mutation. New individuals are generated until a fixed maximum number of individuals is reached.

4 Integration Optimization and Simulation Based on Extendsim

Job shop scheduling system can be easily communicated with Extendsim simulation software by using automation technology based on component object model (COM). The function of automation object is to realize IDispatch interface. The job shop scheduling system and Extendsim simulation system can be connected by using IDispatch interface, as shown in Fig.1, and the concrete implementation process by using VC++ application is as follows.

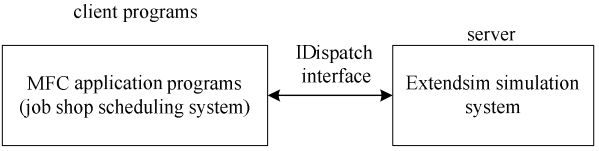

Fig. 1. Connection between client programs and Extendsim simulation model

Step 1. Creating an object by using CLSID
RegOpenKey(HKEY_CLASSES_ROOT, "Extend.Application", &hKey);
RegQueryValue(hKey, "CLSID", ClsidString, &length);
CLSIDFromString (ClsidString, &clsid);
Step 2. Creating an IDispatch interface by using CoCreateInstance (…) function
CoCreateInstance(clsid,NULL,CLSCTX_LOCAL_SERVER,IID_IDispatch,(LPVOID *)&m_pDisp) ;
Step 3. Acquiring a method to Execute DISPID by using GetIDsOfNames(…) function
WCHAR *Name = (WCHAR *) L"Execute";
DISPID executeID;
GetIDsOfNames (IID_NULL, &Name, 1, LOCALE_SYSTEM_DEFAULT, &executeID);
Step 4.Opening an ExtendSim simulation by using Invoke (…) function
CString temp="OpenExtendFile(\"C:\\Extend6LT\\Examples\\Operations Research\\Multitasking CPU.mox\");";
Invoke(executeID,IID_NULL,LOCALE_SYSTEM_DEFAULT,DISPATCH_METHOD,&dp3, NULL,&ei,&uiErr);

Therefore, the optimizing scheduling result can be imported Extendsim simulation model by using IDispatch interface to real time simulate, whereas the simulation results can be feedback to the job shop scheduling system to make the scheduling system better.

5 Example and Result

The following example illustrates the integration optimization and simulation based on Extendsim mentioned above. There is a three-job and three-machine JSP in mechanical engineering, its technological restriction is presented in Table 1.

Table 1. Processing time and processing route

job	machine, time		
1	(2,9)	(1,5)	(3,6)
2	(3,11)	(2,9)	(1,9)
3	(1,20)	(3,7)	(2,8)

(1) Firstly, the GA is used to solve JSP. Parameters of GA are selected as follows: population size N is 20, evolutional generation number G is 50, crossover probability p_c is 0.8, and mutation probability p_m is 0.04. An operation-based encoding method is adopted, and the optimal sequence is [231231312] by using GA.

(2) Secondly, a simulation model is established based on Extendsim, as shown in Fig.2.

(3) The optimal sequence is imported to the simulation model by using IDispatch interface technology. The simulation parameters are shown in Table 2.

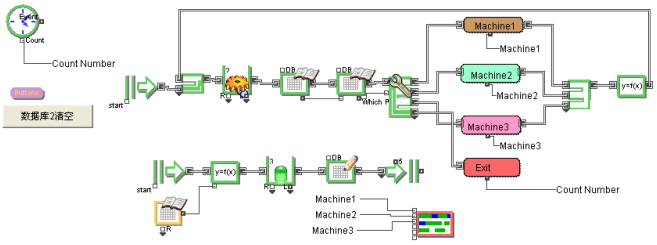

Fig. 2. Simulation model for JSP

Table 2. Utilization of each machine

machine	1	2	3
utilization	0.97	0.74	0.68

The simulation parameters (utilization, etc.) can help us to analyze bottleneck problem in production process and adopt appropriate methods to resolve it. Therefore integration optimization and simulation has an important significance for engineering manufacturing.

6 Conclusions

Manufacturing engineering scheduling is traditionally elaborated in a centralized manner and doesn't consider simulation. This paper presented a simulation combined with GA for JSP in mechanical engineering. In first stage of the scheduling and real-time control system, optimization algorithms for scheduling will reduce drastically the computational burden on simulation, while in second stage, simulation can provide a problem free execution of the predictive plans and can be used to check the validity of the schedule, and most importantly, to improve the engineering schedule and manufacturing.

At these stages, the objective is not to have complex scheduling algorithms but to achieve fast simulation combined with GA optimization. In further work, the embedded local scheduling and dynamic re-scheduling mechanisms will be studied in order to achieve high quality scheduling for practical mechanical manufacturing in a timely way.

Acknowledgements. This paper is supported by the national natural science foundation of China (No. 51175001), Anhui provincial natural science foundation (No.1208085QE94), the doctoral scientific research starting foundation of Anhui Polytechnic University (No.2011YQQ006), universities natural science research project of Anhui province (No. KJ2012B008). The authors would like to thank the referees, the editors and the anonymous reviewers for their helpful comments and constructive suggestions.

References

1. Sonmez, A.I., Baykasoglu, A.: A New Dynamic Programming Formulation of (n m) Flow Shop Sequencing Problems with Due Dates. International Journal of Production Research 36, 2269–2283 (1998)
2. Garey, M.R., Johnson, D.S., Sethi, R.: The Complexity of Flow Shop and Job-shop Scheduling. Mathematics of Operations Research 1(2), 117–129 (1976)
3. Lageweg, B.J., Lenstra, J.K., Rinnooy, K.A.: Job-shop Scheduling by Implicit Enumeration. Management Science 24(4), 441–450 (1977)
4. Haupt, R.: A Survey of Priority-rule Based Scheduling. OR Spektrum 11, 3–16 (1989)
5. Van Laarhoven, P.J.M., Aarts, E.H.L., Lenstra, J.K.: Job Shop Scheduling by Simulated Annealing. Operations Research 40(1), 113–125 (1992)
6. DellAmico, M., Trubian, M.: Applying Tabu Search to the Job Shop Scheduling Problem. Annals of Operations Research 41(3), 231–252 (1993)
7. Croce, F.D., Tadei, R., Volta, G.: A Genetic Algorithm for the Job Shop Problem. Computers & Operations Research 22(1), 15–24 (1995)
8. Fishwick, P.A.: Computer Simulation: Growth Through Extension. Transactions of the Society for Computer Simulation International 14(1), 13–23 (1997)
9. Georges, H., Claire, B.: A Model for Manufacturing Systems Simulation with a Control Dimension. Simulation Modelling Practice and Theory 11, 21–44 (2003)
10. Law, A.M., Kelton, W.D.: Simulation Modelling and Analysis, 2nd edn. McGraw-Hill, New York (1991)
11. Hirano, H.: Genetic Algorithm with Cluster Averaging Method for Solving Job-shop Scheduling Problems. JSAI 27(5), 769–777 (1995)
12. Brizuela, C.A., Zhao, Y., Sannomiya, N.: No-wait and blocking job-shops: Challenging problems for GA's. In: IEEE International Conference on Systems, Man, and Cybernetics, Tucson, Arizona, USA, pp. 2349–2354 (2001)
13. Cheng, R., Gen, M., Tsujimura, Y.: A Tutorial Survey of Job-shop Scheduling Problems Using Genetic Algorithms, Part II: Hybrid Genetic Search Strategies. Computers and Industrial Engineering 36, 343–364 (1999)

Prediction of Aero-Engine Exhaust Gas Temperature Based on Chaotic Neural Network Model

You Gao and Yuli Shen

College of Science, Civil Aviation University of China, Tianjin 300300, China
Gao_you@263.net, 362719862@qq.com

Abstract. This paper proposes a method of forecasting the aero-engine performance parameters exhaust gas temperature (EGT) time series. In order to obtain the forecast of good quality, the similarity theory is applied to the data processing. The method, based on chaos theory and neural network, give the prediction of the EGT series with relative errors less than 1.3%, which indicate that the proposed method makes a significant contribution for accurate forecasting. These important properties may provide us with new method to make prediction and projection of the EGT time series.

Keywords: Engine exhaust gas temperature, Chaotic time series, Lyapunov exponent, Neural network.

1 Introduction

Maintaining a high level of aero-engine reliability by efficient fault diagnosis is becoming important, because certain malfunctioning conditions can be a threat to safety of both human beings and the environment. In response to this demand, systematic methods of engine fault detection and diagnosis have long been sought. The classical diagnostic solutions are based on prediction of engine performance parameters and working status. Previous papers show the complex nonlinearity of variable trend for aero-engine performance parameters. More recently, the investigation of engine performance parameters focus on support vector machine [1-2], wavelet theory [3], neural network [4-6].

The reconstruction of the chaotic dynamics on the phase space shows predictability for chaotic time series. Therefore, on the basis of phase space reconstruction and neural network, we proposed the method to forecast the engine exhaust gas temperature.

2 Data Preprocessing

2.1 EGT Time Series Similarity Correction

The external conditions, such as external temperature and atmospheric pressure, are different for every flight, consequently, the data of engine exhaust gas temperature are usually not used for comparison directly. For solving this problem, we using the similarity theory to elimination of external conditions on the engine EGT sequence effects [7].

D. Jin and S. Lin (Eds.): Advances in Mechanical and Electronic Engineering, LNEE 176, pp. 145–150.
springerlink.com

$$EGT\_cor = (EGT\_obs + 273.15) / \theta T_2 \quad . \tag{1}$$

$$\theta T_2 = \left(TAT + 273.15\right) / 288.15 \quad . \tag{2}$$

Where TAT is atmospheric temperature, EGT_cor and EGT_obs present the parameter corrected value and observed value, respectively.

2.2 Exclude Outliers

If the data has outliers, it will seriously affect the prediction accuracy. Assume the sample bias of measurement data is denoted by δ, then

$$\delta = \sqrt{\frac{\sum_{n=1}^{N}\left(x_n - \bar{x}\right)^2}{N-1}} \quad . \tag{3}$$

Where $x_i (i = 1, 2, \ldots, N)$ is the observed time series, N is the number of sample, $\bar{x}$ is the mean value. If the error $(x_n - \bar{x})$ greater than 3δ, the date x_n will be excluded based on the statistical principles.

And then, we repeat this procedure for the reserved data.

3 Engine Exhaust Gas Temperature Chaotic Characteristics Identification

3.1 Phase Space Reconstruction

From the phase space dynamics, one can estimate the correlation dimension and other quantities to see whether the scalar time series is chaotic or stochastic. Therefore, phase space reconstruction is the first stage in chaotic time series analyses. Applying the delay time τ and embedding dimension *m*, the reconstruction affects the action of model and its prediction directly.

According to Packard et al. and Takens, the method of delays can be used to embed a scalar time series $\{x_n\}_{n=1}^{N}$ into an *m*-dimensional space as follows:

$$X_n = (x_n, x_{n-\tau}, \ldots, x_{n-(m-1)\tau}) \in R^m,\ n = N_0, N_0 + 1, \ldots, N \tag{4}$$

Where $N_0 = (m-1)\tau + 1$, $\tau > 0$ the delay time, and m is the embedding dimension. The methods of selecting the delay time τ generally are autocorrelation function method, the average mutual information method, etc. The methods of selecting embedding dimension m generally are the test algorithm, the false neighbor method and improved the false neighbor method [9]. In this paper, we use C-C method [10] to calculate the embedding dimension and time delay at the same time.

3.2 Chaos Identification

To identify whether chaotic components is exist in time series, the chaos theory, especially the largest Lyapunov exponent is used for the purpose. The size and plus-minus of Lyapunov exponent reflects the stretch and shrinkage characteristics [11] in all directions of the system.

In this paper we use the trajectory tracing method [12] proposed by A.Wolf to calculate the largest Lyapunov exponent.

4 Chaos Neural Network Prediction Model

Owing to feed forward neural network has strong nonlinear approximation ability, the multilayer feed forward neural network model become a popular neural network model. In this algorithm, the selected sample data is used for training the network, and the corresponding prediction model will be established until the results collected in training process converge to the minimum variance. Here we use the three-layer BP network, where have m-dimensional input nodes, q-dimensional hidden layer nodes, and one output node. After the reconstruction, the m-dimensional vector $X_n = (x_n, x_{n-\tau}, \cdots, x_{n-(m-1)\tau})$ is used as the input layer. The number of hidden layer points was obtained through the test of training network as shown in Fig. 1.

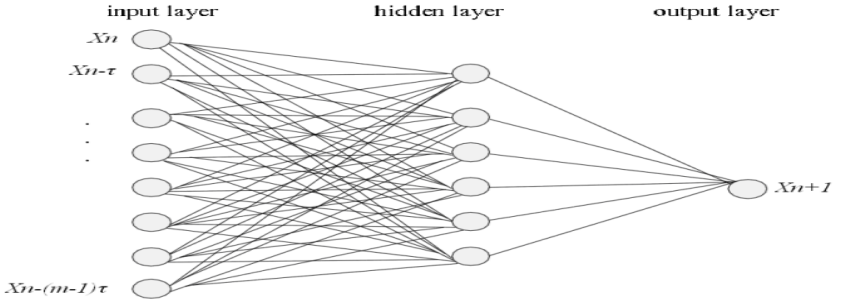

Fig. 1. BP neural network model

5 The References Section

In this paper, we apply the chaos neural network prediction model to analyze the data of aircraft communications address and reporting system (ACARS) collected at an aircraft maintenance company in Beijing. There are types of ACARS data: Take off mode, Cruise mode and Landing mode. The ACARS data includes various aero-engine performance parameters that are recorded at different sampling intervals. The airborne cruise segment data of here is collected for the PW4077D engine, about1000 records. For the convenience of our study, the engine exhaust gas temperature (EGT) data is recorded in time sequence.

For a record $\{x(i)\}$, the algorithm briefly involves the following steps.

Step 1: we determine the similarity correction and exclude outliers for original data. Processed data is shown in Fig. 2.
Step 2: we reconstruct phase space.

By using C_C method, the reconstructed phase space denoted as

$$X_n = (x_n, x_{n-2}, ..., x_{n-10}) \in R^6,\ n = N_0, N_0 + 1, ..., N \tag{5}$$

Where the time delay $\tau = 2$, embedding dimension m=6, $N_0 = (6-1)\times 2 - 1 = 9$.

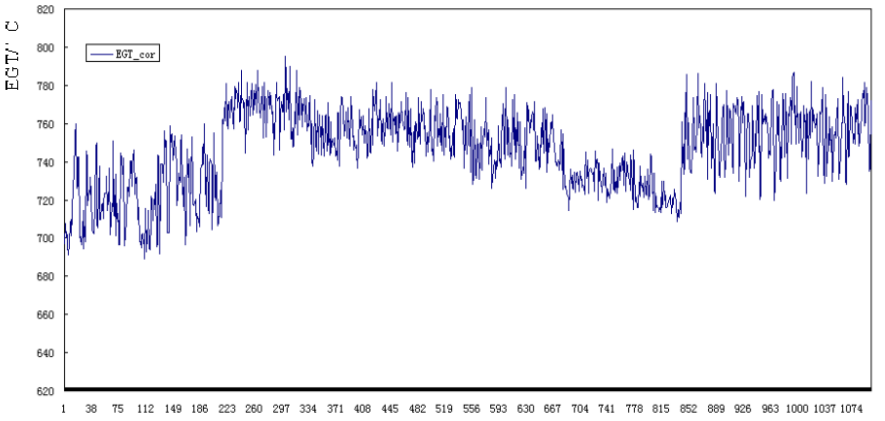

Fig. 2. EGT_cor

By applying trajectory tracing method proposed by A.Wolf, the largest Lyapunov exponent of engine exhaust gas temperature (EGT) is calculated. The value of the largest Lyapunov exponent is 0.0204>0. Thus there exist chaotic properties in engine exhaust gas temperature time series.

Step 3: we forecast the series by chaos neural network prediction model.

By the reconstruction results, there are 6 input nodes and 1 output nodes in the input layer of the neural network. Though training the net, we get the minimum error when the hidden layer has 13 nodes. By using MATLAB neural network toolbox to create 'newff' networks, with 'logsig' transfer function and 'learngdm' learning function, the former 1000 data is employed as training samples. We forecast the 10 data behind the 1000th as shown in Fig. 3. where the original value is given for comparison. We calculate the relative error between the predicted value and the original value to measure the accuracy of the prediction. The results are shown in talbe1.

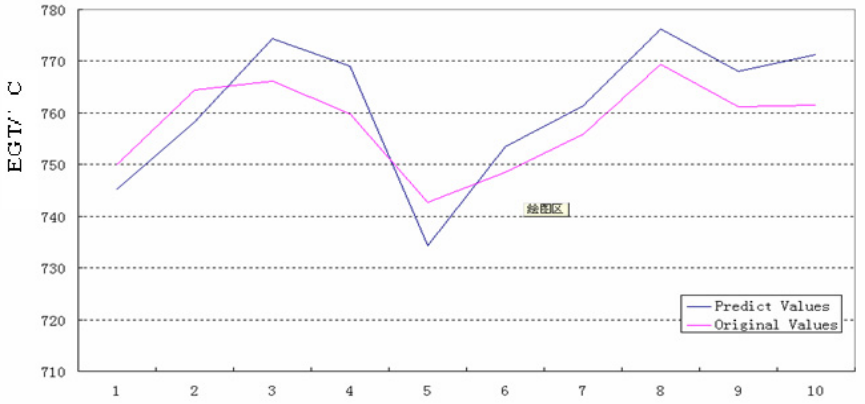

Fig. 3. Comparison of original values and predictive values

Table 1. The Comparative Table of EGT

No	Original Values	Predict Values	Relative Error
1	745.2	750.06	-0.00648
2	758.33	764.43	-0.00798
3	774.43	766.08	0.0109
4	769.11	759.83	0.012213
5	734.34	742.67	-0.01122
6	753.53	748.45	0.006787
7	761.3	755.8	0.007277
8	776.31	769.46	0.008902
9	768.1	761.09	0.00921
10	771.32	761.45	0.012962

It can be seen from Fig. 3 that the trend of predicted values and original values are similar and the error between them is small. In table 1, the prediction relative errors are almost less than 1%, which shows the chaotic neural network prediction for EGT series has better accuracy.

6 Conclusion

This paper introduced the largest Lyapunov exponent in chaos theory and applied it to engine EGT time series. The value of the largest Lyapunov exponent is 0.0204 indicate that the chaotic properties is exist in engine EGT series. On the basis of chaos theory and neural network, the proposed method gives the forecasting values with relative errors less than 1.3%. It is therefore believed that such a combined method of phase space reconstruction and neural network may be applied to widespread field.

Acknowledgments. This work is supported by the Fundamental Research Funds for the Central Universities under Grant No. ZXH 2009B003..

References

1. Wu, B., Wei, X.K., Feng, Y., Shao, C.Q., Yang, J.J.: Applications of Chaotic Support Vector Forecasting Model for Aeroengine. Fire Control & Command Control 36, 29–33 (2011) (in Chinese)
2. Zhang, C.X., Wang, N.: Aero-Engine Condition Monitoring Based on Support Vector Machine. In: SSME 2010 Conference, vol. 12, pp. 335–339 (2010) (in Chinese)
3. Song, Y.X., Peng, P., Shi, Y.S.: Chaos arithmetic for civil aero-engine forecasting. Journal of Aerospace Power 26, 675–679 (2011) (in Chinese)
4. Ding, G., Zhong, S.: Approximation capability analysis of parallel process neural network with application to aircraft engine health condition monitoring. In: Liu, D., Fei, S., Hou, Z., Zhang, H., Sun, C. (eds.) ISNN 2007. LNCS, vol. 4493, pp. 66–72. Springer, Heidelberg (2007)
5. Gencay, R., Liu, T.: Nonlinear modeling and prediction with feed forward and recurrent networks. Physica D. 108, 119–134 (1997)
6. Ding, G., Fu, X.Y., Zhong, S.S.: Aeroengine performance parameters prediction based on process neural network. Computer Integrated Manufacturing Systems 17, 198–207 (2011)
7. Zhou, B.Z.: Design and implementation of QAR data processing system. D. College of Aeronautical Engineering. Civil Aviation University of China (2009) (in Chinese)
8. Takens, F.: Detecting strange atractor in turbulence. Lecture Notes in Math., 366–381 (1981)
9. Wang, H.Y., Lu, S.: Nonlinear time series analysis and its application, pp. 16–21. Science Press, Beijing (2006) (in Chinese)
10. Kim, H.S., Eykholt, R., Salas, J.D.: Nonlinear dynamics, delay times, and embedding windows. Physica D. 127, 48–60 (1999)
11. Anastasios, A.T.: Chaos: From theory to applications. Plenum Press, New York (1992)
12. Wang, H.Y., Lu, S.: Nonlinear time series analysis and its application, pp. 25–28. Science Press, Beijing (2006) (in Chinese)

Visual Simulation of the Robot Welding Station of Car-Body-in-White Floor Assembly

ShengFang Zhang, JianGang Guo, ChangJun Ji, Kui Zeng, and ZhiHua Sha

School of Mechanical Engineering, Dalian Jiaotong University, Dalian 116028, China
frankzhangsf@hotmail.com

Abstract. Visual simulation of the robot welding station is one of the key sections of car-body-in-white welding line process planning which determines the production cycle of the whole automobile. Aims at the problem of lack of accurate and reliable visual simulation of robot welding station, the visual simulation system of robot welding station is presented based on developing platform of Robcad, and technical solutions and key technologies of the visual simulation are analyzed in detail. Finally, take one car-body-in-white floor assembly as an example, the visual simulation of robot welding station is generated. The result shows, applying the system in visual simulation of robot welding station, can shorten the time and increase the accuracy and reliability of car-body-in-white welding line process planning remarkably.

Keywords: Robot welding station, Car-body-in-white, Visual simulation, Robcad, Process planning.

1 Introduction

In order to meet the model-diversity and volume-variability of mixed-flow production, car-body-in-white (CBIW) welding assembly is heading towards the flexible robot welding line direction as a result of increasingly fierce competition in automotive industry. The simulation, as a technical means of system performance analysis, evaluation and optimization, which can analyze the system-configuration rationality, the system-performance satisfaction, and the prediction of system-defect existence, and has become an effective tool of a system scheme demonstration, planning and design, parameters and performance optimization [1,2]. The CBIW welding assembly is composed of robot welding stations which are the most basic and important units, and the robot welding station simulation is critical to optimize the production process, enhance process planning accuracy and shorten the production cycle and cost[3,4].

The CBIW floor assembly welding has many characteristics, such as more welding spots and fixture positioning points, more welding methods, and higher standard of welding technology and welding dimensional accuracy are required, so the welding robots are wildly used in CBIW floor assembly welding and more than 80% of the solder joint is completed by them, so robot welding process simulation is particularly important.

D. Jin and S. Lin (Eds.): Advances in Mechanical and Electronic Engineering, LNEE 176, pp. 151–155.
springerlink.com

2 Technology Program of Robot Welding Station Simulation

The production process of floor assembly welding station is mainly shown as follows: transportation → positioning and clamping fixture → welding → releasing→ transportation. In the above process, the robot is operated as follows: the robot starts from the original point, grabs and assembles the sub-assembly parts, switches the welding torches to spot welding the floor assembly which is clamped by the fixture, after completion of one welding point, welding torches move quickly to the next point to continue the operation. After all the welding tasks are completed, the welding torches will return to work original point.

After analysis of the robot welding station process planning, the robot welding station modeling, simulation and optimization are initiated. Three steps are normally needed to establish welding simulation system:

(1) Design 3D simulation model and establish simulation environment;
(2) Setup parameter of simulation model and control workflow;
(3) Simulate the operation, verification and analysis of the model.

The technology program of robot welding station simulation of CBIW floor assembly is shown in Fig. 1.

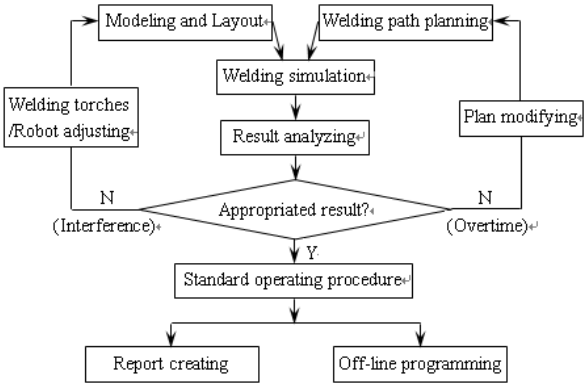

Fig. 1. Its main contents include: the establishment of simulation environment, welding spot and welding path planning, movement simulation, result analysis and offline program output

3 Approach of Robot Welding Station Simulation System

3.1 Foundation of Welding Station Simulation Model

The CBIW floor assembly robot welding station is mainly composed of robots, welding fixtures, transmission equipments, welding clamps, auxiliary equipments and body assembly parts. The accurate CAD-modeling is needed first in order to realize the visual simulation. Robcad[5] simulation data is divided into two categories: project data and library data, and two respectively folders are created to store them according

to classification. Project data contains *ce data and the equipment of demanding model-modification; library data contains digital-analog of production, fixture, general equipment and project-specialized equipment, and station layout. Select the robot type and welding clamp in the ROBOTICS module, and load resources of needed welding robots and other tools from query-available resource directory. The basic element of virtual manufacturing is kinematic simulation. In the kinematic simulation of floor assembly robot welding station, it mainly concerns definition of the fixture and welding clamp and foundation of motional model of station equipments.

3.2 Welding Path Planning

Taking welding workload as layout index and minimizing the working time as target, optimization process of path planning can be achieved by taking various constraints into account. The station welding time is defined by the robot which takes the longest time during multi-robot welding begun at the same time, and the best path is the trajectory which the above robot covers. The constraints of welding path planning are as fellows:

(1) Welding sequence constraint. Welding thermal deformation caused by different welding sequence absolutely affects the quality of welding.
(2) Welding time constraint. Balance the workload of multi-robot when welding task is assigned in order to ensure the workload can be completed at the same time.
(3) Welding space constraint. The center distance of welding spot is generally much smaller than the space which the welding torches takes, so the distance between two welding spots must be taken into account during multi-robot welding.

3.3 Selection of Welding Clamp and Robot and Installation Position

According to process requirement and production capacity, the welding spots will be generally given to each station, and then welding clamps will be generally decided by the condition of each station. Welding clamp electrodes commonly adopt pneumatic drive, servo-drive is usually adopted when precise control is needed, and welding pressure and welding current are determined by plate material, thickness and layer where the welding spots are located. In the robot welding automatic station, man-machine factor is less concerned, integrated pneumatic power frequency welding clamp is mainly chosen, considering of the welding quality, cost and energy saving.

Welding robot is mainly achieved welding, transport, gluing and other operations. This robot welding station adopts Fanuc robots. The installation position of the robot references to the task finish that the welding camps can access to the welding spots. In Robcad simulation environment, firstly, the enveloping surface of robot is created with the aim of all the spots enveloping the range of robot control. AUTOPLATE function can get the accessible points in robot running, then the robot automatically calculates the proper position, and through the plane at the origin point set different colors.

3.4 Simulation of Welding Spots Accessibility and Clamp Position

In order to confirm the accessibility between welding camp and spot, the welding clamp being validated is mounted on the robot, which is used to teach and show each of the stations assigned to welding spots . Welding camp is installed in the flange by the command of MOUNT in Robcad, and edits the welding spots to a group then obtains the welding-path by projection. Proper points between the welding spots are added to ensure the smooth operation of welding. To ensure welding spots quality, the electrode spot of welding clamp must consistent with the center of welding spots, and the electrode axis must coincide with the normal of welding spot.

3.5 Simulation of Robot Welding

The simulation of motion robot welding process is taken by MOTION panel, which includes the initial position and motion path optimization, spot welding and robot operating posture adjustment. In the robots simultaneously work with the completion of each welding task, the timing relationship between robots needs to be creating, and continuous simulation of robot welding is taken. The timing in Robcad existed in the form of Sequence of Operations (SOP), and SOP is set to each object involved in the station to describe logical relationship of objects in the station. The Time Chart of floor assembly station simulation is shown in Fig.2.

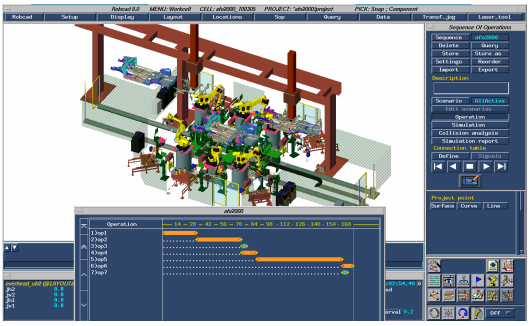

Fig. 2. When the SOP is simulating, the seven time-scales in Time Chart shows the operation and the time processing

4 Operation Example

Taking the robot welding point-fixed station of a certain CBIW floor assembly as an example, through physical modeling, robot planning and welding process planning, simulation modeling, the methods and steps of visual simulation using this system are verified. And also, run the simulation and analyze the result to find the bottleneck of assembly process and validate the process planning. The simulation of robot welding station production capability based on this system is shown in Fig. 3.

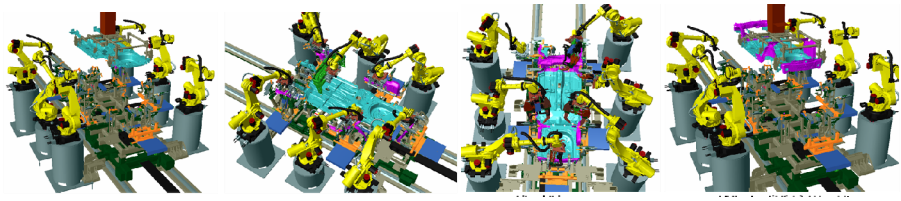

Fig. 3. (a) The work piece is transported to robot welding station by overhead system; (b) The robot fixing sub-floor assembly; (c) The robot welding in welding station; (d) The work piece is transported to next robot welding station by overhead system

5 Conclusions

In this paper, using simulation software Robcad as research and development platform, integrated modeling, planning and simulation technology are studied, the visual simulation system of robot welding station is constructed, and a visual simulation of CBIW floor assembly robot welding station is achieved. The practice shows, the simulation effectively proving the feasibility of the scheme, significantly reducing process planning time, improving process planning accuracy and efficiency, so it has important application value in achieving the CBIW welding assembly simulation.

Acknowledgement. Supported by the Natural Science Foundation of Liaoning Province (No. 201102021), the Excellent Staff Project of Institution of Higher Education of Liaoning Province（LJQ2011048）and the Science and Technology Foundation of Dalian City (2011J21DW008).

References

1. Su, C.: Modeling and Simulation of Manufacturing System. Mechanical Industry Press, Beijing (2008)
2. Yan, J.Q.: Virtual Manufacturing Theory, Technology and Practice. Shanghai Jiaotong University Press, Shanghai (2003)
3. Deng, X.B., Li, S.Q.: The Automobile Assembly Line Simulation Study. Computer Simulation 11(22), 72–74 (2005)
4. Bes, P.J., Mckay, L.N.D.: A Method for Registration of 3D Shape. IEEE Transactions on Pattern Analysis and Machine Intelligence 14(2), 239–256 (1992)
5. Zhang, J.Y., Cai, H.G., Wang, S.G.: A Large Robot Simulation System - ROBCAD. Journal of Harbin Institute of Technology 25(3), 108–109 (1993)

A Method for Auto-detecting Surface Defections of Ring Pieces

Yuhuai Wang[1], Keyong Hu[1], Yongqing Chen[2], and Zhouxiang Shou[1]

[1] Qianjiang College, Hangzhou Normal University, Hangzhou, Zhejiang, China
[2] School of Mechanical Engineering, Ningbo University of Technology, Ningbo, China
wyiya@hotmail.com, hukeyong@tom.com, arching@163.com, shoupan@hz.cn

Abstract. The online surface defects auto-detecting is important for the ring pieces quality. The proposed method implemented on binarization by iteration threshold. It located the optimized contours using the seed growth and calculated radius and central coordinates of ring pieces through the least square fitting. It measured and recognized the features extracted by masking using pixel-counting area. The PLC control circuit was designed. Experimental results show that the method detects 2038 magnetic rings in half an hour with detection rate 95.92% and false detection 2.06%.

Keywords: Machine Vision, Ring Pieces, Location and Optimization, Masking Circle.

1 Introduction

The random defections are often found in the surface of ring pieces. It's difficult to detect these defections by traditional methods. Machine vision technology used in the high-speed online detection of produces is a highly effective non-contact detecting technology [1-6]. Take the magnetic ring used for home appliances (e.g., speaker, microwave oven, etc.) for example, [6] presented an auto-detection method for E-shape magnetic based on gradient histogram of defects image. The main drawback of this method is that it is complex to realize for magnetic rings.

After reducing noise by second order BLPF, this paper studied a method for detecting surface defections of ring pieces and presented an optimum location algorithm of the image contour. Firstly, the image binarization is achieved by iterative threshold algorithm and the contour is pre-located by solving the inner radius and outer radius and the coordinate of ring centre based on seed growth method. Then, the contour is optimized by least square fitting Method. Finally, the defections are recognized by measuring the extracted feature. Detailed approach will be discussed in the following.

1.1 Operation Principle

The detecting system includes several steps. (1) Ring pieces are sent to the assembly line at a fixed cycle time using the feeding cylinder controlled by PLC. (2) The image

D. Jin and S. Lin (Eds.): Advances in Mechanical and Electronic Engineering, LNEE 176, pp. 157–164.
springerlink.com

is captured and conveyed to image acquisition card using the CCD camera driven by the corresponding photoelectric trigger, when the piece arrives at the detecting position. (3) A/D is achieved for the image. (4) The digital image is processed by the program. Firstly, the pre-processing is implemented including denoising, binarization and boundary extraction. Secondly, the features are extracted and analyzed to recognize defections and get the pass or fail signal. Finally, the logical signal is sent to PLC. (5) The defective pieces are eliminated using the cylinder controlled by PLC according to the fail signal. The good pieces will go to next position. (6) Turning over the piece and repeating steps (2)-(5) to detect the defections on the other surface.

The detecting system is mainly composed of computer and PLC. Computer is used to capture and process the image. FX2N-32MR-001 which was selected as PLC with 32 I/O is used to control all kinds of executive mechanisms.

The wiring diagram and ladder diagram are shown as the Fig.1 and Fig.2 respectively. Where, X11 receiving the signal from serial port is set through the communication protocol of host computer to control the outputs of PLC.

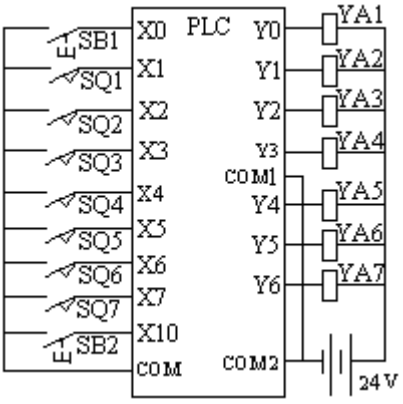

Fig. 1. Wiring diagram

2 Auto-detecting Method

In this paper, the system of coordinates of *roc* for digital image and *xoy* for physical image is introduced. The gray value of pixel is respectively represented by $I(r,c)(r,c,I \in Z^+)$ and $F(x,y)(x,y,F \in R^+)$.

2.1 Iteration Threshold Binarization Algorithm

The process of the algorithm can be separated into the following several steps.

(1) Normalization.
(2) Setting the initial estimated threshold.

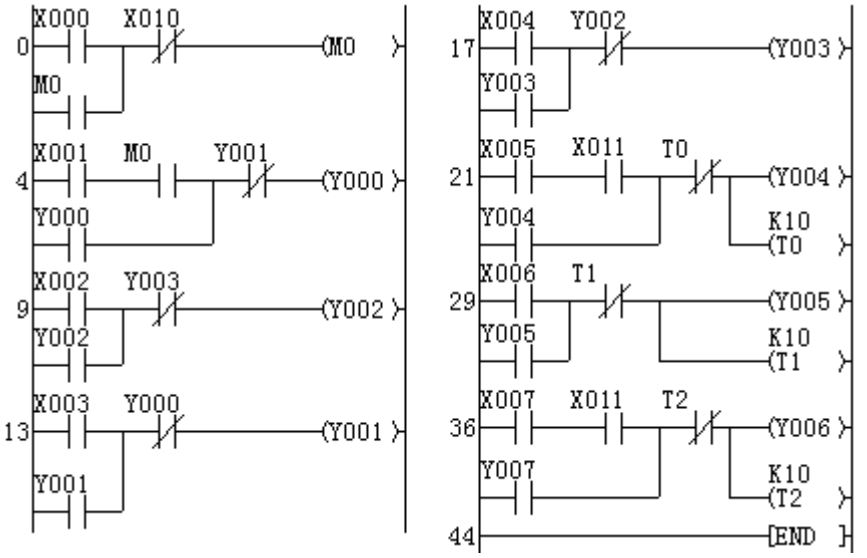

Fig. 2. Ladder diagram

$$T_0 = \{T_k \mid k = 0\} = (I_{\max} + I_{\min})/2$$

(3) Image threshold segmentation.

$$R_1 = \{I(r,c) \mid I(r,c) \geq T_k\} \text{ and } R_2 = \{I(r,c) \mid I(r,c) < T_k\}$$

(4) Calculating the mean gray I_{1mean} and I_{2mean} for R_1 and R_2.

(5) Solving the new threshold.

$$T_{k+1} = (I_{1mean} + I_{2mean})/2$$

If $T_k \neq T_{k+1}$, $k = k+1$. And then be switched to the third step.

(6) Binarization.

$$I(r,c) = \begin{cases} 0 & ,I(r,c) < T_k \\ 1 & ,I(r,c) \geq T_k \end{cases}$$

2.2 Contour Location Using Seeds

The contour of ring is the foundation of creating masked image, used for inspecting effective analysis area of ring pieces surface, which directly relates to the future successful defect inspection and precision.

Some methods for circular pattern recognition are presented in [7-9]. The commonality of [7] is poor. [8] has a burden for time. The complexity of [9]

is $O(N^3)$. Considering with the specific characteristics of ring images, a simple method is presented for locating the contour of inner and outer circle.

Let S_i is $(r_{\min}, c_i)$, where, $r_{\min}$ is the minimum row, when the gray is 1 on the pixel in the every column. In order to reduce the effects of grinding marks, three seeds $S_1(r_{\min 1}, c_1)$ 、 $S_2(r_{\min 2}, c_2)$ and $S_3(r_{\min 3}, c_3)$ are selected on the outer contour. The S_i which is the farthest to the centroid C is adopted as the seed.

In this paper, the coordinates of seeds selected will be as following:

$$\begin{cases} c_i = 90 \times (i-2) + \text{int}(n/2) \\ r_i = r_{\min | I(r,c_i)=1} \end{cases}, i = 1,2,3 \tag{1}$$

Where, *m*×*n* is the spatial resolution. int(·) is the nearest integer of the argument.

The centroid of binary image for ring pieces is obtained by equation (2).

$$\begin{cases} x_C = [\iint\limits_{(x,y)\in D} x dx dy] / [\iint\limits_{(x,y)\in D} dx dy] \\ y_C = [\iint\limits_{(x,y)\in D} y dx dy] / [\iint\limits_{(x,y)\in D} dx dy] \end{cases} \tag{2}$$

To speed up the calculation and to decrease the errors, Equation (2) was dispersed to Equation (3) based on Green's formula.

$$\begin{cases} x_C = \{\sum\limits_{k=1}^{N-1} [y_k (x_{k+1}^2 - x_k^2) - x_k^2 (y_{k+1} - y_k)]\} / \{2 \times \sum\limits_{k=1}^{N-1} [y_k (x_{k+1} - x_k) - x_k (y_{k+1} - y_k)]\} \\ y_C = \{\sum\limits_{k=1}^{N-1} [y_k^2 (x_{k+1} - x_k) - x_k (y_{k+1}^2 - y_k^2)]\} / \{2 \times \sum\limits_{k=1}^{N-1} [y_k (x_{k+1} - x_k) - x_k (y_{k+1} - y_k)]\} \end{cases} \tag{3}$$

Suppose S_1 which is farthest from the C in S_i as the seed point. That is

$$d_{S_1 C} = \max(d_{S_1 C}, d_{S_2 C}, d_{S_3 C})$$

Where,

$$d_{S_i C} = \sqrt{(x_{S_i} - x_C)^2 + (y_{S_i} - y_C)^2}, i = 1,2,3.$$

Based on the S_1 and its m-neighborhood, The contour is pre-located by M points on the boundary of ring pieces.

2.3 Fitting Optimization Algorithm

In order to improve the accuracy of the contour of a ring and masking image and avoid the tracking error caused by defections, the least square fitting optimization algorithm is presented based on M points for the contour.

Suppose a circle curve as

$$(x-x_o)^2+(y-y_o)^2=R_{outer}^2$$

Let $\alpha=-2x_o$, $\beta=-2y_o$ and $\gamma=x_o^2+y_o^2-R_{outer}^2$. We can deduced

$$x^2+y^2+\alpha x+\beta y+\gamma=0$$

The distance from the j-th sampling point (x_j, y_j) to center (x_o, y_o) is R_j. The area of circle is πR_j^2。 Then, the inaccuracy of the circular area is

$$\delta_j=\pi(R_j^2-R_{outer}^2)=\pi(x_j^2+y_j^2+\alpha x_j+\beta y_j+\gamma)$$

Let the function for Square inaccuracy of the area as

$$J(\alpha,\beta,\gamma)=\sum_{j=1}^{M}\delta_j^2=\pi^2\sum_{j=1}^{M}(x_j^2+y_j^2+\alpha x_j+\beta y_j+\gamma)^2$$

According to the extreme conditions of function, when J has the minimum value, parameters α, β and J should be held:

$$\frac{\partial J}{\partial\alpha}=\frac{\partial J}{\partial\beta}=\frac{\partial J}{\partial\gamma}=0$$

Then, we can obtain

$$\begin{cases}(x_o, y_o)=(-\alpha/2,-\beta/2)\\ R_{outer}=(\sqrt{\alpha^2+\beta^2-4\gamma})/2\end{cases} \tag{4}$$

Similarly, the inner contour can also be resolved by the above-mentioned methods. However, to speed up the calculation, considering the concentric characteristics of both inside and outside for ring, the inner contour will be resolved using the center of outer contour and a point on the inner contour.

The S_i which is the closest to the centroid C from three seeds on the inner contour is adopted as the seed. The three seeds should meet

$$I(r_{\min}+1, c_i)-I(r_{\min}, c_i)=-1 \tag{5}$$

2.4 Feature Extraction and Measurement and Defections Recognition

The image Q consisted of the extracted features is obtained by masking between the masked image g and optimized binary image E.

In order to improve the accuracy of the result, g is constructed as following

$$g(r,c)=\begin{cases}1, & R_{inner}^2 \le (r-r_o)^2+(c-c_o)^2 \le R_{\text{outer}}^2 \\ 0, & others\end{cases}$$

Then,

$$Q(r,c) = E(r,c)\times g(r,c) \tag{6}$$

The pixel-counting area and the Minimum Enclosing Rectangle (MER) are adopted to determine defection. We can define an empirical parameter A_{max} as the allowable area and A_f as the pixel-counting area of feature. A_f is the number of pixel on which the gray is 1 in the MER. The feature from Q is recognized as a defection, if $A_f \ge A_{max}$.

3 Experimental Analysis

In half an hour, a total of 2038 magnetic rings pieces are detected. Take the magnetic ring with crack (shown as Fig.3) as an example, the optimum location contour is shown as the red thread in Fig.4. Where, the blue symbol '+' and '■' represent the fitting center of ring and the selected seeds on the contour respectively. The green thread represents a part of located contour. The red thread represents the fitting optimum contour.

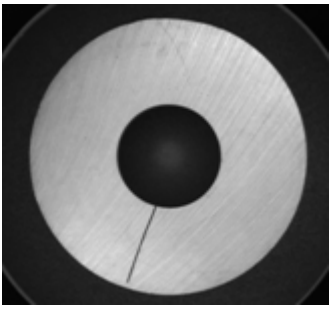

Fig. 3. The captured magnetic ring with crack

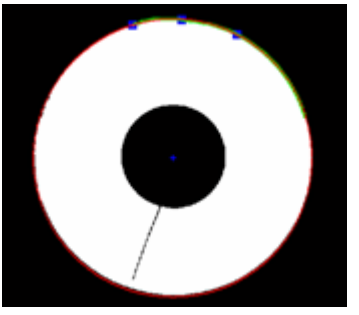

Fig. 4. The optimum binary image

Fig. 5 shows the enlarged view of crack and its MER detected by the presented approach. Where, MER is represented by [x,y,L,W]. In which, (x, y) is the coordinate of the upper-left point. L and W represent respectively the length and width of the MER. The MER is [60.94, 83.02, 10.42, 26.25]. The A_f is 52. The nominal data of magnetic rings detected and the relative error are illustrated in Table 1 and Table 2 respectively. The detected results of defections are shown as Table 3.

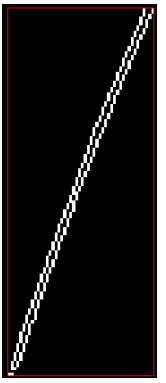

Fig. 5. The enlarged view of crack and its MER

Table 1. The nominal data comparison

	Outer /Inner radius	Center coordinate
Before optimization	52.19/19.53	(74.25,62.50)
Optimization	52.62/20.06	(76.49,62.05)
The true value	52.54/19.85	(76.16,62.25)

Table 2. The relative error

	Before optimization	Optimization
Outer radius	0.67%	0.15%
Inner radius	1.61%	1.06%
horizontal ordinate *x* of the center	2.51%	0.43%
vertical ordinate *y* of the center	0.40%	0.32%

Table 3. Defection results

	Algorithm	Manual
Quantity (pcs)	2038	2038
Crack (pcs)	13	15
Edge defect (pcs)	69	28
Split (pcs)	1	1
Impurity (pcs)	5	5
Qualified (pcs)	1950	1989

The system performance parameters can be got from the table 3.

Efficiency=2038/1800≈1.13 pieces/s

Detection rate= (13+28+1+5)/(15+28+1+5)×100%≈95.92%

False detection rate= (69-28) ×100%/1989≈2.06%

The actual quantity of defected product defected manually is 49, however, the actual quantity got by the algorithm in the paper is 88. There into, the edge defection quantity is 69, but that is 28 by the manual detection, therefore, the false detection is 41. The main reason of this mistake is caused by the depth deference when the edge

defection area meets or exceeds the detection limitation. When it comes to the edge defected magnetic ring with relative small depth, it is the acceptable products, so the manual detection is required for further, however, the work load has been reduced greatly. It evidenced that in the simulation: (1) Contour location of magnetic rings is precise. (2) The optimized contour ring is got by least square fitting. (3) Relative precise ring radius and center coordinate can be got. (4) Feature extraction and measurement and defections recognition are realized.

4 Conclusion

In this paper, an iterative threshold binarization algorithm is introduced; A kind of contour location optimization algorithm of boundary point search and least square fitting is presented, by which the inner and outer radius size and central coordinate was got; And then, the defections are extracted by masking technology and feature such as the pixel-counting area and MER are measured. Through the detection efficiency, detection rate, false detection rate and relative error got by the experiment, the proposed algorithm has the high performance to the normal defections.

Acknowledgments. It is supported by the National Natural Science Foundation of China (61103171), the Science and Technology Department of Zhejiang Province (2011C31048) and Qianjiang College of Hangzhou Normal University (2011QJJL09).

References

1. Lahajnar, F.: Machine vision system for inspecting electric plates. Comput. Ind. 47, 113–122 (2002)
2. Duan, F.J., Zhang, J.X., Ye, S.H.: Study on the Application of Computer Vision Inspection Technique to Electronic Meshes. Opto-Electron. Eng. 23, 66–72 (1996)
3. Lei, L.Y., Zhou, X.J., Pan, M.Q.: Machine Vision System for Inner and Outer Diameters Inspection of a Bearing. Trans. CSAE. 36, 131–134 (2005)
4. Lu, J.P., Little, J.J.: Reflectance and shape from images using a collinear light source. Int. J. Comput. Vision 32, 213–240 (1999)
5. Ying, Y.B., Wang, J.P., Jiang, H.Y.: Inspecting diameter and defect area of fruit with machine vision. Trans. CSAE. 18, 216–220 (2002)
6. Yue, X.J.: Gradient-histogram Based Adaptive Threshold Segmentation Algorithm for Defects Image of Product Surface. J. Nantong Univ. 6, 82–86 (2007)
7. Furusawa, K., Imoto, D., Kitamura, Y., et al.: A Novel Method for Circular Pattern Recognition in a Binary Image Using Two Kings of Resolutions and Its FPGA implementation. In: Proceedings of ITC-CSCC 2001, Tokushima, Japan, pp. 772–775 (2001)
8. Shigemori, K.: A Proposal of Novel Recognition System Using positional information to Detect Circles. In: Proceedings of ITC-CSC 2001, Japan, pp. 1058–1061 (2001)
9. Han, H.: Detect Circles from Intensity Images. J. Wuhan Univ. Technol. 25, 76–78 (2003)

Real-Time Trajectory Tracking of a Wheeled Mobile Robot With Kinematic and Dynamic Constraints

ZiHui Zhang and YueShan Xiong

School of Computer,
National University of Defense and Technology,
Changsha, P.R. China
peter1982.10@163.com, ysxiong@nudt.edu.cn

Abstract. To study the real-time trajectory tracking problem of a wheeled mobile robot, an approach with kinematic and dynamic constraints is suggested. When a desired trajectory is generated in real time, the velocities and accelerations required for real-time trajectory tracking are likely to exceed the bounds of a real mobile robot's velocities and accelerations. Some strategies proposed in this paper for velocity and acceleration constraints are adopted to make the resultant tracking trajectory of a real robot more reasonable in a practical environment. Experimental results of real-time trajectory tracking of sinusoidal curve illustrate that it is an efficient, effective, practical and high-precision approach for a wheeled mobile robot.

Keywords: Trajectory tracking, Wheeled mobile robot, real-time, kinematic constraint, dynamic constraint.

1 Introduction

In recent years, wheeled-based mobile robots have attracted considerable attention in various industrial and service applications[1,2], such as room cleaning and disabled people assistance.

In [3], Oriolo et al. had studied the trajectory tracking problem of a wheeled mobile robot using a dynamic linear feedback controller. In [4], Chwa et al. had investigated a wheeled mobile robot path tracking with sliding mode tracking controller in polar coordinates. In [5], Tzafestas et al. had developed a fuzzy path tracking algorithm for an autonomous nonholonomic mobile robot. Although some promising results are achieved in previous works, it does not mean that trajectory tracking of wheeled mobile robots has been studied in depth.

In this paper, we define the wheeled mobile robot's kinematic constraints as velocity contraints and define the dynamic constraints as acceleration contraints. When a desired trajectory is generated in real time, the velocity and acceleration constraints are taken into account to make the outcomes more practical in a real environment. Simulations of real-time trajectory tracking with sinusoidal curve validate the effectiveness and effeciency of our approach.

D. Jin and S. Lin (Eds.): Advances in Mechanical and Electronic Engineering, LNEE 176, pp. 165–170.
springerlink.com

2 Problem Statement

As it is well known, a wheeled mobile robot under perfect rolling constraints is a nonholonomic system, see Fig.1. These constraints can be defined by $\dot{x}\sin\theta - \dot{y}\cos\theta = 0$, where x, y denote the coordinates of the mobile robot and θ is the heading angle measured from the horizontal axis. Therefore, the kinematics of the wheeled mobile robot can be represented by the following equations. Linear velocity and angular velocity are denoted by ν and ω.

$$\begin{cases} \dot{x}(t) = \nu(t)\cos\theta(t) \\ \dot{y}(t) = \nu(t)\sin\theta(t) \\ \dot{\theta}(t) = \omega(t) \end{cases} \tag{1}$$

A discrete-time version of the dynamic model of the wheeled mobile robot is:

$$\begin{cases} x(t_k) = x(t_{k-1}) + T\nu(t_{k-1})\cos(\theta(t_{k-1}) + T\omega(t_{k-1})/2) \\ y(t_k) = y(t_{k-1}) + T\nu(t_{k-1})\sin(\theta(t_{k-1}) + T\omega(t_{k-1})/2) \\ \theta(t_k) = \theta(t_{k-1}) + T\omega(t_{k-1}) \end{cases} \tag{2}$$

Where T is the sampling period with $t_k = kT$ $(k \in \boldsymbol{Z})$ and $k \geq 1$. The robot's posture in time t_k is defined as follows. Furthermore, Variable $\mathbf{P}_d$ denotes the desired trajectory point to be tracked at current time.

$$\mathbf{P}(t_k) = [x(t_k), y(t_k)]^T \tag{3}$$

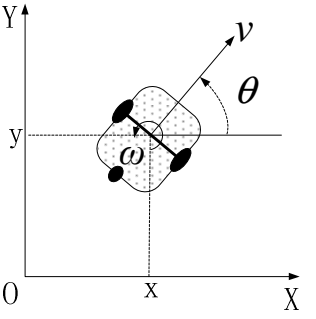

Fig. 1. Wheeled mobile robot kinematic parameters

As mentioned above, the wheeled mobile robot's kinematic and dynamic constraints are defined as velocity and acceleration constraints, which can be formulated as follows. Where ν_{max} and ω_{max} are the maximum velocities allowed for a real robot, and $\dot{\nu}_{max}$ and $\dot{\omega}_{max}$ are the maximum accelerations.

$$\begin{aligned} |\nu(t)| &\leq \nu_{max} & |\dot{\nu}(t)| &\leq \dot{\nu}_{max} \\ |\omega(t)| &\leq \omega_{max} & |\dot{\omega}(t)| &\leq \dot{\omega}_{max} \end{aligned} \tag{4}$$

3 Real-Time Trajectory Tracking Approach

For real-time trajectory tracking, a first order dynamic system is adopted in Eq. (5). Where k_{p1}, k_{p2} and k_{ω} are control gains and $\angle\dot{\mathbf{P}}_1(t_k)$ is the orientation angle of linear velocity $v_1(t_k)$. It can be recognized that the control inputs of $v_1(t_k)$ and $\omega_1(t_k)$ guarantees fulfillment of the trajectory constraint in absence of the kinematic and dynamic constraints. However, these value and their corresponding time derivatives are likely to exceed the bounds of a real mobile robot's velocity and acceleration so that trajectory tracking in a practical environment would fail.

$$\dot{\mathbf{P}}_1(t_k) = \dot{\mathbf{P}}_d(t_k) + k_{p1}[\mathbf{P}_d(t_{k-1}) - \mathbf{P}(t_{k-1})] + k_{p2}[\mathbf{P}_d(t_{k-2}) - \mathbf{P}(t_{k-2})] \tag{5}$$

$$v_1(t_k) = \left\|\dot{\mathbf{P}}_1(t_k)\right\| \tag{6}$$

$$\omega_1(t_k) = k_{\omega}\left[\angle\dot{\mathbf{P}}_1(t_k) - \theta(t_{k-1})\right] \tag{7}$$

3.1 Velocity Constraint

To limit the values of linear and angular velocities, the following strategies are adopted.

$$v_2(t_k) = \begin{cases} v_{max} & \text{if } v_1(t_k) > v_{max} \\ v_1(t_k) & \text{if } v_1(t_k) \le v_{max} \end{cases} \tag{8}$$

$$\omega_2(t_k) = \begin{cases} \text{sign}[\omega_1(t_k)]\omega_{max} & \text{if } |\omega_1(t_k)| > \omega_{max} \\ \omega_1(t_k) & \text{if } |\omega_1(t_k)| \le \omega_{max} \end{cases} \tag{9}$$

$$\dot{v}_2(t_k) = \frac{[v_2(t_k) - v(t_{k-1})]}{T} \tag{10}$$

$$\dot{\omega}_2(t_k) = \frac{[\omega_2(t_k) - \omega(t_{k-1})]}{T} \tag{11}$$

3.2 Acceleration Constraint

Similarly, to limit the values of linear and angular accelerations, the following strategies are adopted.

$$\dot{v}_3(t_k) = \begin{cases} \text{sign}[\dot{v}_2(t_k)]\dot{v}_{max} & \text{if } |\dot{v}_2(t_k)| > \dot{v}_{max} \\ \dot{v}_2(t_k) & \text{if } |\dot{v}_2(t_k)| \le \dot{v}_{max} \end{cases} \tag{12}$$

$$\dot{\omega}_3(t_k) = \begin{cases} \text{sign}[\dot{\omega}_2(t_k)]\dot{\omega}_{max} & \text{if } |\dot{\omega}_2(t_k)| > \dot{\omega}_{max} \\ \dot{\omega}_2(t_k) & \text{if } |\dot{\omega}_2(t_k)| \le \dot{\omega}_{max} \end{cases} \tag{13}$$

$$v_3(t_k) = v(t_{k-1}) + \dot{v}_3(t_k)T \tag{14}$$

$$\omega_3(t_k) = \omega(t_{k-1}) + \dot{\omega}_3(t_k)T \tag{15}$$

Clearly, we have

$$\begin{matrix} |v_3(t_k)| \le v_{max} & |\dot{v}_3(t_k)| \le \dot{v}_{max} \\ |\omega_3(t_k)| \le \omega_{max} & |\dot{\omega}_3(t_k)| \le \dot{\omega}_{max} \end{matrix} \tag{16}$$

And

$$\mathbf{P}_d(t_k) = \mathbf{P}_d(t_{k-1}) + \int_{t_{k-1}}^{t_k} \boldsymbol{\nu}_3(\tau)\, d\tau \tag{17}$$

Although these strategies for velocity and acceleration constraints have limited the values of linear and angular velocity and acceleration, it does not mean that real-time trajectory tracking would be achieved. There has a special case that it would fail. That is to say, when the mobile robot is tracking a large curvature trajectory point with a small angular velocity because of the velocities and accelerations constraints, the robot cannot get this curvature. Therefore, trajectory tracking would not be achieved. To solve this problem, we slow down the linear velocity to increase the curvature of the robot's motion trajectory for good trajectory tracking.

4 Computer Simulation

To validate the effectiveness of our approach, simulation results from sinusoidal curve are presented. The parameters are set as: $T = 0.1s$, $k_{p1} = k_{p2} = 2$, $k_\omega = 0.3$. The maximum value of velocity and acceleration are set as follows.

$$\begin{matrix} \nu_{max}=0.3m/s & \dot{\nu}_{max}=0.55m^2/s \\ \omega_{max}=20deg/s & \dot{\omega}_{max}=90deg^2/s \end{matrix} \tag{18}$$

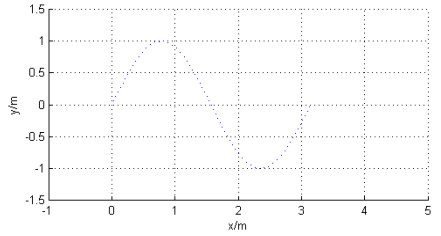

Fig. 2. A sinusoidal curve to be tracked

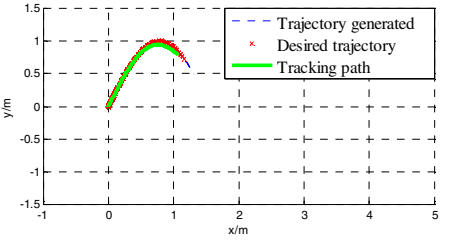

Fig. 3. The mobile robot is passing by the wave crest

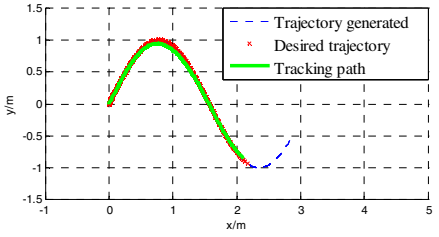

Fig. 4. The mobile robot is passing by the trough

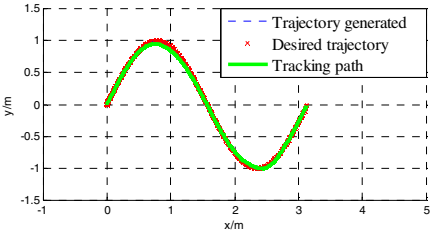

Fig. 5. The complete performed trajectory

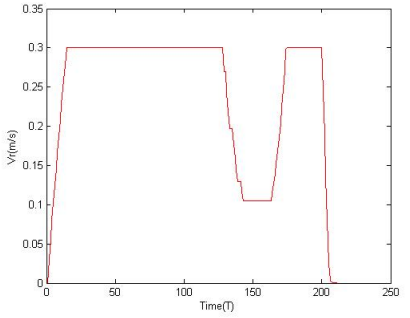

Fig. 6. The robot's linear velocity

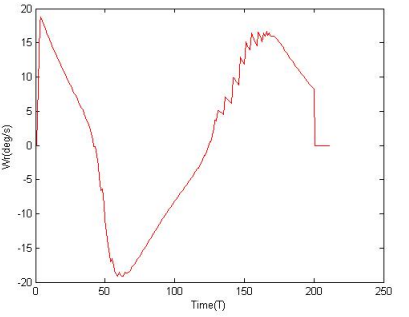

Fig. 7. The robot's angular velocity

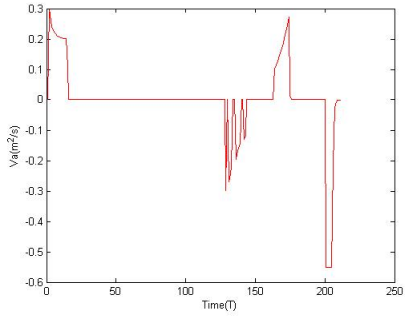

Fig. 8. The robot's linear acceleration

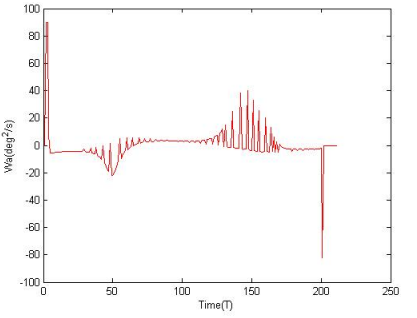

Fig. 9. The robot's angular acceleration

The sinusoidal curve to be tracked is showed in Fig.2. When the mobile robot is passing by the wave crest, due to the kinematic and dynamic constraints, the robot's linear velocity and angular velocity are limited, so that the desired trajectory is beginning to get behind of the trajectory generated in real time, see Fig.3. When the robot is passing by the trough, the difference between them is more distinct, see Fig.4. The complete performed trajectory can be found in Fig.5. We can see from this figure that the tracking error is so small that can be ignored, thus our approach is efficient and high-precision. The linear velocity and angular velocity of the mobile robot are shown in Fig.6 and Fig.7; both of them are within the bounds of velocity constraints. When the robot is approaching the trough, the linear velocity is slowed down to track the trough successfully. The linear acceleration and angular acceleration of the mobile robot are shown in Fig.8 and Fig.9; both of them are within the bounds of acceleration constraints.

5 Conclusion

In this paper, a real-time trajectory tracking approach of a wheeled mobile robot is suggested. We define the kinematic and dynamic constraints as the velocity and

acceleration constraints respectively. When the desired trajectory is generated in real time, the velocity and acceleration constraints are considered to make the results more practical in a real environment. Experiments with sinusoidal curve illustrate that it is a high-presicion and effecient real-time trajectory tracking approach.

References

1. Andres, R., Gustavo, S., Vicente, M., Fernando, D.S.: Formation control and trajectory tracking of mobile robotic systems-a Linear Algebra approach. Robotica 29, 335–349 (2011)
2. Ding, D., Cooper, R.A.: Electric-powered wheelchairs: a review of current technology and insight into future direction. IEEE Control System Magazine 25, 22–34 (2005)
3. Oriolo, G., De, L.A., Vendittelli, M.: WMR control via dynamic feedback linearization: Design, implementation, and experimental validation. IEEE Transactions on Control Systems Technology 10, 835–852 (2002)
4. Chwa, D.K.: Sliding mode tracking control of nonholonomic wheeled mobile robots in polar coordinates. IEEE Transactions on Control Systems Technology 12, 637–644 (2004)
5. Tzafestas, S.G., Deliparaschos, K.M., Moustris, G.P.: Fuzzy logic path tracking control for autonomous nonholonomic mobile robots: design of System on a chip. Robotics and Autonomous Systems 58, 1017–1027 (2010)

Effect of Contact Interface Pressure on Ultrasonic Transducer

Li Zhanhui

Institute of Automobile and Mechanical Engineering,
Changsha University of Science and Technology, Changsha, P.R. China, 41007
Lzh-jdx@hotmail.com

Abstract. The model of ultrasonic propagation through contact interface was established by Hertz contact theory. From the Hertz contact theory, it is found that higher order harmonic wave and waveform distortion occur when the ultrasonic wave propagate through a contact interface between two isotropic solids pressed together. The experiment results show at contact interface pressure is less than 6 kPa, the nonlinear coefficient of the interface layer decreases. When contact interface pressure is in the range of 6 kPa to 10 kPa, higher harmonic wave and nonlinear coefficient is minimum l. When contact interface pressure is more than 10 kPa, the nonlinear coefficient increases as increasing of the interface pressure.

Keywords: contact interface, harmonic wave, ultrasonic transducer, pressure.

1 Introduction

In recent years, ultrasonic bonding has become one of the research focuses in the domain of chip packaging. The ultrasonic bonding technology is making transient micro-interconnection between chip bump and substrate using ultrasonic power, pressure energy and heat energy. Ultrasonic bonding has become a leading technology in chip package, because of which possess a simple, efficient, and lead-free advantage. Ultrasonic is the most critical process parameters in ultrasonic bonding, which plays role of inspired interconnection interface atomic energy and soften metallic materials.

Ultrasonic transducer is the core part of providing ultrasonic energy. Contact interface is the connection interface of different parts in the ultrasonic transducer, including pre-pressure, interface methods and interface materials etc. The bonding tool needs be replaced to meet the needs of different types of chips, so the contact interface between bonding tool and horn is a dynamic coupling interface.

Nonlinear effect at contact interface has been paid more attention by many researchers. J. Qian studied the response of a system of two rigid, massless or massive, surface foundations of arbitrary plan-forms to various harmonic waves under three-dimensional conditions using direct BEM in the frequency domain1. G. A. Rogerson investigated harmonic wave propagation in a pre-stressed, incompressible elastic plate applying a general strain energy function2. D. J. Barnard forecast quantify the strength of diffusion bonds combination of reflected energy and

D. Jin and S. Lin (Eds.): Advances in Mechanical and Electronic Engineering, LNEE 176, pp. 171–177.
springerlink.com

harmonic generation data at unbonded interfaces3. M. Rothenfusser measured second harmonic generation to give early information about failure of adhesive layers4. Jianjun Chen researched on the contact acoustic nonlinearity (CAN), which produced by a bonded solid-solid interface, and calculated the bonding strength5. N. H. Sweilam applies the variational iteration method and Adomian's decomposition method to solve numerically the harmonic wave generation in a nonlinear, one-dimensional elastic half-space model subjected initially to prescribed harmonic displacement6.

The conventional transducer assembly includes a PZT driving element coupled at one end and a capillary coupled to the output end of the transducer. For repair/replacement needs, the capillary is screw-fastened on the assembly. Contact interface conditions (the pressure value on the interface) can affect the transducer performance in packaging practice, but there are few publications dealing with this issue. It was supposed that over-pressure may deform the tip of the transducer while under-pressure may result in inefficient transfer of ultrasonic power, but that needs to be verified.

2 Theory Modeling of the Contact Interface

2.1 Ultrasonic Transducer

In a conventional transducer assembly (in Fig. 1), the ultrasonic system consists of ultrasonic generator, PZT driver, horn, clamping barrel, capillary, chip, workbench, ultrasonic generator and etc[7].

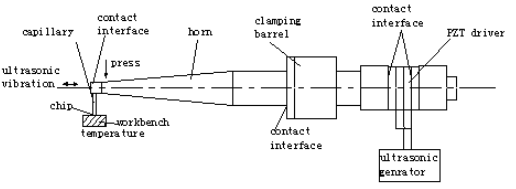

Fig. 1. Ultrasonic transducer and contact interface

In the process of ultrasonic propagation, ultrasonic pass through many contact interfaces. The pressure of contact interface can affect the efficiency of ultrasonic propagation and bonding strength.

2.2 Model of Contact Interface

The contact interface model can be described as Fig.2. Two isotropic elastic half-spaces are contacted together by pressure p_0.

Set a plane compression wave propagating through material 1 normal to the interface. The interactions between this incident wave and the interface give rise to reflected (in material 1) and transmitted (in material 2) plane compression waves (Figure 2a). At the contact asperity, there is reflection wave and transmission wave.

At the gap, there is only reflection wave. The contact area increases with contact interface pressure increasing. To simplified description of ultrasonic propagation, take contact interface between two materials regard as an interface layer. The characteristic of interface layer changes with pressure (Figure 2b).

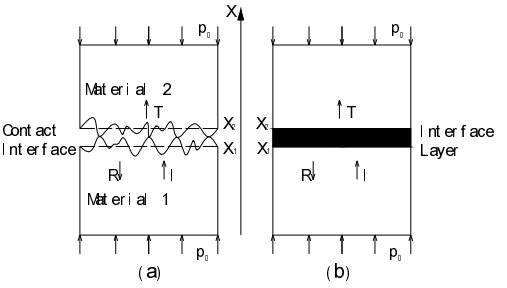

Fig. 2. Ultrasonic propagation at contact interface I: incident wave, R: reflection wave, T: transmitted wave, p_0: contact pressure, x_1 and x_2: two solids

As a nonlinear part, constitutive equation of the contact interface layer is described as:

$$\sigma = E\varepsilon + F\varepsilon^2. \tag{1}$$

Where, σ is the stress, ε is the strain, E and F is first order elastic modulus and second order elastic modulus of interface layer, separately.

Define nonlinearity coefficient of contact interface layer as

$$\beta = \frac{2F}{E}. \tag{2}$$

The ultrasonic wave in contact interface is described as the simple one-dimensional dynamic equations:

$$\frac{\partial^2 u}{\partial t^2} - c^2 \frac{\partial^2 u}{\partial x^2} = \beta c^2 \frac{\partial u}{\partial x}\frac{\partial^2 u}{\partial x^2}. \tag{3}$$

Where c denotes wave velocity

$$c = \sqrt{\frac{E}{\rho}}. \tag{4}$$

Where ρ is the average density of interface layer.

The approximate analytical solution could be found by the approximate analytical method.

The initial condition of equation (3) can be supposed as

$$u(x,t) = A_0 \cos(\omega t - \frac{x}{c}). \tag{5}$$

So, the second-order approximate analytical solution to eq. (3) is:

$$u(x,t) = A_0 \cos(kx - \omega t) - \beta x \frac{A_0^2 k}{8} \cos 2(kx - \omega t). \tag{6}$$

Where k is wave number of ultrasonic wave.

In eq. (6), the first part expresses the fundamental wave, and the second one is its second harmonic wave. The amplitude of second harmonic wave is in proportion to nonlinearity coefficient, propagation distance and wave number.

So A_1 and A_2 is amplitude of fundamental wave and second harmonic wave, separately.

$$\begin{cases} A_1 = A_0 \\ A_2 = -\beta x \dfrac{A_0^2 k}{8}. \end{cases} \tag{7}$$

From eq. (7), the nonlinear coefficient is converted into:

$$\beta = \frac{8A_2}{xA_1^2 k^2}. \tag{8}$$

2.3 Simulation

Implanting eq. (6) with $A_0 = 10^{-6} m$, $\beta = 20000$, $A_0 = 10^{-6} m$, $E = 210GPa$, $\rho = 7890 kg/m^3$, $f = 63000kHz$, $k = 50.1m^{-1}$, we plotted the solution of Eq. (6) in Fig. 3. The nonlinear wave shown in Fig. 3, compared with a linear wave, has some special features such as the generation of high-order harmonic wave which become stronger and stronger with the increase of travel path and the obvious amplitude accumulation. This is due to the fact that the phase velocities of nonlinear wave are variables depending on the nonlinearities of media and strains.

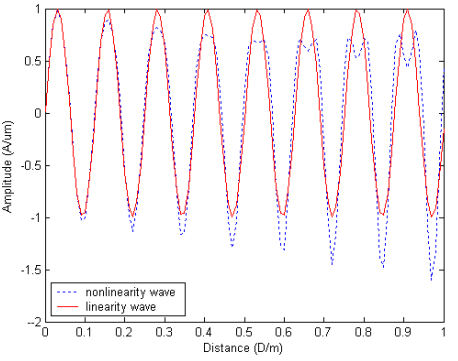

Fig. 3. Analytical solutions of linear (solid line) and nonlinear (dotted line) waves at t = 1 ms

To investigate the effect of nonlinear coefficient on nonlinear ultrasonic, we calculate ultrasonic propagation along time when $\beta = 20000$, $\beta = 15000$ and $\beta = 10000$, respectively. With the nonlinear coefficient increasing, wave distortion increases and the amplitude of second harmonic wave increases (In Fig. 4).

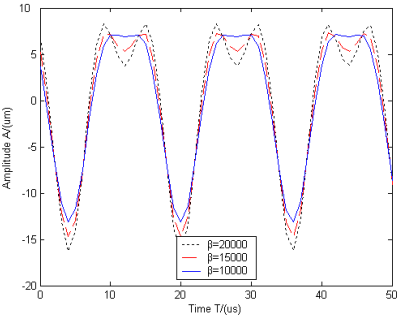

Fig. 4. Nonlinear ultrasonic at $\beta = 20000$ (black dotted line), $\beta = 15000$ (red dashed line), $\beta = 10000$ (blue solid line)

3 Experimental Results

Test as Fig.5.

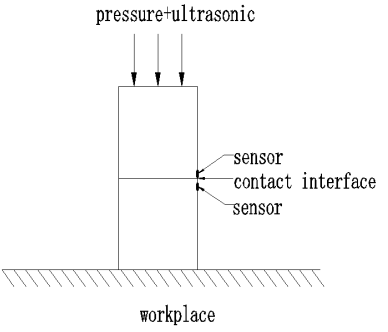

Fig. 5. Ultrasonic test

The vibration is measured using sensor as in Fig. 6. Fig. 6 shows the waveform distortion of the vibration displacement.

Figure 7 shows the frequency spectrum of capillary vibration displacement. In the range of 0-200 kHz, there are three frequency components about 60, 120, 175 kHz, which is the fundamental wave, second harmonic wave and third harmonic wave, respectively. The amplitude of second harmonic wave is closed to amplitude of fundamental wave, so it cannot be ignored.

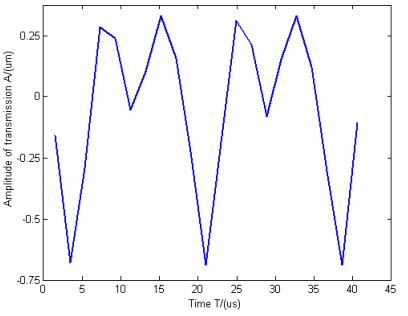

Fig. 6. Vibration displacement distortion

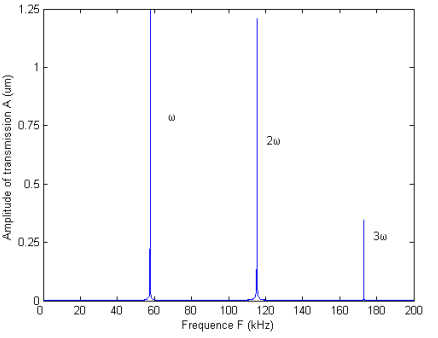

Fig. 7. The higher harmonic wave in capillary vibration

The nonlinear coefficient is calculated by using eq. (8). Nonlinear coefficient versus pressure shows in figure 8, when interface pressure is less than 6 kPa, the nonlinear coefficient decreases with increasing of the contact pressure. When interface pressure is more than 10 kPa, the nonlinear coefficient increases. When interface pressure is in the range of 6 kPa to 10 kPa, the nonlinear coefficient is the least. The possible reasons are: when pressure is small, there is little contact area in contact interface, the first order elastic modulus is small and nonlinear coefficient is large; with pressure increasing, nonlinear coefficient decreases. When pressure is suffice large, interface layer take place plastic deformation, and nonlinear coefficient increases.

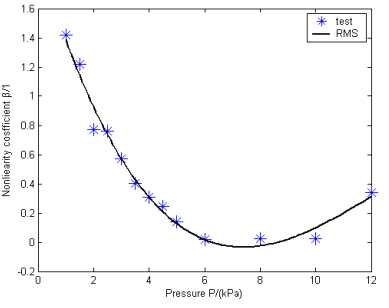

Fig. 8. Nonlinear coefficient versus pressure

4 Conclusions

The main reason of the high-order harmonic generation is nonlinearity of contact interface layer at different contact pressure.

When contact interface pressure is less than 6 kPa, the nonlinear coefficient and bond strength increase with increasing of pressure. When contact interface pressure is more than 10 kPa, the nonlinear coefficient and bond strength decrease with increasing of pressure. When nonlinear coefficient is small, the vibration frequency component of capillary is single-frequency, and help for getting rid of the chip surface oxides and bond success. When nonlinear coefficient is large, the vibration of capillary is disorder, and makes bond failure.

The nonlinear coefficient of ultrasonic propagation is a method of forecast bond strength can be by measure.

References

1. Qian, J., Beskos, D.E.: Harmonic wave response of two 3-D rigid surface foundations. Soil Dynamics and Earthquake Engineering 15, 95–110 (1996)
2. Rogerson, G.A., Sandiford, K.J.: Harmonic wave propagation alonga non-principal directionin a pre-stressed elastic plate. International Journal of Engineering Science 37, 1663–1691 (1999)
3. Barnard, D.J., Dace, G.E., Rehbein, D.K., et al.: Acoustic Harmonic Generation at Diffusion Bonds. Journal of Nondestructive Evaluation 16(2), 77–89 (1997)
4. Rothenfusser, M., Mayr, M., Baumann, J.: Acoustic nonlinearities in adhesive joints. Ultrasonics 38, 322–326 (2000)
5. Chen, J., Zhang, D., Mao, Y., et al.: Contact acoustic nonlinearity in a bonded solid-solid interface. Ultrasonics 44, 1355–1358 (2006)
6. Sweilam, N.H.: Harmonic wave generation in non linear thermoelasticity by variational iteration method and Adomian's method. Journal of Computational and Applied Mathematics 207, 64–72 (2007)
7. Han, L., Zhong, J., Gao, G.: Effect of tightening torque on transducer dynamics and bond strength in wire bonding. Sensors and Actuators A 141, 695–702 (2008)
8. Zuwen, Q.: Nonlinear acoustic. Science Press, Beijing (1992) (in Chinese)

Trajectory Tracking Optimal Control of the Wheeled Mobile Robots Based on Genetic Algorithm

Jianhua Li and Jinwen Li

School of Mechanical & Electronical Engineering, Lanzhou University of Technology, Lanzhou, China

Abstract. The trajectory tracking control optimal problem of the uncertain mobile robot with nonholonomic constraints is analyzed in this paper. A adaptive tracking controller and its Stability are described based on kinematic model. In order to confirm an optimal parameter set among so many control parameters. This paper put forward a optimization index function as an evaluating indicator for genetic algorithm. At last, the optimal controler was implemented on the simulations and the wheeled mobile robot. Results show the effectiveness.

Keywords: Mobile robot, Genetic Algorithm, Optimal Control, Trajectory tracking.

1 Introduction

WMR is one of the well-known system with nonholonomic constrains and it contains a class of mechanical systems characterized by kinematic constrains that are not integrable and cannot therefore be eliminated from the model equations. From Brockett's necessary conditions for stability, one may demonstrate that systems with nonintegrable velocity constraints cannot be stabilized to a point with smooth static-state feedback [2-3]. With this result, the control problems of the nonholonomic system become a challenge task. To stabilize such a system, time-varying feedback laws [4] and discontinuous feedback laws are developed [5]. Murray and Sastry worked on steering a nonholonomic system between arbitrary points by means of sinusoids [6]. Path planning approaches are developed by Latombe [7] and Laumond et al [8]. Despite the validity, these controllers are so complex that they are not easy to design.Therefore, we presented a novel simple and general tracking controller based on the kinematics models[9]. However, It is very difficult to confirm an optimal parameter set because a suitable adjustment must be done among so many control parameters. In this paper, we put forward a function as an evaluating indicator for FGA[1] to find an optimal parameter set. The optimization results is confirmed via computer simulation and their implementation.

2 The Trajectory Tracking Control Problem

The robot possesses three degree of freedom in its positioning which are represented by a posture (Fig1). Where θ is the posture angle, x and y are the coordinates.

D. Jin and S. Lin (Eds.): Advances in Mechanical and Electronic Engineering, LNEE 176, pp. 179–184.
springerlink.com

$$\mathbf{P} = \begin{pmatrix} x \\ y \\ \theta \end{pmatrix} \tag{1}$$

The robot's motion is controlled by its velocity v and rotational velocity ω, which are also function of time. The vehicle's kinematics is defined by a Jacobian matrix J.

$$\begin{pmatrix} \dot{x} \\ \dot{y} \\ \dot{\theta} \end{pmatrix} = \dot{p} = J \begin{pmatrix} v \\ \omega \end{pmatrix} = \begin{pmatrix} \cos\theta & 0 \\ \sin\theta & 0 \\ 0 & 1 \end{pmatrix} \begin{pmatrix} v \\ \omega \end{pmatrix} \tag{2}$$

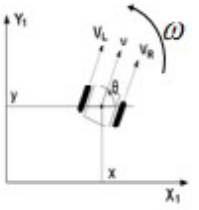

Fig. 1. Mobile Robot with two actuated wheels

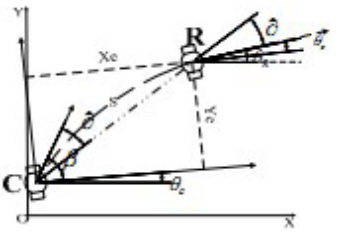

Fig. 2. Error posture and artificial electrostatic field

In the control system, two posture are used, the reference posture $p_r = (x_r, y_r, \theta_r)$, and current posture $p_c = (x_c, y_c, \theta_c)$. A reference posture is the goal posture of the robot (Point R in the fig.2) and a current posture is its real posture (Point C in the fig.2). Defined error posture as P_e

$$\mathbf{P}_e = \begin{pmatrix} x_e \\ y_e \\ \theta_e \end{pmatrix} = \begin{pmatrix} \cos\theta_c & \sin\theta_c & 0 \\ -\sin\theta_c & \cos\theta_c & 0 \\ 0 & 0 & 1 \end{pmatrix} (\mathbf{P}_r - \mathbf{P}_c) \tag{3}$$

An electrostatic artificial field will be used to navigate the wheeled mobile robot[9]. In our controller, we consider the reference posture as a new coordinate. The Point R is the new grid origin and the X-aixs is in the direction of θ_r. So we can show the artificial electrostatic field from reference posture to current posture as wire splice: C-S-R. (Figure 2 illustrates this case)

The following equation is known from the artificial electrostatic field.

$$\begin{cases} \theta_e + 2 \times \partial = \beta \\ \theta_e + \partial = arctg(y_e / x_e) \end{cases} \tag{4}$$

Then

$$\beta = 2arctg(y_e / x_e) - \theta_e \tag{5}$$

Now, we are able to state the architecture of a tracking control system for the robot (Fig.3) The global input of the system is the reference posture $\mathrm{P_r}$ and reference velocities $q_r = (v_r, \omega_r)^T$, which are variables of time. The global output of the system is the current posture P_c. The dotted box stands for the wheeled robot hardware capability of transforming target velocities to real current velocities. The next box is the kinematics Matrix J to produce the derivative of a current posture P_c. The last box is for integration.

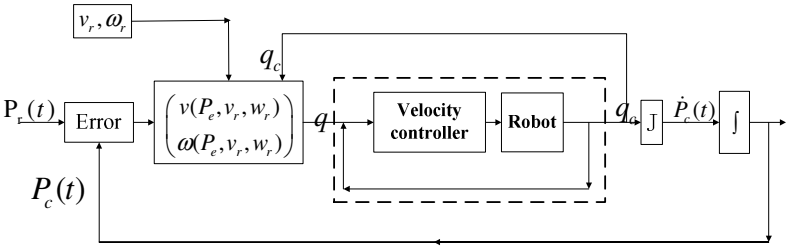

Fig. 3. Architecture of Tracking Controller

From paper [9], The controller is equation (4) Where $K_x, K_y, K_\theta, K_\beta$ are positive constants. The stability of this system is proved through the use of a Liapunov function system[9].

$$\mathbf{q} = \begin{pmatrix} v \\ \omega \end{pmatrix} = \begin{pmatrix} v_r \cos\theta_e + K_x x_e \\ \omega_r + v_r \left(K_\beta (x_e^2 + y_e^2) \sin\beta + K_\theta \sin\theta_e + K_y y_e \right) \end{pmatrix} \tag{6}$$

3 Parameters Optimization Control Simulation

K_x is the error coefficient of x-direction, K_y is the error coefficient of y-direction, K_θ is the error coefficient of posture angle. K_β is the error coefficient of artificial electrostatic field angle. The system is stable for any combination of parameter value of K_x, K_y, K_θ and K_β. However, since we need a non-oscillatory, but not too slow response of a robot, we have to find an optimal parameter set.

It is very difficult to confirm an optimal parameter set because a suitable adjustment must be done among so many control parameters. In the control progress, We hope that the movement of the robot can approximate the target in accordance

with the planned trajectory as soon as possible. Thus, the parameters optimization involves two optimization goals. First, the accumulated value of the angle between the robot's forward direction and the control direction should be as small as possible so that the robot can move according to the electrostatic field line. Second, the accumulated value of position error also should be small enough to move forward quickly. The weighted sum of the above optimization goals can define optimization index function Q as follows:

$$Q = \frac{1}{N}\sum_{i=1}^{N} i \times \left[\frac{\beta_i}{\pi} + \frac{\bar{S}_i}{\bar{S}_0}\right] \tag{7}$$

Where correspond to the number of elapsed time step, is the in fig.2, is the maximum distance between real robot and reference robot, is the distance between real robot and reference robot. From the above equation, the definition of evaluation function involves two subjects, on the one hand the accumulated value of the included angle between the robot's forward direction and the progress's direction should be as small as possible so that the robot can move according to the electrostatic field line direction, on the other hand the accumulated value of position error also should be small enough to move forward quickly.

In order to simplify the analysis in simulation, we consider only situations in which reference posture is moving to the positive direction at a constant velocity. The velocities of the reference robot are selected as follows: $v_r = 0.125(m/s)$ $\omega_r = 0$.

Adaptive Genetic Algorithm [10] and Family Genetic Algorithm [1] are used to optimize and evaluate Q separately to get the better control parameters. Choosing the optimal parameters of FGA $K_x = 1.300127$, $K_y = 6.548126$, $K_\theta = 4.896574$, $K_\beta = 5.658702$ and choosing the optimal parameters of AGA $K_x = 2.498754$, $K_y = 4.987542$, $K_\theta = 7.128735$, $K_\beta = 1.598745$. Figure 5 shows the simulation results with these parameters.

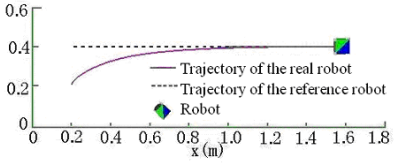

Fig. 4. Control result with the AGA parameter set

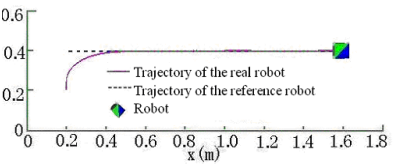

Fig. 5. Control result with the FGA parameter set

From these simulation results, it is obvious that the FGA parameter set is better than AGA parameter set. We confirm that we can find better control parameters through different algorithm.

4 Implementation

The results presented in section 3 were hardware independent. In this section, Parameters optimization control was implemented on the FIFA MIROSOT robot system.

In the following experiments, we use the FGA control parameter set. Robot is required to track the line trajectory. The line is showed in figure 6. The velocities of the reference robot are selected as follows

Fig. 6. The robot is tracking the line trajectory

We can see trajectory tracking process in figure 7. The error posture robot between real robot and reference robot is showed in figure 8.

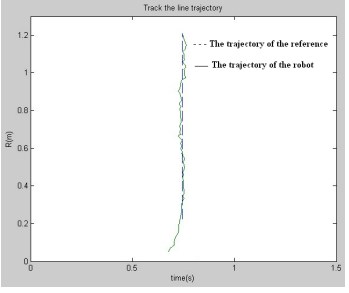

Fig. 7. Track the line trajectory

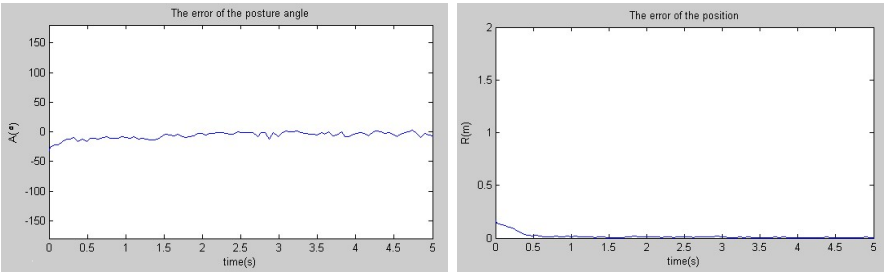

Fig. 8. The error posture versus time (MIROSOT)

Papers not complying with the LNCS style will be reformatted. This can lead to an increase in the overall number of pages. We would therefore urge you not to squash your paper.

5 Conclusion

The trajectory tracking control optimal problem of the uncertain mobile robot with nonholonomic constraints is analyzed in this paper. A adaptive tracking controller and its Stability are described based on kinematic model. In order to confirm an optimal parameter set among so many control parameters. This paper put forward a optimization index function as an evaluating indicator for genetic algorithm. The optimal controler was implemented on the simulations and practical MIROSOT system. Even though we cannot obtain all precise parameters of a wheeled mobile robot in practical application, and as a result, the robot cannot show high performance if we ignore this error. But without question, the trajectory tracking optimal control of the wheeled mobile robots if effective.

References

1. Li, J., Wang, S., Zhuang, J.: Family Genetic Algorithms Based on Gene Exchange and Its Application. Journal of Systems Engineering and Electronics 17(4), 864–868 (2006)
2. Kolmanovsky, I., McClamroch, N.H.: Developments in Nonholonomic Control Problems. IEEE Control System 15(6), 20–36 (1995)
3. Bloch, A.M., Reyhanoglu, M.: Controllability and Stabilizability Properties of a Nonholonomic Control System. In: Proceedings of the 29th IEEE Conference on Decision and Control, pp. 1312–1314. IEEE, Honolulu (1990)
4. Campion, G., Bastin, G., Dandrea-Nove, B.: Structural Properties and Classification of Kinematic and Dynamic Models of Wheeled Mobile Robots. IEEE Transactions on Robotics and Automation 12(1), 47–62 (1996)
5. Andrea-Novel, B., Camption, G., Bastin, G.: Control of Nonholonomic wheeled Mobile Robots by State Feedback Linearization. The International Journal of Robotic Research 14(6), 543–559 (1995)
6. Shim, H.-S., Sung, Y.-G.: Stability and Four-Posture Control for Nonholonomic Mobile Robots. IEEE Transactions on Robotics and Automation 20(1), 148–154 (2004)
7. Tayebi, A., Tadjine, M., Rachid, A.: Invariant manifold approach for the stabilization of nonholonomic systems in chained form: application to a car-like mobile robot. In: 1997 Proceedings of the 36th IEEE Conference on Decision and Control, San Diego, California, USA, vol. 4, pp. 4038–4043 (1997)
8. Fierro, R., Lewis, F.L.: Control of a nonholonomic mobile robot: backstepping kinematics into dynamics. In: Proceedings of the 34th IEEE Conference on Decision and Control, vol. 4, pp. 3805–3810 (1995)
9. Li, J.-H., Wang, S.: Adaptive Trajectory Tracking Control of Mobile Robots Based on Integrated Steering. Journal of Xi'an Jiaotong University 39(3), 252–255 (2005)
10. Jian, Z., Sun'an, W.: Study on Self-Adjusting of Gene Migration Genetic Algorithm. Journal of Xi'an JiaoTiong University 36(11), 359–363 (2002)

A Design of Marine Propulsion Shaft Power Telemetry System

Hongyan Hao and Qingshan Ji

Electromechanical College of Zhejiang Ocean University, zhoushan, zhejiang, 316000, China

Abstract. In order to achieve the marine shaft power's dynamic telemetry, on the basis of the analysis of shaft power measurement's fundamental principles, from both hardware and software, the telemetry system has designed basing on magnetic sensing phase difference type. The system can real-time acquire and analysis process to the torque and rotational speed signal, and online real-time calculate shaft power. It can meet needs of the ship shaft power telemetry and shaft conditions in real-time monitoring.

Keywords: torque, shaft power, telemetry, data acquisition.

1 Introduction

The shaft power is one of the most important performance parameters of the marine diesel engine and its power plant. It can be obtained by indirect measurement of shaft output torque and rotational speed [1]. Online measurement of the ship power system's shaft power, not only can find in diesel engine technology which is in good condition or not, also can determine the match status of the ship power system.

Presently domestic ship shafting shaft power measurement mainly used a vibrating wire torque instrument. When axis reversed, it used the steel strings tighten or relax in the sensors, then the steel string frequency changes measured torque. This torque meter sensor installs complexly, which signal transmission relies on the brush and cable. Between the brush and slip ring clean and good contact should be kept. The sensor's ground wire and the instrument reliably grounded with the hull, to prevent electromagnetic interference. Test environment request is higher. It belongs to a kind of non-contact torque of measurement.

Through a strain-gauge sensor, the strain-gauge torque meter measure the shaft's principal strain under the action of torque. According to different transmission of the strain signal, it is divided into the two methods which are contact and telemetry strain measurement. The telemetry strain measuring is small size and easy installation. During transmission, signal has less impact of environmental noise. It is suitable for the measurement of more complex conditions. Recently shaft power measurement developed rapidly [2-4].

D. Jin and S. Lin (Eds.): Advances in Mechanical and Electronic Engineering, LNEE 176, pp. 185–189.
springerlink.com

2 Measurement Principle

Currently, shaft power of ship shafting through indirect measurement of the output torque and rotational speed of the shaft, gains the shaft power decay, that is, respectively measures torque and rotational speed, and then obtains the power. The formula can be expressed as follows:

$$P = T\omega = T\frac{n \times 2\pi}{60} = T\frac{\pi n}{30} \tag{1}$$

Of which: P- Power (kw);

T- Output torque of shafting (N·m);
N- Rotational speed of shaft (r/min).

Relative to the torque measurement, rotational speed measurement is relatively simple. The measurement means is also more mature. Based on the magnetic sensing phase difference type torque measurement system is designed.

2.1 Torque Measurement

The torque measurement principle is based on the magnetoresistive effect phase difference type, by measuring the relative twist angle θ between the two sections of the shafting, then calculates the bearing torque T. The torque measurement principle is shown in Figure 1.

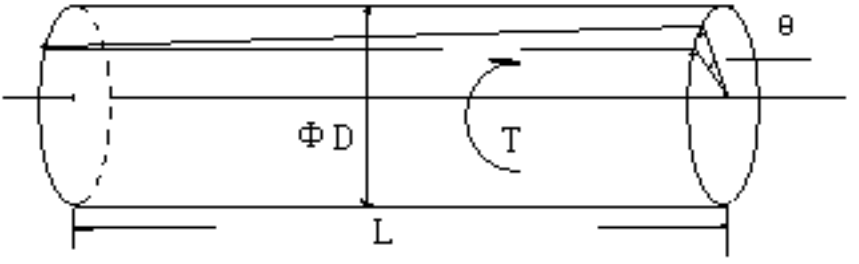

Fig. 1. The torque measurement principle

When the shaft bears torque, on the shaft any two parallel sections of distance L will have a relative twist angle θ. The formula can be expressed as follows:

For the solid shafting: $$\theta = 584\frac{TL}{GD^4} \tag{2}$$

For the hollow shafting: $$\theta = 584\frac{TL}{G\left(D^4 - d^4\right)} \tag{3}$$

Of which: T- Shaft torque (N • m);
G- The material's shear modulus (Pa);

D - Shaft diameter (m);
d - Shaft diameter (m);
θ-torsion angle (°).

When torque is measured, two sections of distance L on the drive shaft were respectively installed the same distribution law magnet. When the shaft rotates, the magnet also rotates. When magnet swept the sideward non-contact installed magnetoresistive sensor, a pulse signal will be produced. By torque T, the axis occurs torsional deformation, and the signal between the two measuring surface produces the phase difference. When axis is not torque, the phase difference between the two sets of signals only have to do with the relative position of magnet and sensor installation, the phase is called the initial phase θ0. While torque is measured, the rotational speed is measured. Then the phase difference θ1 can be calculated. The actual torsion angle should be $\Delta\theta = \theta_1 - \theta_0$.

Getting from the formula (2) or (3):

$$T = \frac{GD^4}{584L} \bullet (\theta_1 - \theta_0) \tag{4}$$

2.2 Rotational Speed Measurement

The rotational speed measurement uses the frequency measurement method. That is, the rotational speed is determined through measuring the number of pulse signals within the prescribed time generated by the magnetoresistive sensor which installed facing the magnet cross-section. The magnetoresistive sensor is installed facing the flywheel. When the shaft rotates, the flywheel turns every magnet, and the magnetoresistive sensor outputs a pulse. The counter counts. The shaft rotational speed can be calculated as follows:

$$n = 60N/\ \ Mt \tag{5}$$

In this formula, n is the measured shaft speed, r/min; T is the counting time, s; N is the pulse number which counter determines in time t; M is the magnet number installed on the flywheel within a round. In this way, the rotational speed measurement without increasing any device can be simultaneously completed when the torque measures.

3 The Composition of the Shaft Power's Dynamic Telemetry System

The ship shafting power's telemetry system is composed of the two magnet ring which fixed installation in the axis of distance L according to certain rules distribution, magnetoresistive sensors, data acquisition systems and computer. The power telemetry system hardware composition is shown in Figure 2.

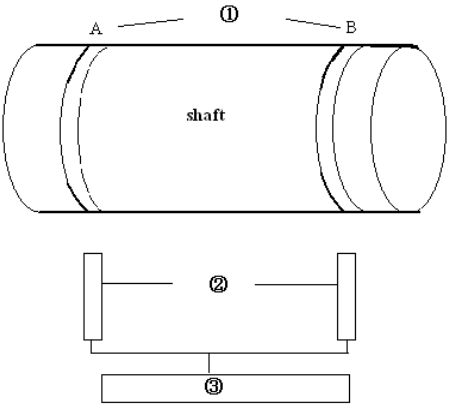

① magnet ring ② magnetoresistive sensor ③data acquisition system

Fig. 2. Magnetic sensing phase difference type power telemetry system hardware composition

Measurement system works through the organic integration of hardware and application software. The magnetoresistive sensor picks up the signal, the data acquisition system processes the signal, and using the shaft power's calculation software of computer calculates and displays data. The test system software consists of data acquisition, parameter setting, signal processing, data display and storage four main modules. The software flowchart is shown in Figure 3.

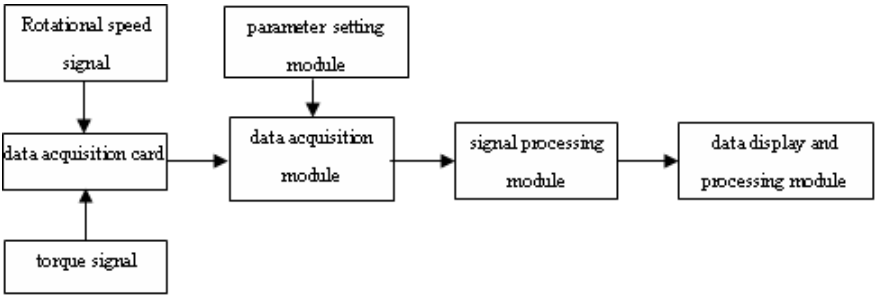

Fig. 3. The shaft power measurement system software flowchart

4 The Test System Error Analysis

This axis power test systems includes test hardware configuration and testing software platform. The various components installation and the processing will cause errors in different degrees. The measured values only closed to the true value by a certain error. The errors of this system mainly come from the corner simulation, data acquisition, as well as torsion angle calculation. Analysis shows that the error is mainly in the following aspects: First, since the measuring device main body is the

flexibility which installs the magnets, every disassembly process can not be exactly the same. Then causing the relative position changed between the magnets. In addition, speed instability, and electromagnetic interference can also affect the measurement results. The above three cases lead to random error, the average processing is needed to reduce its impact on the test results. In the data collection process, two-way signal sampling can not be fully synchronized, which can also cause a phase difference calculation of the error.

5 Conclusion

In this paper, aiming at the problem of the shaft power testing of the ship power system, the shaft power test system based on magnetic sensing phase-difference type was designed. From hardware components and software design two aspects elaborated the principle and build process of the entire test system. In the traditional torque measurement, the signal is not easy to transfer in the rotating body; a shaft diameter is need to a current collector ring; and current collector ring produces difficultly etc., many shortcomings were overcomed. Designed the shaft power test system with high precision, easy to use, can be used the dynamic non-contact measurement of the shafting shaft power in the real ship in complex conditions, with high practical value.

Acknowledgments. This work was supported by Educational Commission of Zhejiang Province of China (Y201121382).

References

[1] Yu, J., Hu, Q., Xu, J.: Design of Shaft Power Measurement System Software Based on Labview. Ship Engineering 32, 61–64 (2010)
[2] Zhou, G., Fan, S.D., Zhong, J.J.: Achievement of the dynamic measurement system of marine engine's shaft power. Ship & Ocean Engineering 36, 56–59 (2007)
[3] Deng, M.W.: Development and using of the multi-slurry ship shaft power real-time measuring instrument. China Water Transport 9, 10–11 (2009)
[4] Gan, S.W., Fan, S.D., Zhou, G.: Design and implementation of power measurement system for marine diesel engine. Marine Engineering 170, 25–27 (2006)

An Expert System for Crane Working Condition Selection

Qianwang Deng[1], Lijing Nie[1], Qin Fan[2], and Yuru Hu[2]

[1] The State Key Laboratory of Advanced Design and Manufacturing for Vehicle Body, Hunan University, Changsha 410082, China
[2] Zoomlion Heavy Industry Science & Technology Development Co., Ltd, Changsha 410082, China
{deng_arbeit,nielijing0406}@163.com

Abstract. This paper gives an intelligent selection algorithm which was applied in the cases, making the crane working condition intelligent selection come true. The selection system is based on visual C++ language rules and describes the establishment of knowledge database knowledge reasoning process and inference model of expert system construction detailedly. In the last part of this paper, the experiment proved the system feasibility. The system will make a contribution to the selection of crane.

Keywords: crane, working condition selection, expert system.

1 Introduction

Expert system is an important branch of artificial intelligence. In 1965 F.A Fischer root developed the world's first DENDRAL expert system by summing up the general problem solution system. In the middle of 1970's, mycin, casnet, prospector, hearsay and a number of other fruitful expert systems have been developed successfully. They were the second generation expert system. By summering up the design method and implementation technique, the fourth expert system, which adopted the latest artificial intelligent technology, such as the large multi-expert cooperative, multidisciplinary collaborative problem solving and parallel reasoning[1] . Expert system has been used widely in Lifting operations and boasts certain research at home and abroad. The German Liebherr company developed the Liccon system, which is their own R&D of auxiliary hoisting scheme selection tool. But the system is not open because its crane data is saved as regular file instead of database. The system can only be applied in their products. Zhejiang Province, Kaiyuan installation company developed the vista hoisting expert system, but it is only used for lifting condition accounting software[2].

2 The Construction of Expert System

The expert system is constructed by the knowledge library module, the reasoning engine, explain tools module and man-machine interface. The knowledge library is an access database, crane information is stored in access data table using the standard of

D. Jin and S. Lin (Eds.): Advances in Mechanical and Electronic Engineering, LNEE 176, pp. 191–195.
springerlink.com

class. Its advantage is that the data storage is flexible and suitable for different types of cranes. The figure.1 is the basic framework of the expert system for crane condition selection.

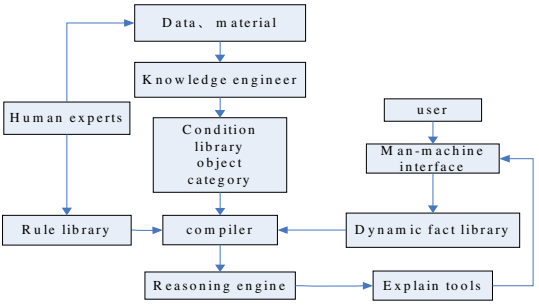

Fig. 1. The framework of the expert system for crane condition selection

2.1 The Establishment of Knowledge Database

Acquisition, representation and use are the three core components of the system development[3]. The knowledge representation means the description of knowledge, using the agreed sign to code into a set of computer knowledge that can be accepted by data structure. The same knowledge may have a variety of representation with different effects.

First-order predicate logic showed that method, production rules, frame representation, semantic network and object-oriented representation are the five methods of knowledge representation[4]. Though there are many mature reasoning methods according to the first-order predicate logic, the reasoning process is too long and can't clearly distinguish the knowledge of the real world. The thinking process of production rules is similar to the way of human, but the efficiency is lower and it can't express structural knowledge. Frame representation method is based on the theory of the framework with strong adaptability, generality and flexible reasoning approach[5]. It can combine the stating knowledge and process knowledge together, but it has problem between the consistency and integrity, and the reasoning method is not fixed, so it will increase the users' burden. The main advantages of semantic network are: provide the object and concept extremely natural framework, but it lacks the named connection standard and accepted system. Object-oriented representation combines more of a single knowledge representation method into a mixture of knowledge expression form according to object-oriented program design principle[6].

The system includes rule library lifting performance table and dynamic facts. Lifting performance tables are prepared by knowledge engineers according to the different types and specifications of cranes. Dynamic library refers to the fact that users input into machine through the man-machine dialogue. And the facts will be the premise condition that drive reasoning machine choose corresponding working conditions. The system will code the production rules and object oriented combination of knowledge expression. Each of the crane arm style will be combined

into category. The attributes of the category include the working condition for amplitude the weight telescopic way and the rate.

2.2 Knowledge Reasoning Process

The system uses the forward reasoning way. The user inputs the fact through the man-machine dialogue, and then the fact will be paired comparison with the data in the condition library. The conditions paired comparison successfully will be pared comparison again with the dynamic fact until all the conditions meet the dynamic fact.

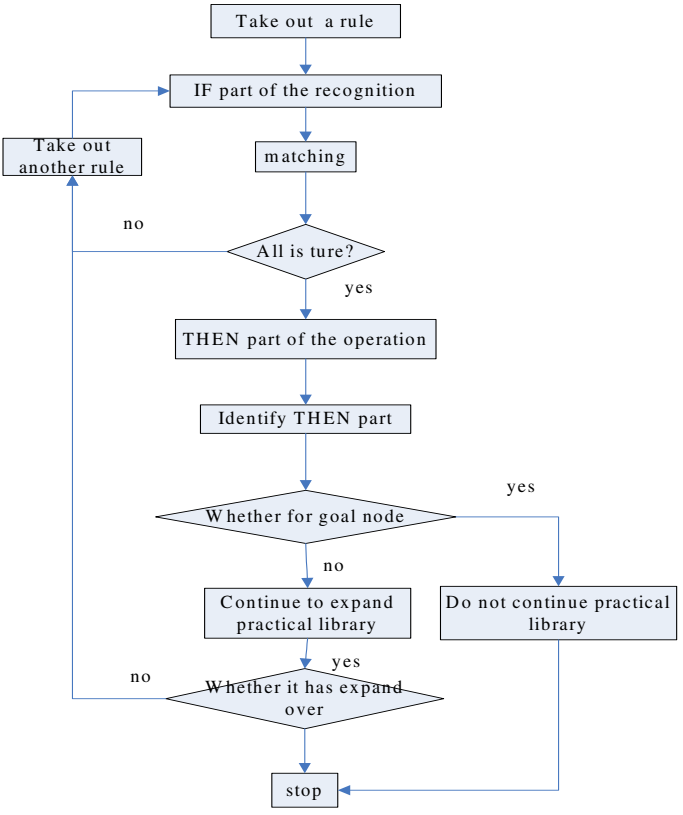

Fig. 2. Forward reasoning process diagram

3 Examples of Application

The following is the application on the selecting of crane condition. The example will provide you the rule library condition library dynamic fact library and man-machine interface. One crane condition should include crane model arm combination balance weight boom length super up state leg telescopic state operating angle range telescopic mode magnification working radius weight and minimum radius.

Condition library:

Condition 1:500 tons (crane model) the boom (arm combination) 125 (balance weight) 17 (boom length) with super up (super up state) and the legs stretched all (leg telescopic state) 360 (operating angle range) 111111 (telescopic mode) magnification(26) 7 (working radius) 191 (weight) 3 (minimum radius)

The dynamic facts are input through the man-machine interface by users, these are the basis of crane condition selecting.

Dynamic fact library:

Fact 1:5 (homework radius), 20 (hoisting height), 100 (hoisting weight), 500 tons, the boom, with super up

Rule library:

Rule 1: If it weighs more than the rated crane hoisting load quantity then it is banned

The figure.3 is the man-machine interface, users input the dynamic fact and select conditions through the man-machine interface. After all is done, users can acquire the right results by clicking the inquire button.

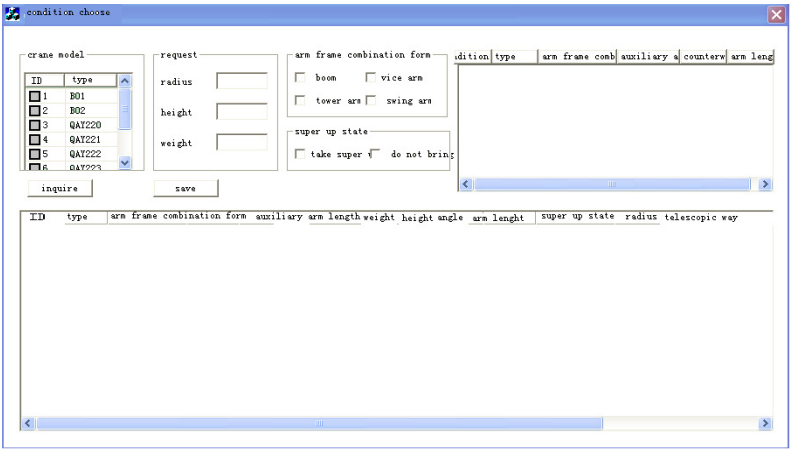

Fig. 3. Man-machine interface

4 Conclusion

This paper studies a set of crane selection expert systems and analyzes its structure. Knowledge expression is the core of the expert system. This system uses the forward reasoning process method and illustrates the design of the user interface and reasoning process. The study of crane has certain effect on intelligent selection. But there are also disadvantages. This system only applies in a special field, but the needs of users are a university of expert system. This needs general expert system that has different kinds of parallel algorithm and knowledge acquisition model and can use a variety of reasoning strategy. I believe that it is completely possible for the continuous improvement and development of expert system.

Acknowledgement. The project is supported by the Science Fund of Chinese State Key Laboratory of Advanced Design and Manufacturing for Vehicle Body No. 60870002.

References

1. Sun, Y., Yin, G., Liu, D., Shen, X.: The Application of Expert System for the Analysis of Typical Working Condition. Sichuan Union University (1996)
2. Wang, H.: The Research and Implementation of Cooperation Lifting Simulation Basing on Open Source. Dalian University of Technology (2009)
3. Parkalgren, L., Jeffrey, J., Rene, E.: US19812011130276, A61N1/365, A, A61, A61N, A61N1 (February 15, 2011)
4. Sun, S.: An expert system incorporating data simulation, feature recognition, model fitting, and data analysis functions. University of Colorado, Denver (2009)
5. IEEE Trial-Use Standard for Artificial Intelligence and Expert System Tie to Automatic Test Equipment (AI-ESTATE): Overview and Architecture, pp. 1232-1995. IEEE
6. Zhang, Y.-D., Wu, L.-N., Wagn, S.-H.: The Development and Application of Expert System, School of Information Science &Engineering. Southeast University, Nanjing 210096, China (2010)
7. Tan, Y.: The Use and Maintenance of Automobile Crane. Machinery Industry Press (2010)

Mechanism Design of the Inspection Robot for Aircraft Fuel Tank

Guochen Niu, Taiwen Li, and Li Wang

Robotics Institute, Civil Aviation University of China,
Tianjin 300300, China
niu_guochen@139.com, taiwenl@126.com, minhang1991@yahoo.cn

Abstract. To improve reliability and security of the aircraft fuel tank inspection and decrease labor intensity of maintenance personnel, an inspection robot is developed. Maintenance workers' work, which include entering the fuel tank and inspecting defects and so on, can be performed by the robot. Approach of switching motion mode is presented based on wheel-tracked mobile mechanism in order to adapt to the particular structure of aircraft fuel tank. Wheeled mechanism and tracked mechanism can be switched to each other at some time. By means of remote control and wireless video transmission, the worker can operate the robot and observe the scenario of fuel tank conveniently. Experimental result shows that the work of the robot is stable and reliable, and the design is reasonable and feasible.

Keywords: aircraft fuel tank, inspection robot, wheel-tracked mechanism, wireless video transmission.

1 Introduction

Aircraft fuel leak is not only a wasteful use of resources, but it is likely to cause the aircraft accidents. To ensure the normal operation of the aircraft, airlines need to regularly check the aircraft fuel tank leaks. However, the maintenance of the tank often takes a long time and even needs to repeat this process several times for completion, which will waste a lot of time and money.

As the internal structure of the aircraft fuel tank is complicated and difficult for operators to determine the leak and corrosion location, so operators usually count on their eyes to check the aircraft fuel tank. The fuel tank is a flammable and explosive environment, where fuel is over the tank mixing with the fuel-gas. People who need to enter the tank must strictly follow the AMM security manual. For anti-explosion, special tools must be taken, and maintenance workers generally need to be armed with exposure suit and aerophore, otherwise it can be harmful to their skin, eyes and respiratory system and even lead to fatal accidents. In addition, the access door of the aircraft fuel tank is so narrow that only one people can enter and check it. During the inspection, the operator in the fuel tank needs a shift at regular intervals (generally half an hour) [1-2], and another people is needed to monitor his situation.

D. Jin and S. Lin (Eds.): Advances in Mechanical and Electronic Engineering, LNEE 176, pp. 197–202.
springerlink.com

Currently, there are already some robots for defect inspection, which can work reliably in harsh terms such as tank or other flammable environments with the capability of climbing over obstacles [3-7]. In 2004, the Electronic and Information Engineering College of London South Bank University developed a floating and crawling robot which could automatically detect damage of fuel tank. Three non-destructive inspection techniques (ultrasonic phased array, eddy current array and alternating electromagnetic field detection array) were adopted to detect weld cracks and erosion of tank plate.

Although it is convenient to apply non-destructive inspection technology for aircraft fuel tank inspection, the device is relatively large and with high cost. In this paper, the robot can transmit the video about the aircraft fuel tank, through which people can observe whether there is a leak or corrosion conveniently. To adapt to the environment of aircraft fuel tank, the wheel-tracked mobile mechanism is designed. In ground control station, operators can control the robot and observe the interior of the aircraft fuel tank at ease. The robot can replace the worker to enter the tank and perform tasks continuously. So it decrease labor intensity, and the efficiency can be raised greatly.

2 Mechanism Design of the Robot

The robot system for defects inspection in aircraft fuel tank consists of two parts: the carrier system and the ground control system, as shown in Fig.1. The carrier system receives control commands from the ground control system, performs defined operation and sends image back; the ground control system provides a human-machine interface for operators, who can send control commands to the carrier system and analyze the status of the fuel tank based on real time image.

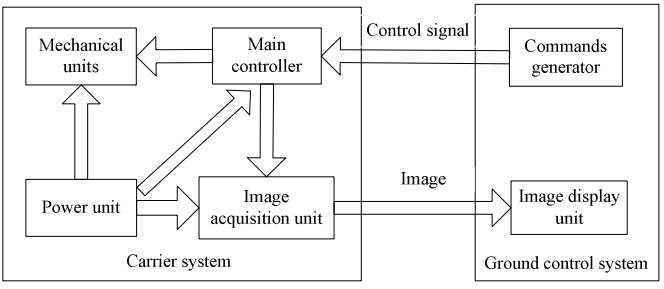

Fig. 1. System components

2.1 Overall System

It is difficult for the robot to crawl on stringers, which are parallel in the bottom of fuel tank. In Boeing 737 wing fuel tank, the span between two stringers is about 160mm. The height and the width of a stringer are about 45mm and 30mm

respectively. For a small robot, it will be easy to bump up and down as moving on stringers, which causes the motor wastage and power dissipation largely.

Because of the homogeneous distribution of stringers, it is very difficult for a wheel mobile robot to crawl and swerve usually. In order to solve these problems, a wheel-tracked mechanism is assembled in the robot. The tracked mechanism is equipped in vertical to ensure the stability of the robot crawling on the stringers. The wheeled mechanism is equipped in horizontal to achieve a flat crawling in stringers. Two mechanisms can switch to each other to adapt to the structure of stringers. Aircraft fuel tank inspection robot is shown in the Fig.2.

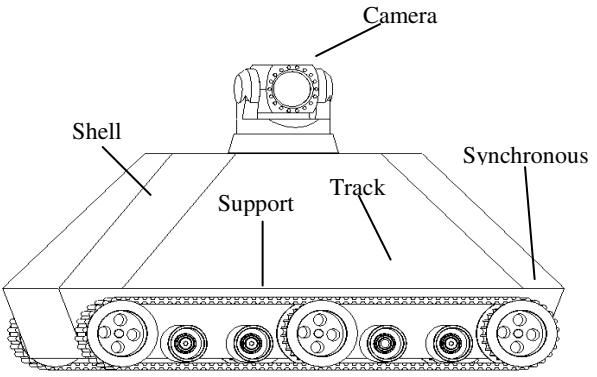

Fig. 2. Aircraft fuel tank inspection robot

The robot can move along x-axis, y-axis and z-axis, shown in Fig.3. The horizontal driving wheels can make the robot move along x-axis, while the vertical driving wheels can make the robot move along y-axis. If angle deviation arises in vertical or horizontal, the robot can return to the appropriate direction through differential control. Lifting motor is used to drive the robot along z-axis in order to switch the wheeled mechanism to tracked mechanism.

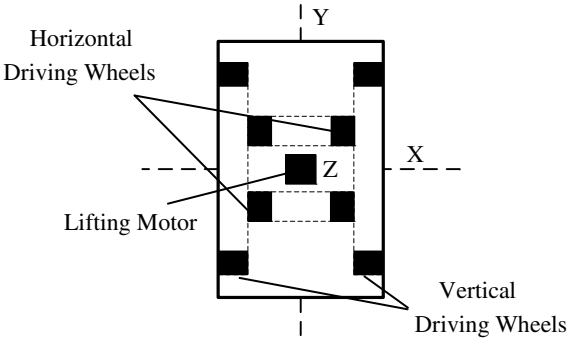

Fig. 3. Robot moving direction

2.2 Mechanism Design

The main mobile mechanism of the robot is the tracked mechanism consisted of the synchronous wheel, Bearing pedestal, shaft coupling, and DC motor, shown in Fig. 4. To enable the robot move smoothly, the length of tracked mechanism should be at least two times of the distance between the outer edges of the two adjacent stringers:

$$L_y \geqslant 2L + s. \tag{1}$$

Where, L_y is the length of tracked mechanism, L represents the space between stringers, and s is the width of a stringer.

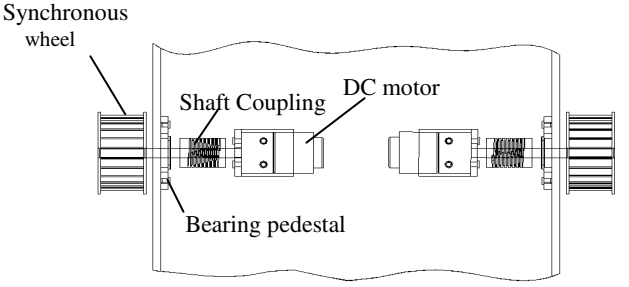

Fig. 4. Vertical driving mechanism

Horizontal mechanism is nested in the vertical mechanism, and consists of the braced frame, wheels and motion control component, shown in Fig.5. Motion control component includes two DC motors and bevel gear transmission mechanisms. It moves between the stringers, so its width must meet the following condition:

$$s \leqslant L_x \leqslant 2L + s. \tag{2}$$

Where, L_x is the width of the horizontal mechanism.

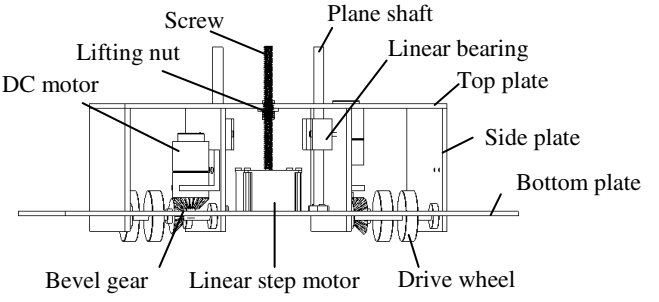

Fig. 5. Horizontal mechanism and lifter

Lifter is connected between the horizontal and vertical mechanism, and consists of a lead screw and a step motor, shown in Fig.5. As the step motor works vertical mechanism will rise or decrease relative to horizontal mechanism. The length of the screw in the lifter must meet the following condition:

$$H_z \geqslant H_x + H_y + h. \tag{3}$$

Where, H_z is the height of the screw, H_x is the height of horizontal wheels from the bottom of the robot in vertical motion mode, H_y is the height of the robot's bottom height from the stringers in vertical motion mode, h is the height of the stringer.

3 Experimental Analysis

The prototype of the robot was developed, whose length, width and height are 480mm, 280mm, and 180mm respectively. A model of aircraft wing fuel tank is made according to a ratio of 1:1 to Boeing 737.As Shown in Fig.6, Fig.6 (a) demonstrates vertical movement of the robot, while Fig.6 (b) demonstrates horizontal movement of it. The vertical track mechanism can ensure it to crawl stably on the stringers, and the horizontal wheel mechanism can make it move smoothly between stringers. Experiment results show that the vertical maximum moving velocity is 17.3 cm/s, horizontal maximum moving velocity is 15cm/s, the switching period between vertical and horizontal mechanisms is 4 seconds, and the wireless remote control range is 100m.

(a) Vertical movements

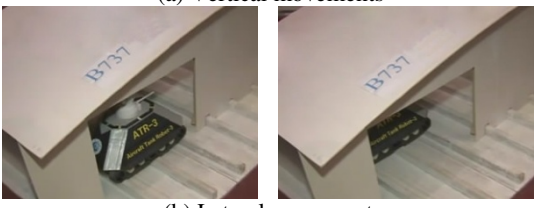

(b) Lateral movements

Fig. 6. The robot is going into the wing fuel tank

4 Conclusion

According to the problem that the manual inspection of the aircraft fuel tank is inefficient and dangerous, a fuel tank inspection robot is designed. The robot system can adapt to the aircraft fuel tank structure with ribs and stringers. It can enter fuel

tank instead of human and monitor the internal scenario in real time, and transfer video information to the ground control system. The coverage of this system is large enough to arrive at regions where are inconvenient or unavailable for maintenance worker. This design not only provides convenience to aircraft fuel tank maintenance, but also reduces work risk and labor intensity.

Acknowledgements. This work was funded by the Fundamental Research Funds for the Central Universities #ZXH2011D008. The support by Robotics Institute of Civil Aviation University of China is acknowledged.

References

1. Bratukhin, A.G.: Ways to increase the reliability of welded joints of high-strength steels in a new generation of aircraft. J. Metal Science and Heat Treatment 39(3), 123–126 (1997)
2. Abolikhina, E.V., Molyar, A.G.: Corrosion of aircraft structures made of aluminum alloys. J. Materials Science 39(6), 889–894 (2003)
3. Fromme, P., Wilcox, P.D.: On the sensitivity of corrosion and fatigue damage detection using guided ultrasonic waves. In: 50th IEEE International Ultrasonics, Ferroelectrics, and Frequency Control, pp. 1203–1206 (2004)
4. Schempf, H., Chemel, B., Everett, N.: Neptune: above-ground storage tank inspection robot system. J. IEEE Robotics & Automation, Society Magazine (1995)
5. Sattar, T.P., Leon Rodriguez, H.E., Shang, J., et al.: Automated NDT of floating production storage oil tanks with a swimming and climbing robot. J. Climbing and Walking Robots, 935–942 (2006)
6. Correia Cruz, A., Silva Ribeiro, M.: In service inspection robotized tool for tanks filled with hazardous liquids—robtank inspect. J. Climbing and Walking Robots, 1019–1031 (2006)
7. Wen, J., Dun, X.M., Miao, S.H., et al.: Structure design and weld seam surmounting characteristic of a wall-climbing robot with variable magnetic adsorption force device. J. Robot 33(4), 405–410 (2011)

Life Cycle Cost Estimated for the Diesel in Mechanical Engineering Based on the BP Neural Network

JiaShan Jin, JunBao Geng, LinKai Sun, and GuoWei Chen

School of Naval Architecture & PowerNaval University of Engineering, 430033, Wuhan, China
82950548@qq.com

Abstract. Expenses estimated for the equipment is an important part in LCC technique. If we can accurately estimate the expenses, we can control the expenses. There are some problems in the general estimated methods. Such as the workload is big, the accuracy of the estimate is not objective. This paper put forward a method based on the BP neural network. This method can use the machine learning, and built the neural network model to estimate the expenses of the equipment.

Keywords: BP neural network, life cycle cost, expenses estimate.

1 Introduction

Life cycle cost (LCC) refers to the total expenses of the equipment which spends in the design, development, production and use of the equipment in the course from project to scrap of the equipment[1]. According to the statistics, generally the use expensive of is several times than the equipment procurement costs in its life cycle. So the equipment life cycle cost prediction research is to determine the key weapons equipment economic life. It has a very important meaning to control and save cost, promote the reliability and maintainability of the equipment, and strengthen the use and maintenance of the equipment scientific management[2]. General commonly used equipment life cycle cost estimation methods are engineering estimation, parameter estimation, analogy method and experts estimate estimation. But these methods have the problem of large amount of calculation and more subjectivity. It often needs detailed data of the operation state to do more accurate estimate, in the practical application of the equipment. In the 1980s, the BP neural network was puts forward which use the error Back Propagation BP (Back Propagation) learning algorithm. In recent years, neural network has a wide range of applications, in solving nonlinear prediction and pattern recognition which have much relevant application [3, 4]. So in the applications, the back propagation algorithm of the BP neural network can be used to have the memory of the training. It can construct the network model and set up the relationship between the parameters and cost. In the application of the diesel, the parameters regression model of life cycle cost of the diesel can establish, then the cost can be controlled though the parameters.

D. Jin and S. Lin (Eds.): Advances in Mechanical and Electronic Engineering, LNEE 176, pp. 203–208.
springerlink.com

2 The Theory of BP Neural Network

2.1 The Concept of BP Neural Network

The BP neural network algorithm is divided into two parts train and work. The training time has two processes which are the input of the information positive dissemination and error back propagation. In the process of positive dissemination, the input information from input level to the hidden level to output layer step by step. If the output value is not the same with the samples are given, calculation the output error, back propagation the error, modification the weights between neurons of each layer to minimum the error.

After further research, Rumelhart and McClelland in 1989 proved three layers of the BP neural network was enough to finish nonlinear mapping from n dimension to m dimension. Along with the development of the network model application, the three BP neural networks become the core essence of the artificial neural network because of its simple structure, adjustable parameter, and more training algorithm[5]. Three layers of BP neural network have strong adaptive learning ability. it can find the corresponding relation of data, analysis the regression modeling more accurately.

The BP neural network trains the network according to certain method through the given data. If the error reaches the set value, stop the calculation, generate network, and then call the network to forecast. Training the network need amount of data demand. If less data, may not train out the ideal network, so the BP neural network only suit for the condition of large amount of data.

2.2 The Structure of the Neural Network

Figure 1 is the three layer neural network model structure which has single output and multi input.

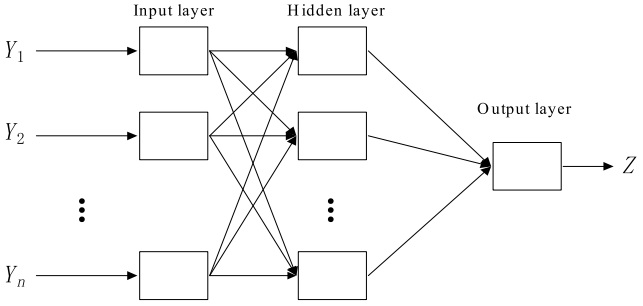

Fig. 1. The model structure of the single output BP neural network

The BP neural network structure includes input layer, hidden layer and output layer. When a pair of learning samples for neural network, the activation vale of neurons disseminate from the input value to output layer though the hidden layer, in the output layer get response vale. Next, according the principle of reduce the error between the target output and actual output, the vale disseminate from the output

layer back to the input layer though the hidden layer. Then the weights between the layers can be correct step by step, the method called "error back propagation algorithm".

2.3 The Training Steps of the BP Neural Network

The following are the calculating process for the neural network algorithm, which provides calculation theoretical basis for design and analysis.

$X_k = [a_{k1}, a_{k2}, \cdots a_{kn}]$, $(k = 1, 2, \cdots N)$, is the training sample, N is the number of training samples.

$$W_{MI}(n) = \begin{bmatrix} w_{11}(n) & w_{12}(n) & \cdots & w_{1I}(n) \\ w_{21}(n) & w_{22}(n) & \cdots & w_{2I}(n) \\ \vdots & \vdots & \vdots & \vdots \\ w_{M1}(n) & w_{M2}(n) & \cdots & w_{MI}(n) \end{bmatrix} \tag{1}$$

Eq. (1) is the weight value between the input layer and the hidden layer for the n times iterations.

$$W_{IJ}(n) = \begin{bmatrix} w_{11}(n) & w_{12}(n) & \cdots & w_{1J}(n) \\ w_{21}(n) & w_{22}(n) & \cdots & w_{2J}(n) \\ \vdots & \vdots & \vdots & \vdots \\ w_{I1}(n) & w_{I2}(n) & \cdots & w_{IJ}(n) \end{bmatrix} \tag{2}$$

Eq. (2) is the weight value between the hidden layer I and the hidden layer J for the n times iterations.

$$W_{JP}(n) = \begin{bmatrix} w_{11}(n) & w_{12}(n) & \cdots & w_{1P}(n) \\ w_{21}(n) & w_{22}(n) & \cdots & w_{2P}(n) \\ \vdots & \vdots & \vdots & \vdots \\ w_{J1}(n) & w_{J2}(n) & \cdots & w_{JP}(n) \end{bmatrix} \tag{3}$$

Eq. (3) is the weight value between the output layer and the hidden layer J for the n times iterations.

$Y_k(n) = [y_{k1}(n), y_{k2}(n), \cdots y_{kp}(n)]$, $(k = 1, 2, \cdots N)$, is the output of the network after n times iterations. $d_k = [d_{k1}, d_{k2}, \cdots d_{kn}]$, $(k = 1, 2, \cdots N)$, is the expected output. η is the learning rate.

The training steps of the network is:

Step 1: set the parameters and variable

Step 2: initialization and set the $W_{MI}(0)$, $W_{IJ}(0)$, $W_{JP}(0)$ as a smaller random nonzero values

Step 3: load sample data X_k.

Step 4: calculate each layer of BP network neurons output signal u and the input signal v.

Step 5: calculate the error $E(n)$ though compare expectations output d_k and the real output $Y_k(n)$, judge whether meet the requirements, Yes to over. No to step 6.

Step 6: the $n+1$ is greater than the maximum iterating times or not, if more than, the study is over, if not greater than, calculation the neurons local gradient δ of each layer.

Step 7: calculate the correction value Δw, and fixed weight values, turn to the step 4.

Step 8: randomly select the sample vector for learning neural network, and return to the step 3, until the neural network error E less than the predefined valve, namely network convergence. If learn times are more than the predefined value, the network can't convergence. When all the training samples were train, the study is over.

3 Example

Though collecting the specific data show in table 1,

Table 1. The life cycle cost of a series Marine diesel

number	X_1	X_2	X_3	X_4	X_5	X_6	X_7	X_8	X_9	X_{10}	X_{11}	X_{12}	Y
1	3460	185	0.7	2000	10000	10	35	1800	20	1500	181177	848435.4	36279.8
2	3480	188	0.8	2500	8000	8	32	2000	25	2000	203475.9	1617032	63593.04
3	3500	190	0.9	3000	8000	8	46	2450	33	3000	365169.4	3784096	137088.9
4	3460	186	0.8	2500	9000	8	40	2300	25	2500	286138	2021290	78117.32
5	3490	189	0.6	2800	8000	10	38	2200	30	3000	344571.7	2037649	118342.8

X_1—The largest continuous power (KW), X_2—Fuel consumption rate (gram per KWH), X_3—Slippery fuel consumption rate (gram per KWH), X_4—Average fault time interval (hours), X_5—average cost of once maintenance (Yuan), X_6—The repair interval of the machine (years), X_7—average once repair cost of the machine (ten thousand Yuan), X_8—Purchase expenses (ten thousand Yuan), X_9—Service years (years), X_{10}—Working time (hours), X_{11}—Temporary maintenance costs (Yuan), X_{12}—Plan maintenance costs (Yuan), Y—life cycle cost (ten thousand Yuan).

Using the MATLAB tools, the influence factors of the diesel cost were took as the neural networks input data, life cycle cost data as prediction output. The forecasting model will be established though training the raw data. Figure 2 is the training effect of the data.

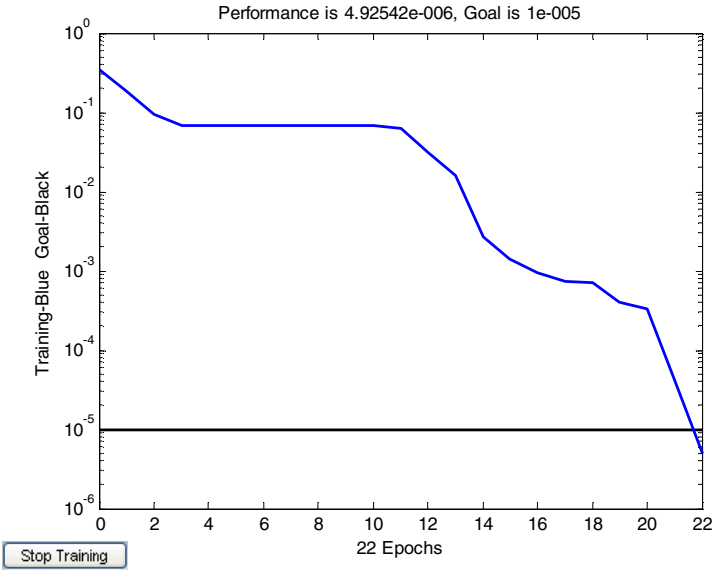

Fig. 2. The figure of training effect

The predict cost will be got though inputting the input data into the trained model. Comparing the predict cost and the real cost we can get the predicted error. Table 2 shows the predict error almost control within 1%, it meet the requirements of engineering application.

Table 2. The data of predict error

number	Real cost (ten thousand Yuan)	Predict cost (ten thousand Yuan)	Predict error(%)
1	36279.8	36640.81	1%
2	63593.04	63943.14	0.55%
3	137088.9	136729.86	-0.26%
4	78117.32	78422.15	0.39%
5	118342.8	118316.21	-0.02%

4 Conclusion

The BP neural network has strong adaptive learning ability. It can find the corresponding relation of data, analysis the regression modeling more accurately. It can establish the diesel cost regression model though the influence factors of the life cycle cost. From the example we can see, the prediction accuracy can meet the requirements of the engineering application, it provide accurate data base for the life cycle cost management in the next step.

References

1. Luo, Y.: The application of the equipment life cycle cost method. The ocean press, Beijing (1992)
2. Guo, W.M., Zhao, L.: Fire Control & Command Control 29, 29 (2004)
3. Li, D.K., Zhang, H.X., Li, S.A.: Fire Control & Command Control 31, 27 (2006)
4. Zhang, W., Hua, X.L.: Journal of air force engineering university (natural science edition) 10, 52 (2009)
5. Luo, Y.B., Hou, Z.Q., Cui, K.L.: Journal of naval aeronautical engineering institute 21, 463 (2006)

Development of Intelligent Liquid Inspection System Based on Machine Vision

Huan-jun Liu

Faculty of Automation, Guangdong University of Technology, Guangzhou, Guangdong, China
hjliu74@163.com

Abstract. This paper presents an intelligent liquid inspection system based on machine vision. The inspection system is designed to capture sequence images of the rotating liquid in the bottle. And the impurities in liquid are inspected by motion analysis. The binary image difference method is put forward to detect the motion regions in sequence images. In order to converting gray image to binary image precisely, this paper employs a novel segmentation algorithm base on unsupervised learning. This algorithm combines the fuzzy C-means method with fuzzy support vector machines, and can subdivide the image into the impurities and background efficiently. The experiments demonstrate the inspection precision of the liquid inspection system is about 96.8%.

Keywords: liquid inspection, machine vision, motion analysis, unsupervised learning.

1 Introduction

Liquid in bottle maybe contain some impurities because of these matters bringing in liquid during production process. Some researches have done for detecting these impurities[1-3]. In this paper a novel intelligent liquid inspection system has been designed for automatic impurity control, by illumination of liquid pharmaceutical products in glass containers.

2 Inspection System Design

Because the particle is small, the impurities maybe sink to bottle bottom. These impurities are difficultly detected. Even if the impurities remain suspended in liquid, they are easy to confuse with trace in bottle. So the dynamic inspection equipment need be employed by liquid inspection machine. This paper presents a dynamic method to capture the liquid images. The inspection system rotates the bottle, and then stops it rapidly. At this time, the bottle is still, and the liquid is yet rotary. If there are impurities in bottle, they will be rotated with liquid. The camera captures the sequence images of liquid. The method of capture image is as fig. 1(a).

When the images are captured, some impurities are very small and difficulty detected. So the illumination need be designed to highlight these small impurities. The design of illumination system is shown in fig. 1(b).

D. Jin and S. Lin (Eds.): Advances in Mechanical and Electronic Engineering, LNEE 176, pp. 209–215.
springerlink.com

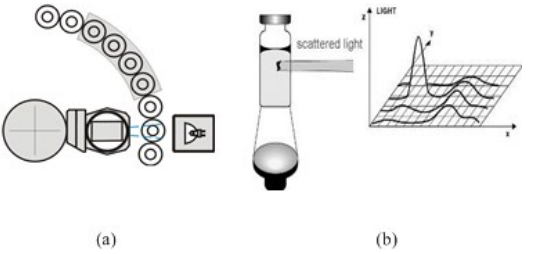

Fig. 1. Inspection system

When the side illumination in black background is employed, the impurities are shown as bright spot on black background.

3 Dynamic Inspection Method

To distinguish impurities from noise, the dynamic inspection is employed. The sequence images are captured, and then the foreign matters are detected by motion analysis. This paper presents a binary image difference method. Firstly, this method segments the image into the targets and background. Then the two binary frames are compared to determine whether they are the same. Because the targets which may be the change regions are directly compare in this method, the inference of noise can be reduced. And if there are holes in difference image, the motion regions can be also detected.

3.1 Image Segmentation

In this method the region segmentation is key thing. Many algorithms for converting a gray image into a binary image are presents. However the image of liquid has different characters. The image of liquid includes targets and background. The impurities in liquid are very small, so the most are of image is background, and the target regions are small. The segmentation result using tradition algorithms is not ideal. To segment these image, a novel algorithm based unsupervised learning is presented. Clustering can be used to divide a digital image into distinct regions for border detection or object recognition [4,5]. This paper puts forward to a novel methods based on unsupervised pattern classification. This method firstly uses Fuzzy C-means methods to classify the image, and then chooses the samples which is high-confidence by fuzzy voting. These samples are used to train the fuzzy support vector machines. Finally the image is classified by trained fuzzy SVM.

The fuzzy c-means objective function $\{x_K\}_{k=1}^{N}$ for partitioning into clusters is given by:

$$J = \sum_{i=1}^{c}\sum_{k=1}^{N} u_{ik}^{p} \left\| x_k - v_i \right\| \tag{1}$$

Where $\{v_i\}_{i=1}^{c}$ are the prototypes of the clusters and the array $[v_{ik}] = U$ represents a partition matrix, $U \in u$, namely

$$u\{u_{ik} \in [0,1] \Big| \sum_{i=1}^{c} u_{ik} = 1 \ \forall k \ \ 0 < \sum_{k=1}^{N} u_{ik} < N \ \ \forall i\} \tag{2}$$

The parameter is a weighting exponent on each fuzzy membership and determines the amount of fuzziness of the resulting classification. The FCM objective function is minimized when high membership values are assigned to voxels whose intensities are close to the centroid of its particular class, and low membership values are assigned when the voxel data is far from the centroid.

Because the pixels in image are not isolated points, the features which can represent the characters of region are chose. The three features are used for FCM, which are as follow.

The feature $fs_1(x, y)$ of point (x,y) is:

$$fs_1(x, y) = gray(x, y) \tag{3}$$

Where $gray(x,y)$ is the gray level of point (x,y).

The feature $fs_2(x, y)$ is:

$$fs_2(x, y) = \frac{\sum_{i=-1}^{1} \sum_{j=-1}^{1} gray(x+i, y+j)}{9} \tag{4}$$

Where gray(x,y) is gray level of point (x,y). $fs_2(x, y)$ is average gray level of the 9 point in neighborhood of point (x,y).

The feature $fs_3(x, y)$ is:

$$fs_3(x, y) = Var(X) = \frac{\sum_{i=-1}^{1} \sum_{j=-1}^{1} (gray(x+i, y+j) - \mu)^2}{9} \tag{5}$$

Where gray(x,y) is gray level of point (x,y), $\mu = \frac{\sum_{i=-1}^{1} \sum_{j=-1}^{1} gray(x+i, y+j)}{9}$.

After classifying the image by FCM according to the features, the high-confidence samples are chose by following condition. First the membership value of the sample is larger than a threshold:

$$fm(x, y) > T_m \tag{6}$$

Where $fm(x, y)$ is a membership value of point (x,y) which is assigned by FCM, and the T_m is a threshold which is 0.8 in this paper.

Second condition is that there are 2 points in neighborhood of the sample which also meets the first condition.

After choosing the samples, these samples are used to train the fuzzy support vectors. SVMs have been used as one of the highest performance classifying systems

because of their ability to generalize well. In this paper, fuzzy support vector machines are presented. It combines fuzzy theory with SVMs.

FSVM consists of fuzzy layer and SVMs. Fuzzification is the function of the fuzzy layer. The features are inputted into the fuzzy layer, and translated into fuzzy outputs. This layer uses Gaussian function as the membership function. The function is as follows:

$$\mu_i(x_i) = \mathrm{e}^{-\left(\frac{x_i - a_i}{b_i}\right)^2}. \tag{7}$$

Then, SVMs are used as the classifier for fuzzy outputs.

Research shows that the use of the hybrid kernel yields a better performance than those with a single common kernel [6]. Hence, the hybrid kernel is applied in this study. The kernel function adopted in this paper is as follows:

$$K(x, x_i^*) = k_1 (x \cdot x_i^*)^d + k_2 \mathrm{e}^{-r|x - x_i^*|^2}. \tag{8}$$

Genetic algorithms (GAs) constitute the global optimization techniques known to be successful in many domains. Thus, a GA based selection of components for FSVM is proposed in this study. This method is employed to optimize FSVM. The accuracy of classification are used to evaluate the performance of classification.

The results of using the method presented by this paper to segment the liquid images are shown in fig. 2.

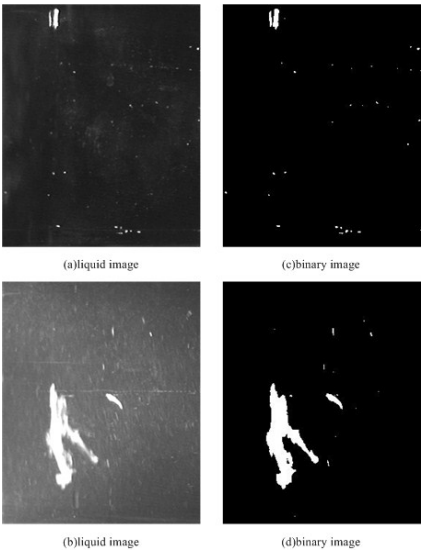

Fig. 2. The binary images

Figure 4 (a) and (b) are the liquid images, and the (c) and (d) is the corresponding binary images.

3.2 Binary Image Difference

After obtaining the segmented images, the two contiguous images are differenced. Suppose contiguous n and n+1 images are $f(x,y,n)$ and $f(x, y, n+1)$, and the segmented images are $b(x,y,n)$ and $b(x,y,n+1)$. The formula of binary image difference is:

$$D(x, y) = b(x, y, n) - b(x, y, n+1) \tag{9}$$

If there are immobile objects in sequence images of liquid, like trace in bottle, these objects will not exist in the differenced image because of no change in different images. If there are moving objects in images, these objects partly exist in the differenced image. By comparing these regions and original image, the moving object can be detected.

According to the differenced image, the still background and motion regions in image can be classified. The region i is a segmented region in nth frame binary, and the point (x_j,y_j) is in this region. The area of region i is N_i. The measure function $BM(i)$ is defined to detect the motion change of region i.

$$BM(i) = \sum_{j=0}^{N} (D(x_j, y_j) - \frac{\sum_{j=0}^{N} D(x_j, y_j)}{N})^2 \tag{10}$$

If there are m segmented regions in nth frame binary image, the average BM_{avg} of the measure values of all region is calculated by formula :

$$BM_{avg} = \frac{\sum_{i=1}^{M} BM(k)}{M} \tag{11}$$

If $BM(i)$ is larger than BM_{avg}, like formula, the region i maybe a motion region.

$$BM(i) > BM_{avg} \tag{12}$$

For avoiding misjudgment, the average gray level comparison is employed to further ensure whether the region is the motion region. If the region i can meet formula (), the average gray level of the region i in original image n and n+1 is compared. The comparison formula is as follow:

$$\left| m_i(n) - m_i(n+1) \right| > T \tag{13}$$

Where $m_i(n)$ is the average gray level of region i in image n; $m_i(n+1)$ is the average gray level of region i in image n+1; and T is a threshold.

If region i can also meet this condition, it can be confirmed as a motion region.

The results of motion analysis are shown in fig. 3 according to the binary image difference.

To avoiding the misjudgment caused by noise, the contiguous 5 frame images of detected liquid are captured to constitute a group images. And the binary image differences are employed to contiguous image. The four results of motion analysis are got. If the motion objects are detected in three results, we can confirm that there are the impurities in the detected liquid.

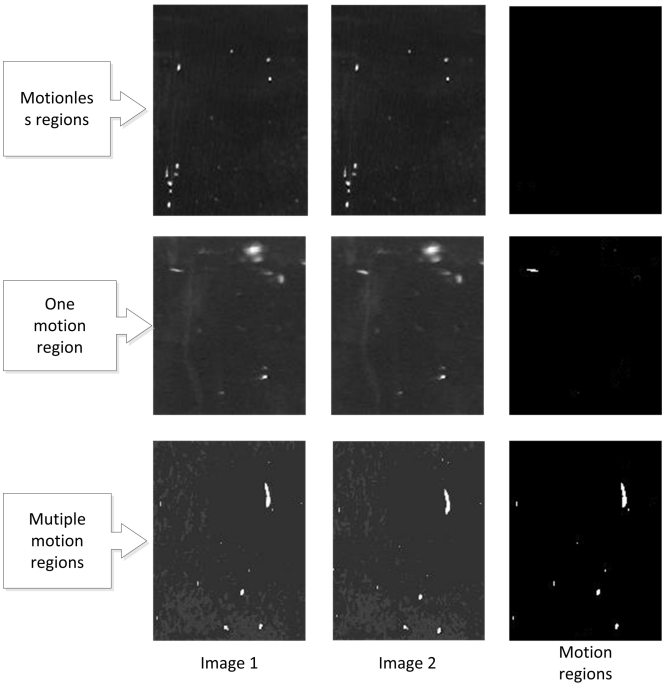

Fig. 3. The results of the motion analysis

4 Experiments

The experimental instrumented are developed according to the design plan in this paper. And then the 400 group sequence images of liquid products are captured. These images are detected manually to confirm if there are impurities in these products. The methods which are presented by this paper are also employed to detect these liquid products. Compared to manual results the detection results are as follow:

Table 1. The inspection results of typical samples(%)

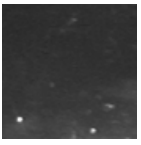	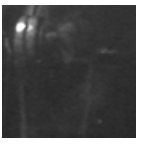		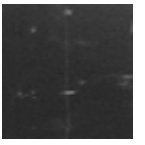	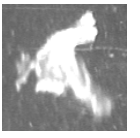
Traces in bottle	Light spots	fibers	Suspended particles	flocs
97	99	94	94	100

And the average inspection accuracy is about 96.8%. The inspection system is proved that it can replace the manual inspection.

5 Conclusion

This paper presents an inspection system based on machine vision to detect the impurities in liquid. Impurities in liquid are difficult to detect by static inspection. Hence dynamic inspection should be employed. The equipment is designed, which can capture sequence images of the rotating liquid in the bottle. Then the binary image difference is put forward to detect the motion regions in sequence images. Firstly, this method segments the image into the targets and background. Second the two binary frames are compared to determine whether they are the same. So the image segmentation is a key thing. This this paper employ a novel segmentation algorithm base on unsupervised learning. This algorithm uses Fuzzy C-means methods to classify the image, and then chooses the samples which is high-confidence by fuzzy voting. These samples are used to train the fuzzy support vector machines. Finally the image is classified by trained fuzzy SVM. This algorithm could segment the impurities and background efficiently. To avoiding misjudgment, the 5 frame liquid images are captured and these contiguous sequences image are analyzed by the binary image difference method. The finally judgment is made according these four motion analysis results. The experiments demonstrate the inspection precision of the liquid inspection system is above 96.8%

References

1. Ishii, A., Mizuta, T., Todo, S.: Detection of foreign substances mixed in a plastic bottle of medicinal solution using real-time video image processing. In: Fourteenth International Conference on Pattern Recognition, Australia, pp. 1646–1650 (1998)
2. Lu, J., Wang, Y.-N., Zhang, J., et al.: On-line detection of foreign substances in glass bottles filled with transfusion solution through computer vision. In: International Conference on Information and Automation, pp. 424–429 (2008)
3. Ge, J., Wang, Y., Zhou, B., et al.: Intelligent Foreign Particle Inspection Machine for Injection Liquid Examination Based on Modified Pulse-Coupled Neural Networks. Sensors (9), 3386–3404 (2009)
4. Zhang, Y., Chung, F.-L., Wang, S.T.: Robust fuzzy clustering based image segmentation. Applied Soft Computing 9(1), 80–84 (2009)
5. Yang, M.-S., Tsai, H.-S.: A Ganssian kernel-based fuzzy c-means algorithm with a spatial bias correction. Pattern Recognition Letters 29, 1713–1725 (2008)
6. Tan, Y., Wang, J.: A support vector machine with a hybrid kernel and minimal Vapnik-Chervonenkis dimension. IEEE Transactions on Knowledge and Data Engineering 16(4), 385–395 (2004)

A Branch and Bound Algorithm to Minimize Makespan on Identical Parallel Machines with Consumable Resources

Fayçal Belkaid, Fouad Maliki, Fethi Boudahri, and Zaki Sari

Manufacturing Engineering Laboratory of Tlemcen
Abou Bekr Belkaid University
B. P. N°119, Tlemcen 13000, Algéria
{f_belkaid,mafouad11,fathi_boudahri}@yahoo.fr,
z_sari@mail.univ-tlemcen.dz

Abstract. In this paper, we study a scheduling problem for minimizing the makespan on identical parallel machines with consumable resources in a node of a supply chain. The goal is to provide a first exact approach to this problem through the use of Branch and Bound method. We propose two new heuristics and apply other with a series of lower bounds that are incorporated into our algorithm. We tested a large number of randomly generated instances that allow us to compare the computation time and quality of lower bounds and heuristics.

Keywords: Scheduling, Makespan, Parallel Machines, Branch and Bound.

1 Introduction

We study a parallel machines scheduling problem of order picking in a platform with a distribution company without manufacturing which manages about 100 stores and several trucks of transport. This platform is connected to a set of suppliers and a set of clients. The manner of working platform is all known. Several ways to make deliveries are identified and many assumptions can be made for departures deliveries, this leads to vehicle routing to make such distributions, while optimizing their costs through scheduling preparation store orders.

This research proposes to include realistic constraints very encountered, but are rarely taken in the literature. Therefore, this study will highlight the importance of this problem in the industry.

Rest of the paper is organized as follows. In Section 2 we make an analysis of the literature. Section 3 describes our problem and the method of resolution. Section 4 describes the new proposed heuristic. Section 5 provides lower bounds. Experiments are made in Section 6. Finally, section 7 concludes the work.

2 Literature Review

In this section, we focus on problems with non-renewable resources.

D. Jin and S. Lin (Eds.): Advances in Mechanical and Electronic Engineering, LNEE 176, pp. 217–221.
springerlink.com

Carlier et al. [1] have addressed the problem of project scheduling where resource units are produced or consumed. They proposed algorithms lists to minimize the makespan. Slowinski [2] addressed a scheduling problem on parallel machines with resource constraints and preemptive jobs. Gafarov and Lazarev [3] made a recent analysis of the complexity of problems in a machine with a consumable resource or he gave special attention to the problem of minimizing the sum of the delays.

Baoqiang, [4] considered a problem to a single machine with fixed delivery dates and temporary storage to minimize the sum of makespan and storage costs. The author has shown that the problem is NP-hard in the strong sense. Carrera et al. [5] dealt with problems in a single machine with consumable resources and fixed delivery dates. The authors conducted a study on the complexity of these problems and they showed that they are NP-hard. They used a branch and bound to solve them.

This article proposes to extend the problem considered by Carrera et al. [5], should parallel machines, that is to say, to combine between: Consumable resources and identical parallel machines.

To our knowledge and after a literature search, we believe that the problem NP-hard type, as defined in this work, has never been studied before.

3 Problem Description and Resolution Method

Our research focuses on the scheduling part of the logistics platform considered. The problem is to perform a set of n jobs , which correspond to order preparation of a set of m identical parallel machines. These machines can handle only one job at a time. We assume that the jobs and machines are continuously available at time t = 0. The execution time of a job j is denoted by p_j. We assume that the intéruptibilité of jobs is not allowed (no preemption). A job j can be run on a machine i, when all necessary components are available. Each job j consumed $a_{j,k}$ units of component k at the beginning of his execution day.

In this paper, we address a problem with a flexible delivery date, this flexible date corresponds to Cmax. So, the criterion to be minimized in this case is Cmax. The notation $\alpha|\beta|\gamma$ corresponding to our NP-hard scheduling problem is:

- $P_m|E(nc), a_{j,k}|Cmax$

E (nc): nc consumable resources defined by the cumulative curves of arrivals shaped staircase.

The aim of this paper is to provide an exact method as Branch And Bound (BAB) for the considered problem. However, we can cite work of Yalaoui and Chu [6] which offers the BAB as an exact method for solving some scheduling problems on parallel machines.

4 Heuristic Methods

In this section, we propose a new heuristic for Cmax. We will note by LPTR, because it is based on LPT rule. We test this technique and show that it gives good results. The three heuristics applied are LPT, LPT-SCD and the proposed heuristic LPTR

- LPT (Longest Processing Time first): we arrange jobs in descending order of their processing time
- LPT-SCD (Decreasing values of processing times divided by consumption of components): we rank the jobs in descending order of their relative processing time and the sum of the components that consume, this technique has been used by Carrera et al. [5].
- LPTR (Longest Processing Time first repeated), we propose this new heuristic which consists in arranging the jobs that can be executed in descending order of their processing time. If two or more jobs have the same processing time, therefore they are classified in order of increasing consumption of components, we repeat these steps on each arrival of a component, that is to say, we apply the LPT between each two arrivals. This technique avoids downtime.

The proposed algorithm LPTR

```
Let L be the list of all jobs;
Until the list L is not empty do;
  For each arrival of any component k do;
  Refresh arrivals Ak curves of all components;
    Until the next arrival of any component does not
    happen to;
    Select the jobs from the list L that can be
     processed;
     Schedule the jobs that can be treated according to
     LPT rule;
    Schedule the jobs that have the same processing time
    in order of increasing consumption of components;
    Handle such jobs selected so that the curves of uses
    are less than or equal to the curves of arrivals;
    end;
  Remove the jobs processed in the list L;
  Refresh Uk utilization curves for all components;
  end;
End.
```

5 Lower Bounds

In this section, we apply two lower bounds used by Carrera et al. [5] in single machine problem for our parallel machines scheduling problem.

5.1 Lower Bounds Using Agreeable Orders

To apply the technique of agreeable orders, we need to cite the lemma used by Carrera et al. "If the decreasing order of processing times *LPT* is identical to the increasing order of component requirement, then the orders are agreeable and minimize the *Cmax*". So, after applying this lemma, we obtain different values of Cmax for each component, and then we retain the maximum value of Cmax among all components (noted k), our lower bound for parallel machines is in the following form:

$$LB1 = Max\left((\max_k Cmax\,(P'(k))/M)\,, \max_j\,(p_j)\right)$$

5.2 Lower Bounds Using Integer Relaxations

In this section, we generalize the lower bounds applied by Carrera et al., [5] to our problem, while accepting the interruptibility of jobs and assuming that the consumption of components is a continuous and uniform during the processing of jobs. We apply the technique of Cochand et al. [7] also used by Carrera et al. [5] our scheduling problems on identical parallel machines. The objective is to minimize the date of last event, corresponding to the end of last job (We denote this by Min(LE)), this involves minimizing Cmax. We denote this Lower bound by LB2.

$$LB2 = Max\left(\,(Min(LE)/M)\,, \max_j\,(p_j)\,\right)$$

6 Computational Experience

This section describes the results obtained by the BAB. We do tests on different sets of randomly generated instances for represent realistic situations. Each job j follows a uniform distribution [1, 100]. We also consider another parameter that represents the dispersion of the components, ie the arrival of components can be grouped at the beginning of the time horizon (denoted RA), or dispersed throughout the time horizon (denoted DA). Each family contains 30 instances of instances with n = {50, 100, 150, 200} jobs and m = {2, 4, 8} machines. For Table 1, GAP represents the relative error, and the CPU is the average computation time (in seconds).

Table 1. Makespan lower bounds comparison

Data set	LB1		LB2	
	GAP	CPU	GAP	CPU
RA	0.44	0.09	0.09	0.13
DA	7.52	0.02	0.01	0.08

In Table 1, we compare the lower bounds for Cmax, we note that LB2 gives good results for RA and DA to LB1, but we can notice that the GAP is relatively small to LB1 and LB2 when arrivals are grouped. For the computation time, it remains small.

For table 2, GAP is the percentage average error between the best lower bound and best upper bound for each family of instances and BESTH shows the percentage of times where a fast approximate method provides the best solution. In the heuristic column, we classify the different heuristics in order of most efficient to least efficient. We note the heuristics used by: LPT by (H1), SCD-LPT by (H2) and LPTR by (H3).

Table 2. Upper and lower bounds comparison for makespan

Data set	GAP Cmax	Heuristics	%BESTH
RA	0.38	H3, H2, H1	33%, 13%, 10%
DA	2.25	H3, H2, H1	30%, 15%, 7%

In table 2, we compare the best lower bound with the best solution obtained by the heuristics, we notice that the gap is small for the Cmax for the family instance RA and worse for DA, this fact is due to downtime associated with resource constraints which disappears after the last arrival component. We also note that the proposed heuristic H3 give good results, in the second position is the heuristic H2 and finally H3.

7 Conclusion

The detailed study of scheduling problems highlighted their importance in the industry. And therefore, to solve this problem we used a BAB. We have developed lower bounds and proposed upper bounds for both hypotheses. These terminals are evaluated by appropriate experiments and promising results were obtained by preliminary tests. For future work, we propose to include a release date for each task and accept interruptibility. Also, meta-heuristics and lower bounds can be developed.

References

1. Carlier, J., Moukrim, A., Xu, H.: The project scheduling problem with production and consumption of resources: A list-scheduling based algorithm. Discrete Applied Mathematics 157(17), 3631–3642 (2009)
2. Slowinski, R.: Preemptive scheduling of independent jobs on parallel machines subject to financial constraints. European Journal of Operational Research 15, 366–373 (1984)
3. Gafarov, E.R., Lazarev, A.A.: Single machine scheduling with a non-renewable financial resource. Working paper (2010)
4. Baoqiang, F.: Scheduling with fixed delivery dates and temporary storage. In: International Conference on Logistics Systems and Intelligent Management, China, pp. 1926–1929 (2010)
5. Carrera, S., Portmann, M.C., Ramdane Cherif, W.: Scheduling supply chain node with fixed components arrivals and two partially flexible deliveries. In: 5th International Conference on Management and Control of Production and Logistics, France (2010)
6. Yalaoui, F., Chu, C.: A new exact method to solve the Pm/ri/∑ci schedule problem. International Journal of Production Economics 100(1), 168–179 (2006)
7. Cochand, M., de Werra, D., Slowinski, R.: Preemptive scheduling with staircase and piecewise linear resource availability. Methods and Models of Operations Research 33, 297–313 (1989)

Research on Performance of Gas Turbine's Intake

Song Wang[1], MingLiang Lu[2], MeiLing Tan[3], and YueHan Xu[4]

[1,2,4] College of Power and Energy Engineering, Harbin Engineering University, Harbin, China
[3] 703th Research Institute of China Shipbuilding Industry Corporation, Wuxi Branch, Wuxi, China
wangsong331@sina.com, 332076285@qq.com, 15961860176.fL9807@sohu.com, yuehanxu@yahoo.com.cn

Abstract. Gas turbine inlet aerodynamics can affect the overall performance of the gas turbine. For this requirement, the design and numerical simulation of gas turbine inlet will provide a reliable basis to design the high performance marine gas turbine. In order to offer reliable basis, in this article two inlet system models of gas turbine are designed and some numerical simulations are carried on according to the requirements mentioned above. The simulation results of the two projects are famous and important to the actual application.

Keywords: marine gas turbine, inlet system, numerical simulation.

1 Introduction

The inlet of marine gas turbine is installed in front of the compressor. It can makes a stable flow, removes the sea water and salt. It is called the filtering device of marine gas turbine. The airflow of gas turbine is very large. We should ensure that the velocity of the airflow in the inlet cannot be too high in order to reduce the flow loss and the velocity is generally controlled within the range of 15m/s～30m/s, so the size of the intake manifold is very large.

Marine gas turbine requires more even airflow and avoids the tremble of the compressor and the instability of gas turbine. The air flows into the regulator chamber from the filter, and the stream turns 90 degrees to enter the compressor. The flow of air in the regulator chamber will inevitably result in uneven flow area, velocity and pressure field distribution, the role of the horizontal pressure gradient and the channel wall boundary layer will produce vortex motion and the secondary flow loss.

We must master its aerodynamics performance before finalizing the design of inlet system. It needs more manpower and material resources as well as longer experimental period to realize characteristic of the different inlet structure absolutely by model experimentation, so numerical simulation studying method has important meaning [1].

Studying the aerodynamic performance of two inlet system models of gas turbine and examining the flow field of gas turbine inlet can provide a reliable reference to the real ship gas turbine inlet designing.

D. Jin and S. Lin (Eds.): Advances in Mechanical and Electronic Engineering, LNEE 176, pp. 223–227.
springerlink.com

2 Numerical Simulation Scheme

2.1 Control Equation

Under the assumptions of Boussinesq, the RANS governing equations are as follows [2].

$$\frac{\partial \rho}{\partial t} + \nabla \cdot \left(\rho \vec{v} \right) = 0 \tag{1}$$

$$\frac{\partial}{\partial t}\left(\rho \vec{v} \right) + \nabla \cdot \left(\rho \vec{v} \vec{v} \right) = \nabla \cdot \left(-pI + \Gamma \right) \tag{2}$$

$$\frac{\partial}{\partial t}\left(\rho E \right) + \nabla \cdot \left(\rho \vec{v} E \right) = \nabla \cdot \left[\left(-pI + \Gamma \right) \cdot \vec{v} \right] - \nabla \cdot \vec{q} \tag{3}$$

And $\mathrm{I} = \left\{ \delta_{ij} \right\}$ is unit tensor; $\Gamma = \left\{ \tau_{ij} \right\}$ is viscous stress tensor; $\vec{q} = \left\{ q_i \right\} = K \nabla \cdot T$ is heat flux vector; $E = e + \frac{1}{2} \vec{v} \cdot \vec{v}$ is the total energy of unit mass of fluid.; the ideal-gas equation : $\frac{p}{\rho} = RT$

Where: ρ —density; v —velocity vector; p —pressure; e —energy per unit mass; k —heat transfer constant; T —temperature; μ —coefficient of dynamic viscosity ;

The viscosity coefficient in the above parameters is changed as the temperature changed. Its value can be drawn by the engineering formula of Sutherland [3]:

$$\frac{\mu(T)}{\mu_0} = \left(\frac{T}{T_0} \right)^{3/2} \frac{T}{(T + T_s)} \tag{4}$$

And $T_0 = 273.16K$; T_s is Sutherland constant, $T_s = 110.4K$; μ_0 is the air viscosity coefficient under the conditions of an atmospheric pressure and temperature is 273K.

2.2 Turbulence Model

The standard *k-ε* model is a typical two-equation model, it is based on one-equation model. Launder and Spalding [4] proposed this model in 1972.

The corresponding transport equations [5]:

$$\frac{\partial (\rho k)}{\partial t} + \frac{\partial (\rho k u_i)}{\partial x} = \frac{\partial}{\partial x_j} \left[\left(\mu + \frac{\mu_t}{\sigma_k} \right) \frac{\partial k}{\partial x_j} \right] + G_k + G_b - \rho \varepsilon - Y_M + S_k \tag{5}$$

$$\frac{\partial(\rho\varepsilon)}{\partial t}+\frac{\partial(\rho\varepsilon u_i)}{\partial x_i}=\frac{\partial}{\partial x_j}\left[\left(\mu+\frac{\mu_t}{\sigma_\varepsilon}\right)\frac{\partial\varepsilon}{\partial x_j}\right]+C_{1\varepsilon}\frac{\varepsilon}{k}\left(G_k+C_{3\varepsilon}G_b\right)-C_{2\varepsilon}\rho\frac{\varepsilon^2}{k}+S_\varepsilon \tag{6}$$

And $C_{1\varepsilon}=1.44$, $C_{2\varepsilon}=1.92$, $C_\mu=0.09$, $\sigma_k=1.0$ and $\sigma_\varepsilon=1.3$.

3 Intake System Designs

The two computational domain models of intake system are shown below.

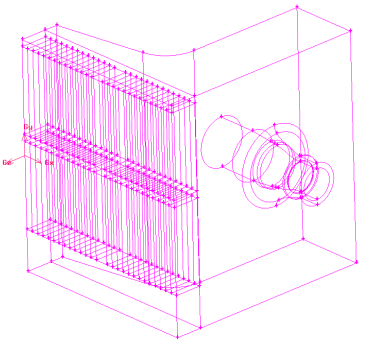

Fig. 1. Model 1

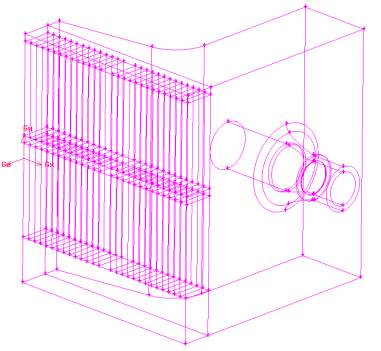

Fig. 2. Model 2

It is can be found that the inlet surface of model 1 is tapered and the inlet surface of model 2 is constant section.

Inlet boundary conditions: pressure inlet, the inlet pressure is standard atmospheric pressure (101325Pa), the intake air temperature is 300K and the airflow direction is the normal direction; porous jump conditions: drag coefficient of the filter; outlet boundary conditions: pressure outlet, exhaust pressure energy (resize it to adjust the flow), the exhaust pressure is 101325Pa; wall boundary conditions: adiabatic, no slip.

4 Results and Analysis

Fig 3 and Fig 4 show the path lines colored by velocity magnitude and Fig 5 and Fig 6 show the velocity distribution on the horizontal section.

For the entire flow field, the velocity distribution is uniform in the regulator chamber, but at the compressor inlet is not. The velocity of compressor inlet is gradually increased along the radial direction from the inner to the outer ring, but the total pressure is gradually reduced along the radial direction from the inner to the outer ring. And the pressure gradient that close to the filter side is larger than the opposite side. Thus, relative to the flow direction of the gas in the compressor, the airflow flows

into the regulator chamber from the lateral. Therefore, the turning of the airflow leads to the partial flow loss.

It is should be noted that the distribution of the total pressure in the regulator chamber is very uniform. In the transition section and compressor section, the total pressure is gradually reduced from the inner to the outer ring along the radial direction. And the total pressure that close to the filter side and the lower side is lower than the opposite sides.

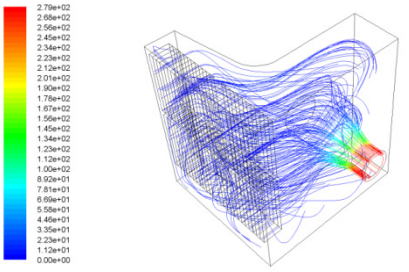

Fig. 3. The path lines of model 1

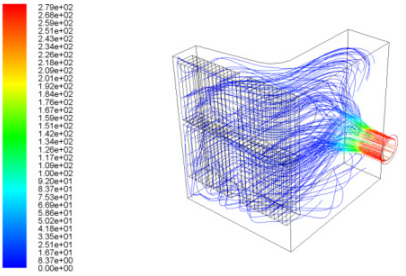

Fig. 4. The path lines of model 2

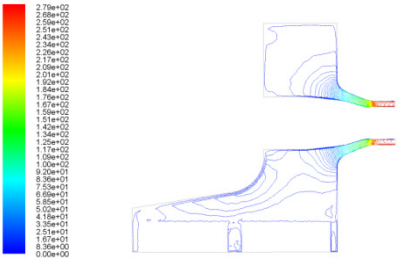

Fig. 5. Velocity contours in section (model 1)

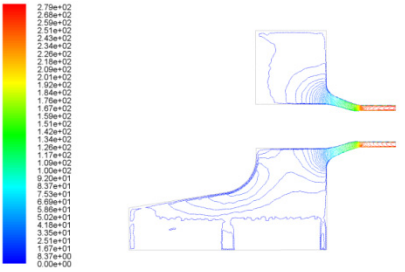

Fig. 6. Velocity contours in section (model 2)

5 Numerical Simulation Results of Compressor Inlet Flow

Table 1 shows the velocity field uniformity calculations on the compressor inlet cross-section at the rated conditions (the flow of 27kg / s). Fig. 7 and Fig. 8 show the simulation results of the velocity field on the cross-section of the compressor inlet in both models. By comparison it can be found that the flow field in model 1 is more uniform than that in model 2. But the structure of model 2 is relatively simple. In practical engineering, we should choose the best solution according to the specific situations.

Table 1. The uniformity of velocity field

Model	$\overline{V}_A$ (m/s)	$\overline{V}_{max}$ (m/s)	$\overline{V}_{min}$ (m/s)	Average uniformity (%)
1	148.21	150.58	143.43	4.82
2	146.59	148.97	141.81	4.89

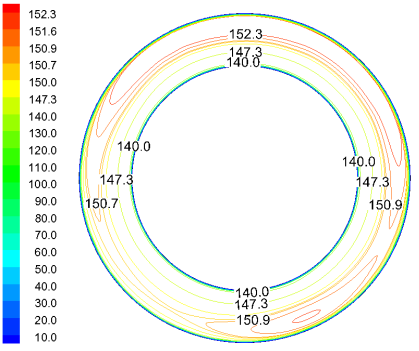

Fig. 7. The velocity on the section (model 1)

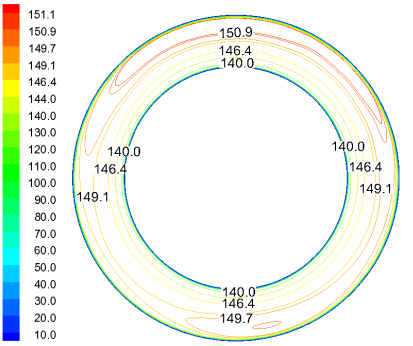

Fig. 8. The velocity on the section (model 2)

6 Conclusions

In this paper, some numerical simulations are carried on researching the flow characteristics of the gas turbine inlet regulator chamber. Conclusions are summarized as follows:

(1) In this paper, numerical simulation methods can be used to determine the impact of two different models on the flow. The geometric models are established in accordance with the actual size when study the flow field of the two models. So that it makes the numerical simulation results to be able to fully reflect the true current state and it can accurately compare the flow field characteristics between the two models.

(2) In this paper, numerical simulation methods have been used to get the uniformity of the velocity field on the compressor inlet cross-section. This article makes a detailed numerical calculation about the velocity distribution on the compressor inlet cross-section and the uniformity characteristics of the cross-section at rated conditions have been researched.

References

1. Shi, B.: The Research on Marine Gas Turbine Inlet Flow Filed. Harbin Engineering University Master's degree thesis, Harbin
2. Mishing, Y.: Diffusion Processes in Advanced Technological Materials. In: Gupta, D. (ed.) Noyes Publications/William Andrew Publishing, Norwich, NY (2004)
3. Liu, Y., Miao, G.: Advanced Fluid Mechanics, pp. 1-15, 148–188. Shanghai Jiaotong University Press, Shanghai (2000)
4. Launder, B.E., Spalding, D.B.: Lectures in Mathematical Models of Turbulence. Academic Press, London (1972)
5. Fluent Inc. FLUENT User's Guide. Fluent Inc. (2003)

A System-Level Compensation Method for Inertial Navigation System

Jiwei Zhang, Xiaodong Xu, and Bo Wang

School of Automation, Beijing Institute of Technology, China
{hellozjw,wb1020}@bit.edu.cn

Abstract. In order to solve the problem about the slow accumulation of error in the INS, this paper offers a system-level compensation method that makes use of characteristics of ship that two sets of ship's INS are independent and backup for each other to convert gyro for navigation into biax-gyro. By proceeding of the output of biax-gyro, gyro's bias was revised. This method not only reduces the size and weight of INS, but also improves the stability of system.

Keywords: system-level compensation, bias, scale factor, azimuth axis, pitching axis, horizontal roller.

1 Introduction

It is common that ship would be furnished more than two sets of INS to guarantee the stability and availability. In the precondition that the two sets of INS run normally and cooperate with each other, the precision of INS was boosted through detection of gyro's bias according to the principle of gyro-supervision[1].

There are two manners including modification of gyro-outputs' variation and calculation of position output-error. For HALE inertial navigation system with high precision, self calibration could detect and compensate constant error in the step of initial alignment[2]. After the constant error was calibrated accurately, the mutative slowly error of inertial instruments becomes the main factor influencing the precision of system. Regarding to this kind of error, this paper provides compensation method form the view of system.

2 Specific Principle and Procedure

In the navigation of ship, two sets of INS work in the same working mode that means they have similar error propagation law. The two sets of INS are respectively noted as sytem1 and system2.

After sytem1 and system2 working for a period time t, a number of output of gyro were collected. Then the average outputs of two systems are[3][5]:

System1:

D. Jin and S. Lin (Eds.): Advances in Mechanical and Electronic Engineering, LNEE 176, pp. 229–233.
springerlink.com

$$\begin{bmatrix} \omega'_{x1} \\ \omega'_{y1} \\ \omega'_{z1} \end{bmatrix} = \begin{bmatrix} \omega_x + \varepsilon_{x1} + \delta_{x1}(0) \\ \omega_y + \varepsilon_{y1} + \delta_{y1}(0) \\ \omega_z + \varepsilon_{z1} + \delta_{z1}(0) \end{bmatrix} \tag{1}$$

where ω'_{x1}, ω'_{y1} and ω'_{z1} are respectively the average output of x, y, z axis of system1. ω_x, ω_y and ω_z are respectively the actual angular velocities of carrier on the direction of three axises. ε_{x1}, ε_{y1} and ε_{z1} are respectively gyro bias of x, y, z aixs of system1. $\delta_{x1}(0)$, $\delta_{y1}(0)$ and $\delta_{z1}(0)$ are the initial bias of pitching axis, horizontal roller and azimuth axis of system1[4].

System2:

$$\begin{bmatrix} \omega'_{x2} \\ \omega'_{y2} \\ \omega'_{z2} \end{bmatrix} = \begin{bmatrix} \omega_x + \varepsilon_{x2} + \delta_{x2}(0) \\ \omega_y + \varepsilon_{y2} + \delta_{y2}(0) \\ \omega_z + \varepsilon_{z2} + \delta_{z2}(0) \end{bmatrix} \tag{2}$$

where ω'_{x2}, ω'_{y2} and ω'_{z2} are respectively the average output of x, y, z axis of system2. ω_x, ω_y and ω_z are respectively the actual angular velocities of carrier on the direction of three axises. ε_{x2}, ε_{y2} and ε_{z2} are respectively gyro bias of x, y, z aixs of system2. $\delta_{x2}(0)$, $\delta_{y2}(0)$ and $\delta_{z2}(0)$ are the initial bias of pitching axis, horizontal roller and azimuth axis of system2.

$\delta_{x1}(0)$, $\delta_{y1}(0)$, $\delta_{z1}(0)$, $\delta_{x2}(0)$, $\delta_{y2}(0)$ and $\delta_{z2}(0)$ are known quantities. Combining equation (1) and (2), following equation is avaliable:

$$\begin{bmatrix} \Delta\omega'_x \\ \Delta\omega'_y \\ \Delta\omega'_z \end{bmatrix} = \begin{bmatrix} \omega'_{x1} - \omega'_{x2} \\ \omega'_{y1} - \omega'_{y2} \\ \omega'_{z1} - \omega'_{z2} \end{bmatrix} = \begin{bmatrix} \varepsilon_{x1} - \varepsilon_{x2} + \delta_{x1}(0) - \delta_{x2}(0) \\ \varepsilon_{y1} - \varepsilon_{y2} + \delta_{y1}(0) - \delta_{y2}(0) \\ \varepsilon_{z1} - \varepsilon_{z2} + \delta_{z1}(0) - \delta_{z2}(0) \end{bmatrix} \tag{3}$$

The normal working state of two systems was shown in the Fig. 1.

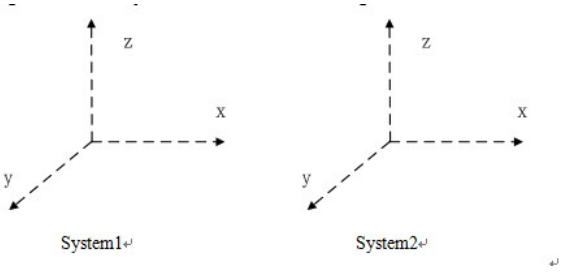

Fig. 1. The normal working state of two systems

When system1 is working normally, the inertial instruments of system2 were rotated around aixses. The rotation scheme is as follows:

The inertial instruments of system2 were rotated 180° around z aixs. Compared with the former position, the direction of x and y axis is reversed. During the rotation of system, the outputs of both the gyros on x and y axis of system1 and system2 were collected. By calculating the average of outputs, ω''_{x1}, ω''_{y1}, ω''_{x2} and ω''_{y2} were obtained:

$$\begin{aligned} \omega''_{x1} &= \omega'_x + \varepsilon_{x1} + \delta_{x1}(0) \\ \omega''_{y1} &= \omega'_y + \varepsilon_{y1} + \delta_{y1}(0) \end{aligned} \tag{4}$$

$$\begin{aligned} \omega''_{x2} &= -\omega'_x + \varepsilon_{x2} + \delta_{x2}(0) \\ \omega''_{y2} &= -\omega'_y + \varepsilon_{y2} + \delta_{y2}(0) \end{aligned} \tag{5}$$

where, ω'_x and ω'_y were respectively the actual angular velocity of x and y axis of carrier.

Through equation (4) and (5), the follows can be got:

$$\begin{bmatrix} \Delta\omega''_x \\ \Delta\omega''_y \end{bmatrix} = \begin{bmatrix} \omega''_{x1} + \omega''_{x2} \\ \omega''_{y1} + \omega''_{y2} \end{bmatrix} = \begin{bmatrix} \varepsilon_{x1} + \varepsilon_{x2} + \delta_{x1}(0) + \delta_{x2}(0) \\ \varepsilon_{y1} + \varepsilon_{y2} + \delta_{y1}(0) + \delta_{y2}(0) \end{bmatrix} \tag{6}$$

Fig. 2. System2 rotated 180°

The inertial instruments of system2 were rotated 180° around x axis. Compared with the former position, the direction of z axis is reversed. During the rotation of system, the outputs of both the gyros on z axis of system1 and system2 were collected. By calculating the average of outputs, ω''_{z1} and ω''_{z2} were obtained:

$$\begin{aligned} \omega''_{z1} &= \omega'_z + \varepsilon_{z1} + \delta_{z1}(0) \\ \omega''_{z2} &= -\omega'_z + \varepsilon_{z2} + \delta_{z2}(0) \end{aligned} \tag{7}$$

where, ω'_z was respectively the actual angular velocity of z axis of carrier.

Through adding the output of z axis in both system1 and system2 up, the follows can be got:

$$\Delta\omega_z'' = \omega_{z1}'' + \omega_{z2}'' = \varepsilon_{z1} + \varepsilon_{z2} + \delta_{z1}(0) + \delta_{z2}(0) \tag{8}$$

According to (6) and (8),

$$\begin{bmatrix} \Delta\omega_x'' \\ \Delta\omega_y'' \\ \Delta\omega_z'' \end{bmatrix} = \begin{bmatrix} \omega_{x1}'' + \omega_{x2}'' \\ \omega_{y1}'' + \omega_{y2}'' \\ \omega_{z1}'' + \omega_{z2}'' \end{bmatrix} = \begin{bmatrix} \varepsilon_{x1} + \varepsilon_{x2} + \delta_{x1}(0) + \delta_{x2}(0) \\ \varepsilon_{y1} + \varepsilon_{y2} + \delta_{y1}(0) + \delta_{y2}(0) \\ \varepsilon_{z1} + \varepsilon_{z2} + \delta_{z1}(0) + \delta_{z2}(0) \end{bmatrix} \tag{9}$$

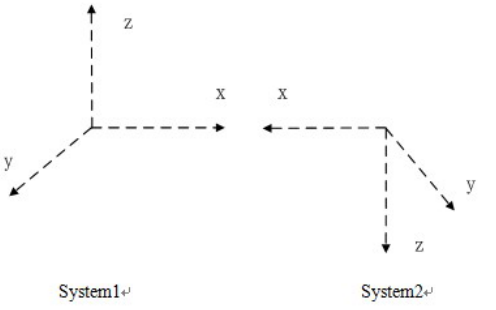

Fig. 3. System2 rotated 180°

The inertial instruments of system2 were rotated 180° around z axis. Then let the inertial instruments of system2 spine 180° around x axis. Obviously, the system2 returns to initial position.

Adding equation (3) and (9) up, the gyro biases of system1 could be acquired:

$$\begin{bmatrix} \varepsilon_{x1} \\ \varepsilon_{y1} \\ \varepsilon_{z1} \end{bmatrix} = \begin{bmatrix} \dfrac{\Delta\omega_x' + \Delta\omega_x''}{2} - \delta_{x1}(0) \\ \dfrac{\Delta\omega_y' + \Delta\omega_y''}{2} - \delta_{y1}(0) \\ \dfrac{\Delta\omega_z' + \Delta\omega_z''}{2} - \delta_{z1}(0) \end{bmatrix} \tag{10}$$

Subtracting equation (3) from equation (9), the gyro biases of system2 could be obtained:

$$\begin{bmatrix} \varepsilon_{x2} \\ \varepsilon_{y2} \\ \varepsilon_{z2} \end{bmatrix} = \begin{bmatrix} \dfrac{\Delta\omega_x'' - \Delta\omega_x'}{2} - \delta_{x2}(0) \\ \dfrac{\Delta\omega_y'' - \Delta\omega_y'}{2} - \delta_{y2}(0) \\ \dfrac{\Delta\omega_z'' - \Delta\omega_z'}{2} - \delta_{z2}(0) \end{bmatrix} \tag{11}$$

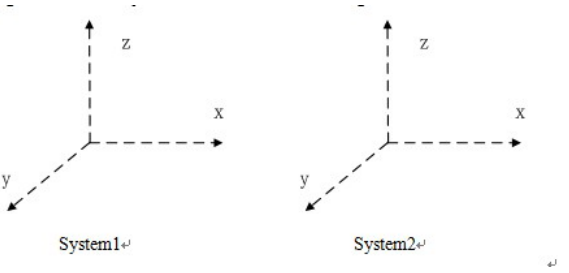

Fig. 4. System2 rotated 180^{o}

The gyro bias of two systems acquired from equation of (10) and (11) helps to improve the system's precision realizing the system- level compensation for the INS.

3 Summary

This paper offers a system-level compensation method that makes use of characteristics of ship that two sets of ship's INS are independent and backup for each other to convert gyro for navigation into gyro, in order to solve the problem about the slow accumulation of error in the INS, By proceeding of the output of gyro, gyro's bias was revised. This method not only reduces the size and weight of INS, but also improves the stability of system. It is positive for the exploration of new compensation methods.

Acknowledgments. This work is supported by the grant from National Program on Key Basic Research Project (973 Program) (No.613121) and National Natural Science Foundation of China (No. 60904086, No. 61104189, No. 61104192 and No. 61127004).

References

1. Ojeda, L., Borenstein, J.: FLEXnav: Fuzzy Logic Expert Rule-based Position Estimation for Mobile Robots on Rugged Terrain. In: Proceedings of IEEE International Conference Robotics and Automation, pp. 317–322. IEEE Press, Washington, DC (2002)
2. Rehbinder, H., Hu, X.: Nonlinear State Estimation for Rigid Body Motion with Low Pass Sensors. Sys. Cont. Let., 183–190 (2000)
3. Leavitr, J., Athanasios, S.J., Bobrow, J.E.: High Bandwidth Tilt Measurement Using Low-cost Sensors. IEEE/ASME Trans. Mechatron. 11, 320–327 (2006)
4. Baerveldt, A.J., Klang, R.: A Low Cost and Low Weight Attitude Estimation System for An Autonomous Helicopter. In: Proceedings of IEEE Conference Intelligent Engineering Systems, pp. 391–395. IEEE Press, Budapest (1997)
5. Rogers, R.M.: Applied Mathematics in Integrated Navigation Systems. American Institute of Aeronautics and Astronautics (2007)

Optimal PID Controller for Integrating Processes with Time Delay Based on Modified Internal Model Methods

Xiaohui Zeng, Yonghui Chen, and Gongquan Tan

Shool of Automation and Electronic Information Engineering, Sichuan University of Science & Engineering, 643000, Zigong, China
xh-z@sohu.com, cyh4180@163.com, tgq77@126.com

Abstract. A modified internal model controller is designed in the paper which satisfies requirements of internal stability and disturbance response of the system. The equivalent feedback controller for the internal model controller is approximated by a traditional PID controller with Maclaurin formula. A robust performance index is structured by maximum sensitivity value and integral of absolute error, and then the damping ratio and the time constant of PID parameters are determined. Simulation results show that the method proposed is effective for different integrating processes with time delay and the performance and the robustness of control systems are good and satisfactory.

Keywords: Integrating process with time delay, Modified internal model controller, PID controller, Robust performance.

1 Introduction

Integrating processes with time delay exists often in industrial processes. System performances and stabilities of such processes are affected easily by time delays and it is difficult to get satisfactory control performance. A PID parameter optimization method with two degrees of freedom based on modified internal model methods is proposed. The damping ratio and the time constant are optimized according to the robustness of the system and then optimal PID control can be achieved.

2 The Design of the Internal Model Controller

A feedback control system with filter is as shown in figure 1. Parameters y and u in the system response to inputs r and d are

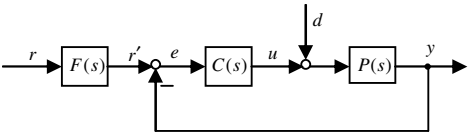

Fig. 1. The feedback control system with filter

D. Jin and S. Lin (Eds.): Advances in Mechanical and Electronic Engineering, LNEE 176, pp. 235–240.
springerlink.com

$$\begin{bmatrix} y \\ u \end{bmatrix} = \begin{bmatrix} P(s)Q(s) & P(s)[1-P(s)Q(s)] \\ Q(s) & -P(s)Q(s) \end{bmatrix} * \begin{bmatrix} r' \\ d \end{bmatrix} \tag{1}$$

In which, affine function $Q(s) = C(s)/[1+P(s)C(s)]$.

If Q(s), P(s)Q(s) and P(s)[1-P(s)Q(s)] is stable, then the closed-loop control system is stable. For a stable process, internal stability of the closed-loop system can be assured only if Q(s) is stable.

Otherwise, for stead step disturbance response without differences, disturbance transfer function should satisfy the constrain of

$$\lim_{s\to 0} \frac{y}{d} = \lim_{s\to 0} P(s)[1-P(s)Q(s)] = 0 \tag{2}$$

Internal model controller Q(s) should guarantee the interference suppression performance and the robust stability of the closed-loop system. And feed-forward compensator F(s) functions to improve the tracking performance of the system.

For an commonly integrating model exists in the industry[1]

$$P(s) = \frac{Ke^{-Ls}}{s(Ts+1)} \tag{3}$$

Where K, T and L are speed gain, inertia time and delay time constant of the process respectively.

For processes with small inertia ($T/L<1$), internal model controller is selected as

$$Q(s) = \frac{(\beta s+1)s/K}{\lambda^2 s + 2\lambda\xi s + 1} \tag{4}$$

In which, λ and ξ are adjustable time constant and damping ratio individually.

Corresponding disturbance transfer function and tracking transfer function are

$$\frac{y}{d} = \frac{Ke^{-Ls}}{s(Ts+1)}[1 - \frac{(\beta s+1)e^{-Ls}}{(\lambda^2 s^2 + 2\lambda\xi s+1)(Ts+1)}] \tag{5}$$

$$\frac{y}{r} = \frac{F(s)(\beta s+1)e^{-Ls}}{(\lambda^2 s + 2\lambda\xi s+1)(Ts+1)} \tag{6}$$

When equation (5) satisfies equation (2), the coefficient β should be $\beta = 2\lambda\xi + T + L$

At the same time, the feed-forward compensation function used to improve the tracking performance of the system is $F(s) = (Ts+1)/(\beta s+1)$.

For processes with large inertia ($T/L>1$), internal model controller is selected as

$$Q(s) = \frac{(\alpha s^2 + \beta s+1)s(Ts+1)/K}{(\lambda^2 s + 2\lambda\xi s+1)^2} \tag{7}$$

Corresponding disturbance transfer function and tracking transfer function are

$$\frac{y}{d} = \frac{Ke^{-Ls}}{s(Ts+1)}[1 - \frac{(\alpha s^2 + \beta s + 1)e^{-Ls}}{(\lambda^2 s^2 + 2\lambda\xi s + 1)^2}] \tag{8}$$

$$\frac{y}{r} = \frac{F(s)(\alpha s^2 + \beta s + 1)e^{-Ls}}{(\lambda^2 s + 2\lambda\xi s + 1)^2} \tag{9}$$

When equation (8) satisfies equation (2), the coefficient β should be $\beta = 4\lambda\xi + L$.

For improving response speed of disturbances, disturbance transfer function pole -1/T should be cancelled, that is equation (8) should satisfy following condition.

$$\lim_{s \to -1/T}[1 - \frac{(\alpha s^2 + \beta s + 1)e^{-Ls}}{(\lambda^2 s^2 + 2\lambda\xi s + 1)^2}] = 0 \tag{10}$$

Therefore, coefficient α is

$$\alpha = \beta T - T^2 + (\lambda^2 / T - 2\lambda\xi + T)^2 e^{-L/T} \tag{11}$$

At last, feed-forward compensation function $F(s) = 1/(as^2 + \beta s + 1)$ is used to suppress overshoot of step tracking response of the system.

3 Parameters Optimization of the PID Controller

Assume function $G(s)$ can be represented by Maclaurin series, that is

$$G(s) = sK \cdot C(s) = sK \cdot \frac{Q(s)}{1 - P(s)Q(s)} \tag{12}$$

In which, C(s) is equivalent feedback controller for the internal model controller.

Equivalent feedback controller $C(s)$ is approximated by a regular ideal PID controller, that is

$$C_{PID}(s) = K_c(1 + 1/sT_i + sT_d) \approx C(s) \tag{13}$$

For small inertia integrating processes with time delay, parameters of improved internal model PID controller are

$$\begin{cases} K_c = \dfrac{T_i}{K(\lambda^2 + 2\xi\lambda T + \beta L - L^2/2)} \\ T_i = \beta + T - \dfrac{\lambda^2 T + L^2(L - 3\beta)/6}{\lambda^2 + 2\xi\lambda T + \beta L - L^2/2} \\ T_d = \dfrac{\beta T}{T_i} + T_i - \beta - T - \dfrac{L^3(4\beta - L)/24}{T_i(\lambda^2 + 2\xi\lambda T + \beta L - L^2/2)} \end{cases} \tag{14}$$

For large inertia integrating processes with time delay, parameters of improved internal model PID controller are

$$\begin{cases} K_c = \dfrac{T_i}{K(2\lambda^2 + 4\lambda^2\xi^2 - \alpha + \beta L - L^2/2)} \\ T_i = \beta + T - \dfrac{4\lambda^3\xi + \alpha L + L^2(L-3\beta)/6}{2\lambda^2 + 4\lambda^2\xi^2 - \alpha + \beta L - L^2/2} \\ T_d = \dfrac{\alpha + \beta T}{T_i} + T_i - \beta - T - \dfrac{\lambda^4 - \alpha L^2/2 + \beta L^3/6 - L^4/24}{T_i(2\lambda^2 + 4\lambda^2\xi^2 - \alpha + \beta L - L^2/2)} \end{cases} \tag{15}$$

Assume the robustness performance index is

$$J = IAE \cdot M_s^b = \int_0^\infty |e(t)|\,dt \cdot (\max_{\omega>0} |S(j\omega)|)^b \tag{16}$$

In which, b is exponential weighting factor and b>0, $S(j\omega)$ is the sensitivity function of the system and $e(t)$ is the error function under disturbances.

For small inertia integrating processes with time delay, take a first-order integrating process with time delay for example, that is the model described by equation (3) when K=1, T=0, L=1. PID parameters of the modified internal model method are determined according to equation (14). M_S-*IAE* characteristics of the system with different time constant λ under two damping ratios are as show in figure 2(a). characteristics of PID proposed by Chengqiang Ying[2] (named Y-PID), Jianguo Wang[3] (named W-PID) and Ahmad Ali[4] (named A-PID) are also shown in the figure.

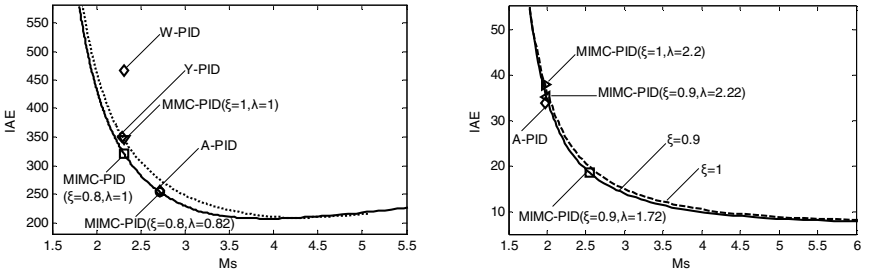

(a) First-order integrating (b) Double integrating

Fig. 2. M_s-*IAE* characteristics of different integrating processes with time delay under different PID controls

As shown in figure2(a), the robustness of W-PID control is poor. Parameter determination of Y-PID is under critical damping ratio ξ=1 and parameter determination of A-PID is when damping ratio ξ=0.8. MIMC-PID control proposed in the paper is the PID control when b=1.5 in equation (16). The resulting robustness and performance of the system is more reasonable.

For large inertia integrating processes with time delay, take a double integrating process with time delay for example

$$P(s) = \frac{K_a e^{-Ls}}{s^2} \tag{17}$$

The process is described by equation (3) when $K=K_aT$ and T is great. That is

$$P(s) \approx \frac{K_a e^{-Ls}}{s(s+1/T)} = \frac{K_a T e^{-Ls}}{s(Ts+1)} \tag{18}$$

Assume K_a=1, L=1 in equation (17), and PID parameters of the modified internal model method is obtained according to equation(15). M_S-*IAE* characteristics of the system with different time constant λ under two damping ratios are as show in figure 2(b). characteristics of A-PIDare also shown in the figure. The performance of A-PID control is slightly better than MIMC-PID control when ξ=0.9, λ=2.22 or ξ=1,λ=2.2 with almost same M_S. But both the robustness and performance of the system under MIMC-PID control when ξ=0.9, λ=1.72 are better (the situation when b=2 with the best robustness in equation (16)).

For integrating processes described by equation (3), when b=1.5~2 in equation (16), the robustness and performance of the system under MIMC-PID control are satisfactory.

4 Simulations

Assume a first-order integrating process with time delay [2] is

$$P(s) = \frac{e^{-5s}}{\mathrm{s}} \tag{19}$$

Parameters of each PID controller are as followings: A-PID: K_c=0.2200, T_i=13.6000, T_d= 1.90, W-PID: K_c=0.1733, T_i=20.2378, T_d=2.1912, Y-PID: K_c=0.1733, T_i=20.2378, T_d=2.1912, MIMC-PID: K_c=0.1942, T_i=16.8103, T_d=1.7160, β=14.8989 when ξ=1 and λ=1,K_c=0.1903, T_i=14.9400, T_d=1.6125, β=13.1167 when ξ=0.8 and λ=1, K_c=0.2178, T_i=13.6061, T_d=1.7369, β=11.6151 when ξ=0.8 and λ=0.82. Set-points of the system and disturbance step responses for each PID control are as shown in figure 3(a).

Assume a double integrating process with time delay is

$$P(s) = \frac{e^{-s}}{s^2} \tag{20}$$

Parameters of each PID controller are as followings: A-PID: K_c=0.1300, T_i=7.7800, T_d=3.940, MIMC-PID: K_c= 0.1284, T_i=9.7161, T_d=3.8162, α=37.9239, β=9.795 when ξ=1 and λ=2.2, K_c=0.1282, T_i=8.8763, T_d=3.7009, α=34.0592, β=9.0039 when ξ=0.9 and λ=2.22, K_c=0.1952, T_i=7.2302, T_d=3.0681, α=22.0622, β=7.2009 when ξ=0.9 and λ=1.72. Set-points of the system and disturbance step responses for each PID control are as shown in figure 3(b).

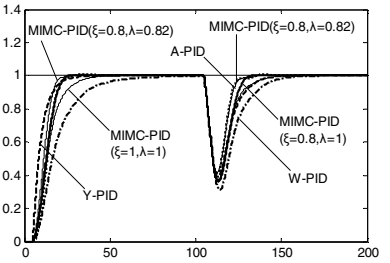

(a) First-order integrating

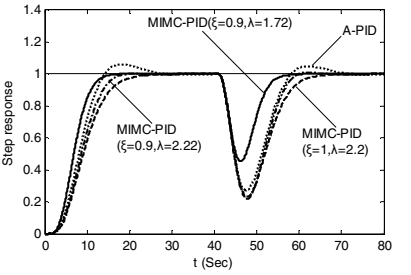

(b) Double integrating

Fig. 3. Step responses of different integrating processes with time delay under different PID control

5 Summary

A two degree of freedom PID controller based on modified internal model method with set filter for integrating processes with time delay is designed in the paper. The simulation results show that robustness and performance of the system under proposed method are satisfactory when b=1.5~2. PID design method proposed by Admad Ali is a little conservative for the control of large inertia integrating processes with time delay. It means the selection of proper optimizing index is quite important for the design of the controller and robustness index in the paper is generally applicable. PID design based on internal model theories can reduce the search space dimension of parameter optimization which may not guarantee global optimum of PID parameters, and it is a sub-optimal method.

References

1. Tan, G., Chen, Y., Zeng, X., Fu, C.: Design method of PID controller for unstable processes with time delay in time domain. Chemical Automation and Instruments 38(3), 284–287 (2011)
2. Ying, C., Yue, J.: Modified Control for Self-irregulating Processes Plus Time Delay. Control and Decision 24(10), 1593–1596, 1600 (2009)
3. Wang, J., Gu, Y., et al.: Optimal PID Control for A Kind of Self-irregualting Objects. Journal of Scientific Instrument 29(1), 148–151 (2008)
4. Ali, A., Majhi, S.: Integral Criteria for Optimal Tuning of PI/PID Controllers for Integrating Processes. Asian Journal of Control 13(2), 328–337 (2011)

Optimal Design of PV/Wind/Battery Systems by Genetic Algorithms Considering the Effect of Charge Regulation

Juan M. Lujano Rojas, Rodolfo Dufo-López, and José L. Bernal-Agustín

Department of Electrical Engineering, University of Zaragoza,
Calle María de Luna 3, 50018, Spain
lujano.juan@gmail.com,
{rdufo,jlbernal}@unizar.es

Abstract. Hybrid power systems (HPS) play an important role in the social development of areas located far from the electric grid. The optimal sizing of these systems is difficult to determine due to the variable nature of renewable energy resources and the complex behavior of their components. An important device of HPS is the charge controller as it protects the battery bank against extreme operational conditions, directly affecting the acceptance of charge from the battery bank and consequently the ability of the system to store energy. This paper presents a study about optimization of stand-alone PV/wind/battery hybrid power systems based in a genetic algorithm that considers the effect of charge regulation in the energy capture of the battery bank.

Keywords: Genetic Algorithms, Hybrid power systems.

1 Introduction

Autonomous renewable energy systems are an important option for rural electrification in many places around the world. Designing these types of systems is difficult due to the variability of renewable resource and the complex behavior of some components. Many algorithms have been proposed to find the optimal combination of power sources to meet energy demands. The following possible combinations were tested: [1] direct algorithm [2], design space methodology [3], particle swarm optimization [4], linear programming [5], simulated annealing [6], genetic algorithm [7], and hybrid genetic-simulated annealing [8]. The charge controller protects the battery bank against excessive charge or discharge conditions using voltage set points. For example, when the battery bank voltage reaches a high voltage set point, the charge controller disconnects the renewable generator, and when low voltage set point is reached, the charge controller disconnects the load. In systems with high power from a renewable source, high charge currents produce a premature disconnection of renewable generators; consequently, the state of charge of the battery bank results in low values [9]. In this paper, a study about optimization of hybrid power systems with photovoltaic panels, wind turbines, an inverter, and a lead acid battery bank using a genetic algorithm, which considers the influence of charge controller in the performance of the system, is carried out. The paper is organized as

D. Jin and S. Lin (Eds.): Advances in Mechanical and Electronic Engineering, LNEE 176, pp. 241–247.
springerlink.com

follows: Section 2 describes the mathematical model of a PV/wind/battery system, and the implementation of the genetic algorithm is explained in Section 3. A case of study is analyzed in Section 4, and conclusions are presented in Section 5.

2 PV/Wind/Battery System Model

The next sections describe mathematical models for each components of a typical hybrid system with several photovoltaic panels, wind turbines, a lead acid battery bank, an inverter, and a load coupled in AC.

2.1 Wind Turbine

Wind turbines are commonly modeled based on their power curve. Fig. 1 shows several wind turbines with small capacities.

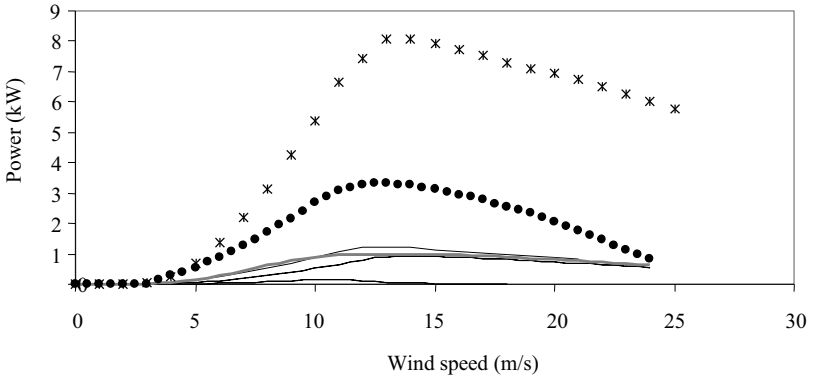

Fig. 1. Typical wind turbines power curves

2.2 Photovoltaic Panel

The power of the photovoltaic generator is calculated using equations (1) and (2) [10].

$$P_{PV} = P_{STC}\left\{\frac{G}{G_{STC}}\left[1+\alpha(T_c-25)\right]\right\} \tag{1}$$

$$T_c = T_a + \left(\frac{NOCT-20}{800}\right)G \tag{2}$$

where G is the incident solar radiation in W/m^2, G_{STC} is the solar radiation at standard test conditions, T_c is cell temperature ºC, T_a is ambient temperature in ºC, α is the temperature coefficient in %/ºC, and $NOCT$ is the nominal operation cell temperature in ºC.

2.3 Lead Acid Battery Bank

In this paper, a simplification of the general lead acid battery model proposed in [11] and [12] is used. The capacity of the battery is calculated using equations (3) and (4).

$$C_T = 1.67 C_{10}(1 + 0.005\Delta T_a) \tag{3}$$

$$C = \frac{C_T}{1 + 0.67\left(\frac{I}{I_{10}}\right)^{0.9}} \tag{4}$$

where C is the capacity at constant current I, C_T is the maximum capacity, C_{10}, and I_{10} are the capacity and discharge current after 10 hours, respectively.

The efficiency (η_b) during charge ($I>0$) and discharge ($I<0$) is calculated using Equation (5) [12].

$$\eta_b = \begin{cases} 1 - \exp\left[\left(\frac{20.73}{I/I_{10} + 0.55}\right)(SOC - 1)\right] & I > 0 \\ 1 & I < 0 \end{cases} \tag{5}$$

where SOC is the state of charge calculated according to Equation (6) [12].

$$SOC = \begin{cases} \frac{Q}{C}\eta_b & I > 0 \\ 1 - \frac{Q}{C}\eta_b & I < 0 \end{cases} \tag{6}$$

where $Q=\int I dt$ is the charge supplied or subtracted during the charge or discharge processes, respectively. The charge regulator disconnects the renewable generators when the battery bank voltage reaches a specific value. Equation (7) [11] allows us to estimate the SOC in this moment and then represents the effect of charge regulation in the acceptance of the battery bank charge.

$$V = (2 + 0.16\frac{Q}{C}) + \frac{I}{C_{10}}\left(\frac{6}{1 + I^{0.6}} + \frac{0.48}{(1 - Q/C_T)^{1.2}} + 0.036\right)(1 - 0.025\Delta T_a) \tag{7}$$

where V is battery voltage per cell during the charge process and $\Delta T_a = T_a - 25$.

2.4 Inverter

The efficiency (η_p) of the inverter could be described using Equation (8).

$$\eta_p = \frac{P_l}{\varepsilon P_{inv} + (1 + \zeta)P_l} \tag{8}$$

where P_l is the alternant current load, P_{inv} is the rated power of the inverter, ε and ζ are parameters determined using experimental data.

3 Mono-Objective Optimization

The problem of finding a combination of photovoltaic panels, wind turbines, and lead acid batteries that minimize the costs of the system, thus guaranteeing a determined level of reliability, is solved using the genetic algorithm described below.

3.1 Optimization Criteria

The variables considered are net present cost (*NPC*) and energy index of unreliability (*EIU*). *NPC* have been defined according to equations (9) and (10) [1].

$$NPC = \frac{(ACC + ARC + AMC)}{CRF(i, j)} \tag{9}$$

$$CRF(i, j) = \frac{i(1+i)^j}{(1+i)^j - 1} \tag{10}$$

where *ACC* is the annualized capital cost, *ARC* is the annualized replacement cost, *AMC* is the annualized maintenance cost, *CRF(i,j)* is the capital recovery factor, *i* is the real interest rate, and *j* is the project lifetime. *EIU* have been defined according to Equation (11).

$$EIU = \frac{ENS}{E_0} \tag{11}$$

where *ENS* is the energy not supplied and E_0 is the total energy demanded.

3.2 Genetic Algorithm Implementation

To find the combination of renewable energy sources and lead acid batteries that minimize the *NPC* during the *j* years, the genetic algorithm could be implemented in the following ways [13]:

1. Adjust the number of individuals in the population (Ψ), number of generations (χ), crossing rate (ϕ), mutation rate (ω), and *EIU* required (EIU_0).
2. An individual is represented as an integer vector $|\varphi|\beta|\lambda|\mu|\delta|\gamma|$ that contains a representation of solar generator manufacturer (φ), number of PV panels in parallel (β), battery manufacturer (λ), number of batteries in parallel (μ), wind generator manufacturer (δ), and number of wind turbines in parallel (γ). The initial population with Ψ individuals is randomly obtained.
3. For each individual in the population, the *NPC* and *EIU* are evaluated, and then an arbitrarily high value of *NPC* is assigned for those individuals with an *EIU* higher than EIU_0.
4. With $k=1,2,..,\Psi$, the aptitude (Φ_k) of individual *k* is obtained according to its rank in the population, rank 1 for the best individual and rank Ψ for the worst individual. Fitness function is shown in (12).

$$\Phi_k = \frac{(\Psi + 1 - k)}{\sum_{k=1}^{\Psi} (\Psi + 1 - k)} \tag{12}$$

5. Reproduction, crossing, and mutation are carried out to obtain the next generation. Reproduction is done using the roulette-wheel methods, crossing is done using the one crossing point method, and mutation is done by randomly changing the components of some individuals.
6. The steps described from 3 to 5 are repeated until χ generation is reached. The best solution obtained is that which has a lower *NPC* and an *EIU* at least lower than the required EIU_0.

4 Case Study

A PV/wind/battery system installed in the Netherlands in 2009 was analyzed. The installation site is the K13 meteorological station. Wind speed time series are provided by the Royal Netherlands Meteorological Institute [14]. The hourly solar radiation time series was generated synthetically according to Graham and Hollands' methodology [15] using information provided by NASA [16] for this location. The load is assumed to require 900W over 24 hours.

The genetic algorithm explained in Section 3 was implemented in MATLAB to find the combination of PV panels, wind turbines, and battery bank capacity that guarantee at least *EIU*=0.1. The wind turbines considered are showed in Figure 1. For the PV generator, capacities between 0.175kW and 4.375kW were considered, and for the lead acid battery bank, capacities between 200Ah and 3,000Ah and strings between 1 and 10 were considered. The rated capacity of the inverter is 900W with ε=0.0064 and ζ=0.0942. The economic analysis was carried out considering 35 years of project lifetime, a 5% interest rate, and a 3% inflation rate. For wind turbines, we considered 15 years of lifetime and capital cost between 1700€ and 30000€, and operation and maintenance cost between 50€ and 140€, respectively. The lifetime of the inverter is estimated at 20 years and its acquisition cost is estimated at 700€; the operation and maintenance cost is considered negligible. The lifetime of considered batteries is between 8 years and 20 years, and its capital cost is considered 250€/kWh. For a PV panel, its lifetime is considered 20 years, a capital cost of 4€/W is used, and operation and maintenance costs are considered negligible. Fig. 2 shows the evolution of net present cost in the optimization for 100 individuals in the population, 10 generations, crossing rate of 0.9, and a mutation rate of 0.01. After 10 generations, a hybrid system with 11 PV panels of 175W each, a wind turbine of 1kW, a battery bank of 1,000Ah, and a floating lifetime of 20 years is suggested. The *EIU* value obtained is 0.0675.

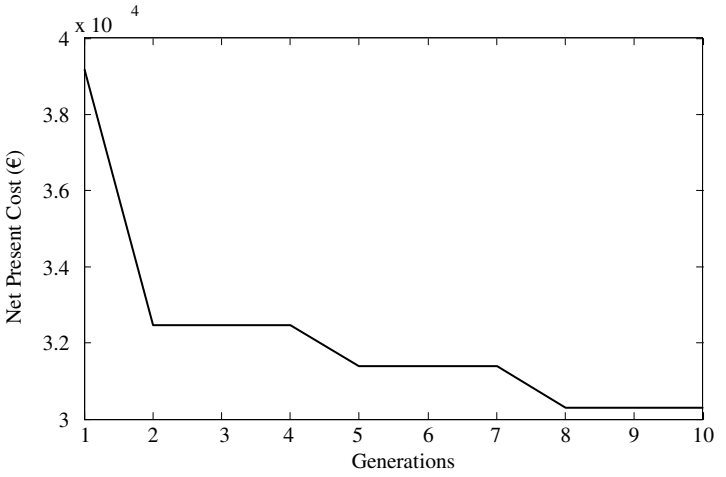

Fig. 2. Evolution of Net Present Cost in the optimization

5 Conclusions

In this paper, a genetic algorithm was used to find the optimal combinations of photovoltaic panels, wind turbine, and battery bank capacity in a typical hybrid power system to guarantee a determined level of reliability. The model presented in this paper is able to consider the coulombic efficiency, the charge controller operation, and many different types of photovoltaic panels, wind turbines, and battery bank capacities in the mono-objective optimization problem. These characteristics allow us to obtain fast and realistic results from the sizing process.

Acknowledgments. This work was supported by the "Ministerio de Ciencia e Innovación" of the Spanish government under Project ENE2009-14582-C02-01. Furthermore, the authors would like to thank the Royal Netherlands Meteorological Institute and NASA for providing the wind speed and solar radiation data for the case of study presented in this paper.

References

1. Lambert, T., Gilman, P., Lilienthal, P.: Micropower System Modeling with HOMER. In: Farret, F.A., Simões, M.G. (eds.) Integration of Alternative Sources of Energy, pp. 379–418. John Wiley & Sons, Inc. (2006)
2. Belfkira, R., Zhang, L., Barakat, G.: Optimal sizing study of hybrid wind/PV/diesel power generation unit. Solar Energy 85, 100–110 (2011)
3. Roy, A., Kedare, S.B., Bandyopadhyay, S.: Application of design space methodology for optimum sizing of wind-battery systems. Applied Energy 86, 2690–2703 (2009)

4. Boonbumroong, U., Pratinthong, N., Thepa, S., Jivacate, C., Pridasawas, W.: Particle swarm optimization for AC-coupling stand alone hybrid power systems. Solar Energy 85, 560–569 (2011)
5. Kanase-Patil, A.B., Saini, R.P., Sharma, M.P.: Integrated renewable energy systems for off grid rural electrification of remote area. Renewable Energy 35, 1342–1349 (2010)
6. Ekren, O., Ekren, B.Y.: Size optimization of a PV/wind hybrid energy conversion system with battery storage using simulated annealing. Applied Energy 87, 592–598 (2010)
7. Dufo-López, R., Bernal-Agustín, J.L., Yusta-Loyo, J.M., Domínguez-Navarro, J.A., Ramírez-Rosado, I.J., Lujano, J., Aso, I.: Multi-objective optimization minimizing cost and life cycle emissions of stand-alone PV-wind-diesel systems with batteries storage. Applied Energy 88, 4033–4041 (2011)
8. Carapellucci, R., Giordano, L.: Modeling and optimization of an energy generation island based on renewable technologies and hydrogen storage systems. International Journal of Hydrogen Energy 37, 2081–2093 (2012)
9. Corbus, D., Newcomb, C., Baring-Gould, E.I., Friedly, S.: Battery voltage stability effects on small wind turbine energy capture. Technical report, U.S. National Renewable Energy Laboratory (2002)
10. Lorenzo, E.: El Generador Fotovoltaico. In: Electricidad Solar: Ingeniería de los Sistemas Fotovoltaicos, pp. 93–120. PROGENSA (1994)
11. Copetti, J.B., Chenlo, F.: Lead/acid batteries for photovoltaic applications. Test results and modeling. Journal of Power Sources 47, 109–118 (1994)
12. Copetti, J.B., Lorenzo, E., Chenlo, F.: A general battery model for PV system simulation. Progress in Photovoltaic 1, 283–292 (1993)
13. Dufo-López, R., Bernal-Agustín, J.L.: Design and control strategies of PV-Diesel systems using genetic algorithms. Solar Energy 79, 33–46 (2005)
14. Royal Netherlands Meteorological Institute, `http://www.knmi.nl/`
15. Graham, V.A., Hollands, K.G.T.: A method to generate synthetic hourly solar radiation globally. Solar Energy 44, 333–341 (1990)
16. NASA, `http://eosweb.larc.nasa.gov/sse/RETScreen/`

Fuzzy Control for Variable-Speed Constant-Frequency Generators

Zhiming Yang and Xiaorong Wang

Chongqing University of Science and Technology, Chongqing, China
yzm-cq@126.com, wxrong88@163.com

Abstract. Due to high operation efficiency and control flexibility, the AC excited double-fed induction generator can not only realize Variable-speed constant-frequency (VSCF),a new typed operational mode for the doubly fed induction generator based wind power generation system is proposed based on the grid-connected power transmission. A control method aimed at increasing efficiency and maximizing energy capture using the stator flux-orientation control technology is introduced. the excitation controller was achieved using fuzzy-PID control. The results of simulation and experimental study testify the feasibility of the proposed strategy, meanwhile validate the optimal power efficiency tracking and optimal wind power capturing can be achieved.

Keywords: Variable-speed Constant-frequency generator. Maximal wind energy capture. Fuzzy-PI Control.excitation control.

1 Introduction

Variable-speed constant-frequency wind generating technology is getting increasing recognition for its characteristic of high efficiency and practicability over constant speed wind turbine generator system[1,2]. This kind of machine has been added to the main type of large scale wind turbine generator system.To maintain the optimum blade tip speed ratio in order to obtain the maximum wind energy under lower wind speed based on the variation of wind and to store or deliver some energy in order to enhance the flexibility of gear system and get stable output of power under higher wind speed ,the angular speed of wind wheel is mainly used to control the variable speed wind turbine generator system[3]. Because the energy gotten by the wind machine is proportional to the cube of the wind speed. When the input wind varies very large and fast, the gain of the wind machine will change accordingly. In the classical control, to realize the fast control, the accurate mathematical model of the wind generator system is needed.But this is very difficult because of the uncertainty of air kinetics and the complexity of power electronics. The model built is only adapted to the special system and in a particular time. The varying degree influences the energy transformation process of the wind generator system. This is caused by the change of the Reynolds number, the erosion by rain and deposit on the blade, the aging of the wind machine and the change of the air condition. Wind turbine is a high order,nonlinear, strong coupled and multiple variables time varied system. It is very difficult to obtain the proper result by using open loop control or general PID control.

D. Jin and S. Lin (Eds.): Advances in Mechanical and Electronic Engineering, LNEE 176, pp. 249–254.
springerlink.com

Using fuzzy control can overcome this difficulty[4]. Changing the reverse moment of force and rotation speed of generator to realize the variant of speed is done by changing the wound voltage of the stator. The simulation model and result and the PID control result are also given in this paper. According to the low and high wind speed we designed two fuzzy controllers respectively.

2 Type Style and Fonts

By using a synchronously rotating reference frame as shown in Fig. 1, the voltage, current, and flux linkages of the three phases of the stator can be transferred to directaxis, quadrature-axis, and zero-sequence components, respectively. Because the three phases are in equilibrium states, based on the q-d axis synchronously rotating reference frame, the voltage equation of the DFIG can be obtained as follows[5]:

3 Mathematic Model of DFIG

Dq coordinate system is two phase synchronous the haste rotating coordinate system T, D-axis transform the stator flux vector dq coordinate system. Consequently, Therefore, the d - axis and q-axis magnetic components are: ψd1 = ψ1, ψq1 =0[5].

DQ coordinates the equations of motion of the generator voltage, flux and torque is:

$$\begin{aligned} u_{d1} &= -R_1 i_{d1} - d\psi_{d1}/dt + \psi_{d1}\omega_1 \\ u_{q1} &= -R_1 i_{q1} - d\psi_{q1}/dt + \psi_{q1}\omega \end{aligned} \quad . \tag{1}$$

$$\begin{aligned} u_{d2} &= -R_2 i_{d2} - d\psi_{d2}/dt + \psi_{d2}\omega_1 \\ u_{q2} &= -R_2 i_{q2} - d\psi_{q2}/dt + \psi_{q2}\omega_1 \end{aligned} \quad . \tag{2}$$

$$\begin{aligned} \psi_{d1} &= L_1 i_{d1} - L_m i_{d2} \\ \psi_{q1} &= L_1 i_{q1} - L_m i_{q2} \end{aligned} \quad . \tag{3}$$

$$\begin{aligned} \psi_{d2} &= L_1 i_{d2} - L_m i_{d1} \\ \psi_{q2} &= L_1 i_{q2} - L_m i_{q1} \end{aligned} \quad . \tag{4}$$

$$\begin{aligned} T_L - T_e &= \frac{Jd\omega_r}{p_n dt} \\ \omega_r &= \frac{d\theta}{dt} \\ T_e &= p_n L_m (i_{d1} i_{q2} - i_{q1} i_{d2}) \end{aligned} \quad . \tag{5}$$

Where: R1 and R2 is the equivalent resistance of the induction motor stator and rotor windings; L1, L2 and Lm is the induction motor self and mutual inductances, the stator and rotor windings; id1, iq1, id2, iq2 are induction motor d, q-axis stator and

rotor current; ud1, uq1, ud2, uq2 are induction motor d, q-axis stator and rotor voltage; ψd1, ψq1, ψd2, ψq2 are induction motor d, q-axis stator and rotor flux; ω1 and ωs are induction motor speed and slip speed.

Ignore the resistance of the induction motor stator windings, generator stator flux and the stator terminal voltage vector angle difference of 90. Therefore, the generator stator flux oriented vector control system can be greatly simplified. For the induction motor d-axis stator flux and the neglect of the stator winding voltage, flux and voltage equations:

$$\begin{aligned} d\psi_1 &= 0 \\ u_1 &= \omega_1 \psi \end{aligned} \quad . \tag{6}$$

Simplifying equation (2,3):

$$\begin{aligned} d\psi_1 &= -L_m L_{m2} \\ i_{q2} &= 0 \end{aligned} \quad . \tag{7}$$

Equation (7) into equation (1) can be:

$$\begin{aligned} \psi_{d2} &= L_2 i_{d2} \\ \psi_{q2} &\neq 0 \end{aligned} \quad . \tag{8}$$

By the induction motor voltage and flux equations can be derived[6,7]

$$\begin{aligned} u_{d2} &= u'_{d2} + \Delta u_{d2} \\ u_{q2} &= u'_{q2} + \Delta u_{q2} \end{aligned} \quad . \tag{9}$$

$$\begin{aligned} \Delta u_{d2} &= -b\omega_s i_{q2} \\ \Delta u_{q2} &= a\omega_s \psi_1 + b\omega_s i_{d2} \end{aligned} \quad . \tag{20}$$

With a=-Lm/L1,b=L2-L2m/L1.

By equation (1)-(10), one can design induction motor VSCF Maximum Wind Energy Wind Power System tracking control strategy, shown in Figure2.

4 Fuzzy-PI Control Theory and Design

When large discrepancies (|e|≥e0), Fuzzy controller output is chosen as a control volume. a small deviation (|e|≤e0) PI controller output is chosen as a control volume[8]. The variable structure fuzzy-PI control of the DFIG is shown in Fig. 3.

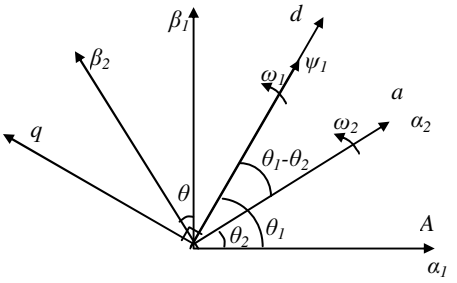

Fig. 1. Coordinate transformation relations

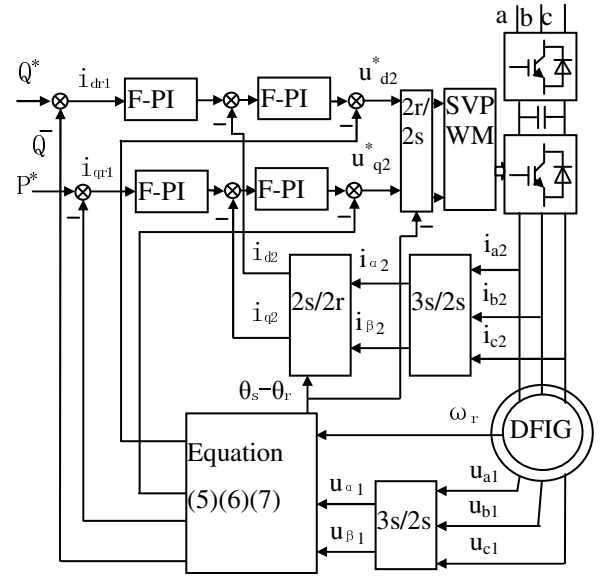

Fig. 2. DFIG system control block diagram

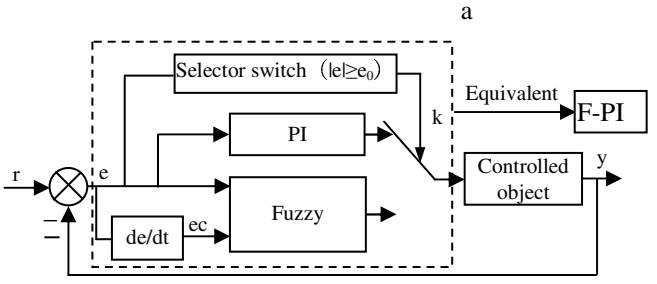

Fig. 3. The structure chart of variable structure fuzzy-PI control

5 Simulation Results

Simulation of the experimental parameters: three-phase four-pole double-fed induction generator; rated power is 2.2kW. rated voltage is 220V. The stator resistance and leakage inductance is 0.446Ω,2mH. rotor resistance and leakage inductance respectively is 0.8276Ω,2 mH. mutual inductance is 68.421mH: Synchronous speed is 1800r/min.

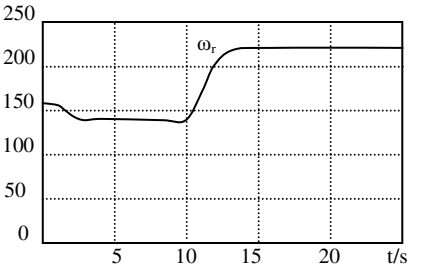

Fig. 4. Wind velocity ν and generator angle speed ωr

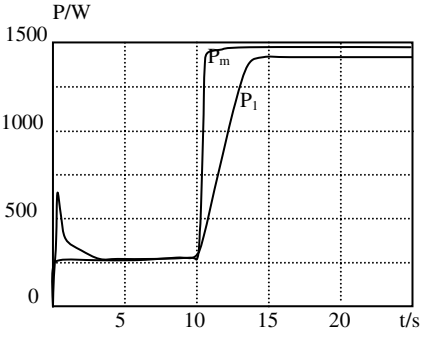

Fig. 5. Output active power P1 of the generator and output mechanical power Pm of the wind-turbine

Induction motor load before the students run, grid connection. The load operation is 0.5s. After grid connection of wind speed 4m / s. Project in a 10 to 6.8 m / s wind speed increases. Figure 4 is a process of change of the angular velocity of wind speed and induction motor.

Figure 5 is the power curve of the induction motor. The induction motor-output active power and mechanical power output changes Figure 5 shows the situation the best output of the wind sensor turbine power curve.

6 Conclusion

This paper analyzes the system model based on the characteristics of induction motors. We have the largest wind power, to capture the optimal power control strategy of vector control and fuzzy control adaptive factor. The stator active power control, to achieve maximum wind power tracking control. Compared with the traditional PID control strategy has the following advantages: the wind in the steady state and dynamic induction motor unit to achieve maximum wind tracking; based on vector control and fuzzy control, adaptive control system for maximum wind energy capture can be provide a good dynamic and static performance measurement of wind speed, robustness. The experimental results confirmed the effectiveness of the control strategy of the largest wind power can be achieved. The test results have good practical value.

7 Project Funding

This research is funded by Research Foundation of The Natural Foundation of Chongqing City, the project No. is cstc2011jjA80022.

References

1. Moroine, L., Azim, E.: Fuzzy logic control for active suspension of a non-linear full-vehicle model. In: Proceedings of IEEE Intelligent Vehicles Symposium, Xi'an, China, pp. 677–684 (June 2009)
2. Yazhou, L., Mullane, A., Lightbody, G., et al.: Modeling of the wind turbine with a doubly fed induction generator for grid integration studies. IEEE Trans. Energy Convers. 121(1), 257–264 (2006)
3. Liu, Q., He, Y., Zhang, J.: Investigation of Control for AC-exited VSCF Wind Power Generation System Connected to Grid. Proceedings of the CSEE 26(3), 109–115 (2006)
4. Ma, W., Yu, J., Wu, G., Chen, G.: Doubly-fed Wind Power Generation System Maximum Power Point Tracking Control Strategy. Transactions of China Electrotechnical Society 24(4), 202–208 (2008)
5. Hui, L., Be, H.: Control strategy of maximizing the wind enrgy for wind turbines with a dfig. Acta Energiae Solaris Sinica 29(7), 797–804 (2008)
6. Chi, F., Wang, X., Wang, X.: A new wind power grid connection method based on fractional frequency transmission system. Automation of Electric Power Systems 32(4), 59263 (2008) (in Chinese)
7. Cao, J.: Multivariable self-tuning feed forward PID controller and its application in coordinated control. Proceedings of the CSEE 9(1), 48–55 (1989) (in Chinese)
8. Lie, X.: Direct active and reactive power control of DFIG for wind energy generation. IEEE Trans. Energy Convers. 21(3), 750–758 (2006)

Adaptive Fuzzy Controller for Air Conditioning System

Lepeng Song, Huanhuan Chen, Huiming Wu, and Zhiming Yang

Chongqing University of Science and Technology, Chongqing, China
{slphq,chenhuahua}@163.com, 530699609@qq.com, yzm-cq@126.com

Abstract. To solve the control problem of temperature, the process of Air Conditioning System temperature parameter is not easy and timely. Adaptive fuzzy PID control method was proposed. PID control was to maximize the use of fast Air Conditioning System temperature. Adaptive Fuzzy PID was used to improve the accuracy of the temperature Air Conditioning System. The system static and dynamic performance was ideal. The MATLAB simulation of the Adaptive fuzzy PID controller and a PID controller were carried out on the Air Conditioning System temperature. Results showed that: Response time of PID control was 1.17 s., maximum overshoot was about 19.4%,. response time of Adaptive fuzzy PID was 0.46 s., and maximum overshoot didn't exceed 3.29%.The stability accuracy and rapidity of the system were able to satisfy the Air Conditioning System technical requirements.

Keywords: Adaptive Fuzzy PID Control. Air Conditioning System. Simulink.

1 Introduction

With the widespread use of large air-conditioning, energy supply and demand is becoming more and more serious conflicts. Therefore, a higher requirement for its energy efficiency has been put forward. Because interference factors of the change of room temperature are many parameters vary considerably in process of the air temperature control, it's hard to build an accurate mathematical model. The control of central air conditioning system has many characteristics such as time-varying, nonlinear and strong delay. The traditional control easily causes the central air conditioning system to oscillate, so its control effect may fluctuate in a wide range. It not only increases the system's power consumption, but also easily prevents the system from achieving the stability of a given value in a long time and achieving ideal control effect. Fuzzy control and classic PID control are combined in different forms to constitute the composite Fuzzy-PID controller, which is able to eliminate limit cycle oscillations in theory[1]. However, it is difficult to choose and coordinate parameters between fuzzy control and PID control when they switch. This paper establishes a In this paper, simulink to create a simulation model of the room temperature change controlled by air conditioning according to the characteristics of temperature change in a conditioned room. To mention the traditional use of fuzzy PID control on behalf of, the results can be seen from the simulation, air-conditioning system control effect has been significantly improved.

D. Jin and S. Lin (Eds.): Advances in Mechanical and Electronic Engineering, LNEE 176, pp. 255–260.
springerlink.com

2 Air Conditioning System Model

For convenient analysis, the conditioned room cans be regarded as a single-capacity object. The outside heat through the palisade structure into indoor needs long time delay, so here the heat is considered through the palisade structure from outside to inside. Thus the mathematical expression can be concluded as follows[2]

$$C_1 \frac{dt_n}{dt} = (L\rho c t_s + q_n) - (L\rho c t_n + \frac{t_n - t_0}{r}) \tag{1}$$

Where q_n is room heat dissipating capacity, kJ/h, C_1 is capacity coefficient, kJ/℃, r is heat resistance of constant temperature room's palisade structure, h·℃/kJ, t_0 is outdoor air temperature, ℃, L is air supply, m^3/h, ρ is the density of air, kg/m^3, c is air constant pressure specific heat, kJ/kg, t_n is indoor air temperature, ℃, t_s is supply air temperature, ℃. The mathematical expression of air conditioning room can be concluded as follows(2)-(6):

$$T_1 \frac{d\Delta t_n}{dt} + \Delta t_n = K' \Delta L + K'' \Delta q_f \ . \tag{2}$$

$$T_1 = \frac{C_1}{L_0 \rho c + \frac{1}{r}} \ . \tag{3}$$

$$K' = \frac{\rho c (t_s - t_{n0})}{L_0 \rho c + \frac{1}{r}} \ . \tag{4}$$

$$K'' = \frac{1}{L_0 \rho c + \frac{1}{r}} \ . \tag{5}$$

$$\Delta q_f = \Delta q_n + \frac{\Delta t_0}{r} \ . \tag{6}$$

Δq_f is indoor heat change which is converted from the change of inside and outside interference, kJ/h, ΔL is air supply change, m3/h,. Δt is the output parameters of constant temperature room, ℃. The foot mark "0" in the formula expresses steady state.

ΔL and Δq_f are the inputs of temperature room, ΔL is on regulation effect and Δq_f is on interference effect. When the effect of temperature room pure time-delay is considered, regulating channels of conditioned room mode are expressed by transfer function as follows:

$$G(s)=\frac{Ke^{-\tau_1 s}}{T_1 s+1} \quad . \tag{7}$$

Where K is amplification coefficient, T_1 is inertia time constant, s, τ_1 is pure lag time, s.

3 Air Conditioning Fuzzy-PID Control System

The structure of Fuzzy-PID system is as shown in Fig.1, In this control system, Fuzzy controller are realized by PLC. So can lower costs, improve systematic dependability and stability, obtain the good control result [3-6].

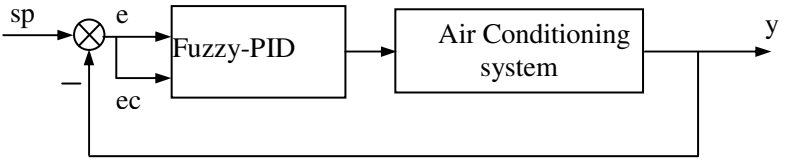

Fig. 1. Air Conditioning system of Fuzzy-PID

4 Fuzzy Controllers And Algorithms Designed

Fuzzy self tuning PID controllers based of PID algorithm, according the error of the present system E and rate of change of error EC, utilize fuzzy control rule to fuzzy reasoning, and inquire the fuzzy matrix form carries on parameter adjustment.

When E is bigger, in order to make the system have fast following performance, should fetch bigger Kp and smaller Kd, for avoid system respond greater going beyond and suiting well, should limit function of integral at the same time, usually fetch Ki =0;

When E and EC being medium-sized, in order to make the system have smaller overshoot, should fetch smaller Kp ,person who fetch of Kd of great impact to system, fetch Ki adapting to;

When E is smaller, in order to make the system have good robustness and stability, should fetch bigger Kp and Ki, Kd fetching value should be appropriate, in order to avoid oscillation near the equalization point.

This controller set up the fuzzy regular form suitable on the foundation of the experience knowledge accumulated in long-term practice, to get about ΔKp、△Ki、△Kd fuzzy rule table, see Table 1 - Table 3:

Table 1. K_p Fuzzy Rules

e	ec						
	-3	-2	-1	0	1	2	3
-3	3	3	2	2	1	0	0
-2	3	3	2	1	1	0	-1
-1	2	2	2	1	0	-1	-1
0	2	2	1	0	-1	-2	-2
1	1	1	0	-1	-1	-2	-2
2	1	0	-1	-2	-2	-2	-3
3			-2	-2	-2	-3	-3

Table 2. K_i Fuzzy Rules Table

e	ec						
	-3	-2	-1	0	1	2	3
-3	-3	-3	-2	-2	-1	0	0
-2	-3	-3	-2	-1	-1	0	0
-1	-3	-2	-1	-1	0	1	1
0	-2	-2	-1	0	1	2	2
1	-2	-1	0	1	1	2	3
2	0	0	1	1	2	3	3
3	0	0	1	2	2	3	3

Table 3. K_D Fuzzy Rules

e	ec						
	-3	-2	-1	0	1	2	3
-3	1	-1	-3	-3	-3	-2	01
-2	-1	-1	-3	-2	-2	-1	0
-1	0	-1	-2	-2	-1	-1	0
0	0	-1	-1	-1	-1	-1	0
1	0	0	0	0	0	0	0
2	3	-1	1	1	1	1	3
3	3	2	2	2	1	1	3

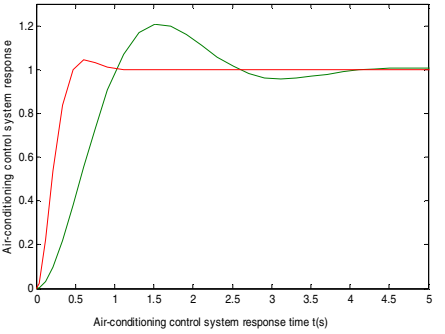

Fig. 2. Air-conditioning control system response

The fuzzy controller adopts the center of gravity (COG) to defuzzification. PID controller according to getting real-time 3 parameters（ΔK_P、ΔK_i、ΔK_d）, Output the exact value signal to the motor, and then armature voltage contol the actual air temperature.

5 Simulation and Analysis

According to the system parameter setting, simulation model is created in Matlab\Simulink. The traditional PID and the fuzzy adaptive PID of simulation curve is compared. The steady and dynamic characteristics are studied. The simulation result is shown in Figure 2.

6 Conclusion

It can be seen from the simulation figure that the self-tuning control of adaptive fuzzy PID controller has smaller overshoot and shorter adjustment time, and its dynamic

response and steady-state characteristics are superior to those of conventional PID control. When the response of adaptive fuzzy PID controller is near to the balance and has tended to deviate, the speed of curve's change becomes slower because of the Integral process. After several times, the response of system ecomes stable at the balance at last. In the variable integral coefficients adaptive fuzzy PID controller, integral parameter's self-setting control can be adjusted automatically according to the change of process. Thus, this kind of controller has better adaptive ability, self-adapting ability and good robustness.

The fuzzy control combine PLC control system, Not only have PLC's feature, such as reliable, flexible, adaptability, has but also raised the intelligent of the control system greatly.

PLC system based fuzzy control is suitable for many situation, the easy module of software, standardization, compared with the situation that PLC PID attached module, have flexible programming, less limiting conditions, such characteristics as fuzzy variable and fuzzy rules are not limited by hardware, have reduce the systematic development cost, has expanded the range of application [7-9].

7 Project Funding

This research is funded by Research Foundation of The Natural Foundation of Chongqing City, the project No. is cstc2011jjA80022.

This research is funded by Research Foundation of Chongqing University of Science & Technology, the project No. is CK2011Z16.

This research is funded by outstanding innovation and personnel training scheme of Chongqing University of Science & Technology, the project No. is 4.

References

1. Wang, Y.: Fuzzy Inferences Methodologies for Cognitive Informatics and Computational Intelligence. In: Proc. 8th IEEE International Conference on Cognitive Informatics (ICCI 2009), pp. 241–248. IEEE CS Press, Hong Kong (2009b)
2. Xing, L., Yang, S.: Fuzzy-PID Controller with Variable Integral Parameter for Temperature Control in Variable Air Volume Air Conditioning Systems. In: ICECE 2010, pp. 1050–1053 (2010)
3. Moroine, L., Azim, E.: Fuzzy logic control for active suspension of a non-linear full-vehicle model. In: Proceedings of IEEE IntelligentvVehicles Symposium, Xi'an, China, pp. 677–684 (June 2009)
4. Wu, X., Zhou, J.: A novel possibilistic fuzzy c-means clustering. ACTA Electronica Sinica 10, 1996–2000 (2008)
5. Yu, H., Luo, H.: A Novel Possibilistic Fuzzy Leader Clustering Algorithm. In: Sakai, H., Chakraborty, M.K., Hassanien, A.E., Ślęzak, D., Zhu, W. (eds.) RSFDGrC 2009. LNCS(LNAI), vol. 5908, pp. 423–430. Springer, Heidelberg (2009)
6. Grantner, J.L., Fodor, G.A., Tamayo, P.A., Gottipati, R.: Design of a reconfigurable state transition algorithm for fuzzy automata. Int. J. Gen. Syst. 37(1), 103–126 (2008)

7. Nanayakkara, T., Sahin, F., Jamshidi, M.: Intelligent Control Systems with An Introduction to System of Systems Engineering. CRC Press, Boca Raton (2010)
8. Sun, F., Li, L., Li, H.X., Liu, H.: Neuro-fuzzy dynamic-inversionbasedadaptive control for robotic manipulatorsłdiscrete time case. IEEE Transactions on Industrial Electronics 54(3), 1342–1351 (2007)
9. Liang, C., Wang, X.: Variable-Rate Fertilization Control System Based on Fuzzy PID Control Strategy. In: ICECE 2010, pp. 2511–2514 (2010)

Fault Diagnosis of Diesel Engine Based on EMD and TFD

Jinming Lu, Zhenzhen Liu, and Kangle Wang

School of Energy and power Engineering, Jiangsu University of Science and Technology, Zhenjiang Jiangsu 212003, China
Ljm2801jm@163.com

Abstract. A new diagnosis method for diesel engine faults is presented, which is based on EMD and time-frequency distribution image processing. The vibration signals of cylinder head surface is obtained under the different conditions, such as the normal condition、the valve clearance faults condition and stop misfire condition. Each raw signal is decomposed into a finite number of intrinsic mode function components by the EMD method. The analytic signal is transformed from reconstructed signal of IMF1 and IMF2 component. The image processing of the proper time-frequency distribution can reveal running conditions of diesel.

Keywords: Diesel engine, Fault diagnosis, Empirical mode decomposition (EMD), Hibert-Huang transform(HHT), Time-frequency distribution(TFD), Image processing.

1 Introduction

The cylinder head vibration signal is time variant and non-stationary multidimensional signal, which contains the response of multiple exciting forces in different time. All of these factors make the application of vibration-based techniques to diesel engines very difficult. Yong Xia etc.[1,2] proposed a new diesel engine fault diagnosis method based on image processing. The texture features of gray images and features of grey histogram were extracted, and the valve train faults can be classified effectively with BP neural network. Chengdong Wang etc.[3] proposed a method of using ambiguity function images in fault diagnosis for diesel valve train. The process of fault diagnosis for valve train was transformed to the classification of ambiguity function images. By using six indexes, such as Euclidean distance, similarity, J-divergence and so on, the testing images were classified into eight types, which correspond to eight states of valve train.

The image processing method for diesel engine fault diagnosis still exits some problems. First, the position of first sampling data responding to working cycle must be the same. Usually the top dead centre (TDC) is taken as the sampling starting time. Second, the time length of sample data must be the same, such as one cycle period. Furthermore, the accuracy of analysis result is affected by the signal noise largely. The grey histogram of the signal time-frequency distribution equals compressing the diagram. The most space information is lost and diesel engine fault diagnosis is quite difficult.

A new diagnosis method for diesel engine faults which based on EMD and TFD image processing is presented in this paper.

D. Jin and S. Lin (Eds.): Advances in Mechanical and Electronic Engineering, LNEE 176, pp. 261–266.
springerlink.com

2 Method

2.1 EMD Decomposition

According to Norden E. Huang and Z.H. Wu[4,5,6], any signal consists of different simple intrinsic mode of oscillation, Each mode can be linear or non-linear and have the same number of extrema and zero-crossings. There is only one extremum between successive zero-crossings. Each mode should be independent of the others. In this way, each signal $s(t)$ could be decomposed into a number of IMFs (c_i). Each IMF represents a simple oscillatory mode compared with the simple harmonic function. So that

$$s(t) = \sum_{i=1}^{n} c_i + r \tag{1}$$

Here r is the residual signal, which is a monotonic function from which no more IMFs can be extracted.

2.2 Time-Frequency Image Feature Extraction

Suppose the time-frequency image $tfr(t, f)$ have m points in time axis and n points in frequency axis. $G(i, j)$ represents the amplitude of the time-frequency image in point i in time axis and point j in frequency axis. $\overline{G}$ is the mean value. σ is the variance and σ_{AB} is the covariance.

The evaluate index of structure comparability is

$$Q_{AB} = \frac{\sigma_{AB}^2}{\sigma_A \sigma_B} \frac{2\overline{G}_A \cdot \overline{G}_B}{(\overline{G}_A^2 + \overline{G}_B^2)} \frac{2\sigma_A \sigma_B}{\sigma_A^2 + \sigma_B^2} \tag{2}$$

Here, the first item is the correlation coefficient, the second item is the gray distortion, and the third item is the contrast distortion. The index combine the subjectivity and impersonality and surpass to traditional evaluate index, which reflects the difference in the structure and vision character.

The absolute distance between image A and image B is

$$D_{AB} = \frac{1}{m \cdot n} \sum_{i=1}^{m} \sum_{j=1}^{n} \left| G_A(i, j) - G_B(i, j) \right| \tag{3}$$

The Euclidean distance between image A and image B is

$$E_{AB} = \sqrt{\frac{1}{m \cdot n} \sum_{i=1}^{m} \sum_{j=1}^{n} \left| G_A(i, j) - G_B(i, j) \right|^2} \tag{4}$$

First order time moment is

$$f_m(t) = \frac{\int_{-\infty}^{\infty} f \cdot tfr(t, f) df}{\int_{-\infty}^{\infty} tfr(t, f) df} \tag{5}$$

Second order time moment is

$$B^2(t) = \frac{\int_{-\infty}^{\infty} f^2 \cdot tfr(t,f)df}{\int_{-\infty}^{\infty} tfr(t,f)df} - f_m^2(t) \tag{6}$$

3 Cylinder Vibration Signal Analysis

To study the characteristics of the vibrations generated from the diesel engine, a 3110 diesel engine was chosen for our investigation. The diesel is a water-cooled four-stroke engine with three cylinders using direct fuel injection. Abnormal clearance of a valve train may be caused by incorrect positioning of the valve's rocket lever adjusting screw. To create abnormal clearance in the intake valve train of cylinder 1, the valve rocket lever screw was turned to adjust the gross valve tappet clearance from normal value 0.3mm (A) to tight clearance value 0.1mm (D) and excessive clearance value 0.9mm (C). The vibration signals were measured in normal condition, misfire condition (B) and abnormal clearance conditions at a rotating speed of 700r/min. The top dead centre (TDC) before ignition is taken as the sampling starting time. The signal which length is one working cycle is decomposed by EMD method. The reconstructed signal is made by IMF1 and IMF2, and the low frequency component is removed.

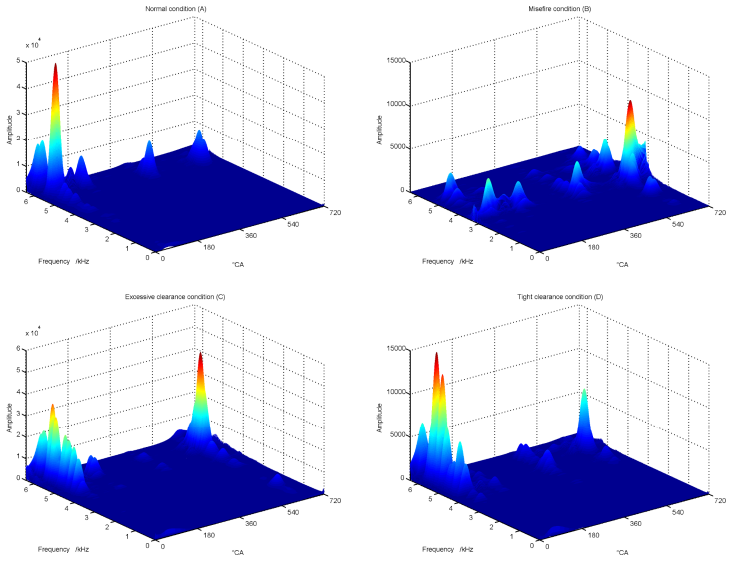

Fig. 1. TFD of reconstructive signals

The pseudo Wigner-Ville time-frequency distribution (SPWD), the Absolute distance ratio of SPWD is showed as Fig.1. The SPWD is similar in same work condition and distinctness between different work conditions. The signal can be classified according to the first main component with the largest amplitude.

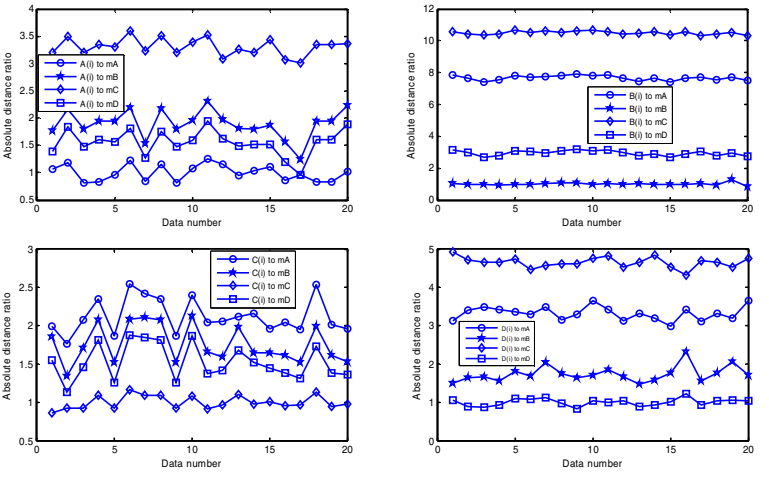

Fig. 2. Absolute distance ratio of SPWD

Absolute distance ratio between each SPWD and the mean SPWD is showed in Fig.2. The absolute distance ratio close to 1 means belonging to this work condition by any possibility. Otherwise means not belonging to this work condition by any possibility. The condition B,C and D is distinguished from other conditions well, and some data in condition A have some difficult to be distinguished. The result is similar by using the Euclidean distance.

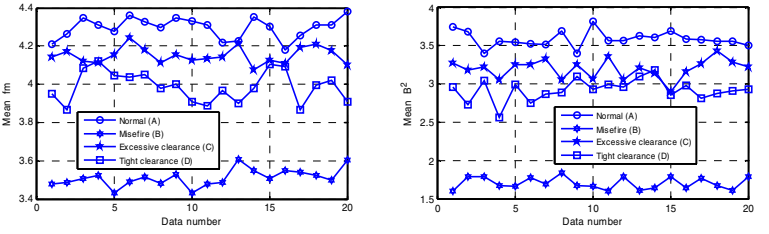

Fig. 3. Time moment of SPWD

Fig.3 showed the first order time moment and the second order time moment, the value of misfire condition is smallest and different obviously with other conditions. Normal condition and abnormal clearance conditions can also be distinguished except for some data.

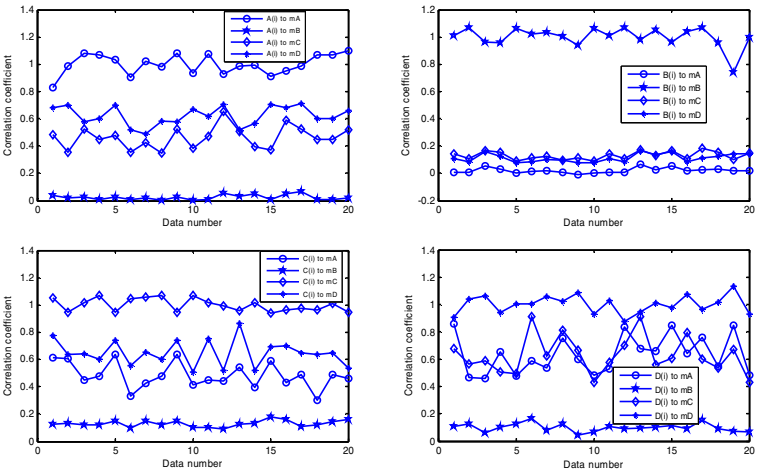

Fig. 4. Structure resemblance of SPWD

The similarity of each data is compared in Fig.4, the SPWD of data is similar to the mean SPWD in the same condition, and it's not similar in different conditions. The threshold value may be set 0.55, the data belong to this condition when the resemblance value above this threshold. Otherwise it is not belong to this condition.

4 Conclusion

A new diagnosis method for diesel engine faults is presented, which is based on EMD and time-frequency distribution image processing. Absolute distance ratio of SPWD and Euclidean distance can distinguish the misfire and abnormal clearance of valve train conditions well. Normal condition and abnormal clearance conditions can also be distinguished except for some data.

The SPWD image may be transferred some phase angle for the position of first sampling data responding to working cycle not the same and this may cause confusion. But this problem can be avoided by using time moment of image which only require the same time length of data.

References

1. Xia, Y., Zhang, Z., Shang, B., Guo, M., Zhang, Y.: Fault Diagnosis for ICE Based on Image Processing and Neural Networks. Transactions of CSICE 19(4), 356–360 (2001)
2. Xia, Y., Shang, B., Zhang, Z., Xue, M., Guo, M.: Research on Fault Diagnosis for Internal Combustion Engines Using Wavelet Packet and Image Processing. Transactions of CSICE 19(1), 62–67 (2001)

3. Wang, C., Zhang, Y., Xia, Y.: Study on the Use of Ambiguity Function Images in Fault Diagnosis for Diesel Valve Train. Transactions of CSICE 22(2), 162–168 (2004)
4. Huang, N.E., Shen, Z., Long, S.R.: The empirical mode decomposition and the Hilbert spectrum for nonlinear and non-stationary time series analysis. Proc. R. Soc. Lond. A. 454, 903–995 (1998)
5. Wu, Z.H., Huang, N.E.: Ensemble empirical mode decomposition: A noise-assisted data analysis method. Advances in Adaptive Data Analysis 1(1), 1–41 (2009)
6. Wu, Z.H.: The multi-dimensional ensemble empirical mode decomposition method. Advance in Adaptive Data Analysis 1(3), 339–372 (2009)

Research on the Proposal to Improve the Stability of Crane Rotary Mechanism from Mechanics Stability

Qi Liu

Wuhan University of Technology, Wuhan, 430063, China
936430013@qq.com

Abstract. As a solution to the inadaptation of crane rotating mechanism to mechanical load characteristics, Closed-loop control system is proposed. Through an experiment, compare the closed loop control system and the original system in the aspects of Control performance and mechanics stability. The result states that the closed loop control system has its superiority in adapting to mechanical load characteristics, and it has a prosperous application in port machinery.

Keywords: crane, rotating mechanism, closed-loop control system, mechanics stability.

1 Introduction

Portal crane as the most typical port carrying machine in docks and harbors is widely used all over the world [1].Portal crane is characterized by complicated structures, and portal crane which has big mechanisms and wide lifting weight, (usually 40T-45M and 40T-43M model) is usually used in bulk terminal. There are many problems such as gears and motor shaft in portal crane in the long-term working process of converters.

2 Analysis of the Issue

According to the practical experience in using, maintenance and repairing, load parameters of portal crane, influenced by many factors such as air velocity, inertia, installation and human factors, it is very hard for detail calculate of the actual load characteristic parameters. Especially for the 40T model crane, when it's under maximum load conditions, load parameter of rotating mechanism has a random and drastic variation. Machine mechanism is easily to get broken and structure cracking as the big inertia and big shock during starting and stopping of rotating mechanism[2]. So configuration inverter capacity and frequency converter is the key to adapt to the mechanical load characteristics. A new way to control with closed loop control system was proposed according to the comparison with open loop control system, the effectiveness of which was verified by experimental results.

D. Jin and S. Lin (Eds.): Advances in Mechanical and Electronic Engineering, LNEE 176, pp. 267–270.
springerlink.com

Through investigating the working conditions, collecting the designing information and data as well as analyzing, the author gives some advices for reference. The following factors explain problems in practical application of closed loop control system in the rotating mechanism:

(1) High requirements of encoder installation: Given the fact that encoder is installed by hand in our country; the installation of encoder has a high precision requirement ①the rotation axis of encoder can't bear high load when installing encoder ②the angle deviation in axial direction should be less than 3 degree[3] ③the installation of encoder support has a strict concentricity requirement so that encoder has a smooth rotary action ④The vertical setting up of rotary motor makes it hard to replace encoder's coupling. Problems above make the application of closed loop control system impossible for factories.

(2) Complicated situation for wiring technology: The receiving signal process of encoder is easily interfered so that the normal operation of system will be disturbed as well as other electrical equipment[4]. There are national standard for encoder's wiring technology. Encoder's cable should be laid separately with other cable and is in a pipe alone. But those problems are ignored in frequency conversion portal cranes' early promotion.

3 Comparison among the Closed Loop Control System and the Original System

Despite the problems above, the designing of the control system should be based on the frequency characteristics and practical load changes. The table following is a comparison between the closed loop control system and the original system.

Table 1. Comparison between two control system

No.	Character	Without PG control (open loop control)	With PG control (closed loop control)
No.1	Control system	Without PG electric control	With PG electric control
No.2	Function	Control motor without PG, it can be adopted if the precision requires generally	Control motor with PG, can meet High precision demand
No.3	Range of speed control	1:100	1:1000
No.4	Velocity control accuracy	± 0.2%	±0.02%
No.5	Starting torque	150%1HZ	150%1min-1
No.6	Zero-serve controlled system	No	yes

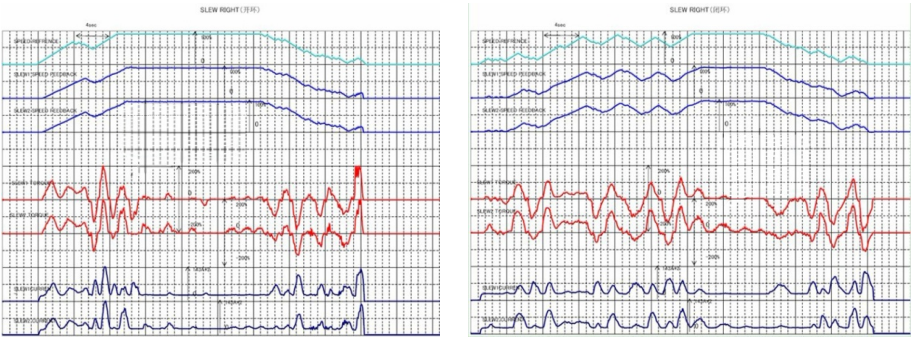

(a) open loop control (b)closed loop control

Fig. 1. Comparison of current control

According to figure 1, the result that current in the original system exceeds 200% many times during acceleration and deceleration period will increase load on inverters. The closed loop control system has smooth current in the test which will have a positive impact on motor and mechanism.

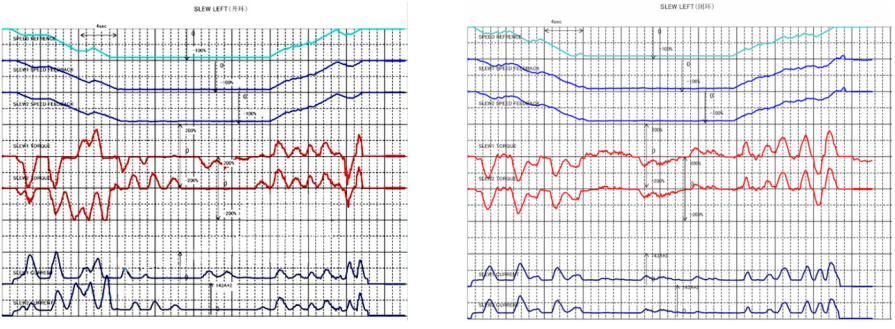

(a)open loop control (b) closed loop control

Fig. 2. Comparison of current control

According to figure 2, current in the original system exceeds 200% many times while the closed loop control system has smooth current in the test.

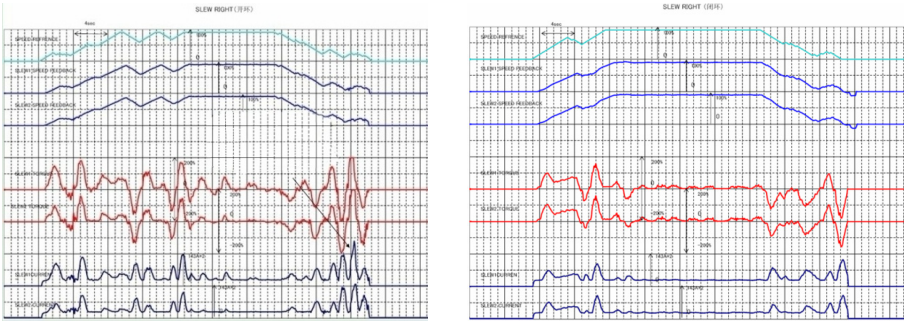

(a) open loop control (b) closed loop control

Fig. 3. Comparison of current control

According to figure 3, the original system can't have a properly reflection to driver's action. And the violent changing current will break actuators and mechanism. The closed loop control system will make a smooth reflection to control precisely.

4 Conclusion

The data above states that the closed loop control system has its superiority in adapting to mechanical load characteristics. The practical application of closed loop control system will improve the effectiveness of rotating mechanism, decrease responding time and protect micro-actuator from violent changing current. Given the face that rotating mechanism is easily broken, the practical application of closed loop control in rotating mechanism is very necessary.

References

1. Hu, J., Wang, W.: Method and technology of designing 40t single arm portal crane. Port Operation (SP), 6–7 (1999)
2. Hou, W.: Transformation of rotating mechanism of portal crane 21(3), 49–50 (2001)
3. Li, J., Wu, Q.: New installation bearing of high-speed encoder. Port Operation (2), 21 (2011)
4. Zhang, Y.: Disturbance in frequency converter application and its control measures. Electric Power Construction 27(1), 63–65 (2006)

The Research of Ultrasound Parameters Affecting the Stability of Bio-diesel Fuel for Mechanical Engineering

Xiao-li Wei[1,2], Shu-yang Wang[1], and Zhuo Wang[1]

[1] Mechanical and Electrical Engineering Institute, Northeast Forestry University, Hare bin, 150001, China
[2] Engineering Institute, Northeast Agriculture University, Hare bin, 150030, China

Abstract. In order to improve the stability of bio-diesel fuel, the system which is combination of ultrasonic and bio-diesel fuel use ultrasonic as the additional energy, and investigate the Ultrasonic frequency, waveforms, power and ultrasonic time factors and the effects of bio-diesel fuel stability. Optimal operating parameters of ultrasonic generator were studied by orthogonal experiment. The ultrasonic generator could adjust frequency, power, waveform and treating time flexibly in order to compare the stability of bio-diesel fuel under different conditions. According to the results, treating time had the most significant in fluency on the stability, power and frequencies were less important than it and waveform was the least.

Keywords: emulsification, Stability, operating parameters, orthogonal experiment.

1 Introduction

Biomass diesel phacoemulsification is actually biomass diesel emulsion preparation, which is the two immiscible liquids, namely biomass oil droplets dispersed in the form to another and immiscible liquids diesel[1], therefore , in the preparation of emulsion in the process to require huge phase interface, in order to make the system interface can greatly increase, thus needs a certain energy to complete the preparation, and ultrasound in the liquid can produce the spread of an important phenomenon, namely to bubbles or cavity in liquids constantly generate, grow up and implosion, In the medium to micro and very short time to form the hot spot, its temperature above 500K, the pressure of several hundred to several thousand atmospheres, for chemical reaction with enormous energy, accelerate the reaction speed[2]. Phacoemulsification compared with other emulsification, droplets can spread thin and narrow distribution, high efficiency, good dispersion, increasing the stability of emulsion. This paper aimed at the ultrasonic on biomass diesel oil emulsifying effect and stability are studied experimentally, for ultrasonic emulsified biomass diesel technology laid the foundation for further popularization and application.

D. Jin and S. Lin (Eds.): Advances in Mechanical and Electronic Engineering, LNEE 176, pp. 271–275.
springerlink.com

2 Ultrasound

Ultrasound is actually a kind of wave, therefore can be used as a load information and the detection of carrier; ultrasound is a form of energy, can accelerate the chemical reaction or trigger the new reaction channel.

Ultrasonic effect can be attributed to the following three basic action form [3]: Mechanical effect; Thermal effect; Cavitation effect.

2.1 Main Factors Influencing Ultrasonic Cavitation

In the ultrasonic cavitation effect of "high" and "high voltage" and mechanical action, will induce cavitation bubbles within the high temperature decomposition, chemical bond breaking, free radical generation and related reaction, resulting in the chemical effect, promote the chemical reaction . And ultrasonic cavitation effect and the nature of the liquid, the acoustic field and environmental factors related. The description of these factors in many related physical parameters will affect the cavitation effect, such as nucleation, cavitation bubble of vibration, growth and collapse. The main influence factors include: ultrasonic frequency, ultrasonic power, ultrasonic excitation waveform and the action time.

(1) Ultrasonic Frequency: Early people thought that, since the sonochemical reaction is the main driving force of acoustic cavitation, so as long as the irradiation with strength greater than the cavitation threshold of the acoustic, acoustic chemical reaction occurs, and the acoustic frequency appears unrelated. However, current research suggests, ultrasonic cavitation threshold and ultrasonic frequency is closely related to, the higher the frequency, the higher the cavitation threshold, in other words, the higher the frequency, in a liquid to produce cavitation needed for sound intensity and sound power is greater; low frequency, cavitation is easy to produce, while at low frequencies, liquid subjected to compression and rarefaction has a longer time interval. Instand high frequency ultrasonic contrast ultrasound swelling phase corresponding to shorter time [3]; Studies have found that [4], low frequency ultrasonic activation of the cavitation bubble radius is significantly larger than the high frequency ultrasonic cavitation bubble, So the cavitation bubble inclusions and cavitation bubble collapse release energy is bigger, So hydroxyl radicals in unit of time should be the yield of the larger, make every time cavitation produce hydroxyl radicals and the concentration of hydrogen radical is larger. So, in the vast majority of the action of ultrasonic chemical reactions are used in low frequency ultrasonic wave, and the frequency range is from 20 KHz to 50 KHz.

(2) Ultrasonic Waveform: Different with different waveforms of exciting current harmonic types, the harmonic frequency domain and energy in the frequency domain of the distribution and attenuation characteristics are also different. Therefore during phacoemulsification, different current waveforms are produced by different cavitation effect [5]. Usually in order to obtain stable cavitation intensity, need enough pulse width, but also in a certain pulse width, cavitation intensity will show a maximum value phenomenon. Currently for the phacoemulsification emulsified factors of the best studies have many, but most research is confined to the ultrasonic frequency, power, time and temperature factors, very few people take into account the effects of ultrasonic

excitation waveform and on the stability of emulsion, However different excitation waveform currents caused by the oscillation amplitude attenuation level is different, the situation will affect the ultrasonic cavitation effect. In this paper, on the basis of the excitation waveform as a reference factor, and setting a reference waveform of sine wave, cosine wave triangle wave and square wave pulse. And make the best of biomass diesel phacoemulsification process parameters studied.

(3) Ultrasonic Power: Typically, greater than the liquid above the cavitation threshold, improving the sound intensity can make the chemical reaction under ultrasonic cavitation yield increase, enhanced cavitation. Cavitation threshold is causes the liquid to produce cavitation required minimum sound intensity. But the sound intensity has certain limits, exceed this limit, the cavitation bubble in the ultrasonic expansion phase may be increased too much, that it in acoustic compression phase collapse to occur, so that the action of ultrasonic chemical yield tends to saturation even decline.

(4) Action Time of Ultrasonic Wave: Some people have with high frequency (820 KHz) and low frequency (28KHZ) ultrasonic action, adopt different ultrasonic chemical detection method to study the action of ultrasonic chemical reaction rate and the relationship between the action times of ultrasonic wave. Found in a certain time range (10min), under the effect of ultrasonic chemical reaction yield and action time of ultrasonic wave is proportional to the increase of [7].

3 Experimental Materials and Experimental Apparatus

3.1 Raw Materials

The experiments of biological fuel oil production by Northeast Forestry University, 0 # diesel, sorbitan monooleate (Span80) and polyoxyethylene sorbitan monooleate (Tween80), twelve sodium alkyl benzene sulfonate and octanol.

3.2 Experimental Apparatus

Currently on the market has not yet forming factors can be adjusted for each ultrasound phacoemulsification equipment, laboratory study is carried out using ultrasonic cell Mill beaker test, there is uneven distribution of unipolar probe energy, non-adjustable operating parameters and other issues[7,8]. According to this study the main factors affecting phacoemulsification phacoemulsification and design characteristics of ultrasonic wave trough occurrence frequency control device, the device using DDS technology of ultrasonic excitation frequency, stimulus waveform, power and other operating parameters adjusted freely in order to biomass diesel phacoemulsification experimental study of the optimum parameters.

The ultrasonic wave trough controlled variable frequency generator features:

(1) Ultrasonic generator frequency is variable. The ultrasonic generator frequency range in 20KHZ-200KHZ, and a three parameter adjusting key, step , frequency plus key and frequency cut keys, according to test needs to adjust the size of excitation frequency[8].

(2) Ultrasonic generator waveform is controllable. The ultrasonic generator in order to meet the various test and experiment technology needs, signal generator can generate sine wave, triangle wave and square wave pulse wave signal.
(3) Ultrasonic generator power can be adjusted. The ultrasonic generator power adjustment ranges from 40Wto 200W.
(4) Trough structure, uniform distribution of ultrasonic. Around the tank are equipped with ultrasonic transducers, to avoid the probe-type ultrasonic transducer, the problem of uneven energy distribution.

4 Experimental Methods

4.1 Compound Emulsifier Choice and the Best HLB Value Determination

Emulsifiers selected by many to be the ultimate test when HLB=5, so that the stability and the absorption coefficient reaches a peak, so the compound emulsifier HLB=5; choose methanol as emulsion and the content of 20%; In addition, the biological oil content on emulsion properties influence, not too little dosage to achieve the purpose of saving diesel emulsion, dosage too much effect on emulsion stability and its combustion performance, but also the internal combustion engine and its components caused by corrosion, In the experiment through the different biological fuel volume under the optimum HLB value for the investigation, if the biological oil content in the 10%-30% range, emulsified fuel oil stability is relatively good.

4.2 Emulsification Biomass Diesel Orthogonal Test Method

According to the above emulsifier ratio of 40ml emulsion, placed in the groove type variable frequency controlled waveform ultrasound emulsification instrument, at a certain frequency, power, waveform and time using ultrasound emulsification process, The main factors of phacoemulsification ultrasonic frequency, ultrasonic type, ultrasonic power and processing time, four levels of each factor selected, the application of L16 (4^4) orthogonal test table, as shown in Table 1:

Table 1. Orthogonal experimental design

Level/Factor	A Frequency /KHZ	B Power /W	C Time/min	D Waveform
1	30	20	2	Sine wave
2	40	30	5	Cosine wave
3	60	40	8	Triangle wave
4	80	60	10	Square-wave pulse

5 Results and Analysis

The designed conditions, the stability of the bio-diesel fuel was measured after emulsifying by ultrasonic. The results as shown in the experiment range R reflects the influence degree of the various factors on the test results. We can get from the experiment data $R_3 > R_2 > R_1 > R_4$. In the four selected factors including frequency and power, the processing time and ultrasonic irradiation waveform, the most influential factor on the stability of emulsified fuel in the process of ultrasonic emulsification is the processing time, followed by ultrasonic power and ultrasonic frequency, the least excitation current waveform. From the experiment that the best role, ultrasonic operating conditions for A1 B2 C2, namely in ultrasonic power D4 for 30W, the processing time for 8 minutes, ultrasonic frequency for 30KHZ and ultrasonic wave for square wave pulsed, ultrasonic emulsification oil stability effect best. Through verification test, the condition of ultrasonic emulsion stability of ESI2 is 114.8, and the results of orthogonal test.

References

1. Fang, H.: The influence of ultrasonic wave on diesel emulsion. Petroleum Chemical Industry (8), 615–618 (2001)
2. Rozenberg, L.D.: High-Intensity Ultrasonic Fields. Plenum Predd, New York (1971)
3. Dai, Y.: Under the effect of Ultrasonic Deep Desulfurization of high sulfur fuel, Harbin Institute of Technology, pp. 17–22 (2009)
4. Zhao, Y.Y., Feng, R., Yun, Y.X.: Frequency to the sound of the formation of the influence of hydroxyl radicals. Acoustic Technology 17(1), 12–14 (1998)
5. De-Ping, F., Chen, S.L.: Vibration waveform interference effects on dendritic growth. Journal of Synthetic Crystals 15(4), 35–39 (1989)
6. Xue, Y.W., Ji, M.: Ultrasonic power of the ultrasonic cracked. The influence of sludge. Journal of Chemical Engineering 58(4), 1037–1039 (2007)
7. Wang, L., Wang, S.: Influence of emulsification bio fuel stability of experimental study. Eight One Farming Cultivate University Journal 10(5), 26–29 (2010)
8. Jiang, J., Yang, S.: Groove type ultrasonic generator for improving sludge dewatering performance. Application of Basic Science and Engineering 12(6), 852–859 (2009)

A Real-Time Optimized Trajectory Planning for a Fixed Wing UAV

Jian Yang[1], Mi Dong[1,*], and Yan Tang[2]

[1] School of Info. Science & Engineering, Central South University, Changsha, Hunan 410083, China
[2] Department of Mechanical Engineering, Embry-Riddle Aeronautical University, Daytona Beach, FL 32114, USA
dm1221@tom.com

Abstract. The problem of determining an optimal feasible trajectory, for a fixed wing flying UAV moving in a dynamical 3-D space, is addressed in this paper, and an analytical solution is proposed. With explicitly considering the boundary conditions and kinematic constraints as well as by satisfying the collision avoidance criterions, trajectories are described in terms of three parameterized polynomials, and the families of feasible trajectories are found. Then, the desired near shortest trajectory is chosen from the feasible trajectories by optimizing a performance index with respect to L2 norm. This trajectory and its associated steering controls are achieved analytically. Computer simulations validate that this approach is computationally efficient and real-time implementable.

Keywords: Trajectory generation, obstacle avoidance, piecewise parameterizations, fixed wing.

1 Introduction

A lot of research efforts have been directed toward trajectory planning, and many techniques have been proposed. Among them, the method of potential field pioneered in [1] is widely used, and its basic idea is that, in planning a trajectory, potential fields are built around obstacles and pathways to expel the trajectory from obstacles and to bring the trajectory close to the final destination. Also popular are the spline method [2] and exhaustive search methods [3]. In the spline method, a sequence of splines is used to generate a path through a given set of waypoints in 3-D space. However, the prior knowledge of waypoints needed may not be available due to the fact that the environment is dynamic. On the other hand, in an application of a search-based algorithm, the space is typically divided into regions and a safe path is found for the vehicle by starting at the initial condition and successively searching adjacent regions to the goal. There have been efforts in applying numerical iteration methods to address the presence of vehicle kinematics and dynamics in 3-D trajectory planning. In these methods, obstacle avoidance criterion and kinematic model are typically converted into a set of inequality and equality constrains, and

* Corresponding author.

D. Jin and S. Lin (Eds.): Advances in Mechanical and Electronic Engineering, LNEE 176, pp. 277–282.
springerlink.com

numerical iterations are used to approximate or determine the path that satisfies all the constraints. In particular, semi definite programming is used in [4], nonlinear point-mass model is studied in [5], and nonlinear dynamic programming is applied in [6]. All these approaches provide a feasible and collision free trajectory, but they require perfect knowledge of the environment and their numerical iterations make them adequate only for offline path planning.

The objective of this paper is to present a real-time optimized trajectory generation algorithm for flying UAVs. The algorithm is based upon polynomial parameterization and online optimization.

2 Problem Formulation

Consider operations of a fixed wing flying UAV in a dynamically-changing environment with moving obstacles. The vehicle is needed to move from initial configurations $q_0 = (x_0, y_0, h_0, \gamma_0, \varphi_0)$ at time t_0 to terminal configurations $q_f = (x_f, y_f, h_f, \gamma_f, \varphi_f)$ at time t_f, where (x, y, h) is vehicle's coordinates, v stands for its velocity, γ refers to the directional angle and φ denotes the flight-path angle. To solve the corresponding trajectory planning problem, we adopt the following mathematical abstraction that reflects real-world applications:

- Vehicle: It has a limited sensing range (radius R_s) and operational velocity $v(t) = [\dot{x}, \dot{y}, \dot{h}]^T$. Physical envelope of the vehicle is assumed to be a sphere centered at $O(t) = (x, y, h)$ and of radius γ_o
- Obstacles: The ith obstacle (for any $i \in \{1, \cdots, N\}$ has a spheriform envelope centered at $O_i(t) = (x_i, y_i, h_i)$ and of radius r_i with velocity $v_i(t) = [v_{i,x}, v_{i,y}, v_{i,h}]$

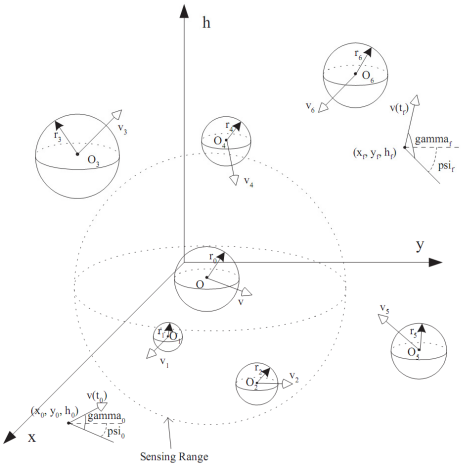

Fig. 1. Flying vehicle moving in a dynamic environment

To this end, the trajectory planning problem of this paper is mathematically formulated as the following optimization problem:

$$\begin{aligned} &\min J(\mathrm{q},\dot{\mathrm{q}}) \\ &\quad s.t.\ \mathrm{q}(t_0)=\mathrm{q}_0\ ,\ \mathrm{q}(t_f)=\mathrm{q}_f,\ M(\mathrm{q},\dot{\mathrm{q}})=0 \\ &\qquad (x-x_i)^2+(y-y_i)^2+(h-h_i)^2\geq(r_0+r_i)^2, i=1,\ldots,n \end{aligned} \tag{1}$$

For the fixed wing UAV, the detailed $M(q,\dot{q})=0$ are shown as follows:

$$\begin{aligned} &\dot{x}=\upsilon\cos\gamma\cos\psi,\quad \dot{y}=\upsilon\cos\gamma\sin\psi,\quad \dot{h}=\upsilon\sin\gamma \\ &\dot{\upsilon}=\frac{F_T}{M}-g\sin\gamma,\quad \dot{\gamma}=\frac{F_N\cos\sigma}{M\upsilon}-\frac{g\cos\gamma}{\upsilon} \end{aligned} \tag{2}$$

where g is the gravitational acceleration, the controls are F_T, F_N, and bank angle σ. For the pilot, they are "throttle", "stick pull-push", and "stick left-right".

3 Optimal Real-Time Trajectory Planning for Fixed Wing UAV

Let $T_m=t_f-t_0$ be the time for the fixed wing UAV to complete its maneuver and T_s be the sampling period such that $\bar{k}=T_m/T_s$ is an integer, that centers of obstacles O_i are located at (x_i^k,y_i^k,h_i^k) at $t=t_0+kT_s$, and that these objects are all moving with known constant velocities t for $t\in[t_0+kT_s,t_0+(k+1)T_s]$, where $k=0,1,\cdots\bar{k}-1$. The trajectories of fixed wing UAV are described by

$$x(t)=\left(B_1^k\right)^{-1}Y_1^k\left[1\ t\ t^2\ t^3\right] \tag{3}$$

$$y(x(t))=\left(B_2^k\right)^{-1}\left(Y_2^k-A_2^kb_4^k\right)\left[1\ x\ x^2\ x^3\right]+b_4^kx^4 \tag{4}$$

$$h(t)=\left(B_3^k\right)^{-1}\left(Y_3^k-A_3^kc_4^k\right)\left[1\ t\ t^2\ t^3\right]+c_4^kx^4 \tag{5}$$

where

$$B_1=B_3=\begin{bmatrix}1 & t_0 & t_0^2 & t_0^3\\ 0 & 1 & 2t_0 & 3t_0^2\\ 1 & t_f & t_f^2 & t_f^3\\ 0 & 1 & 2t_f & 3t_f^2\end{bmatrix},\quad Y_1=\begin{bmatrix}x_0\\ \upsilon_0\cos\gamma_0\cos\psi_0\\ \upsilon_f\cos\gamma_f\cos\psi_f\end{bmatrix}$$

$$A_2=\begin{bmatrix}(x_0)^4\\ 4(x_0)^3\\ (x_f)^4\\ 4(x_f)^3\end{bmatrix},\quad B_2=\begin{bmatrix}1 & x_0 & (x_0)^2 & (x_0)^3\\ 0 & 1 & 2x_0 & 3(x_0)^2\\ 1 & x_f & (x_f)^2 & (x_f)^3\\ 0 & 1 & 2x_f & 3(x_f)^2\end{bmatrix},\quad Y_2=\begin{bmatrix}y_0\\ \tan\psi_0\\ y_f\\ \tan\psi_f\end{bmatrix}$$

For $t \in [t_0 + kT_s, t_0 + (k+1)T_s]$,the collision avoidance criterion is

$$\left(x - x_i^k - v_{i,x}^k \tau\right)^2 + \left(y - y_i^k - v_{i,y}^k \tau\right)^2 + \left(h - h_i^k - v_{i,h}^k \tau\right)^2 \geq \left(r_i + r_0\right)^2 \tag{6}$$

where $\tau = t - t_k$ for $t \in [t_0, t_f]$.

Theorem 1. Consider a flying UAV, whose kinematics model is given by (2), moving in an environment with dynamically moving and static obstacles, and its trajectories are parameterized by equations (3), (4) and (5). Under boundary conditions q_k and q_f, the trajectories, avoiding *n* obstacles, are mapped into collision-free intervals of b_4^k, which is

$$\Omega = \left\{ b_4^k : b_4^k \notin \cup_{i=1}^n \left(\underline{d}_i^k, \overline{d}_i^k \right) \right\} \tag{7}$$

where $\underline{d}_{1,i}^k$ and $\overline{d}_{1,i}^k$ are the upper and lower bound, incurring collision to the ith obstacle, respectively. ♦

Considering all these issues, a performance index is proposed as follows:

$$J_k\left(b_4^k\right) = \int_{t_k}^{t_f} \left[\left(x - x_l\right)^2 + \left(y - y_l\right)^2 + \left(h - h_l\right)^2 \right] dt \tag{8}$$

The point (x_l, y_l, h_l) belongs to the "initial straight line", that is, the beeline between the start point and the end point.

Theorem 2. Consider the flying UAV, whose kinematic constraint is in the form (2), operating in an environment with static and dynamically moving obstacles. Its trajectories are expressed by polynomials (3), (4) and (5), for which only a free parameter b_4^k needs to be determined. Let Ω be the set of b_4^k generating collision-free trajectories, solved from inequalities (6). Then, the projection of

$$b_4^{k*} = \frac{\int_{t_k}^{t_f} \left[f_1 f_2 + f_3 f_4 - f_1 y_0 - f_3 h_0 - f_1 \dfrac{\left(y_f - y_0\right)\left(x - x_k\right)}{x_f - x_0} - f_3 \dfrac{\left(h_f - h_0\right)\left(x - x_k\right)}{x_f - x_0} \right] dt}{\int_{t_k}^{t_f} \left[\left(f_1\right)^2 + \left(f_3\right)^2 \right] dt} \tag{9}$$

on the set Ω generates near shortest collision-free trajectory while minimizing performance index (8). The definition of the projection is

$$P_\Omega^{b_4^{k*}} = \left\{ b_4^{k*} \in \Omega : \left\| b_4^{k**} - b_4^{k*} \right\| \leq \left\| b_4^k - b_4^{k*} \right\|, \forall b_4^k \in \Omega \right\}$$ ♦

4 Simulation

In the scenario of simulation, all quantities conform to a given unit system, for instance, meter, meter per second, etc. The sampling period is chosen to be T_s= 1s for convenience. Three obstacles are presented in the scenario: one is static and the other

two are moving. The flying UAV and three obstacles are denoted by balls with different colors, and they are drawn every 5 seconds. We use "x" marks the starting position and "star" denotes the ending position. The velocity of the moving obstacles will change in each 10s and the settings are as follows:

- Flying UAV parameters: $r_0 = 1$, $R_s = 10$.
- Boundary conditions: $q_0 = (0, 0, 0, 1, \pi/6, \pi/4)$ and $q_f = (30, 20, 10, 2, \pi/5, \pi/10)$, $t_0 = 0$ and $t_f = 40$.
- Moving obstacles parameters:

$$v_1^0 = [0,0,0]^T, v_1^1 = [0,0,0]^T, v_1^2 = [0,0,0]^T, v_1^3 = [0,0,0]^T$$
$$v_2^0 = [-0.4,0.4,0.2]^T, v_2^1 = [0.2,-0.1,-0.4]^T, v_2^2 = [1,0.2,0.4]^T, v_2^3 = [0.6,0.2,0.2]^T,$$
$$v_3^0 = [0.1,0.2,-0.3]^T, v_3^1 = [0.2,0.2,0.4]^T, v_3^2 = [-0.1,-0.3,-0.3]^T, v_3^3 = [0.4,0.4,-0.2]^T.$$

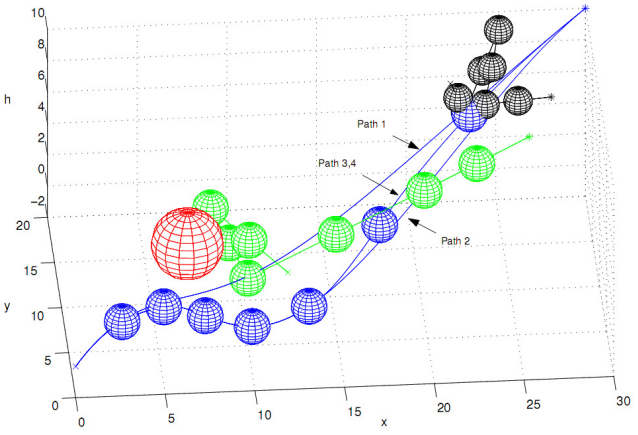

Fig. 2. Evolvement of the optimal trajectory

With the optimal solution proposed in this paper, the simulation result shows that the fixed wing UAV avoid the static and moving obstacles effectively in the 3-D space.

5 Conclusion

A method for planning the trajectory of a fixed wing vehicle moving in a dynamically changing environment has been developed. It is a parameterization approach, since the real-time and feasible trajectory is expressed by parameterized polynomials. The only requirement to obtain the solution of an adjustable parameter makes it possible to generate the realtime trajectory. Also demonstrated was the effectiveness of the optimal solution.

Acknowledgments. This work was supported by the National Young Teacher Foundation under Grant 2011QNZT037.

References

1. Khatib, O.: Real-time obstacle avoidance for manipulator and mobile robots. Int. J. Robot. Res. 5, 90–98 (1986)
2. Judd, K.B., Mclain, T.W.: Spline based path planning for unmanned air vehicles. In: AIAA Guidance, Navigation, and Control Conference and Exhibit, Montreal, Canada (August 2001)
3. Fujimura, K.: A hierarchical strategy for path planning among moving obstacles. IEEE Transactions on Robotics and Automation 5, 61–69 (1989)
4. Frazzoli, E., Mao, Z.H., Oh, J.H., Feron, E.: Resolution of conicts involving many aircraft via semidefnite programming. AIAA Journal of Guidance, Control and Dynamics 24, 79–86 (2001)
5. Menon, P.K., Sweriduk, G.D., Sridhar, B.: Optimal strategies for free-flight air traffic conflict resolution. AIAA Journal of Guidance, Control and Dynamics 22, 202–211 (1999)
6. Raghunathan, A.U., Gopal, V., Subramanian, D., Biegler, L.T., Samad. 3d, T.: conflict resolution of multiple aircraft via dynamic optimization. In: AIAA Guidance, Navigation and Control Conference and Exhibit, Austin, TX (August 2003)

Irregular Graphics Nesting Algorithm in the Hull Construction Automatic Nesting System

Ying Mei

Computer and Information Engineering Department
Guangzhou Maritime High College
Guangzhou, 510725, China
yzsmcg@sina.com

Abstract. The paper discusses the irregular parts nesting problem based on an improved immune genetic algorithm, and a NIGA based on crowing mechanism is proposed. GA, an improved immune genetic algorithm, and NIGA are applied to practical experiments respectively to solve and optimize the nesting problem, and we compare the results. In solving the large-scale nesting problem, the application of immunity operator and niche genetic algorithm based on crowing mechanism improves the global optimization performance and velocity of convergence. The improved algorithms are effective and feasibility for solving the hull construction automatic nesting problem

Keywords: irregular graphics nesting algorithm, nesting problem, niche technology.

1 Introduction

The optimized solution of the kind of problem (the nesting problem of the large-scale regular nesting-graphics and irregular graphics) is based on the stochastic algorithm, and the study is to find a fast convergent stochastic algorithm (the heuristic algorithm). In the forepart study, we use an improved immune genetic algorithm to avoid the shortcoming of prematurity convergence of genetic algorithm. Then we'll discuss the niche technology combined with the improved immune genetic algorithm, and use it to solve the irregular graphics nesting problem in the hull construction automatic nesting system. The global search using the algorithm is based on the diversity.

In the study of the nesting optimized algorithm of the hull building automatic nesting system, we practice cluster analysis for irregular graphics at first, which is based on area, bitmap enveloping rectangle coverage (bitmap enveloping circle coverage) and approximately ratio of long axes and short axes.

To solve the problem of 2D irregular nesting problem, there are two solutions: one is to use the regular graphics envelope before the irregular graphics nesting (we can use rectangle, parallelogram and hexagon); the other is to pack the irregular graphics directly. The paper discusses using appropriate nesting algorithm to solve the 2D irregular graphics' direct nesting problem.

D. Jin and S. Lin (Eds.): Advances in Mechanical and Electronic Engineering, LNEE 176, pp. 283–288.
springerlink.com

2 The Irregular Graphics Nesting Algorithm Based on the Improved Immune GA

2.1 Problem Solving

The goal is to put more parts ($\{p_1, p_2, ..., p_t\}, 1 \le t \le n, n$ is the number of nesting parts) without overlaps in the given rectangle sheets (L_S , W_s) and get the maximal utilization of materials. t is the number of actually nesting parts; the goal is to maximize the utilization ratio of materials, and the residual materials can be reused. So, the goal of solution is

$$Object = \max\{\sum_{j=1}^{t} S_{pi} / W_u * L_u\}, 0 < W_u \le W_s, 0 < L_u \le L_s$$

Here W_u , L_u is the maximum width and length that the nesting parts occupy the nesting area from the left-bottom point of the nesting area.

The goal of 2D nesting cutting problem is to put more parts without overlaps in the given sheets and get the maximal utilization of materials. However, they are all NP-hard problems. In particular, with the increasing of dimensions of regular nesting-graphics and irregular graphics, the complexity of computation increases rapidly. How to increase the time of nesting and improve the utilization ratio of materials is the focus and we try to find an appropriate balance point between them as the final choice.

And the fitness function is as the following: Here, I_i means the coding of the individual i.

$$Fitness(I_i) = Object = \max\{\sum_{j=1}^{t} S_{pi} / W_u * L_u\},$$
$$0 < W_u \le W_s, 0 < L_u \le L_s$$

We use the decimal system coding. One nesting graphics is called one integer series I_1, $I_1 = \{p_{11}, p_{12,\cdots,} p_{1n}\}$, which is composed by the parts serial number. Each integer represents one irregular graphics, and the positive integers represent that the parts is not rotated. The negative integer represent that the parts is 90 degree rotation.

2.2 Bottom-Left Nesting Principle

We use bottom-left principle: the nesting parts' position $(x, y) = \arg\{\min\{L_i\}\}$ or $\min\{W_i, when \arg\{\min\{L_i\}\}\}$ is not unique. Here, (x, y) is the top left coordinate. L_i and W_i is the occupied material's maximal length and width after nesting i parts.

2.3 The Choice of Genetic Operators

The selection operator: the selecting operation introduces the similarity operator and the concentration operator, and it uses the conception of information entropy. It's as the following:

$$A_{apI_1I_2} = \sum_{j=1}^{n} W_j V_j$$

$$V_j = \{1, p_{1j} = p_{2j}; 0, p_{1j} \neq p_{2j}\}$$

Here, W_j is the weight when we form the similarity operator, and it means the number on the j position is the same. If the times are h that the number on the front corresponding positions is continuously same, the weight of the similarity is $h+1$. The original the selecting operation in proportion is changed into the following selection rate:

$$S_{I_i} = \frac{fitness(I_i)\prod_{t=1}^{m}(1-A'_{I_iI_t})}{c_{I_i}\sum_{j=1}^{m} fitness(I_j)}$$

Here, $A'_{I_iI_t} = \{A_{I_iI_t}, A'_{I_iI_t} \geq A_{g2}; 0, A'_{I_iI_t} < A_{g2}\}$, and A_{g2} is the given threshold.

According to the irregular graphics nesting problem, we need to have an accurate similarity definition. We can consider the different rotation angle or turnover mark when we get the individual similarity. For example:

I_1

1	25	1	2	25	1	3	15	1	4	25	0	5	80	1

I_2

1	25	1	2	25	1	3	15	1	4	25	0	5	80	1

I_3

1	25	0	2	25	1	3	25	0	4	25	1	5	80	1

In anterior simplified discussion, $A_{apI_1I_2} = A_{apI_1I_3} = 15$. Here, $\gamma_i = 1$. And we have the modified definition: if the corresponding parts' position coding number is the same but the rotation angle or turnover isn't the same, the similarity operator need to subtract 0.6(reference value). At this time, $A_{apI_1I_2} = 15, A_{apI_1I_3} = 13.8$. It can show that the modified similarity definition embodies the similarity degree between the individuals.

In solving the irregular graphics nesting problem, we comprehensively consider the fitness degree and similarity degree to decide which individual can be chosen. The paper reserves the anterior m/3 with the high fitness value and the anterior m-m/3 with the low concentration value for the individual selection.

3 The Graphics Nesting Algorithm Based on the Improved Niche Immune GA

Then we'll discuss the niche technology combined with the improved immune genetic algorithm We also consider using the niche technology based on the crowing mechanism in the improved immune genetic algorithm for optimal selection. The algorithm is as the following: (1) To generate N initial antibody to form the initial population, and get every individual's similarity and fitness. Then preserve the first N/CF (in the paper, $CF=3$) individuals with high fitness and preserve the first $N-N/CF(N<M)$ individuals with low similarity for implementing the individual selection and forming the antibody population. (2) GA evolves the antibody population. Selection operation, calculate the individual I_i selection rate according to the fitness and similarity; crossover operation; mutation operation. (3) The niche technique selection operation. (4) Termination criterion. If it doesn't meet the terminal conditions, the first N individuals in step (3) are regarded as the new next generation population and go to the step (2) for further operation; if it satisfies the termination, we'll get the optimal result. The algorithm ends.

4 Testing

4.1 The Example Description and the Results Comparison

The rectangle nesting example:

To design a nesting problem that has the multi-optimal results: The rectangle panel with the 100% utilization ratio that is combined by 10 small rectangle parts for nesting. And we respectively use the genetic algorithm, the improved immune GA and the improved niche immune GA for the nesting problem.

The nesting rectangle set is: {(1500,1000), (500,500), (500,1000), (500,250), (500,1250), (500,1500),(500,750), (500,250), (1500,500), (500,20000)}。

The partial parameter settings are as the following: $P_{\mathrm{var}s}=1e-4$, the optimization parameter precision(if it's the vector, each parameter uses the different parameter); $P_c=[0.6,0.99]$, the adapting crossover probability(if it's the scalar quantity, the probability is invariable); $P_m=[0.01,0.1]$, the adapting mutation probability(if it's the scalar quantity, the probability is invariable); $Sigma=[3,0.01]$, genotype niche radius and expression niche radius.

In the experiment, for resolving the contradictions which arise between retaining high fitness results and the spreading results, we use the immune operator's algebra threshold G_g and the immune operator's concentration threshold G_g to control the algorithm: when the operation algebra $G\geq G_g$ and the concentration $C\geq G_g$, we use the improved immune operator. Here $G_{g1}=10;G_{g2}=20$. The experiment

results are as the following, the results show the comparison of generation of convergence of three algorithms, and m means the population size:

Table 1. Comparison of generation of convergence of three algorithms

Group Size	GA	The improved immune GA	The improved niche immune GA
m=7	25	13	12
m=8	3	2	3
m=9	8	7	7
m=10	5	5	5
m=11	7	5	4
m=12	5	5	3
m=13	9	7	6
m=14	3	3	3
m=15	6	6	6

The irregular parts nesting example:

For a group of irregular graphics, we use GA, the improved immune GA and the improved niche immune GA for the nesting problem, the results is as the following graphics:

Here, m=12, the convergence generation of three algorithms is 87, 78 and 77, the material utilization ratio is 77.31%.

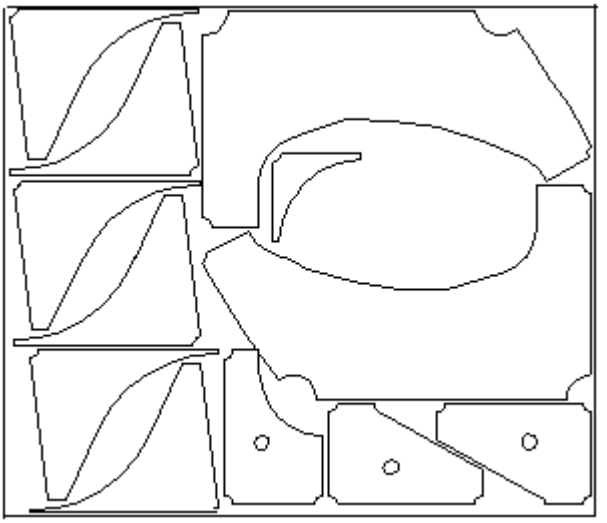

Fig. 1. Example of results of irregular nesting graphics

4.2 The Analysis of the Experiment Results

When we respectively use the GA, the improved immune GA and the improved niche immune GA, the latter two can fast skip from local optimization. When the population size is larger, the latter two algorithms have better global optimization and the convergence rate, the algorithms are efficient and practicable.

5 Conclusion

For solving the irregular parts nesting problem in the hull building automatic nesting system, the paper introduces an improved immune GA and the niche technology. By comparisons of more experiments, in the large-scale irregular parts nesting process, the IGA and the NIGA can find satisfied nesting results fast and stably, and at the same time we can improve the efficiency of the material cutting to a certain degree.

References

1. Song, Y.-N.: Study of Algorithm of Graphic-Matching, Control of Nesting and Contacting in Two-Dimensional Nesting System. South China University of Technology, Guangzhou (2004)
2. Wu, S., Cao, J.: Optimal Layout of Silicon Steel Sheet Based on Niche Immune Genetic Algorithm. Computer Engineer 5, 181–183 (2008)
3. Zhang, Z.-Z., Zhang, W.-Y.: A Novel Niche Genetic Algorithm of Accurate Optimization Performance. Computer Applications 8, 1903–1905 (2005)
4. Shi, J.-Y., Feng, M.-G.: Niche Genetic Algorithm for Two Dimensional Irregular Parts Optimal Layout. Journal of Engineer Design 4, 171–174 (2007)
5. Jiang, X.-B., Lv, X.-Q., Liu, C.-C.: Improved Genetic Algorithm for Nesting Problem of Rectangles. Computer Engineering and Applications 44(22), 244–248 (2008)

Robot Localization Combining Stereo Vision and Artificial Landmark

Xiaoming Dong[1,*] and Benyue Su

School of Computer & Information, Anqing Teachers College
Linghu South Road 128, Anqing, Anhui Province, China
xiaoming.dong@ia.ac.cn, bysu@aqtc.edu.cn

Abstract. The artificial landmark is useful to resolve the problem of data association, meanwhile the stereo vision is useful to the accuracy of the location, in this paper, an effective method is proposed for indoor robot self-localization combining artificial landmarks with stereo vision. Experiments show the effectiveness and robustness of the method in various environments.

Keywords: mobile robot, pose estimation, artificial landmark.

1 Introduction

Landmarks are important to accomplish the task of robot self-localization and navigation. There are two kinds of landmarks which are natural landmarks and artificial landmarks [1-3]. natural landmarks can be the vertical lines in corridor or number plate of door[4], or more abstract feature as SIFT(Scale-Invariant Features) in journal[5]. Though the effectiveness has been confirmed in many researches, the obvious shortcoming can't be ignored that almost all of the natural landmarks only can be used to specified environment. Comparing with natural landmarks, artificial landmark is more powerful and easier to be recognized. In this paper, to make the robot localization more robust and accurate, we combine the artificial landmark and stereo vision to implement the task of robot localization. Considering of the characters whether the landmark can present enough information, and self error correcting, etc. we choose the MR code as the the artificial landmark needed [6].

The paper is organized as follows. In section 2, we present the structure of the MR code and discuss the method of its detection and recognition. In section 3, MR code is combined with stereo vision to implement the task of robot self-localization, the method is verified effective in various experiments and this is given in Section 4. The conclusions are given in section 5.

2 The Structure of MR Code

A prototype of MR code with 8x8 units is shown in Fig.1, The MR code has some characteristics. Utilizing the computation of the cross ratio, the landmark pattern show

* This work is supported by the natural science project of Anhui Provincial Education Department under Grant No.KJ2012B090, KJ2009A123 and KJ2011B086.

D. Jin and S. Lin (Eds.): Advances in Mechanical and Electronic Engineering, LNEE 176, pp. 289–293.
springerlink.com

invariant characteristics under different viewing angles and illumination; its unit modules contain the binary information encoded by binary BCH code. As in Fig.1, using BCH(63, 45, 3) to encode the binary information, such a MR code can provide 2^{45} different landmarks. In order to meet the needs of using the vision system of the mobile robot to recognize the MR code from the environment robustly and read the code value correctly, we mainly pay our attention to the design of its shape and the distribution of the unit modules in it. A mobile robot can recognize its location or the objects it faces using its vision system by simply recognizing the information represented by the MR code. In the next parts of this section, we will do some explanation about the design of its appearance. Using the five vertexes of the extracted outline, the coordinate of the five vertices can be easily computed combining the stereo vision, so the pose of the robot is confirmed relative to the landmark.

To show the effectiveness of this method, the algorithm to detect and recognize the MR landmark is shown briefly as follows. The process is mainly completed by four steps.

1. Extracting lines. Canny edge detector is used to extract edges to calculate projective invariants.
2. Calculating invariants. Since the lines are detected by the canny detector, the pairs of cross ratio invariants can be computed according to the contour of the landmark.
3. Determining homography matrix. Before translating the binary value of unit modules, the homography matrix $\mathbf{H}$ is computed to. Because the contour of the landmark is confirmed, the coordinates of the five vertexes are determined.
4. Reading and decoding. After the homography matrix $\mathbf{H}$ is determined, given a new image $\mathbf{I}_P$, which has the same size as the image of the MR code. According to the homography matrix $\mathbf{H}$ .the new image can be mapped to the MR code, so the the binary information can be obtained by searching at the positions of unit modules.

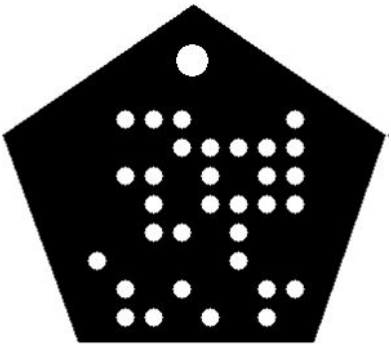

Fig. 1. A prototype of MR code

3 The Position Calculation of the Stereo Vision

The research of binocular vision is based on human visual system [7]. When a pair of points in the images captured by the binocular vision, the correspondent

three-dimensional coordinates in real world can be calculated. So when a mount point of the MR landmark is detected by the binocular vision, the distance between robot and landmark can be calculated through the disparity of the same point in the two images. The principle can be represented as follows.

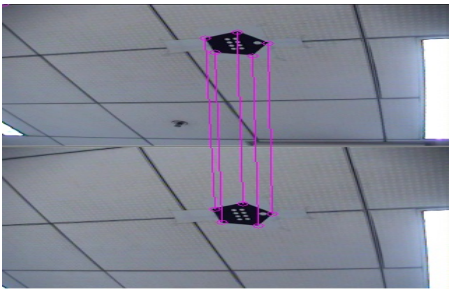

Fig. 2. The correspondent vertices of landmark in the different image

Fitting the plane according to the five vertices, we can the pose of robot. The process can be described as follows.

Assumed that $p_i(x_i, y_i)$ is a point in the plane $ax_i + by_i + cz_i = d$ $(d^2 + b^2 + c^2 = 1)$, the distance is described as

$$D_i = ax_i + bx_i + cx_i - d \tag{1}$$

To obtain the optimized object plane, we must meet the object function:

$$S = \sum_{i=1}^{n} D_i^2(x_i, y_i) \tag{2}$$

And this is equal to solve the follow function:

$$WH = 0 \tag{3}$$

$$W = \begin{pmatrix} \sum_{i=1}^{n}(x_i - x_0)^2 & \sum_{i=1}^{n}(x_i - x_0)(y_i - y_0) & \sum_{i=1}^{n}(x_i - x_0)(z_i - z_0) \\ \sum_{i=1}^{n}(x_i - x_0)(y_i - y_0) & \sum_{i=1}^{n}(y_i - y_0)^2 & \sum_{i=1}^{n}(z_i - z_0)(y_i - y_0) \\ \sum_{i=1}^{n}(x_i - x_0)(z_i - z_0) & \sum_{i=1}^{n}(z_i - z_0)(y_i - y_0) & \sum_{i=1}^{n}(z_i - z_0)^2 \end{pmatrix} \tag{4}$$

$$x_0 = \sum_{i=1}^{n} x_i, y_0 = \sum_{i=1}^{n} y_i, z_0 = \sum_{i=1}^{n} z_i \tag{5}$$

This eigenvector problem can be easily solved; however, we must determine how to select the correct eigenvector to get the result of the function. Using the SVD, we choose the singular vector corresponding to the smallest singular value, since under these conditions the singular values are the square roots of the eigenvalues.

4 Experiments and Analysis

Some experiments have been carried out in various conditions. The robot localization experiment is implemented in stereo vision combining the artificial landmark MR code. To calculate the position of the mobile robot in world coordinate, the external camera parameters must be determined; Table 1 shows the calibration result of stereo vision.

Table 1. External Camera Parameters

Translation vector p	result	-436.77377 -6.12314 8.138701
	variance	3.22473 2.86419 3.46239
Rotation matrix R	result	0.0163 0.9973 -0.0710 0.9818 -0.0294 -0.1874 -0.1890 -0.0666 -0.9797
	variance	0.03684 0.03972 0.00505

The experiment shows that in the measurement of monocular vision, the error is below 10cm at distance of 150cm or so, meanwhile in the stereo vision; the error decreases about 3cm.

In addition, since the measured angles and distances are computed by hand, a certain amount of error due to human inaccuracy is also expected. Therefore, the precision of the proposed method is good enough for the navigation of indoor mobile robot.

5 Conclusions and Future Work

The artificial landmark is useful to the problem of data association among correspondent points meanwhile the stereo vision is useful to the accuracy of the

localization. In this paper, an effective method of indoor robot self-localization combining artificial landmarks with stereo vision is proposed. Firstly, we analysis the structure of the artificial landmark MR code and show that the landmark has some good characters to implement the task of robot self-localization, we compared the way using the stereo vision and the monocular vision to localize the robot respectively, the experiment shows that stereo vision can get better result. The hybrid method is not only robust to lights and angles, but also can be implemented in real-time, and it can meet the requirement of the self-localization of the indoor mobile robots. Our future work will mainly consider the problem of the robot navigation. Implementing the SLAM (simultaneous localization and map building) is the next object to combine the artificial landmark and stereo vision.

References

1. Guo, Y., Xu, X.: Landmark Design Using Projective Invariant for Mobile Robot Localization. In: Proceedings of SPIE, pp. 852–857 (2006)
2. Sonka, M., Hlavac, V., Boyle, R.: Image processing, analysis, and machine vision, 2nd edn., pp. 170–173. Brook/Cole, Thomson Asia Pte. Led., USA (2002)
3. Becker, C., Salas, J., Tokusei, K., Latombe, J.-C.: Reliable Navigation Using Landmarks. IEEE International Conference on Robotics and Automation, 401–406 (1995)
4. Shi, W., Samarabandu, J.: Corridor Line Detection for Vision Based Indoor Robot Navigation. In: Canadian Conference on Electrical and Computer Engineering, pp. 1988–1991 (May 2006)
5. Se, S., Lowe, D., Little, J.: Vision-based Mobile Robot Localization And Mapping using Scale-Invariant Features. In: IEEE International Conference on Robotics and Automation, pp. 2051–2058 (May 2001)
6. Zheng, R., Yuan, K.: MR code for indoor robot self-localization. In: 7th World Congress on Intelligent Control and Automation, pp. 7449–7454 (June 2008)
7. Matthies, M.S., Maimone, M.W.: Rover navigation using stereo ego-motion. Robotics and Autonomous Systems 43(4), 215–229 (2003)
8. Lu, C., Hager, G., Mjolsness, E.: Fast and Globally Convergent Pose Estimation from Video Images. Pattern Analysis and Machine Intelligence 22(6), 610–622 (2000)

A New Method for the Inverse Kinematics of 6-DOF Manipulator Based on Dual Quaternion

Yurong Nan and Panfeng Wu

College of Information Engineering, Zhejiang University of Technology, Hangzhou, China
Wupanfengxx@126.com

Abstract. The inverse kinematics of 6-DOF manipulator is one of the main concerns and difficult problem in robotics. This dissertation presents a new method for the inverse kinematics of 6-DOF manipulator based on dual quaternion which uses dual quaternion to respect both rotation and translation in a single transformation vector. So all the revolute joints of 6-DOF manipulator can be denoted by dual quaternion. The simulation was provided to verify the feasibility and precision of the proposed new method.

Keywords: 6-DOF, series manipulator, inverse kinematic, dual quaternion.

1 Introduction

The inverse kinematics of a robot manipulator is one of the most basic and important research questions in robot. It's directly related to the motion analysis of robot manipulator, off-line programming, trajectory planning and real-time control. While the hand of a robot manipulator is fixed at a point or a posture in the rectangular space, the inverse kinematics algorithm of robot manipulator will be used to solve the joint angle (or the joint coordinates) for every DOF of the robot manipulator. As a result, the inverse kinematics algorithm is an essential part of the robot control. The structure of traditional robot manipulator tends to be more special. For example, the axes may be parallel or intersecting. Without coupling between the posture and position of robot manipulator, it's easy to use the way of variable separation to achieve inverse solution. For another kind of complex robot manipulator, it can't use the way of variable separation because of the highly coupling of its posture and position. Then it must resort to the numerical algorithms.

The numerical algorithms can be divided into three classes: (1) Numerical analysis method [1], Newton-Raphson method [2] and so on. These algorithms can meet the real-time requirements, but be more difficult to achieve all the inverse solutions. Furthermore it must be given the appropriate initial value. (2) Optimization algorithm [3], Particle swarm optimization (IPSO) algorithm [4], Genetic algorithm [5] and so on. These algorithms have a large convergence range, and can achieve all the inverse solutions. But generally they have bad performance of real-time. (3) Position and posture iterative algorithm [6]. This algorithm can achieve all the inverse solutions more rapidly. But when the position and posture of robot manipulator are highly coupled, the iterative process will be divergent. This paper proposes a new method to

D. Jin and S. Lin (Eds.): Advances in Mechanical and Electronic Engineering, LNEE 176, pp. 295–302.
springerlink.com

solve inverse solutions of the 6-DOF robot manipulator based on dual quaternion which can meet the real-time and accuracy of the robot manipulator's inverse kinematics algorithm.

2 Description of Dual Quaternion

Set $q = a + bi + cj + dk\ (a,b,c,d \in R)$, i, j, k can meet the condition as follows[7] :

$$\begin{cases} i^2 = j^2 = k^2 = -1 \\ ij = -ji = k \\ jk = -kj = i \\ ki = -ik = j \end{cases} \tag{1}$$

then q can be called a quaternion, where i, j, k represent the imaginary unit. Their relationship shows as (1). If $a^2 + b^2 + c^2 + d^2 = 1$, it can be called a unit quaternion.

$\overline{q}$ is the conjugate quaternion of q ,

$$\overline{q} = a - bi - cj - dk \tag{2}$$

The unit quaternion can be shown as,

$$q\overline{q} = 1 \tag{3}$$

In this paper, the quaternion is shown as,

$$q = (s, v) \tag{4}$$

Where s represents the scalar quantity a , v represents the vector $bi + cj + dk$. Let, $q_1 = [s_1, v_1]$ and $q_2 = [s_2, v_2]$ denote two unit quaternions. In this case, multiplication process is shown as [8]

$$\begin{aligned} q_1 * q_2 &= (s_1 + v_1) * (s_2 + v_{22}) = \\ & s_1 * s_2 - v_1 \cdot v_2 + v_1 \times v_2 + s_1 * v_2 + s_2 * v_1 \end{aligned} \tag{5}$$

Or

$$q_1 * q_2 = [s_1 s_2 - v_1 \cdot v_2, s_1 v_2 + s_2 v_1 + v_2 \times v_1] \tag{6}$$

Where $(\cdot)$, $(\times)$ and $(*)$ are dot product, cross product and quaternion multiplication, respectively.

In the three-dimensional space, the rotation which rotate around the unit vector $u=(u_x,u_y,u_z)$ for the angle θ can be shown as unit quaternion [9],

$$\cos(\theta/2)+\sin(\theta/2)(u_x i+u_y j+u_z k) \tag{7}$$

$$q=[\cos(\theta/2),\sin(\theta/2)<u_x,u_y,u_z>] \tag{8}$$

The unit quaternion can describe the rotation of rigid body as (8) shows, but can't describe the displacement relationship of rigid body in the three-dimensional space. A displacement can be composed of rotation and translation in the three-dimensional. In this paper the unit quaternion q can denote the rotation of rigid body. The translation vector can be shown as $p=(p_x,p_y,p_z)$. So the dual quaternion can be denote as,

$$Q(q,p)=([\cos(\theta/2),\sin(\theta/2)<u_x,u_y,u_z>],<p_x,p_y,p_z>) \tag{9}$$

In the same manner as (6), the multiplication process of two dual quaternions is denoted as,

$$Q_1Q_2=(q_1,p_1)*(q_2,p_2)=(q_1*q_2,q_1*p_2*q_1^{-1}+p_1) \tag{10}$$

where, $q_1*p_2*q_1^{-1}=p_2+2s_1(v_1\times p_2)+2v_1\times(v_1\times p_2)$.

A unit quaternion inverse requires only negating its vector part,

$$q^{-1}=[s,-v] \tag{11}$$

Then the inverse of dual quaternion can be written as,

$$Q^{-1}=(q^{-1},-q^{-1}*p*q) \tag{12}$$

where, $-q^{-1}*p*q=-p+[-2s(v\times(-p))+2v\times(v\times(-p))]$.

3 Inverse Kinematics Problem Statement

The inverse kinematics of robot manipulator is very important in Robot which is directly related to the motion analysis, offline programming, trajectory planning and so on. To solve the inverse kinematics problem, the conversion relationship between the revolute joints and dual quaternion can be defined as

$$[R_w,T_w]=([w,<a,b,c>,<p_x,p_y,p_z>]) \tag{13}$$

where (R_w,T_w) represents the known orientation and translation of the robot end-effector with respect to the base. Let $Q_i(1\le i\le 6)$ denotes kinematics

transformations describing the spatial relationships between successive coordinate frames along the manipulator linkages such as [10]

$$Q_1(q_1, p_1), Q_2(q_1, p_2) \cdots Q_6(q_6, p_6).$$

And set:

$$S_i = Q_i Q_{i+1} \cdots Q_6 \tag{14}$$

$$L_{j+1} = Q_j^{-1} L_j \tag{15}$$

where $1 \le i \le 6$ and $1 \le j \le 5$ respectively. Note that $L_1 = [R_w, T_w]$. In order to extract joint variables as functions of s, v, p_x, p_y, p_z and fixed link parameters, appropriate S_i and L_{j+1} terms are equated, such as $S_1 = L_1, S_2 = L_2 \cdots S_6 = L_6$.

4 Example

The rigid body model and coordinate frame attachments of the RS robot manipulator with Euler wrist are given in Fig.1 where $\theta_1, \theta_2, \theta_3, \theta_4, \theta_5, \theta_6$ and d_3 are the joint variables for revolute and prismatic joints, respectively and also l_1 and l_2 denote the link lengths.

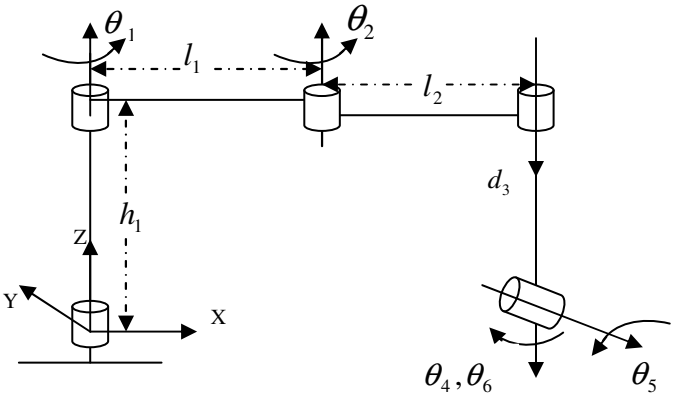

Fig. 1. Rigid body model and coordinate frame attachments of the RS robot

The transformation relationship for each revolute joints of robot manipulator with respect to the base can be expressed as follows:

$$Q_1 = ([\overline{c}_1, \overline{s}_1 k], < l_1 c_1, l_1 s_1, h_1 >) \tag{16}$$

$$Q_2 = ([\overline{c}_2, \overline{s}_2 k], < l_2 c_2, l_2 s_2, 0 >) \tag{17}$$

$$Q_3 = ([1, 0], < 0, 0, -d_3 >) \tag{18}$$

$$Q_4 = ([\overline{c}_4, -\overline{s}_4 k], < 0, 0, 0 >) \tag{19}$$

$$Q_5 = ([\overline{c}_5, -\overline{s}_5 j], < 0, 0, 0 >) \tag{20}$$

$$Q_6 = ([\overline{c}_6, -\overline{s}_6 k], < 0, 0, 0 >) \tag{21}$$

Where, $\overline{\theta}_i$, $\overline{s}_i$, $\overline{c}_i$, s_i and c_i represent $\theta_i / 2$, $\sin(\theta_i / 2)$, $\cos(\theta_i / 2)$, $\sin(\theta_i)$ and $\cos(\theta_i)$, respectively. Their inverse solutions can be achieved by the equation (11).

The equations can be achieved by (14) as follows:

$$S_6 = Q_6 = ([\overline{c}_6, -\overline{s}_6 k], < 0, 0, 0 >) \tag{22}$$

$$S_5 = Q_5 S_6 = ([\overline{c}_5 \overline{c}_6, < \overline{s}_5 \overline{s}_6, -\overline{s}_5 \overline{s}_6, -\overline{c}_5 \overline{s}_6 >], < 0, 0, 0 >) \tag{23}$$

$$S_4 = Q_4 S_5 = ([S_{41}, < S_{42}, S_{43}, S_{44} >], < 0, 0, 0 >) \tag{24}$$

where,

$$S_{41} = \overline{c}_5 \overline{c}_{(4+6)} = \cos(\theta_5 / 2)\cos(\theta_4 / 2 + \theta_6 / 2),$$

$$S_{42} = -\overline{s}_5 \overline{s}_{(4-6)} = -\sin(\theta_5 / 2)\sin(\theta_4 / 2 - \theta_6 / 2),$$

$$S_{43} = -\overline{s}_5 \overline{c}_{(4-6)} = -\sin(\theta_5 / 2)\cos(\theta_4 / 2 - \theta_6 / 2),$$

$$S_{44} = -\overline{c}_5 \overline{s}_{(4+6)} = -\cos(\theta_5 / 2)\sin(\theta_4 / 2 + \theta_6 / 2).$$

$$S_3 = Q_3 S_4 = ([S_{31}, < S_{32}, S_{33}, S_{34} >], < 0, 0, -d_3 >) \tag{25}$$

Where $S_{31} = S_{41}, S_{32} = S_{42}, S_{33} = S_{43}, S_{34} = S_{44}$.

$$S_2 = Q_2 S_3 = ([S_{21}, < S_{22}, S_{23}, S_{24} >], < l_2 c_2, l_2 s_2, -d_3 >) \tag{26}$$

where, $, S_{22} = \overline{s}_5 \overline{s}_{2-4+6}, S_{23} = -\overline{s}_5 \overline{c}_{2-4+6}$ 和 $S_{24} = \overline{c}_5 \overline{s}_{2-4-6}$.

$$S_1 = Q_1 S_2 = ([S_{11}, < S_{12}, S_{13}, S_{14} >], < S_{15}, S_{16}, h_1 - d_3 >) \tag{27}$$

where, $S_{11} = \overline{c}_1\overline{c}_5\overline{c}_{(2+4+6)} - \overline{s}_1 S_{24}$, $S_{12} = \overline{s}_5\overline{s}_{1+2-4+6}$, $S_{13} = -\overline{s}_5\overline{c}_{1+2-4+6}$,
$S_{14} = \overline{c}_1 S_{24} + \overline{s}_1\overline{c}_5\overline{c}_{2+4+6}$, $S_{15} = l_2 c_{1+2} + l_1 c_1$ and $S_{16} = l_2 s_{1+2} + l_1 s_1$.

$$L_1 = ([w, < a, b, c >], < p_x, p_y, p_z >) \tag{28}$$

L_2 can be achieved by (15),

$$L_2 = Q_1^{-1} L_1 = ([L_{21}, < L_{22}, L_{23}, L_{24} >], < L_{25}, L_{26}, p_z - h_1 >) \tag{29}$$

where, $L_{21} = w\overline{c}_1 + c\overline{s}_1$, $L_{22} = a\overline{c}_1 + b\overline{s}_1$, $L_{23} = b\overline{c}_1 - a\overline{s}_1$, $L_{24} = c\overline{c}_1 - w\overline{s}_1$,
$L_{25} = p_x c_1 - l_1 + p_y s_1$ and $L_{26} = p_y c_1 - p_x s_1$.

$$L_3 = Q_2^{-1} L_2 = ([L_{31}, < L_{32}, L_{33}, L_{34} >], < L_{35}, L_{36}, p_z - h_1 >) \tag{30}$$

where $L_{31} = \overline{c}_2 L_{21} + c(\overline{s}_2\overline{c}_1) - w(\overline{s}_2\overline{s}_1)$, $L_{32} = \overline{c}_2 L_{22} + \overline{s}_2 L_{23}$, $L_{33} = \overline{c}_2 L_{23} - \overline{s}_2 L_{22}$,
$L_{34} = \overline{c}_2 L_{24} - \overline{s}_2 L_{21}$, $L_{35} = p_x c_{1+2} - l_2 + p_y s_{1+2} - l_1 c_2$, $L_{36} = p_y c_{1+2} - p_x s_{1+2} + l_1 s_2$.

$$L_4 = Q_3^{-1} L_3 = ([L_{41}, < L_{42}, L_{43}, L_{44} >], < L_{45}, L_{46}, L_{47} >) \tag{31}$$

where, $L_{41} = \overline{c}_2 L_{21} + c(\overline{s}_2\overline{c}_1) - w(\overline{s}_2\overline{s}_1)$, $L_{42} = \overline{c}_2 L_{22} + \overline{s}_2 L_{23}$, $L_{43} = \overline{c}_2 L_{23} - \overline{s}_2 L_{22}$,
$L_{44} = \overline{c}_2 L_{24} - \overline{s}_2 L_{21}$, $L_{45} = p_x c_{1+2} - l_2 + p_y s_{1+2} - l_1 c_2$, $L_{46} = p_y c_{1+2} - p_x s_{1+2} + l_1 s_2$
and $L_{47} = d_3 - h_1 + p_z$.

θ_2, θ_1 and d_3 can be achieved according to the equal relationship between S_1, S_2, S_3 and L_1, L_2, L_3.

$$\theta_2 = \arctan 2(\pm\sqrt{1-a^2}, a) \tag{32}$$

where, $a = \dfrac{p_x^2 + p_y^2 - l_2^2 - l_1^2}{2 l_1 l_2}$.

$$\theta_1 = \arctan(\frac{-p_x}{p_y}) \pm \arctan(\frac{\sqrt{p_x^2 + p_y^2 - (l_2 s_2)^2}}{l_2 s_2}) \tag{33}$$

$$d_3 = h_1 - p_z \tag{34}$$

According to the equal relationship between S_4 and L_4, the equations can be achieved as follows:

$$\overline{s}_5^2 = L_{42}^2 + L_{43}^2 \tag{35}$$

$$\overline{c}_5^2 = L_{41}^2 + L_{44}^2 \tag{36}$$

$$\tan(\overline{\theta}_4 + \overline{\theta}_6) = -\frac{L_{44}}{L_{41}} \tag{37}$$

$$\tan(\overline{\theta}_4 - \overline{\theta}_6) = \frac{L_{42}}{L_{43}} \tag{38}$$

where, $\overline{c}_5\overline{c}_{(4+6)} = L_{41}, -\overline{s}_5\overline{s}_{(4-6)} = L_{42}, -\overline{s}_5\overline{c}_{(4-6)} = L_{43}$ and $-\overline{c}_5\overline{s}_{(4+6)} = L_{44}$.

Above all, θ_4, θ_5 and θ_6 can be achieved.

$$\theta_4 = \arctan(-\frac{L_{44}}{L_{41}}) + \arctan(\frac{L_{42}}{L_{43}}) \tag{39}$$

$$\theta_5 = \arctan 2(\pm\sqrt{L_{42}^2 + L_{43}^2}, \sqrt{L_{41}^2 + L_{44}^2}) \tag{40}$$

$$\theta_6 = \arctan(-\frac{L_{44}}{L_{41}}) - \arctan(\frac{L_{42}}{L_{43}}) \tag{41}$$

Set $L_1 = ([5, <10, 25, 30>] < 10, 15, 25>)$, $l_1 = 100$, $l_2 = 300$, $h_1 = 400$.

So the inverse solutions of 6-DOF robot manipulator can be achieved in Fig.2.

θ_1 /rad	θ_2 /rad	d_3 /mm	θ_4 /rad	θ_5 /rad	θ_6 /rad
0.9828- 3.7881i	3.1416- 1.0945i	375	-0.4255 -3.0915i	0.2119- 0.1407i	0.9723+ 1.7911i
-2.1588 +3.7881i	3.1416- 1.0945i	375	1.1191+ 0.7214i	0.1724- 0.1962i	-0.6246 -1.9733i
0.9828- 3.7881i	-3.1416 +1.0945i	375	-0.4255 -0.9025i	0.2119- 0.1407i	0.9723+ 1.7911i
-2.1588 +3.7881i	-3.1416 +1.9045i	375	1.1192+ 2.9109i	0.1726- 0.1964i	-0.6246 -1.9733i
0.9828- 3.7881i	3.1416- 1.0945i	375	-0.4255 -3.0915i	-0.2119 +0.1407i	0.9723+ 1.7911i
0.9828- 3.7881i	-3.1416 +1.0945i	375	-0.4255 -0.9025i	-0.2119 +0.1407i	0.9723+ 1.7911i
-2.1588 +3.7881i	3.1416- 1.0945i	375	1.1191+ 0.7214i	-0.1724 +0.1962i	-0.6246 -1.9733i
-2.1588 +3.7881i	-3.1416 +1.0945i	375	1.1192+ 2.9109i	-0.1726 +0.1964i	-0.6246 -1.9733i

Fig. 2. All the inverse solutions of robot manipulator

5 Conclusion

This paper proposes a new method for the inverse kinematic of 6-DOF manipulator based on dual quaternion which use dual quaternion to denote the revolute joints of

robot manipulator through the transform relationship between them. To achieve the inverse solutions of robot manipulator, this paper uses the characteristic of dual quaternion. The simulation has been provided to verify the feasibility and precision of the proposed new method.

References

1. Liu, D., Wang, T.: Algorithm combined analytical and numerical solutions for robot inverse kinematics. Journal of Beijing University of Aeronautics and Astronautics 33(6), 727–730 (2007) (in Chinese)
2. Angeles, J.: On the numerical solution for inverse kinematics problem. Int J. Robotics Research 4(2), 21–37 (1985)
3. Xu, J., Wang, W.: Two optimization algorithm for solving robotics inverse kinematics with redundancy. In: IEEE International Conference on Control and Automation, ICCA 2007, pp. 3021–3028 (2007)
4. Du, Y., Wu, Y.: Application of IPSO algorithm to inverse kinematics solution of reconfigurable modular robots. In: 2011 International Conference on Mechatronic Science, Electric Engineering and Computer, pp. 19–22 (2011)
5. Shen, X.-N., Li, S.: Multi-object Genetic Algorithm for Inverse Kinematics Problem of Redundant Manipulator. Journal of System Simulation 20(2), 399–403 (2008) (in Chinese)
6. Bi, Z., Cai, H.: Inverse Kinematics Problem of 6-DOF Manipulator. Robot 16(2), 92–97 (1994)
7. Ni, Z., Liao, Q.: Dual Four Element Method for Inverse Kinematics Analysis of Spatial 6R Manipulator. Journal of Mechanical Engineering 11(45), 25–29 (2009) (in Chinese)
8. Mandic, D.P., Jahanchahi, C.: A quaternion gradient operator and its application. IEEE Signal Processing Letters 1(18), 47–50 (2011)
9. Pham, H.-L., Predereau, V.: Position and orientation control of robot manipulators using dual quaternion feedback. Intelligent Robots and System(IROS), 658–663 (2010)
10. Caccavale, F., Siciliano, B.: Quaternion-based kinematic control of redundant spacecraft/manipulator system. In: Proceedings of the 2001 IEEE International Conference on Robotics and Automation, pp. 435–440 (2001)

A New Algorithm for Evolutionary Structural Optimization in Mechanical Engineering

HongYu Jiao[1,2], QiCai Zhou[1], WenJun Li[1], and Ying Li[2]

[1] College of Mechanical Engineering, Tongji University, 201804, ShangHai, China
[2] College of Mechanical Engineering, Changshu Institute of Technology, 215500, SuZhou, China

Abstract. In this paper, a new algorithm for evolutionary structural optimization is proposed. At each iteration, a more optimal design will be obtained by continuously removing low-stress elements with certain proportion. The amount of removed elements is controlled by a single parameter: the reference Von Mises stress. The convergence of the iteration is determined by a performance index of the structure. It is found that the proposed ESO algorithm has many advantages over the classical ESO and FG ESO in term of efficiency and robustness.

Keywords: evolutionary structural optimization, optimal design, the reference Von Mises stress.

1 Introduction

In 1993, Xie.Y.M and G.P.Steven introduced an approach called evolutionary structural optimization (ESO) [1]. ESO is based on the simple idea that the optimal structure can be produced by gradually removing the ineffective material from the design domain. ESO has been received extensive attention because it can be easily implemented and linked to existing finite element analysis packages [2-5]. Also, the resulting optimal design provides a clear profile to topology and therefore easy to manufacture.

Y.M.Xie and G.P.Steven adopt a parameter which is rejection ratio. RR is defined in the form of a polynomial as equation (1). The method adopts polynomial to form RR, but the related coefficient is difficult to choose during the optimization process.

$$RR = a_0 + a_1 \times SS + a_2 \times SS^2 + a_3 \times SS^3 \quad , \tag{1}$$

where RR is rejection ratio. a_0, a_1, a_2, a_3 are specified according to experience. SS is steady state number.

H.Kim and M.J.Garcia develop a faster and improved structural optimization method [6-8] which combines fixed finite element analysis (FG FEA) and evolutionary structural optimization (ESO). ESO optimizes a structure by removing a few elements at each iteration. FG methods allow fast mesh generation, fast solution and fast re-evaluation of the modified meshes. The implementation of FG into the ESO process which is called FG ESO eliminates the need for regenerating the mesh and a few arithmetic calculations replace the full regeneration of the stiffness matrix every time when the structure is modified [9-10]. This greatly reduces the solution time. But it will lead to require too many iterations because of a low RR value.

D. Jin and S. Lin (Eds.): Advances in Mechanical and Electronic Engineering, LNEE 176, pp. 303–309.
springerlink.com

In this paper, a new algorithm for evolutionary structural optimization method is imposed. At each iteration, a more optimized structure will be obtained by continuously deleting low-stress elements with certain proportion. The amount of removed material is controlled by a single parameter: the reference Von Mises stress σ_{ref}^{k}.The reference Von Mises stress σ_{ref}^{k} is determined by the maximum Von Mises stress $\sigma_{\max}^{k}$, the minimum Von Mises stress $\sigma_{\min}^{k}$ and the removal percent of volume V_{rp}.

In the new ESO method, a convergence criterion based on a performance index is introduced to monitor and ultimately to terminate the optimization process. The new ESO algorithm is very effective in significantly improving performance index of structure. An example in this paper shows that the proposed ESO algorithm has many advantages over the classical ESO and FG ESO in term of efficiency and robustness.

2 Optimization Model of ESO

The problem of topology optimization with stress constraints for continuum structures may be stated mathematically as equations (2).

$$Find \qquad X = \{x_1, x_{2,} \ldots, x_n\} \tag{2.a}$$

$$Minimize \qquad f(x) = \sum_{i=1}^{n} x_i w_i \tag{2.b}$$

$$Subject \quad to \quad \sigma \le \sigma_{\max}^{*} \tag{2.c}$$

$$x_i \in \{0,1\}, \quad i = 1,2, \ldots, n \tag{2.d}$$

where $f(x)$ is the objective function and X is the vector of design variables. The binary design variable x_i declares the absence (0) or presence (1) of an element. w_i is the volume or weight of the ith element. $\sigma_{\max}^{*}$ is the maximum Von Mises stress which the structure is allowed. n is the number of elements in domain.

3 New Algorithm for ESO

For isotropic material, Von Mises criterion is used to evaluate. The Von Mises stress of each element can be calculated by equation (3).

$$\sigma = \sqrt{(\sigma_x^2 + \sigma_y^2) - \sigma_x \sigma_y + 3\tau_{xy}^2} \tag{3}$$

At each iteration, the maximum Von Mises stress $\sigma_{\max}^{k}$ and the minimum Von Mises stress $\sigma_{\min}^{k}$ are collected to calculate the stress range σ^{k} as equation (4).

$$\sigma^{k} = \sigma_{\max}^{k} - \sigma_{\min}^{k} \tag{4}$$

where $\sigma_{\max}^k$ is the maximum Von Mises stress at k th iteration. $\sigma_{\min}^k$ is the minimum Von Mises stress at k th iteration. σ^k is the range of Von Mises stress at k th iteration.

The range of Von Mises stress at k th iteration is divided into 100 intervals. Each interval is defined as equation (5).

$$l^k = \frac{\sigma^k}{100} = \frac{\sigma_{\max}^k - \sigma_{\min}^k}{100} \tag{5}$$

Function $ff(j)$ is defined as equation (6). When $j=0$, $ff(0)=\sigma_{\min}^k$ .When $j=100$, $ff(100)=\sigma_{\max}^k$. It means that function $ff(j)$ varies from $\sigma_{\min}^k$ to $\sigma_{\max}^k$ when j varies 0 to 100.

$$ff(j) = \sigma_{\min}^k + j \times l^k \quad j = 0,1,2,3\ldots,100 \tag{6}$$

Elements can therefore be chose if they satisfy equation (7) and m is the number of elements which satisfy equation (7).

$$\sigma_i \le ff(j) \qquad i = 0,1,2,3\ldots\mathrm{m} \tag{7}$$

Function $V_{rp}(j)$ is defined as equation (8) which is the percent of volume which satisfy equation (7).

$$V_{rp}(j) = \frac{m}{n^k} \quad , \tag{8}$$

where n^k denotes the total number of elements at k th iteration.

The relation between $V_{rp}(j)$ and j is fitting in the form of a polynomial as equation (9).

$$f(j) = V_{rp}(j) = a_0 + a_1 j + a_2 j^2 + \ldots + a_n j^n \tag{9}$$

At each iteration, low-stress elements with certain percent are removed. When the removal percent of volume (V_{rp}) equals to a constant, the variable j is solved as equation (10).

$$j = f^{-1}(V_{rp}) \tag{10}$$

The relation between the reference Von Mises stress σ_{ref} and j is represented as equation (11).

$$\frac{\sigma_{\text{ref}} - \sigma_{\min}^k}{\sigma_{\max}^k - \sigma_{\min}^k} = j \quad , \tag{11}$$

where σ_{ref} is the reference von Mises stress.

The reference von Mises stress σ_{ref} is calculated as equation (12).

$$\sigma_{ref}^k = \sigma_{\min}^k + f^{-1}(V_{rp}) \times (\sigma_{\max}^k - \sigma_{\min}^k) \tag{12}$$

At each iteration, the i th element is removed if the Von Mises stress of the i th element satisfies equation (13).

$$\sigma_i \le \sigma_{ref}^k \tag{13}$$

4 Performance Index and Convergence Criterion

Performance index (PI) can be introduced to identify the performance of various optimal designs. Thus, the definition of the performance index should be directly related to the optimization objective. In the present case, the performance index is defined as equations (14).

$$PI^k = M_0 / M_k \quad k = 1,2,3,\ldots \tag{14.a}$$

$$M^k = \sum_{i=1}^{n} \frac{\sigma_i^k}{\sigma_{\max}^k} v_i^k \tag{14.b}$$

$$M_0 = \sum_{i=1}^{n} \frac{\sigma_i^0}{\sigma_{\max}} v_i^0 \tag{14.c}$$

When the structure satisfies the convergence criterion defined as equation (15), an optimum for the present removal ratio of volume is assumed to be obtained.

$$error_k = \frac{|PI_k - PI_{k-1}|}{PI_k} \le error \tag{15}$$

5 Example

The classic Michell type structure is fixed at both supports as shown in Fig.1.The dimensions of the rectangular domain are 200 mm by 100 mm. The thickness of the plate is 1 mm. A 100 N concentrated force is applied at the center of bottom edge. The linear material is used with Young's modulus E=210 GPa and Poisson's ratio v=0.3. The ESO parameters are set to be V_{rp} =0.02 and $error = 0.001$.

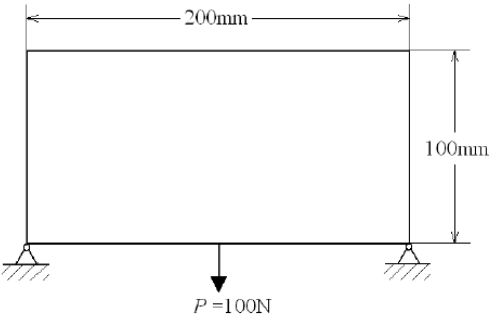

Fig. 1. Design domain of a Michell type structure

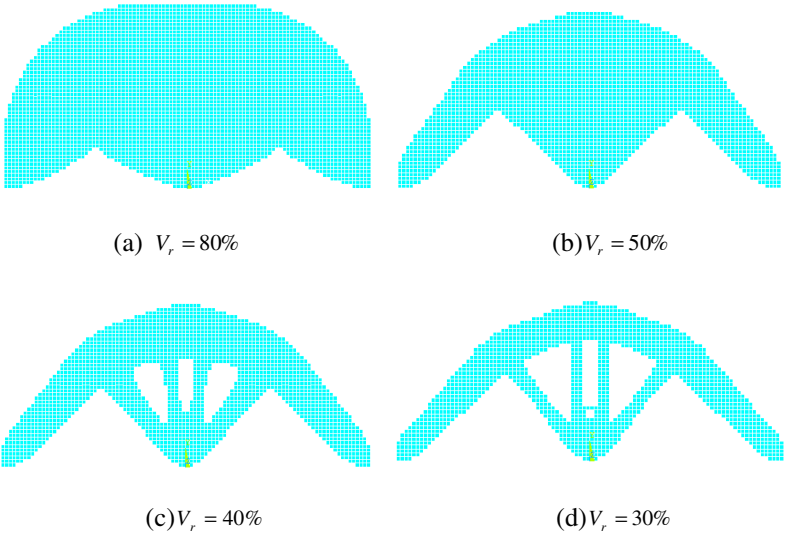

Fig. 2. Optimal designs with various volume ratio: (a) $V_r = 80\%$; (b) $V_r = 50\%$; (c) $V_r = 40\%$;(d) $V_r = 30\%$;

The evolutionary history of the structure is shown in Fig.2 (a)-(d) with various volume ratio V_r .Fig.3 shows the history of the performance index of optimums during the whole evolution processes. The performance index increases continuously until the final remained volume arrives. The highest performance index of the design is 3.050114. Thus, the performance of the design improves significantly comparing with the initial full design with $PI = 1$.

During the optimization process, low-stress elements with certain proportion are removed at each iteration. The number of removed elements decreases smoothly as the increasing of iteration shown in Fig.4, which leads to the stable descending of the volume ratio in Fig.5. It is exactly what we are looking for.

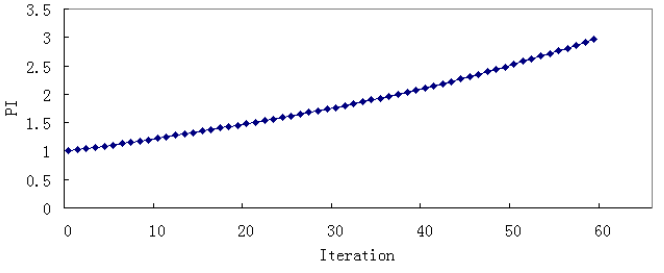

Fig. 3. Evolutionary history of the performance index

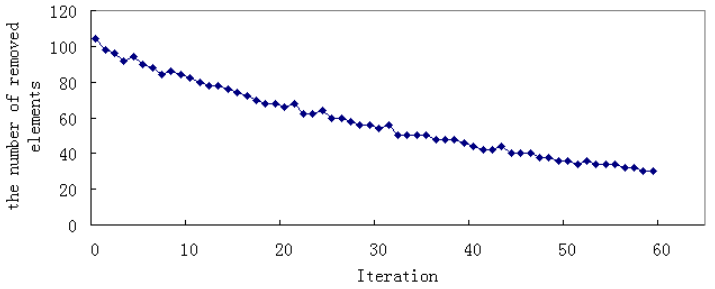

Fig. 4. Evolutionary history of the number of removed elements

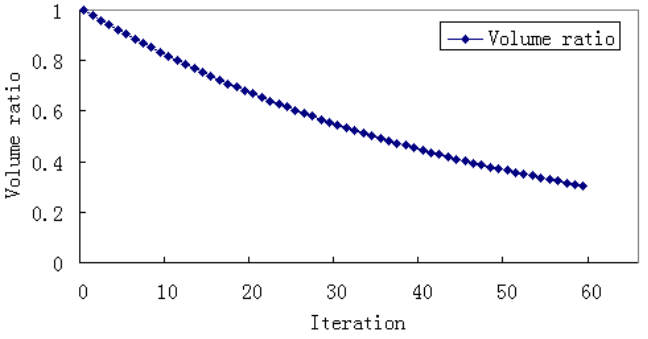

Fig. 5. Evolutionary history of volume ratio

The maximum Von Mises stress increases slowly from 29.90013 MPa to 33.144427 MPa and the minimum Von Mises stress increases slowly from 0.002448 MPa to 1.490636 MPa. It can be seen that the minimum Von Mises stress increases shown in Fig.5 because the elements on low-stress region are removed.

6 Conclusion

In this paper, a new algorithm for evolutionary structure optimization has been developed. An example has demonstrated the capability of the new ESO method to optimize a structure by removing material. The developed ESO method has several advantages over classical ESO and FG ESO:

1. The removing of material is controlled by a single parameter: the reference Von Mises stress.
2. During the optimization process, low-stress elements with certain proportion are removed at each iteration.
3. The proposed ESO method is more efficient than the classical ESO and FG ESO because of relatively few iterations.

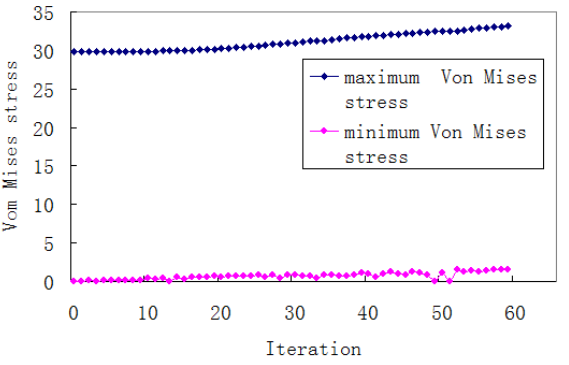

Fig. 6. Evolutionary history of Von Mises stress

References

1. Xie, Y.M., Steven, G.P.: A simple Evolutionary Procedure for Structural Optimization. Comput. Struct. 49, 885–896 (1993)
2. Ansola, R., Veguería, E.: A simple evolutionary topology optimization procedure for complicant mechanism design. Finite Elements in Analysis and Design 44, 53–62 (2007)
3. Huang, X., Xie, Y.M., Burry, M.C.: A new algorithm for Bi-directional evolutionary structural optimization. JSME International Journal 49, 1091–1099 (2006)
4. Jia, H., Beom, H.G.: Evolutionary level set method for structural topology optimization. Computers and Structures 89, 445–454 (2011)
5. Xie, Y.M., Huang, X.: Recent development in evolutionary structural optimization for continuum structures. IOP Science (2010)
6. Querin, Q.M., Steven, G.P., Xie, Y.M.: Evolutionary Structural Optimisation by an Additive Algorithm. Finite Elements Anal. Design 34, 291–308 (2000)
7. Tanskanen, P.: The Evolutionary structural optimization method: theoretical aspects. Comput. Methods Appl. Mech. Engrg. 191, 5485–5498 (2002)
8. Kim, H., Garcia, M.J.: Introduction of fixed grid in evolutionary structural optimisation. Engineering Computations 17, 427–429 (2000)
9. GarcõÂa, M.J.: Fixed grid finite element analysis in structural design and optimisation, PhD thesis, University of Sydney, Australia
10. GarcõÂa, M.J., Steven, G.P.: Displacement error for fixed grid FEA elasticity problems. In: GarcõÂa, M.J., Steven, G.P. (eds.) 3rd Colombian Congress in Finite Elements, Medellin (1996)

Numerical Simulation and Optimization of Centrifugal Fan

Tao Sun, Yu Li, YueHan Xu, and ZhongYi Wang

College of Power and Energy Engineering, Harbin Engineering University, Harbin, China
{suntao01,yuehanxu}@yahoo.com.cn, 471646757@qq.com, wzy@hrbeu.edu.cn

Abstract. The centrifugal fan is a kind of turbo machinery. It is widely used in ventilating and refrigerating of buildings, mines, factories, tunnels, vehicles, watercrafts and refrigerant towers; drying and selecting of corn; charging and advancing of hovercrafts and so on. Comparing with axial fan, it has advantages of volume and weight. In this paper the inner flow field in the centrifugal fan is numerically simulated and its flow characteristics are analyzed, based on the high pressure centrifugal fan 9-16№15.9D.

Keywords: centrifugal fan, numerical simulation, standard k-ε turbulent model, blade shape.

1 Introduction

High-pressure centrifugal fan is made of air inlet, impeller group, scroll Group.[1] In order to make the import and export of boundary conditions more consistent with actual and inlet airflow more stable and uniform, we add an extension in both imports and exports region.[2]

Impeller is the core of the centrifugal fan. The structural parameters of the impeller plays a key role for its efficiency.[3] And the blade is the key to the core. Therefore, this article will try to optimize the blades so that its efficiency can be improved.[4]

After analysis the numerical simulation results of centrifugal fan with the original blade-shaped, it's found that there is a negative pressure zone in the suction surface at the impeller inlet. The specificity of this region have a great relationship with the shape of the blade imports.[5]

The blade type is changed to what is shown in Figure 1. Without changing the blade inlet angle and outlet angle, the curvature of the blade is reduced so that air can flow more stably.

2 Numerical Simulation Scheme

In order to calculate centrifugal fan, we need to build three parts of physical model consists of air inlet, impeller group, scroll group. According to the calculation of the

D. Jin and S. Lin (Eds.): Advances in Mechanical and Electronic Engineering, LNEE 176, pp. 311–315.
springerlink.com

actual needs and a series of Boolean operations to simplify, finally we get the flow path as Figure 1 shows.

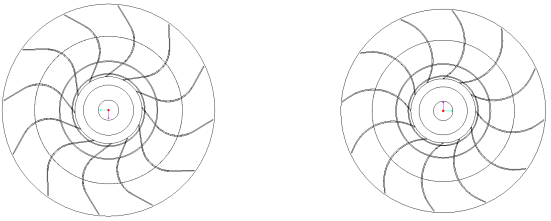

(a) Before improved (b) After improved

Fig. 1. The shape of blades

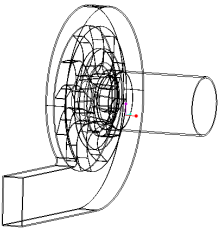

Fig. 2. Computed field

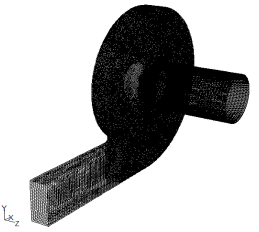

Fig. 3. Girds of computed field

The girds of computed field are shown in figure 3. The computed field is divided by unstructured grids and more girds are placed in where the fluid velocity changes violently in order to improve the accuracy.

Boundary Conditions

Inlet: pressure-inlet; total pressure is zero ; the temperature is set to the default.

Outlet: pressure-outlet; outlet temperature is set to default.

3 Numerical Simulation Results

Keep all other conditions remain unchanged, we do the numerical simulation again and calculate and compare the results. In the same flow rate, we analysis the total pressure contour in the middle surface of the impeller (z = 106mm) .After improved, total pressure increased at the inlet of centrifugal impeller, and negative pressure area reduced a lot.[6] After improved, total pressure distribution is more stable and pressure loss has also been reduced, as Figure 4 showed.

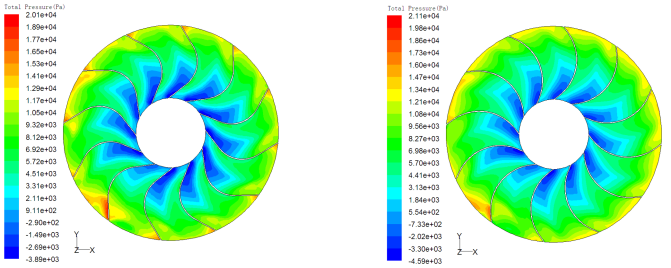

(a) Before improved (b) After improved

Fig. 4. Total pressure contours of impeller mid-plane (Z= 106mm)

Before Improved, the maximum of turbulence intensity appear in the impeller inlet. However, after improved, although the maximum turbulence intensity is still in the impeller inlet, but the area of high turbulence intensity decreased a lot, it has become very small, the turbulence intensity of impeller also declined. Overall, the improved strength of the turbulence, in addition to several larger near the exit of volute, the remaining is declined. It also shows the feasibility of improving the shape of blades. Changes on blade shape are mainly for the negative pressure area and low speed area of the impeller. Now we can see from the diagram, area of turbulence intensity reduced significantly in the main research areas.

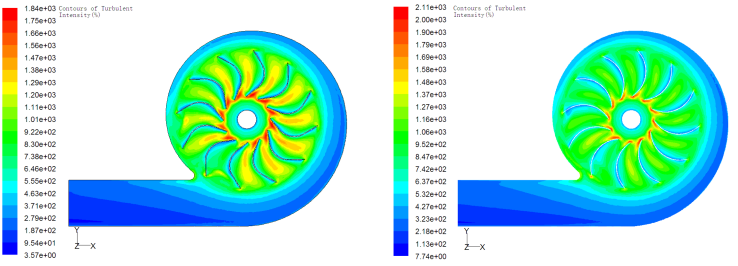

(a) Before improved (b) After improved

Fig. 5. Turbulence intensity in the middle section (z = 106mm)

4 Experimental Study and Analysis

The performance curve shoes that, total pressure, internal efficiency and internal efficiency are all turned better in improved centrifugal fan. [7] This shows that in the same conditions blade which is improved is better than the original one. From the flow rate - total pressure characteristic curve we can see, total pressure goes down when traffic increase. In the improved blade centrifugal fan, the whole pressure has increased. This part of total pressure is mainly coming from the reduction of losses in the entrance.

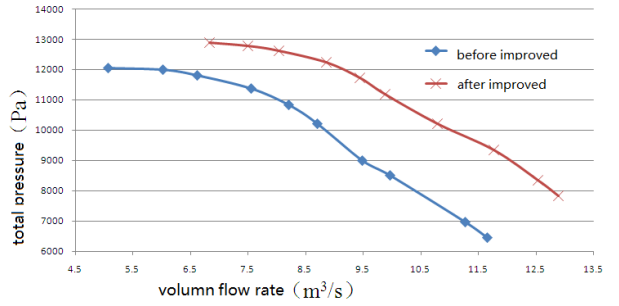

(a) Flow and total pressure of the characteristic curve

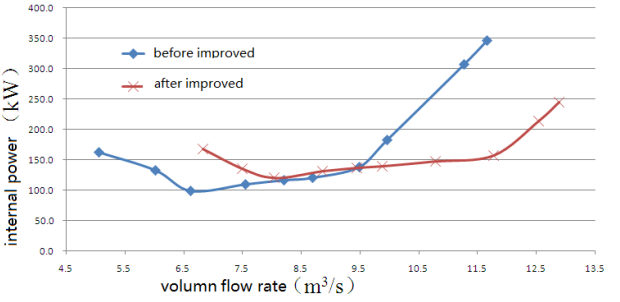

(b) Traffic and internal power curve

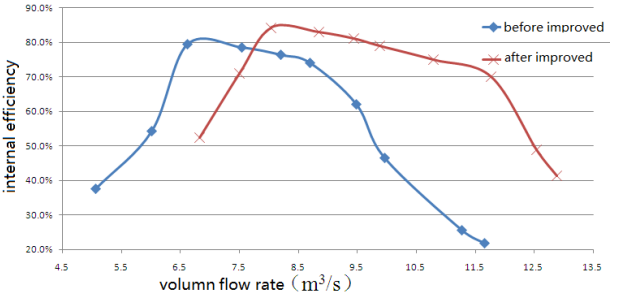

(c) Flow and internal efficiency curves

Fig. 6. Centrifugal fan performance curves

5 Conclusion

Based on above statements, we could see the fan's ability had an obvious improvement after blade improved. With total pressure increased, the total pressure loss of imports has also been reduced. Internal efficiency is much better than original type especially at the large flow of time. It can be seen that optimal improvement is effective and provide a certain basis for future improvement and optimization.

References

[1] Shen, T.Y.: Centrifugal impeller flow theory. Zhejiang University Press, Zhejiang (1986)
[2] Wu, Y., Chen, Q., Liu, S.R.: Ventilators and compressors. Tsinghua University Press, Beijing (2005)
[3] Zhu, C., Xiaodong other side: Centrifugal fan impeller channel simulation and its applications. Mechanics and Engineering - Du Qinghua Academy to Celebrate 80th Birthday Anthology 4, 423–431 (1994)
[4] He, H.: Centrifugal fan the whole flow field numerical simulation. Master Thesis (March 2001)
[5] Li, X., et al.: Centrifugal fan machine steady flow numerical simulation. Engineering Thermophysics 23(4), 450–463 (2002)
[6] Area Yingda, C.-I.: Cabinet with multi-blade centrifugal fan air flow field numerical simulation. Fan Technology 4, 22–25 (2004)
[7] Li, Z., et al.: Within the centrifugal turbo machinery unsteady flow numerical calculation. Fan Technology (4), 10–16 (2004)

High-Performance Speed Control of Permanent Magnet Synchronous Motors Using Extended Kalman Filter

XinZhong Ding[1], ChengRui Zhang[1], HuXiu Li[1], and LeHua Yu[2]

[1] School of Mechanical Engineering, Shandong University, Jinan, 250061, China
[2] School of Control Science and Engineering, Shandong University, Jinan 250061, China
{xinzhong.ding,zhangchengrui}@gmail.com

Abstract. When a low-resolution photoelectric encoder was used for the speed detection, only the average speed during the sampling period can be obtained. Under low-speed conditions, detection lag makes the speed controller unstable. This paper presents a novel permanent magnet synchronous motor (PMSM) drive technique using an optimal state estimator for high-performance speed control. In the proposed algorithm, a state estimator based on the extended Kalman filter (EKF) was used to provide exact estimation for instantaneous currents, speed, position and disturbance load torque in a random noisy environment. Then, the anti-disturbance ability and the robustness to variations of the mechanical parameters were studied. Finally, an experimental platform was built to verify the efficiency of this method. The results show a precise speed control over a wide range of speeds and the proposed system is robust to modeling error and system noise.

Keywords: extended Kalman filter, state estimator, permanent magnet synchronous motor, speed control.

1 Introduction

Precise speed control through correct speed detection is an essential requirement in the field of high-performance motion control such as robotics and machine tool applications. An ordinary speed feedback signal is easily lost during the sampling interval, especially in a low-speed range. Recently, the instantaneous observer theory has been developed to obtain the motor speed in the low-speed region [1-4]. However, the observers do not have good noise-rejection properties in a noisy environment and may fail to find a stable position and detect the speed [5].

The Kalman filter is a random state estimator which possesses smoothing properties and noise-rejection capability to the system and measurement noise. In this paper, a new speed control technique using an EKF state estimator for wide-speed operation was presented. The estimator was used to estimate the output currents, angular velocity, angular position and the disturbance torque instantaneously. Experiments were carried out to show the effectiveness of the proposed estimator at very low speed with the low-resolution quadrature encoder of 1024 pulse per revolution (p/r) mounted on the PMSM.

D. Jin and S. Lin (Eds.): Advances in Mechanical and Electronic Engineering, LNEE 176, pp. 317–322.
springerlink.com

2 Adaptive State Estimator

2.1 Modeling of State Estimator

The unsaturated electrical model of the PMSM is expressed in the following formulas

$$\frac{\mathrm{d}i_\alpha}{\mathrm{d}t} = -\frac{R_s}{L_s} i_\alpha + \omega_e \frac{\psi_f}{L_s} \sin\theta_e + \frac{u_\alpha}{L_s}$$

$$\frac{\mathrm{d}i_\beta}{\mathrm{d}t} = -\frac{R_s}{L_s} i_\beta - \omega_e \frac{\psi_f}{L_s} \cos\theta_e + \frac{u_\beta}{L_s}. \tag{1}$$

Where, i_α, i_β, u_α and u_β are the αβ-components of the stator currents and voltages; R_s, L_s are the stator resistance and inductance; ψ_f is the permanent magnet flux linkage; ω_e is the rotor electrical angular velocity; θ_e is the rotor electrical angular displacement.

According to Newton's law, the dynamic torque balance equation is expressed by the following

$$\frac{\mathrm{d}\omega_e}{\mathrm{d}t} = \frac{n_p}{J}\left(T_e - \frac{B}{n_p}\omega_e - T_l\right). \tag{2}$$

Where, n_p is the number of pole pairs; J is the system inertia moment including rotor and load inertia; B is the viscous friction coefficient; T_e is the electromagnetic torque developed by the motor; T_l is the equivalent load torque.

The equivalent load torque T_l is introduced as an augmented state variable which includes the variations in the nonlinear viscous friction torque and the torque due to the torque constant variation [6]. Since the sampling frequency of the current loop is much higher than that of the equivalent load torque variation. Thus

$$\frac{\mathrm{d}T_l}{\mathrm{d}t} = 0. \tag{3}$$

Combining (1), (2) and (3), the state equations are given by the following

$$\frac{\mathrm{d}\boldsymbol{x}}{\mathrm{d}t} = f(x) + \boldsymbol{B}_e\boldsymbol{u}$$

$$\boldsymbol{y} = \boldsymbol{C}_e\boldsymbol{x}. \tag{4}$$

Where

$$\boldsymbol{x}=\begin{pmatrix} i_\alpha & i_\beta & \omega_e & \theta_e & T_l \end{pmatrix}^{\mathrm{T}}, \boldsymbol{u}=\begin{pmatrix} u_\alpha & u_\beta & T_e \end{pmatrix}^{\mathrm{T}}, \boldsymbol{y}=\begin{pmatrix} i_\alpha & i_\beta & \theta_e \end{pmatrix}^{\mathrm{T}}$$

$$f(x)=\begin{pmatrix} -\frac{R_s}{L_s}i_\alpha+\omega_e\frac{\psi_f}{L_s}\sin\theta_e \\ -\frac{R_s}{L_s}i_\beta-\omega_e\frac{\psi_f}{L_s}\cos\theta_e \\ -\frac{B}{J}\omega_e-\frac{n_pT_l}{J} \\ \omega_e \\ 0 \end{pmatrix}, \boldsymbol{B_e}=\begin{pmatrix} \frac{1}{L_s} & 0 & 0 \\ 0 & \frac{1}{L_s} & 0 \\ 0 & 0 & \frac{n_p}{J} \\ 0 & 0 & 0 \\ 0 & 0 & 0 \end{pmatrix}. \quad (5)$$

2.2 Currents, Speed and Torque Estimator

For a real system, the modeling inaccuracies and measurement noise should be considered for high-performance speed control. These noises are assumed to be zero-mean Gaussian white noise [7] and known covariance matrix $\boldsymbol{Q}$ and $\boldsymbol{R}$. The values for the elements of $\boldsymbol{Q}$ are determined by the uncertainties and variabilities in the system model parameters and the quantization error of continuous equations discretization. On the other hand, the elements of $\boldsymbol{R}$ depend on the quantization error of A/D conversion and shaft angular position, the accuracy of the shaft encoder and analogue noise in currents measurement. Eventually, the process for on-line estimation of discrete state variables $\boldsymbol{x}(k)$ with EKF is given by [8]

$$\tilde{\boldsymbol{x}}(k+1)=\hat{\boldsymbol{x}}(k)+T_s\left\{f\left[\hat{x}(k)\right]+\boldsymbol{B_e}\boldsymbol{u}(k)\right\}$$

$$\tilde{\boldsymbol{y}}(k+1)=\boldsymbol{C_e}\tilde{\boldsymbol{x}}(k+1)$$

$$\tilde{\boldsymbol{P}}(k+1)=\hat{\boldsymbol{P}}(k)+T_s\left[\boldsymbol{F}(k)\hat{\boldsymbol{P}}(k)+\hat{\boldsymbol{P}}(k)\boldsymbol{F}^{\mathrm{T}}(k)\right]+\boldsymbol{Q}$$

$$\boldsymbol{K}(k+1)=\tilde{\boldsymbol{P}}(k+1)\boldsymbol{C_e}^{\mathrm{T}}\left[\boldsymbol{C_e}\tilde{\boldsymbol{P}}(k+1)\boldsymbol{C_e}^{\mathrm{T}}+\boldsymbol{R}\right]^{-1}$$

$$\hat{\boldsymbol{x}}(k+1)=\tilde{\boldsymbol{x}}(k+1)+\boldsymbol{K}(k+1)\left[\boldsymbol{y}(k+1)-\tilde{\boldsymbol{y}}(k+1)\right]. \quad (6)$$

Where, $\tilde{\boldsymbol{x}}(k)$ and $\hat{\boldsymbol{x}}(k)$ are the predictive and estimated values of state variables; $\tilde{\boldsymbol{P}}(k)$, $\hat{\boldsymbol{P}}(k)$ are the predictive and estimated values of covariance matrix; T_s is the sampling period; $\boldsymbol{F}(k)$ is the gradient matrix which is given by

$$\boldsymbol{F}(k) = \left.\frac{\partial f(x)}{\partial \boldsymbol{x}}\right|_{\boldsymbol{x}=\hat{\boldsymbol{x}}(k)}.$$

From the EKF estimator, the estimated current $\hat{i}$, angular velocity $\hat{\omega}_e$ and angular displacement $\hat{\theta}_e$ are used in the current controller, speed controller and position controller as feedback values respectively. Due to the filtering action of EKF, most of the noise and ripple in feedback current is reduced, and the estimated torque $\hat{T}_l$ is used for feedforward control which can decrease the torque ripple of the motor effectively.

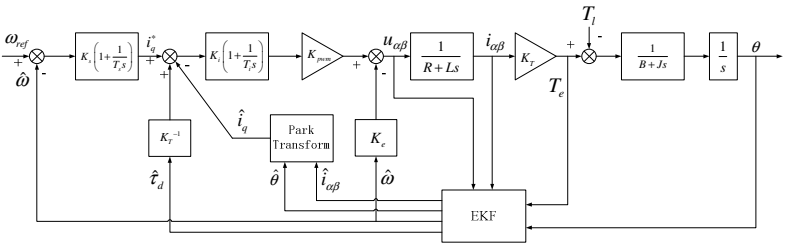

Fig. 1. Speed servo system with EKF estimator

3 Experiments

The configuration of the experimental system is shown in Fig. 2. The control system adopts all-digital architecture including the current loop, speed loop and position loop. The control of phase currents has been obtained with the field oriented control (FOC) by space vector PWM (SVPWM).

Fig. 3 shows the influence of the state estimator on speed control. Fig. 3-a represents the speed response when the speed command is ±500 rpm and the comparison between the measured speed ω_{enc} by M/T method using 1024 p/r encoder and estimated speed ω_{est} by the proposed method. It is shown that the estimated speed has smaller fluctuations and overshoots than measured speed, which gives smooth and low-noise speed feedback. Fig. 3-b is the same case as Fig. 3-a except that the speed command is ±1 rpm. In this figure, the average detection with a low-resolution encoder makes the speed response unstable due to the lack of speed information. Comparatively, the proposed method still provides a precise speed estimation and inertia identification under very low speed.

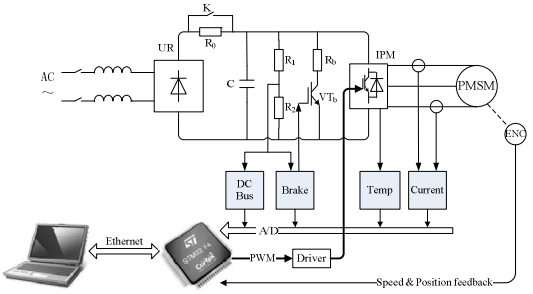

Fig. 2. Experimental configuration

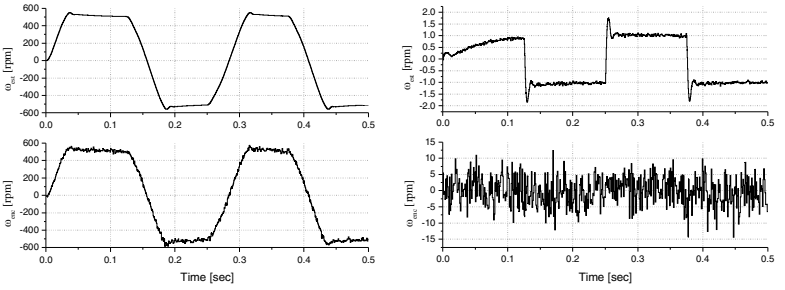

(a) (b)

Fig. 3. Speed response of the proposed estimator when speed command is a (*±500 rpm*) and b (*±1 rpm*)

4 Conclusions

This paper proposes a new PMSM drive technique using the EKF-based adaptive state estimator for high-performance speed control with a low precision quadrature encoder to estimate instantaneous currents, speed, position and disturbance load torque. The performance of the strategy has been studied by experiments. The results show that the motor can operate smoothly at 1 rpm and its speed ripple is below 0.2 rpm with fast dynamic response. The proposed strategy is also proven to have a high performance at ordinary-speed range.

Acknowledgments. This work is supported by the National Natural Science Foundation of China (Grant No. 51075241) and Scientific and Technological Projects of Shandong Province Grant of China (Grant No. 2009GG10004006).

References

1. Yang, X.H., Jiang, J.G.: Precise instantaneous speed detection for permanent magnet synchronous motors. Transactions of China Electrotechnical Society 26, 71–76 (2011)
2. Wang, M.S., Kung, Y.S., Thi, H., Chang, C.M.: Superior low-speed control of a permanent magnet synchronous motor with digital encoder. Journal of Systems and Control Engineering 225, 281 (2011)
3. De Angelo, C., Bossio, G., Solsona, J., Garcia, G.O., Valla, M.: A rotor position and speed observer for permanent-magnet motors with nonsinusoidal EMF waveform. IEEE Transactions on Industrial Electronics 52, 807–813 (2005)
4. Seung-Ho, S., Seung-Ki, S.: An instantaneous speed observer for low speed control of AC machine. In: Applied Power Electronics Conference and Expositioned, pp. 581–586. IEEE Press, California (1998)
5. Heui-Wook, K., Seung-Ki, S.: A new motor speed estimator using Kalman filter in low-speed range. IEEE Transactions on Industrial Electronics 43, 498–504 (1996)
6. Taeg-Joon, K., Dong-Seok, H.: High-performance speed control of electric machine using low-precision shaft encoder. IEEE Transactions on Power Electronics 14, 838–849 (1999)
7. Salvatore, L., Stasi, S.: Application of EKF to parameter and state estimation of PMSM drive. IEE Proceedings B Electric Power Applications 139, 155–164 (1992)
8. Wang, C., Sun, Y., Xia, J., Yang, J.: Modern Motor Control Technology. China Machine Press, Beijing (2006)

Fiber Bragg Grating Strain Sensor Applied in Security Monitoring of Road Tunnel Structure

Yan Chen[1], YongBen Lin[1], Chuan Li[1], and QingQin Li[2,*]

[1] Faculty of Information Engineering and Automation, Kunming University of Science and Technology, Kunming City, China, 650051
[2] Kunming Metallurgy College, Kunming City, China, 650033
chy01@sina.com, 154073620@qq.com

Abstract. By monitoring tunnel structure and analyzing measurement datum, structural deformation trend was predicted and the level of tunnel structure safety was evaluated in order to timely find early disease and timely warn and safeguard driving safety. Fiber Bragg grating surface strain sensors were applied in monitoring the lining cracking and the deformation of Jiulong double-arch tunnel left of Yunnan Xiao-Mo Expressway. 20 crack sections had been monitored for nearly a year. The monitoring results indicated that after temperature was compensated, the strain of Fiber Bragg grating strain sensor was in the normal range (max-243με) and indicated that tunnel structural was stability and normal in the monitoring period.

Keywords: Fiber Bragg grating, Tunnel, Lining, Strain Sensor.

1 Introduction

Road tunnel safety is related to people's life and socio-economic activities [4]. Built tunnel structure should have good carrying capacity, durability and the life of meeting the durability requirements. In General, the scale of highway tunnel engineering is larger. Some tunnel reach several kilometers to dozen kilometers and often pass through many different time domain and environmental spatial. Engineering conditions are complex. Environment's conditions are very bad. In the course of construction and operating, tunnel is influenced by various factors (such as geology, design and climatic conditions, etc). In addition, materials itself become old and maintenance is not timely. In use, [6] diseases (such as lining cracking, dislocation, falling blocks and water seepage, etc) were occurred, which endangered traffic safety and even forced the closure of traffic. Therefore, it is important to monitor tunnel structure for timely finding early diseases and for timely warning.

In this paper, fiber Bragg grating surface strain sensors was applied in monitoring the health of tunnel structure. The lining cracking and the deformation of Jiulong double-arch tunnel left-line of Yunnan Xiao-Mo Expressway were Long-term monitored. Tunnel secondary lining's structural deformation and stress were known. By analyzing measurement data, structural deformation trend was predicted and the

* Corresponding author.

D. Jin and S. Lin (Eds.): Advances in Mechanical and Electronic Engineering, LNEE 176, pp. 323–328.
springerlink.com

level of the tunnel structure safety was evaluated in order to provide key technical parameters for disposal.

2 Principle

Measurement principle of fiber Bragg grating strain is shown in figure 1.

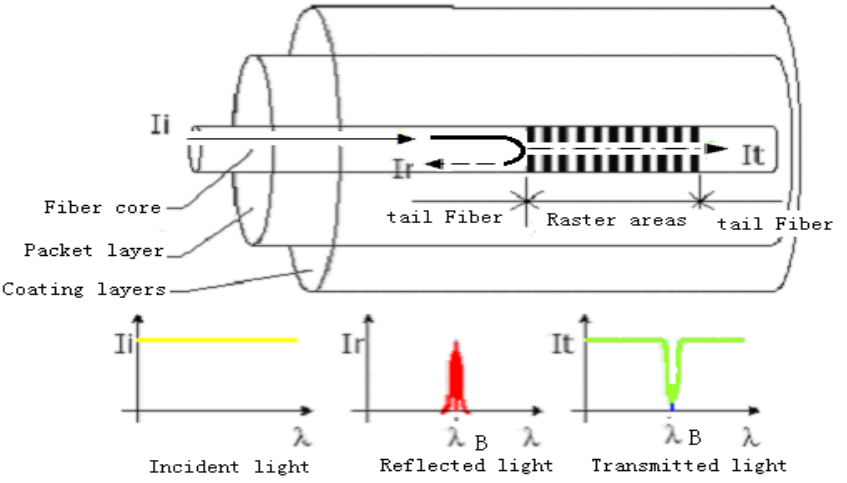

Fig. 1. Principle

When a wide-spectrum light beam (λ) goes through fiber Bragg grating, a single spectrum light is reflected by grating. Central wavelength (λ_B) of the reflected light is in connection with the effective refractive (neff) and the grid period (Λ). If the fiber Bragg grating suffers strain or ambient temperature changing, the effective refractive (neff) and the grid period (Λ) will change and will lead to grating reflection wavelength shift ($\Delta\lambda_B$). Through monitoring the reflection wavelength shift ($\Delta\lambda_B$), it can be got that the temperature and the strain change at the point of fiber Bragg grating sensor. Wavelength shift ($\Delta\lambda_B$) with temperature and strain can be used formula (1) expression [1], [2], [3], [5].

$$\Delta\lambda_B = \lambda_B S_\varepsilon \Delta\varepsilon + \lambda_B S_T \Delta T \tag{1}$$

The first is effected by strain (Δε) and the second is effected by temperature (ΔT). S_ε is strain sensitivity coefficient of the sensor. S_T is the temperature coefficient of the sensor. Fiber Bragg grating strain sensors were laid in the appropriate lining sections. Simultaneously, the temperature inside the structure was measured. Temperature effect was eliminated by temperature correction. So it was possible that the stress and the deformation of monitored sections were known.

2.1 Application Object

Jiulong double-arch tunnel which its width is 10.5M and its arching height is 6.75m and its buried depth is 25~69m is the structure of curved wall. Passing through: the zones of squeezed into pieces, fractured granite, weak weathered crannied granite which crannies is still developing, highly weathered rock mass which is loosely and a small fissure water. In construction, irregular crack, width for 1~3mm, appeared on the right side of left tunnel arch. As shown in figure 2.

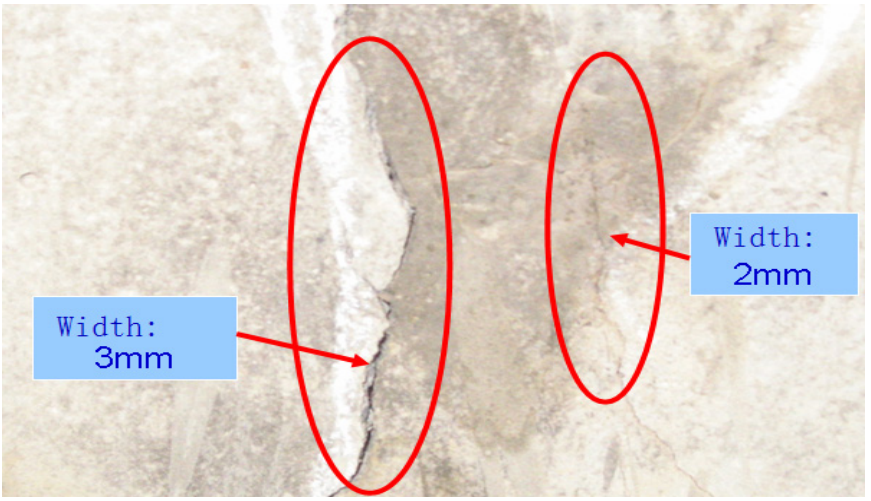

Fig. 2. Second lining crack pictures

By measuring and analyzing the stress and the deformation of second lining of tunnel, technical support was provided for further construction, trend prediction of structural deformation, assessing safe level of the tunnel structure, detecting early disease, timely warning and safeguard driving safety in the future.

2.2 Emplaced Sensors and Sensor Network Architecture

1) Emplaced Sensors

In the scope of K6+120~+310 (K6: calibration pile. After the pile, the positive number is the distance away from the pile. Unit: meters), interval 10m Design a monitoring section so that left tunnel's cracks regional (K6+130~+302) could be monitored for long time. Twenty monitoring sections were design. Each section arranged seven fiber Bragg grating surface strain sensors and one temperature compensation sensor. As shown in figure 3.

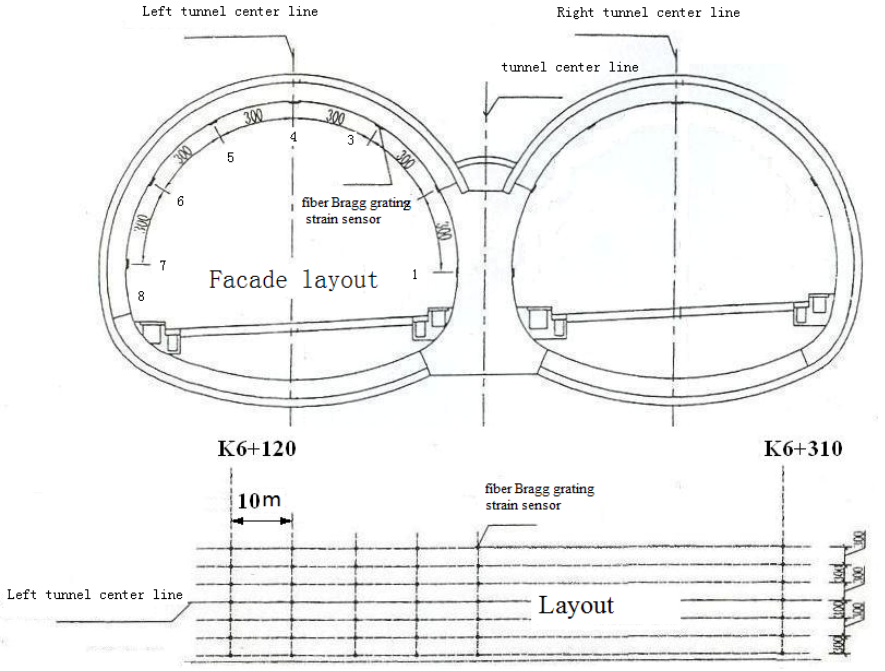

Fig. 3. Fiber Bragg grating sensor arrangement

On K6+120 monitoring section, sensor's serial numbers and layout position are shown in table 1. On other monitoring sections, sensor's number rule is the same with table 1 and laying position is also similar.

Table 1. K6+120 section sensor's serial numbers

numbers	Sensor categories	Serial numbers	Layout position
1	Strain	K6+120_1	Arched wall bottom-right
2	Strain	K6+120_2	Arched wall right
3	Strain	K6+120_3	Hance right
4	Strain	K6+120_4	Top
5	Strain	K6+120_5	Hance left
6	Strain	K6+120_6	Arched wall left
7	Strain	K6+120_7	Arched wall bottom-left
8	Temperature	K6+120_8	

2) Sensor Network Architecture

Demodulation instrument's 1~20 channel were occupied by sensors on 20 monitoring sections. On every section, seven fiber Bragg grating surface strain sensors and one temperature compensation sensor were connected in series. Between adjacent sensors in each channel, 0 ℃ wavelength is greater than 3nm. As shown in figure 4.

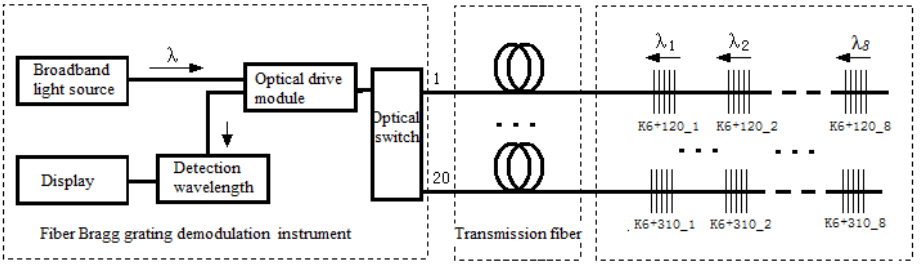

Fig. 4. Fiber grating sensor network chart

2.3 Results and Analysis of the Data

In nearly a year, in which went through spring, summer, autumn, winter and stepped across rain and dry seasons, twenty five measurements had been done. Maximum strain of fiber Bragg grating strain sensor was in arched wall bottom-right of K6+290 section (recorded maximum temperature was 27.8 °C and minimum temperature was 20.3°C). After temperature effect was eliminated, strain was -243με. And the strain of other fiber Bragg grating strain sensors was in $-100\mu\varepsilon < \Delta\varepsilon < 100\mu\varepsilon$. As shown in figure 5.

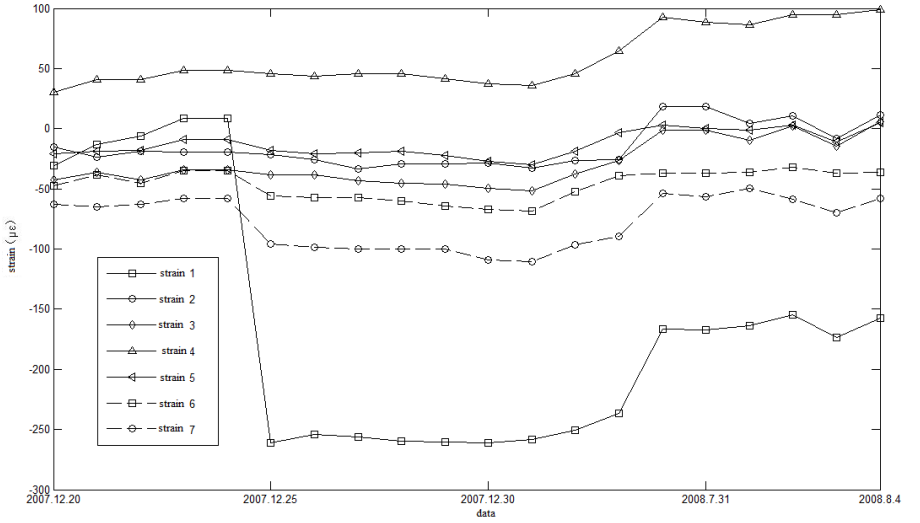

Fig. 5. Monitoring strain curves of K6+290 section

On Other 19 sections, recorded curves were similar to figure 3. The strain of fiber Bragg grating strain sensors was in $-200\mu\varepsilon < \Delta\varepsilon < 200\mu\varepsilon$ (recorded maximum temperature difference: 8.4°C). It was indicated that the deformation of tunnel was within the normal range.

4 Conclusions

In this paper, fiber Bragg grating surface strain sensors were applied in long-term monitoring the Lining cracking and the deformation of Jiulong double-arch tunnel left of Yunnan Xiao-Mo Expressway to understand the stress and deformation of tunnel secondary lining and to provide technical support for further construction of disposal. By measuring and analyzing, structural deformation trend was predicted and the level of the tunnel structure safety was evaluated, early disease was detected for timely warning and safeguard driving safety in the future. 20 crack sections had been monitored for nearly a year, in which went through spring, summer, autumn, winter and stepped across rain and dry seasons. The monitoring results indicated that the strain of fiber Bragg grating strain sensor was in the normal range and that the tunnel structural was stability and normal in the monitoring period.

References

1. Li, C., You, J., Li, Y.N., Wan, Z., Chen, Y., Xu, X.P., Xu, J.C.: Double Thimble Type Fiber Bragg grating Temperature Sensor. Optical Technique 36(2), 1–4 (2010)
2. Cao, M., Chen, Y., Wang, D.-D., Xu, X.-P., Xu, J.-C.: Two-Pipe Fiber Bragg grating Temperature Sensor Applied in Cable Trench and Cable Pit. In: 2011 International Conference on Advanced in Control Engineering and Information Science, CEIS 2011, pp. 710–714 (2011)
3. Li, C., et al.: FBG: Principles, Techniques and Applications, pp. 114–116. Science Publishing house, Beijing (2005)
4. Ding, Y., Shi, B., Sui, H.-B.: Tunnel Structural Health Monitoring System and Fiber Optic Sensing Technology. Journal of Disaster PreVention and Mitigation Engineering 25(4), 375–380 (2005)
5. Zhang, Y.-J., Kang, R.-X., Lou, J.-B., Wei, B., Li, J., Chen, L.-J., Su, Y.-L.: Distributed temperature sensor based on fiber grating of cable. Laser & Infrared 40(4), 405–409 (2010)
6. Liu, H.-J., Xia, C.-C., Zhu, H.-H., Luo, X.: Studies on Tunnel Damage. Chinese Journal of Underground Space and Engineering 3, 947–953 (2007)

Analysis of the Robot Positioning Error Based on Jacobian Matrix

Lizhe Qi[1], Leibin Yu[2], Wei Wang[1], Lei Chen[2], and Chao Yun[1]

[1] Robotics Institute, Beihang University, Beijing 100083, China
[2] Shanghai aircraft manufacturing co., Ltd, Shanghai 200436, China
lizhe-qi@sohu.com

Abstract. In order to calibrate the industrial robot's positioning error effectively, the mathematical model of six-DOF robot positioning error is built based on the Jacobian matrix, the positioning parameters, the angle parameters and the length parameters that how to affect the robot positioning error is analyzed and its simulated result is given at last. It is a foundation for calibration the parameters error of robot ulteriorly.

Keywords: industrial robot, positioning error, jacobian matrix.

1 Introduction

The repeat positioning accuracy of industrial robot is higher enough to use, but its absolute positioning accuracy is poor. In order to improve the performance of robot and expand its application scope, the parameters of robot kinematics model should be calibrated to reduce its absolute positioning error. There are four steps for the calibration process: modeling, measurement, parameter identification and error compensation [1]. There have been many domestic and foreign scholars researching on a variety of robot positioning error analysis and compensation method based on matrix transformation, vector and other forms of expression [2-6], but due to too many factors influencing the robot positioning error, the actual calibration result is not ideal based on the theoretical analysis formula. In order to calibrating a robot positioning error effectively, it is necessary to analyze the rule of various parameters how to affect the positioning error. For this issue, TING K et al refer to that it is only need to improve the precision of key factors and can relax the error of secondary factors appropriately to simply the calibration process [7]; Wang Wei et al analyze the precision of 3R robot by Orthogonal Experimental Design and draw its end error distribution and the factors sequence diagram that influence of end error under a complex surface task [8].

In this paper, the mathematical model of six-DOF robot positioning error is built based on the Jacobian matrix, the positioning parameters, the angle parameters and the length parameters is analyzed that how to affect the robot positioning error and its simulated result is given at last. The rule of various parameters affecting the positioning error is shown by the simulated result. This work is a foundation for calibration the parameters error of robot ulteriorly.

D. Jin and S. Lin (Eds.): Advances in Mechanical and Electronic Engineering, LNEE 176, pp. 329–334.
springerlink.com

2 Mathematical Model of Robot Positioning Error

In order to describe the kinematic positioning relationship among all the links and joints, the D-H model is used and its geometric parameters are shown by Fig.1.

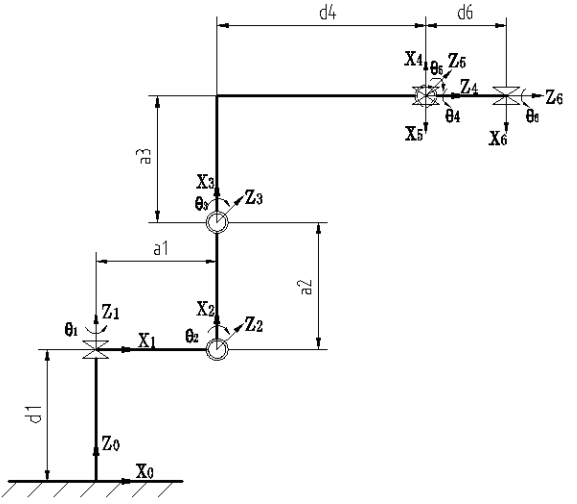

Fig. 1. The geometric parameters defined in D-H model of 6 DOF robot, the θ_i is the angle from X_{i-1} to X_i around Z_i; the d_i is the distance from X_{i-1} to X_i along Z_i; the α_i is the angle from Z_{i-1} to Z_i around X_{i-1}; the a_i is the distance from Z_{i-1} to Z_i along X_{i-1}.

The D-H model transformation matrix can be obtained as follows:

$$^{i-1}\mathbf{T}_i = Rot(x_{i-1},\alpha_{i-1})Trans(x_{i-1},a_{i-1})Trans(z_i,d_i)Rot(z_i,\theta_i) \tag{1}$$

So, the kinematic mathematical model of tool plate for the six-DOF robot is this:

$$^{T0}\mathbf{T}_B = \prod_{i=1}^{6} {}^{i-1}\mathbf{T}_i \tag{2}$$

From the equation above, we have:

$$\begin{cases} f_{bx}(X_b,Y_b,Z_b,g)=0 \\ f_{by}(X_b,Y_b,Z_b,g)=0 \\ f_{bz}(X_b,Y_b,Z_b,g)=0 \end{cases} \tag{3}$$

Where X_b,Y_b,Z_b represent the position of the tool plate, g is a vector including all geometric parameters and f_{bx}, f_{by}, f_{bz} represent function vector. Differentiating all the equations against all the variables X_b,Y_b,Z_b,g:

$$\begin{aligned}
&\frac{\partial f_{bx}}{\partial X_b}dX_b+\frac{\partial f_{bx}}{\partial Y_b}dY_b+\frac{\partial f_{bx}}{\partial Z_b}dZ_b+\sum_j\frac{\partial f_{bx}}{\partial g_j}dg_j=0\\
&\frac{\partial f_{by}}{\partial X_b}dX_b+\frac{\partial f_{by}}{\partial Y_b}dY_b+\frac{\partial f_{by}}{\partial Z_b}dZ_b+\sum_j\frac{\partial f_{by}}{\partial g_j}dg_j=0\\
&\frac{\partial f_{bz}}{\partial X_b}dX_b+\frac{\partial f_{bz}}{\partial Y_b}dY_b+\frac{\partial f_{bz}}{\partial Z_b}dZ_b+\sum_j\frac{\partial f_{bz}}{\partial g_j}dg_j=0
\end{aligned} \tag{4}$$

Rewrite it as:

$$\begin{bmatrix}
\frac{\partial f_{bx}}{\partial X_b} & \frac{\partial f_{bx}}{\partial Y_b} & \frac{\partial f_{bx}}{\partial Z_b}\\
\frac{\partial f_{by}}{\partial X_b} & \frac{\partial f_{by}}{\partial Y_b} & \frac{\partial f_{by}}{\partial Z_b}\\
\frac{\partial f_{bz}}{\partial X_b} & \frac{\partial f_{bz}}{\partial Y_b} & \frac{\partial f_{bz}}{\partial Z_b}
\end{bmatrix}\begin{bmatrix}dX_b\\dY_b\\dZ_b\end{bmatrix}=\begin{bmatrix}
-\sum_j\frac{\partial f_{bx}}{\partial g_j}dg_j\\
-\sum_j\frac{\partial f_{by}}{\partial g_j}dg_j\\
-\sum_j\frac{\partial f_{bz}}{\partial g_j}dg_j
\end{bmatrix} \tag{5}$$

In a compact form, it becomes:

$$\mathbf{J}_1 d\mathbf{P}=\mathbf{J}_2 d\mathbf{g} \tag{6}$$

So, the mathematical model of robot positioning error based on the jacobian matrix can be obtained as follows:

$$d\mathbf{P}=\mathbf{J}d\mathbf{g} \tag{7}$$

Where, the **J** is the jacobian matrix that describes the relationship between the errors of the robot's tool plate position and the errors of all of the robot's parameters, it equals:

$$\mathbf{J}=(\mathbf{J}_1^{-1}\mathbf{J}_2)=\begin{bmatrix}
\frac{\partial f_{bx}}{\partial X_b} & \frac{\partial f_{bx}}{\partial Y_b} & \frac{\partial f_{bx}}{\partial Z_b}\\
\frac{\partial f_{by}}{\partial X_b} & \frac{\partial f_{by}}{\partial Y_b} & \frac{\partial f_{by}}{\partial Z_b}\\
\frac{\partial f_{bz}}{\partial X_b} & \frac{\partial f_{bz}}{\partial Y_b} & \frac{\partial f_{bz}}{\partial Z_b}
\end{bmatrix}^{-1}\begin{bmatrix}
-\frac{\partial f_{bx}}{\partial g_1} & -\frac{\partial f_{bx}}{\partial g_2} & \cdots & -\frac{\partial f_{bx}}{\partial g_{24}}\\
-\frac{\partial f_{by}}{\partial g_1} & -\frac{\partial f_{by}}{\partial g_2} & \cdots & -\frac{\partial f_{by}}{\partial g_{24}}\\
-\frac{\partial f_{bz}}{\partial g_1} & -\frac{\partial f_{bz}}{\partial g_2} & \cdots & -\frac{\partial f_{bz}}{\partial g_{24}}
\end{bmatrix} \tag{8}$$

3 Analysis of the Robot Positioning Error and Its Simulation

Based on the mathematical model of robot positioning error, there are three categories of parameters and theirs errors influencing the robot positioning error, they are:

- ✧ the robot positioning parameters($\theta_1 \sim \theta_6$), and the corresponding sub vector or matrix is denoted by $\mathbf{g}_a$ and $\mathbf{J}_a$
- ✧ the angle parameters($\alpha_1 \sim \alpha_6$), and the corresponding sub vector or matrix is denoted by $\mathbf{g}_b$ and $\mathbf{J}_b$
- ✧ the length parameters($d_1 \sim d_6, a_1 \sim a_6$), and the corresponding sub vector or matrix is denoted by $\mathbf{g}_c$ and $\mathbf{J}_c$

And from the equation (7) above, we have:

$$d\mathbf{P} = \mathbf{J}_a d\mathbf{g}_a + \mathbf{J}_b d\mathbf{g}_b + \mathbf{J}_c d\mathbf{g}_c \tag{9}$$

This equation describes that the robot positioning error is an integrative effect by the positioning parameters and theirs errors, the angle parameters and theirs errors and the length parameters and theirs errors. The section below will analyze and simulate the robot positioning error independently and the object of analysis is the robot of IRB2400 manufactured by the ABB Robotics Corporation, Sweden. It is a six DOF articulated robot which used high precision, speed reduction gears. This robot is widely used in industry, in general, and the flexible manufacturing industry, in particular.

3.1 Analysis of the Robot Positioning Error Affecting by Positioning Parameters

Ignoring other factors, the mathematical model is simplified and the positioning error δ_a will be:

$$\delta_a = \left\| \mathbf{J}_a d\mathbf{g}_a \right\|_2 \tag{10}$$

Assuming that the error of the positioning parameters is 0.1 degree and the sample number of robot position is 1000, the simulated result of robot positioning error is shown by Fig.2.

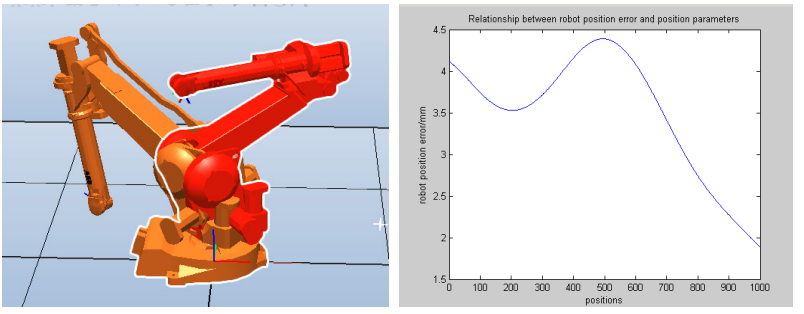

Fig. 2. Robot configuration and the error simulation result, the left figure shows the robot two limit positions, the right figure shows the simulated result of robot positioning error when there are only had positioning parameter errors and the robot is moved from one limit positioning to the other

3.2 Analysis of the Robot Positioning Error Affecting by Angle Parameters

Ignoring other factors, the mathematical model is simplified and the positioning error δ_b will be:

$$\delta_b = \left\| \mathbf{J}_b d\mathbf{g}_b \right\|_2 \tag{11}$$

Assuming that the error of the angle parameters is 0.1 degree and the sample number of robot positioning is 1000, the simulated result of robot positioning error is shown by Fig.3.

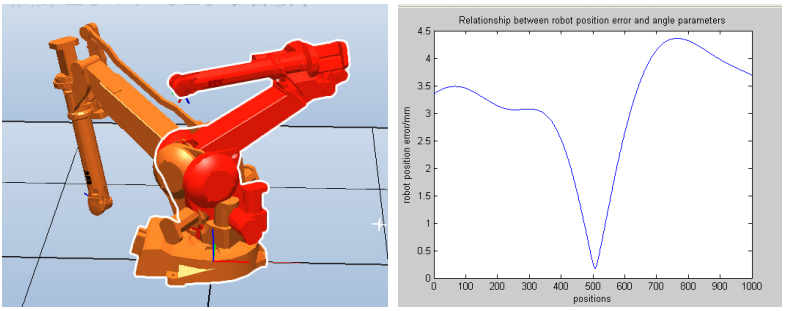

Fig. 3. Robot configuration and the error simulation result, the left figure shows the robot two limit positions, the right figure shows the simulated result of robot positioning error when there are only had angle parameter errors and the robot is moved from one limit positioning to the other

3.3 Analysis of the Robot Positioning Error Affecting by Length Parameters

Ignoring other factors, the mathematical model is simplified and the positioning error δ_c will be:

$$\delta_c = \left\| \mathbf{J}_c d\mathbf{g}_c \right\|_2 \tag{12}$$

Assuming that the error of the positioning parameters is 0.2 mm and the sample number of robot positioning is 1000, the simulated result of robot positioning error is shown by Fig.4.

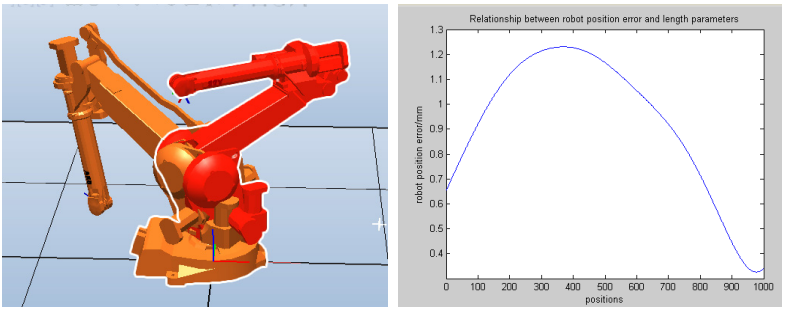

Fig. 4. Robot configuration and the error simulation result, the left figure shows the robot two limit positionings, the right figure shows the simulated result of robot positioning error when there are only had positioning parameter errors and robot is moved from one limit positioning to the other

4 Conclusion

From the simulated result, we can know that:

- ✧ different robot position generates different robot positioning error when there are various parameter errors
- ✧ different type of parameter errors results in different robot positioning error when there is the same robot position
- ✧ the positioning parameters and the angle parameters are more sensitive then the length parameter for robot positioning error

These rules can be used for sensitivity analysis of the parameters affecting robot positioning error and simply the calibration process ulteriorly.

Acknowledgments. This research is sponsored by the innovation foundation from the manufacturing engineering technology research center of the National commercial aircraft.

References

1. Jiao, G.: Analysis and synthesis of robot pose errors. Beijing University of Technology, Beijing (2002)
2. Bai, Y., Zhuang, H.Q., Roth, Z.S.: Experiment study of PUMA calibration using a laser tracking system. In: Proceedings of the IEEE International Workshop on Soft Computing in Industrial Applications, Piscataway, USA, pp. 139–144 (2003)
3. Alici, G., Shirinzadeh, B.: A systematic technique to estimate positioning errors for robot accuracy improvement using laser interferometry based sensing. Mechanism and Machine Theory 40, 879–906 (2005)
4. Cui, H., Zhu, Z., Gan, Z., Brogardh, T.: Kinematic analysis and error modeling of TAU parallel robot. Robotics and Computer-Integrated Manufacturing 21, 497–505 (2005)
5. Yu, A., Bonev, I.A., Zsombor-Murray, P.: Geometric approach to the accuracy analysis of a class of 3-DOF planar parallel robots. Mechanism and Machine Theory 43, 364–375 (2008)
6. Paziani, F.T., Di Giacomo, B., Tsunaki, R.H.: Robot measuring form errors. Robotics and Computer-Integrated Manufacturing 25, 168–177 (2009)
7. Ting, K., Long, Y.: Performance quality and tolerance sensitivity of mechanisms. Transactions of the ASME 118, 144–150 (1996)
8. Wei, W., Chao, Y.: Orthogonal Experimental Design to Synthesize the Accuracy of Robotic Mechanism. Journal of Mechanical Engineering 45, 18–24 (2009)

Research on Measurement and Analysis of Load Spectrums Based on Actual Equipment Experiment and Virtual Prototyping

Huibin Hu[1,2], Lijun Cao[1], Xinwen Cao[2], Shuxiao Chen[2], Jianzhong Jin[2], Yan Sun[2], and Linlin Li[2]

[1] Department of Mechanical Engineering, Shijiazhuang Mechanical Engineering College, 050003 Shijiazhuang, Hebei Province, China
[2] Military Operational Center, Shijiazhuang Army Command College 050010 Shijiazhuang, Hebei Province, China
{huhuibin_bin,caolijun_jun}@163.com

Abstract. Component's load spectrums under various running conditions are the basis of stress and strain analysis, fatigue life prediction and reliability analysis. Self-Propelled Gun has complicated running conditions, which are usually described by running speed, gearshift and road. Traditional experimental measurement methods of load spectrums are impossible to measure all components' load spectrums. Virtual prototyping of Self-Propelled Gun is established and firstly adopted to measure the load spectrums of torsion shaft. The comparison between results of two different methods verifies the credibility and accuracy of virtual prototyping. Virtual experiments based on virtual prototype supplement the load spectrums which actual equipment experiments can not supply effectively.

Keywords: load spectrum, torsion shaft, virtual prototype, Self-Propelled Gun.

1 Introduction

The fatigue lives and fatigue reliabilities of running system of Self-Propelled Gun are the references to determine appropriate maintenance cycles. Components' load spectrums under various running conditions are the basis of fatigue lives and fatigue reliabilities calculation. The running condition can be mainly described by running speed, running gearshift and road. The running speed and road roughness are main vibration driving sources of Self-Propelled Gun and main external causes of component's fatigue failure. But the working conditions of running system are very complicated. The running roads include all grades of pavement. If components' load spectrums are measured only based on experiments, the testing cost is very huge. Because many components are encapsulated in equipment, it is impossible to measure their load spectrums.

In order to supplement the experimental data and acquire complete load spectrums, a new kind of measurement method of load spectrums combined actual equipment experiment and virtual prototype is first put forward in this paper. Virtual prototyping of Self-Propelled Gun is established in Pro/E and ADAMS. Its credibility and

D. Jin and S. Lin (Eds.): Advances in Mechanical and Electronic Engineering, LNEE 176, pp. 335–341.
springerlink.com

accuracy are verified. Torsion shaft is the main buffer and damping component of running system of Self-Propelled Gun. So it is taken as research object to measure the load spectrums. The comparison between actual experiment data and virtual test results of virtual prototype verifies their complementarity, which provide complete and accurate load spectrums for torsion shaft.

2 Actual Equipment Experiment

Normal method is adopted to carry out actual equipment experiments. Running roads include farmland, fluctuation land, sand plain etc. Measuring parameters are vertical displacement between second loading wheel axis and chassis, axis accelerations speeds of second and fifth loading wheels, running speed of Self-Propelled Gun.

2.1 Measurement Principle

It is difficult to install strain gauges on the torsion shaft to measure its strain and stress. So we measure the torque of torsion shaft indirectly by the displacement between the axis of loading wheel and vehicle body. The measurement principle is shown as Figure 1:

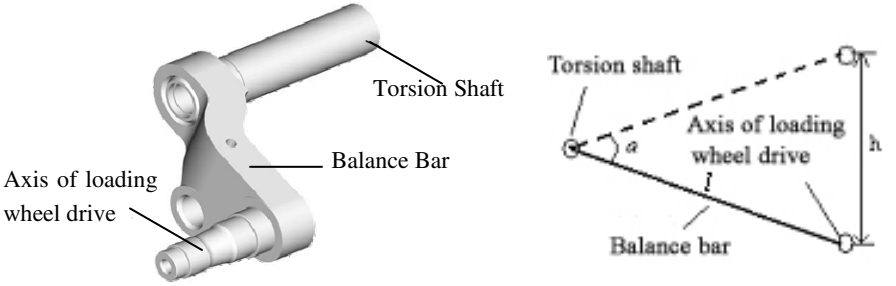

a) Installation position of torsion shaft b) Computational principle of torsion shaft's torque

Fig. 1. Measurement Principle of Torsion Shaft's Torque

From Figure 1, it is can be seen that the loading wheel and vehicle body are connected by the balance bar. The axis of loading wheel drive the balance bar rotate around the torsion shaft. Therefore, the torque T of torsion shaft can be calculated by Formula (1):

$$T = \frac{GI_p(2\arcsin\frac{h}{2l} + a_0)}{L} \tag{1}$$

Where

GI_p —the torsional stiffness of torsion shaft;

a_0 —the torsion angle of torsion shaft in static balance state;

L—the length of torsion shaft;

l—the axis distance between torsion shaft and loading wheel.

2.2 Sensor Installation

Because torsion shaft is installed in vehicle and bear huge torque, traditional torque measurement method, such as strain-gauge method, is difficult to measure the load spectrums of torsion shaft. Therefore, we adopt indirect method to acquire the torque of torsion shaft by measuring the relative displacement between loading wheels and vehicle.

Linear displacement sensor is installed between the axis of second loading wheel and vehicle. The installation is shown as Figure 2. Stationary bracket protruded from step is linked with the floating arm of displacement sensor. The floating arm of displacement move with the loading wheel in its fluctuating process and produce corresponding electric voltage signal. The upper fixed part of displacement sensor is linked with vehicle by stationary bracket. The displacement sensor measures the vertical displacement of loading wheel relative to vehicle, which is the computational basis of torque of torsion shaft.

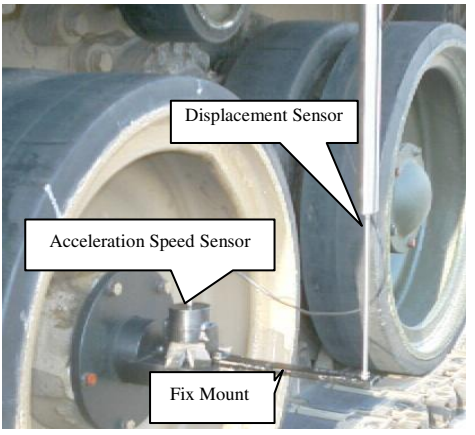

Fig. 2. Acceleration and displacement sensors on the second load-bearing wheel

The type of linear displacement sensor is LDC6000. Its sensitivity is 15.03mv/mm. And its measuring range is ±150mm. The type of electricity amplifier is YE6600. The type of recording instrument is Sony PC216AX. It have 16 channels. Its maximum sampling frequency is 20K. And its measuring range is ±20V.

Power spectral density method of vertical acceleration is adopted to measure road roughness. Acceleration sensors are installed on the axles of the second and fifth loading wheels. The type of acceleration sensor is CA-YD-107. Its measurement sensitivity is 5.36pc/ms-2. The type of electricity amplifier is YE6600. The type of recording instrument is Sony PC216AX. It have 16 channels. Its maximum sampling frequency is 20K. And its measuring range is ±20V.

In Self-Propelled Gun's running process, the driving wheel rotates between the emitter and receiver poles of photoelectric sensors. The photoelectric sensors produce uncontinuous impulse signals. The linear speed of the driving wheel's rim can be

regarded as the running speed of Self-Propelled Gun. The transition relationship is shown as Formula (2):

$$v = \frac{2\pi r}{kT} \tag{2}$$

Where v is the linear speed of the driving wheel's rim, which is equal to the running speed of Self-Propelled Gun. R is the effective rotary radius. K is the teeth number of the driving wheel. T is the period of impulse signals produced by photoelectric sensors.

3 Virtual Prototyping

The virtual prototype of Self-Propelled Gun is established through six steps:

1) Establish components' three-dimensional solid models in Pro/E according to their design drawings and compute components' quality characteristics.
2) Establish virtual prototype based on ATV module of ADAMS.
3) Modify the physical dimensions and track-center distance according to design drawings, and adjust components' installation positions.
4) The qualities of transmission system, control system, power system and firepower system are added on vehicle body.
5) Define related dynamical models.
6) Add kinetic constraints.

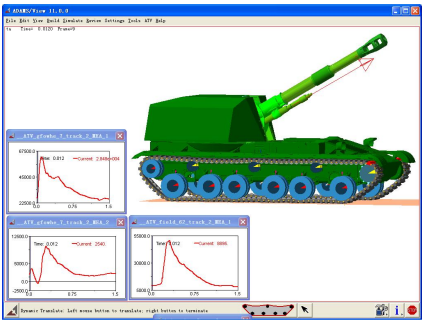

Fig. 3. Virtual prototyping of Self-Propelled Gun

4 Comparison between Results of Two Different Methods

Actual experiments and virtual prototyping simulation methods are adopted to obtain torsion shaft's load spectrums. Figure 4 and Figure 5 are load spectrums of torsion shaft of E-class road and 3-grade condition obtained by actual experiment and virtual prototyping simulation.

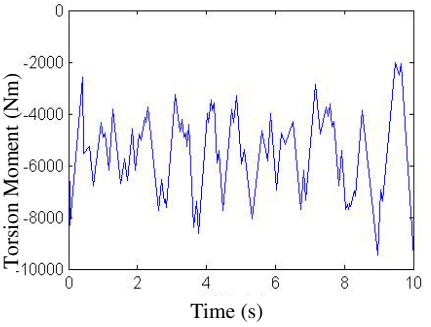

Fig. 4. Load spectrum of torsion shaft on E-class road and 3-grade condition based on experiment

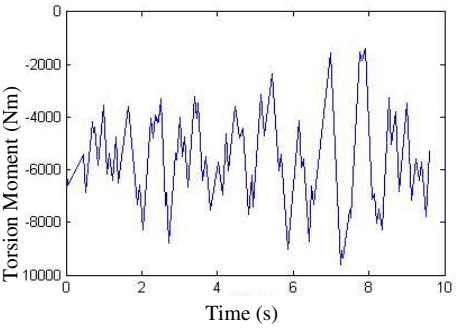

Fig. 5. Load spectrum of torsion shaft on E-class road and 3-grade condition based on Virtual prototyping

To prove the accuracy and credibility of simulation results based on virtual prototyping, several contrast methods are used to measure the consistency between simulation results and experimental data.

a. Contrast of between steady-state parameters of actual measured values and simulation data for torsion shaft load.
b. Analysis of power spectrum in time-domain signal between measured torsion moment and simulation torsion moment. The contrast of torsion moment obtained by actual measurement and simulation is shown as Figure 6:

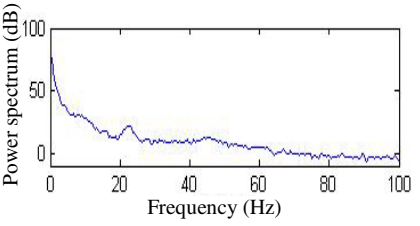

a) Power spectrum of measured torsion moment

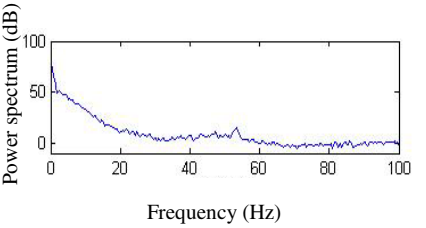

b) Power spectrum of simulation torsion moment

Fig. 6. Contrast of torsion moment obtained by two different kinds of methods

Shapes of spectral line, heights of spectral peak, frequency width of two kinds of power spectrums are similar, which indicate the credibility of established virtual prototyping.

5 Analysis of Local Strain and Stress Spectrum

The superficial stress state of torsion shaft in pure torsion condition is shown as Figure 7. There is maximum shearing stress τ on the surface of torsion shaft. The stresses on main plane have 45° angle to the axial line. The stresses on main plane include maximum tension stress σ_1 and maximum compression stress σ_3. They are equal to maximum shearing stress. All the above stresses are maximum on surface and equal to zero on the central axis.

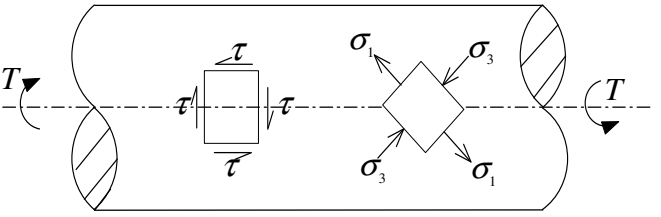

Fig. 7. The superficial stress state of torsion shaft in pure torsion condition

According to elastic mechanics theory, the maximum tension stress is

$$\sigma_1 = \tau = \frac{TD}{2I_p} = \frac{16T}{\pi D^3} \tag{3}$$

Where T is the torque on torsion shaft, it is the polar moment of inertia, D is the diameter of torsion shaft.

Based on the load data, the local strain and stress distribution of torsion shaft under D-class pavement and 3 gearshift can be resolved. The time histories of mean values of strain and stress are shown as Figure 8:

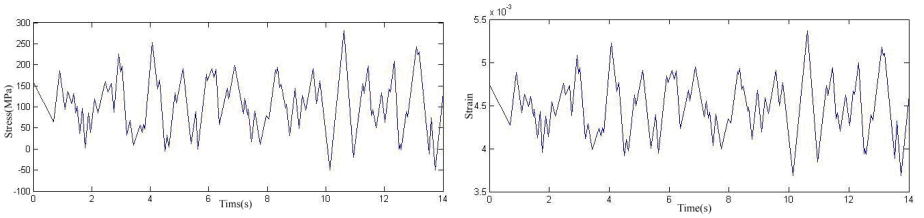

a) Stress b) Strain

Fig. 8. Local stress-strain mean value of D class road 3 gear

From Figure 8, it can be seen that the D-class pavement is flat, the strain and stress diagram of torsion shaft is similar. This is because that the strain concentration section of torsion shaft is in linear-elastic deformation state, the strain and the stress varies proportionally. In this case, the fatigue reliability should be analyzed by high-cycle fatigue theory.

References

1. Joe, H.: Asymptotic efficiency of the two-stage estimation method for copula-based models. Journal of Multivariate Analysis 94(2), 401–419 (2005)
2. Olsson, A., Sandberg, G., Dahlblom, O.: On Latin hypercube sampling for structural reliability analysis. Structural Safety 25, 47–68 (2008)
3. Melchers, R.E.: Search-based importance sampling. Structural Safety (9), 117–128 (1990)

The Study of Surface Smooth Finish of Spinneret Hole Bottom Manufactured by Drills of Different Materials

Bo Gao, Quan Sun, and Chongchang Yang

Engineering Research Center of Advanced Textile Machinery, Ministry of Education, Shanghai, P.R. China
College of Mechanical Engineering, Donghua University, Shanghai, P.R. China

Abstract. The resistance of the melts in spinning can be reduced by improving the surface finish of spinnerets, avoiding eddy current and decreasing the frequency of lousiness and breaking of fibers, to improve efficiency in the production of the finished product and quality. High-speed steel and carbide drill have a significant impact on the surface smooth of spinnerets considering their carbon content and other alloy elements and their own texture multiphase. According to the three chosen materials, this paper analyzes and compares the differences in the surface finish of spinneret hole bottom though mechanical engineering experiments and draws the conclusion that the best way to get smooth surface finish is processed by carbide drill, and the higher the spindle rotation speed of the tool, the better the surface finish.

Keywords: Spinneret hole bottom, Surface finish, High-speed steel, Cemented carbide.

1 Introduction

Spinneret, one key component of a spinning machine, is an important equipment for the manufacture of chemical fibers. The high precision of spinneret is the crucial element to ensure the quality of fiber goods and spinning technology. The performance of fiber products is linkde directly with the spinneret hole type, structure and precision. [1]The hole bottom processing is one of the most vital processes during the whole manufacturing of spinnerets and the quality of the follow-up fibers are influenced by the surface smoothness of the spinneret hole bottom.

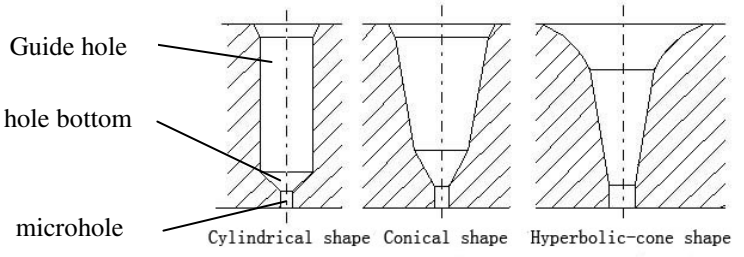

Fig. 1. Structures of spinneret hole

D. Jin and S. Lin (Eds.): Advances in Mechanical and Electronic Engineering, LNEE 176, pp. 343–348.
springerlink.com

SUS630 and 1Cr18Ni9Ti, the main ingredients of spinnerets, have good corrosion and acid resistance. From practical production, it has been learned that, stainless steel in difficult to machine and it's difficult to ensure the manufacturing quality with a rapid tool wear.

On one hand, in order to improve the quality of fiber goods, avoiding melt fracture and reducing the lousiness and breaking of fibers, the precision of length and diameter of spinneret hole, as well as its surface smoothness finish, needs to request strictly. One the other hand, there exits the elastic deformation and high shear stress at the bottom in the place where melt flows into the micro hole from the guide-hole. Good surface finish could help to reduce the flow resistance of melt and avoid eddy current. Based on the importance of smooth surface finish of hole bottom, this article analyzes and compares the cutting experiment results of common high speed steel, cobalt high speed steel and cemented carbide.

2 Performance Analysis of High-Speed Steel and Cemented Carbide Structure

2.1 High-Speed Steel

As we all known, most of the carbide elements in high-speed steel are combined with W, Mo, Cr, and V to generate the carbide, the grinding performance of ordinary high-speed steel is good, the decarburization is insensitive, overheating tendency is not obvious when hardening, and the resistance to plastic deformation ability of ordinary high-speed steel is strong enough, but the carbon content of ordinary high-speed steel is rich, the distribution is uneven, the strength and toughness of ordinary high-speed steel is not high enough , what's more ,the thermoplastic of ordinary high-speed steel is poor.

The high-speed steel added with cobalt can improve the thermal stability of the steel and carbide precipitation in tempering, and increase the dispersion hardening effect; thereby the high temperature hardness and antioxidant capacity will be improved. Cobalt cannot form carbide, and mostly it exists in austenite and ferrite. During the tempering process, cobalt is not only can inhibit and delay the precipitation of certain special carbides, but also can hinder the precipitated phase of aggregation. Therefore, in tempering or using process, the particles precipitated from the cobalt high-speed steel is much finer than precipitated from high-speed steel without cobalt, and the degree of aggregation is much lower.[2]

2.2 Cemented Carbide

The major components of cemented carbide are: tungsten carbide (WC), titanium carbide (TiC), tantalum carbide (of TaC), niobium carbide (NbC), etc. Cemented carbide is made of tungsten carbide with high hardness and high melting point using powder metallurgy method, and its hardness is up to 78 ~ 82HRC, far higher than the high-speed steel; what's more, carbide is a brittle material with low capacity to withstand cutting vibration and shock.[3] In this test we use YW Carbide, such as

tungsten, tantalum, titanium and niobium. An appropriate increase in Co content will significantly increase the flexural strength of this type of cemented carbide, while increasing the content of TaC and refining of grain, the ability to resist crack propagation can be improved, which can withstand mechanical shock, and thermal shock caused by temperature cycling, it will have a high bending strength and impact toughness, can reduce the collapse of the knife when cutting, and it will have a good thermal conductivity ability to pass the cutting heat, and its grinding performance is also very good, making it easy to grind a sharp cutting edges. Table 1 is the typical YW carbide's composition and it's performance.

Table 1. Composition and performance of typical yw carbide

steel grade	composition	Hardness (HRC)	Strength (/Ma)	density /g.cm-3
YW1	WC+6%TiC+4%Ta(Nbc)+6%Co	79	1209	12.8~13.3
YW2	WC+6%TiC+4%Ta(Nbc)+8%Co	77	1350	12.6~13.0

3 Analysis of Experiments and the Results

The material of this experiment is SUS630 stainless steel. And its chemical components and mechanical performances are in Table 2 and Table 3.

Table 2. Chemical components of sus630 stainless steel

Element	C	Mn	Si	Cr	Ni	Cu	S	P
Concentration	≤0.07	≤1.00	≤1.00	15.50~17.50	3.0~5.0	3.0~5.0	≤0.03	≤0.03

Table 3. Mechanical performances of sus630 stainless steel

Elongation	**Tensile strength**	**Yield strength**	**Hardness**
16%	930MPa	725MPa	HRC32

Experimental equipment: NL-36 vertical machining center, microemulsion cutting fluid for stainless steel processing.

3.1 Different Performance Results of Spinneret Hole Bottom Manufactured by Twist Drills of Different Materials under the Same Technology Conditions

There are three kinds of twist drills: ordinary HSS twist drill Φ2.5mm, cobalt HSS twist drill Φ2.5mm(cobalt content ≥4.5%) and carbide twist drill Φ2.5mm. And the edges of the three are sharpened to 90º by fine grinding wheel E28. The three kind of twist drills drilled 144 holes separately with the same spindle speed 1500r/min and feed rate 30mm/min. The surface smoothness finish of the holes bottom was observed with a stereomicroscope. The results are shown in the following figures.

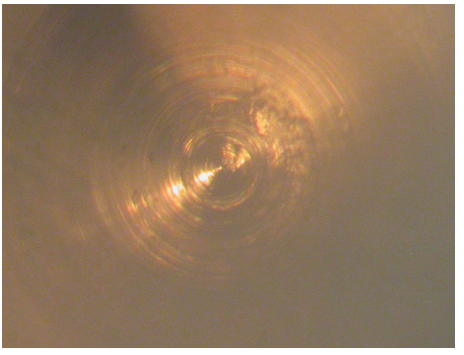

Fig. 2. Surface smoothness by ordinary HSS twist drill

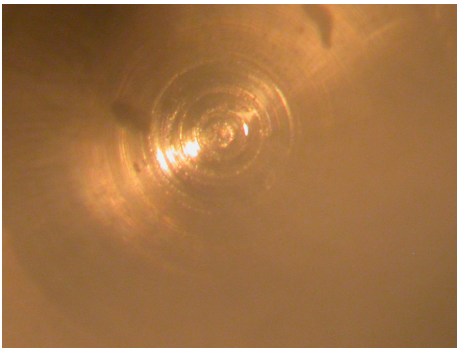

Fig. 3. Surface smoothness by cobalt HSS twist drill

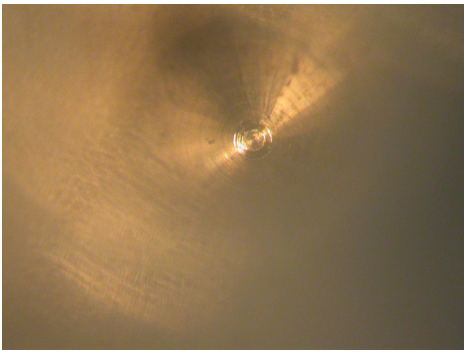

Fig. 4. Surface smoothness by carbide twist drill

By comparing Figure 2 and Figure 3, it can be learned that there exit spiral grains on the hole bottom surfaces processed by all the three kinds of HSS twist drills. There are also "scratch" on the surfaces processed by ordinary HSS twist drill. That is because of the cutting heat which generats in the process of cutting stainless steel and disappears easily due to the poor thermal conductivity of stainless steel. The cutting heat can react with oxygen, hydrogen, nitrogen and other elements in the air to form hard and brittle compounds that cause the welding and adhesion wear of tool leading to tipping, as shown in Figure 5.[4]However, because of the compact structure of HSS, spiral grains still exit on the surface drilled by cobalt twist drill.

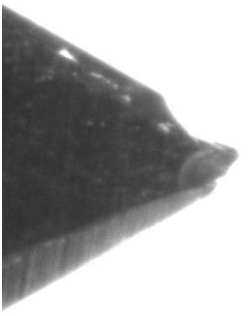

Fig. 5. The phenomenon of" avalanche knife"

Through the comparison of figure 3 and figure 4, the surface shown in figure 4 is more smooth than that of figure 3. And this is because cemented carbide is a type of material in which it is metal carbides in the hard phase and iron family metals as metal bonds. Cemented carbide is gained by powder metallurgical process. The stronger the bonding force between hard phase and binding phase, the better properties of a alloy performance.[5] Cemented carbide takes both advantages of high melting point of carbide and high ductility of metal bonds, processing high wear resistance corrosion resistance and high-temperature resistance. With the compact and uniform structure of cemented carbide, the holes processed by cemented twist drill have smooth surface.

3.2 Different Performance Results of Spinneret Hole Bottom Manufactured by Cemented Twist Drill under Different Spindle Speeds

Ordinary cemented carbide twist drill Φ2.5mm, microemulsion cutting fluid, feed rate at 20mm/min and 30mm/min. Change the spindle rotation speeds and the result is as follows.

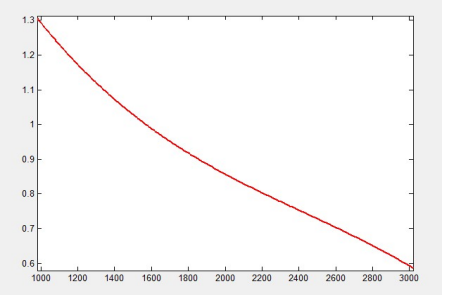

Fig. 6. 20mm/min, Results of different rotation speeds

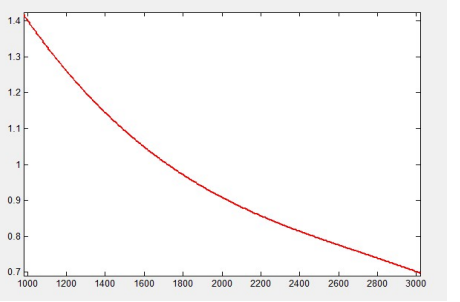

Fig. 7. 30mm/min, Results of different rotation speeds

According to the figure 6 and figure 7, with the increase in spindle rotation speeds, the hole bottom surface become more and more smooth, because low spindle speed leads to the decreasing depth of cut under the same feed rate. However, with excessive acceleration of spindle rotation speed, the wear of cutting tool get more rapidly due to the untimely cooling of cutting edge. And even the breaking of the drill would happen because of too large cutting force.

By comparing the surface finish of hole bottom processed by the three kinds of drills, the surface quality drilled by cobalt twist drill is better than that by ordinary twist drill and the best smooth surface is processed by carbide drill and the higher the spindle rotation speed the better the surface finish. There are also other factors that affect the surface smoothness finish. Taking cutting fluid for example, different kinds of cutting liquid would produce different effects. Microemulsion cutting fluid is chosen in this testing. The surface quality is better if vegetable oil is used as cutting fluid during machining.

4 Conclusion

Spinneret is mainly made of stainless steel, which is difficult to machine and its surface finish is not good with the cutting-tool wearing rapidly. Grinding performance of ordinary high-speed steel is good, but it can easily form hard brittle compounds with stainless steel under high temperature, easy to stick and collapse the knife, bring about “surface scratches" in the bottom of the hole; The red hot and wear resistance performance of cobalt high speed steel is much better as compared with ordinary high-speed steel, but because of the compactness of their organization, the bottom surface of the tooling holes still have spiral lines; carbide material has high melting point of the carbides and good ductility of bonding metal, and the strength and hardness of carbide material is high, also it has good wear resistance of high temperature, wear and corrosion. Surface finish of the machining bottom of the hole is good enough to meet the processing requirements of the spinneret and is beneficial to spinning. Proved by the mechanical engineering experiments, the higher the rotational speed, the better the surface finish of the drilling hole’s bottom.

Acknowledgments. Fund name: The Fundamental Research Funds for the Central Universities of Donghua University(additional).

References

1. Guo, L., Yang, C.: The Processing technology of Spinneret plate with large ratio of length to diameter of micro hole. Tool Technology (2008)
2. Shuai, N.: The Processing technology of Cobalt high speed steel hot forging. Forging Technology (1985)
3. Chen, J., Shen, X.: Study on Machinability of stainless steel. Electrical and Mechanical Product Development and Innovation (2004)
4. Ding, Z., Peng, T., Li, S.: Principle of metal cutting and cutting tool. Machinery Industry Press, Beijing (1985)
5. Chen, Y., Du, Q., Dong, W.: Metal cutting tools and practical technology. Chemical Industry Press, Beijing (2008)

Numerical Simulation on the Influence of Altitude on Jet Flow Field

BoWei Liu[1], Yi Jiang[1], Yang Song[2], and ShaoZhen Yu[1]

[1] Department of Aerospace Engineering, Beijing Institute of Technology, Beijing, 100081, China
[2] Social Security Troop of Beijing Municipal Public Security Bureau, Beijing, 100088, China
borylau@163.com

Abstract. In order to analyze the influence of altitude on the missile jet flow field, based on U.S. Standard Atmosphere (1976), the point trajectory of a certain ballistic missile was obtained by solving the equations of missile flight without control which is established in the vertical plane, then the technology of secondary programming with Fluent was used to simulate the jet flow field on the trajectory below 30km, which was based on the Navier-Stokes equations and the RNG $k-\varepsilon$ turbulence model. The results showed that as the altitude increased, the static pressure and static temperature became lower, mach-number became higher, and the spreading range of jet flow field became farther.

Keywords: jet flow, standard atmosphere, vertical plane trajectory, secondary programming.

1 Introduction

As the flight altitude changes, the characteristic of missile jet flow field changes, which will affects the aerodynamic drag and base pressure of the missile, then causes projectile dispersion [1]. Meanwhile, it will affect the concealment of the missile. Therefore, it is necessary to research the characteristic of jet flow at different altitude.

Firstly, by solving the equations of missile flight without control which is established in the vertical plane, the point trajectory of a certain ballistic missile was obtained, and the part blow 30km was chose for following compute. Secondly, the technology of secondary programming with Fluent [2] was used to conduct the numerical simulation on a certain missile jet flow field at different altitude. Finally, the regular pattern of jet flow field changing with altitude was researched.

The U.S. Standard Atmosphere (1976) [3] was chose to calculate the atmospheric environment parameter in real time [4], then it was integrated into the program which used the technology of secondary programming with Fluent. This method helped to reduce the workload of data entry and calculus of interpolation.

The results showed that as the altitude increased, the static pressure and the temperature gradually reduced, the static pressure and the temperature gradually reduced, the mach-number increased, and the spreading range of jet flow field became farther.

D. Jin and S. Lin (Eds.): Advances in Mechanical and Electronic Engineering, LNEE 176, pp. 349–355.
springerlink.com

2 Calculation Theory and Model

2.1 Missile Point Motion Equations in the Vertical Plane

The earth was assumed as a static homogeneous ball, and missile as a mass point, the missile's movement in the horizontal plane was ignored, then got the missile point motion equations in the vertical plane, which is defined in Eq(1) [5].

$$\begin{cases} g = g_0 (R_m / h)^2 \\ \dot{x} = v \cos\theta \\ \dot{y} = v \sin\theta \\ \dot{v} = (P \cos\alpha - X)/m - g \sin\theta \\ \dot{\theta} = (P \sin\alpha / m + Y / m - g \cos\theta)/V \\ \dot{m} = -m_c \end{cases} \tag{1}$$

The Fourth-order-Runge-Kutta method was used to solve Eq(1), and the calculation step was chose as 0.01s.

2.2 Flow Governing Equations

In this question, the flow field researched has good axial symmetry, so the three-dimensional question was simplified to a two-dimensional question. Meanwhile, the air was assumed as steady ideal gas with single component. The calculation was based on the Navier-Stokes equations which were composed of continuity equation, momentum equation and energy equation, and on the state equation of ideal gas, which are described in Eq(2) and Eq(3)[6].

$$\begin{cases} \nabla \cdot (\rho \vec{V}) = 0 \\ \vec{V} \cdot \nabla \vec{V} = \vec{f} + \frac{1}{\rho} \nabla P \\ \frac{V^2}{2} + \frac{k}{k-1} \frac{P}{\rho} = const \end{cases} \tag{2}$$

$$P = \rho R T \tag{3}$$

2.3 RNG $k-\varepsilon$ Turbulence Model

RNG $k-\varepsilon$ turbulence model also called Renormalization Group $k-\varepsilon$ turbulence model, it uses the renormalization group method to instantaneous Navier-Stokes equations, and can deal with the flow problem which is with high strain rate and large bending flow line[7]. It is described in Eq(4).

$$\begin{cases} \rho \dfrac{dk}{dt} = \dfrac{\partial}{\partial x_i}\left[\left(\alpha_k \mu_{eff}\right) \dfrac{\partial k}{\partial x_i} \right] + G_k + G_b - \rho\varepsilon - Y_M \\ \rho \dfrac{d\varepsilon}{dt} = \dfrac{\partial}{\partial x_i}\left[\left(\alpha_k \mu_{eff}\right) \dfrac{\partial \varepsilon}{\partial x_i} \right] + C_{1\varepsilon} \dfrac{\varepsilon}{k}\left(G_k + G_{3\varepsilon} G_b\right) - C_{2\varepsilon} \rho \dfrac{\varepsilon^2}{k} + C_{2\varepsilon} \rho \dfrac{\varepsilon^2}{k} - R \end{cases} \tag{4}$$

2.4 Model and Calculation Conditions

The computational domain used the two-dimensional axisymmetric form, and the nozzle shape was ignored. It was shown in Fig. 1 and Fig. 2, AB is the nozzle exit, it used pressure inlet boundary condition, the total temperature, total pressure and static pressure at this face were given in computing; AE is the symmetric axis, it used axis boundary condition; BC, CD and DE used pressure far field boundary condition, the static temperature, static pressure and inlet mach number.

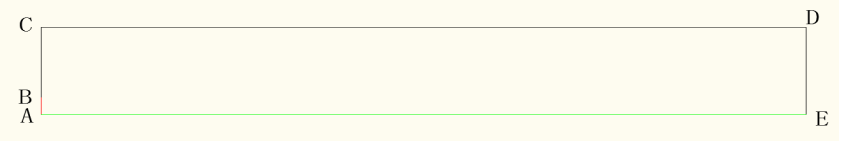

Fig. 1. Computational domain

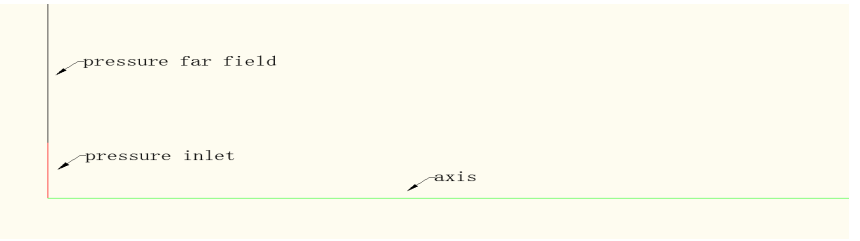

Fig. 2. Local amplification of computational domain

The inlet mach number was calculated as the ratio of missile velocity which was gained by trajectory calculation mentioned above to the local sound velocity. The local sound velocity is described in Eq(5). Table 1 shows 5 typical inlet mach number at different altitude.

$$a = 20.05\sqrt{T} \tag{5}$$

Table 1. Typical inlet mach number in different altitude

Altitude (km)	0	5	10	15	30
Mach Number	0	1.35	2.22	3.06	4.98

2.5 Calculation Process

The Fluent command flow template was used to conduct the auto calculation of jet flow field at different altitude. The flow chart of calculation process was shown in Fig 3.

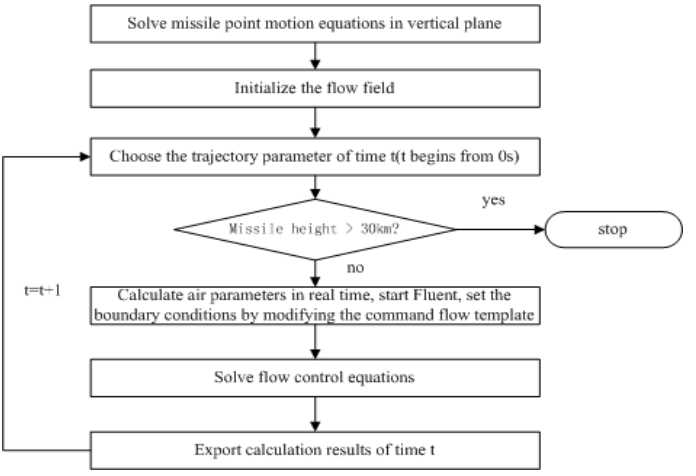

Fig. 3. The flow chart of calculation process

3 Results and Discussion

Firstly the flow field at single altitude was discussed. Fig. 4 to Fig.6 shows the static pressure, static pressure and mach number along the nozzle axis at 0km. As can be seen from the graphs, the initial segment of jet flow field was from 0m to 5m, turbulence transition segment was from 5m to 25m, and fully development segment was the area after 25m. In initial segment, there was a core area next to the nozzle exit, which was about 6m long. In this area, the static pressure and static temperature were constant, and the static pressure was lower than atmospheric pressure, so the nozzle was at over expanded state at 0km. After the core area, the first step appeared, the static pressure and static temperature fell acutely, and the mach number increased seriously along the nozzle axis. In the turbulence transition segment, the considerable oscillation of parameters appeared. In the fully development segment, static pressure fell to atmospheric pressure gradually, and mach number fell to inlet mach number slowly. As to static temperature, it fell too, but was still close to 1000k.

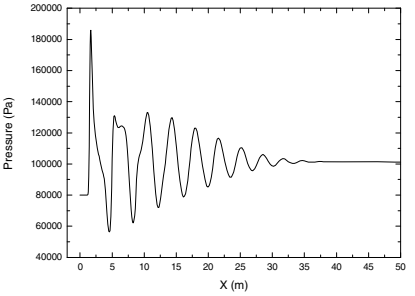

Fig. 4. Static pressure along nozzle axis at 0km

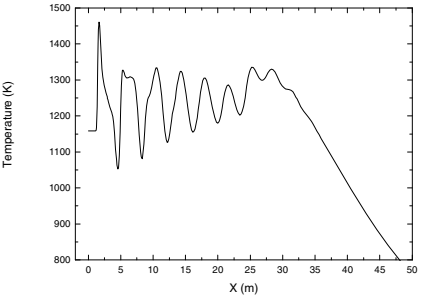

Fig. 5. Static temperature along nozzle axis at 0km

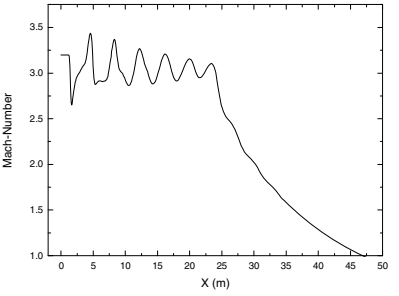

Fig. 6. Mach number along nozzle axis at 0km

Secondly, 0km, 5km, 10km, 15km and 30 km were chose as the typical altitude, Fig. 7 to Fig. 9 shows the static pressure, static pressure and mach number along the nozzle axis at different altitude. As the altitude increased, static pressure became lower, and finally achieved atmospheric pressure of each altitude; static temperature became lower too, the reducing speed became slower, but it was still much hotter than atmospheric temperature at each altitude; mach number became bigger. To different altitude, parameters at nozzle exit were same, it was because that they were mainly affected by structure and working condition of the engine, but in this calculation model, the nozzle shape was ignored, and the state of the nozzle exit were same.

Fig. 10 shows the mach number contours at typical altitude. As the altitude increased, the number of wave nodes became fewer, the length of single wave node was longer, mach disk was clearer, and the spreading range of jet flow field became farther [8]. There were core areas with same size at different altitude, which states were same to nozzle exit.

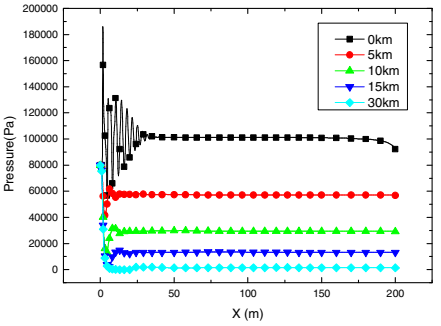

Fig. 7. Static pressure along nozzle axis at typical altitude

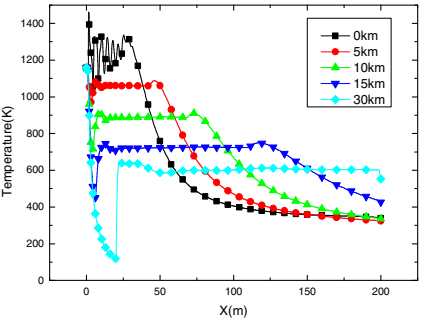

Fig. 8. Static temperature along nozzle axis at typical altitude

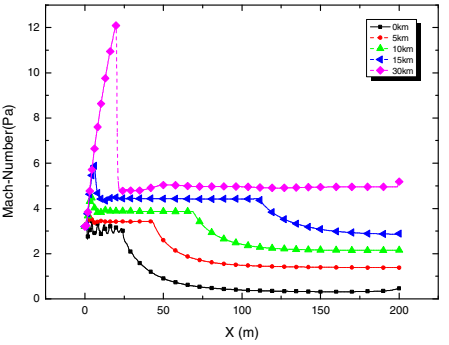

Fig. 9. Mach number along nozzle axis at typical altitude

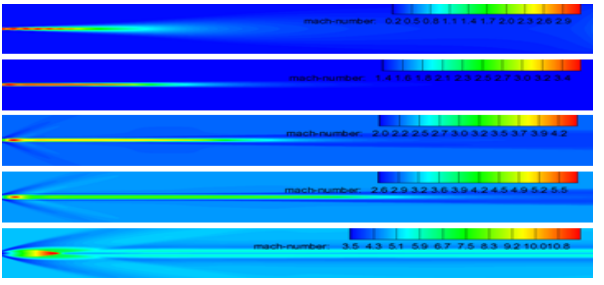

Fig. 10. Mach number contours at 0km, 5km, 10km, 15km and 30km

4 Conclusions

(1) As altitude increased, to the same point at nozzle axis, static pressure became lower; static temperature became lower in initial segment and turbulence transition segment, the regular pattern in fully development segment was not

clear; mach number became higher; the spreading range of jet flow field became farther; jet flow field was at over expanded state at low altitude and became under expanded state at high altitude, because atmospheric pressure became lower and lower.

(2) To a certain altitude, at the end of jet flow field, static pressure fell to atmospheric pressure, and mach number fell to inlet mach number, however, static temperature still was much higher than atmospheric temperature, the jet flow kept high temperature in quite a large area.

(3) There were core areas which had same size and parameters at different altitude, the possible reason was that the nozzle shape was ignored and the state of the nozzle exit were same in this calculation model, which had the main influence on parameters of the area close to nozzle exit.

References

1. Zhang, F.: Rocket Jet Flow Dynamics. Harbin Institute of Technology Press (2004)
2. Xiao, H., Gao, C., Dang, Y., Yang, Y., Wang, G.: Secondary Programming with Fluent and It's Application in Rocket Dynamic Calculation. Aeronautical Computer Technique 05, 59–61 (2009)
3. U.S. Standard Atmosphere, National Oceanic and Atmospheric Administration (1976)
4. Yang, B.: Formulae Expressing of Standard Atmospheric Parameter. Journal of Astronautics 01, 86–89 (1983)
5. Qian, X., Lin, R., Zhao, Y.: Missile Dynamics. Beijing Institute of Technology Press (2000)
6. Zhao, C., Jiang, Y.: Gas Jet Flow Dynamics. Beijing Institute of Technology Press (1998)
7. Fu, D.: Application of Numerical Simulation in Aerospace Launching Technology. National Defense Industry Press (2011)
8. Chang, J., Zhou, C., Li, J.: Numerical Analysis around Flow Field of Rocket in High-low Altitude. Journal of System Simulation 16, 60–63 (2007)

The Research of Mobile Robot Avoid Obstacle Based on Kalman Filter Forecast Combined with Vector Field Rectangular Algorithm

Shigang Cui, Ting Zhang, Li Yang, Li Zhao, and Genghuang Yang

Tianjin Key Laboratory of Informational Sensing & Intelligent Control
Tianjin University of Technology and Education, Hexi, 300222, Tianjin, P.R. China
{cuisg,jinshihui,ygenghuang}@163.com, zilin0723@126.com,
52203881@qq.com

Abstract. Intelligent obstacle avoidance is the key technology of independent robot completing the given task. This paper is mainly aimed at uncertain environments, used the kalman filter algorithm to realize accurately predict estimate of dynamic obstacles, and combining with vector field rectangle method avoid unknown obstacles in real time, at the last conducted simulation of the mobile robot real-time avoiding obstacle in the MATLAB environment.

Keywords: Intelligence obstacle avoidance, Kalman filter forecast, Vector field rectangle method.

1 Introduction

The robot is known as one of "the 20 th century's greatest invention", the appearance of robot and application, which greatly promoted the development of industrial production, aerospace, military, medical care and other fields, it is also greatly convenient to people's life. The variety and complexity of the motion environment, which decide the problem of mobile robot autonomous obstacle-avoiding, it is the key research to the robot field, it also is the key to realize intelligent technology of robot. The safety and accessibility are the main index during the robot obstacle avoidance, accordingly, it have been put forward to solve many method and strategy of robot obstacle avoidance under unknown environment, but it still difficult to avoid obstacle effectively in the dynamic uncertainty environment .

2 The Basic Principle of Kalman Filtering

Kalman published a paper about solving the problem of discrete data linear filtering by using a recursive method (A New Approach to Linear Filtering and Prediction Problems) in 1960. In this article, a new method that overcoming the shortcomings of the wiener filtering is come up, and that is what we today call kalman filtering method. Kalman filter is used widely and powerful, it can estimate in the past and current status of the signal, and even can estimate future state, even if does not know the exact nature of the model. The basic idea is: the minimum mean square error as the best estimation,

D. Jin and S. Lin (Eds.): Advances in Mechanical and Electronic Engineering, LNEE 176, pp. 357–362.
springerlink.com

using the state space model of the signal and noise, using the estimate of the past moment and the observation data of the present moment to update the estimates of state variable, find out the estimate of the present moment. The algorithm according to the established system equation and observed equation to make the meet the minimum mean square error estimate for the signal which needing to deal with.

Kalman filter include two main process: estimated and correction. Estimated process build prior estimate of the current state by using time update equation. Forward calculate the current state variables and error covariance estimated values in time, so that structure a priori estimate for the next time; Calibration process is responsible for feedback, and founded the posteriori estimation of the improvement current state based on measuring update equations in the process of prior estimate and the current estimate of measured variables. Such a process, we call it estimated a forecast-calibration process, the corresponding estimation algorithm called forecast-calibration algorithm. The following are discrete kalman filtering time update equations and state update equations.

Time update equations:

$$\widehat{X_k}^- = A\widehat{X}_{k-1} + B\widehat{U}_{k-1} \quad . \tag{1}$$

$$P_k^- = AP_{k-1}A^T + Q \quad . \tag{2}$$

Status update equations:

$$K_k = P_k^- H^T (HP_k^- H^T + R)^{-1} \quad . \tag{3}$$

$$\widehat{X_k} = \widehat{X_k}^- + K_k (Z_k - H\widehat{X_k}^-) \quad . \tag{4}$$

$$P_k = (I - K_k H)P_k^- \quad . \tag{5}$$

In the above, the amount stated below:

A : The $n \times n$ state transformation matrix is used in the X_{k-1}.

B : The $n \times 1$ control input matrix is used in control vector U_{k-1}.

H : It is $m \times n$ order observation model matrix, it maps the real state space to observation space.

P_k^- : It is $n \times n$ order prior estimate covariance matrix

P_k : It is $n \times n$ order a posteriori estimation error covariance matrix

Q : It is $n \times n$ order process noise covariance matrix

R : It is $m \times m$ order process noise covariance matrix

I : It is $n \times n$ order unit matrix

K_k : It is $n \times m$ order matrix, called kalman gain or mixed factor, the function is to make a posteriori estimation error covariance minimum.

3 The Basic Principle and the Simulation of Vector Field Rectangle Method

3.1 Determined CV Value

Vector field rectangle method is used the grid trust model, it is the researchers of the Carnegie-Mellon university put forward the obstacles probability model in the 1980 s, it is the common environment modeling method, it can unify describe sensor data from different types sensors, and have strong adaptability for such easy to produce inaccurate ultrasonic measurement data of sensors. Grid trust model is described robot's working environment with a 2 d array, each one of these elements represent a grid, each grid has a credibility CV value, used to say distribution of obstacles in this region. The higher the CV value, says the box exists the higher possibility of obstacles, without the place of obstacles, the CV value is 0.

3.2 Calculation Obstacles Density

Robot sensors have the largest measuring range, it is a circle with the robot to the core, the radius $d_{\max}$. During the robot marching forward, it can test the coordinate grid of the obstacles is (x_i, y_j) within the measured scope, the coordinates of the robot is (x_r, y_r) . Thus we can measure the obstacles to the grid robot distance is $d_{i,j}$, and the vector Angle θ between the obstacles gird and robots.

The robot must to select the right direction every time before meeting the obstacle, in order to avoid obstacle, we selected a resolution α , divided the selection of the robot into $n = \frac{360}{\alpha}$ interval, then calculated the density of obstacles falling into each interval:

Fall into the *k* interval obstacles:

$$k = \frac{\theta}{\alpha} \quad . \tag{6}$$

Obstacles make the contribution to the interval density value:

$$m_{i,j} = (c_{i,j})^2 (a - bd_{ij}) \quad . \tag{7}$$

Therefore it can be calculated the interval density values of obstacles:

$$h_k = \sum_{i,j} m_{ij} \ . \tag{8}$$

3.3 The Choice of Robot Direction

Set a threshold λ , the selected below the value of the obstacles density area called "candidate" area, and then determine the distribution of the activity window "wide

valley" and "narrow way" based on the number of consecutive candidate, robot preferred option "wide valley" area as travel direction. Recorded the left zone of "wide valley" in the continuous candidate as k_l, the right zone notes for k_r, at the same time recorded the area between the robot and the target of connections as k_g. When k_g is located in k_l and k_r, it is preferred k_g as candidate direction; If not, the robot can compare the near degree between "narrow way" and the zone which k_g in and the approach degree between the area between k_l and k_r and the zone which k_g in, and then choose the near k_g area as travel direction.

4 The Simulation of Robot Obstacle Avoidance Based on Kalman Filter Forecast Combined with Vector Field Rectangle Method

The procedure flow chart is shown in fig.1.

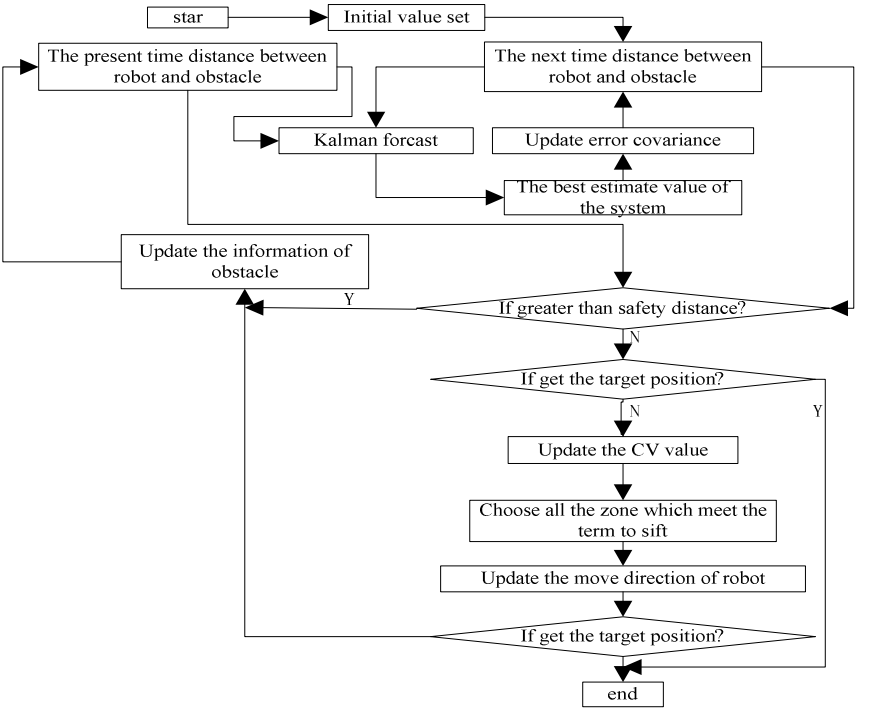

Fig. 1. The procedure flow chart

The simulation result is shown in fig.2 diagram.

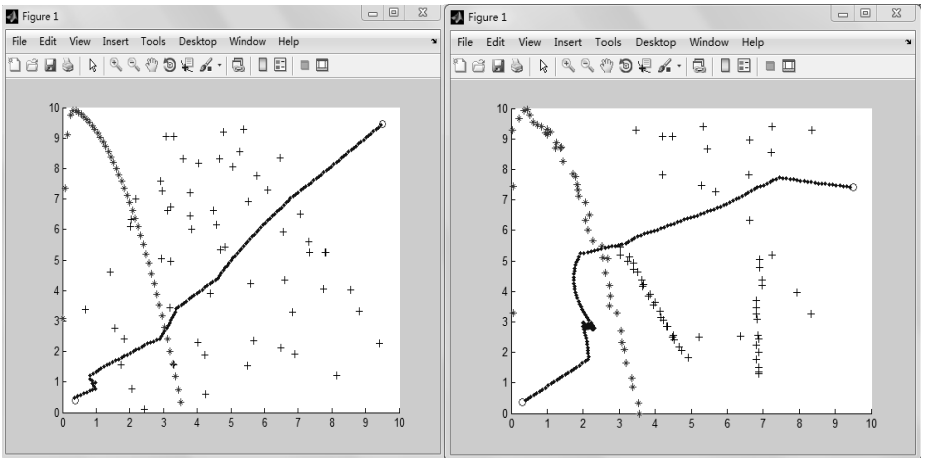

Fig. 2. The simulation result

In the above figure, "+" all represent static obstacles, red "*" are representative of the dynamic obstacles do gearshift sports, blue "*" are representative of the robot route. We can see the robot can very good avoid the static and dynamic obstacles and eventually smooth get to its destination from the fig.2.

5 Conclusion

This paper introduces the principle and the design of the algorithm based on Kalman filter forecast combined with vector field rectangle method, and make the simulation in the MATLAB environment, the simulation results show that the based on Kalman filter forecast combined with vector field rectangle method can effectively and security achieve avoid the obstacles under the uncertain environment, effectively resolve the problem that robot has no prior knowledge for obstacles information especially dynamic obstacles so can only according to detect the current environmental information to take measures of obstacle avoidance which bring with collision to dynamic obstacles.

Acknowledgments. This work was supported by the national natural science foundation of china which the high rate of Internet devices based parallel light scientific research problems, 61178048.

This work was also supported by the twelve-five planning of the Educational Ministry of China 2011 annual issue, the practice research of effectively dovetailing the innovation education between high school and university based on robot, BFA1100491.

References

[1] Ma, Z., Yuan, C.: Mobile robot navigate and avoid obstacles real time based on grid. Robotic (1996)
[2] Wang, H.: Dealing with random digital signal. Scientic Press, Beijing (1998)
[3] Zhang, S., Wu, M., Cao, W.: An avoiding obstacle algorithm under part of dynamic environment. Computer Technology and Automation (2003)
[4] Jing, X.: Kalman filtering and the basic of application. National defense Press, Beijing (1973)
[5] Thongchai, S., Suksakulchai, S., Wilkes, D.M., Sarkar, N.: Sonar Behavior-Based Fuzzy Control for a Mobile Robot. In: Proceedings of the IEEE International Conference on Systems Man, and Cybernetics, pp. 435–440 (2000)
[6] Zhuang, Y., Xu, X.-D., Wang, W.: Mobile Robot Geometric-topological Map Building and Self-localization. Control and Decision 20(7), 815–822 (2005)
[7] Yairi, T., Hori, K.: Map Building By Mobile Robots With Incomplete and Qualitative Observation. In: SICE 2003 Annual Conference, Fukui University, Japan, pp. 1482–1486 (2003)
[8] He, W., Liang, X.: SLAM Problem of Mobile Robots in Unknown Environment. Control & Automation 21(3), 179–180 (2005)
[9] Jia, X.: The vector field rectangular avoidance research of mobile robot based on kalman filtering (2009)
[10] Xu, G., Tan, M.: The present situation and development trend of the mobile robot. Robot Technology and Application (03), 7–14 (2001)

The Floating Crane Gear Fault Classification Model Based on Weighted Kernel Least Squares Support Vector Machines*

BinHuang Lu, YongQi Chen**, and QingE Dai

School of Science and Technology, Ningbo University, Ningbo, China
lingfen7781@163.com

Abstract. Weighted kernel least squares support vector machine is presented to solve the problem of fault diagnosis for floating crane gear box. In Weighted kernel least squares support vector machines, the linear function, the polynomial function and the RBF function are combines as the kernel function. The weight of each function is selected by genetic algorithms. Experiment result proves that the floating crane gear fault recognition rate based on the proposed method is better than the traditional least squares support vector machines.

Keywords: Weighted kernel support vector machine, crane gear box, fault diagnosis, genetic algorithms.

1 Introduction

With the strong generalization ability, the small number of training samples and the excellent non-linear processing capacity and other characteristics, Support Vector Machines (SVM) has developed rapidly in recent years [1-4]. SVM is also very appropriate to solve these problems existing in equipment fault diagnosis, such as the highly cost of getting training samples and nonlinear characteristics of samples. But, the wide application of SVM is limited by it's a disadvantage: It is difficult to select an appropriate kernel function for any data set. For this reason, this issue proposes a weighted kernel least squares support vector machines model (WKLS_SVM). This model makes use of the linear kernel function, the polynomial kernel function and RBF kernel function in least squares support vector machines (LS_SVM) [5]. The weight parameters of the kernel functions are determined by genetic algorithms. The proposed weighted kernel least squares support vector machines model is used in the fault diagnosis system of the floating crane gear box. The experiment result illustrates the classification precision. Furthermore, the least squares support vector machines is compared with the proposed method to indicate the advantage of the proposed method.

* This work was supported by natural science foundation of Ningbo (No. 2009A610074), Scientific Research Fund of Zhejiang Provincial Education Department (Y201119567), SRIP project of Ningbo University in 2012.
** Corresponding author.

D. Jin and S. Lin (Eds.): Advances in Mechanical and Electronic Engineering, LNEE 176, pp. 363–368.
springerlink.com

2 Weighted Kernel Least Squares Support Vector Machines

2.1 The Introduction of Least Squares Support Vector Machines

LS-SVM is a learning algorithm [1]. It uses a hypothesis space of linear function in a high dimensional feature space by using the kernel theory. This algorithm is trained by optimization theory. LS_SVM has been applied in many applications. Given training dataset $\{X_t, Y_t\}, i = 1, \cdots, n$, LS-SVM supposes the Hyperplanes as the following:

$$y = w^T \varphi(x) + b \tag{1}$$

where x , y are input variable and output variable, $\varphi(x)$ is a nonlinear function which maps the feature space of input into a higher dimension feature space and can be reached by the kernel strategy. w is a coefficient determining the margin of support vectors and b is a bias term.

The coefficients (w, b) are determined by minimizing the following regularized risk function and using the equality constraints.

$$\begin{aligned} &\min J(w,e) = \frac{1}{2} w^T w + \frac{1}{2} c \sum_{i=1}^{n} e_i^2 \qquad (c > 0) \\ &y_i [w^T \varphi(x_i) + b] = 1 - e_i \qquad i = 1 \cdots N \end{aligned} \tag{2}$$

where e_i is the nonnegative error variable and used to construct a soft margin hyper plane. In equation (2), the first term, measures the inverse of the margin distance. In order to obtain the minimum structural risk, the first term should be minimized. C is the regularization parameter determining the fitting error minimization and smoothness. This optimization problem including the constraints can be solved by using the Lagrange function as following:

$$\min L(w,b,e,\alpha) = \frac{1}{2} w^T w + \frac{1}{2} c \sum_{i=1}^{n} e_i^2 - \sum_{i=1}^{n} \alpha_i \{ y_i [w^T \varphi(x_i) + b] - 1 + e_i \} \tag{3}$$

This optimization problem can be solved by the following equation matrix:

$$\begin{bmatrix} 0 & y^T \\ y & u \end{bmatrix} \begin{bmatrix} b \\ a \end{bmatrix} = \begin{bmatrix} 0 \\ L_n \end{bmatrix}$$

$$y = [y_1 \cdots y_N]^T, \quad a = [a_1 \cdots a_n]^T, \quad L_n = [1 \cdots 1_N]^T$$

$$u = \begin{bmatrix} y_1 y_1 \varphi(x_1)^T \varphi(x_1) + 1/c & \cdots & y_1 y_n \varphi(x_1)^T \varphi(x_n) \\ \vdots & \ddots & \vdots \\ y_N y_1 \varphi(x_n)^T \varphi(x_1) & \cdots & y_N y_N \varphi(x_n)^T \varphi(x_n) + 1/c \end{bmatrix} \tag{4}$$

From this equation, it can be deduced:

$$b = \frac{y^T u^{-1} L_n}{y^T u^{-1} y}$$
$$a = u^{-1}[1 - y]b \tag{5}$$

Finally, the decision function of the classifier of LS_SVM can be expressed as following:

$$f(x) = sign[\sum_{i=1}^{n} a_i y_i \varphi(x_i)\varphi(x) + b] \tag{6}$$

For this time, the LS_SVM model has been deduced. The functional form of $\phi(\mathbf{x}_i)$ doesn't need to be known since it is defined by the kernel function $K(\mathbf{x}_i, \mathbf{x}_j) = \phi(\mathbf{x}_i)^t \phi(\mathbf{x}_j), i = 1, \cdots, n, j = 1, \cdots, n$. Different kernel functions present different mappings from the input space to the high dimension feature space. The common used kernels for regression problem are given as following:

Linear kernel: $K(\mathbf{x}, \mathbf{y}) = \mathbf{x}^t \mathbf{y}$

Polynomial kernel: $K(\mathbf{x}, \mathbf{y}) = (\mathbf{x}^t \mathbf{y} + 1)^d$

RBF kernel: $K(\mathbf{x}, \mathbf{y}) = \exp(-\frac{\|\mathbf{x} - \mathbf{y}\|^2}{2\sigma^2})$

2.2 Weighted Kernel Least Squares Support Vector Machines

In least squares support vector machines, only a kernel function can be selected for any data set. But, every kernel functions have own advantages. A kind of kernel function can not be suit for any data set. For this reason, the WKLS_SVM is obtained based on LS_SVM. The new regression function is obtained as the following:

$$y = w^T [m1\varphi_1(x) + m2\varphi_2(x) + m3\varphi_3(x)] + b \tag{7}$$

The coefficients (w, b) are determined by minimizing the following optimization problem:

$$\min J(w, e) = \frac{1}{2} w^T w + \frac{1}{2} c \sum_{i=1}^{n} e_i^2 \qquad (c > 0)$$
$$y_i \{w^T [m1\varphi_1(x) + m2\varphi_2(x) + m3\varphi_3(x)] + b\} = 1 - e_i \qquad i = 1 \cdots N \tag{8}$$

This optimization problem can be solved by the following equation matrix:

$$\begin{bmatrix} 0 & y_1 & \cdots & y_n \\ y_1 & y_1 y_1 \varphi(x_1)^T \varphi(x_1) + 1/c & \cdots & y_1 y_n \varphi(x_1)^T \varphi(x_n) \\ \vdots & \vdots & \ddots & \vdots \\ y_n & y_1 y_n \varphi(x_1)^T \varphi(x_n) + 1/c & \cdots & y_n y_n \varphi(x_n)^T \varphi(x_n) + 1/c \end{bmatrix} \begin{bmatrix} b \\ a_1 \\ \vdots \\ a_n \end{bmatrix} = \begin{bmatrix} 0 \\ 1 \\ \vdots \\ 1 \end{bmatrix}$$

$$\varphi(x_1) = m1\varphi_1(x_1) + m2\varphi_2(x_1) + m3\varphi_3(x_1)$$

$$\varphi(x_n) = m1\varphi_1(x_n) + m2\varphi_2(x_n) + m3\varphi_3(x_n)$$

$$\varphi_1(x_i)\varphi_1(x_j) = k_1(x_i, x_j) = x_i^t x_j$$

$$\varphi_2(x_i)\varphi_2(x_j) = k_2(x_i, x_j) = (x_i^t x + 1)^2$$

$$\varphi_3(x_i)\varphi_3(x_j) = k_3(x_i, x_j) = \exp(-\frac{\|x_i - x_j\|^2}{2\sigma^2}$$

$$\varphi_1(x_i)\varphi_2(x_j) = k_4(x_i, x_j) = \sqrt{\varphi_1(x_i)\varphi_1(x_i)\varphi_2(x_j)\varphi_2(x_j)}$$

$$= \sqrt{k_1(x_i, x_i)k_2(x_j, x_j)}$$

$$\varphi_1(x_i)\varphi_3(x_j) = k_5(x_i, x_j) = \sqrt{\varphi_1(x_i)\varphi_1(x_i)\varphi_3(x_j)\varphi_3(x_j)}$$

$$= \sqrt{k_1(x_i, x_i)k_3(x_j, x_j)}$$

$$\varphi_2(x_i)\varphi_3(x_j) = k_6(x_i, x_j) = \sqrt{\varphi_2(x_i)\varphi_2(x_i)\varphi_3(x_j)\varphi_3(x_j)} \quad (9)$$

$$= \sqrt{k_2(x_i, x_i)k_3(x_j, x_j)}$$

From these equations, the decision function of WKLS_SVM can be deduced as:

$$f(x) = sign\{\sum_{i=1}^{n} a_i y_i [m1\varphi_1(x_i) + m2\varphi_2(x_i) + m3\varphi_3(x_i)] \quad (10)$$

$$[m1\varphi_1(x) + m2\varphi_2(x) + m3\varphi_3(x)] + b\}$$

2.3 WKLS_SVM Weight Parameters Optimization Based on Genetic Algorithms

In the WKLS-SVM model, the appropriate kernel functions weight parameters are selected by the genetic algorithms. k_1, k_2 and k_3 is regarded as chromosomes of genetic algorithms [6], then, these chromosomes are evaluated in the current iteration and selected in the next iteration according to their fitness values. The chromosomes with higher fitness values are more likely to be selected in the next iteration. After the

selection process, genetic operations such as crossover, mutation, and inversion are operated on the selected chromosomes, causing them to evolve in hope that desirable characteristics can be passed from iteration to iteration. The detail steps of genetic algorithms for WKLS_SVM weight parameters is obtained as following:

Step1: Take the weighted kernel parameters $(m1, m2, m3)$ as chromosomes and set crossover, mutation parameters, give training samples $\{X_t, Y_t\}, i = 1, \cdots, n$.

Step2: use the samples and chromosomes $(m1, m2, m3)$ to train WKLS-SVM and get the classification precise of all chromosomes.

Step3: regard the classification precise as fitness function of genetic algorithms and selected some chromosomes in the next iteration.

Step4: update the chromosomes according to crossover, mutation and inversion operations.

Step 5: Evaluate the objective values of all particles.

Step 6: If a stopping criterion is met, then output the optimal chromosome $(m1, m2, m3)$ as the the optimal weight value; otherwise go back to Step (3).

Step7: Finally, obtain the LS-SVM model at the best optimal weighted kernel parameters and get the output data.

3 Experimental Results

Floating crane gear box fault is used to verify the effectiveness of the WKLS_SVM. There are 3 modes for the gear box: The normal mode, The gear wear, The gear teeth broken. Nine samples are used to train WKLS_SVM. Three groups of the normal mode, three groups of gear wear, three groups of the gear teeth broken. 40 samples are used to test WKLS_SVM. As well as compared with the fault diagnosis based on LS_SVM for the same sample. The diagnosis results is in the table1, The results shows that WKLS_SVM performance is significantly better than the LS_SVM. The weight parameters is automatically selected by genetic algorithms and is obtained in talble1.

Table 1. Comparison results of LS_SVM and WKLS_SVM

Method	Verification rate	Weight parameters
LS_SVM	95%	1
Optimized LSVM	97.5%	[0.71, 0.65.0.38]

4 Conclusions

In this issue, weighted kernel least squares support vector machines is proposed to improve the classification precision. Floating crane gear fault diagnosis experiment demonstrates the effect of the proposed method.

References

1. Suykens, J.A.K., Vandewalle, J.: Least Squares Support Vector Machine Classifiers. Neural Processing Letters 9, 293–300 (1999)
2. Chunfu, L., Shengde, W.: Fuzzy Support Vector Machines. IEEE Transactions on Neural Networks 13, 464–471 (2002)
3. Mangasarian, O.L., Musicant, D.R.: Lagrangian Support Vector Machines. Journal of Machine Learning Research 1, 161–177 (2001)
4. Scholkopf, B., Smola, A.J., Williamson, R.C.: New Support Vector Algorithms. Neural Computation 12, 207–1245 (2000)
5. Suykens, J.A.K., Brabanter, J., Lukas, L., Vandewalle, J.: Weighted Least Squares Support Vector Machines: Robustness and Sparse Approximation. Neurocomputing 48, 85–105 (2002)
6. Franklin, A., Karjalainen, P.: Using genetic algorithms to find technical trading rules. Journal of Financial Economics 51, 245–271 (1999)

A Novel Lagrangian Support Vector Machine and Application in the Crane Gear Fault Diagnosis System*

MingYang Sheng, YongQi Chen**, and QingE Dai

School of Science and Technology, Ningbo University, Ningbo, China
lingfen7781@163.com

Abstract. Lagrangian support vector machine (LSVM) owns good generalization ability. But traditional LSVM regards all attributes of samples owning the same important degree in training process. In fact, some attributes are more important than others for training LSVM. In this issue, a novel LSVM is proposed. The different weight parameter for the different attribute is obtained by particle swarm optimization. The crane gear fault diagnosis experiment is accomplished to demonstrate the effect of the novel LSVM.

Keywords: Lagrangian support vector machine, attribute, fault diagnosis, particle swarm optimization.

1 Introduction

LSVM owns the strong generalization ability, the small number of training samples and the excellent non-linear processing capacity and other characteristics [1], so LSVM has achieved rapid development in recent years. As the best small-sample learning theory, LSVM has become the research focus in the field of artificial intelligence and machine learning. SVM is very appropriate in the application of equipment fault diagnosis due to the highly cost of getting training samples and nonlinear characteristics of samples. Although LSVM owns many advantages, LSVM regards each attribute of samples owning the equal contribution to the performance of LSVM. However, when LSVM is used in the fault diagnosis system, some attributes occupy a major position in the fault classification, and other attributes may be redundant indicator [2-4]. For these reasons, this issue proposes a weight LSVM. This method give each attribute a different weight parameter by particle swarm optimization. The important attribute is given a large weight in order to play a more important role in training LSVM. Finally, the crane gear fault diagnosis experiment is accomplished to demonstrate the effect of the novel LSVM.

* This work was supported by natural science foundation of Ningbo (No. 2009A610074), Scientific Research Fund of Zhejiang Provincial Education Department (Y201119567), SRIP project of Ningbo University in 2012.
** Corresponding author.

D. Jin and S. Lin (Eds.): Advances in Mechanical and Electronic Engineering, LNEE 176, pp. 369–373.
springerlink.com

2 Weighted Lagrangian Support Vector Machine

2.1 The Introduction of Least Squares Support Vector Machines

LS-SVM is a learning algorithm [1]. It uses a hypothesis space of linear function in a LS-SVM is a learning algorithm [1]. It uses a hypothesis space of linear function in Given training dataset $\{(\mathbf{x}_1, y_1), \cdots (\mathbf{x}_n, y_m)\} \subset \chi \times R$, where χ denotes the space of the input patterns, $\phi(x)$ is a nonlinear function which maps the feature space of input into a higher dimension feature space and can be reached by the kernel strategy. ω is a coefficient determining the margin of support vectors and b is a bias term. The coefficients (ω, b) are determined by minimizing the following regularized risk function and using the equality constraints.

$$\min J(w,e) = \frac{1}{2}(\omega'\omega + b^2) + \frac{1}{2}c\sum_{i=1}^{N}\xi_i^2 \qquad (c>0)$$

$$s.t.\ y_i[(\omega \cdot x_i) + b] + \xi_I \geq 1 \qquad i = 1 \cdots m \tag{1}$$

This optimization problem including the constraints can be solved by using the Lagrange function as following:

$$\min L = \frac{1}{2}\omega'\omega + b^2 + \frac{1}{2}c\sum_{i=1}^{N}\xi_i^2 - \sum_{i=1}^{N}\alpha_i\{y_i[(\omega \cdot x_i) + b] + \xi_i - 1\} \tag{2}$$

The LSVM Algorithm is based directly on the Karush-Kuhn-Tucker necessary and sufficient optimality conditions for the dual problem:

$$0 \leq \alpha \perp (Q\alpha - e) \geq 0 \tag{3}$$

These optimality conditions lead to the following iterative scheme for LSVM algorithm:

$$\alpha^{i+1} = Q^{-1}(e + ((Q\alpha^i - e) - \lambda\alpha^i)_+), i = 0,1,\cdots, \lambda > 0 \tag{4}$$

2.2 Weighted LSVM Based on Particle Swarm Optimization

In weight LSVM, a weight matrix is construct for each training samples as follows:

$$\mathbf{w} = \begin{bmatrix} w_1 & 0 & 0 \\ 0 & \ddots & 0 \\ 0 & 0 & w_m \end{bmatrix} \tag{5}$$

By the weight $\mathbf{w}$, the training samples of LSVM are converted:

$$\mathbf{x}_i = [w_1 x_{i1} \quad \cdots \quad w_m x_{im}] \tag{6}$$

Each attribute own its weight parameters. The large weight leads to a important role in training LSVM. The kernel functions is also changed:

(1)Weight RBF kernel function:

$$K^w(\mathbf{x_i w}, \mathbf{y_j w}) = \exp(-\sum_{p=1}^{n}(x_{ip}w_p - w_p y_{jp})^2 \Big/ 2\sigma^2 = \exp(-(\mathbf{x_i} - \mathbf{y_j})^T \mathbf{w}\mathbf{w}^T(\mathbf{x_i} - \mathbf{y_j}) \Big/ 2\sigma^2)$$

(2)Weight linear kernel function:

$$K^w(\mathbf{x_i w}, \mathbf{y_j w}) = \sum_{p=1}^{n} x_{ip}\mathbf{w}^p\mathbf{w}^p y_{jp} = \mathbf{x_i}^T \mathbf{w}\mathbf{w}^T \mathbf{y_j}$$

(3)Weight polyminal kernel function:

$$K^w(\mathbf{x_i w}, \mathbf{y_j w}) = (1 + \sum_{p=1}^{n} x_{ip} w^p w^p y_{jp})^d = (1 + \mathbf{x_i}^T \mathbf{w}\mathbf{w}^T \mathbf{y_j})^d$$

The decision function of weight LSVM is:

$$f(\mathbf{x}) = sign\left[\sum_{i=1}^{n} a_i y_i K(\mathbf{x}_i \mathbf{w}, \mathbf{x w}) + b\right] \tag{7}$$

From this decision function, the smaller w_i leads to the smaller impact to the Gaussian kernel and classification results. When w_i is equal to 0, then the ith attribute disappears from the calculation of the kernel function and have no impact on the classification results.

In the kernel function of weight LSVM, the weight parameters are selected by the particle swarm optimization. PSO was developed by Kennedy and Eberhart [5] to model the birds flocking and fishes school for food. PSO starts with a random initialization of individuals in the search space and works on the social behavior of the particles in the swarm. The weight w_i is selected based on PSO in this issue. w_i are regarded as the swarm. The algorithm of weight parameters selection method based on PSO can be summarized as following:

Step1: Regard the weight parameters w_i as particles and initialize n_{sw} particles with random positions $x_i^k = w_i$ and velocities $v_i^k = v_i, i = 1, \cdots n_{sw}$, Moreover, training samples and test samples are also given here;

Step2: LSVM is trained by training samples. Then one can obtain the classification precision of the test samples by the trained LSVM for each particle;

Step3: Regard the classfication precision as fitness value;

Step 4: If the max iteration times is met, output the optimal particle as weight LSVM parameters. Otherwise, go to Step (5).

Step 5: Generate n_{sw} new particles of PSO from the current particle.

Step6: $k = k + 1$ and go to step 2.

3 Experimental Results

Large floating crane gear fault classification is used to illustrate the effect of the weight LSVM. The gear faults of training samples, including gear wear, the rotor pitting fault samples, gear crack fault samples and normal samples. A floating crane gear box failure set is made of the gear box, drive motor, inverter and sensor components. The floating crane gear box vibration fault, signals are often transient signals. the singular points of these mutations in the signal contains a wealth of fault information. For example, the signal of a normal gear reflects on the power spectrum, the meshing frequency and its harmonic components. The meshing frequency composition, its high-order harmonic decreases in turn. At the same time, the low frequency gear shaft rotation frequency and its higher harmonics makes lower. In the event of gear wear, the meshing frequency and its harmonic components remain unchanged, but the amplitude are changes and high-order harmonic amplitude increases. In addition, a increased wear may also result in fractional harmonics. A tooth broken will be the rotation frequency of the frequency characteristics. It can use the Lipschitz exponent of the singularity to characterize its size through the discrete wavelet transform in different scales of values. It is difficult to achieve in other mathematical methods, mainly due to the discrete wavelet function is equivalent to a band-pass filter different frequency signals, and enable different scales by a different band channel separation. The singular point of the fault signal can be transformed to different frequency components of the floating crane gear box by discrete wavelet. the discrete wavelet transform to approximate part of the layer can be expressed as:

$$A_j = \sum_{-\infty}^{+\infty} f(n)\phi_{j,k}(n) = \sum_{-\infty}^{+\infty} f(n)\frac{1}{\sqrt{2^j}}\phi\left(\frac{n-k2^j}{2^j}\right) \tag{8}$$

Which is the wavelet function, scaling function, the time series of large floating crane gear box failure. Similarly, the details of the discrete wavelet transform part of the fault signal in the first layer can be expressed as:

$$D_j = \sum_{-\infty}^{+\infty} f(n)\psi_{j,k}(n) = \sum_{-\infty}^{+\infty} f(n)\frac{1}{\sqrt{2^j}}\psi\left(\frac{n-k2^j}{2^j}\right) \tag{2}$$

Based on the above formula, the three-layer decomposition of the floating crane failure signal, has been a hierarchical approximation and detail signals by computing the energy parameters of the different frequency bands of the time series of gearbox failure. When gearbox failure, the energy of the signal within the same band appear significant differences compared with the normal state. Different energy changes represent different fault information, these energy parameters can be converted as the fault feature vectors.

Set the optimization space of the weight vector $0 < w \le 1$, the initial 15 groups of weight. The penalty coefficient of LSVM is 1.7 the radial width of the Gaussian kernel function 0.13. After 50 iterations of particle swarm optimization, the weights parameters are selected $w = [0.4607, 0.8611, 0.6972, 0.5426, 0.7373, 0.2715]$. The fault classification precision achieved as 98.5%. In order to illustrate the effect of weight LSVM, the comparison results of LSVM and weight LSVM are list in table 1.

Table 1. Comparison results of LS_SVM AND WEIGHT LSVM

Method	LSVM	Weight LSVM based on
w	$w_i = 1, i = 1, \cdots, 6$	$w = [0.4607 \quad 0.8611 \quad 0.6972$ $0.5426 \quad 0.7373 \quad 0.2715]$
Classification precision	92.7%	98.5%

4 Conclusions

In this issue, weight LSVM is proposed to improve the classification precision. Floating crane gear fault diagnosis experiment demonstrates the effect of the proposed method. The fault classification accuracy improvement is very important, especially in a variety of fault types and the complexity of the equipment. For this reason, weight LSVM play important role in production safety.

References

1. Mangasarian, O.L., Musicant, D.R.: Lagrangian Support Vector Machines. Journal of Machine Learning Research 1, 161–177 (2001)
2. Chuang, C.C.: Fuzzy Weighted Support Vector Regression With a Fuzzy Partition. IEEE Transactions on Systems, Man, and Cybernetics—part b: Cybernetics 37, 1287–1299 (2007)
3. Judong, S., Syaub, Y.R., Leea, E.S.: Support Vector Fuzzy Adaptive Network In Regression Analysis. Computers and Mathematics with Applications 54, 1353–1366 (2007)
4. Ash, C., Turksen, I.B.: Fuzzy Functions With Support Vector Machines. Information Sciences 177, 5163–5177 (2007)
5. Kennedy, J., Eberhart, R.: Particle Swarm Optimization. In: Proc. IEEE Int. Conf. on Neural Networks, pp. 1492–1948. IEEE Press, Perth (1995)

Research on Inverted Pendulum Control Based on LQR

Hui Fang, Wei Tang, and Enrang Zheng

Shaanxi University of Science and Technology,
710021 Xi'an China
qyfanghui@126.com

Abstract. In this paper, the author constructs a mathematical model of linear single inverted pendulum with the Newton-Euler method, and analyzes the design approach of LQR control of linear single inverted pendulum on this basis. Through the comparative simulation between different values of Q and R, the way of valuing Q and R in LQR control method of single inverted pendulum is presented. Results of the analysis in this paper have a certain theoretically instructive significance for researches in this area.

Keywords: inverted pendulum, LQR, control.

1 Introduction

Inverted pendulum is a non-linear, strongly coupled, multivariable and absolutely unstable system. Because there are lots of similarities between controlling inverted pendulum and controlling rocket launch and robot walking, its control process can effectively reflect many key problems of control. Thus, inverted pendulum is an important experimental device of studying control theory. Many control theories and control methods can be conducted with physical verification through inverted pendulum experiment.

2 The Mathematical Model of Linear Single Inverted Pendulum

The linear single inverted pendulum can be abstracted as a system composed of a cart and a homogeneous rod without air resistance and all kinds of frictions, shown in Fig.1:

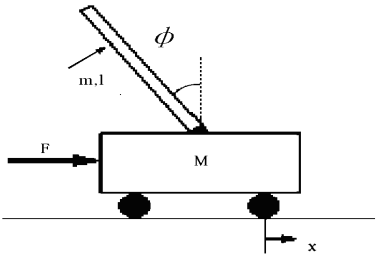

Fig. 1. Linear single inverted pendulum

D. Jin and S. Lin (Eds.): Advances in Mechanical and Electronic Engineering, LNEE 176, pp. 375–380.
springerlink.com

The mass of the cart is M and the mass of the pendulum rod is m. The length between the rotation axis and the rod centroid is l. The position of the cart is x. The angle between the pendulum rod and the vertical direction is ϕ, and the force added to the cart is F. Assume that the friction coefficient of the cart is b and the inertia of the pendulum rod is I, the state space equation of linear single inverted pendulum system can be acquired through modeling of Newton-Euler method:

$$\begin{bmatrix} \dot{\phi} \\ \ddot{\phi} \\ \dot{x} \\ \ddot{x} \end{bmatrix} = \begin{bmatrix} 0 & 1 & 0 & 0 \\ \frac{mgl(M+m)}{I(M+m)+Mml^2} & 0 & 0 & \frac{-mlb}{I(M+m)+Mml^2} \\ 0 & 0 & 0 & 1 \\ \frac{m^2gl^2}{I(M+m)+Mml^2} & 0 & 0 & \frac{-b(I+ml^2)}{I(M+m)+Mml^2} \end{bmatrix} \begin{bmatrix} \phi \\ \dot{\phi} \\ x \\ \dot{x} \end{bmatrix} + \begin{bmatrix} 0 \\ \frac{ml}{I(M+m)+Mml^2} \\ 0 \\ \frac{I+ml^2}{I(M+m)+Mml^2} \end{bmatrix} u \tag{1}$$

$$y = \begin{bmatrix} \phi \\ x \end{bmatrix} = \begin{bmatrix} 1 & 0 & 0 & 0 \\ 0 & 0 & 1 & 0 \end{bmatrix} \begin{bmatrix} \phi \\ \dot{\phi} \\ x \\ \dot{x} \end{bmatrix} + \begin{bmatrix} 0 \\ 0 \end{bmatrix} u \tag{2}$$

which is expressed as $\dot{x} = Ax + Bu$

$y = Cx + Du$, so

$$A = \begin{bmatrix} 0 & 1 & 0 & 0 \\ \frac{mgl(M+m)}{I(M+m)+Ml^2} & 0 & 0 & \frac{-mlb}{I(M+m)+Ml^2} \\ 0 & 0 & 0 & 1 \\ \frac{m^2gl^2}{I(M+m)+Ml^2} & 0 & 0 & \frac{-b(I+ml^2)}{I(M+m)+Ml^2} \end{bmatrix},$$

$$B = \begin{bmatrix} 0 \\ \frac{ml}{I(M+m)+Ml^2} \\ 0 \\ \frac{I+ml^2}{I(M+m)+Ml^2} \end{bmatrix},$$

$$C = \begin{bmatrix} 1 & 0 & 0 & 0 \\ 0 & 0 & 1 & 0 \end{bmatrix}, \quad D = \begin{bmatrix} 0 \\ 0 \end{bmatrix}$$

3 LQR Method

LQR refers to linear quadratic regulator. The LQR problem represents such a physical concept: If a system deviates from the zero state due to external disturbance, then what kind of control u should be imposed so that the system can be back near the zero state, satisfying that the quadratic objective function is the minimum.

LQR method is aimed at the state equation $\dot{x} = Ax + Bu$. Through determining the matrix K of the optimal controlled variable $u(t) = -Kx(t)$, the control

performance index $J = \int_0^\infty (x^T Qx + u^T Ru)dt$ reaches its minimum. Q is a positive definite (or positive semi-definite) Hermitian or a real symmetric matrix, and R is a positive definite Hermitian or a real symmetric matrix. Q and R represent relative importances of error and energy loss respectively. Each element in the diagonal matrix of Q represents the relative importance of each index error respectively[4]. The controller gain of LQR is:

$$K = LQR\ (A,B,Q,R)$$
$$u(k) = -Kx$$

The control of LQR method is illustrated in Fig. 2:

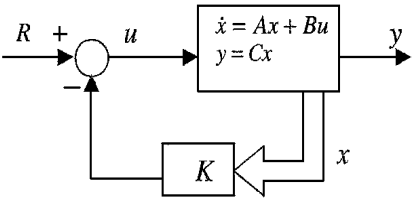

Fig. 2. Linear feedback controller

4 The Study on LQR Control of Linear Single Inverted Pendulum

4.1 The Control of Inverted Pendulum

The objective of inverted pendulum control is to exert a force F (u, controlled variable) on the cart pedestal so that the cart will remain at a predetermined location and the rod will not fall, which means the vertical deviation will not go beyond a predefined angle range. There are altogether four control targets, namely angle ϕ and angle rate $\dot{\phi}$ of the single inverted pendulum, cart position x and cart rate $\dot{x}$.

4.2 LQR Control and Simulation Analysis of Inverted Pendulum

With the Matlab tool function lqr, the corresponding feedback gain matrix K of the optimal controller can be dertermined, K = LQR (A,B,Q,R). For a specific single inverted pendulum system, A and B are determinate. So the key point, as well as the difficulty, of LQR control of inverted pendulum lies in the selection of Q and R. The two parameters, Q and R, are used to balance sensitivities of the system on input variable and state variable. As for the inverted pendulum system illustrated in formula (1)and formula (2), $Q_{1,1}$, $Q_{2,2}$, $Q_{3,3}$ and $Q_{4,4}$ of the matrix Q respectively represent the sensitivity of cart position, cart velocity, angle of pendulum rod and angular velocity of pendulum rod.

Set model parameters of an actual single inverted pendulum as: M = 1.096Kg, m=0.109Kg, b=0.1N/m/sec, *l*=0.25m, I=0.0034 Kg • m • m, and the sampling frequency T=0.005s. So, corresponding to state space equations (1) and (2), there are:

$$A=\begin{bmatrix} 0 & 1 & 0 & 0 \\ 31.5397 & 0 & 0 & -0.2671 \\ 0 & 0 & 0 & 1 \\ 0.7132 & 0 & 0 & -0.0890 \end{bmatrix}, \quad B=\begin{bmatrix} 0 \\ 2.6708 \\ 0 \\ 0.8903 \end{bmatrix}$$

(1) Choose R=1, Q=diag[1, 1, 1, 1], and conduct Matlab programming simulation. Results are as shown in Figure 3a and 3b.

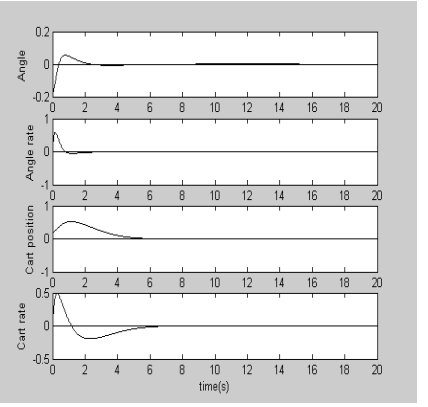

Fig. 3a. Responses of inverted pendulum controlled by LQR

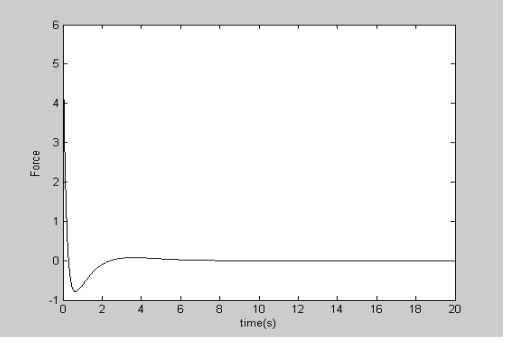

Fig. 3b. Output of LQR controller

(2) Choose R=1, Q=diag[100, 10, 1, 1], and conduct Matlab programming simulation. Results are as shown in Figure 4a and 4b.

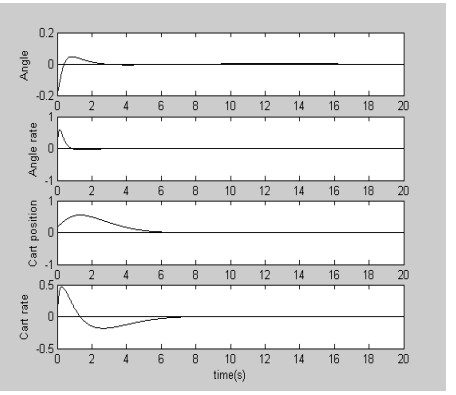

Fig. 4a. Responses of inverted pendulum controlled by LQR

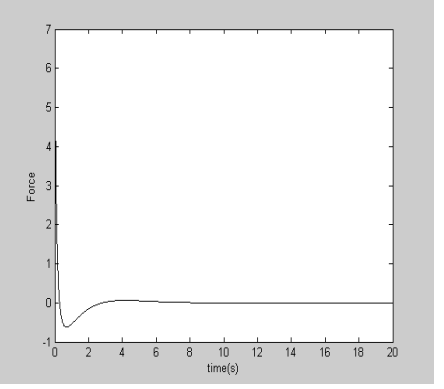

Fig. 4b. Output of LQR controller

(3) Choose R=0.1, Q=diag[1, 1, 1, 1], and conduct Matlab programming simulation. Results are as shown in Figure 5a and 5b.

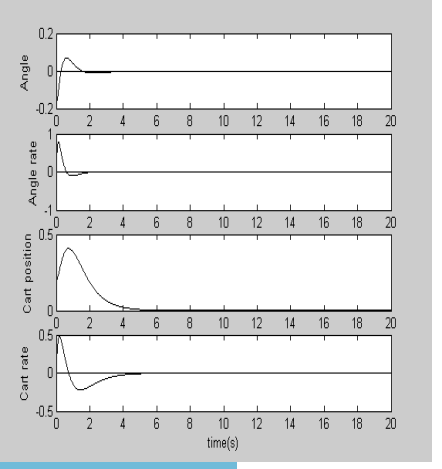

Fig. 5a. Responses of inverted pendulum controlled by LQR

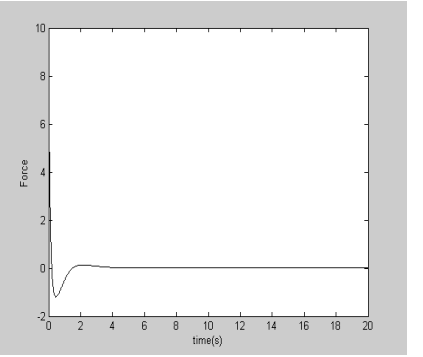

Fig. 5b. Output of LQR controller

It can be seen from the above simulations that LQR control of single inverted pendulum has a good control effect for different values of Q and R.

5 Conclusion

Through simulation study, it can be concluded that the optimal control of single inverted pendulum can be realized by LQR. Besides, the Q and R selection of LQR control of single inverted pendulum can be conducted in this way: the simplest case is to suppose that R=1 and Q is a unit matrix. It is able to adjust controller through changing nonzero elements in matrix Q so as to get the desired response. It is not only able to adjust the time of the cart of arriving at the designated position through adjusting $Q_{1,1}$, but also able to adjust the time needed by the pendulum rod of achieving stability and the effect of stability through adjusting $Q_{3,3}$.

References

1. Googol Technology (Shenzhen) Co., LTD. Googol Pendulum System and Automatic Control Experiment (2002)
2. Wu, S.: Application of Optimal Control. Xi'an Jiaotong University Press, Xi'an (1988)
3. Zheng, D.: Linear System Theory. Tsinghua University Press, Beijing (2002)
4. Liu, J.: Advanced PID Control of MATLAB Simulation. Publishing House of Electronics Industry, Beijing (2004)
5. Dan, H., et al.: Inverted Pendulum Control System Based on LQR Optimal Control Regulator. Microcomputer Information (Measurement and Control) 20(2), 37–38 (2004)

Simulation and Optimization of the Hydraulic System of 3000T Automatic Hydraulic Machine

Zhaomei Xu, Yuwei Dong, and Gang Yang

Faculty of Mechanical Engineering, Huaiyin Institute of Technology, Huaian, JiangSu, China
fuyun588@163.com, {1229849292,46710016}@qq.com

Abstract. The hydraulic model was set up and the dynamic simulation was processed under the AMESim simulation environment by analyzing the working principle of the 3000T Hydraulic Machine. The relation curves versus time were obtained, which represented the working process of the press part. Then some defects of the hydraulic system were appeared according to the curves, and they were optimized and improved eventually

Keywords: Hydraulic Machine, Hydraulic System, AMESim Simulation.

1 Introduction

Automatic hydraulic machine is the most critical equipment of the production line of modern hydraulic equipment. As technology continues to progress and development of hydraulic, hydraulic press hydraulic system stability, reliability, accuracy also raised higher and higher requirements. The level of domestic hydraulic machine is close to and even some over the level of foreign advanced hydraulic press. Hydraulic system design by means of experience, and theoretical work rarely. Using simulation software AMESim hydraulic machine hydraulic system simulation, can be determined that the hydraulic system design is reasonable, if designed to achieve the desired in order to effectively shorten the design cycle.

This article is drawn according to a particular design 3000T hydraulic press. The hydraulic system will have a strong vibration and sound of gun Ming, during the debugging process at some stage. In order to solve this problem fastly and low-cost, we use the simulation software AMESim modeling and model simulation. And a work cycle of the pressure curve analysis of the curve, and ultimately where the problem lies was found out. So, the hydraulic system has been improved to solve practical problems.

2 3000T Hydraulic System Working Principle

The dual-pump and dual-circuit hydraulic system of the hydraulic press, together with the upper and lower cylinder prefill valve structure, the whole system has a flow of hydraulic lines, and low power consumption.

D. Jin and S. Lin (Eds.): Advances in Mechanical and Electronic Engineering, LNEE 176, pp. 381–387.
springerlink.com

According to the structural characteristics of the hydraulic press, hydraulic system simulation needs, under the premise does not affect the simulation results, simplified under the cylinder structure, designed to suppress part of the hydraulic schematic shown in Figure 1:

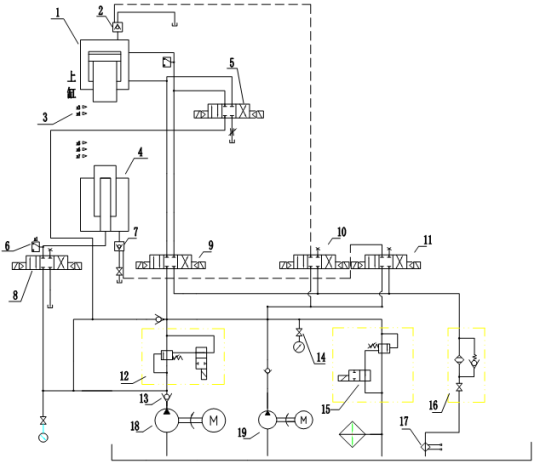

1. upper cylinder 2, 7 Charging Valve 3, press contact 4, lower cylinder 5, 8, 9, 10, 11, directional valve 6, pressure sensor 12, 15 relief valve 13 check valve 14 pressure gauge 18, 19 hydraulic pump 16, filter 17 thermometer

Fig. 1. Hydraulic machine principle

When the hydraulic syestm was started, Of particular note is that the cylinder prefill valve when the cylinder fast downlink up the oil on the cylinder, while valve 5 right. Under the cylinder fast uplink cylinder prefill valve 7 to open up the oil, the solenoid valve 8 Left. Reach the preset pressure contact at the start pressure, the electromagnetic relief valve 12 is closed, the system produces 3MP pressure, while the upper and lower cylinder filling valve is closed, the piston cavity into the oil, valve 3 left The upper and lower cylinder interconnected confluence get 25MP pressure. Another pressure contact is reached, the upper and lower cylinder unloading tank upstream, under the tank up, bricks launched the mold, pick up the launch by the clamp. Then under the tank filling valve is opened, fall under the tank by gravity, into the next work cycle.

Should be noted that, due to the set pressure of the electromagnetic relief valve 13 is set for 3MP electromagnetic relief valve 12 and 13 relative to the pump 16 is connected in series, so a 25MP pressure, the electromagnetic relief valve set pressure of 14should be set to 22MP.

3 Hydraulic System AMESim Model

According to the Hydraulic schematic diagram, the hydraulic system simulation model was set up. Given the special structure of the upper and lower cylinder, if only using the AMESim library, and the principle of internal structure can not be fully expressed, Therefore, in order to get a more accurate simulation results, the model of the upper and lower cylinder were established by the HCD library.

For one specific hydraulic system, the purpose of analysis was different, when the model meet the requirements, the model was smaller as simple as possible. When the press hydraulic system was modeled, little effect on the simulation results of a secondary factor can be ignored. Once the pressing process, for example, the specific modeling results shown in Figure 2.

In this model, due to the fall of the lower cylinder by gravity the above cavity was directly through the fuel tank. Meanwhile, in order to facilitate the modeling cylinder structure was simplified as a hydraulic cylinder. The purpose of this simulation is to find out the sound of the gun Ming action, so this simplifies does not affect the conclusions.

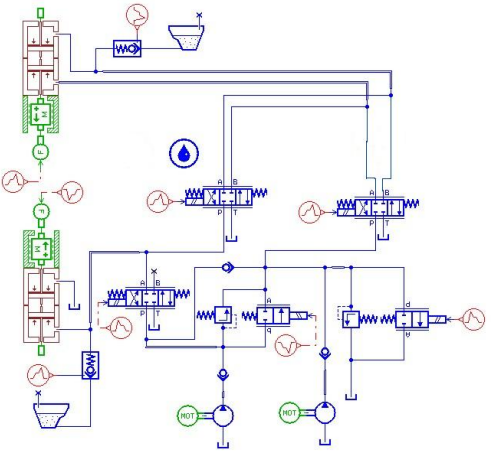

Fig. 2. AMESim model of the hydraulic schematic

4 Simulation Results and Analysis

According to the actual work process parameter values, the simulation parameters were set and the simulation model was run. The upper and lower cylinder displacement, pressure and velocity curve were drawn up.

Run a certain speed on the cylinder, and then pressurized 4s, followed by packing 2s. Displacement, pressure and acceleration curve shown in Fig.3,4,5,6:

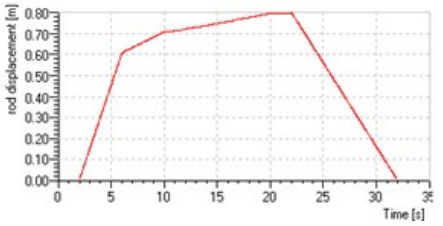

Fig. 3. Upper cylinder displacement curve

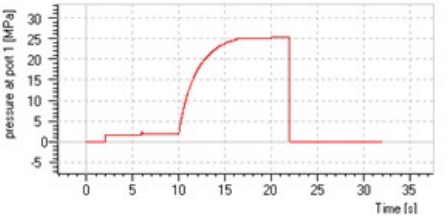

Fig. 4. Upper cylinder pressure curve

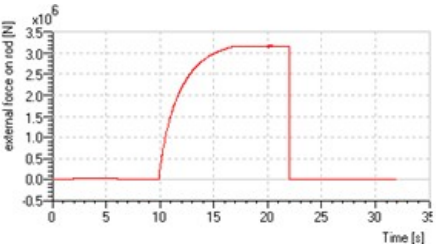

Fig. 5. The force curve of upper cylinder

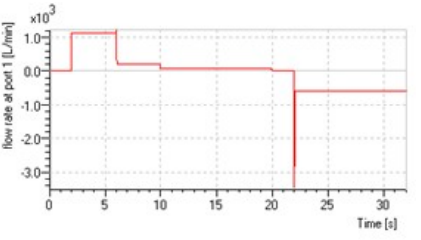

Fig. 6. Upper cylinder flow curve Piston rod

Seeing from the working chamber pressure carve, there was a great sudden drawdown of the difference. During the system holding pressure, the pressure of the working chamber there is a difference between a great plummeted. Causing the machine to the system in the packing process, the compressibility of hydraulic oil and mechanical parts to produce elastic deformation, and thus it save considerable energy. If immediately change at this time, it will instantly generate strong vibration and sound of gun sound and the vibration of the piping, affecting the normal working of the hydraulic press.

5 Improvement Analysis of the Hydraulic System

From the above analysis, in order to solve the great sound and vibration in the hydraulic press return, it was necessary to make the chamber on the cylinder controlled pressure relief, and wait on the chamber pressure to a lower and then transferred to the return.

This can be to install a pressure relief circuit in the system and change Relief measures taken between the pressure in the system warranty, thus to eliminate system vibration and fulmination. Figure 7 Relief Valves for Use in the loop.

When the valve is in the position shown, the remote control port relief valve 2 through the throttle valve 3 and one-way valve back to tank. Adjust the throttle valve opening size can change the relief valve opening speed, that adjust the speed of the

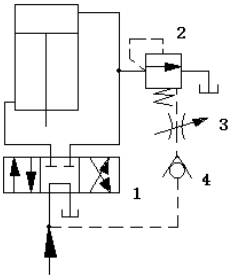

Fig. 7. Unloading loop

cylinder chamber pressure oil pressure release. Adjust the pressure relief valve 2 should be greater than the system to adjust the relief valve pressure relief valve 2 also played the role of safety valve.

The improved system schematic shown in Figure 8. The part inside the dashed border is the join Relief loop.

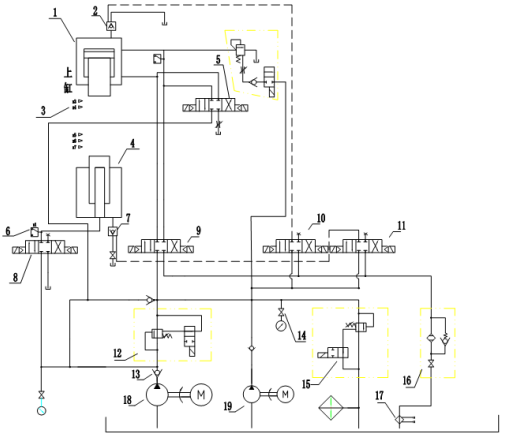

Fig. 8. Improved hydraulic schematic

The unloading relief valve electromagnet only in the relief of the return to power, the rest of the time to maintain power failure. Holding pressure after the end of the return trip before the electromagnets first power, the working cylinder chamber high-pressure fluid is compressed energy through the relief valve gradually released, will not produce the sound of the gun Ming.

Shown in Figure 9 for the installation of the loop pressure release system working cylinder circuit AMESim model.

The Relief circuit simplifies the combination of a pilot pressure relief valve and a signal source. The part inside the dashed border is the join Relief loop.

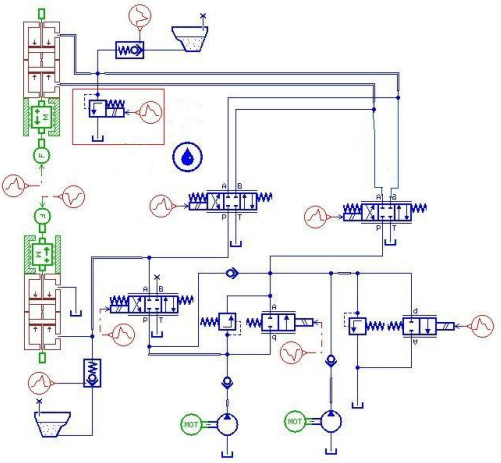

Fig. 9. AMESim model improved

6 The Improvement of the Hydraulic System Simulation Analysis

Improved system simulation run, set the pressure release time for the 4s, the working cylinder pressure dropped from 25MP to 5MP. After the installation of circuit pressure relief work in front of the cylinder in the system working cylinder cavity pressure curve and improve the working chamber pressure curve shown in Figure 10.

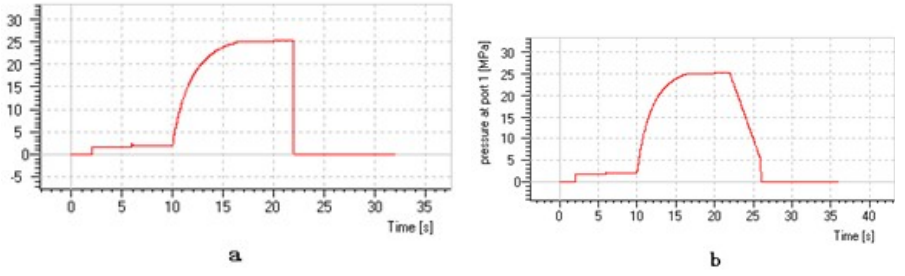

Fig. 10. Before and after improvement on the cylinder pressure curve

It is evident from the figure, the improved system 4s after the end of the packing, gently working cylinder chamber pressure gradually decreased to 5MPa high pressure plummeted, the system will not produce the gun Ming. Improved speed are showed in Fig.11.

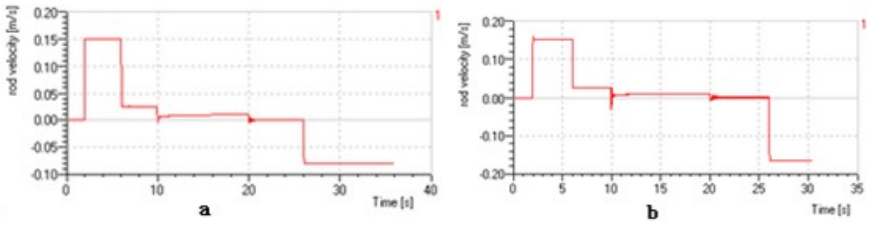

Fig. 11. On the cylinder speed before and after improvement

7 Conclusion

In this paper, the impact fulmination 3000T hydraulic press process, through the analysis of the existing hydraulic system works, the establishment of the AMESim model and analyze the simulation model and found that the impact of the preliminary design of the system change to pressure problem. Were analyzed to address these issues is proposed to improve the installation of pressure relief circuit improvement program. Improved system simulation analysis to determine the system is basically correct.

When these theoretical results are applied to actual production, found that the method is indeed greatly reduce the impact blasting song almost eliminated, greatly reducing the noise pollution, to extend the life of the equipment.

References

[1] Li, H., Li, J.: Mechanical / hydraulic system modeling and simulation software AMEsim. Computer Simulation 23(12), 294–297 (2006)
[2] Bian, H., Dai, S.: Four-universal hydraulic machine hydraulic system. Mechanical Engineers (7), 92–94 (2007)
[3] Su, D., Yu, J.: Hydraulic simulation technology AMEsim and applications. Mechanical 33(11), 35–37 (2006)
[4] Cheng, Y., Liu, Z.: Stamping and plastic molding equipment. Science Press, Beijing (2005)
[5] Fu, Y., Qi, X.: System modeling and simulation based on AMESim. Beijing University of Aeronautics & Astronautics Press, Beijing (2006)

Study on the Comparison of Driving Configuration for Hybrid SUVs

Sijia Zhou, Jingyan Xia, Jiangqi Long, Pingdan Xu, Jun Chu, and Yi Zhang

Wenzhou University, College of Mechanical & Electrical Engineering,
Zhejiang Wenzhou 325035, China
zhousj@wzu.edu.cn, {1004222950,494161858,48113319,
87903101}@qq.com, longjiangqi@163.com

Abstract. Two kinds of parallel hybrid power trains are selected and applied to a certain SUV chassis. According to the typical configurations and functions, the components of the two power trains include ISA, engines, batteries and transmissions. Then, simulations are carried out in a certain SUV model. The target of the simulations is to achieve a better fuel economy and emission as well as meet the required driving performances.

Keywords: SUV, Hybrid electric vehicle, Simulation.

1 Introduction

The researches on new energy resources vehicles are taken by some countries nowadays because of the requirement of automotive energy-saving and environment protection. Electric vehicles are one of the main selections. Due to the reasons of technology and cost, purely electric vehicles and fuel-cell vehicles were not taken as the major development targets; however, Hybrid electric vehicles are good choice between performance and environment protection. Now, the SUV are increasing quickly, and the researches are putting more and more their attentions on SUVs.

2 Selection and Comprehensive Analysis of the Driving Type

According to the connecting structure of the power train parts, the HEV power train can be divided into three basic structure types: series type, parallel type and complex type. In parallel type HEV, the working state of engine and motor could be independent or connected with each other. The motor could be used to drive the whole vehicle in low speed, but in the stable middle or high speed conditions, the driving forces could be only supplied by the engine. The dynamics of vehicle can be proved by the combined power of engine and motor with a device in high speed or acceleration conditions. The America Renewable Energy National Laboratory researches showed that the fuel economy in parallel type HEV is 6% higher than the series type with similar parts.

D. Jin and S. Lin (Eds.): Advances in Mechanical and Electronic Engineering, LNEE 176, pp. 389–393.
springerlink.com

According to the analysis above, the fuel economy can be improved by the parallel hybrid system with a low cost. Therefore, the parallel power train of SUV is mainly researched in this paper.

2.1 The Parameter of the Simulation

Three types of SUV were analyzed in this paper. There were traditional SUV configuration, ISA parallel configuration and ordinary parallel configuration. The motor located in the midst of engines and clutch is named ISA parallel configuration. The motor located in the midst of transmission and clutch is called ordinary parallel configuration. Their power train structures are shown in figure 1 & table 1.

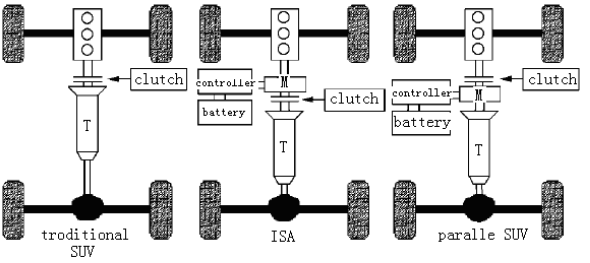

Fig. 1. Three types of SUV

Table 1. Vehicle parameters

mass of traditional body $\mathbf{m}_o$	Loaded with quality **m**	Windward area
1603 kg	1739 kg	2.66 m^2
The radius of the wheel **r**	Rolling resistance coefficient $\mathbf{f}_r$	Drag coefficient
0.343 m	0.015	0.44

The power to meet the required driving performance is certain. The efficiency of the whole vehicle is decided to the work efficiency of engines, work efficiency of ISA, charge-discharge efficiency of batteries and controller efficiency. The efficiency of the whole vehicle can be decreased if the hybrid mixing degree is too low or too large. So the selection of mixing degree can be considered with the fuel economy, fuel emission and manufacturing cost. Considering the successful parallel hybrid electric vehicles include the Insight of Toyota Company, the Dodge ESX3h of Daimler Chrysler AG and the model of Argonne Nation Laboratory using the mild hybrid configuration, the mild hybrid of parallel configuration was discussed in this paper.

According to the automobile theory, vehicle driving in maximum speed, the power demand is

$$P_v = (\frac{C_D A\ v_{\max}^{\ 2}}{21.12} + mgf_r) \times \frac{v_{\max}^{\ 2}}{3600} \times \frac{1}{\eta} \quad . \tag{1}$$

Where P_v is power demanded, $v_{\max}$ is maximum speed, η is transmission efficiency.

When the SUV with 10 $km.h^{-1}$ speed goes up a slope with gradient 17°, the power demand is

$$P_i = mgv \sin \alpha \quad . \tag{2}$$

The dynamic performance of SUV could be considered at the designing of whole vehicle. Therefore, calculating power could be choose the bigger date. The requires is

$$P_{e\max} = P_{m\max} \geq \max\{P_v, P_i\} \quad . \tag{3}$$

Where $P_{e\max}$ is the maximum power of engine, $P_{m\max}$ is the maximum power of motor.The engine become the unique power source when the designed mild hybrid SUV driving in cruising speed. The equation is

$$P_e^* = P_e + P_{acc} + P_i + P_{chr} \quad . \tag{4}$$

Considering the two selected conditions, the economic cruising speed is 70 ~ 80 km/h, the cruising P_e^* is 20 ~ 24 kW. The cruising P_e^* could be possibly cross the region of fuel economy at the universal characteristic of the engine in order to reducing the emission and fuel consumption.

2.2 The Simulation and Result Analysis

The dynamic, fuel economy and emission of three types of SUV were simulated and compared in ECE and US06 conditions with ADVISOR software.

The table 2 shows the dynamic simulation result of comparison among three types of SUV. The dynamic performance of hybrid SUV is stronger than the traditional SUV from the table 2. The change of the dynamic performance is decided by the different output characteristics and connection with the motor and engine. The permanent magnet motor with large power is applied in ordinal parallel SUV and the work efficiency in motor with a bigger power is far higher than the engine as well as contains a certain overload capacity. Because of this, the max speed for ordinal parallel SUV is improved greatly. The ISA parallel SUV with a lighter weight made its acceleration performance better than that of the ordinal parallel SUV.

Table 2. Dynamic comparison among three types of SUV

type	Maximum speed Vmax /(km/h)		0~100(km/h) Acceleration time/s		60~100(km/h) Acceleration time/s	
	speed	rate	time	rate	time	rate
traditional SUV	164.4	0	14.6	0	7.9	0
ISA parallel	170.9	+3.95%	11.95	-18.15%	6.9	-12.66%
ordinal parallel	174	+5.84%	13.1	-10.27%	7.4	-6.33%

The table 3 shows the fuel economy simulation result of comparison among three types of SUV. The fuel economy of hybrid SUVs are better than the traditional SUV. The effect of fuel saving can be improved above 20% in city condition and high condition also can be improved by nearly 10%. Though the weight of hybrid SUVs are heavier thus having to overcome larger rolling and acceleration resistance, the work efficiency of engine in hybrid are higher and the barking energy can be used again. The energy efficiency can be improved largely with these strategies.

Table 3. Fuel economy comparison among three types of SUV

type	100km fuel consumption/L ECE city		100km fuel consumption/L US06 high speed	
	fuel consumption	rate	fuel consumption	rate
traditional SUV	12.5	0	10.2	0
ISA parallel	9.6	-23.2%	9.3	-8.82%
ordinal parallel	10	-20%	9.1	-10.78%

The table 4 shows the emission simulation result of comparison among three types of SUV. The emission of hybrid SUV can be improved greatly from the table 7. The main harmful emissions of hybrid SUV are decreased obviously compared with traditional SUV. The harmful emissions HC are reduced 1/4~1/3. The emissions of CO in hybrid SUV are only the half of traditional SUV. The emissions of NO_x are decreased to nearly 50%. The emission of hybrid SUV could be improved by transformation the existing purification out of engine based on the characteristic of parallel SUV.

Table 4. Emission comparison among three types of SUV

type	HC/(g/km)		CO/(g/km)		NOx/(g/km)	
	emission	rate	emission	rate	emission	rate
traditional SUV	0.348	0	2.175	0	0.316	0
ISA parallel	0.244	-29.88%	1.052	-51.63%	0.198	-37.34%
ordinal parallel	0.258	-25.86%	1.08	-50.34%	0.16	-49.37%

3 Summary

The three types of hybrid SUV, two hybrids and one traditional, with similar body structure, chassis and engine were comparative studied in this paper. The dynamic, fuel economy and emission are compared in traditional SUV and hybrid SUV based on their different transmission structures. In the results, the fuel economy and emission are improved greatly and the dynamic is also improved some in hybrid electric vehicle.

Acknowledgments. The authors acknowledge the financial support from the Zhe Jiang province public welfare project (No.2010C31094; No.2011C21068), Wenzhou university program (11jg58B).

References

1. Cuddy, M., Wipke, K.: Analysis of the Fuel Economy Benefit of Drive train Hybridization. SAE paper 970289, 101–103 (1997)
2. National Renewable Energy Laboratory. Advanced Vehicle Simulator (February 9, 2001), http://www.ctts.nrel.gov/analysis
3. Colli, V.D., Tomassi, G., Scarano, M.: Single wheel longitudinal traction control for electric vehicle. IEEE Transactions on Power Electronics 21(3), 799–803 (2006)
4. Pusca, R., Ait-Amirat, Y., Berthon, A., et al.: Modeling and simulation of a traction control algorithm for an electric vehicle with four separate wheel drives. IEEE Transactions on Industrial Electronics, 1671–1675 (2002)

The Five-Axis NC Machining Simulation and Optimization

Anjiang Cai, Liang Qiang, Shihong Guo, and Zhaoyang Dong

Xi'an University of Architecture & Technology, Xi'an, Shanxi, 710055, China

Abstract. The supporting technology of five-axis CNC machine is establishing virtual machining platform, correcting NC program and process simulation and optimization, which can make the efficient machining technology come true. Taking non-orthogonal 5-axis CNC machine tools DMC70ev as the object, NC machining simulation platform based on the VERICUT was constructed. Taking surface machining for example, the optical design mathematical model based on constant volume removal rate and constant chip thickness optimum method was established and the toolpath optimization was carried out. The research result has realized five-axis process simulation of NC machining and the verification of NC program correctness, which improves the processing efficiency and quality, the application level, quality of NC machining technology for enterprises, and it will promote the development of modern manufacturing technology.

Keywords: VERICUR, Virtual machining, Modeling, Feed rate Simulation.

Foundation Item: Shanxi Province industrialization projects of the Education Department (2011JG15).

1 Introduction

With the merits of high degree of automation, flexible and high machining precision, the five-axis CNC machine tools has been widely applied in the field of modern manufacturing, especially in high-performance processing of large and heterogeneous complex parts. But its performance and efficiency is not satisfactory now, there are still some application technical difficulties unresolved, such as the tool interference, the posture control of the tool processing space, the feed rate optimization, the verification of five axis NC program. Therefore, the construction of the virtual processing platform, verification of the NC program and the simulation and optimization for the process are the important basic technologies of five-axis CNC machine tools for efficient machining.

2 The Five-Axis Machining Simulation Based on VERICUT

As an advanced simulation software for NC machining, VERICUT can be used to verify the collision, interference, over-cut, owes-cutting and unreasonable cutting parameters which may arise in NC programs, and has been widely used in aviation, aerospace, shipbuilding, electronics, automobile, locomotive, mold and other companies which using multi-axis CNC machining. Taking non-orthogonal 5-axis

D. Jin and S. Lin (Eds.): Advances in Mechanical and Electronic Engineering, LNEE 176, pp. 395–401.
springerlink.com

CNC machine tools DMC70ev as the object, non-orthogonal axis CNC machine tools, the surface processing for example, the research for five-axis NC machining simulation and optimization was done based on VERICUT.

2.1 The Construction of Five Axis NC Machining Simulation Platform

The construction of NC machining simulation platform includes the establishment of the machine model, setting the machine system parameters, customizing the control system and the establishment of tool libraries. DMC70ev has a quite complicated structure, it is a typical five-axis CNC machine tools with two-axis rotary table, the five axis is realized by way of worktable rotation, X-axis, Y-axis, Z-axis are linear axises, B-axis, C-axis are rotation axises, B-axis is a non-orthogonal axis in Cartesian coordinate system, the space angle is 45°with Y-axis, and the control system is Millplus IT V530. Taking VERICUT as a platform, a machine model was established via measuring the size required for the machine geometrical model, establishing machine components tree, adding the model to the components tree, the machine parameters was set in the meantime; according to program format of Millplus IT V530 system and machining requirements, the control system was customized on the basis of calling "heimplum. ctl" existing in the VERICUT , the tool library required for was built, so the machining simulation was realized. It can test interference, collisions, overtravel and other machining issues which may occur in the actual machining process and optimize the process, five-axis NC machining simulation platform established is shown in Figure 1.

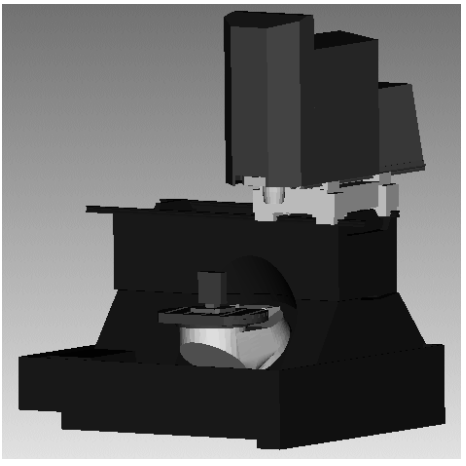

Fig. 1. The five-axis NC machining simulation platform

2.2 The NC Machining simulation Instance Based on VERICUT

After adding parts, rough and fixture to the five-axis NC machining simulation platform established, the machining simulation environment was completed by

transferring NC program, loading the control system, setting the machine parameters and structural variables, customizing special instructions. Figure 2 shows the momentary scene of the second step for machining a surface on five-axis NC machining simulation platform, the left view shows the process of removing the rough material, the right view shows the movement of five-axis CNC machining, which can observe interferences, collisions between the fixture, tool and machine components and the movement of CNC machine tools easily, the verification of accuracy of NC program was realized. After the simulation process, the over-cut, owes-cutting and other process issues can be checked through AUTO-DIFF function, measurement function and the log file existing in VERICUT, which can replace the trial cut.

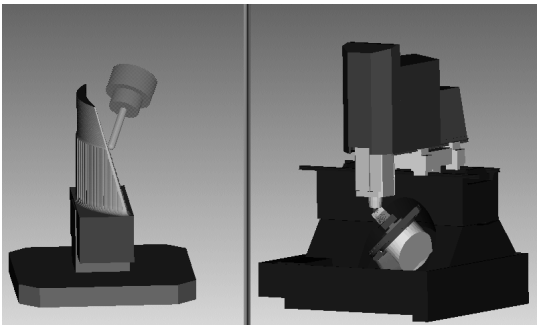

Fig. 2. The momentary scene of machining simulation

3 The Toolpath Optimization Based on VERICUT

Optimized design is a modern design method on the principle of optimization, its purpose is to seek the optimal design parameters and obtain the process design with best technical and economic indicators. The toolpath optimization based on VERICUT divides the original NC program each step into multiple segments through calculating volume removed for each step of NC program, then set an optimum feed rate for each block, more efficient and more security NC program will be created, but it does not change the trajectory of the program, so there will be no error machining results.

3.1 The Establishment of a Mathematical Model for Optimized Design

Each design has specific requirements and constraints, the optimized design should convert the design issues into mathematical model that generally includes the design variables, objective function and constraints.

3.1.1 Determine the Optimized Design Variables

Design variables are independent parameters that can be adjusted and optimized in the design process, the more design variables, the more complex for the design, so the design parameters should be minimized on the premise of meeting the design conditions, cutting depth, cutting width and feed rate is the main factors affecting the

cutting efficiency, so the optimized design variables of the mathematical models based on VERICUT are as follows:

$$X=[A_d,\ \ R_w,\ \ F]^T$$

A_d represents cutting depth, R_w represents cutting width, F represents feed rate.

3.1.2 Determine the Objective Function

The objective function is the indicator used to evaluate the design project, which is generally classified into two groups: single-objective and multi-objective. The optimized design mathematical model based on VERICUT is to improve machining efficiency on the premise of guaranteeing quality, so shorting the machining time is taken as the optimized design goals. Which is defined as follows:

$$T\ (X)\ =T\ [A_d,\ \ R_w,\ \ F]^T$$

T(X) is the design variable, it should be shorten one third after optimized design.

3.1.3 Determine the Constraints

Constraints are to restrict the values of the design variables, which are generally classified into two groups: inequality and equality constraints. The design variables of this subject required to meet the following design conditions:

The constraint for cutting depth:

$$g_1\ (X)\ =\Delta-\ A_d\geq 0$$

That Δ represents machining allowance.

The constraint for cutting width:

$$g_2\ (X)\ =D-\ R_w\geq 0$$

That D represents tool diameter.

The constraint for feed rate:

$$g_3\ (X)\ =F-F_{min}\geq 0$$

$$g_4\ (X)\ =F_{max}-F\geq 0$$

That $F_{max,}$ F_{min} were the maximum, and the minimum feed rate of the machine tools allowed.

3.2 The Optimization Instance Based on VERICUT

The objective function and constraints are nonlinear functions which can be seen from the above mathematical model, so the solution is quite complex, the optimization module of VERICUT provides the function of setting optimal constraints and calculating the objective function(machining time) automatically. VERICUT provides two main methods for toolpath optimization: 1)optimization methods at constant volume removal rate mainly used for rough machining, its purpose is to remove the material as soon as possible, and keep constant material removal volume in different cutting conditions. 2)optimization method at constant chip thickness mainly uesd for

semi finish and finish machining, its purpose is to improve machining efficiency, extend tool life and ensure the quality by changing the feed rate during the cutting process. Taking the surface machining on DMC70ev CNC machine tools for example, the toolpath optimization based on VERICUT was illustrated, machining this part is divided into two steps: rough and finish machining, which used two optimization methods respectively.

3.2.1 The Optimization Process

The toolpath optimization based on VERICUT includes two steps: 1)the establishment of optimized tool library, 2)the NC program optimization by transferring the optimized tool library. The tool library optimization using VERICUT is used to set feed rate and spindle speed and other optimization data for tools in different cutting conditions. The optimal parameters were fixed by adjusting them constantly with practical experience. Figure 3 shows parameter settings window using optimization methods at constant volume removal in the first step of rough machining. Cutting depth A_d=1.5mm, cutting width R_w=10mm, the constant volume removal rate Vo_l=15000mm^3/min, Fmin, Fmax, the maximum cutting width and the maximum material removal rate can be set up by the "limit" button in this window, after that, the optimized tool library was established, the NC program machining the surface can be optimized by transferring the optimized tool library.

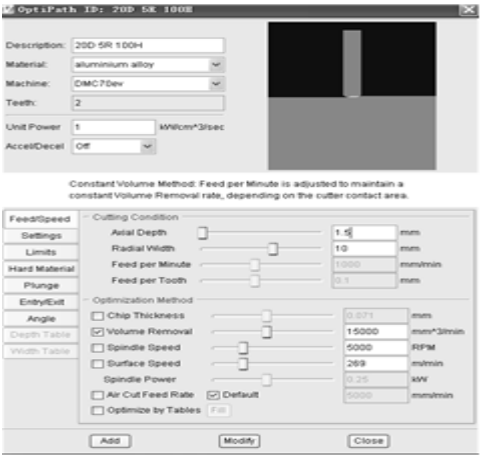

Fig. 3. "Optimized tool library settings"

3.2.2 The Optimization Results

After the NC program optimization of surface machining finished, the results can be analyzed through status and graphs, the log files can also show the optimized information. As table 1 show, the time of surface machining saved 40.8 percent after optimization, which make the optimization purpose come true.

Table 1. The comparison for man-hour of fore and aft optimization unit

Tool number	Man-hour fore optimization (T1)	Man-hour aft optimization (T2)	Optimization rate
T1	355.9561	217.5648	38.9%
T2	167.7534	92.3541	44.9%
Total hours	523.7095	309.9189	40.8%

The comparison for the NC program of fore and aft optimization is shown in Figure 4, the feed rate in the NC program fore optimization is a fixed value (1000mm/min), while the NC program aft optimization is divided into multiple segments, and each segment set a reasonable feed rate according to the cutting state, which improves the machining efficiency. the number of segments the NC program divided depends on the size of resolution set while establishing optimized tool library, the smaller the resolution is, the more sick the NC program divided.

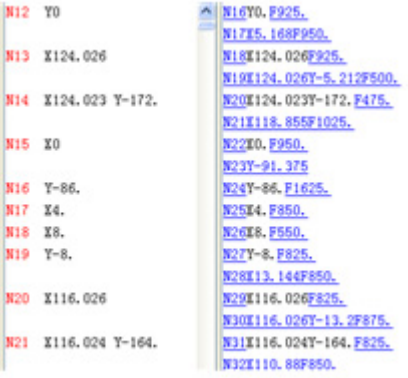

Fig. 4. Comparison for the NC program of fore and aft optimization

4 Conclusion

An important way to promote the performance and efficiency of five-axis CNC machine tools is to establish a virtual machining system, it can verify the correctness of the NC program instead of trial cut, and optimize the processing technical. Five-axis NC machining simulation platform based on VERICUT was constructed, and the toolpath was optimized, all these provide instructional methods and reference examples for surface machining simulation of five-axis CNC technology. Which has solved practical process issues, replaced trial cut, and improved the machining efficiency and quality.

References

1. Yang, S.: NC machining simulation technology based on Vericut. Tsinghua University press, Beijing (2010)
2. Luo, L.-Q., Zhang, D., Li, Z.-M.: Study of CNC Machining Simulation and Optimization Based on VERICUT. Journal of Hubei University of Technology 21(3), 186–188 (2006)
3. Yun, W.-S., Ko, J.H., Lee, H.U., et al.: Development of a virtual machining system, part3: cutting process simulation in transient cuts. International Journal of Machine Tools & Manufacture 42, 1617–1626 (2002)
4. Zhang, Y., Gui, G.: NC Machining Simulation and Optimization Based On VERICUT. Modern Manufacturing Technology and Equipment 4(185), 75–185 (2008)
5. Jian, G.: Mechanical Optimize Design Basis. Science Press, Beijing (2000)
6. Nie, W., Li, G., Xu, Z.: Research and Application of CNC Machining Optimization Based on VERICUT. Manufacturing Automation 29(2), 84–86 (2007)

Regulation against Unknown Sinusoidal Signals in an Active Suspension System

Zhizheng Wu and Fei Peng

Department of Precision Mechanical Engineering, Shanghai University,
#149 Yanchang Road, Shanghai, China, 200072
zhizhengwu@shu.edu.cn

Abstract. This paper presents an adaptive regulation approach in an active suspension system against exogenous disturbances consisting of a linear combination of sinusoids with unknown amplitudes, frequencies and phases. The design of the regulator is based on considering a parameterized set of stabilizing controllers for the linear system. The goal of the adaptation is to search within the set of stabilizing controllers for a controller that yields regulation in the closed loop system.

Keywords: Regulationm, adaptive, sinusoidal disturbance.

1 Introduction

This paper presents a regulation approach for linear systems subject to sinusoidal exogenous inputs with unknown frequencies, amplitudes and phases. The problem of regulation against unknown sinusoidal exogenous inputs is of a significant practical importance, and is motivated by a number of applications such as vibration and noise cancellation. A number of approaches have been presented in the literature to address this problem, including using disturbance observers [1], phase locked loops [2,3], internal model approach [4-8]. An adaptive regulation approach is proposed in this paper, which involves constructing a parameterized set of stabilizing controllers for the system, and tuning the Q parameter in the adaptive controller to achieve regulation against unknown sinusoidal signals. The effectiveness of the approach is verified in a benchmark test of an active suspension system simulator involving various unknown combinations of sinusoidal disturbances.

2 Design of the Regulator

Consider the discrete-time linear system model given by:

$$\sum: \begin{cases} x(k+1) = Ax(k) + Bu(k) + Ew(k) \\ y(k) = C_y x(k) + D_{yw} w(k) \\ e(k) = C_e x(k) + D_{ew} w(k) \end{cases} \tag{1}$$

D. Jin and S. Lin (Eds.): Advances in Mechanical and Electronic Engineering, LNEE 176, pp. 403–407.
springerlink.com

where $x \in \mathbb{R}^n$ is the state vector, $u \in \mathbb{R}$ is the control input, $y \in \mathbb{R}$ is the measurement signal to be fed to the controller, and $e \in \mathbb{R}$ is the performance variable to be regulated. The disturbance $w \in \mathbb{R}^s$ is of the form $w = [w_1 \quad \cdots \quad w_s]^T$ where each $w_j, j = 1, \cdots, s,$ is of the form:

$$w_j(k) = \sum_{n=1}^{k^j} c_n^j(k) \cos\left(\omega_n^j(k)k + \phi_n^j(k)\right) + c_0^j \tag{2}$$

with unknown (or slowly time-varying) amplitudes $c_n^j(k)$, frequencies $\omega_n^j(k)$, and phases $\phi_n^j(k)$, and possible offsets c_0^j, $j = 1, \ldots, s$.

The parameterized controllers consist of the interconnection of two blocks with a fixed block J and a stable system (parameter) Q that can be chosen as desired [7,8]. The parameter Q is given by:

$$\begin{aligned} x_Q(k+1) &= A_Q x_Q(k) + B_Q\left(y(k) - \hat{y}(k)\right) \\ y_Q(k) &= C_Q x_Q(k) \end{aligned} \tag{3}$$

whereas the J block is given by:

$$\begin{aligned} \hat{x}(k+1) &= (A + LC_y + BK)\hat{x}(k) - Ly(k) + By_Q(k) \\ u(k) &= K\hat{x}(k) + y_Q(k) \\ y(k) - \hat{y}(k) &= y(k) - C_y\hat{x}(k) \end{aligned} \tag{4}$$

where K and L are such that $(A + BK)$ and $(A + LC_y)$ are stability matrices, respectively. The plant Σ and the block J can be combined into a single block T. The dynamics of the system T can be represented as follows:

$$\begin{bmatrix} x(k+1) \\ \tilde{x}(k+1) \\ e(k) \\ y(k) - \hat{y}(k) \end{bmatrix} = \begin{bmatrix} A + BK & BK & E & B \\ 0 & A + LC_y & -E - LD_{yw} & 0 \\ C_e & 0 & D_{ew} & 0 \\ 0 & -C_y & D_{yw} & 0 \end{bmatrix} \begin{bmatrix} x(k) \\ \tilde{x}(k) \\ w(k) \\ y_Q(k) \end{bmatrix} \tag{5}$$

where $\tilde{x}(k) = x(k) - \hat{x}(k)$. Therefore, we have that:

$$\begin{bmatrix} e(k) \\ y(k) - \hat{y}(k) \end{bmatrix} = \begin{bmatrix} T_{11} & T_{12} \\ T_{21} & T_{22} \end{bmatrix} \begin{bmatrix} w(k) \\ y_Q(k) \end{bmatrix} \tag{6}$$

Let $W(z)$ and $E(z)$ denote the Z transform of the disturbance input w and the performance variable e respectively. The closed loop system performance variable is then given by

$$E(z) = F_{T,Q}(z)W(z) = [T_{11}(z) + T_{12}(z)Q(z)T_{21}(z)]W(z)$$

Consider the Q parameter as $Q(z)=\sum_{i=1}^{n_Q}\theta_i\psi_i(z)$, where $\psi_i(z)=z^{1-i}F(z)$, $i=1,\cdots n_q$, and $F(z)$ is a weighted function. Define the parameter vector

$$\theta=\left[\theta_1,\cdots,\theta_{n_Q}\right]^T \tag{7}$$

In the case where the disturbance input properties are unknown and possibly time varying, it is desired to introduce adaptation in the controller design process. The aim of the adaptation is to tune the parameter vector θ in so that it converges to the desired parameter vector θ_0 needed to achieve regulation. Let q^{-l} denote the l time step delay operator, and $Q_k=\sum_{i=1}^{n_Q}\theta_i(k-1)q^{1-i}$. The performance variable $e(k)$ is then given by:

$$e(k)=[T_{11}(q^{-1})+T_{12}(q^{-1})Q_kT_{21}(q^{-1})]w(k) \tag{8}$$

Define $r(k)=T_{21}(q^{-1})w(k)=y(k)-\hat{y}(k)$ and

$$v_1(k)=T_{12}(q^{-1})r(k)$$

$$\tilde{e}(k)=e(k)-[T_{12}(q^{-1})Q_k-Q_kT_{12}(q^{-1})]r(k)$$

Set $\phi(k)=[-v_1(k),\cdots,-v_1(k-n_q+1)]^T$, then the parameter $\hat{\theta}(\cdot)$ can be performed using the following recursive least squares algorithm:

$$\begin{aligned}\hat{\theta}(k+1)&=\hat{\theta}(k)+\lambda(k+1)P(k+1)\phi(k+1)\tilde{e}(k+1)\\ P^{-1}(k+1)&=\lambda(k+1)[P^{-1}(k)+\phi(k+1)\phi^T(k+1)]\end{aligned} \tag{9}$$

with $\hat{\theta}(0)=0$, $P(0)=P_0>0$, and where $\lambda(k)$ is a time varying forgetting factor satisfying $0<\lambda_{\min}\le\lambda(k)\le\lambda_{\max}<1$.

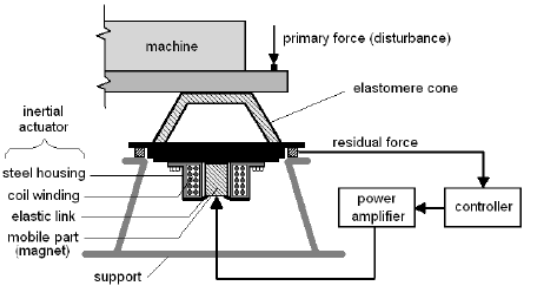

Fig. 1. Scheme of the active suspension system

3 Disturbance Cancellation in an Active Suspension System

The designed adaptive regulator is applied to an active suspension system. Figure 1 shows the scheme of the active suspension system. It consists on a passive damper, an inertial actuator, a load, a transducer for the residual force, a controller, a power amplifier and a shaker. The inertial actuator will create vibrational forces which can counteract the effect of vibrational disturbances. A model of the system, as given in (1), was obtained using system identification, where w is the excitation of the shaker, u is proportional to the inertial actuator input and y is the residual force. The sampling frequency is *800* Hz. The frequencies in the narrow band disturbances are located in the range 45 to 105 Hz. The parameter Q is selected to be of the form $Q(z) = F(z)\sum_{i=1}^{6}\theta_i z^{1-i}$ where $F(z)$ is a low pass filter with a cut-off of frequency of 200Hz. The forgetting factor in the estimation algorithm is a constant $\rho = 0.95$. The initial conditions of the algorithm are $\hat{\theta}(0) = 0_{6\times1}$ and $P(0) = 10^6 I$ where I is a 6×6 identity matrix.

The results of rejection of a single time varying sinusoidal disturbance within 45 and 105 Hz are verified. The magnitude of the disturbance is in all the cases as *Amp* =0▷1V. Time domain results for the step applications of the disturbance (from 45Hz to 105Hz every 5Hz) are summarized in table 1. The similar results are also obtained for multiple sinusoidal signals. Figure 2 illustrates the closed loop system response for the case of a disturbance frequency of [65-85-105]Hz.

Table 1. Time domain results (1 sinusoid)

	Minimum value (disturbance freq.)	Maximum value (disturbance freq.)
Transient duration	66ms(45Hz)	151ms(105Hz)
Transient norm2	$4.31\cdot10^{-1}$ (45Hz)	$2.32\cdot10^{-0}$ (105Hz)
Transient maximum	$1.87\cdot10^{-1}$ V(55Hz)	$4.12\cdot10^{-1}$ V(105Hz)
Global attenuation	47.80dB(45Hz)	82.48dB(100Hz)

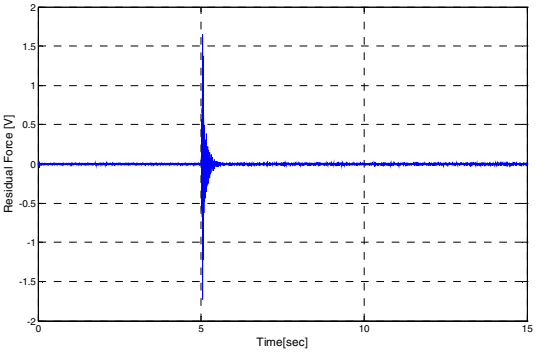

Fig. 3. Adaptive rejection of a sinusoidal disturbance with frequencies [65-85-105]Hz

4 Conclusion

The problem of adaptive regulation against disturbances represented as a linear combination of unknown sinusoidal signals is presented, where the adaptive regulator design approach based on tuning the Q parameter in a parameterized set of stabilizing controllers is proposed. The developed regulator is applied to the problem of vibration suppression in an active suspension system.

Acknowledgment. This work was supported by the National Natural Science Foundation of China (51075254), the Shanghai Pujiang Program (11PJ1404000), the Innovation Program of Shanghai Municipal Education Commission (11YZ16).

References

1. Marino, R., Santosuosso, G.L., Tomei, P.: Robust adaptive compensation of biased sinusoidal disturbances with unknown frequency. Automatica 39, 1755–1761 (2003)
2. Pigg, S., Bodson, M.: Adaptive algorithms for the rejection of sinusoidal disturbances acting on unknown plants. IEEE Transactions on Control Systems Technology 18(4), 822–836 (2010)
3. Bodson, M., Douglas, S.C.: Adaptive algorithms for the rejection of sinusoidal disturbances with unknown frequency. Automatica 33(12), 2213–2221 (1997)
4. Serrani, A.: Rejection of harmonic disturbances at the controller input via hybrid adaptive external models. Automatica 42, 1977–1985 (2006)
5. Hoagg, J.B., Santillo, M.A., Bernstein, D.S.: Discrete-time adaptive command following and disturbance rejection with unknown exogenous dynamics. IEEE Transactions on Automatic Control 53, 912–928 (2008)
6. Landau, I.D., Constantinescu, A., Rey, D.: Adaptive narrow band disturbance rejection applied to an active suspension - an internal model principle approach. Automatica 41, 563–574 (2005)
7. Ben Amara, F., Kabamba, P.T., Ulsoy, A.G.: Adaptive sinusoidal disturbance rejection in linear discrete-time systems - Part I: Theory. ASME Journal of Dynamic Systems, Measurement and Control 121(4), 648–654 (1999)
8. Wu, Z., Ben Amara, F.: Adaptive regulation in bimodal linear systems. International Journal of Robust and Nonlinear Control 20(1), 59–83 (2009)

A Study on CAD System for Bending Die Based on UG

Jun Su and Yan Ma

Henan Polytechnic Institute, Nanyang Henan, China
Hygy2011@126.com

Abstract. In this paper , it has been designed that the module of continuous bending die calculation, process design, process scheme, parts design and UG die holders for diagonal sets design by using UG software , improved the efficiency of the design.It has improved the efficiency and achieved intelligence and automation by through establishing CAD system of the continuous mold design.

Keywords: Bending die, UG, CAD system, Module; Design.

1 Process Calculation Module

Process calculation modules include four parts,such as power calculations, material utilization calculation, convex and concave parts of the Die size calculation,and central computing power.

1.1 Force Calculation

For choicing the press and design molds reasonably,it is calculated blanking force and bending forces . Normally, after cutting blanking pieces,due to elastic deformation, the radial expanded, while the sheet metal holes along the radial,it occoured elastic contraction. At the same time, the parts which rushed down and also try to restore the elastic and bending . The results of the two elastic recovery, materials and parts would infarct in the die, and the rest of the sheet in the convex modules tightly after punching. It is said the unloading force which from the punch or waste will be unloaded. Push out the pieces from the top which force along the direction of cutting in the concave die ,it is said pushing force. Many factors affect these forces, mainly it concludes that the mechanical properties, die clearance, material thickness, shape and size of the parts and lubrication and so on.

Calculated free bending force, for wedge-shaped bending part:

U- shaped bending part:

$$F_z = \frac{0.7KBt^2\sigma_b}{r+t}$$

For the bengding die who has top or pressure device,its top force F_d or pressure force F_y , can approximately take 30%-80% of the bending force F_z ,that is:

$$F_d \quad (\text{or } F_y) = \text{K } F_z$$

D. Jin and S. Lin (Eds.): Advances in Mechanical and Electronic Engineering, LNEE 176, pp. 409–414.
springerlink.com

1.2 Size Calculation for the Parts of Convex and Concave

Edge size calculation for the part of blanking.The mold size precision is primary factor that who influence on the size calculation for the part of blanking, the reasonable gap is depending on edge size and tolerances.

Size calculation for the part of bending.①Punch radius r,as figure 1.When r/t is small, the punch radius is equal to the inner bend radius r, but should not be less than the minimum radius $r_{\min}$ 。

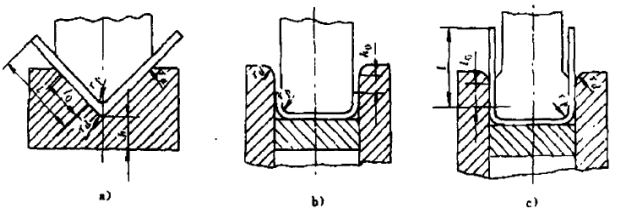

Fig. 1. The structure and size for bending die

②matrix radius rd

In practice, matrix radius is usually selected according to the material thickness t:

When t<2mm, r_d =(3-6)t

When t=2-4mm, r_d =(2-3)t

When t>4mm, r_d =2

Matrix radius cannot choose too small, so as to avoid scratches on material surface, even indentation. radius should be as same as the both sides, otherwise, the blank will shifting when it bends.

2 Process Design Module

2.1 Analysis for Bending Radius

Radius should be larger than minimal bending radius, but not too large, so as not to affect the accuracy. Minimum bend radius is only used when it is necessary in the structure.

2.2 Analysis for the Minimum Straight Edge Height

Side length should not be too small,usually L>R┼2t,as figure 2. When L is too small,straight edge (not deformation area) in the mold is too small and it is not easily to creat enough moment ,it is very difficult to obtain precise shape for the parts.

2.3 Analysis for the Distance of the Hole to the Center of Bend Radius

They should be a certain distance between the the edge of the hole and the deformation zone,lest the shape deformation.The distance a which from the hole to the center of bend radius R should be two times greater than or equal to a thickness t , that is $a \geq 2t$,as figure 2.

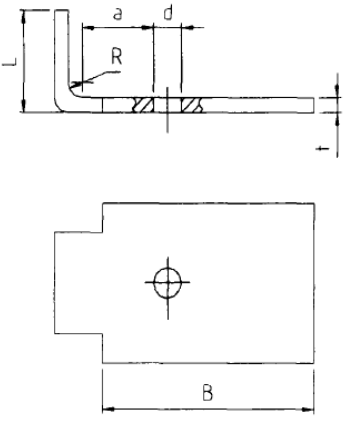

Fig. 2. The structure and size for bending die

3 Process Scheme Determined Module

After the analysis,you can proceed to make bending process program. There are many factors that affect the process scheme determined,such as punching process number, stamping sequencing, process combination, mold structure and so on. It is researched that the design of continuous bending die in this text, therefore, using this system,should have the conditions for that mass production of multi-processes bending die.

4 Parts Design Module

According to their function,they can be divided into parts and auxiliary structural components who constituted by the stamping parts and components. The parts of process structure take patr in finishing stamping process directly and effected with blank directly; the parts of auxiliary structure does not directly effect with blank, but it is guaranteed for the mold process or effectd for the mold perfectly.

4.1 Bending Punch Design

Bending punch structure, shown in Figure3.When the height of bending parts is larger,we should use the punch type structure,that is figure 3 (a) ;when the height of bending parts is smaller,we should use the punch type structure,that is figure 3 (b).

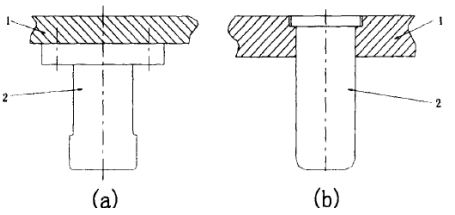

1.Punch-retainer plate 2. Bending punch

Fig. 3. Bending punch structure

4.2 Blanking Punch Design

The part of punching have common structure is circular cross section ,shown in figure 4. In order to enhance the strength ahd stiffness of the punch ,and to avoid stress concentration, the punch made of smooth transition ladder,one of the biggest ladder used to guarantee the punch without being pulled out in unloading. Figure 4 (a) shows a small circle punch for the small hole,diameter ϕ 1-8mm,to improve strength,in the middle increase transition ladder, the end department adopts riveting open type after assembly,instead of shoulder; figure 4 (b) shows a circle punch for the small hole,diameter ϕ 1-15mm, the part of ladder which coordinate with the punch plate are entended down,in order to enhance its strength; figure 4 (c) shows for the middle hole,diameter ϕ 8-30mm,for the larger diameter, can not increase the transition ladder in the middle; blanking circle holes or blanking punch often used the structure as shown in figure 4(d), the punch using screw, pin or screws and nest stand on the template directly , don't use the punch fixed;

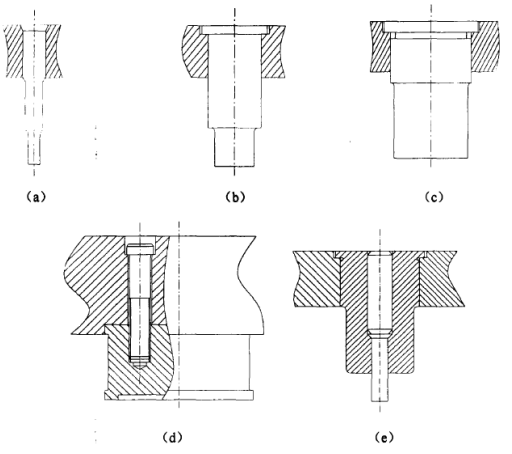

Fig. 4. Circular punch structure

According to the above several types, in this system designed the punching as multi-step cylinder model, and set parameters for diameter and length in each step.

4.3 Blanking Cavity Design

For this cavity,using another method of setting up feature,except the parameter driving technology that provided by UG,creat programming method.The structure type of cavity hole divided by pattern,there are several types,shown in figure 5.

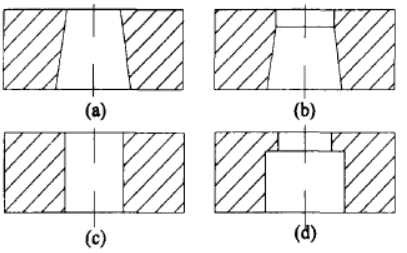

Fig. 5. The structure of punching cavity hole

(l) Cone-shaped cavity. Figure 5 (a), (b) for the cone-shaped cavity.This type has sharp blade,a small taper, it is difficult to accumulate part or waste material in the orifice, wear and spiltting forces of orifice are smaller,service life is relatively longer.However,edge strength lower,the edge size increase with the amount. This cavity fits for discharging material which workpiece simple for punching shape,less accuracy ,sheet thinner.The effective height in the wall of cavity edge should keep the actual size does not exceed the limit size after a limited number of sharpening; meanwhile,the clearance increasing between the punch and cavity should be allowed to increase in a range,to ensure the blanking quality.

(2)Cylindrical-type cavity. Figure 5(c), (d) for the cylindrical-type cavity.This type has high strengh ,make easy,the hole size changeless after grinding,no signicant effcct on punching clearance. But it is easy to accumulate the part and waste material in the hole,thereby the push force increasing, and due to the friction increasing,wear and tear on the wall of depth hole are increasing,so the total life of the cavity is reducing. In addition, the hole of cavity may form the reversed cone after wearing, make the workpiece or waste rebounded from the hole to the cavity surface,cause practical difficulties.This cavity fits for punching workpiece which complex shape,higher accuracy ,or a piece of punching.

5 UG Die Holders for Diagonal Sets Design

Finally, using VisualC++ 6.0 to prepare the user interface, to achieve the connection with interface ,dabatase and UG.

In the UG ,drawing the parts parameter model of contious bending die, and finishing parameter settings.Choose Microsoft. Office Access2003 database, import the bending die parts standard data which in the standard of the machinery industry into the database. Using Microsoft Visual c + + 6.0 ,build a a good man-machine interface,to realize how to control contious bending die parameter model by through vc + + language and correlation function in the UG development package,to achieve continuous bending die with D design.

References

1. Jing, Y.: A Study to Advanced Die and Manufacturing Technologies. Die and Mould Technology (5), 68–70 (2001)
2. Chen, H., Wang, G., Li, Z., et al.: Application on client /server model in Die CAD. Computer Aided Design and Graphics Journal (12), 152–155
3. The Chinese mechanical engineering society, China mold and die design canon editorial committee. China die and mould design canon. Jiangxi science and technology press, Jiangxi (2002)
4. Yuan, G., Zhao, Z., Peng, Y., Ruan, X.: Application on AHP for progressive dies strip layout system. Journal of Shanghai Jiaotong University 34(10), 1411–1412 (2000)
5. Yong, C.: Research of Two Dimensional Irregular Auto-Nesting Algorithm. Zhejiang University (2003)
6. Qiao, X.: Study and Development CAD System of Progressive Bending Die Based on Pro/Engineer, Tianjin Technology, University, vol. (3), pp. 28–54. (2008)
7. Hu, Y.: Rearch and implementation on optimum layout technology in mould CAD system. Nanjing University of Aeronautics and Astronautics (2004)
8. Zhao, H.: Future of CAD and relevant technology. To D / CAM Computer Design and Manufacturing Employers (4), 9–11 (2000)

A Modified Satellite Selection Algorithm Based on Satellite Contribution for GDOP in GNSS

Guangyao Li[1,2], Chengdong Xu[1,2], Pengfei Zhang[2], and Chunsheng Hu[2]

[1] Key Laboratory of Dynamics and Control of Flight Vehicle, Ministry of Education of the People's Republic of China
[2] School of Aerospace Engineering, Beijing Institute of Technology, No.5 South Zhongguancun Street, Haidian District, Beijing, 100081, China
Liguangyao283@163.com

Abstract. In Global Navigation Satellite System (GNSS), the visible satellites combination which has a better geometry distribution can provide better positioning accuracy. Geometry Dilution of Precision (GDOP) can be used to measure the positioning accuracy. The direct satellite selection algorithm (DSSA) is a time-consuming algorithm because it would calculate all GDOP values associated with different combinations to choose the smallest one. In this paper, based on each satellite's contribution for GDOP, a modified satellite selection algorithm (MSSA) is proposed which is dependent on a fixed contribution value. Through the theory analysis, the computational complexity of the MSSA is far less than that of the DSSA. Meanwhile, the result of simulation experiment indicates that the calculation precision of the MSSA is almost close to that of the DSSA.

Keywords: GNSS, satellite contribution value, modified satellite selection algorithm, GDOP.

1 Introduction

Global Navigation Satellite System (GNSS) is a time measuring and positioning navigation system based on satellite radio. It can provide positioning data with different accuracy online or offline for different users on aeronautics, astronautics, land, and sea. With the development of GNSSs, the number of global navigation satellites continues to increase[1]. Thus, time and coordinate transformations among different GNSSs should be taken into account for calculation, and they have been researched in some papers[2][3]. The combination of different GNSSs will provide more visible satellites in the same epoch moment. This will improve the navigation accuracy and reliability, but the computational complexities will increase exponentially[4]. Furthermore, the requirement of calculation speed is increasing for receivers of users in engineering, especially for high dynamic users' receivers, and this will add the receivers' burden. For satellite navigation and positioning calculation, when the number of visible satellites used to calculate reaches a certain value, the improvement of positioning accuracy is inconspicuous[5]. In addition, for the number of the receiver channels is restricted, it needs to choose a combination

D. Jin and S. Lin (Eds.): Advances in Mechanical and Electronic Engineering, LNEE 176, pp. 415–421.
springerlink.com

which has a good geometry distribution for calculation. Thus, how to choose the visible satellites to form the combination fast is significant. Geometry Dilution of Precision (GDOP) is used to be a measurement for satellite selection. Based on each satellite's contribution for GDOP, a modified satellite selection algorithm (MSSA) is proposed in this paper.

2 Related Knowledge of GDOP

2.1 The Geometrical Meaning of GDOP

The accuracy of positioning is decided by two main factors: one is observations' accuracy which is caused by the navigation satellite itself, the signal transmission error and the receiver's error; the other is geometry distribution of visible satellites. The amplification degree of measurement error which caused by geometry distribution of visible satellites is called GDOP[6][7]. A smaller GDOP value indicates that the geometry is better, which yields a better positioning accuracy. The more dispersed the distribution of satellites is, the smaller the GDOP value is. On the contrary, the more concentrated the distribution of satellites is, the larger the GDOP value is. It can be shown in Fig. 1.

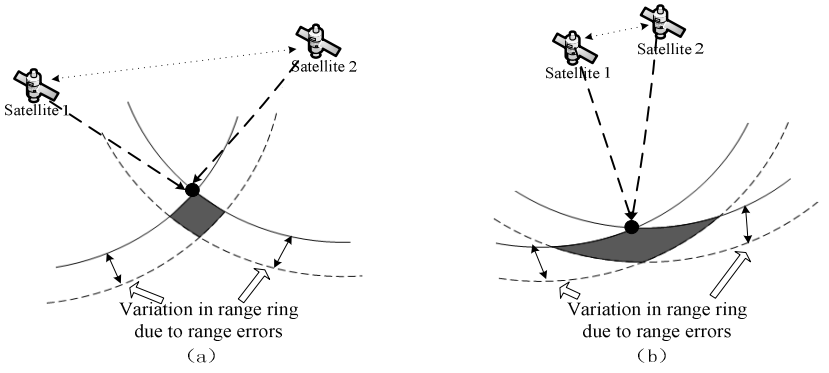

Fig. 1. Relative geometry of satellites and possible locations of receivers

The range between a satellite and a receiver is measured including an error. The solid range rings in Fig. 1 are formed by the true range between a satellite and a receiver, and the regions between the solid range ring and the dashed range ring indicate the error bands. Furthermore, the shaded regions indicate the set of locations of receivers with error. With the same measurement error variation, the accuracy of the computed location is very different for the two cases. The Fig.1 (a) is the situation that the GDOP value is smaller. We can see the range of satellite 1 and satellite 2 is larger, and the error band is smaller. The Fig.1 (b) is the situation that the GDOP value is bigger, and the error band is also bigger. The situation of more satellites is similar to that of the two satellites. This is the geometrical meaning of GDOP.

2.2 The Calculation Method of GDOP

In GNSS, in order to calculate the receiver's 3-dimensional coordinate (x_u, y_u, z_u) and the clock offset t_u, it needs at least four satellites. The formula (1) can be used to calculate single pseudorange ρ_j [6]. The (x_j, y_j, z_j) denotes the *j*th satellite's position in three dimensions.

$$\rho_j = \sqrt{(x_j - x_u)^2 + (y_j - y_u)^2 + (z_j - z_u)^2} + ct_u = f(x_u, y_u, z_u, t_u) \tag{1}$$

It is known that the unknown user's position and the unknown receiver's clock offset can be considered to consist of an approximate component and an incremental component. This can be shown in formula (2).

$$f(x_u, y_u, z_u, t_u) = f(\hat{x}_u + \triangle x_u, \hat{y}_u + \triangle y_u, \hat{z}_u + \triangle z_u, \hat{t}_u + \triangle t_u) \tag{2}$$

When the number of satellites is equal to or more than four, the pseudorange equations can be linearized with Taylor's series expansion at the approximate point and associated predicted receiver clock offset (x_u, y_u, z_u, t_u). It can be expressed as formula (3).

$$\begin{bmatrix} \triangle\rho_1 \\ \triangle\rho_2 \\ \triangle\rho_3 \\ \vdots \\ \triangle\rho_n \end{bmatrix} = \begin{bmatrix} a_{11} & a_{12} & a_{13} & 1 \\ a_{21} & a_{22} & a_{23} & 1 \\ a_{31} & a_{32} & a_{33} & 1 \\ \vdots & \vdots & \vdots & \vdots \\ a_{n1} & a_{n2} & a_{n3} & 1 \end{bmatrix} \begin{bmatrix} \triangle x_u \\ \triangle y_u \\ \triangle z_u \\ -c\triangle t_u \end{bmatrix} + \begin{bmatrix} v_{\rho 1} \\ v_{\rho 2} \\ v_{\rho 3} \\ \vdots \\ v_{\rho n} \end{bmatrix} \tag{3}$$

In the formula (3), $\triangle\rho_j$ is the pseudorange increment and $(\triangle x_u, \triangle y_u, \triangle z_u)$ is the user's 3-dimensional coordinate increment. $v_{\rho i}$ denotes a random noise with an expected value of *0*. *H* is the $n \times 4$ matrix and (a_{j1}, a_{j2}, a_{j3}) are the unit vectors pointing from the linearization point to the location of the *i*th satellite. GDOP can be calculated by matrix *H*, and the calculation formula is as follows:

$$GDOP = \sqrt{trace(H^T \bullet H)^{-1}} \tag{4}$$

It involves matrix inversion and matrix multiplication, whose computational complexity will be greatly increased with the dimensions of matrix *H* growing.

3 Satellite Selection Algorithm

As mentioned earlier, it only needs to choose the combination which has a good geometry distribution for calculation. The combination with minimum GDOP value is considered as the best one. The direct satellite selection algorithm (DSSA) is to calculate all GDOP values of different combinations, but the computational complexity is large. In order to reduce the computational complexity, the researchers

have proposed many approximate calculation methods, such as the neural network algorithm, the support vector machine, the genetic algorithm and so on[8]. They have reduced the computational complexity partly. In this paper, visible satellites are selected based on each satellite's contribution for GDOP of the combination. For avoiding too many matrix inversions and matrix multiplications, it can improve the efficiency of calculation.

3.1 Single Satellite's Contribution for GDOP

Supposing that H_m is an observation matrix of m satellites, and the observation matrix that removed the *i*th satellite from the m satellites is H_{m-1}^i. As pointed out in [5], the relationship between the two matrixes is as follow:

$$H_m^T H_m = {H_{m-1}^i}^T H_{m-1}^i + h_i^T h_i \tag{5}$$

Recording $(H_m^T H_m)^{-1}$ as G_m, the following formula can be got according to Sherman-Morrison formula[5]:

$$G_{m-1}^i = ({H_{m-1}^i}^T H_{m-1}^i)^{-1} = (H_m^T H_m - h_i^T h_i)^{-1} = G_m + G_m {h_i}^T (1 - h_i G_m h_i^T)^{-1} h_i G_m \tag{6}$$

where $(1 - h_i G_m h_i^T)$ is a scalar, and recorded as λ_{mi}. The further formula about the GDOP values of the $m-1$ satellites and the m satellites is as follow:

$${GDOP_{m-1}^i}^2 = trace G_{m-1}^i = GDOP_m^2 + trace(G_m h_i^T h_i G_m / \lambda_{mi}) \tag{7}$$

It can also be expressed as follows:

$${GDOP_{m-1}^i}^2 - GDOP_m^2 = trace(G_m h_i^T h_i G_m / \lambda_{mi}) \tag{8}$$

From the formula, it can be seen that the changed value of $GDOP^2$ resulted from the *i*th satellite is $trace(G_m h_i^T h_i G_m / \lambda_{mi})$, which is recorded as ΔG. The bigger the ΔG_i is, the larger the *i*th satellite's contribution for $GDOP_m$ is. And it indicates that the *i*th satellite should not be removed because the $GDOP_m$ will change largely. So the *r* satellites with higher ΔG can be chosen from *m* satellites, and form a combination which has a better geometry distribution to replace the all visible satellites. This method can reduce the times of matrix inversion and matrix multiplication, so the calculation efficiency will be improved.

3.2 Satellite Selection Algorithm Design

Obviously, at a certain moment, the GDOP value associated with *m* satellites changes very little when removing off a few satellites for calculation. The algorithm in paper [9] is based on a fixed satellite number six over time, but it has limitation when the number of satellites with higher ΔG is more than six. So the following modified satellite selection algorithm (MSSA) is designed.

Algorithm: If the *i*th satellite's contribution values ΔG_i is smaller than a threshold γ, the GDOP value will changes very little when removing off it. According to the experiments, the threshold can be set as an empirical value $\gamma = 0.15$, which can ensure that the difference of GDOP values are small than 0.2. Remove the satellites whose contribution values are smaller than γ from visible satellites. In this way, it can find out the satellites which are important for calculation, and the number of the selected satellites is changing over time. The algorithm process is as follows:

- Calculate the current satellites' positions through ephemeris data.
- Find out the current visible satellites by earth obscuration angle.
- Calculate all visible satellites' contribution values ΔG_i.
- Rank the visible satellites in the order of ΔG_i.
- If the ΔG of each visible satellite is larger than or equal to γ, the selection result is the all visible satellites. Otherwise proceed to the next step.
- Remove the satellites whose ΔG are smaller than the γ, and the rest of the satellites are selected.

The number of selected satellites is changing over time. The threshold γ can be reset according to requirement of accuracy.

3.3 Computational Complexity Analyses

The calculation complexities mainly depend on the times of matrix inversion and matrix multiplication. If using the DSSA to select the *n* satellites combination whose GDOP value is minimum from the *m* visible satellites, it must calculate all GDOP values of *n* satellites combinations. The times of matrix inversion and matrix multiplication are both C_m^n, this is a time consuming work. Using the MSSA, for calculating *m* satellites' ΔG, it only needs one matrix inversion and $5 \times m + 1$ matrix multiplications. When the satellites are selected more frequently, the calculation complexities are greatly different. Supposing that four satellites are selected, the calculation times are compared between DSSA and MSSA. The result is shown in table 1:

Table 1. Comparison of the computational complexity for selection

The number of Visible satellites	DSSA		MSSA	
	matrix inversion times	Matrix multiplication times	matrix inversion times	matrix multiplication times
8	70	70	1	41
9	126	126	1	46
10	210	210	1	51
11	330	330	1	56
12	495	495	1	61
13	715	715	1	66
14	1001	1001	1	71

The table 1 indicates that the calculation times of the DSSA is far more than that of the MSSA when the difference between selection number and the visible satellite number is larger. And with the number of visible satellites increasing, the accelerated speed of calculation times in the DSSA is faster.

4 Simulation Experiments

The MSSA can be used to all GNSSs, so the experiment takes GPS navigation system for example. Supposing that the receiver is in Beijing (116°E, 40°N), the earth obscuration angle is 5°, the observation time is 24 hours and the sampling time-interval is 30 seconds. The experimental result of MSSA is as follows:

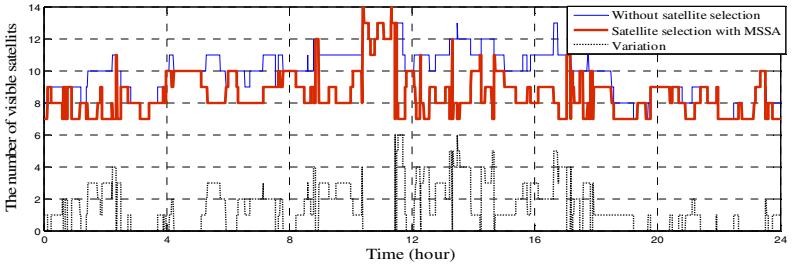

Fig. 2. The number of visible satellites for calculation

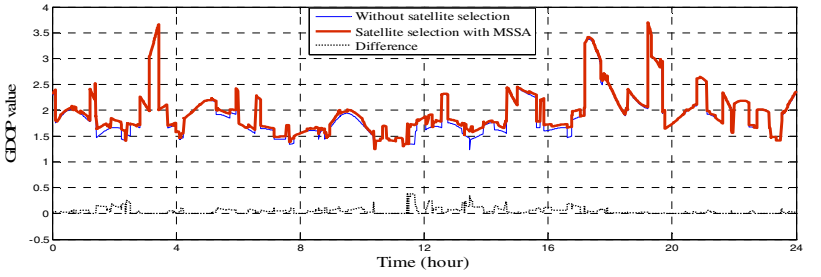

Fig. 3. The GDOP values in different time

In Fig. 2, the fine line denotes the number of all visible satellites in different time, and the bold line denotes the satellite number using the MSSA with a threshold 0.15, and the dot line is the difference between them. The result shows that the reduction of the numbers is obvious at some time. The average difference is 2.1, and the selection result is satisfactory. At the same time, the variation of accuracy is very little showed in Fig. 3. The fine line denotes the GDOP values in different time calculated by all visible satellites. The bold line denotes the GDOP values using the MSSA. The difference between them is very little, and the average is 0.09, and the maximum value is 0.4.The variation of accuracy is very little.

5 Conclusions

This paper describes the necessity of the selection on visible satellites when the number of receiver's channel is restricted and the requirement of calculation speed is increasing for high dynamic users' receivers. Based on each satellite's contribution for GDOP, the MSSA is proposed. The visible satellites are selected by a fixed contribution value γ .The theoretical analysis result shows that the calculation complexity of the MSSA is less than that of the DSSA. So it increases the speed of satellite selection. Meanwhile, by comparing the difference of GDOP values, the result of simulation experiment shows that it can reach a high precision. In addition, if the empirical value γ is set more reasonable, the selected result will be more perfect. This will be considered in the future work.

Acknowledgments. This work was supported by the National High-Tech. R&D Program, China (No.2011AA120505) and the National Natural Science Foundation, China (No.61173077).

References

1. Hofmann-Wellenhof, B., Lichtenegger, H., Wasle, E.: GNSS-Global Navigation Satellites Systems GPS,GLONASS,Galileo & More. Springer Wien, NewYork (2008)
2. Zhang, P., Xu, C., Hu, C., Chen, Y.: Coordinate transformations in satellite navigation systems. In: 2011 International Conference on Electronic Engineering, Communication and Management, EECM 2011, Beijing, pp. 249–257 (2011)
3. Zhang, P., Xu, C., Hu, C., Chen, Y.: Time Scales and Time Transformations among Satellite Navigation Systems. In: The 3rd China Satellite Navigation Conference, CSNC 2012, Guangzhou (2012)
4. Bo, X., Shao, B.: Satellite selection algorithm for combined GPS-Galileo navigation receiver. In: Forth International Conference on Autonomous Robots and Agents, Wellington, New Zealand, pp. 149–154 (2009)
5. Cong, L., Abidat, A.I., Tan, Z.: Analysis and Simulation of GDOP of Satellite Navigation. Acta Electronica Sinica 34(12), 2204–2208 (2006)
6. Kaplan, E.D., Hegarty, C.J.: Uderstanding GPS: Principles and Applications, 2nd edn. Artech House Publisher (2006)
7. Kihara, M.: Study of a GPS satellite selection policy to improve positioning accuracy. In: Proc. of IEEE Position Location Navigation Symp., Las Vegas,NV,USA, pp. 267–273 (1994)
8. Wu, C.-H., Ho, Y.-W.: Genetic Programming for the Approximation of GPS GDOP. In: 2010 International Conference on Machine Learning and Cybernetics, pp. 2944–2949 (2010)
9. Cong, L., Tan, Z.: Satellite selection algorithm to improve precision and real-time performance of GPS positioning. Systems Engineering and Electronics 30(10), 1914–1917 (2008)

Parametric Design of Helical Gear Based on UG

Erbao Peng and Hongge Zhang

Henan Polytechnic Institute,Nanyang Henan, China
Yang09200@163.com

Abstract. The secondary development was made on UG by Visua1C++ to achieve the mutual-use between UG / Open API and UG / Open Grip. Database was applied in the UG secondary development to complete the parametric design of involute helical gear, a helical gear library was established through database technology, and gear information which has been completely designed was stored. Searching function in this secondary development makes gear parametric design more convenient. This secondary development truly realized the application of the product data management idea in design.

Keywords: UG/Open API, Helical gear, database, Parameter, VB.

1 UG Software Development Two Times

UG / OPen two development module of UG software as the two development tools, and is convenient for users to carried out two times the development work, the module of the UG system user tailoring and development, to meet the user's demand of development. UG / Open including the following several parts: UG / OpenMenuscrint development tools, UG software interface for user development, without programming to UG standard menu to add, recombination, cut or in the UG software integrated user software function; UG / OpenuIStyle development tool is a visual editor, used to create similar UG interface, using the tool, the user can provide UG / Open application development is independent of hardware platform interface; UG / OpenAPI development tools, provides UG software direct programming interface, support C, C + +, Fortran and Java mainly senior language; UG / OpenG P development tool is a rent similar to the APT UG development language, using the tool users can generate NC automated or automatic modeling and other users of the special application.

1.1 UG/OPen MenuScript

Use of this tool can realize user menu. UG / Open MenuScript support UG main menu and pop-up menu design and modification, it can change the UG menu layout. To add a new menu item to perform user GRIP, API two, User Tools development program file and operating system command.

Application of UG / Open MenuScript programming there are two ways to realize the menu customization: ① to add the menu file, developers to add menu file

D. Jin and S. Lin (Eds.): Advances in Mechanical and Electronic Engineering, LNEE 176, pp. 423–428.
springerlink.com

corresponding to the menu, the menu file is after the user to edit, compliance with the requirements of their own menu file.② editorial standard menu file, developers edit the existing standard menu file. This approach will change the original UG interface, can not be restored. Developers can use the text editor, such as Notepad editor UG menu file. UG / Open API UG / Open API program and UG / Open MenuScript program interface function.

1.2 UG/OPen UIStyler

UIStyler: is the development of UG dialog visualization tools, generates dialog can be integrated with UG, allow users more convenient, more efficient to interact with UG operation. Use of this tool can avoid the complex graphical user interface CUI programming, directly to the dialog box controls the basic function of combination generates different dialog. Developers to enter the UG, click Application UIStyler can enter the dialog interface design. The interface includes a tool bar and the three window: object browser window, the resource editor window as well as the design of dialog window. Application tool capable of rapid clicks on the icon, in the design of the dialog box to add delete controls, dialog box interface design object browser window to display the dialog box controls on all the information, select a controls can in the resource editor window corresponding to the operation of the two resource editor window is used to set the modify the control properties, news operation two design dialog window used to display the dialog interface.

1.3 UG/OPen Grip

UG provides a UG / OpenGrip CRIP language editor, with this tool can edit, modify, compile, link program. GRIP language and common language, has its own grammatical structure, program structure, internal function, as well as with other general purpose programming language to call each other's interface. A GRIP statement is composed of one or several GRIP commands, GRIP command CRIP language is the basic component of. The GRIP programming language is the language for engineers, is simple, easy to learn, easy to use features, but the preparation procedure of long, complex, must consider the procedures of the various details. Therefore, the GRIP language commonly used in the development of some small procedures.

1.4 UG/OPen API

UG/OPen API procedures according to compile the situation can be run in two different environments, Intemal and Extemal.Exteral types to exe way can be directly in the running under the operating system, independent of the UG system, the type to display graphics and user interaction, but can be printed and generating computer graphics metafile (CGM; Intemal) type can only be run under UG environment. The program with DLL (Dynamic Link Library) way was transferred to UG process space, once the loading is resident in the memory, the types and Extemal types compared his merit is can

connect faster and smaller and can interact with the user program. Internal type program can be run from the UG graphical interface to call, in addition to the UG / Open MenuScript, User Exits, User Tools and UG / Open GRIP call.

The UG / OPenAPI program using C or C + + programming language. Based on the WindowsNT operating system and UG software development in VC++6.0 environment. In the VC environment to build a UG two development project has two kinds of methods. One is the use of UG / OpenAPPWizard the wizard to set up the basic framework: the VC in hand to build a UG / Open API project. The first method developers as long as the wizard step by step to carry out to complete the project basic frame. Compared to the first method, the second method is more cumbersome, it must be in the VC manual configuration of works in a variety of settings, in order to build UG software and VC connection. The method is much more complicated, it must be in the VC manual configuration of works in a variety of settings, in order to build UG software and VC connection. So it is best to use UG / Open AppWizard two development project to build. Through the above research, the system adopts UG / Open MenuScript custom menu, through uG / OpenAPI compiler, using VisualC++6.0 as a development tool, UG two development function.

2 Database Construction

Most of the current database uses the relational model, which uses two dimensional table is represented in the form of the entity and the entity links between data model. From the user's perspective, the relationship between logical structure is a two-dimensional table. Usually the design of database structure is at least the conceptual design, logical design and physical design of 3 stage.

2.1 Concept Design

Conceptual design conceptual design model, it is the key to the design of the database. In the conceptual design phase of work to be done is to make every kind of user information demand into the preliminary design of database. Concept design goal is generated reflecting system information needs of the database concept structure, i.e. the concept model. The conceptual model is independent of the DBMS database, which is a database table structure design is the most important stage. Current concepts of design in general with the entity relationship model (EntityRelationshipMedel) also known as ER model to represent the. This model directly from the real world in the abstract entity and entity relation, and then use the entity relationship diagram ER. The ER model is simple in design, easy to understand, truly reflect the needs of users. In the ER model has 3 basic elements.

Figure 1 shows the gear machining simulation system of cut gear entity and entity ER diagram of preshaving hob. The links between entities according to the actual needs to be identified as a contact, through the gear parameters to calculate the corresponding tool parameters, and uses the calculated parameters of finish machining simulation.

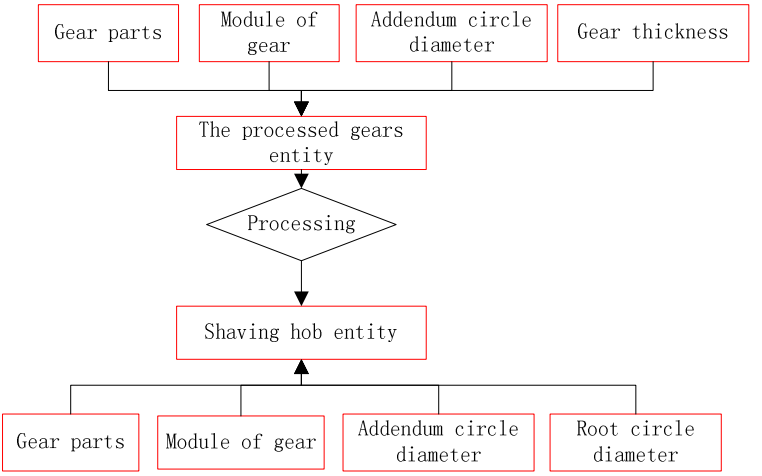

Fig. 1. The entity-relation diagrams of the gear and pre-shaving ho

2.2 Logic Design

ER model representation of conceptual model can be accepted by a user model. It is independent of any a kind of data model, but also for any one specific database management system support, so need to the conceptual model is converted to a specific computer database management system (DBMs) supported by the data model, the process of database logical design.

The ER model into relation model refers to the ER model entity relationship model and contact conversion for each relation, each relationship is a two-dimensional table.Table 1 shows the gear machining simulation system is processed gear entity structure.

Table 1. The entity structure of the machined gear

Attribute	Data type
Gear part number	
Gear modulus m	
Gear tooth number z	
Gear pressure angle a	
Gear helix angle β	
Gear pitch circle tooth thickness	
Addendum circle diameterda	
Root circle diameterdf	
Gear thickness s	
Tooth thickness for shaving stock	
Cutter tooth and gear tooth top radial clearance number	

3 UG Helical Gear Parametric Design

Gear is one of the many products of the main components, especially in machinery industry have a wide range of applications, thus changing the traditional design method, using modern design method, designed to improve efficiency, is especially meaningful.This module to involute helical gear as example, in addition to the completion of involute helical gear parametric design, through the database technology to build a helical gear base, will have completed the design of the gear information storage, and a search function, a great convenience to gear parametric design, the real product data management thought is applied to the design of the.Client layer mainly completes the helical gear helical gear storage, information inquiry, information deletion and helical gear helical gear parametric modeling two data layer is mainly used to store the data information of helical gear, for the customer provides the data support, system components such as shown in Figure 2.

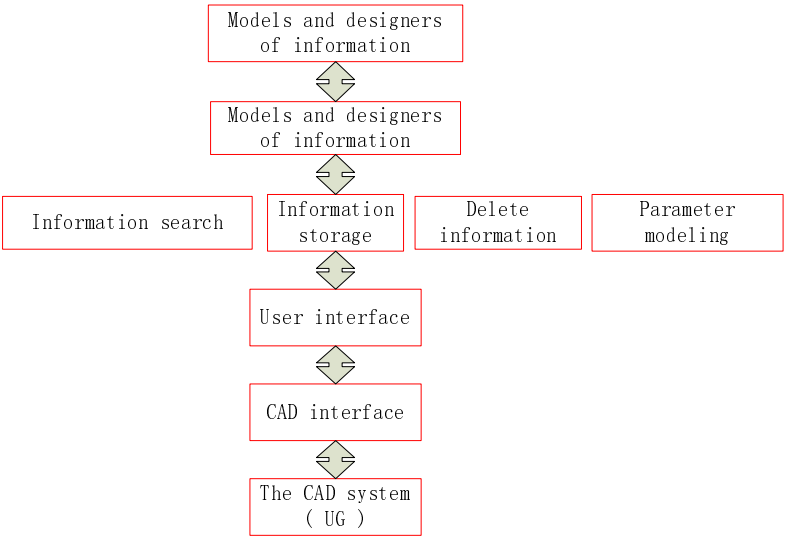

Fig. 2. General system design

3.1 System Database

Database application stored in the warehouse, during application development occupies the very important position, simple data design process is divided into the database logical design and physical design of two parts. The system uses access relational database, the logical database design as shown in table 2.

Table 2. The entity structure of the involute helical gear

Attribute	Data type
Gear number	Text
Modulus m	Real number
Number of teeth z	Real number
Pressure angle a	Real number
Spiral angle β	Real number
Tooth width b	Real number

3.2 The Use of UG / Open MenuScript Making the System Menu

Menu script file extension *. Men file, you can use Notepad to create and edit, file syntax (which behind the ACTION menu for the action to be performed, the system is the dialog file name):

```
VERSION 120
EDITU_GATEWAY_MAIN_MENUBAR
AFTER UG_APPLICATION
CASCADE_BUTTON gear_menu
LABEL
END_OF_AFTER
MENU gear_menu
BUTTON bevelgear
LABEL
ACTIONS beveigear.Dlg
END_OF_MENU
```

References

1. Daniel, S., Rainer, W.: Product configuration framework–asuoey. IEEE Intelligent System 4(13), 42–49 (1998)
2. Kotha, S.: Mass customization: Implementing the Emerging Paradigm For Competitive Advantag. Strategic Management Joumal, 21–42 (1995) (specialedition)
3. Da Silveria, G., Borenstein, D., Fogliatto, F.S.: Mass Customization: Literature Review and Research Directions. Intemational Joumal of Production Economics 72(l), 1–13 (2001)
4. Chou, H.-T., Kim, W.: A unifying framework for version control in a CAD environment. In: Proceedings of the12th International Conferenceon Very Lalge Database(VLDB), Kyoto, Japan, pp. 336–334 (1986)
5. Strphane, G., Genevieve, J.: A framework for Programming multiversion databases. Data and Knowledge Engineering 36(l), 29–53 (2001)
6. Gunter, A., Kuhn, C.: Knowledge-based configuration-Survey and fture directions. In: Proceedings of the 5th Biannual German Conference on Knowledge-Based Systems, pp. 47–66. Springer, Wurzburg (1999)
7. Getting Started Guide for Boriand Together 2006 for EcllPse. Togethersoft Corporation (2005)

Study on Nondestructive Inspection of Pears Quality Based on Mechanical Engineering Method

Jie Wu[1], Jiali Yang[2], and Kang Tu[2]

[1] Department of Food Engineering, Bengbu College, Bengbu AnHui Province, China, 233030
[2] College of Food Science and Technology, Nanjing Agricultural University, Nanjing, Jiangsu Province, China
Kangtu@njau.edu.cn

Abstract. Acoustic impulse response method as one of the mechanical engineering techniques was used to monitor the qualities of pears (c.v. Housui and c.v. Niitaka). Stiffness, SSC/TA (soluble solids content/total acid) of the pears and the nondestructive stiffness coefficient (S) were measured during the storage. The results indicated that S correlated well with the quality parameters and the models developed were all at significant levels ($P < 0.05$). It was found that the stiffness coefficient of pears with inner decay showed significant different with the control group and fruit weight loss rate can be considered as an important parameter in detecting degree of inner decay of pears.

Keywords: Pears, acoustic impulse, stiffness, quality.

1 Introduction

Housui pears (Pyrus pyrifolia Nakai, c.v.Housui) and Niitaka pears (Pyrus pyrifolia Nakai, c.v.Niitaka) are widely planted in the south of China because of their high quality and high economic value. The quality of pear fruit is determined by several internal and external factors. External factors such as shape, mass and color can be measured easily, but internal attributes such as firmness, sugar, acid content and the absence or presence of internal defects are difficult to assess. There are many techniques available to measure fruit quality. Acoustic impulse response as one of the mechanical engineering techniques is a non-destructive measurement. The response frequencies of the intact fruit are obtained by recording the sound wave, which is produced by an impact on the fruit without damaging the fruit.

In an experiment with apples [1], the acoustic technique was very effective and its sensitivity to firmness was greater than that of penetrometer measurements, and the correlation between both methods varied according to the cultivars and freshness. The response frequencies of the intact fruit were significantly correlated with fruit firmness and sensory measurements [2]. The technique also could be used to monitor the change in conference pear quality with time [3]. At present, there has no reported on the acoustic impulse response technique monitoring the quality of Housui and Niitaka pears.

On the other hand, it is difficult to detect the internal defects of pears nondestructively. Recently, some non-destructive technologies, such as near-infrared

D. Jin and S. Lin (Eds.): Advances in Mechanical and Electronic Engineering, LNEE 176, pp. 429–435.
springerlink.com

reflectance, time-resolve reflectance spectroscopy, have been applied in detecting brown heart in pears and water core in apples [4-5]. However, these technologies for inspecting the internal condition are very limited in functionality and affordability now.

The objectives of this work were to: 1) investigate the correlation between quality parameters and the nondestructive stiffness coefficient and develop appropriate regression models of the two kinds of pears; 2) detect the internal defects of pears based on acoustic impulse response in a simple and quick way.

2 Materials and Methods

2.1 Fruit Material and Storage

Pears (c.v. Housui and c.v. Niitaka) were harvested from Suining, Jiangsu Province of China. They were selected according to uniform color and size and divided into four groups. Group A of Housui pears were stored under controlled conditions (20 ℃ , 80 % RH) for 18 days and Group B of Housui pears were stored under 2-4 ℃ and 95% RH conditions for 30 days. Group A were measured first non-destructively and then destructively on every 3 days interval, while Group B on 5 days. Group C of Niitaka pears stored 20 ℃, 80 % RH and Group D of Niitaka pears stored 2-4 ℃, 95% RH were measured repeatedly on 5 days, respectively.

2.2 Measurements

1) Acoustic measurements

The pear was measured in the similar way as [6]. It was proposed that a mathematical model for the interpretation of the vibrant behavior of intact fruit [7]. They showed that the so-called stiffness coefficient S can be estimated satisfactorily as follows:

$$S=f^2m^{2/3} \tag{1}$$

where f is the first resonance frequency in Hz, and m is the fruit mass in g. S can be used to indicate firmness of the fruit.

The measurement set up is shown in Fig.1.

2) Quality measurements

The stiffness coefficient (*S*), *SSC/TA*, maximum force, and modulus of elasticity were measured on 10 pears of each group.

The maximum force (F_{max}) was measured with a universal testing machine (TA.XT2i, UK). The skin of the pears was pared at four locations equally spaced on the circle of fruit equator. The maximum force was recorded when a metal cylinder (P/5, diameter 5 mm) penetrates into the pear flesh to a depth of 10 mm with a speed of 1.0 $mm.s^{-1}$. The testing machine was programmed to get F_{max} and the depth (*d1*), 60 % F_{max}(*F*) and the depth (*d2*), $\Delta F= F_{max}-F$, $\Delta d= d1-d2$. The modulus of elasticity was calculated as follows:

$$E= (\Delta F/s)/(\Delta d/d) \tag{2}$$

Where *d* is maximum penetration, and *s* is the area of the cylinder. The measurement is as shown in Fig. 2.

The soluble solids content (*SSC*) was determined in pear juice with a digital refractometer and the total acid (*TA*) was measured according to GB12293-90 (Chinese standard).

3) Simulation and detection of the internal defects of pears

The Niitaka pears were injected with conidial suspension of *Penicillium expansum* (1 $\times 10^5$/ml) of 15 μl, 20 μl, 25 μl respectively into the core. Then the injected pears were stored under controlled conditions (20 ℃ and 80 % RH) for 3 days.

The inner decay of pears which had been sliced off was observed and pictures were taken. After image processing, the percent of rotten area of flesh could be calculated. The pears were classified into four level according to the percentage of rotten area, Grade 0 (0 %), Grade 1 (0 %-10 %), Grade 2 (10 %-25 %), Grade 3 (＞25 %).

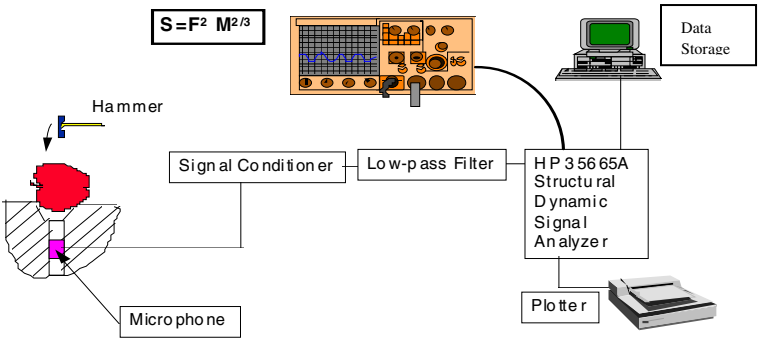

Fig. 1. Acoustic impulse response measurement system

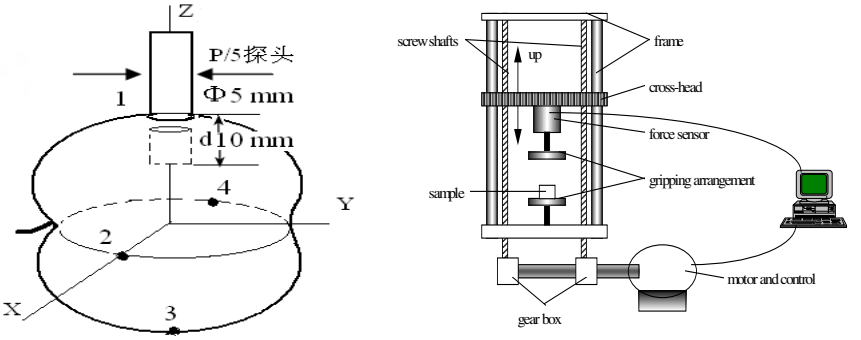

Fig. 2. Pear sample (left) and firmness measurement system (right)

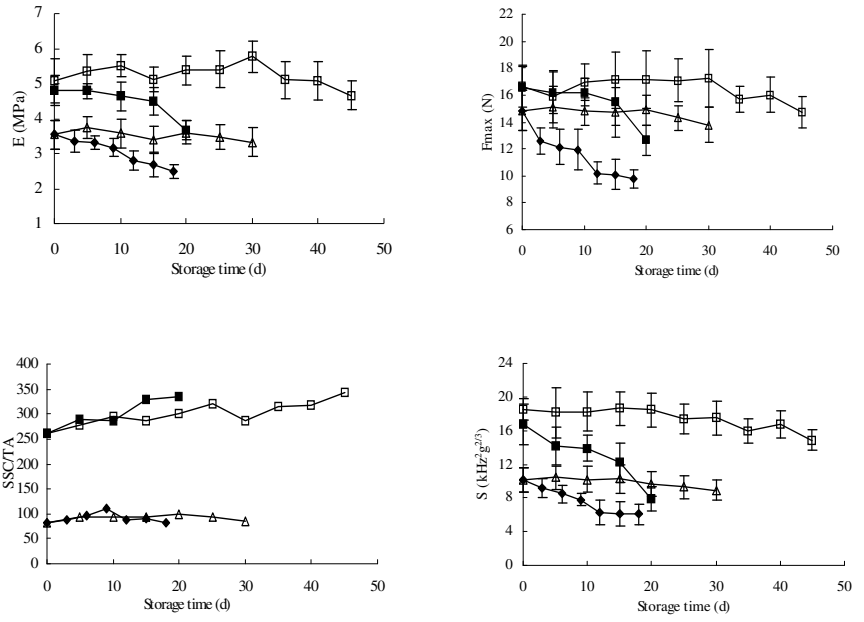

Fig. 3. Changes of modulus of elasticity (E), maximum force at compression (Fmax), SSC/TA and the stiffness coefficient S of Group A (◆), Housui pears stored at 20 ℃, 80 % RH, Group B (△), Housui pears stored at 2-4 ℃, 95% RH, Group C (■), Niitaka pears stored at 20 ℃, 80 % RH, and Group D (□), Niitaka pears stored at 2-4 ℃, 95% RH.

3 Results

Figure 3 shows the evolution of maximum force at compression F_{max}, modulus of elasticity E, *SSC/TA* and the stiffness coefficient S of Housui and Niitaka pears. As expected, the F_{max} and E measured destructively and S measured non-destructively decreased, while pears in shelf life changed more significantly and quickly. The *SSC/TA* of Housui pears increased first, but began to fall later in storage time. In contrast the *SSC/TA* of Niitaka pears rose steadily. Generally, E, F_{max}, *SSC/TA* and S of Housui pears were lower than those of Niitaka pears.

The correlation coefficients between S and E, F_{max}, *SSC/TA* are given in Table 1. The correlation coefficients of pears in shelf life (Group A and Group C) were all higher than those of pears in cold storage (Group B and Group D). It may be due to S which was changed distinctively in shelf stored pears. For pears in shelf life, the correlations between the F_{max}, E and S were significant ($P < 0.01$) and *SSC/TA* was negatively correlated with S ($P < 0.05$).

In cold stored pears, the correlations were also high ($P < 0.05$). This could be logically expected since the changes in all parameters reflect the process of fruit maturation. However, there was a very poor correlation between the $H°$ and S. From Table 1, it could be noticed that modulus of elasticity E was better correlated with S

than F_{max} in the four groups. Since F_{max} could be influenced by a number of factors, such as individual difference, test point difference, the turgor pressure, the structure, size and composition of the cells, while E can reflect the mechanical property of the flesh considering force and deformation. Besides, Table 1 suggested that the correlation between the E, F_{max}, *SSC/TA* and S of Niitaka pears is better than that of Housui pears.

Table 1. Correlation Coefficients of measured parameters

Group	Parameters			
	Fmax	*E*	*SSC/TA*	*H°*
Group A	0.8710**	0.8915**	-0.7869*	0.4839
Group B	0.7320*	0.7847**	-0.6603*	0.3963
Group C	0.8347**	0.8715**	-0.7194*	0.4160
Group D	0.7502*	0.7778**	-0.6170*	—

Correlation between quality parameters for pears (c.v. *Housui and* c.v. *Niitaka*).
** and * indicate significant difference at 0.01 and 0.05 levels, respectively.

The regression models described the prediction of Housui and Niitaka pears quality, including Group A, Group B, Group C and Group D, in function of the stiffness coefficient S can be found in Table 2. For Niitaka pears (Group C and Group D), the models could be fit to the data with a linear regression procedure with SAS 8.2, while a quadratic regression procedure for Housui pears (Group A and Group B). Accordingly, these indicated that the model could predict quality of Housui and Niitaka pears on shelf or during cold storage.

Table 2. Regression models of destructive parameter as function of stiffness factor

Group	Parameters	Regression equation	R^2	Significant levels (P)
Group A	Fmax	-0.1661S2+3.8264S-6.6322	0.7959	<0.01
	E	-0.0263S2+0.6697S-0.3016	0.8175	<0.01
	SSC/TA	-1.0886S2+33.282S-158.51	0.6917	<0.05
Group B	Fmax	-0.6866S2+13.967S-56.125	0.7291	<0.01
	E	-0.0765S2+1.6741-5.4936	0.7639	<0.01
	SSC/TA	-2.8856S2+106.19S-881.58	0.6297	<0.05
Group C	Fmax	0.8367S+3.8220	0.7451	<0.01
	E	0.2212S+1.4529	0.7709	<0.01
	SSC/TA	-8.7496S+412.85	0.6882	<0.01
Group D	Fmax	0.0859S+1.5287	0.6027	<0.01
	E	0.1306S+2.9958	0.6338	<0.01
	SSC/TA	-15.732S+574.47	0.5707	<0.05

Table 3. General analysis on the test results among different

Parameters	Grades of Decay			
	0	1	2	3
The stiffness coefficient S ($kHz^2 \cdot g^{2/3}$)	17.61	14.20	12.94	12.77
Rate of weight loss (%)	0.68	0.79	0.96	1.17

Table 4. Comparison of S and weight loss rate inner deacy levels of pears

Parameters	DF	Mean squares	F value	Significant levels (P)
The stiffness coefficient	3	63.06	13.30	<0.01
Weightlessness rate	3	0.48	22.40	<0.01

In Table 3, the test result shows that pears at four decay levels have different S and weight loss rate values. After doing the ANOVA analysis with SAS 8.2, the differences of S and weight loss rate among the four decay grade of pears were significant ($P < 0.01$), which is presented in Table 4.

In Table 5, for the stiffness coefficient S, it was clear that the differences between Grade 0 and other grades were significant, while among Grade 1, Grade 2, and Grade 3 were not. The result indicated that the stiffness coefficient S of inner decay of pears had significant differences with normal pears (Grade 0), however, S is not able to indicate different degree of inner decay. For weight loss rate, the difference between Grade 0 and Grade 1 was insignificant, while among other grades were all significant. Consequently, the rate of weight loss should be considered as an important parameter indicating degree of inner decay of pears.

Table 5. The ANOVA analysis

Grades of Decay	Average Value of Difference	
	S (kHz2·g2/3)	weight loss rate
0−1	3.4031*	-0.10637
0−2	4.6715*	-0.32125*
0−3	4.8378*	-0.53081*
1−2	1.2684	-0.21488*
1−3	1.4347	-0.42444*
2−3	0.1663	-0.20956*

* indicate significance at 0.05 levels.

4 Conclusions

The acoustic impulse response technique as one of the mechanical engineering methods appeared to be a valuable method to monitor the quality of Housui and Niitaka pears. The study confirmed that impulse response measurements in Housui and Niitaka pears correlated well with internal quality parameters (E, F_{max}, SSC/TA) of the fruit under shelf and cold storage conditions. The developed regression models based on stiffness factor S, were able to estimate the quality of Housui and Niitaka pears. In this method, the measurements of Housui pears were more reliable than that of Niitaka pears. The

results of the experiment also showed that S and weight loss rate were important parameters in detecting inner decay of pears. It laid a theoretical basis for applying non-destructive acoustic impulse response technique to monitor the internal defects of pears.

References

[1] De Belie, N., Schotte, S., Coucke, P., De Baerdemaeker, J.: Development of an automated monitoring device to quantify changes in firmness of apples during storage. Postharvest Biol.Technol. 18, 1–8 (2000)
[2] Galili, N., De Baerdemaeker, J.: Performance of acoustictest methods for quality evolution of agricultural products. In: ISMA Conference, Leuven, Belgium (September 1996)
[3] Dewulf, W., Jancok, P., Papadiamantopoulou, E., Nicola, B., De Roeck, G.: Monitoring of the firmness of a Conference pear using experimental modal analysis. In: Proceedings of ISMA23 Conference on Noise and Vibration Engineering, Leuven, vol. III, pp. 1489–1496 (1998)
[4] Throop, J.A., Rehkugler, G.E.: Application of computer vision for detecting watercore in apples. Transactions of ASAE 32(6), 2087–2092 (1989)
[5] Zerbini, P.E., Grassi, M.: Nondestructive detection of brown heart in pears by time-resolve reflectance spectroscopy. Postharvest Biology and Technology 25(1), 87–97 (2002)
[6] Chen, H., De Baerdemaeker, J.: Effect of apple shape on acoustic measurements of firmness. Journal of Agricultural Engineering Research 56, 253–266 (1993)
[7] Cooke, J.R., Rand, R.H.: A mathematical study of resonance in intact fruits and vegetables using a 3-media elastic sphere model. Journal of Agricultural Engineering Research 18, 141–157 (1973)

Design of Austenitic Stainless Steel Solution Treatment Device

Yue Liu[1], Wei Wang[2], LiGuo Tian[3], Meng Li[3], and BeiBei Guan[3]

[1] Tianjin Modern Vocational Technology College, Tianjin, 300222, China
[2] School of Electric and Automatic Engineering, ChangShu Institute of Technology, ChangShu, JiangSu, 310027, China
[3] Tianjin Key Laboratory of Information Sensing&Intelligent Control, Tianjin University of Technology and Education, Tianjin, 300222, China
{liuyue201202,tlg1234,limeng-3260711}@163.com

Abstract. All Heat treatment is an important basic technology in the process the mechanical manufacturing, heat treated parts can have special properties, and high quality, long service life, so the heat treatment equipment is directly related to the heat treatment technology level and the quality of workpieces. It designed a set of solution treatment device for austenitic stainless steel, used to enhance the corrosion resistance of austenitic stainless steel pipe. The device used a STM32F103VE microcontroller as the control core, using PI control algorithm to realize temperature control. After tested, the device has good stability, fast response, and accurate temperature control.

Keywords: Austenitic, Solution treatment, STM32F103VE micro-controller, μC/GUI.

1 Introduction

In the process of using the austenitic stainless steel pipe, under the action of cold stress the intergranular corrosion could occurred easily, which is a common and serious phenomenon. How to prevent stainless steel intergranular corrosion is a difficult point for the heat treatment technology. At present, a commonly used method for the cold-deformated austenite stainless steel pipe is solution treatment [1]. Carbides solubility in austenite is very low at room temperature, along with the increase of the temperature, the solubility of carbides in austenite is increased, when heated to 1050℃ above, all the carbide can be dissolved in austenite, after rapid cooling the supersaturated solid solution can be obtained, namely homogeneous single-phase austenite, this process is called as the solution treatment [2].

After solution treatment, for austenitic stainless steel pipe, anti-intergranular corrosion ability and plasticty, toughness and stress problems after cold deformation are greatly improved. The austenitic stainless steel solution treatment device designed in the paper, combined with heat treatment technology, sensor technology and

D. Jin and S. Lin (Eds.): Advances in Mechanical and Electronic Engineering, LNEE 176, pp. 437–442.
springerlink.com

microelectronics technology, completed the solution treatment of austenitic stainless steel pipe through hardware circuit of control system and modular software system.

2 Overall Design of the System

The key technology for austenitic stainless steel solution treatment lies in the selection of heating method and temperature control in the heating process, which is related to solution treatment quality. According to the requirement of heat treatment technique and the application of intelligent control technology in heat treatment technology, the device proposed in the paper uses STM32F103VE micro-controller as control core, and uses the contact-type resistance to heat, infrared temperature sensor and thermocouple to measure temperature and compressed air for cooling; it acquires the signal such as temperature, current in the process of treatment, and ensure the implementation of solution treatment technique through reasonable control algorithm, the overall structure of the system as shown in Fig.1.

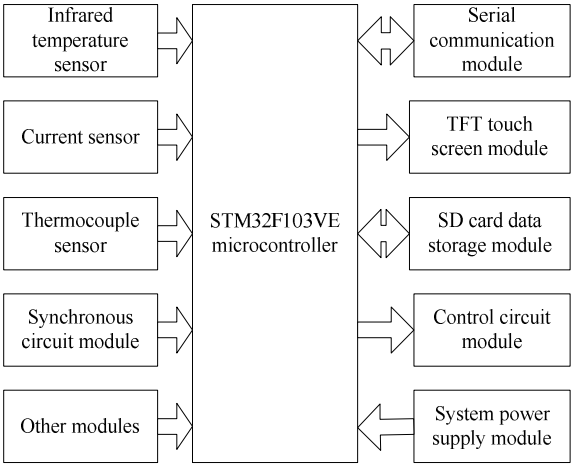

Fig. 1. The overall structure of the system

3 System Hardware Realization

The control system hardware of the austenitic stainless steel solution treatment device uses a STM32F103VE microcontroller as the main control core, collocated in periphery with infrared temperature sensor, thermocouple temperature sensor and a current sensor and some other data acquisition circuits, temperature control circuit, serial communication circuit, SD card data storage circuit and other control circuits, to achieve the solution treatment of austenitic stainless steel pipe.

3.1 Microcontroller Module

STM32F103VE used ARM Cortex-M3 as the kernel for is a high performance, low cost, low power 32-bit RISC processor, its basic frequency reach up to 72 MHz, and it uses a single power supply; the clock signal comes from 8 MHz external crystal oscillator; with 512 KB on-chip FLASH and 64 KB RAM, it fully meets the requirements of bus gateway for the data buffers and program space; rich reinforced I/O ports and peripheral connected to the two APB bus, it contains three 12–bit ADC,4 general16-bit timer and a 2 timer PWM, also contains the standard and advanced communication interface: 2 I2C, 3 SPI, 5 USART, 1 USB and 1 CAN; STM32F103VE has DMA function, which can provide the high-speed data transmission between the peripheral and internal memory, or internal memory and internal memory [3].

3.2 Sensor Acquisition Circuit

Sensor acquisition circuit is mainly used for real-time signal acquisition in the process of solution treatment for austenitic stainless steel such as temperature, current signal, its core is the 12-bit ADC integrated by STM32F103VE internally. STM32 12-bit ADC is a successive approximation type A/D converter, it has up to 18 channels, can measure 16 external signal source and 2 internal signal source; the A/D conversion of each channel can be implemented by a single, continuous, discontinuous or scanning mode; ADC results can be stored in 16-bit data register by the way of left align or right align; characteristic of analog watchdog allows the application program to detect whether the input voltage exceeds the user defined high/low threshold.

3.3 Temperature Control Circuit

The Temperature control is the hard core of the austenitic stainless steel solution treatment device, related to quality of solution treatment. The main part of temperature control circuit is power regulator, which is composed of two anti-parallel thyristors and reactor, transformers, protection circuit. After the thyristors chopping, reactor filtering, and transformer adjustment, the input voltage is converted as the heating power; trigger pulse for the thyristors comes from the system control circuit [4].

In the process of heat treatment, the STM32 control system take a sample of temperature of the workpiece in real time through the infrared temperature sensor, and then compared with the preset temperature curves, after that, according to the current temperature deviation, in accordance with a control algorithm to calculate the required heat input and converted it into corresponding heating current, which is the given current for power regulator; at the same time, the current sensor takes a sample of output current, according to deviation of the actual current and the given value, calculates the conduction angle of thyristors in power regulator for next cycle, and generates a trigger pulse to trigger the thyristors, so as to change voltage for the stainless steel pipe and adjust the quantity of heat, thus realizes the temperature control. The thyristors trigger circuit diagram as shown in Fig.2.

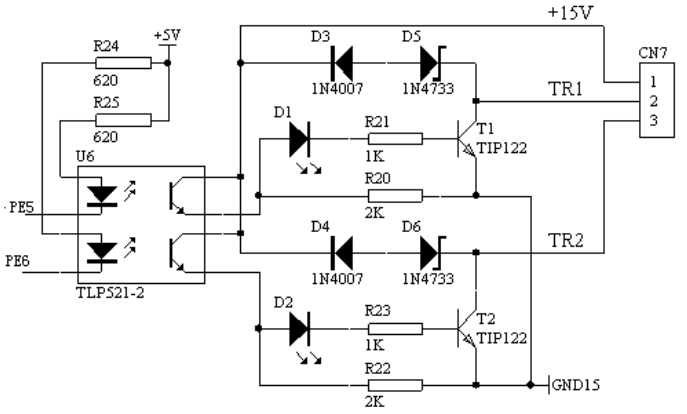

Fig. 2. The thyristor trigger pulse schematics

4 System Software Realization

The software system of austenitic stainless steel solution treatment device adopts modularized design idea, according to the practical use, it mainly divided into the following function module: sampling conversion task, temperature control task, human-computer interaction task, serial communication task and so on, considering each task's characteristic, such as multiple or untime, software system transplants μC/OS-II embedded operating system, using μC/OS-II operating system to realize the multi task processing [5]. μC/OS-II is specially designed for the embedded system, and is Hard Real Time and multitasking kernel, its kernel is simplified, multiple task management function is relatively perfect, and has good real-time performance; Furthermore, it can be cut, solidified, and source code is open, also has strong portability.

4.1 Design of Master Control program

The μC/OS-II operating system allows to run 64 tasks simultaneously, and each task should have its independent stack space and the only task priority. There are 8 tasks were used by the system kernel, 4 tasks were used by operating system, the remainder is used by user. The software system of the austenitic stainless steel solution treatment device consists of sampling conversion task, temperature control task, human-computer interaction task and serial communication tasks etc. the entire application is controlled by μC / OS-II operating system, the main control program flow diagram as shown in Fig.3.

4.2 Design of Human-Computer Interaction Interface

In the software system, human-computer interaction interface module is the bridge of connection between human and machine, which could reflect the solution treatment

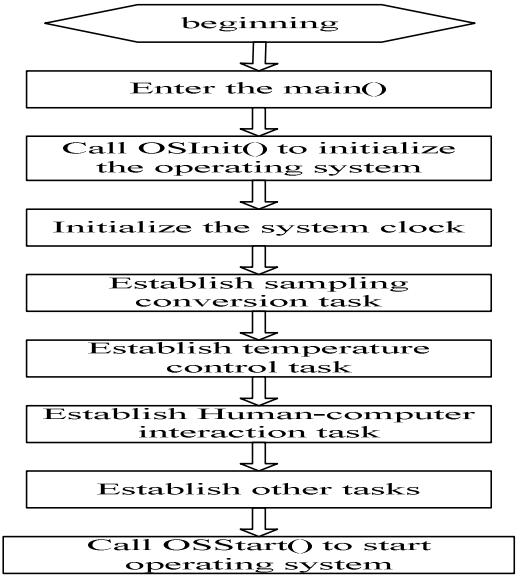

Fig. 3. The flow diagram of the main control program

process intuitively, including parameter display, parameter setting and communication with upper computer. This paper adopts the embedded graphics system μC/GUI to compile the human-computer interaction interface. μC/GUI is a dedicated to embedded graphic support software, it can work in a single task or multitasking system environment, μC/GUI is suitable for the majority of black/white and color LCD applications, providing extensible 2D graphics library, window manager, extensible fontlib and other controls, and can support a keyboard, a touch screen and a mouse input[6]. Human-computer interaction interface diagram as shown in Fig.4.

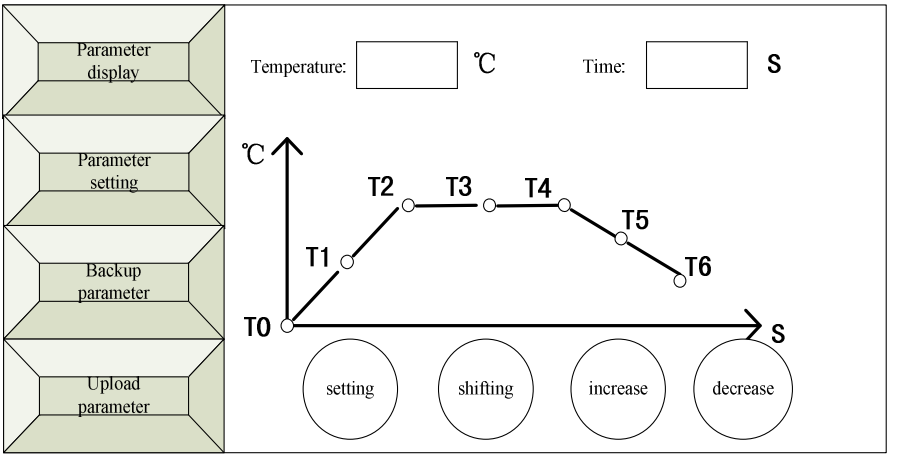

Fig. 4. The sketch map of Human-computer interface

5 Conclusion

In recent years, along with rapid development of the intelligent control research in the control domain, leading the intelligent control technology into the heat treatment process control accords with the development trend of modern industry. In view of the existing problem in reliability, solid solution treatment effect and the production process automation level of the present production equipment during the course of austenitic stainless steel solution treatment, the paper designed the austenitic stainless steel solution treatment device used a STM32F103VE microcontroller as the core. After tested, the device can meet the design requirements in stability, response characteristic and control accuracy.

References

1. Lin, J., Yang, G.: Density Experimental Study on Austenitic Stainless Steel Solution Treatment. Theory Pressure Vessel 4, 14–17 (1999)
2. Ma, Y.Z., Wang, W., Liang, W.D.: The Contact-type resistance Heating Stainless Steel Solution Treatment Device. New Technology and New Process 11, 26–28 (2000)
3. Wang, Y.H., Xu, W., Hao, L.P.: STM32 Series ARM Cortex-M3 Microcontroller Principles and Practice. Beijing University of Aeronautics and Astronautics Press, Beijing (2008)
4. Gao, G., Guo, X.L.: Improvement of the Thyristor Dipulse Trigger. Industrial Heating 2, 44–46 (2000)
5. Shao, B.B.: Embedded Real-time Operating System μC/OS-II. Beijing University of Aeronautics and Astronautics press, Beijing (2003)
6. Ge, X.: Using μC/GUI to Develop Graphical User Interface. Computer Engineering and Design 26, 1–3 (2005)

Research on a Novel Thermoelectric Generator Module Made of Bismuth Telluride

Zheng Zhang and Yushan Chen

School of Mechanical and Automotive Engineering,
South China University of Technology,
Guangzhou, Guangdong, 510640, China

Abstract. In this paper, a structure of the high power density thermoelectric generator is presented. The main part of the generator is located inside the pipe, expanding the heat exchange area. The centralized cooling is used in the cooling channel, in where the low temperature part of conversion element and fins are installed. In the conversion element, a lot of thermocouple arrays are installed connected with the parallel thin thermocouples, metal wires and transitional conductors to a loop that can transmit heat and current. By means of computer simulations of the convective heat transfer and steady-state circuit, the numerical calculations show that the conversion elements have good temperature distribution and lower resistance value, and the load characteristic of the thermoelectric generator is improved.

Keywords: Thermoelectric Generator, module, structure, CFD, heat transfer enhancement, steady-state circuit.

1 Introduction

The efficiency and output power of the thermoelectric generator are related to the temperature difference between cold side and hot side and thermoelectric figure of merit. Improving figure of merit has been a central topic of research in the field of thermoelectric materials. Actually the figure of merit (ZT) of thermoelectric materials widely used is not more than one. In practical system design, series and parallel with a large number of thermocouples are the chief connection method in thermoelectric circuit. Therefore, this paper mainly studies a new structure of efficient heat exchanger and low-resistance conversion components of the thermoelectric generator.

2 Model Establishment

The structure of heat exchanger is the key to gaining heat energy maximally, setting up large-scale thermoelectric conversion element and establishing efficient thermoelectric circuit. Based on the theory of heat transfer enhancement, the heat exchanger can increase the heat transfer rate in three aspects: using the form of built-in convective heat transfer to replace the form of heat conduction to increase the heat

D. Jin and S. Lin (Eds.): Advances in Mechanical and Electronic Engineering, LNEE 176, pp. 443–448.
springerlink.com

transfer coefficient; expanding the heat exchange area in the same volume to increase the number of conversion components; centralized cooling to enhance the cooling effect.

Figure 1 (a) shows the structure of a high power density thermoelectric generator designed for exhaust system of a light bus. And the thermoelectric convection device with cross-shaped section is shown in Figure 1 (b). Where 1 represents the passage of heat flow and heat source of thermoelectric circuit; 2 represents the thermoelectric conversion device with cross-shaped section, which locates its high temperature segment in the hot channel, and makes its external surface as heat interchanging area; cooling channel 3 is the cold source of the thermocouple conversion circuit, with low temperature segment of the generator inside; 5 represents an adiabatic layer used for eliminating the thermal interference between the hot channel and cooling channel; 6 is an arched conversion component which adhere to the tube wall. T_h, P_h and C_h stand for the temperature, pressure and flow rate of high temperature exhaust respectively; Tc, Pc and Cc stand for the temperature, pressure and flow rate of low temperature exhaust respectively, $T_h > T_c$; the form of heat exchange between exhaust and node of thermocouple is heat convection transfer.

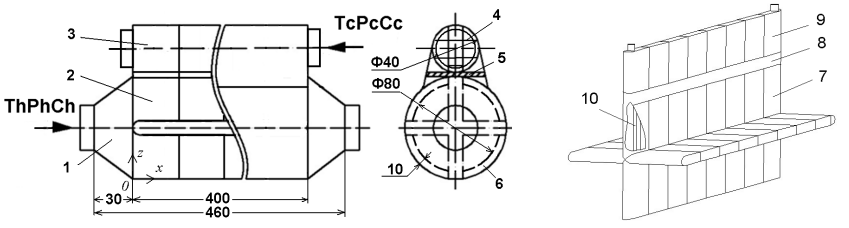

(a) (b)

Fig. 1. (a) Model of thermoelectric system (b) centralized cooling conversion conversion element of cross shape

In the two channels of the heat exchanger, incompressible and turbulent fluids exchange thermal by the way of convective heat transfer. General form of the governing equation in three-dimensional Cartesian coordinate shows below:

$$\frac{\partial(\rho u\phi)}{\partial x}+\frac{\partial(\rho v\phi)}{\partial y}+\frac{\partial(\rho w\phi)}{\partial z}=\frac{\partial}{\partial x}\left(\Gamma\frac{\partial\phi}{\partial x}\right)+\frac{\partial}{\partial y}\left(\Gamma\frac{\partial\phi}{\partial y}\right)+\frac{\partial}{\partial z}\left(\Gamma\frac{\partial\phi}{\partial z}\right)+S \quad . \tag{1}$$

Where: Φ is flow physical quantity; u, v and w are velocities of components; ρ represents the fluid density; Γ represents diffusion coefficient; S is source item.

The three-dimensional steady-state heat conduction equation of conversion element is:

$$\frac{\partial^2 T}{\partial x^2}+\frac{\partial^2 T}{\partial y^2}+\frac{\partial^2 T}{\partial z^2}+\frac{\Phi}{k}=0 \quad . \tag{2}$$

Where: T represents temperature; k represents the thermal conductivity; Φ is internal heat source here, where it refers to the Joule Heat of conversion element ($\Phi=I^2R$).

The built-in thermoelectric conversion module is shown in Figure 2. The parallel thermocouple group is shown in figure 2 (a), where 1 is bonded with the N-type and P-type semiconductor material directly; for the transition conductor, 3 is also made by N-type and P-type semiconductor material; 4 is connected with the output. In the direction as shown in the arrow B, Figure 2 (b) presents two parallel thermocouple groups connected through a metal deflector 6. A pair of N-type and P-type transition conductors form the cold side joint, incorporated in a complete thermoelectric circuit.

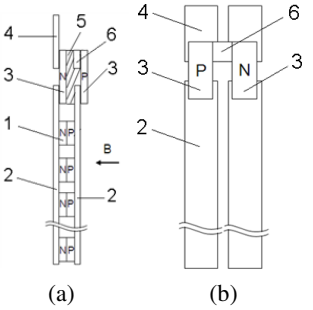

Fig. 2. Structure of thermocouples arrays

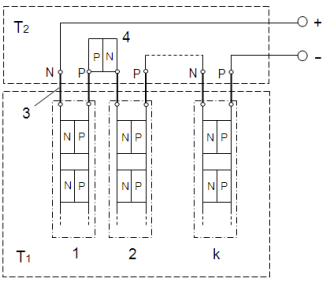

Fig. 3. Mixed circuit of centralized cooling conversion element

A thermoelectric circuit can be seen as an active two-terminal network, equivalent to a power model composed of a resistor in series with an electromotive force.

As shown in Figure 3, parallel circuit with n couples has been in series m times, the total number of the power element is n×m. Though the Seebeck coefficient, electrical resistively and thermal resistance are temperature-dependent, when DC operating point analysis is applied, the circuit can be seen as a linear circuit. According to the basic circuit theory, the matrix equation based on the node is given by:

$$AY_bA^TU_n=A(I_g-Y_bU_g)\ . \tag{3}$$

Where: A represents an incidence matrix; Y_b is admittance matrix of branch b; U_b is branch voltage vector; U_g is current source vector; I_g is parallel current vector.

3 Calculation and Analysis

We mainly research on a four-cylinder turbocharged diesel, and focus on three conditions: rated power, maximum torque and idle speed. The initial value of the engine exhaust is shown in Table 1.

Table 1. Data of the engine

Engine condition	Exhaust temperature (K)	Exhaust velocity (m/s)	Exhaust pressure (bar)
Rated Power	731.6	97.9	1.0577
maximum torque	698.6	65.5	1.0158
idle speed	625	19.9	0.9839

To make the result more accurate, an overall model of the thermoelectric generator is established based on Figure 1. There is no heat exchange between the hot channel and cooling channel, but convective heat transfer between the solid and fluid. So the temperature difference between the cold side and the hold side is established. STAR-CD is used for fluid-solid-heat coupling calculation. The temperature distribution of the solid wall can be obtained when the calculation of convective heat transfer is complete.

In the Figure 4 (a), curves 1, 2 and 3 represent the variation of average temperature along with the axial direction in the hot part when the engine is working on the conditions of rated power, maximum torque and idle running respectively. It can be seen that the curves are high at the entrance then gradually decreased. This is because of the heat conduction of thermoelectric element and part of thermal energy turning into power. As the thermal conductivity of the metal in the surface, temperature does not change significantly. There seems to be the same tendency in the cold passage in Figure 4 (b).

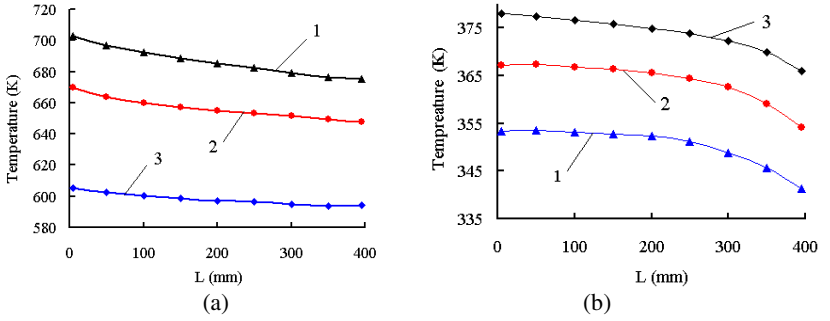

Fig. 4. Variation of temperature along with the axial direction

To be compared with HZ-14, a thermocouple is designed to be the same section area (5×5mm) and made of the same thermoelectric material. The trend of a thin thermocouple changing with the arm length is shown in Figure 5. It is shown that the resistance value decreases linearly with the arm length decreases. When the arm length is reduced to 0.5mm, the resistance can be decreased by 83.2%. So it is efficient to reduce the resistance of conversion element by using thin arm thermocouple.

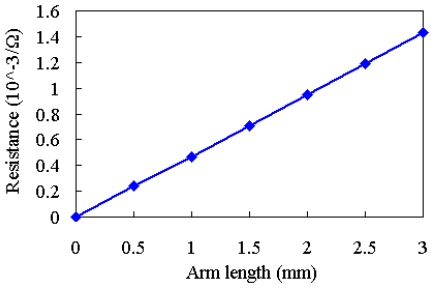

Fig. 5. Variation of resistance along with arm length

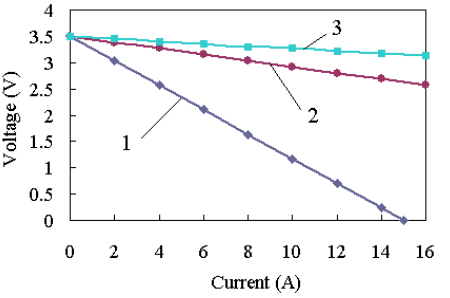

Fig. 6. Volt-ampere characteristic

When the thermoelectric generator works with loading, output power is determined by the load. When the load changes, the smaller the internal resistance of the power supply, the change of terminal voltage is smaller, so the ability to drive the load is greater. Therefore, we can take the analysis methods of EDA technology to research the external performance which can be used to evaluate the design of the generator. It is easy to gain the volt-ampere characteristic of the conversion circuit.

Figure 6 shows the comparison of the volt-ampere characteristic. Where Series 1 represents the experimental results of HZ-14 conversion element, the line with a slope of -0.232 suggests that internal resistance of the conversion element is relatively large, consuming too much power. In order to make the comparison, series 2 and 5 are calculated with the same geometry size and voltage. In the series 2, the module series 2 is a thermocouple array with four couples in parallel and series 49 groups. In the volt-ampere characteristic of series 2, the slope of the linear part is -0.058. Series 5 is a thermocouples array of six couples in parallel and series 49 groups. In the volt-ampere characteristic of series 5, the slope of the linear part is -0.038. Obviously, the more the thermocouples have been connected in parallel, the smaller the slope is, and the stronger the capacities of driving load will be.

4 Conclusion

The utilization of exhaust heat can be improved by taking measures in the structure of the heat channel and cooling channel separated, hot and cold fluid reverse flowing and using forced convection heat transfer. Setting up the conversion element internally rather than externally has increased the heat exchange area effectively. Taking the form of centralized cooling in the cold channel can enhance the cooling effect and have a good temperature distribution. The results of simulations show that the special series and parallel circuit has decreased the internal resistance of component by 83.2%. The load characteristic of temperature difference power has been improved efficiently and the volt-ampere characteristic is more ideal.

References

1. John, W. F.: Vehicular Thermoelectrics: A New Green Technology. In: Proceedings of DEER 2011 (2011)
2. Vedernikov, M. V., Iordonishvili, E. K.: Loffe origin of modern semiconductor thermoelectric energy conversion. In: Proceedings of ICT, pp. 24–28 (1998)
3. Chen, J., Lin, B.W., Lin, G.: Optimal design of a multi-couple thermoelectric generator. J. Semiconductor Science and Technology 2(15), 184–188 (2000)
4. Bass, J.C., Elsner, N.B.: Design Study and Experience with Thermoelectric Generators for Diesel Engines. In: Proceedings of Society of Automotive Engineers, pp. 451–455 (1991)
5. Velimir, J., Saeid, G.: Design, Fabrication and Testing of Energy-Harvesting Thermoelectric Generator. Hi-Z Technology, Inc.
6. Chen, M.: System Modeling and Validation of a Thermoelectric Fluidic Power Source: Proton Exchange Membrane Fuel Cell and Thermoelectric Generator (PEMFC-TEG). Journal of Electronic Materials 39(9), 1593–1160

The Application of Rough Programming Based on Inclusion Degree in Mechanical Engineering

Fachao Li and Ying Jing

Hebei University of Science and Technology, 050018, Shijiazhuang, Hebei, China
lifachao@tsinghua.org.cn, 932023729@qq.com

Abstract. In this paper, for the decision problem under rough environment, we first analyze the essential characteristic of rough programming based on inclusion degree in mechanical engineering systematically, then we give the general expression of rough programming for mechanical engineering. And we construct the rough programming model based on synthesis effect by using direct effect and indirect effect (denoted by BSE-RPM for short). Finally, we analyze the effectiveness and characteristics of BSE-RPM by a example. The results indicate that this model can integrate the decision making consciousness into decision making process effectively. And this method can be effectively used in mechanical engineering.

Keywords: Rough set, Decision making, Rough Programming, Inclusion degree, Effect synthesis function, mechanical engineering.

1 Introduction

Rough set theory [1] has been extensive concerned by academic circles and application fields. Many scholars study on rough set theory and get many beneficial achievements. For instance, [2] expanded traditional rough set theory and presented variable precision rough set model. [3] studied the knowledge reduction method through adjusting variable precision. [4] presented a novel approach for mining association rules based on rough set theory. [5] used the rough sets based on tolerance relation to discuss attribute reduction in incomplete decision systems. [6] proposed an attribute reduction method in the Bayesian Version of variable precision rough set model. [7] proposed a way to attribute reduction of consistent and inconsistent covering decision systems with covering rough sets. And [8] analyzed the characteristics of knowledge reduction systematically based on rough set theory and proposed decision table reduction based on conditional information entropy.

All the results above mainly focus on the reduction of information system, and the research on rough programming theory and method are less mentioned. [9] defined rough programming problem, proposed the concepts of local rough optimal solution and global rough optimal solution of rough programming problem based on distance function and approximation, and studied on the roughness of optimal solution for rough programming problem. But the above discussions merely considered the roughness of solution, didn't think about the equivalence classes' function and characteristics of their effect on decision. [10] classified rough programming problems into three classes according to the place of the roughness of feasible set and objective function and then

D. Jin and S. Lin (Eds.): Advances in Mechanical and Electronic Engineering, LNEE 176, pp. 449–454.
springerlink.com

discussed the feasible set, optimal solution and optimal value of one kind of rough programming problems. But it didn't think about the effect of equivalence classes on decision. These researches reflect the current situation of rough programming. Compared with the successful application of rough set theory in data mining, the research on rough programming is relatively backward. The reason is that structural characteristics of rough programming problem can't be described systematically.

The main contributions of this paper are listed as follows. Firstly we analyze the essential characteristics of rough programming problem and propose general descriptive format of it. Secondly, we put forward the concept of direct effect and indirect effect, and then establish the rough programming model based on synthesis effect (denoted by BSE-RPM for short). Thirdly, we analyze the constructing idea and procedures of BSE-RPM by using inclusion degree as measurement pattern of indirect effect. Finally, we analyze the effectiveness of BSE-RPM through a medical case. This method can be effectively used in mechanical engineering.

2 Preliminaries

In 1984, based on an equivalence relation on U, Pawlak [1] put forward the concept of rough set and constructed the basic frame of rough set theory. It is an effective method for dealing with uncertain information in decision making process.

Definition 2.1. (see [1]) Let U be a finite set and R be an equivalence relation on U, $[x]_R = \{y \mid (x, y) \in R\}$ be the R-equivalence classes of x, $U/R = \{[x]_R \mid x \in U\}$,

$$\underline{R}(X) = \{x \mid x \in U, \text{ and } [x]_R \subset X\}, \tag{1}$$

$$\overline{R}(X) = \{x \mid x \in U, \text{ and } [x]_R \cap X \neq \phi\}. \tag{2}$$

If X is the union of some elements of U/R, X is called R-definable (or R-exact set). Otherwise X is called a R-indefinable (or R-rough set). And $\underline{R}(X)$ is called R-lower approximation set of X, $\overline{R}(X)$ is called R-upper approximation set of X. For convenience,

$$C_R(x) = \frac{|[x]_R \cap X|}{|[x]_R|} \tag{3}$$

is called R-believable degree of x accords with X. Here we use $|A|$ to express the number of elements of A. It is easy to see that $C_R(x)$ reflects the degree of X includes equivalence class $[x]_R$, and describes the roughness of x with respect to X in approximation space (U, R) from partial views.

3 Analysis on Essential Characteristic of Rough Programming Based on Inclusion Degree in Mechanical Engineering

The core of programming problem is selecting decision scheme to optimize the criteria in certain region. And its general form as follows:

$$\begin{cases} \max f(x), \\ \text{s. t. } x \in X. \end{cases} \tag{4}$$

In (4), X is the subset of U (called feasible region), and $f(x)$ is a function with quantitative characteristics on U (called objective function). In the decision process of practical problems, we not only consider (4), but also care the relation between elements of U. For instance:

Case: To strengthen the market competitiveness, the production enterprise wants to choose a staff responsible for technical innovation. Development of this item involves substantive cooperation. So when choosing the staff, we must take specialty advantages, working ability, coordinate ability, physical condition and team composition into consideration, and we also must guarantee project success and protect core technology. If we regard X as the set of candidates, U as the set of people who have close cooperative research relationship R with the staffs in this company, $f(x)$ as comprehensive measurement of specialty advantages, working ability, coordinate ability, physical condition of candidates, $[x]_R$ as the set of people who have relationship R with x (means potential available resources of x), this question is a decision making problem with form (4) related to R. In view of R-upper (lower) approximation is foundation of rough set theory, this programming is called rough programming and denoted as:

$$\begin{cases} \max f(x), \\ \text{s. t. } x \in_R X. \end{cases} \tag{5}$$

Here, U is a universe and $X \subset U$, $f(x)$ is a function with quantitative characteristics on U, is a quantitative index reflecting that scheme x is good or not (called direct effect of scheme x) R is some relationship on U. For convenience, suppose that X is a crisp subset of U, $f(x)$ is a nonnegative real-valued function on U and R is equivalence relation on U.

The set $[x]_R$ that has relationship R with x always has indirect effect on the performance of x (called indirect effect of scheme x). So when we make a decision, we should combine direct effect and indirect effect at the same time. If indirect effect is interpreted as a mapping G from U/R to [0, 1] (called indirect effect function), the synthesis problem of direct effect and indirect effect can be abstracted as a mapping $S(u, v)$ from $[0, \infty) \times [0, 1]$ to $[0, \infty)$ (called effect synthesis function and satisfies the following properties: 1) For any u or v, $S(u, v)$ is non-decreasing. 2) $S(u, 1)$ is strictly monotonously increasing. Where u denotes $f(x)$ and v denotes $G([x]_R)$), then model (5) can be transformed into model (6):

$$\begin{cases} \max S(f(x), G([x]_R)), \\ \text{s. t. } x \in X. \end{cases} \tag{6}$$

Considering the measure model of indirect effect D and effect synthesis operator $S(u, v)$ are the core of model (6), we call (6) rough programming model based on synthesis effect (denoted by BSE-RPM for short) in the following.

4 Effect Metric Model Based on Inclusion Degree

It is an effective method with good vivacity and strong operation to use $D(A \subset B) = |A \cap B|/|A|$ to measure the degree of B includes A, so $D([x]_R \subset X)$ shows the degree of $[x]_R$ accords with X (like the believable degree $C_R(x)$ of R in part 2). It shows the potential value of x. And for the case in part 3, $C_R(x)$can be considered as the degree of team members belong to the company. $C_R(x)$ is the bigger, the better for protecting core technology. If we use $C_R(x)$to measure indirect effect of $[x]_R$, model (6) can be transformed into (7):

$$\begin{cases} \max S(f(x), C_R(x)), \\ \text{s.t. } x \in X. \end{cases} \tag{7}$$

The analysis above shows that rough programming can be transformed into specific programming problem by choosing metric pattern of indirect effect $G([x]_R)$ and synthesis effect operator $S(u, v)$.

5 Example Analysis

Case Description: The drug D was developed to treat liver's cancer. It could kill cancer cells and inhibit the growth and reproduction of them. But it could kill normal human cells at the same time. The clinical tests showed that:

1) Using the drug for one course implies to kill 30% of cancer cells. 2) Using the drug for two courses implies to kill 50% of cancer cells and 0.1% of normal cells. 3) Using the drug for three courses implies to kill 70% of cancer cells and 0.3% of normal cells. 4) Using the drug for four courses implies to kill 90% of cancer cells and 0.5% of normal cells. 5) Using the drug for five courses implies to kill 100% of cancer cells and 0.8% of normal cells. Try to select therapeutic scheme.

The main purpose of this therapeutic scheme is to kill cancer cells. So if $f(x)$ means the satisfaction degree of killing cancer cells x and we only consider killing cancer cells, making the therapeutic scheme can be generalized into a programming problem as (4), Here, U means the total cells include the cancer cells and the normal human cells. X means the total liver cancer cells. And $f(x)$ are shown in Table 1 (in Table 1, X_i is the liver cancer cells killed in the ith courses):

Table 1. The value of $f(x)$

x	$x \in X_1$	$x \in X_2$	$x \in X_3$	$x \in X_4$	$x \in X_5$
$f(x)$	0.3	0.5	0.7	0.9	1.0

Define an equivalence relation R on U as:

$$R = \left\{ (x, y) \middle| \begin{array}{l} x \text{ and } y \text{ satisfy one of the conditions: 1) the cells killed in the} \\ \text{same course; 2) the cells were not killed after treatment.} \end{array} \right\} \tag{8}$$

The defined equivalence relation R makes a partition to U as $E_i=\{x| x$ is killed in the ith course$\}$, i=1, 2, 3, 4, 5, $E_6=\{x \mid x$ is not killed after treatment$\}$. Then the essence of making therapeutic scheme is to solve the rough programming problem as (5). During the treatment, the less the quantity of normal human cells killed is, the better the effect is, so we measure indirect effect of equivalence class E_i by the approaching degree of total normal cells be killed from the first to the ith course Y_i and the damage limit (when damage is larger than 1% may lead to heart failure), that is, $G(E_i)=1-Y_i$. And the indirect effect values of each equivalence class were shown in Table 2.

Table 2. The indirect effect values of every equivalence class

$[x]_R$	E_1	E_2	E_3	E_4	E_5
The accumulative number of normal cells (%)	0	0.1	0.3	0.5	0.8
$G([x]_R)$	1.0	0.9	0.7	0.5	0.2

If taking $S(u, v)=u(1+kv^{\alpha})$ as the synthesizing operator of direct effect and indirect effect, then we can get the following general programming problem (9).

$$\begin{cases} \max f(x)(1+k(G([x]_R))^{\alpha}), \\ \text{s. t. } x\in X. \end{cases} \tag{9}$$

Then we can make the therapeutic scheme according to the specific situation of the patients. The decision results of different parameters are shown in Table 3:

Table 3. The decision results of different parameters

x			$x\in X_1$	$x\in X_2$	$x\in X_3$	$x\in X_4$	$x\in X_5$
$f(x)$			0.3	0.5	0.7	0.9	1.0
$G([x]_R)$			1	0.9	0.7	0.5	0.2
$S(f(x), G([x]_R)$	k=0.5	α=0.5	0.4500	0.7372	0.9928	1.2182	1.2236
		α=1.0	0.4500	0.7250	0.9450	1.1250	1.1000
		α=1.5	0.4500	0.7135	0.9050	1.0591	1.0447
	k=1.0	α=0.5	0.6000	0.9743	1.2857	1.5363	1.4472
		α=1.0	0.6000	0.9500	1.1900	1.3500	1.200
		α=1.5	0.600	0.9269	1.1099	1.2182	1.0894
	k=1.5	α=0.5	0.7500	1.2115	1.5785	1.8546	1.6708
		α=1.0	0.7500	1.1750	1.4350	1.5750	1.3000
		α=1.5	0.7500	1.1403	1.3149	1.3773	1.1342
	k=2.0	α=0.5	0.9000	1.4487	1.8713	2.1727	1.8944
		α=1.0	0.9000	1.4000	1.6800	1.8000	1.4000
		α=1.5	0.9000	1.3538	1.5199	1.5364	1.1789

From Table 3, it is easy to see that the optimization results are closely related to the selection of synthesizing operator. If k and α are regarded as the parameters reflecting the decision making consciousness, the above discussions show that BSE-RPM can integrate decision making consciousness into decision making process effectively.

6 Conclusion

In this paper, we analyze the essential characteristic of rough programming based on real project backgrounds, and put forward the rough programming model based on utility synthesis (BSE-RPM). Then we analyze the performance of BSE-RPM by an example. The results indicate that our model has good interpretability, and can integrate the decision making consciousness into decision process effectively. This method can be effectively used in mechanical engineering.

Acknowledgments. This work is supported by the National Natural Science Foundation of China (71071049) and the Natural Science Foundation of Hebei Province (F2011208056).

References

1. Pawlak, Z.: Rough sets. International Journal of Computer and Information Sciences 11(5), 341–356 (1982)
2. Ziarko, W.: Variable precision rough set model. Journal of Computer and System Sciences 46(1), 39–59 (1993)
3. Mi, J.-S., Wu, W.-Z., Zhang, W.-X.: Approaches to knowledge reduction based on variable precision rough set model. Information Sciences 159(3), 255–272 (2004)
4. He, C.-B., Chen, Q.-M.: Approach for mining association rules based on rough set. Journal of Computer Applications 30(1), 25–28 (2010)
5. Meng, Z., Shi, Z.: A fast approach to attribute reduction in incomplete decision systems with tolerance relation-based rough sets. Information Sciences 179(16), 2774–2793 (2009)
6. Ślezak, D., Ziarko, W.: Attribute reduction in the Bayesian Version of variable precision rough set model. Electronic Notes in Theoretical Computer Science 82(4), 263–273 (2003)
7. Chen, D., Wang, C., Hu, Q.: A new approach to attribute reduction of consistent and inconsistent covering decision systems with covering rough sets. Information Sciences 177(17), 3500–3518 (2007)
8. Wang, G.-Y., Yu, H., Yang, D.-C.: Decision table reduction based on conditional information entropy. Chinese Journal of Computers 25(7), 759–766 (2002)
9. Ebrahim, A.: Youness: Characterizing solutions of rough programming problems. European Journal of Operational Research 168(3), 1019–1029 (2006)
10. Osman, M.S., Lashein, E.F., Youness, E.A., Atteya, T.E.M.: Mathematical programming in rough environment. Optimization 60(5), 603–611 (2011)

Fitting Methodologies of Freeform Curve and Surface Model for Mechanical Parts in Commercial Software

Lufang Zhao, Hanwei Liang, Siyuan Cheng, and Xiangwei Zhang

Guangdong University of Technology, 510006 Guangzhou, China
lfzhao@gdut.edu.cn

Abstract. Reverse engineering, as one of the advanced methods of design, has being widely used in product development and innovation redesign. And in mechanical engineering, freeform product design has been the main focus of reverse engineering. In this paper, the mature commercial software CATIA was used as the platform, the various fitting methods of freeform curves and surface model were studied. By this way, a CAD model fit to the original design intent can be obtained, at the same time, the quality of the surface can be guaranteed. By used actual mechanical parts as examples, those fitting methods were proved to be effective way to reverse modeling of freeform surface products.

Keywords: Reverse engineering, Freeform curves, Freeform surface, Fitting.

1 Introduction

Reverse engineering(RE), as one of the advanced methods of design, has being widely used in product development [1]. RE is an important tool with which to generate CAD models [2]. Freeform product design has been the main focus of conventional RE in mechanical engineering. Since their "natural" parameters are hard to be defined and extracted, in redesign with deformation we propose dealing with freeform product models by extracting global and local product definition parameters that are defined by international, domestic or industrial de-facto standards; or by user-defined key parameters. Designers can produce new design variations by editing the product definition parameters [3]. Reverse engineering(RE) starts in the physical environment with the goal of conversion from the physical models to digital models that can be further used by CAD/ CAE/CAM applications, and its application ranged from the simply copy to reverse modelling supporting rapidly innovative design, which is playing an important role in product design [4].

The terminal aim of reverse engineering was to innovation redesign of mechanical parts, a precondition for redesign is extracting sectional feature with parametric sketch and reverse reconstructing exact CAD model. But for freeform products, the major parts are freedom curves and surface. Some products are even natural model or handwork's model which combined art and function from aesthetics engineer, it have no any regulation in surface, it is difficult and impossible to identify the feature, so it is unnecessary to match with scanned surface or multi-sectional surface, the one and only way is curve and surface fitting by the point to a line and surface to pure free-form curve and surface, it can got parametric models which can be easily modified,

D. Jin and S. Lin (Eds.): Advances in Mechanical and Electronic Engineering, LNEE 176, pp. 455–460.
springerlink.com

therefore, the mature commercial software of CATIA as the platform, studying the fitting method of freeform curves and surface model is very practical and important.

2 Freeform Curve and Surface Fitting

2.1 Concept to Fitting

Given a set of ordered data $P_i(i = 0,1\cdots,n)$, these data can be obtained from physical measurements or be given by the designer, construct a curve through these data, it called interpolation of these data, the construction curve is called interpolation curve, the mathematical method called curve interpolation.

Creating curve by interpolation method, the advantage is resulting curve must go through all measured data, so the error between curve and data is zero, the disadvantage is the curve control points will be relatively increased with data increasing, also, if noise be present in these data, data should be pretreated to remove noise and ensure smoothness before curve fitting by interpolation. In some cases, if the measured data are rough or error are large, construct a curve strictly through these given data, maybe the established curve is not smooth, although the data can be pretreated, it will lose geometry characteristic of curve too. Then we can construct a curve which in some sense is most similar to these given data, this method is called be approximate to given data, the constructed curve called the approximation curve, the mathematical method is called curve approximation. Using curve approximation, first step is defining a permissible error value, and set the number of control points of curve, based on all measured data, calculate one curve by least-squares method, and measure the distance between data and the curve, if the maximum distance greater than permissible error, you need to increase the number of control points and re-do curve fitting by least-squares method until the error can meet requirement.

2.2 Fitting Method

Free curve fitting in CATIA is to obtain NURBS curves by approximation [5], which according to the point cloud or mesh surface to gain free curve, there are two main methods: one is getting some scanned line firstly, fit by the scanned line, and generate a free curve, according to the order, segment of curve and other parameters, it can meet our requirements. Second is selecting control point directly in point cloud or mesh surface to generate free curve by 3D curve command of CATIA software, next will discuss the application in CATIA for two methods respectively.

1 Curve Fitting. For curve fitting, first is scanning line and position determination, fitting, it is be done in second step. Based on curvature analysis result of mesh surface, surface can be composed by different surface plates, and curvature analysis can calculate boundary or surface trend of different surface plates, at the same time it provides helpful information to our feature division. Curvature analysis diagram, as shown in Figure 3, it is helpful to easily obtain scanned line in the boundary of curvature, directly getting the scanned line by boundary of grid surface or projection

of plane is feasible too. In addition, in order to obtain the section feature, the cutting plane and the grid surface intersection can be obtain scanned lines, as a preparative for the section feature extraction [6-7].

After got the scanned line, we can fit these curve with free curve fitting tools provided by CATIA, Shown in Figure 1, after set up the tolerance between the curve and the mesh surface, permissible maximum order and the maximum number of segments, we can fit and set the view to be merged into the actual error curve, the curvature map, the order and the number of segments, etc. so than we can control quality of fitting curve and can see whether it can meet our requirements.

2 Curve Extraction. Curve extraction is that directly selecting the control point or node on the grid or point cloud to curve feature [8], by the use of "3D curve" tool provided by CATIA, Shown in Figure 1, generate the freedom black curve according to the selected four points.

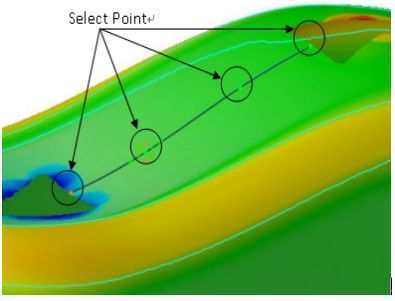

Fig. 1. Extracting curves

These curve and mesh surface have larger error and only the selected points in the grid surface completely, but the curve extracted in this way can freely extract curve feature based on user's division mode of surface, the error also can be eliminated by using the surface, then projecting onto the grid surface and fitting, so this method of curve extraction also has a great advantage.

3 Surface Fitting. CATIA provide a more complete method of surface fitting for different user's requirement, as elementary quadric fitting, pure free-form surface fitting, surface mesh fitting and so on.

(1) Elementary quadric surface. Elementary quadric include flat, cylindrical, conical surface, spherical, etc. For such surfaces, CATIA provide a "basic surface recognition" tool, as shown in Figure 2, so it can fit after set the fitting error and specify the type of surface, it is an important content of feature extraction method, because it not only accurately extracted the feature of original product, but also can be easily re-edit.

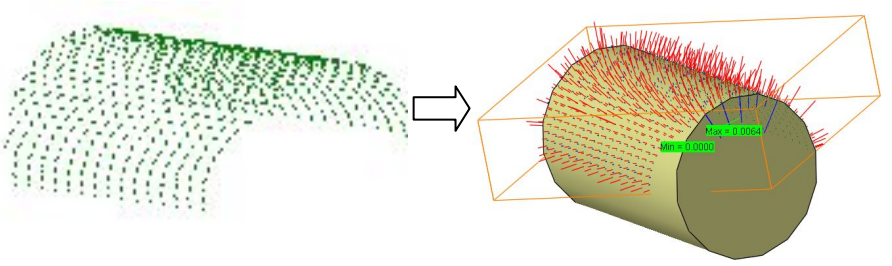

Fig. 2. Extraction of elementary quadric surfaces

If re-edit them, we only need to modify the related parameters, it can greatly facilitate the re-design task to basic surface, Can be easily re-define the axis, the cylindrical surface can meet constraint relations among associated surface.

(2) Pure free-form surfaces. For more complex single free-form surface, "POWERFIT" tool provided by CATIA can be played an important role in fitting into a NURBS pure free-form surface according to the parameters such as error and order. It didn't be restricted by shape and boundary constraints, Shown in Figure 3, field A is free-form surfaces, fitting method can be used to extract.

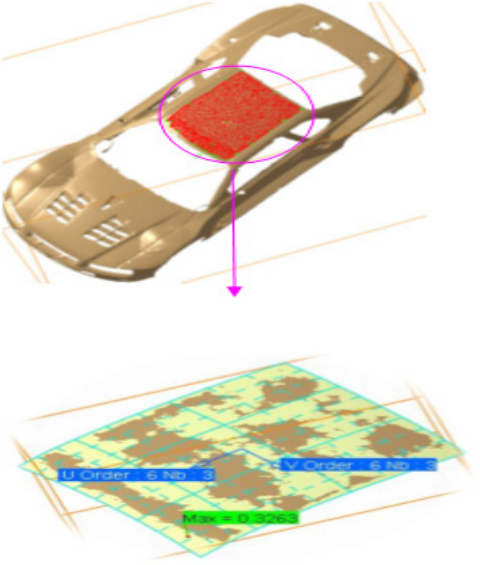

Fig. 3. Fitting of freeform surface

The maximum fitting error and the order of the surface can be found from Figure 3, as a rule, the free-form surfaces have some quality requirement in surface. Figure 4 show the result data of fitting. Zebra grain analysis data in Figure 5 shown the zebra stripes are smoothing transition, it can be seen it has a high surface quality.

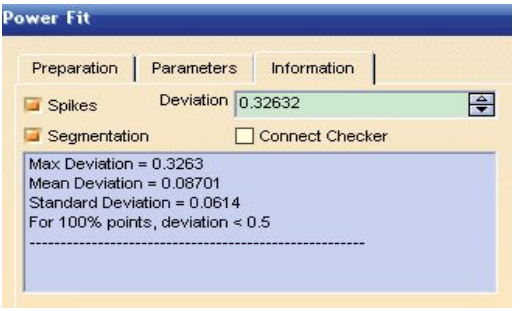

Fig. 4. Result data of fitting

Fig. 5. Zebra grain analysis

(3) Surface mesh. This tool can simultaneously fit multiple NURBS pure freedom surface, at the same time, it can ensure the G0 or G1 continuity between fitted surface patches and boundary of surface, But the condition is that must establish closed curve grid. It is very effective to pure free-form surface fitting with larger area and larger variation in curvature, as shown in Figure 6.

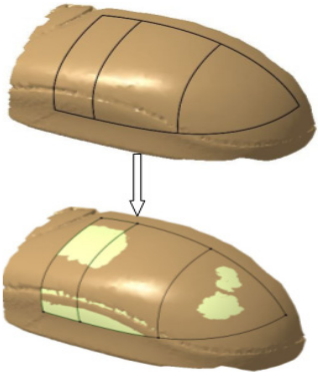

Fig. 6. Fitting of surface network

Analyze the surface quality, and can be seen, the surface quality is better than surface plates with the pure free-form surface fitting, and shown in Figure 7.

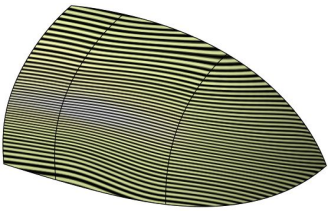

Fig. 7. Zebra grain analysis

3 Conclusions

Focusing on the freeform products in mechanical engineering, which have no obvious regular sectional feature in surface, this paper studied the fitting method of freeform curve and surface model for mechanical parts with mature commercial software of CATIA. Through that there is an approach to redesign for the non-parametric surface as the structural CAD model. So it can get a CAD model and fit to the original design intent, at the same time, the quality of the surface can be guaranteed. By using actual mechanical parts as example in this paper, those fitting methods were proved to be an effective path to reverse modeling of surface products.

Acknowledgement. It is a project supported by the National Natural Science Foundation of China (No. 50805025), the higher education and research institutions science and technology project of Dongguan (201010810205), and the 2010 Undergraduate's innovative experiment project (1184510014).

References

1. Ye, X., Liu, H., Chen, L., Chen, Z., Pan, X.: Computer-Aided Design 40, 812–827 (2008)
2. Barbero, B.R.: Computers & Industrial Engineering (2008), doi: 10.1016/j.cie.2008.07.023
3. Soni, K., Chen, D., Lerch, T.: The International Journal of Advanced Manufacturing Technology 41, 948–959 (2009)
4. Ke, Y., Fan, S., Zhu, W., Li, A.: Computer-Aided Design 38, 485–506 (2006)
5. Dassault, `http://www.3ds.com/`
6. Piegl, L.: Computer Aided Design 9, 538–546 (1989)
7. Thingvold, J., Cohen, E.: In: Proceedings of the 1990 Symposium on Interactive 3D Graphics, pp. 129–137 (1990)
8. Bo, L., Cheng, S., Zhang, X., Yang, X.: In: 2010 WASE International Conference on Information Engineering, vol. 3, pp. 189–192 (2010)

Parameter Tuning Research on Digital AC Servo Controller System

Erbao Peng and Zhe Wang

Henan Polytechnic Institute, Nanyang Henan, China
Yang09200@163.com

Abstract. Through the PID regulator can accurately realize proportional, integral and differential controlling law. The control system can achieve approximate processing and simply transfer function. Second-order optimal tuning is applied to set current loop Pl regulator, and the current loop is simplified into a section of inertia link in this paper. At last, Symmetric optimal setting is applied to set parameters of speed loop PI regulator.

Keywords: Servo control, regulator, controller, parameter, setting.

1 PID Controller Tuning Method Works

Engineering setting method, if the problem is simplified, find out the main contradiction. The first is the first choice of regulator structure, in order to ensure the stability of the system and steady-state precision, and design of regulator parameters to meet the dynamic performance requirements.

1.1 Tuning into the Classic Type I System Controller Design

As shown in Figure 1 of the system, which controller consists of two links, using proportional integral (PI) controller, i.e.

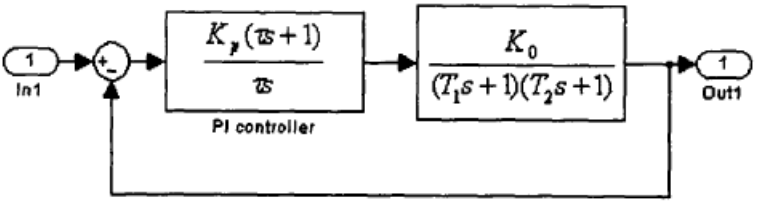

Fig. l. Transform double-inertial object into I system by PI controller

$$W_C(S) = K_P(\tau S + 1)/\tau S \tag{1}$$

Take $\tau = T_1$, elimination of large inertia, after correction for open loop transfer function:

D. Jin and S. Lin (Eds.): Advances in Mechanical and Electronic Engineering, LNEE 176, pp. 461–466.
springerlink.com

$$W(s)=W_c(s)W_o(s)=K_p(\tau s+1)\frac{K_p(\tau s+1)}{\tau s}\frac{K_0}{(T_1s+1)(T_2+1)}=\frac{K_pK_0}{s(T_2s+1)} \tag{2}$$

According to" mode is the best system" setting principle, namely takes the ξ = 0.707, $KT = 0.5$, $K = K_PK_0/\tau$, T=T 2 here, at this time of regulator parameters for:

$$\begin{cases} K_p = T_1 \big/ 2T_2K_0 \\ \tau = T_1 \end{cases} \tag{3}$$

1.2 Correction of a Ttypical Type II System Controller Design

As shown in Figure 2 of the system, system control object has an integral link and an inertia link, using proportional integral controller, system open loop transfer function:

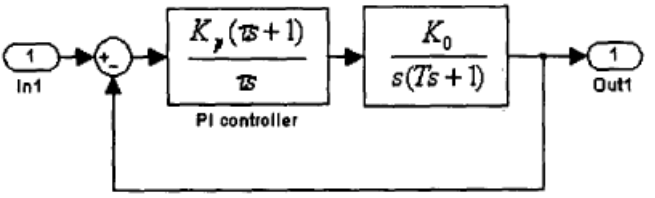

Fig. 2. Transform integal-inertial object into Ⅱ system by PI controller

$$W(s)=W_c(s)W_o(s)=\frac{K_p(\tau s+1)}{\tau s}\frac{K_0}{s}\frac{K_0}{(Ts+1)}=\frac{K(\tau s+1)}{s^2(Ts+1)} \tag{4}$$

Among them $K = K_PK_0/\tau$, type is a typical type standard system structure. According to the $r_{\max}$ maximum phase margin criterion, h=5, then the:

$$\begin{cases} K = K_pK_0 \big/ \tau = h+1 \big/ 2h^2T^2 \\ \tau = hT \end{cases} \tag{5}$$

PI regulator parameter:

$$\begin{cases} K_p = 0.6 \big/ TK_0 \\ \tau = 5T \end{cases} \tag{6}$$

Because many controlled objects and can not directly use the regulator is a typical system., then to do some simplified control object.

2 Current Loop For Parameter Tuning Of Pl Controllers

CNC AC position servo control system of dynamic structure diagram of Figure 3, the system consists of a controller, PWM converter, servo motor and filter. The yellow part is the current loop, mainly by the forward filter, PI controller, limiting link, motor armature part and a feedback link. Due to the current detecting unit feedback signal contains AC component, and a low-pass filter, T_{ief} for the current filter time constant, its size according to the selected delay effect, filter, for the balance of this delay, the forward channel also has a time constant and the same filter. Similarly, the speed loop of a two filter is so.

By the current loop can be seen in the inner motor back EMF generated cross feedback, it represents the rotational speed of the current ring effect. But due to the speed of links have not been designed, therefore it is considered the BEMF is difficult. In the actual system, due to the electromagnetic time constant is much smaller than the electric drive system of electrical time constant, so the current regulation process than speed change process more quickly, so the counter electromotive force of current loop is a slow interference, and the interference is very small, can be neglected. Therefore, the current loop can be expressed as, As shown in Figure 3 to 6 below:

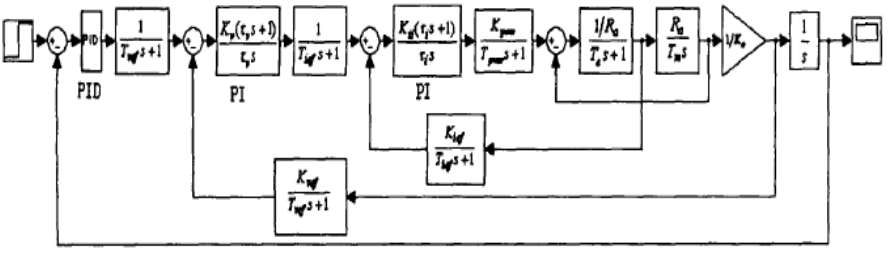

Fig. 3. Typical servo system

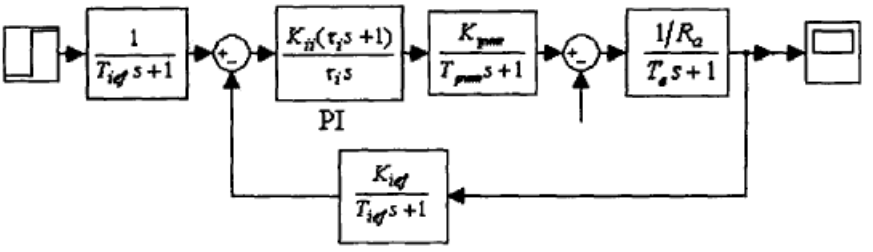

Fig. 4. Current loop

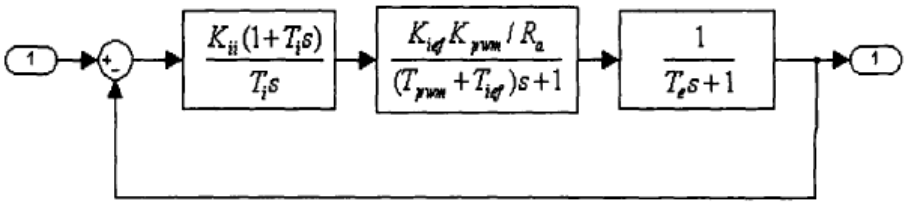

Fig. 5. Current loop with feedback

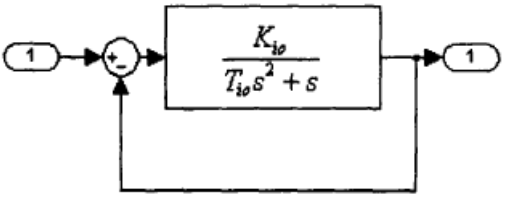

Fig. 6. SimPlified chart of current loop

In the design of regulator when the first limiting part will be removed, in Figure 3.4 the feedback link into unity feedback system, the feedback loop time constant pressure to the open-loop transfer function link to, are shown in Figure 5 of the dynamic structure diagram, in which. From steady state requirements, hope current can do no static error, to obtain good stalling characteristics, from the dynamic point of view, the current loop is tracking current overshoot is given, the smaller the better, so will the current loop correction into type I The system, using PI regulator, its transfer function:

$$W_{ACR}(s) = K_H(T_I + 1)/T_i \tag{7}$$

3 Speed Loop Tuning of Pl Parameters

Speed ring as shown in figure 7.

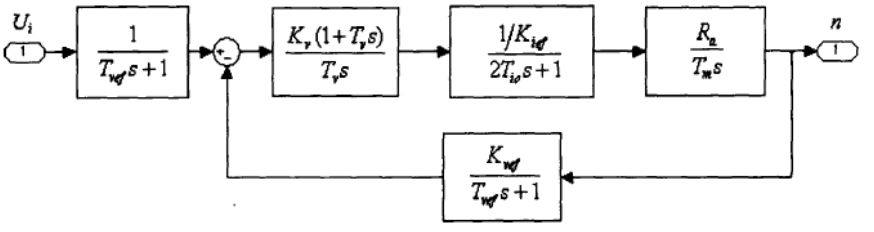

Fig. 7. Speed loop

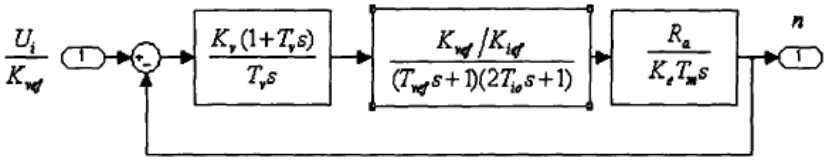

Fig. 8. Speed loop with feedback

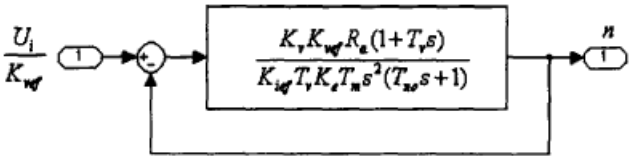

Fig. 9. Simplified chart of speed loop

The velocity loop feedback into units of feedback as shown in Figure 8, again after the merger after further simplification, make, are shown in Figure 9 of the transfer function. By the graph 9 can have the speed loop transfer function is:

$$W(s)=\frac{K_pK_{vef}R_a(T_vs+1)}{K_{ief}T_vK_eT_ms^2(T_{m0}s+1)}=\frac{K_{m0}(T_vs)}{s^2(T_{m0}+1)} \tag{8}$$

In which

$$K_{n0}=\frac{K_vR_aK_{vef}}{K_{ief}T_vK_eT_m} \tag{9}$$

Speed regulator comprises, and two parameters, according to the typical type system to determine its parameters, i.e.

$T_v=hT_{m0}$ According $M_{\min}$ to the guidelines for the identification of system parameters:

$K_{n0}=\frac{h+1}{2h^2TT_{m0}^{\ 2}}$ Then $K_v=\frac{(h+1)K_{ief}K_eT_m}{2hR_aKvefT_{m0}}$ Intermediate frequency bandwidth h optic system for dynamic performance requirements to decide, no special requirements 5 is good.

4 Meng Huan PlD Parameter Tuning

In servo system, in addition to the current loop and speed loop, and a position outside the ring, ring in position controller with PID controller. Position loop PID parameters mainly take the trial-and-error method, according to the engineering experience of adjusting, the integral and differential link parameter is set to zero, equivalent to only a proportional system, gradually increase the proportion of link gain, until the system unit step response curve is oscillating, then adjust the differential and integral link.

References

1. Hang, C.C., Loh, A.P., Vasnani, V.U.: Relay feed back auto-tuning of caseade controllers. IEEE Trans. on Control. Syst. Teeh. 2(1), 42–45 (1994)
2. MeCormaek, A.S., Godfrey, K.R.: Rule-based auto-tuning based on frequency domain identifieation. IEEE Trans. on Control Svst. Teeh. 6(l), 43–61 (1998)
3. Noroozi, N., Roopaei, M., Jahromi, M.Z.: Adaptive fuzzy sliding mode control scheme for uncertain systems. Communications in Nonlinear Science and Numerical Simulation 14(11), 3978–3992 (2009)
4. Li, Y.: The Optimization of Servo Parameters on CNC, Dalian University of Technology, pp. 22–29 (2009)
5. Li, Y.: The Optimization of Servo Parameters on CNC, Dalian University of Technology, pp. 22–29 (2009)
6. Mudia, R.K., Deyb, C., Leec, T.-T.: An improved auto-tuning scheme for PI controllers. ISA Transactions 47, 45–52 (2008)

The Cooperative Control of the Vehicle Steering/ Anti-lock Braking System Using the Coordination Variables

Guo Li and Hui Wang

Automation School, University of Science and Technology in Beijing, Beijing, China
{guo6396,yilianyoumeng008}@sina.com

Abstract. A new two-level cooperative control system was proposed for the vehicle's steering antilock braking stability fields. The architecture was composed with the execution layer and the cooperation layer. The uncertain parameters and coupled interference deteriorated the performance of the systems, so the vehicle anti-lock brake control system was designed based on the sliding mode robust adaptive controller. The yaw moment and the front wheel angle robust sliding mode controllers were designed to improve the respond, adaptive robustness and stability of vehicles. It was quite feasible because of its analytical form. Finally, the validity of the control algorithm was validated by simulation results.

Keywords: Robust adaptive control, Cornering braking, Cooperative control, Coupled interference and uncertain parameters.

1 Introduction

This essay designed a two-level cooperative control system, which was composed of the execution layer and the cooperation layer. On the execution, vehicle's velocity sliding mode robust adaptive controller was designed to track the optimal value. On the cooperation layer, the coordination variables were devised. Then the coordination variables were passed to the execution layer. After the coordination variables cooperated, anti-lock braking controller and the steering controller would finish the cooperative task together. Finally the validity of the control algorithm was validated by detailed simulation results.

2 Anti-lock Braking Controller

The wheel sliding mode adaptive control system was shown at figure 1. Four wheels had four systems like this. A single wheel model[4] was as following:

$$\begin{aligned} F_x &= -m_1\dot{v} = \mu F_z . \\ J\dot{\omega} &= F_x R - T_b \end{aligned} \tag{1}$$

In which m_1 was the mass of every wheel. J was the wheel's moment of inertia. F_z was the wheel's vertical load. μ was the adhesion coefficient. μF_z usually changed

D. Jin and S. Lin (Eds.): Advances in Mechanical and Electronic Engineering, LNEE 176, pp. 467–472.
springerlink.com

uncertainly to reflect the coupled interference the vehicle's steering made to the longitudinal.

Let's $\overline{\omega} = \omega - \omega_d$, then the equation (1) could be changed into: $\dot{\overline{\omega}} = \frac{R}{J}\mu F_z - \dot{\omega}_d - \frac{1}{J}T_b$

According to the error $\overline{\omega}$, designed the sliding mode plane alternate function:

$$s = (\omega - \omega_d) + k_0 \int_0^t (\omega - \omega_d) d\tau$$

ω_d was the vehicle's expected spin velocity. The sliding mode plane defined as $s = 0$ the system state set. Chose the const $g \succ 0$, $h \succ 0$ and the Lyapunov function: $V = \frac{1}{2} g s^2 + \frac{1}{2} h \overline{\mu}_F^2 \succ 0$

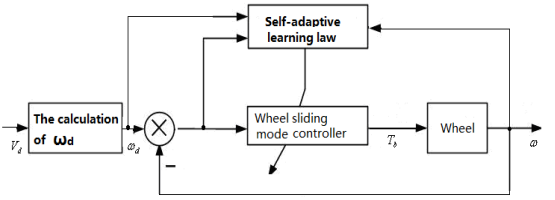

Fig. 1. Wheel Sliding Mode Adaptive Controller

The control variable T_b and the self adaptive law could be shown below: $T_b = J\left[\frac{R}{J}\hat{\mu}_F - \dot{\omega}_d + k_0(\omega - \omega_d) + k_3 \operatorname{sgn}(s)\right]$

$$\dot{\hat{\mu}}_F = \frac{gR}{hJ} s \cdot \tag{2}$$

In the equation: $\mu_F = \mu F_z$, $\hat{\mu}_F$ was the estimation value of μ_F. $\overline{\mu}_F = \hat{\mu}_F - \mu_F$ expressed the error. Chose the const $k_3 \succ 0$. Then : $\dot{V} = gs\left(\frac{R}{J}\mu_F - \frac{R}{J}\hat{\mu}_F - k_1 \operatorname{sgn}(s)\right) + h\overline{\mu}_F \dot{\hat{\mu}}_F$

$\dot{V} = -k_3 g |s| \prec 0 \cdot$

The system was uniformly asymptotic stability. Then : $\lim_{t \to \infty} s = 0$.

In order to eliminate the buffeting in the control variable equation (2), we drew into the border layer using the continuous saturation function sat(.) to replace the symbolic function sgn(.). Let $k_{30} = k_3 / \phi > 0$ be the sliding mode parameter and the thickness of the border layer φ=0.01. The equation below was to compute ω_d **:** $\omega_d = (1 - \lambda_d) V_d$

λ_d was the optimal sliding rate. Because the sliding rate's slope symbols of the curve between the tire friction sliding curve rate peak are different, the optimal sliding rate can be got from the equation below[4]: $\lambda_d(t_k) = \lambda_d(t_{k-1}) + d \operatorname{sgn}\left(\frac{\partial \mu_x}{\partial \lambda}\right)$

In the equation d was the positive step const. The optimal sliding rate can be got from the equation above. When $\frac{\partial \mu_x}{\partial \lambda} \succ 0$, increase d. When $\frac{\partial \mu_x}{\partial \lambda} \prec 0$, decrease d. The detail computation of V_d can be seen in section four.

3 Steering Robust Sliding Mode Controller

A two degree-of-freedom model that was commonly used[4]:

$$\dot{E}(t)=AE(t)+BU+(A-A_d)X_d-E_d\delta_d+w(t). \tag{3}$$

In which $E(t)=\begin{bmatrix}e_1\\e_2\end{bmatrix}=\begin{bmatrix}\beta-\beta_d\\\gamma-\gamma_d\end{bmatrix}=X-X_d$, $A=\begin{bmatrix}-\frac{k_1+k_2}{mv} & -\frac{ak_1-bk_2}{mv^2}-1\\-\frac{ak_1-bk_2}{I} & -\frac{a^2k_1+b^2k_2}{Iv}\end{bmatrix}$, $B=\begin{bmatrix}\frac{k_1}{mv} & 0\\\frac{ak_1}{I} & \frac{1}{I}\end{bmatrix}^T$

$X=[\beta\quad\gamma]^T$, $U=[\delta\quad M_z]^T$

k_1、k_2 were the cornering characteristics parameters of the front and the back wheel. M_z was the whole vehicle's longitudinal braking yaw moment that was needed. ν was the vehicle's velocity. δ was the aided front wheel's active steering angle. γ was the whole vehicle's yaw angular velocity. a was the distance between the center of mass to the front axle and b was the distance between the center of mass to the back axle. m was the whole mass of the vehicle. I was the moment of inertia around the center of mass. The vector w(t) was an unmeasured interference. Choose the four steering model as the referred model and δ_d was the steering angle from the steering input to the steering angle. The expected state variable was: $X_d=[\beta_d\quad\gamma_d]^T$. In which, the parameters A_d, E_d in the expected referring model were certainly known[4][5]. Let's choose the properδand the equation below : $BU_b=BU+(A-A_d)X_d-E_d\delta_d$.

Compute the whole vehicle's yaw moment M_z andδ:

$$U=U_b-B^{-1}(A-A_d)X_d+B^{-1}E_d\delta_d. \tag{4}$$

Then the error system could be changed into:

$$\dot{E}=AE+B_0\delta_0+w(t). \tag{5}$$

In which $U_b=\begin{bmatrix}1\\0\end{bmatrix}\delta_0$, $B_0=B\begin{bmatrix}1\\0\end{bmatrix}=\begin{bmatrix}\frac{k_1}{mv}\\\frac{ak_1}{I}\end{bmatrix}$.

Let the switching vector function in the slip plane be:

$$S=E(t)+K_3\int_0^t E(\tau)d\tau. \tag{6}$$

In which $K_3=p_0I$ was a diagonal matrix, the number $p_0\succ 0$. I was the corresponding suitable unit array. When the equation above was zero, that was S=0, define the system's state set as the two sliding mode plane. Let's consume Q was a suitable positive definite matrix: $V=\frac{1}{2}S^TQS$.

The active front wheel steering controlled variable δ_0:

$$\delta_0=-(S^TQB_0)^{-1}(S^TQAE+p_0S^TQE)-k_4\,\mathrm{sgn}(S^TQB_0). \tag{7}$$

Then $\dot{V} = -k_4 \left| S^T Q B_0 \right| + S^T Q w(t) \prec 0$

$$k_4 \succ \frac{\left\| S^T Q \right\| d_0}{\left| S^T Q B_0 \right|}, when \left\| S \right\| \succ \phi$$
$$k_4 \succ 0, when \left\| S \right\| \le \phi \tag{8}$$

k_4 can be self-adjustable. In order to eliminate buffeting, the boundary layer was drawn into and the function sat(.) in equation (7) was replaced by the function sgn(.). The impact of the controlled variable (4)(7)(8), the system state variables all can reach the sliding plane S=0 and $\lim_{t \to \infty} E(t) = 0$.

4 Cooperative Control

The cooperative control method using the coordination variable can be seen in figure 2. This is a two-level cooperative control structure.

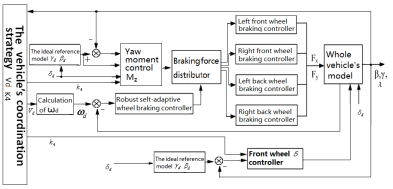

Fig. 2. The cooperative method

The upper centralized coordination strategy was used to calculate V_d、k_4. The lower distributed coordination strategy T_b、U could be got from the equation (2) and (4)(7). The cooperative variable were V_d、k_4.

Given the condition without interference w(t)=0. From the equation (6) and $\dot{V} = -k_4 \left| S^T Q B_0 \right|$, because S(t) was arbitrary function, then : $\dot{S}(t) = -k_4 B_0 sat\left(S^T Q B_0\right)$. That was: $\dot{E}(t) = -K_3 E - k_4 B_0 sat\left(S^T Q B_0\right)$.

Let the common cooperative goal be the optimal performance index: $J_0 = \frac{1}{2} \int_0^{t_f} \left(E^T Q_1 E + q_1 v^2 + q_2 k_4^2 \right) dt$

In which Q_1、q_1、q_2 were the chosen positive definite matrix and positive const.

Let $J_0 \to \min$., compute the v•and made it the longitudinal braking controller's expected velocity V_d=v•, then compute k_4 and made it the steering controller's cooperative variable. Calculate the optimal solution k_4 of the feedback coefficient on-line.

Definition: Function Hamilton was: $H = \frac{1}{2}\left(E^T Q_1 E + q_1 v^2 + q_2 k_4^2 \right) + \sigma^T \left(-K_3 E - k_4 B_0 sat(S^T Q B_0) \right)$

In which σ was the vector function, $\sigma = [\sigma_1 \quad \sigma_2]^T$. Choose $Q_1 = q_0 I$, $q_0 \succ 0$. It's noted that outside the border S=0, $\left\| S^T Q B_0 \right\| \succ \phi$, $sat\left(S^T Q B_0\right)$was a const.

From $\dot{\sigma}(t)=-\frac{\partial H}{\partial E}$, we can calculate the vector function σ:

$$\begin{aligned}\dot{\sigma}_1 - p_0\sigma_1 + q_0 e_1 = 0\\ \dot{\sigma}_2 - p_0\sigma_2 + q_0 e_2 = 0\end{aligned}. \tag{9}$$

From $\frac{\partial H}{\partial v}=0$, $\frac{\partial H}{\partial k_4}=0$, we can deduct the optimal expected tracking line v^*、$k_4^{\bullet}$:

$$\begin{aligned}v &= -\left(\frac{k_1 k_4}{q_1 m}\sigma_1 sat\left(S^T Q B_0\right)\right)^{1/3}\\ k_4 &= \frac{\sigma^T B_0}{q_2} sat\left(S^T Q B_0\right)\end{aligned}. \tag{10}$$

The wheel braking controller in figure 2 is the wheel's longitudinal sliding mode self-adaptive controller. The yaw moment controller M_z and the front wheel δ controller are gotten from the equations (4)(7)(10). While the coordination strategy is gotten from the equation(8)(9)(10) to compute the cooperative value v^*、$k_4^{\bullet}$,$Vd=v^*$.

The distribution strategy of the wheel's braking force can be seen in reference[7].

5 Simulation Analysis

5.1 Vehicle Simulation Model

It could be devided into the vehicle's longitudinal dynamical balanced equation, transverse dynamical balanced equation and the yaw moment dynamical balanced equation. The tire model would apply the adhesion coefficient sliding ration magic formula which was rather commonly used and relatively accurate.

5.2 Simulation Result

The vehicle's coefficient for simulation and PID controller's chosen coefficient could be seen in reference [4]. The separate control means the braking and steering control were under PID control without cooperative control. The cooperative control means the control this text contains. Choose the changes of vertical load and coupled interference as following: μF_z=200sin(10t)N,‖w(t)‖=100N. h=5, g=2, p_0=3, q_0=3, q_1=q_2=2, q_3=0.5. k0=3. c_0=Δ=0.1. Now in the condition that λ_d=0.8 , PID controller with adjusted parameters was applied to control the vehicle's steering and braking. In the road condition, there were changes that λ_d=0.15, the wheel's vertical load 10% besides there had the coupled interference. Then the simulation of the cooperative control system was conducted, which would be compared with the simulation result under PID control without refreshing parameters. The vehicle started at the initial speed of 50km/h in the road. When t=0s, the steering braking simulation began.

From figure 3, it could be seen that the setting time of cc is fast, the surplus is less, the amplitude is small and tracking is steady. The setting time is about t=2.5s. From the comparison it could seen that although the one with PID controller would still be quiet at last, it's setting time was too long, about t=3.8s. On the contrary, yaw velocity with cooperative controller was smooth, steady and safe.

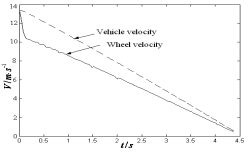

Fig. 3. Velocity simulation results under cooperative control

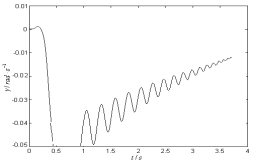

Fig. 4. Yaw velocity with PID controller

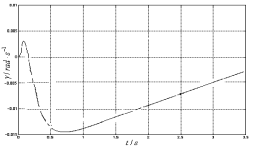

Fig. 5. Yaw velocity with cooperative controller

6 Conclusion

From the simulation result, when there was coupled interference and the vehicle's vertical load was uncertain, the separate PID control had greater tracking error. While the cooperative control could improve the interaction between two systems and at the same time compensate the interference. The whole system expressed good robust self-adaptive optimal performance index and the real time could reach its need.

Acknowledgements. Supported by Beijing Natural Science Foundation (The Cooperative Control of the Vehicle Steering/brake Uncertain Systems 4112038).

References

1. Chen, W.W., Chu, C.B.: Electric power steering system and anti-lock braking system based on layered coordinated control. Journal of Mechanical Engineering 45(7), 188–195 (2009)
2. Chen, L., Nie, J.M.: Intelligent control of dynamic performance of vehicle electric power steering and active suspension integrated system. Journal of Mechanical Engineering 45(6), 128–133 (2009)
3. Esmailzadeh, E., Goodarzi, A., Vossoughi, G.R.: Optimal Yaw Moment Control Law for Improved Vehicle Handling. Mechatronics 13, 659–675 (2003)
4. Xu, W.: Research on the Anti-Lock Brake System in Motor Swerve. University of Science and Technology Beijing, Beijing (2008)
5. Li, G.: The Adaptive Robust Controller of Antilock Brake System of Electric Vehicles. Acta Autonatica Sinica 32(3), 444–448 (2006)
6. Li, G.: Antilock brake fuzzy controller of electric vehicles. Control Theory & Applications 22(1), 134–138 (2005)
7. Li, G., Feng, Z., Wang, X.: The self-regulating cooperative control of the steering / antilock braking system of the vehicles. Application Research of Computers 27(11), 4189–4192 (2010)

The Nonlinear Decoupling Cooperative Controller of the Steering/Antilock Braking System of the Vehicle

Guo Li and Sha Peng

Automation School, University of Science and Technology in Beijing,
Beijing, China
guo6396@sina.com, turesha@163.com

Abstract. Firstly, a nonlinear decoupling control system is proposed for the cooperative control of the vehicle's steering and antilock braking systems. The control architecture is composed with the steering controller and the braking controller. The system is decoupled by using the differential geometry theory. Then the decoupled system is linearized through feedback linearization method, which ensures the global stability of the system. In order to guarantee the dynamic desired property of the system, the pole-displacement method is applied to the decoupled and liberalized system. The uncertain parameters and coupling disturbances deteriorate the performance of the systems, so parameters identification and robust controller are devised. Finally, the stability and the validity of the control algorithm are validated by simulation results.

Keywords: Robust adaptive control, Cornering braking, Cooperative control, Coupled interference and uncertain parameters.

1 Introduction

Steering stability and braking security has been increasingly high demanded with the continuous improvement of vehicle dynamic performance. The vehicle antilock braking system (ABS) has greatly improved security of motor cars. Presently scholars at home and abroad often designed different controller for single-wheel model, Such as PID control, fuzzy control, sliding mode control, optimal control and so on. Some related researches are for two degrees of freedom for the linear shift model and tracking controller based on the yaw moment and the front wheel steering angle. Anti-lock braking for steering and three degrees of freedom non-linear integrated model for the steering and antilock braking system, especially considering the uncertain parameters and coupling interference of non-linear control study has not been seen jet[1] ~ [4].It is difficult for traditional linear control to achieve satisfactory control performance, so nonlinear decoupling robust control must be studied [5] ~ [9].

Nonlinear decoupling controller has been designed for non-linear steering and braking integrated model. Differential geometry and feedback control matrix is selected to get non-linear steering and braking decoupling control strategy. The uncertain parameters and coupling disturbances deteriorate the performance of the systems, so parameters identification and robust controller are devised. Then the brake force distribution policy applicable to the complex work condition is presented.

D. Jin and S. Lin (Eds.): Advances in Mechanical and Electronic Engineering, LNEE 176, pp. 473–478.
springerlink.com

Finally, the stability and the validity of the control algorithm is validated by simulation results.

2 Nonlinear Comprehensive Model of the Vehicles

The three degrees of freedom integrated nonlinear dynamic model of vehicle can be got from the literature [3]. Vehicle lateral force balance is expressed as follow:

$$\dot{\beta} = \frac{k_f + k_r}{m v}\beta + \left(\frac{a k_f - b k_r}{m v^2} - 1\right)\gamma - \frac{k_f}{m v}\delta$$

Where k_f, k_r are the front rear cornering parameters, and β is the vehicle slip angle.

The equation of vehicle yaw motion torque balance is expressed as follow[3]:

$$\dot{\gamma} = \frac{a k_f - b k_r}{I}\beta + \frac{a^2 k_f + b^2 k_r}{I v}\gamma - \frac{a k_f}{I}\delta - \frac{M_z}{I} + \frac{M_n}{I}$$

Where I is the vehicle moment of inertia around the centroid. M_z is the vehicle yaw moment generated by longitudinal braking force.

The equation of automobile brake vertical force balance is expressed as follow[3]:

$$\dot{v} = \beta\gamma v - \frac{k_f}{m}\left(\beta + \frac{a}{v}\gamma\right)\delta - \frac{\sum_{i=1}^{2} F_{xi}}{m} + \frac{f}{m} \tag{1}$$

Where F_{X1} is the ground braking force of the two front wheels, F_{X2} for the two rear wheels, F_{y2} for the first two wheel lateral force, and δ is active steering angle of the front wheel.

Obviously, (1) is a three freedom degrees and nonlinear model, with strong coupling. Where M_n, f are the corresponding freedom degrees interference force and interference torque, which reflects the coupling and external environment interference between steering and brake system.

3 Nonlinear Decoupling Controller

3.1 Nonlinear Control Theory

The multiple-input multiple-output system: $\dot{X} = f(X) + \sum_{j=1}^{m} g_j(X)u_j$

$$y_i = h_i(X) \tag{2}$$

Its relative degree $r_i(X_0)$ is to : $L_{g_i} L_f^{r_i - 1} h_i(X_0) \neq 0, i = 1, 2, \ldots m$

3.2 Steering/Brake Nonlinear Decoupling Controller

Nonlinear decoupling controllers designed as noted in Lemma .

$$g_1(X)=\left[-\frac{k_f}{mv}\quad -\frac{ak_f}{I}\quad -\frac{k_f}{m}\left(\beta+\frac{a}{v}\gamma\right)\right]^T \qquad g_2(X)=\left[0\quad -\frac{1}{I}\quad 0\right]^T,$$

$$g_3(X)=\left[0\quad 0\quad -\frac{1}{m}\right]^T$$

$$f(X)=\begin{bmatrix}\dfrac{k_f+k_r}{mv}\beta+\left(\dfrac{ak_f-bk_r}{mv^2}-1\right)\gamma\\ \dfrac{ak_f-bk_r}{I}\beta+\dfrac{a^2k_f+b^2k_r}{Iv}\gamma\\ \beta\gamma v\end{bmatrix}$$

Output $h_1(X)=\beta, h_2(X)=\gamma, h_3(X)=v$. State variable $X=[\beta\quad \gamma\quad v]^T$. Control input $U=\left[\delta\quad M_z\quad \sum_{i=1}^{2}F_{xi}\right]^T$. It is calculated as follow:

$$L_{g_1}h_1(X)=-\frac{k_f}{mv}, L_{g_1}h_2(X)=-\frac{ak_f}{I}$$

$$L_{g_1}h_3(X)=-\frac{k_f}{m}\left(\beta+\frac{a}{v}\gamma\right),$$

$$L_{g_2}h_2(X)=-\frac{1}{I}, L_{g_3}h_3(X)=-\frac{1}{m}$$

We can get the controller calculated on this basis following the lemma:

$$\begin{aligned}\delta&=\frac{k_f+k_r}{k_f}\beta+\frac{ak_f-bk_r}{k_fv}\gamma-\frac{mv\gamma}{k_f}-\frac{mv}{k_f}v_1\\ M_z&=-(a+b)\beta k_r+\frac{(a+b)bk_r}{v}\gamma+mav\gamma+mvav_1-Iv_2\\ \sum_{i=1}^{2}F_{xi}&=-\frac{(\beta v+a\gamma)(k_f+k_r)}{v}\beta\\ &\quad-\gamma(\beta v+a\gamma)\left(\frac{ak_f-bk_r}{v^2}\right)\\ &\quad+2mv\beta\gamma+ma\gamma^2+m(\beta v+a\gamma)v_1-mv_3\end{aligned} \tag{3}$$

After decoupling, $\dot{\beta}=v_1$, $\dot{\gamma}=v_2+\frac{M_n}{I}$, $\dot{v}=v_3+\frac{f}{m}$, v_1, v_2, v_3 are new input with disturbance interference. Let, $V(t)=\frac{1}{2}\left((\beta-\beta_d)^2+(\gamma-\gamma_d)^2+v^2\right)$.

Control law:

$$\begin{aligned} v_1 &= -\lambda_1(\beta-\beta_d)+\dot{\beta}_d \\ v_2 &= -\lambda_{20}(\gamma-\gamma_d)+\dot{\gamma}_d-\lambda_{21}\operatorname{sgn}(\gamma-\gamma_d) \\ v_3 &= -\lambda_{30}v-\lambda_{31} \end{aligned} \tag{4}$$

Where: $\lambda_1, \lambda_{20}, \lambda_{30}$ are positive numbers and larger than zero. $\lambda_{21} > \frac{\|M_n\|}{I}, \lambda_{31} > \frac{\|f\|}{m}$. β_d, γ_d are the desired trajectory and expected reference model state variables [9]. Then, $\dot{V}(t) < 0$.

System is asymptotic convergence and stability. Take (4) into (3) that is non-linear control law. This is a non-linear decoupling controller. It can be seen from Controller structure that the project can be achieved.

3.3 The Parameter Identification of Wheel Side Slip Characteristic

Change the first two equations into discrete shift equation:

$$Y(k) = \Phi^T(k)\theta + \eta(k) \tag{5}$$

Where: Y is the output. The amount of external interference satisfies $\|\eta\| \le \Delta$.

$$Y(k) = \begin{bmatrix} \beta(k)-\beta(k)+T\gamma(k) \\ \gamma(k)-\gamma(k-1)+\frac{T}{I}M_z(k) \end{bmatrix}$$

$$\theta = \begin{bmatrix} k_f & k_r \end{bmatrix}^T, \eta(k) = \begin{bmatrix} 0 & \frac{T}{I}M_n \end{bmatrix}^T$$

$$\Phi^T = \begin{bmatrix} \frac{T(\beta v + a\gamma - \delta v)}{m v^2} & \frac{T(\beta v - b\gamma)}{m v^2} \\ \frac{T(a^2\gamma + a\beta v - av\delta)}{Iv} & \frac{T(b^2\gamma - bv\beta)}{Iv} \end{bmatrix}$$

Parameter identification takes good real-time projection algorithm with dead zone:

$$\begin{aligned} \hat{\theta}(k+1) &= \hat{\theta}(k)+\alpha(k)\Phi(k)\left(c_0 I_0 + \Phi^T\Phi\right)^{-1} e(k) \\ e(k) &= Y(k)-\Phi^T(k)\hat{\theta}(k) \\ \alpha(k) &= \begin{cases} I_0 & \|e(k)\| \succ 2\Delta \\ 0 & \|e(k)\| \le 2\Delta \end{cases} \end{aligned} \tag{6}$$

Where $c_0 > 0$ is a constant avoiding that the inverse matrix doesn't exist. I_0 is the second-order unit matrix. $\Delta = \frac{\|M_n\|}{I}$.Distribution design of braking force of each wheel is seen in [6].

4 Simulation Analysis

Simulation is completed in the environment of matlab / simulink. Let $\lambda_1 = 3$, $\lambda_{20} = 3$, $\lambda_{30} = 3$ $\lambda_{21} = \lambda_{31} = 6$, $c_0 = c_1 = 3$, $\Delta_1 = \Delta = 0.1$. Separate control refers the braking and steering control with PID control and no coordination. Coordination control refers to the control of this paper.

To verify the effect of the coordination controller, the analog simulation is carried in the condition of Steer braking, adhesion coefficient $\mu = 0.8$. Load variation of Vertical wheel F_n changes. Parameters $k_{f0} = 94000N.rad^{-1}$, $k_{r0} = 85000N.rad^{-1}$ changes about 8%. Environmental interference $M_n = 160\sin 10tNm$, $f = 50\cos 3tN$. Now the changes of road $\mu = 0.2$.

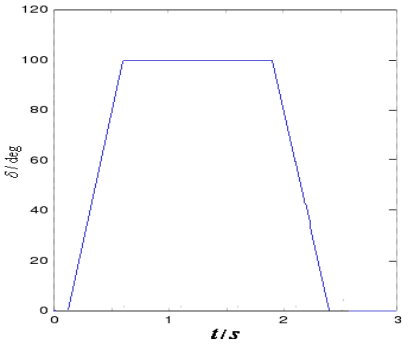

Fig. 1. Input command

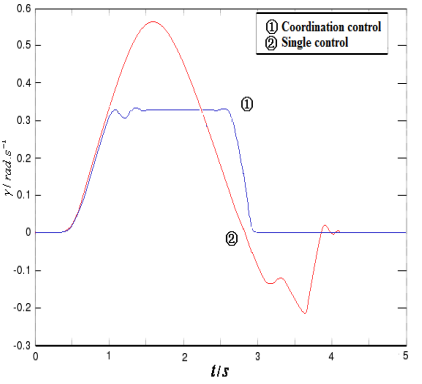

Fig. 2. Yaw velocity

When driving a straight line, braking suddenly, and the input curve of steering wheel steering angle is shown in Fig.1.Fig.2 is the yaw rate contrast curve of vehicle working with individual controller and with coordination control in steering brake condition. From the figure, when the coordinated controller working, the vehicle yaw rate oscillation amplitude reduced, and the simulation curve is gentler, and faster convergence in the expectation to improve the steering stability during braking.

Fig.3 is the contrast curve of sideslip angle vehicle working with individual controller and with coordination controller in a vehicle braking turn. From simulation diagram, sideslip angle will close to 0. However, the oscillation amplitude of sideslip angle is relatively small when the coordinated controller working earlier close to 0 than without coordinated controller, improving the handling of a car.

Fig.4 is the simulation results of wheel speed with coordinate control. It can be seen that regulation time of coordination control is fast and with small overshoot, small amplitude oscillations, and tracking stability.

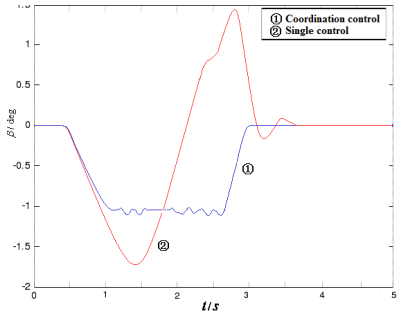

Fig. 3. Slide slip angle at vehicle CG

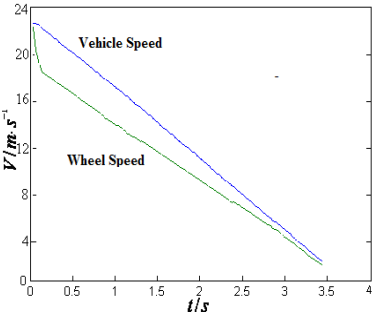

Fig. 4. Velocity simulation result

Acknowledgements. Supported by Beijing Natural Science Foundation (The Cooperative Control of the Vehicle Steering/brake Uncertain Systems 4112038).

References

1. Esmailzadeh, E., Goodarzi, A., Vossoughi, G.R.: Optimal Yaw Moment Control Law for Improved Vehicle Handling. Mechatronics 13, 659–675 (2003)
2. Liu, H.: Research on the Integrated Controller of the Steering/Braking Stability for the Vehicles. University of Science and Technology Beijing, Beijing (2010)
3. Chen, W., Chu, C.: Electric Power Steering System and Anti-lock Braking System Based on Layered Coordinated Control. Journal of Mechanical Engineering 45(7), 188–195 (2009)
4. Yu, Z., Zhang, L.: A study on coordination of direct yaw moment control and variable wheel slip control for vehicle stability. Automotive Engineer 28(9), 844–848 (2006)
5. Li, G.: The Adaptive Robust Controller of Antilock Brake System of Electric Vehicles. Acta Autonatica Sinica 32(3), 444–448 (2006)
6. Li, G.: Antilock brake fuzzy controller of electric vehicles. Control Theory & Applications 22(1), 134–138 (2005)
7. Li, G.: The Adaptive Robust Controller of Mobile Satellite Antennas Systems. Control Theory & Applications 24(2), 134–138 (2007)
8. Li, G., Liu, H.W., Wang, X.: The cooperative control of the steering / antilock braking system of the vehicles. Control Theory & Applications 27(12), 1700–1708 (2010)
9. Isidori, A.: Nonlinear control system, 3rd edn., pp. 175–225. Publishing House of Electronics Industry, Beijing (2005)

The μ Robust Control for the Steering System of the Vehicles

Guo Li and YanJie Hou

Automation School, University of Science and Technology in Beijing, Beijing, China
guo6396@sina.com, hyjiexxx@foxmail.com

Abstract. The uncertain parameters and coupling disturbances deteriorate the performance of the systems, so the μ robust control system is proposed for the control of the vehicle's steering system. To improve the robust performances of the whole system, the μ robust controller of the vehicle steering system is designed based on the front wheel angle. The result of simulation proves that the control system is correct and feasible. It improves the vehicle stability and steering performance.

Keywords: vehicle steering system, uncertain parameters and coupling disturbances, μ robust control.

1 Introduction

Description of vehicle steering control when the vehicle was outside interference to maintain steering stability against interference with the ability to travel. Often used yaw moment and active steering angle before waving a combination of precisecontrol of steering track the desired trajectory path. The optimal control is more used, [1] [3] [4] but most did not consider how to improve the robust control performance.

In vehicle steering, due to the centrifugal force caused by a non-zero steering angle and the existence of longitudinal braking force, the load of each tire shifts, thus the maximum longitudinal adhesion and the cornering properties stiffness of each tire are altered.

Vehicle parameter uncertainty change, steering Angle and longitudinal braking force mutual coupling interference and road conditions interference, increased the difficulty of the steering control. Therefore, the robust control performance must be studied to improve [2] [5] [6] [7] [8] [9].

In paper [2], the vehicle steering system model has a parameter uncertainty change. For two degrees linear model of vehicle, using μ recursive method in the design of *D-K* get vehicle turned to the robust controller. Papers on wheels, before and after the cornering characteristics parameters change is always the same assumptions is not reasonable, The maximum rank factorization are no parameter perturbation out, so controller design conservative is bigger.

In paper [3], Using classical stratified control system for linear time-invariant systems and brake at the same time to control, Without considering how to design the

D. Jin and S. Lin (Eds.): Advances in Mechanical and Electronic Engineering, LNEE 176, pp. 479–485.
springerlink.com

system of robust performance, The text of the stratified controller of real-time performance and synergy is not good.

Steering and brake simultaneously, the dynamics in addition to front, rear tire cornering properties parameter uncertainty changes, the vehicle mass and moment of inertia changes also occur uncertain. In paper[8], The perturbation of important parameters is not taken into account in.

The research content of this paper is steering control. The cooperative control system designed to focus on the cooperative control among sub-systems of the vehicle is to solving the coupling problem between the steering system and the ABS during the vehicle cornering braking, parameters not sure change and road conditions interference problems.

Firstly, μ robust controller is designed by combining front-wheel angle control with yaw moment control. It can dynamically compensate for the interference coming from the braking control to the longitudinal braking and make the whole system have good real-time performance, stability and robustness, Track precision meet the requirements, and Particular simulation results validate the validity of the designed control algorithm.

Then, cooperative error is defined and cooperative model of the vehicle is built. The μ robust cooperative controller of the longitudinal brake is designed. And various errors decay to zero with the same decay rate.

2 The Robust Controller of the Steering System

In designing the μ robust controller of the steering system, linear two degrees of freedom model[1]-[4] is used.

$$E\dot{\bar{X}} = A\bar{X} + B\delta + E\left(AX_d - \dot{X}_d\right) + B_0 M \tag{1}$$

Where,

$$\bar{X} = X - X_d,\ X = [\beta \quad \gamma]^T,\ M_n = [\xi_1 \quad \xi_2]^T,\ X_d = [\beta_d \quad \gamma_d]^T,\ E = diag(m \quad I)$$

$$B_0 = [0 \quad 1]^T,\ A = \begin{bmatrix} -\dfrac{k_1 + k_2}{v} & -\dfrac{ak_1 - bk_2}{v^2} - m \\ -(ak_1 - bk_2) & -\dfrac{a^2 k_1 + b^2 k_2}{v} \end{bmatrix},\ B = \begin{bmatrix} \dfrac{k_1}{v} \\ ak_1 \end{bmatrix}\ B = \begin{bmatrix} \dfrac{k_1}{v} \\ ak_1 \end{bmatrix} \tag{2}$$

Where, ξ_1 and ξ_2 are corresponding interferences, including the model error, road disturbances and so on. v is the velocity of the vehicle. δ is the additional front wheel active steering angle. a is the axis distance between centroid and the front wheels. b is the axis distance between centroid and the rear wheels. I is the moment of inertia around the centroid,m is the mass of the vehicle, β is the side slip angle is the yaw rate. k_1、k_2, which are impacted by steering system and suspension system, are respectively cornering properties parameters of the front wheels and the rear wheels. Then (1) can be rewrite as:

$$E\dot{\overline{X}} = A\overline{X} + B\delta + Hd \tag{3}$$

$$H = \begin{bmatrix} 1 & 0 \\ 0 & 1 \end{bmatrix}, d = \begin{bmatrix} d_1 + \xi_1 \\ d_2 + \xi_2 \end{bmatrix}, d_1 = -\frac{k_1 + k_2}{v}\beta_d - \left(\frac{ak_1 - bk_2}{v^2} + m\right)\gamma_d - m\dot{\beta}_d, \tag{4}$$
$$d_2 = -(ak_1 - bk_2)\beta_d - \frac{a^2 k_1 + b^2 k_2}{v}\gamma_d - I\dot{\gamma}_d$$

Where, k_1, k_2, m, I are uncertain nonlinear variations, which have a greater impact for the control system of the steady-state and dynamic properties, and make the control tracking performance deteriorate. However, too many parameters to consider in the μ design perturbation, the controller will be very conservative, and the adjustment of the weighting function is also more difficult. Then:

$$k_1 = k_{10} + \Delta_1\delta_1,\ k_2 = k_{20} + \Delta_2\delta_2,\ m = m_0 - c_0\delta_1\Delta_1 - c_1\delta_2\Delta_2, \\ I = I_0 - c_2\delta_1\Delta_1 - c_3\delta_2\Delta_2 \tag{5}$$

Where, c_0, c_1, c_3, c_4 are positive numbers.

Two perturbation parameters δ_1, δ_2 descriptor system is investigated,

$$\left(E + \sum_{i=1}^{2}\delta_i E_i\right)\dot{\overline{X}} = \left(A + \sum_{i=1}^{2}\delta_i A_i\right)\overline{X} + \left(B + \sum_{i=1}^{2}\delta_i B_i\right)\delta + Hd \\ e = M\overline{X} + Nd + V\delta,\ y = C\overline{X} + Qd \tag{6}$$

Where, $e = [\beta - \beta_d \quad \gamma - \gamma_d \quad \delta]^T$ is evaluation of output vector, $y = [\overline{x}_1 + d_1 + \xi_1 \quad \overline{x}_2 + d_2 + \xi_2]$ is measured output vector, d is interference. Consider the purpose of interference by adding the appropriate weighting function can be ignored when the expression of model reduction of higher order resonant modes and the impact on the system to be robust compensation [10]. Then,

$$M = \begin{bmatrix} 1 & 0 \\ 0 & 1 \\ 0 & 0 \end{bmatrix}, V = \begin{bmatrix} 0 \\ 0 \\ 1 \end{bmatrix}, C = Q = \begin{bmatrix} 1 & 0 \\ 0 & 1 \end{bmatrix}, N = 0 \tag{7}$$

To avoid the perturbation expansion of the scope to reduce conservative, perturbation is out using maximum rank decomposition method using. Then,

$$E_0^{-1}[E_i \quad A_i \quad B_i] = L_i[R_i \quad W_i \quad Z_i] \tag{8}$$

Where, i=1, 2. Let matrix of the left rank be q_i and we should ensure that $L_i \in R^{n \times q_i}$, $Z_i \in R^{q_i \times n_u}$ and $R_i, W_i \in R^{q_i \times n}$ are full column ranks.

$$E_0 = diag(m_0 \quad I_0),\ E_1 = diag(-c_0\Delta_1 \quad -c_2\Delta_1),\ E_2 = diag(-c_1\Delta_2 \quad -c_3\Delta_2) \tag{9}$$

Similarly, matrix A_0, A_1, A_2 and B_0, B_1, B_2 can be obtained. Then,

$$L = [L_1 \quad L_2] = \begin{bmatrix} -\sqrt{\frac{c_0\Delta_1}{m_0}} & 0 & -\sqrt{\frac{c_1\Delta_2}{m_0}} & 0 \\ 0 & -\sqrt{\frac{c_2\Delta_1}{I_0}} & 0 & -\sqrt{\frac{c_3\Delta_2}{I_0}} \end{bmatrix} \tag{10}$$

$$R = \begin{bmatrix} R_1 \\ R_2 \end{bmatrix} = \begin{bmatrix} \sqrt{\frac{c_0\Delta_1}{m_0}} & 0 \\ 0 & \sqrt{\frac{c_2\Delta_1}{I_0}} \\ \sqrt{\frac{c_1\Delta_2}{m_0}} & 0 \\ 0 & \sqrt{\frac{c_3\Delta_2}{I_0}} \end{bmatrix}, W = \begin{bmatrix} W_1 \\ W_2 \end{bmatrix} = \begin{bmatrix} \frac{1}{v}\sqrt{\frac{\Delta_1}{c_0 m_0}} & \left(\frac{a}{v^2} - c_0\right)\sqrt{\frac{\Delta_1}{c_0 m_0}} \\ a\sqrt{\frac{\Delta_1}{I_0 c_2}} & \frac{a^2}{v}\sqrt{\frac{\Delta_1}{I_0 c_2}} \\ \frac{1}{v}\sqrt{\frac{\Delta_2}{c_1 m_0}} & -\left(\frac{b}{v^2} + c_1\right)\sqrt{\frac{\Delta_2}{c_1 m_0}} \\ -b\sqrt{\frac{\Delta_2}{I_0 c_3}} & \frac{b^2}{v}\sqrt{\frac{\Delta_2}{I_0 c_3}} \end{bmatrix} \tag{11}$$

$$Z = \begin{bmatrix} Z_1 \\ Z_2 \end{bmatrix} = \begin{bmatrix} -\frac{1}{v}\sqrt{\frac{\Delta_1}{c_0 m_0}} & -a\sqrt{\frac{\Delta_1}{I_0 c_2}} & 0 & 0 \end{bmatrix}^T, L = [L_1 \quad L_2] = \begin{bmatrix} -\sqrt{\frac{c_0\Delta_1}{m_0}} & 0 & -\sqrt{\frac{c_1\Delta_2}{m_0}} & 0 \\ 0 & -\sqrt{\frac{c_2\Delta_1}{I_0}} & 0 & -\sqrt{\frac{c_3\Delta_2}{I_0}} \end{bmatrix} \tag{12}$$

Defined 1: Given transfer function $K(s)$ and $\Theta(s)$, then $K(s)$ and $\Theta(s)$ on the linear fractional transformation formula is

$$\left.\begin{aligned} F_l(\Theta, K) &= \Theta_{11}(s) + \Theta_{12}(s)K(s)[I - \Theta_{22}(s)K(s)]^{-1}\Theta_{21}(s) \\ F_u(\Theta, K) &= \Theta_{22}(s) + \Theta_{21}(s)[I - K(s)\Theta_{11}(s)]^{-1}K(s)\Theta_{12}(s) \end{aligned}\right\} \tag{13}$$

Where, $\Theta(s) = \begin{bmatrix} \Theta_{11}(s) & \Theta_{12}(s) \\ \Theta_{21}(s) & \Theta_{22}(s) \end{bmatrix}$. System (2) can be describe by $\begin{bmatrix} e \\ y \end{bmatrix} = F_u\left(G_P, \Delta\right)\begin{bmatrix} d \\ u \end{bmatrix}$,

$$G_P = \left[\begin{array}{c|ccc} \frac{\hat{A}}{W - R\hat{A}} & \frac{L}{-RL} & \frac{\hat{H}}{-R\hat{H}} & \frac{\hat{B}}{Z - R\hat{B}} \\ M & 0 & N & V \\ C & 0 & Q & 0 \end{array}\right], \hat{\mathbf{A}} = \mathbf{E}^{-1}\mathbf{A}, \hat{\mathbf{B}} = \mathbf{E}^{-1}\mathbf{B}, \hat{\mathbf{H}} = \mathbf{E}^{-1}\mathbf{H}, \tag{14}$$

Then,

$$\hat{\mathbf{H}} = \mathbf{E}^{-1}\mathbf{H}, \sup_{\omega} \mu_{\tilde{\Delta}}\left(F_l\left(G_P, K\right)\right) \le \inf_{D \in \Psi} \left\| \left(DF_l\left(G_P, K\right)D^{-1}\right) \right\|_\infty \tag{15}$$

During designing integrated μ, D-K iteration is used, that means successive using of D and K to minimize.

a) Choose an appropriate calibration matrix, make D and D^{-1} are stability;

b) D(s), using the method of H∞ solve the minimization problem on K(s), find out the optimal solution; By solving the Riccati equation or LMI;

c) Fixed K(s), Solving the $\inf_{D \in \Psi} \left\| DF_l\left(G_P, K\right)D^{-1} \right\|_\infty$ *convex optimization problem, get D(s) and notes for D_w;*

d) Compare D(s) and D_w, if both close to, by the (2) get controller K(s) is the optimal controller. Otherwise, make D(s)= D_w, return (b).

Using the Matlab Robust Control Toolbox dkit recursive procedure twice to $\left\| DF_l\left(G_p, K\right)D^{-1} \right\|_\infty = 0.984$.

Third, the performance is not significantly improved, Therefore, using the second recursive controller. Re-use in Matlab balreal and modred reduced order processing functions, and finally get a third-order controller.

In the case of different speeds, find a dual-input $(\beta \quad \gamma)$ and single-output (δ) controller offline. The controller in the car at high speed is especially important role. The controller of $v = 50km/h$ is

$$\delta(s) = \frac{0.38(s+63.9)(s+89.6)}{(s+1.6)(s^2+786s+6.3\times10^5)}(\beta(s)-\beta_d(s)) + \frac{0.17(s+53.7)(s+48.6)}{(s+3.3)(s^2+657s+45.3\times10^3)}(\gamma(s) \quad (16)$$

Take inhibition parameter perturbation weighting function $W(s)$, load disturbance weighting function $W_d(s)$ and input weighting function $W_u(s)$ as

$$W(s) = diag\left\{\frac{0.79(s^2+36s+409.6)}{s^2+58s+357.3} \quad \frac{0.15(s^2+44s+510)}{s^2+77s+573}\right\}.$$
$$W_d(s) = diag\left\{\frac{0.6(s+120)}{s+3.57} \quad \frac{1.3(s+162)}{s+5.86}\right\}.W_u(s) = \frac{13(s+380)}{s+6523} \quad (17)$$

Used in the calculation [7] shows the basic parameters of automotive steering systems. The bode results of the K(S) controller is shown in fig.1.

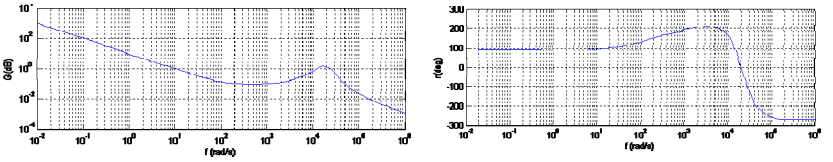

Fig. 1. The Bode results of the controller

3 Simulation Analysis

Simulation is done in matlab/simulink. How to choose parameters used in simulation, and the parameters of PID controller and detailed simulation condition of the control are presented in [7]. Select vertical load variable quantity as $c_0 = 1.2m_0/k_{10}$, $c_1 = 1.4m_0/k_{20}$, $c_2 = 1.44I_0/k_{10}$, $c_3 = 1.96I_0/k_{20}$, $\Delta_1 = 0.3k_{10}$. Two different conditions are considered in the simulation. The first condition is that the vehicle is controlled by the separate control and the other condition is that the vehicle is controlled by the cooperative control.

In the condition of road surface $\lambda_d = 0.8$, the controller of the vehicle, controlled by PID controller whose parameters have been defined, controlled the vehicle to steer. Under steering on the off road, control effect of the cooperative controller is verified. The condition of the road surface changes as $\lambda_d = 0.2$ and the uncertain change of the wheel vertical load is 10% based on the basic value. In the road outside to break conditions, test the controller designed. Simulation of the control system μ compared with the result of PID controller whose parameters aren't reset.

The vehicle is running on the road at the initial speed of 50 km/h. When $t = 0s$, the steering simulation was begun to execute.

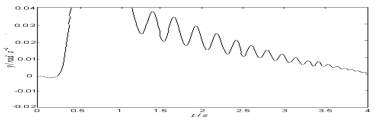

Fig. 2. Yaw velocity with PID controller

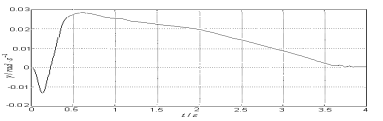

Fig. 3. Yaw velocity with cooperative controller

Fig.2 shows the yaw velocity with PID controller. Fig.3 shows the yaw velocity with μ controller. Through comparing we can see, vibration amplitude of the vehicle is lager which is under PID controlling even goes stable at last, while setting time is longer(about t=4s). That runs though the whole process. On the contrast, the one with the μ control has smooth, stable and safe yaw velocity. Return to zero in about 3.6s.

4 Conclusion

The μ control is better than individual control. Especially when the vehicle has important parameters which are not sure or the coupling to interfere. When the good PID control alone, tracking error becomes large, even the phenomenon of large oscillation. The μ steering control can still accurately track the specified value, improve the auto steering system dynamic performance, and improve the car turned to the precise tracking performance. The vehicle control system showed good performance and robust real-time fast.

Acknowledgments. This research was supported by Beijing Natural Science Foundation (The Cooperative Control of the Vehicle Steering/brake Uncertain Systems 4112038).

References

1. Esmailzadeh, E., Goodarzi, A., Vossoughi, G.R.: Optimal Yaw Moment Control Law for Imp roved Vehicle Handling. Mechatronics (13), 659–675 (2003)
2. Yin, G.D., Chen, N., Wang, J.X.: A stuay on μ synthesis control for four wheel steering system to enhance vehicle lateral stability. Journal of Dynamic Systems, Measurement and Control 133(1), 1–6 (2011)
3. Chen, W., Chu, C.: Electric Power Steering System and Anti-lock Braking System Based on Layered Coordinated Control. Journal of Mechanical Engineering 45(7), 188–195 (2009)
4. Li, G.: The Adaptive Robust Controller of Antilock Brake System of Electric Vehicles. Acta Autonatica Sinica 32(3), 444–448 (2006)
5. Li, G.: Antilock brake fuzzy controller of electric vehicles. Control Theory & Applications 22(1), 134–138 (2005)
6. Li, G.: The Fuel Cell Control System of Electric Vehicles. Control Theory & Applications 25(2), 289–293 (2008)

7. Wang, X.: Research on the Anti-Lock Brake System in Motor Swerve. University of Science and Technology Beijing, Beijing (2008)
8. Li, G., Liu, H.W., Wang, X.: The cooperative control of the steering/antilock braking system of the vehicles. Control Theory & Applications 27(12), 1700–1708 (2010)
9. Li, G.: The μ Robust Controller of Mobile Satellite Antennas Systems. Engineering Science 9(6), 22–26 (2007)

A Study on the Compatibility of Sandwiched Tube-Type Airbag in Rhomboid Vehicle

Jing Huang[1], Jikuang Yang[1], and Lin Hu[2]

[1] State Key Laboratory of Advanced Design & Manufacture for Vehicle Body, Hunan University, 410082 Changsha Hunan, China
huangjing926@163.com
[2] School of Automotive and Mechanical Engineering, Changsha University of Science and Technology, 410004 Changsha Hunan, China

Abstract. The traffic safety has been paid more and more attention currently. Airbags have being widely equipped in passenger vehicles to protect the occupants from vehicle collisions, and the new shape of vehicle brings forward a novel conception for improve the traffic safety. In this paper, the problem of compatibility was studied when applied this new type of airbag in rhomboid vehicle. The FE models of the new airbag and rhomboid vehicle were developed and validated, and the virtual test and regression analysis was used to process the airbag matching.

Keywords: Sandwiched Tube-type Airbag, Rhomboid Vehicle, Compatibility, Virtual Testing, Regression Analysis.

1 Introduction

Airbags have been proven to be very helpful in protecting drivers and passengers in many cases of automotive crashes. However, side-effects may be in responsible for occupant injuries. One common side-effect is that it may harm occupants, especially for occupants with small size, when it deploys improperly on crash [1-3]. In order to achieve occupant protection during a crash using an airbag that must fully-deploy rapidly in less than 50 milliseconds. The airbag dissipate the frontal crash forces experienced by the driver over a larger body area and gradually decelerate the occupant's head and torso to prevent contact with other interior surfaces. However if an occupant positioned extremely close to the airbag module, he will expose to a large force when the airbag begins to inflate. Two phases of airbag deployment have been associated with large forces which caused injuries: the punch-out phase and the membrane-loading phase. According to the findings from the biomechanics research, the passenger car accident investigation and the laboratory crash test, the chest and the neck are the most vulnerable body segments during airbag interaction with the OOP occupant. It has been found that chest injuries are often associated with the airbag "punch out" force and occurs at a very early stage of the airbag deployment, but neck injuries are more likely induced by the "membrane" loading at a relatively late deployment stage [4]. It is believed that the side-effects would be minimized if

D. Jin and S. Lin (Eds.): Advances in Mechanical and Electronic Engineering, LNEE 176, pp. 487–493.
springerlink.com

the early development pattern of the airbag can be controlled, such as through an adaptive airbag [5]. Development of a proper airbag system depends on several factors, including the structure of the airbag, the inflation system, the ignition system and the ignition time etc. The traditional airbag would require quick response of a ignition system and a powerful inflation system, which may increase injury risks to OOP occupants and result in higher costs. To increase the efficiency of an airbag for OOP occupant protection, a new type of airbag-sandwiched tube-type airbag (STAB) [6] was developed and the airbag matching of STAB in rhomboid vehicle using virtual testing and regression analysis was studied.

2 The Numerical Model

2.1 The Airbag Model

The STAB is mainly made up of three parts: upper cushion, middle trachea and lower cushion. In the circumference direction, where the cushion links with trachea, placed flexible rubber to exert restriction to make the upper and lower cushion keep flat. This way can control the shape of the airbag, avoid the trachea to be crooked and out of shape because of the cushion inflate too thick. The middle trachea is divided into two kinds, the circumference six tracheas is one kind, they are used to connect the upper and lower cushions, when inflation, the air get into the airbag' lower cushion from inlet firstly, then flow into the upper cushion through the circumference six tracheas subsequently. The bottom of the center trachea is close, it means that, the center trachea could be inflated and stood upright until the air enters upper cushion, plays a supporting role. This design can avoid the high-speed air act on human body directly.

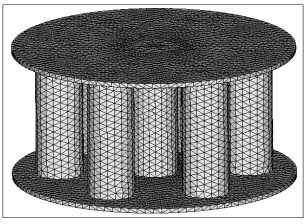

Fig. 1. The airbag FE model

Altair HyperMesh is used as a preprocessor to create the FE model of the airbag used in this study and the FE airbag model was constructed for simulation in LS-DYNA. The STAB system is modeled with 18408 Belyschko-Tsay membrane elements. The material properties of Nylon 66 are assigned to the membrane elements. The contact interface is defined between the airbag and the dummy's head, neck, chest and hands. The self-contact interface is also defined within the airbag system.

2.2 The Rhomboid Vehicle Model

The four wheels of rhomboid vehicle are arranged as rhombus, there is each wheel in front shaft and rear shaft respectively, which are steering wheels; on the right and left of the centre shaft there is each wheel respectively, which are driving wheels. The engine system is loaded in the middle of the chassis; the whole vehicle body takes the form of streamlined kinds of rhombus. The rhomboid vehicle is easier to operation, lighter, and has better aerodynamics performance as well as better performance of absorbing the collision energy, then can provide passengers with better protection.

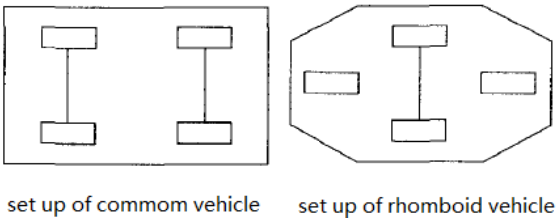

Fig. 2. The rhomboid vehicle set up

The rhomboid vehicle FE model was set up according to the real measurement and structure of the vehicle prototype, shown in Fig.3(a). There are 501265 nodes, 489513 elements in the whole model, including the frame, front suspension, rear suspension, vehicle body, driving system, seat, steering wheel and tires.

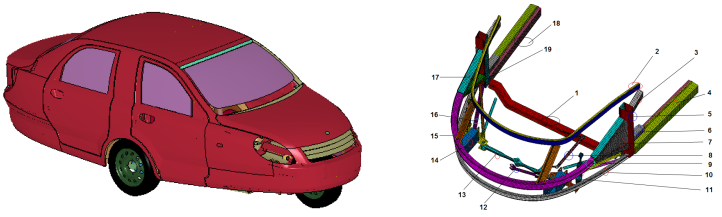

Fig. 3. (a) The rhomboid vehicle FE model (b) The material setting

The selection of material model is very important in FEM, the material setting of the rhomboid vehicle main parts are shown in figure 3(b), parts 2,9,10,14,15,16 are SPCC, yield limit is 180Mpa; parts 1,3,4,5,6,7,17 are SAPH440, yield limit is 395Mpa; parts 8,11,12,13 are rigid, yield limit is 210Mpa.

2.3 The Human Model

According to the test protocol of the C-NCAP frontal 100% rigid barrier impact test, a 50% HYBRID-III dummy with standard safety belt was set in the driver seat.

3 The Model Experimental Validation

3.1 The Airbag Model Validation

To support computational modeling efforts, the static airbag deployment test is performed. Fig.4 displays the simulation results as well as the test results of the airbag interior pressure. It is shown that the overall shapes of response obtained from simulations and those measured from tests are similar. So this computational model can be used as the base model in the further study.

3.2 The Whole Model Validation

The whole FE model are validated by comparing the results of test and simulation of the C-NCAP frontal 100% rigid barrier impact test, so the simulation condition is the same with real world test. According to the protocol of test, place a Hybrid Ⅲ 50th percentile male dummy in the driver seat, in other seats, the dummies are replaced by the counterweights of 78kg and 48kg, shown in Fig.5. And the testing speed is 50km/h.

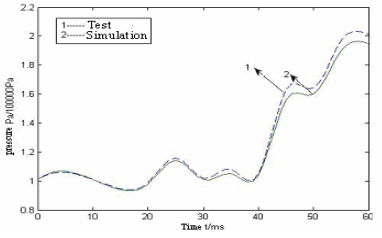

Fig. 4. STAB interior pressure in test and simulation

Fig. 5. The dummy setting

Fig.6 shows the B pillar acceleration, Fig.7 shows the dummy head acceleration of the test and simulation.

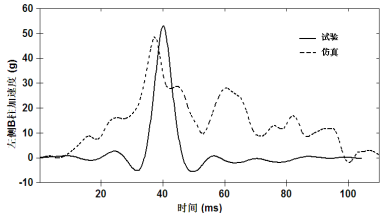

Fig. 6. The B pillar acceleration curve

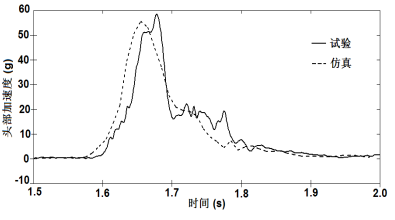

Fig. 7. The dummy head acceleration curve

It can be seen that the curves trend are the similar, so this computational model can be used as the base model in the further study.

4 The Airbag Matching in the Rhomboid Vehicle

4.1 Design Variables and Control Levels

The performance of airbag module might be affected by a number of the design parameters, including airbag structure, vent hole, inflator tank pressure characteristics, fabric material property etc, in this paper, the influence of inflator characteristics and trigger time are analyzed and discussed. The design variables and their control levels are shown in Table 1.

Table 1. Design variable and control levels

Design variable	Level		
	1(base line)	2	3
E=mass flow rate	Base-level	85%	115%
F=pressure slope	Base-level	85%	115%
G=trigger time	20ms	10ms	30ms

4.2 Definition of Object Function

According to the findings from the biomechanics research, the passenger vehicle accident investigation, and the laboratory crash test, head is the most vulnerable segment during airbag interaction with occupant. In order to evaluate STAB's protection performance synthetically, the minimizing occupant injuries, the head injury criterion HIC15 is chosen as the object function.

$$\text{Min } HIC = f(\mathrm{E},\mathrm{F},\mathrm{G}) \qquad \text{s.t.} \quad \begin{array}{l} 85\% \le \mathrm{E} \le 115\% \\ 85\% \le \mathrm{F} \le 115\% \\ 10 \le \mathrm{G} \le 30 \end{array}$$

4.3 Simulation and Results

After the formulation of design problem, full fact tests are conducted to provide enough representative test dataThe whole 27 simulation results are as following: 583.5, 442.3, 458.0, 533.0, 437.0, 452.5, 649.0, 478.5, 531.0, 466.8, 455.5, 478.0, 450.5, 465.8, 467.5, 466.5, 460.3, 470.0, 834.8, 652.3, 960.3, 749.0, 701.5, 884.5, 877.3, 833.8, 1140.3.

4.4 Results Analysis

The stepwise regression was used to analyze the simulation results, as table 2, 3, 4 shown.

Table 2. Analysis of variance

Source	DF	SS	MS	F-value	Prob>F
Model	6	941769	156961	48.43	<0.0001
Error	20	64818	3240.89		
Total	26	1006586			

Table 3. Fitting effect

Root MSE	57.49	R-square	0.9442
Dep Mean	606.96	AdjR-sq	0.9146
C.V.	9.47		

Table 4. Coefficient of stepwise analysis

Variable	DF	Parameter Estimate	Standard Error	F	Prob>|F|
INTERCEP	1	8235.74	1278.01	41.52	<0.0001
X1	1	-14763	2203.94	44.87	<0.0001
X2	1	-1617.13	735.85	4.83	0.0399
X3	1	-36.78	11.04	11.10	0.00033
X11	1	6651.23	1032.94	41.46	<0.0001
X12	1	1897.22	730.40	6.75	0.0172
X13	1	41.92	10.96	14.64	0.0011

The regression equation based on the simulations is as follows:

$$HIC15 = 8235.74 - 14763E - 1617.13F - 36.78G + 6651.23E^2 + 1897.22E \cdot F + 41.92E \cdot G$$

The determination coefficient R^2 is 94.42%, the P value <0.0001, therefore the regression equation is credible.

Solving the regression equation and get the optimized value, when mass flow rate equals 95.66% base line, pressure slope equals 85% base line, trigger time equals 10ms, HIC15 achieves minimum of 401.2. Whe we proved the regression equation credibility and used above optimal values for design parameters with LS-DYNA code, we obtained the HIC15 from the simulation is 429.3, the relative error is 6.5%, so the formulation is fairly reliable in the given range of control levels.

5 Conclusions

This paper studied on the airbag matching of the new sandwiched tube-type airbag in rhomboid vehicle using virtual testing and regression analysis. Results show that there are major parameters that are sensitive to occupant injuries, the order of influence of the design variables on the peak value of head injury is as follows: mass flow rate> trigger time> pressure slope. The STAB system has good potential to provide effective protection to occupants as the traditional airbag system would do when it applied in the new shape of vehicle-the rhomboid vehicle.

Acknowledgments. The study is sponsored by “The Return-from-abroad Foundation of Ministry of personal of the P.R.China(2010)”, “111 Program (No. 111-2-11)”and the Autonomous Subject Program of the State Key Laboratory of Advanced Design and Manufacturing for Vehicle Body (No. 60870004).

References

1. Morris, C.R., Zuby, D.S., Lund, A.K.: Measuring Airbag Injury Risk to Out-Of-Position Occupants. ESV16, ; Paper number 98-S5-O-08, 1036-1043
2. John, W., John, D., Joseph, D., et al.: Assessment of airbag deployment loads with the small female hybrid III dummy. In: Proceedings of the 37th Stapp Car Crash Conference, pp. 121–132; SAE paper, No 933119
3. Axel, M., Heinz-dieter, A.: The airbag folding pattern as a means for injury reduction of out-of-position occupants. In: Proceedings of the 39th Stapp Car Crash Conference, pp. 19–32; SAE paper, No 952704
4. Mu, W.: Driver out-of-position injuries mitigation and advanced restraint features development. In: ESV 17th Conference
5. Yang, J.K., Håland, Y.: Modeling of adaptive passenger airbag systems in car frontal crashes. In: Proc. of the 15th Int. Technical Conf. on the Enhanced Safety Vehicles, Melbourne, Australia, May 13-16, pp. 486–501 (1996); SAE paper no. 976041
6. Zhong, Z.H., He, W.: Sandwiched Tube-Type Airbag (2005); Patent CN200410046609.9
7. Roychoudhury, R., Sun, D., Hamid, M., Hanson, C.: In: 5th Percentile Driver Out of Position Computer Simulation (2000); SAE paper, No 2000-01-1006

Simulation and Optimization of Vehicle Ride Comfort on Random Road

Lin Hu[1], Jing Huang[2], and Fangyi Li[1]

[1] School of Automotive and Mechanical Engineering, Changsha University of Science and Technology, 410004 Changsha Hunan, China
hulin888@sohu.com
[2] State Key Laboratory of Advanced Design & Manufacture for Vehicle Body, Hunan University, 410082 Changsha Hunan, China

Abstract. Vehicle ride comfort is one of the most important performances of vehicle; the research of automotive ride comfort is getting more and more important. In this paper, the subsystems dynamics analysis models were established separately, such as front suspension, rear suspension, person-chair system, steer system, tire and transmission subsystems, and then a vehicle dynamics analysis model is assembled by these subsystems in software-ADAMS. The dynamics analysis model is validated by the sample vehicle experiment results and used to analyze the ride comfort on random road. Finally, the influence and optimization of the spring stiffness, the shock absorber damping and the tire stiffness on vehicle ride comfort is studied.

Keywords: Vehicle, Ride comfort, Simulation, Optimization.

1 Introduction

Smoothness is called the riding comfortableness。 It is the main performance of the modern automobile with high speed and high efficiency. The target quality of the smoothness affects directly the performance display, the travel system's life as well as human's working efficiency and health. So how to guarantee the automobile has good smoothness has already attracts designers' attention. In recent years, with development of the computer technology, the theory of random vibration, the testing method as well as the systems dynamics, Simulation of vehicle ride comfort is to be more comprehensive and much closely approach to the fact.

Based on above purpose, this article used the software ADAMS, which developed with multi-body system dynamics to establish the dynamics simulation model of the full vehicle, and has made the simulation and analysis of ride performance. Then it gives the appraisal to the A vehicle through the ISO2631-1997 principle.

2 The Model of Entire Vehicle Dynamics Simulation

The automobile is a complex system which is made of the wheel, suspension, automobile body, engine, transmission, steering subsystem and so on. When we

D. Jin and S. Lin (Eds.): Advances in Mechanical and Electronic Engineering, LNEE 176, pp. 495–501.
springerlink.com

discuss the ride comfort. We mainly consider the vibration caused by the road surface roughness. The road input passes to the human body through the tire, suspension, the seat cushion that is elastic damping part. These constitute the automobile vertical vibration system interacted. In order to improve computing speed of the model, we can simplify secondary influence factors to ride comfort under the condition in which the model is accurate.

2.1 Front and Rear Suspension System

The front suspension of the vehicle is the double wishbone independent suspension. It mainly contains the up-down cross arm, shock absorber, helical spring and stabilizer bar. The rear suspension is the type of multi-link independent suspension which mainly contains the helical spring, the shock absorber, the longitudinal propelling rod, stabilizer bar and so on. Front end of the longitudinal propelling rod is connected with the automobile body and rear end is connected with the suspension. This is used to transmit the traction and braking effort.

The front and rear shock absorbers are displaced by restrains (DAMPER). Because the shock absorber damping is a non-linearity, we need to load damping characteristics of an damping shock absorber into DAMPER property file by the SPLINE curve. Similarly, we load the helical spring elastic characteristic into SPRING property file by the SPLINE curve. These could guarantee the precise of the model.

2.2 Steering System

The steering system of the vehicle is the rack and pinion steering system, and mainly includes the steering wheel, steering axle, steering column, drive shaft, steering tie rod, gear rack diverter and the boost steering system.

According to the corresponding connection relations, we can add on the corresponding restraint to constitute the steering system in ADAMS/CAR. The assist characteristic of the assist steering system can be indicated with property file which is possible to use similar method with the damping characteristic curve. This may the accurate simulate force outputs of the steering system during its steering.

2.3 Human-Chair System

Simplify the human-chair system model. The human body quality is 75Kg, the chair elastic characteristic and damping characteristics realizes with the rubber bush, of which the elastic characteristic and damping characteristics may use property file to realize. Using the rubber bush is possible reasonable to simulate force that person receives sitting in the chair from each direction movement.

Because the automobile body physique has no influence to the simulation result in the simulation of the vehicle comfort, we can simplify the automobile body to the spheroid which contains all physical property parameter of the automobile body.

2.4 Entire Vehicle Model Establishment

We establish the subsystem model assembled with ADAMS/CAR, and then we guarantee the model movement to be normal through the suitable debugging. Entire vehicle model is shown in Figure 1.

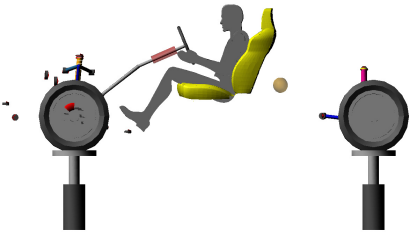

Fig. 1. Entire Vehicle Model

3 Simulation Analysis of Entire Vehicle Model

3.1 Establishment of Tire Model

The ADAMS software has provided 4 kinds of tire models, which are named the Fiala model, UA (university of Arizona) model, Smithers model and DELET model. In addition the user also may define the model. After we evaluate characteristic of these 4 kind of tire models and consider this topic need, so we use the DELET model. The DELET model data file In the ADAMS software is composed by eleven together, each one has the independence data unit which may simulate the tire separately the different operating mode and has the high precision. Also this kind of tire model also has the good toughness.

3.2 Road Surface Productions

The road surface structure needs to satisfy certain random distribution rule, and it also conform to the road surface which the ADAMS tire model requests. This is the main point and difficulty to establish model. According to National Standards GB7031-86"Vehicles Vibrate Input-Road surface Flatness Expression Method", the road surface undulation displacement power spectral density fitting expression uses the equation below:

$$G_d(n)=G_d(n_0)\left(\frac{n}{n_0}\right)^{-w} \quad n>0 \tag{1}$$

Here:n_0—Reference frequency, n_0=0.1m^{-1};$G_d(n_0)$—Road surface undulation coefficient,m^2/m^{-1}; $G_d(n)$—Road surface undulation, m^2/m^{-1}; w—Frequency index, Empirical value $w=2$.

According to the spatial frequency and the temporal frequency relations, its expression is

$$f = v \times n \qquad G_q(f) = \frac{G_q(n)}{y} \tag{2}$$

Here, f is temporal frequency, n is vehicle speed

$G_q(f)$—Road surface time displacement power spectral density.

Through the research of the r power spectral density of road roughness, time and the inverse transformation function in the ADAMS software, we develop the visual software with VC++ to generate the road surface which is the B level road surface this article needs.

4 Random Road Surface Smoothness Analysis

To simulate ride comfort experiment of the entire vehicle in full load operating mode according to the ride comfort random input travel testing[2] of our country. In this article the automobile uses the speed of 70 Km/h commonly used to travel with the uniform speed in the B level road surface that the random road surface input travel testing method stipulated. In the survey of ride comfort to the automobile, ISO2631-1:1997(E) defines the sitting posture of man model inspired[3]. When we make comfortable evaluation, we not only considerate line vibrations in 3 direction on chair area of bearing place, but also consider angular oscillations of 3 directions as well as line vibrations in 3 direction on the chair seat back cushion and foot area of bearing two entrance point. Altogether there are 3 entrance points 12 axial vibrations. This standard is that the human body has different sensitivity to the different frequency vibration. It gives each axial 0.5~80Hz frequency weighting function (asymptote), we consider the different point and axial vibrations which affected to the human body and also give longitudinal vibration axis weighting factor k. Table 1 has given 3 entrance points and 12 axial that select frequency weight function and corresponding axis weighting coefficient k separately.

The weighting acceleration root mean square value in x, y and z directions, can be obtained by integral equation of the auto power spectral density function which this longitudinal vibration acceleration function is

$$a_{wi} = \left[\int_{80}^{0.5} W_i^{\,2}(f) G_{ai}(f) df \right]^{\frac{1}{2}} \tag{3}$$

Here, a_{wi} — Weighting acceleration root mean square value in x, y and z directions, $i = x, y, z$

$G_{ai}(f)$—Weighting acceleration power spectral density function in x, y and z directions, $i = x, y, z$

w_i —Frequency weighting function in x, y and z directions, $i = x, y, z$ .Frequency weighting function $w(f)$ (asymptote) may be expressed by following formula:

$$w_k(f)=\begin{cases}0.5 & (0.5<f<2)\\ f/4 & (2<f<4)\\ 1 & (4<f<12.5)\\ 12.5/f & (12.5<f<80)\end{cases}\qquad w_c(f)=\begin{cases}1 & (0.5<f<8)\\ 8/f & (8<f<80)\end{cases}$$

$$w_e(f)=\begin{cases}1 & (0.5<f<1)\\ 1/f & (1<f<80)\end{cases}$$

$$w_d(f)=\begin{cases}1 & (0.5<f<2)\\ 2/f & (2<f<80)\end{cases}$$

The various pictures above express separately the acceleration and power spectral density curve of the 3 points measured. Figure2 to Figure7 expresses the three direction line accelerations and angle acceleration on the chair bearing surface. Figure8 to Figure10 expresses three direction line accelerations on the backrest bearing surface. Figure11 to Figure13 expresses the three direction line accelerations on the foot bearing surface.

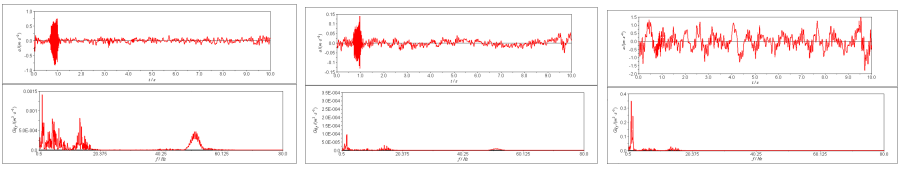

Fig. 2. The curve of the longitudinal/ lateral/ vertical acceleration and acceleration power spectral density values on the chair

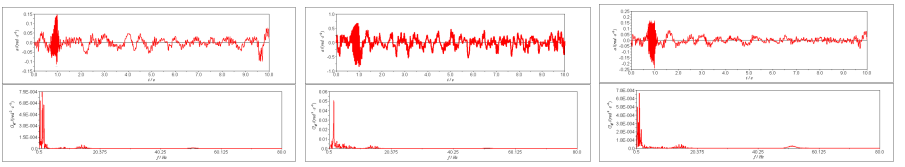

Fig. 3. The curve of the rolling/ pitch/ yaw angle acceleration and acceleration power spectral density values in this direction on the chair area of bearing

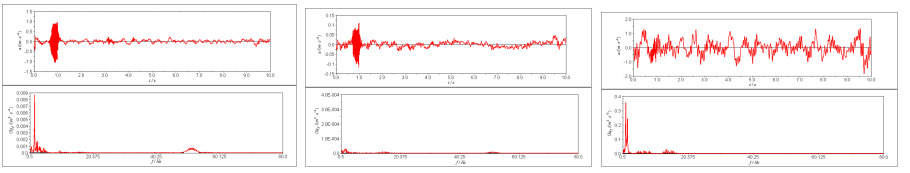

Fig. 4. The curve of the longitudinal/ lateral/ vertical acceleration and acceleration power spectral density values on the backrest

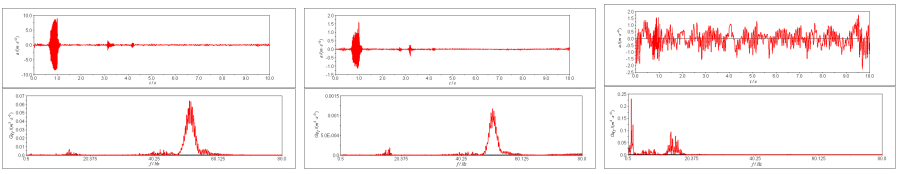

Fig. 5. The curve of the longitudinal/ lateral/ vertical acceleration and acceleration power spectral density values on the foot bearing surface

In the chart the upper part expressed the line acceleration in this direction, the lower part expresses the acceleration power spectral density curve in this direction.

Through computation, the weighting acceleration root mean square value and total weighting acceleration root mean square value of the vehicle at the speed of 70 Km/h are followed in the Table 1.

Table 1. Each axial weighting acceleration and total weighting acceleration of the vehicle speed at 70 Km/h

Position	Name of Coordinate Axis	Frequency Weighting Function	Axis Weighting f Coefficient k	Weighting Acceleration (rms) a_w $m \cdot s^{-2}$	Peak Value Coefficient k
Chair area of bearing	x_s	w_d	1.00	0.0300	4.9
	y_s	w_d	1.00	0.0069	4.2
	z_s	w_k	1.00	0.3009	5.1
	r_x	w_e	0.63	0.0092	4.3
	r_y	w_e	0.40	0.0302	4.9
	r_z	w_e	0.20	0.0028	4.1
Backrest	x_b	w_c	0.80	0.0514	4.2
	y_b	w_d	0.50	0.0029	4.1
	z_b	w_d	0.40	0.1477	4.7
Foot	x_f	w_k	0.25	0.0353	4.4
	y_f	w_k	0.25	0.0048	4.1
	z_f	w_k	0.40	0.1582	5.4
$a_y = (\sum a_{yj}^{\,2})^{\frac{1}{2}}$				0.3785	

5 Conclusions

Through the survey and evaluation method in international standard ISO2631-1:1997(E), considering the influence of the different position as well as the different direction vibration to the human body, we may reflect comprehensive and accurately how comfortable the person feels riding this vehicle. After above simulation analysis

we may know that when the automobile goes on the B level road surface at the speed of 70 Km/h, its total weighting acceleration root-mean-square value is small, this shows its smoothness is good, and it reflects this vehicle has good ride comfort. Also computed result above may provide the instruction to optimize this vehicle smoothness further.

Acknowledgments. The study is sponsored by "The Return-from-abroad Foundation of Ministry of personal of the P.R.China(2012)".

References

1. Sheng, Y.Z.: Automobile Theory. Machinery Industry Press, Beijing (2002)
2. Testing Method of Vehicle Ride Comfort under Pulse Input. The National Standard in People's Republic of China GB/T5902 (1986)
3. ISO 2631-1: Mechanical vibration and shock—Evaluation of human exposure of human exposure to whole-body vibration- Part1: General requirements (1997)

Research on Optimal Guidance Law of Autonomous Underwater Vehicle

ChangBo Liu and Hao Ding

Navy Submarine Academy, Qingdao, Shandong, China

Abstract. A high performance guidance law can help Autonomous Underwater Vehicle (AUV) to catch target faster and with less energy. The equations of relative motion between AUV and target are built firstly. Then the optimal control theory is used, and a new AUV nonlinear optimal guidance law is obtained by considering of minimum energy controls in the course of pursuit. Simulation is taken on to verify the performance of the optimal guidance law. And the results show that comparing with the H∞ guidance law, the optimal guidance law can help AUV overtake target in less time, and the azimuth angle of target line of sight is always staying at the initial numerical values. Furthermore, the normal load doesn't increase along with the decrease of distance between AUV and target. So the optimal guidance law is effective for AUV.

Keywords: guidance law, optimal control, AUV.

1 Introduction

The performance of guidance law is a key factor for AUV to catch target successfully. The traditional guidance law is invalid when the maneuverability of target is good[1]. So it is necessary to design effective nonlinear guidance law to help AUV catch target.

Many scholars have studied the application of nonlinear optimal control in aerocraft [2-7]. The guidance strategy of AUV is same as aerocraft in nature. There are more and more works on nonlinear guidance law of AUV these years[8-10]. However, there are fewer researches on nonlinear optimal guidance law for AUV. For example, the reference [10] studied on a nonlinear optimal guidance law for torpedo in case of hitting a target vertically. While the target's maneuverability is getting better and better, it is necessary for AUV to design nonlinear optimal guidance law in order to catch target effectively.

Firstly, the relative motion model of AUV and target is built. Then the nonlinear optimal control theory is used to get the optimal guidance law of the system. Finally, the guidance performance is compared with H_∞ guidance method by simulation.

2 Description of the Problem

Both AUV and target are taken as particles and their relative motion model is show as figure 1. Without loss of generality, we can make such assumption, the target at point S and AUV at point O at a certain time. The parameters are defined as follows: R is the

D. Jin and S. Lin (Eds.): Advances in Mechanical and Electronic Engineering, LNEE 176, pp. 503–507.
springerlink.com

distance between the AUV and target, line OS is called the target line of sight, q is the azimuth of the target line of sight, q_K is the ideal course angle, q_T and q_S are the real course angle of AUV and target, v_T and v_S are the velocity of AUV and target, u is the acceleration of AUV and is also the controller. The relative motion model between AUV and the target can be written as:

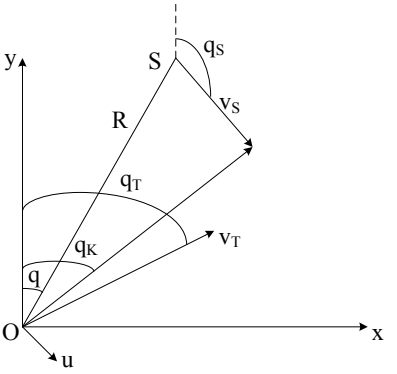

Fig. 1. The relative motion of AUV and target

$$\dot{y}(t) = v_S(t)\cos q_S(t) - v_T(t)\cos q_T(t)\,. \tag{1}$$

$$u(t) = v_T(t)\dot{q}_T(t)\,. \tag{2}$$

For obtaining the optimal trajectory, the relative motion model can be linearized at angle q_K:

$$\dot{y}(t) = v_S(t)\cos q_K(t) - v_T(t)\cos q_K(t) + v_T(t)\sin q_K(t)\Delta q\,. \tag{3}$$

$$u(t) = v_T(t)\dot{q}_K(t)\,, \tag{4}$$

where Δq is the difference between q_K and q_T. The assumption can be made as:

$$\dot{y}(t) = v_y(t)\,,\ \ p(t) = \dot{v}_T(t) \Big/ v_T(t)\,. \tag{5}$$

We can get that:

$$\dot{v}_y = pv_y - pv_S\cos q_S - u_y\,, \tag{6}$$

and $u_y = u\sin q_K$.

So the state equation can be written as follows:

$$X = AX + BU + W\,, \tag{7}$$

where $X = [y(t), v_y(t)]^T$, $A = \begin{bmatrix} 0 & 1 \\ 0 & P \end{bmatrix}$, $B = [1,-1]^T$, $U = u_y$, $W = [0,-pv_S\cos q_S]^T$.

3 Nonlinear Optimal Guidance Law

The optimal guidance law u_y makes the performance parameter J reach its minimum when $y(t_f)=0$, where

$$J = \frac{1}{2}\int_0^{t_f} [u_y(t)]^2 \, dt . \tag{8}$$

The Hamilton function can be constructed as:

$$H = \frac{1}{2}u_y^2 + \lambda^T AX + \lambda^T BU + \lambda^T W . \tag{9}$$

The equations can be get as following:

$$\dot{X} = \frac{\partial H}{\partial \lambda} . \tag{10}$$

$$\dot{\lambda} = -\frac{\partial H}{\partial X} = -A^T \lambda . \tag{11}$$

And the control equation is:

$$\frac{\partial H}{\partial u_y} = 0 . \tag{12}$$

The initial and finishing conditions are:

$$y(0) = y_0 , \quad y(t_f) = 0 , \quad \lambda(t_f) = 0 . \tag{13}$$

Finally, we can obtain the optimal guidance law as following:

$$u_y(t) = \frac{G(t)}{t_k^2}[t_{k0} v_y(t) + y(t) + (t_{k0} - t_k) v_T \cos q_T] , \tag{14}$$

where $t_k(t) = -\dfrac{\int_t^{t_f} v_T(\tau) d\tau}{v_T(t)}$, $t_{k0}(t) = t_f - t$, $G(t) = \dfrac{t_k^3(t)}{\int_t^{t_f} t_k^2 d\tau}$.

On the other hand, the load character of AUV is an important factor to appraise the guidance method performance. In same condition, the less the load is, the better the performance is. The normal load is defined as:

$$n = \frac{|u_y|}{g} , \tag{15}$$

where g is the acceleration of gravity constant.

4 Simulation and Discussion

To verify the performance of the nonlinear optimal guidance law, the simulation is taken on and compared with the H_∞ guidance law. The initial conditions and the parameters of the system are assumed as: q=π/3rad, q_T=π/6rad, q_S=4π/3rad, R=1000m, v_T=30m/s, v_S=20m/s. The results are shows in figure2 to figure 4, where the real line stands for the optimal guidance law and the broken line stands for the H_∞ guidance method.

Figure2 to figure 4 show that when the nonlinear optimal guidance law is applied, the AUV take 100.3s to overtake the target, the azimuth of the target line of sight q stays at the initial numerical value, and the oscillation amplitude of normal load n decreases gradually, and finally value is 0.1. While under the H_∞ guidance method, the AUV take 104.8s to overtake the target, the oscillation amplitude of q increase gradually, and the maximum value are 1.1 rad. When AUV comes close to the target, the numerical value of n increased to 0.2.

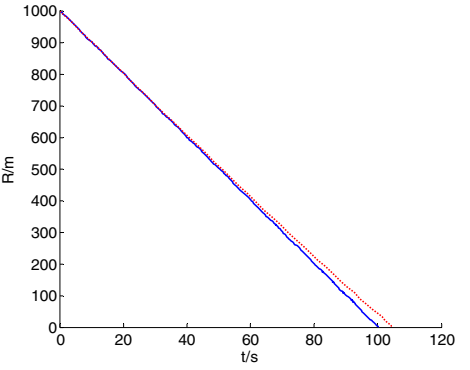

Fig. 2. The curves of distance between AUV and the target

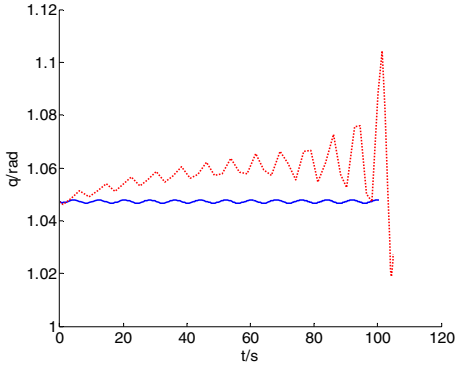

Fig. 3. The curves of azimuth of the target line of sight

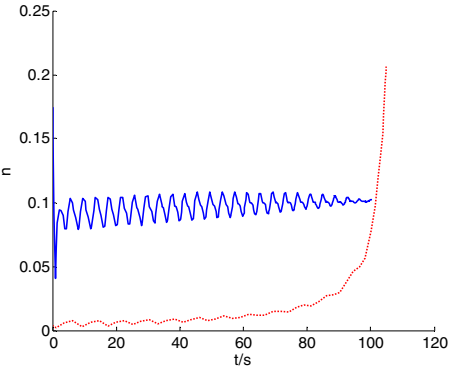

Fig. 4. The curves of AUV's normal load

5 Conclusion

The nonlinear optimal theory is used to design guidance law for AUV. The performance of the nonlinear optimal guidance law is validated by simulation. The results show that comparing with the H_∞ guidance method, the optimal guidance law can make AUV overtake the target in less time, the azimuth angle of the target line of sight is always staying at the initial numerical value and the oscillation amplitude of normal load decreases gradually. In a word, the performance of the nonlinear optimal guidance law is better than the H_∞ guidance method obviously.

References

1. Liu, X.G., Song, K.: Study on optimal terminal guidance law for maneuvering targets. Journal of Air Force Engineering University (Natural Science Edition) 3, 18–21 (2002)
2. Xu, M., Wu, Q.X., Jiang, C.S.: Research on three-dimensional optimum guidance law for air-to-air missile attacking maneuvering target. Aero Weaponry 6, 7–12 (2005)
3. Vinh, N.X., Kabamba, P.T., Takehira, T.: Optimal Interception of a Maneuvering Long Range Missile. Acta Astronautic 48, 1–19 (2001)
4. Cai, L.J., Zhou, F.Q.: One Nonlinear Optimal Missile Guidance Law. Journal of Astronautics 20, 36–40 (1999)
5. Luo, D.L., Wu, W.H., Han, Q., Shen, C.L.: Study on optimal proportional law. Aeroplane Design 3, 45–49 (2004)
6. Tsao, L.P., Lina, C.S.: A new optimal guidance law for short-rang homing missiles. Proc. Natl. Counc. 24, 422–426 (2000)
7. Wang, Y.D., Zhou, J., Guo, J.G.: An optimal guidance law based on zero miss-distance. Computer Simulation 26, 57–60 (2009)
8. Ding, H., Wang, D.S., Wang, H.: Design of nonlinear guidance law for torpedo. Torpedo Technology 15, 18–21 (2007)
9. Ding, H.: Research on nonlinear control in entire trajectory and guidance strategy in trace for torpedo. Naval University of Engineering, Wuhan (2009)
10. Jing, W., Yan, W.S.: A Kind of optimum guide law for a torpedo hitting a target vertically. Journal of Missile and Guidance 25, 138–140 (2005)

GVMS: A GPS/GSM Based Vehicle Management System for the Army

Zhidong Sun[1] and Jiandong Sun[2]

[1] 71573 Troops, No.33, Junmin Road, Laiyang, Shandong, China
[2] College of Software, Shandong University, Jinan, China
zdsun71573@gmail.com, jdsun@sdu.edu.cn

Abstract. In the army, managerial capacity for a large number and various types of vehicles is limited, accuracy is not high, and management method is simple and not flexible enough. GPS/GSM based Position System provides real-time and accurate positioning and Vehicle Management System offers various ways to process and control the position information. GVMS is proposed to combine the advantages of both systems which is successfully implemented and evaluated on twenty vehicles in the military areas. Management and military combat have improved so much.

Keywords: GPS, GMS, Vehicle Management System.

1 Introduction

Millions of vehicles should be well managed in the army currently while these vehicles are always in various types and conditions. Without the powerful management systems, it is difficult to control the various vehicles especially in wartime. Vehicle Management Systems help to manage a vehicle of vehicle by gaining control of travel records and time. These advanced systems could help to manage fuel consumption, velocity, load balancing, vehicle positioning. To construct a vehicle management system, we can make use of location finding techniques, asset tracking, etc. Invariably the success, accuracy and economics of a Vehicle Management System are dependent on the type of location finding techniques used. Location finding techniques can be applied to the vehicle management system to solve these above problems.

Since Global Positioning System (GPS) [1] has been widely used in many management systems to find the location, it can be well used into Vehicle Management as the location finding technique. GPS is a satellite-based navigation system made up of a network of 24 satellites placed into orbit by the U.S. Department of Defense. GPS was originally intended for military applications, but in the 1980s, the government made the system available for civilian use [2]. GPS works in any weather conditions, anywhere in the world, 24 hours a day. There are no subscription fees or setup charges to use GPS. GPS satellites circle the earth twice a day in a very precise orbit and transmit signal information to earth. GPS receivers take this information and use triangulation to calculate the user's exact location. GPS enable the tracking of all kinds of mobile assets accurately and provide their real time

D. Jin and S. Lin (Eds.): Advances in Mechanical and Electronic Engineering, LNEE 176, pp. 509–514.
springerlink.com

positions to the user on a 24 by 7 basis over the General Packet Radio Service (GPRS)/GSM link. While the GPS provides the latitude/longitude information of the mobile asset a given time, this information can be transmitted to any place using the GPRS radio link. Location finding techniques are of various kinds with each technique implying impacts on requirements like accuracy, coverage, location determination, speed and ultimately, costs for the operator, just to name a few. Location finding techniques can be broadly divided into Network based techniques, use of smart devices at fixed locations and GPS based techniques. Geographic information system, geographical information science, or geospatial information studies is a system designed to capture, store, manipulate, analyze, manage, and present all types of geographically referenced data. In the simplest terms, GIS is the merging of cartography, statistical analysis, and database technology [3]. A GIS can be thought of as a system--it digitally creates and "manipulates" spatial areas that may be jurisdictional, purpose or application-oriented for which a specific GIS is developed. Hence, a GIS developed for an application, jurisdiction, enterprise or purpose may not be necessarily interoperable or compatible with a GIS that has been developed for some other application, jurisdiction, enterprise, or purpose. What goes beyond a GIS is a spatial data infrastructure (SDI), a concept that has no such restrictive boundaries.

There are already some integrated management systems which can be used in vehicle managing. Currently, the vehicle managing system communication platform includes conventional communications network, cluster communication network, GSM network, CDPD (Cellular Digital Packet Data, cellular digital packet data) network and the GPRS network and other programs [4]. Communication platform in front of the four have their own drawbacks. Conventional communication network channel utilization is low, usually a large district system, the coverage is small, only build a small system, although the cluster communication network channel utilization has increased, it takes time channel is established, the system in TDMA (Time Division Multiple Access) transmission mode, the system is too large, real-time is not assured, and the error rate is relatively high. GSM short message service communication is used more as a, because of its large coverage area, and can roam the country [5]. However, the delay problem is the system bottleneck, especially in network messaging center over-load, severe obstruction and real-time performance in the vehicle managing system, cannot be guaranteed. Although the CDPD network has higher transmission speed, the area that the network construction covers is relatively small. Combination of transmission rate, frequency utilization, network latency, coverage, and many other considerations, we use the GPRS network as a communications platform, as transmission speed GPRS with a large, high-frequency utilization to support multiple network protocols, and supports roaming and so on. GPRS-based vehicle monitoring system is full use of GPRS to support IP protocol and can access external data network is characterized by realization.

To combine these techniques and get better performance, we present GVMS: a GPS/GSM Based Vehicle Management System .It combines the applications of GIS, GPS, GPRS and the Internet for tracking of vehicle vehicles. As a component of an enterprise solution, it is designed to manage and track a large vehicle. The key features of the system are an open-source GIS platform, real-time location information update, and a web-based user interface.

2 GVMS Architecture

A high level architecture diagram that shows various building blocks of the solution for mobile asset tracking is given as Figure 1.

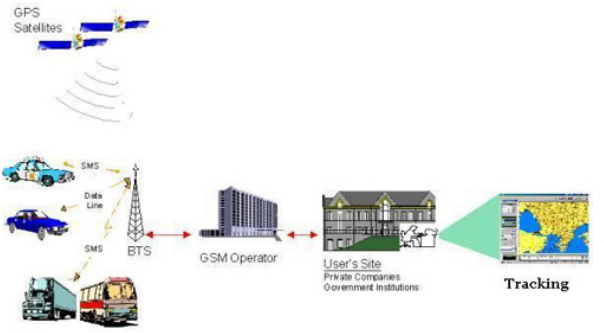

Fig. 1. Architecture of GVMS

Inside the Vehicle, there needs to be an Asset Track box which would need to interface to the vehicle data port, typically called On Board Diagnostics port, version II (OBDII). Through this OBDII port, the Asset Track box can obtain various parameters as indicated below.

Engine parameters: Speed, Engine Throttle, Brake Status, Gear Selected, Active Handling (traction control), Drive Train setting, RPM, service due, Odometer, Mass Airflow Sensor (MAF), etc. Safety parameters: Seat Belt, ABS, Air Bag (multilevel) Front/Rear, braking action or lack thereof, Fuel Tank Level, Seat Occupancy, Error codes, etc. Other: Front/back light status, headlight dip status, indicator status, windscreen wiper status, etc.

There are several parameters that can be sampled and based on these samples, decisions about various attributes of the vehicle can be made to take appropriate and necessary actions such as killing the ignition to various other activities.

A system level block diagram of the various components for such a monitoring system is given in Figure2. It is a standard N-tier model using a web services based architecture. Asset Track Box is the device installed on the car. Asset Track Box interfaces with the Car Engine Management System using a CAN Interface through the OBDII port for getting the speed, forces and related information. It would also interface with the onboard GPS unit to get the position information. The data is transferred to the Backend DB gateway using HTTP/SOAP or relevant protocol over a GPRS network.

A network-load-balanced server cluster can be used to implement a high-available and reliable gateway server to handle the high volume of incoming data. Each of the cluster server can be configured to scale-up by increasing the in system resources (CPU, memory) and scaled-out by adding more servers to handle future increases in data volumes, on demand.

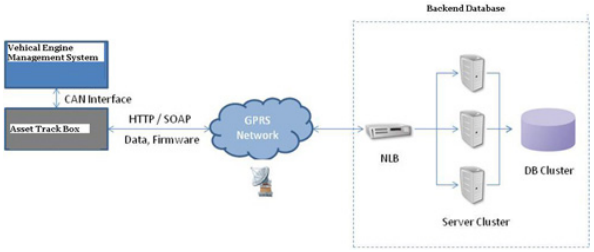

Fig. 2. System Level Block Diagram

The data received by the gateway server cluster is stored, after verification, into a DB Cluster (MS-SQL or Oracle Database). A robust Asset Track box hardware and software architecture enables system upgrades to these boxes remotely (both firmware and system software including applications) and enables the possibility of deploying additional services above the standard features on this box as they become available or provide a simple upgrade to existing application services. A device management feature takes care of roll back of the software versions to previous stable versions in the event of a new upgrade being detected to be not fully operational.

3 Details of GVMS Systems

Various building blocks and our solution approach and technology recommendations are discussed in this section:

3.1 Hardware Specifications

The tracking unit collects the location information via the GPS, formats this information into a system-specific packet format and sends it to the server via GPRS. If GPRS is unavailable at any time, time-stamped data packets are stored in a temporary storage unit to be uploaded when GPRS becomes available again. Thus, the movement information of a vehicle is not lost even in the event of a communications failure.

Asset Track Box is the device that will be installed in the vehicle (independent of Make or Model) and will transmit data about speed, position, forces etc through the GPRS network to a gateway server by interfacing appropriately with the OBDII data port of the vehicle. The device will have GPS capability to provide real-time position data. This device will also receive periodic firmware updates from the server when an update is available. A proposed hardware and software specification for this device is given below. This is a preliminary specification and might change based on the final requirements.

The GPS chipset/CPU is the main operational unit of the tracking device. It communicates with each of the other operational units via its I/O interfaces. The GPS receiver within the tracking unit will collect the latitude, longitude and speed information and send to the microcontroller. Then the GSM module communicates with the microcontroller to access and send this data to the server via a previously

established GPRS connection. First, the unit will establish a GPRS connection with the server, and then establish a TCP/IP socket connection with the data sent as IP data packets over this connection. The general hardware sample is shown in Figure 3.

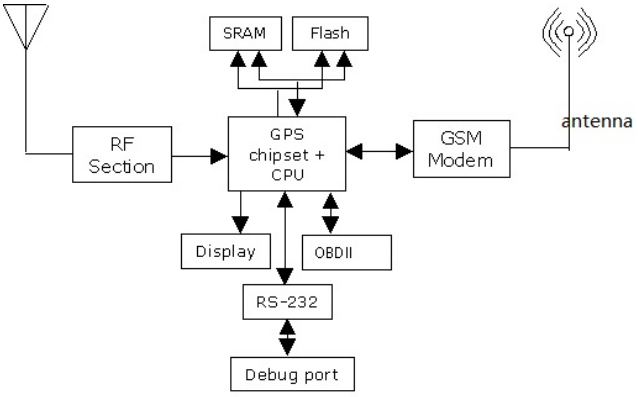

Fig. 3. General Hardware Sample Diagram

3.2 Software Specifications

Software stack on the Asset Track Box can be based on an embedded Operating System like Embedded Linux or XP-Embedded. Our recommendation is to use embedded Linux, but the choice would depend upon the hardware and the integration API with the Car Engine Management System. Java or C/C++ can be used if the platform is Linux. There could be a software frame work which may be required to make some of these features seamless for integration and upgradability.

Since GVMS is web-based, the main software components of the system are the socket communication server, the web server work and the GIS map server. The socket communication server is the central server component that communicates with the tracking units. It establishes TCP/IP socket connections with the remote hardware units. When a client (a remote tracking device) connects, the server will authenticate and acknowledge the client. Then, the server will The web application will retrieve the data from the database server and do preprocessing for further operations as requested by the user.

Communication between Asset Track Box and the gateway server can be implemented using HTTP/HTTPS/SOAP protocols over the GPRS network. Data will be sent to the gateway server using HTTP/SOAP protocols. Firmware and application updates from gateway server to the Asset Track Box will be using proprietary protocols implemented over standard HTTP/SOAP. Any communication to the gateway will be authenticated and packets encrypted using SSL/HTTPS. The main geo information components are Locations, Geo-fences, Routes and Tours. Results from the test-bed shown that user can monitor and track the real-time physical location and conditions of their vehicles via Internet or Short Message Service (SMS).

4 Conclusions

The opportunities created by Vehicle Management Systems are immense and it is likely to have a far-reaching impact. For the GIS solution providers, this pro-vides the opportunity of taking the power of GIS technologies and blending it with new systems to gain wider grounds.

With the success of the case study in the army, GPS-GSM is viable solution for a Vehicle Management System because of its universal appeal to all scenarios whether within city limits or covering remote areas. Smart Devices could be a very good option for fixed route Fleet services, which do not require real time tracking of vehicle because of its cost effectiveness. However, for the consumer and the implementers a careful understanding of service requirements, availability of technologies and the economics will define the kind of and the alternatives of a Vehicle Management System to be used.

The proposed system is successfully implemented and evaluated on twenty vehicles including buses and cars in some areas. Results from the test-bed shown that user can monitor and track the real-time physical location and conditions of their vehicles via Internet or SMS. The web-based fleet management software also helped the army to manage vehicles more effectively.

References

1. Badino, H., et al.: Visual topometric localization. In: IEEE Intelligent Vehicles Symposium (IV), pp. 794–799 (2011)
2. Rantakokko, J., et al.: Accurate and reliable soldier and first responder indoor positioning: multisensor systems and cooperative localization. IEEE Wireless Communications 18, 10–18 (2011)
3. Jaehoon, J., et al.: Trajectory-Based Data Forwarding for Light-Traffic Vehicular Ad Hoc Networks. IEEE Transactions on Parallel and Distributed Systems 22 (2011)
4. Chao, G., Jiming, L.: Modeling and predicting the dynamics of mobile virus spread affected by human behavior. In: IEEE International Symposium on a World of Wireless, Mobile and Multimedia Networks, WoWMoM 2011, pp. 1–9 (2011)
5. Ghazali, R., et al.: Integrating Cadastral GIS Database into GPS Navigation System for Locating Land Parcel Location in cadastral surveying. In: 2011 IEEE 7th International Colloquium on Signal Processing and its Applications (CSPA), pp. 469–473 (2011)
6. Trigo, G., et al.: Vehicle Heading Estimation Using a Two Low-Cost GPS Receiver Configuration. In: 2011 IEEE 73rd Vehicular Technology Conference (VTC), pp. 1–5 (2011)
7. Ndoye, M., et al.: A Recursive Multiscale Correlation-Averaging Algorithm for an Automated Distributed Road-Condition-Monitoring System. IEEE Transactions on Intelligent Transportation Systems 12, 795–808 (2011)
8. Malleswaran, M., et al.: Performance comparison of HONNs and FFNNs in GPS and INS integration for vehicular navigation. In: 2011 International Conference on Recent Trends in Information Technology (ICRTIT), pp. 223–228 (2011)

Development and Realization of an Amphibious Vehicle Simulator for Driver Skill Training

Shutao Zheng[1,1], Zhengmao Ye[1,2], Junwei Han[1,3], and Jinhong Li[2,4]

[1] School of Mechatronics Engineering, Harbin Institute of Technology, China
[2] Oriental Cambridge of Harbin, China
{Zhengshutao77,lijinhong80}@163.com, {yezm,hjw}@hit.edu.cn

Abstract. Driving simulator provides an available method to train driver's operation skill without actual vehicle. Amphibious driving simulator was built to solve the driver's operation skill in water problem. Hardware components and system structure were given, a real-time simulation computer system adopting Ethernet and Local bus based on PC was used to solve the information exchange between computers and simulated cabin. In order to reduce developing cycle and improve maintainability and perform efficiency, the vehicle dynamical model in water was realized based on COTS software Matlab/Simulink. Experiments shows that the simulator can fulfill the requirement of driver's operation skill training and the performance of the simulator can keep consistent with actual amphibious vehicle.

Keywords: Driving simulator, amphibious vehicle, real-time simulation, vehicle dynamical model, COTS.

1 Introduction

With the rapid development of computer and simulation technology, driving simulators have been widely applied in research and educational fields for the advantages such as controlled and repeatable environment etc. Driving simulators date back to the early 1970s which continued for two decades and implemented using the VPI-SU simulator [1]. According to the components, complexity and capability of driving simulators, three kind level of driving simulators was proposed by Saluaar: Low-level simulator, Middle-level simulator and High-level simulator [2]. Low-level simulators are associated with PC, pedals and steering wheels which are among the most popular to use for the low cost and simple operation. Mid-Level simulators generally include a mockup cabin and projection screens or multi-LCD-monitor linked with PC for operation environment and scenario simulation. High-level simulators are more advanced and sophisticated simulators with high fidelity, validity and realism, which generally include the components of mid-level simulators and have a 6-DOF Stewart platform driven by Hydraulic or Electric for support the movement same as the actual vehicle.

The design and development of a driving simulator should not only be guided by the intention to create the most realistic driving environment possible but also by the necessity to replicate drivers' interaction with vehicle controls and surrounding

D. Jin and S. Lin (Eds.): Advances in Mechanical and Electronic Engineering, LNEE 176, pp. 515–520.
springerlink.com

instruments. A driving simulator can be divided into different subsystems such as sound, control loading, visuals, vehicle model and scenario. All these systems work together to create the illusion that the driver is actually in control of a real vehicle.

Amphibious vehicle is a special vehicle which can move on land as well as on water. It has an important application in transportation and military field because of the capability from land to water and reverse which frees from the bridges and ships. It is very difficult to drive the vehicle running in water along the prescriptive route because of the stochastic action of ocean wave to the vehicle. The performance of vehicle has been tested adopting country standard and industry standard such as GJB524-88 [3] and CB/Z 220-87 [4] etc, though the experiments were processed in still water. Secondly the obtained operation skills of drivers generally only include on land and in still water, whether the skill can be used in ocean wave is not certain. Third it is dangerous and high cost if the operation skills of drivers needed obtained by adopting actual vehicle in ocean wave. It is the best way to solve the problems that an amphibious driving simulator was built. The character of amphibious vehicle and operation skill of drivers in ocean wave can be obtained through the high level simulator.

This paper shows the development and realization of an amphibious driving simulator. Several main phases of the driving simulator development, design considerations, hardware selection, computer system structure, fabrication, installation, software development and correction of the driving simulator were detailed given. First this paper gives the driving simulator's hardware construction based on virtual design software and the consideration; secondly it gives the real-time simulation computer system's components and software module distribution; third vehicle dynamical model diagram according to the amphibious vehicle's construction was given, in order to reduce the developing cycle effectively, improve code quality and execute efficiency, COTS (Commercial-Off-The-Shelf)software and Rapid Control Prototype (RCP) technology based on Matlab/Simulink was used; Finally experiments and validation of driving simulator were processed.

2 Development of Amphibious Driving Simulator

2.1 Hardware Structure and Component of Driving Simulator

The development of driving simulator is a complex task [5]. Fig.1 shows you the hardware components of amphibious vehicle driving simulator. It is composed of 6-DOF motion system driven by hydraulic, central operation station, simulated cabin, visual system, instrument system, control loading system and audio system which provides the motion cueing, visual cues, auditory cues and feeling cues.

6-DOF motion system is key equipment of driving simulator which provides the high fidelity motion cueing. The motion system can simulate the interaction between vehicle and below 4 level ocean waves. Motion washout software and servo control software are located in the motion control computer to accomplish the pose and acceleration washout from real-time simulation computer and motion status control. In order to convenient connect with the simulated cabin; a general interface was designed on the up platform which can change the cabin easily.

Visual system was used to simulate the periscope scene which is composed of three 12 inch LCD and one graphic generation computer. In order to obtain the real-time generation of the detailed virtual environment, 4-core processor and two graphic cards were used.

Simulated cabin is the reproduction of actual cabin, vehicle cabin instruments, controls and switches all have to be integrated in simulated cabin and interfaced with the simulation software to reproduce the normal operation of a real amphibious vehicle and measure driver's inputs during experiment.

A multi-channel sound system composed of three speakers and a sub-woofer was installed in the simulated cabin which was used to generate vehicle sounds (e.g. engine sounds during vehicle start and acceleration/deceleration) and sounds from surrounding vehicle and waterworks.

Central operation station was used to place the computers and other accessories. Five 19 inch LCD was used, one is used to provide the operation interface which to control simulator connecting with Instructor operation computer, one is used to monitor the driver's operation connecting with KVM switch, and the other three is used to display the training scenario connecting with three video distribute which the visual signals from the visual computer.

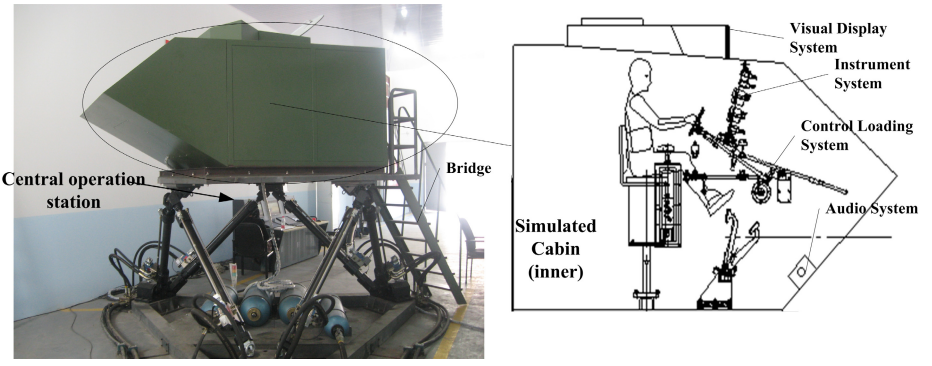

Fig. 1. Amphibious vehicle driving simulator system structure

2.2 Real-Time Simulation Computer System of Driving Simulator

Real-time simulation computer system is composed of real-time simulation computer, visual computer, instructor computer, motion system computer and data acquisition and control computer, Ethernet network and Local bus. Fig.2 shows you the network topology structure of driving simulator.

UDP/IP protocol was used to change information between computers except data acquisition and control computer, CAN bus was used to change data between simulated cabin and real-time simulation computer.

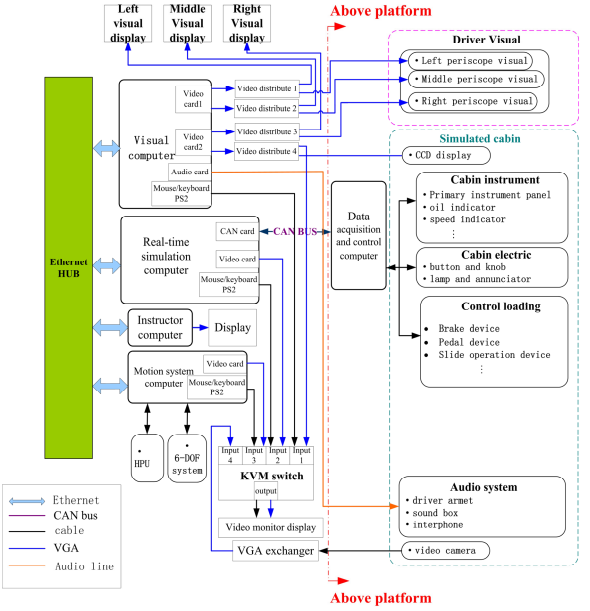

Fig. 2. Real-time simulation computer system structure of driving simulator

2.3 Software Components and Vehicle Dynamic Model Developing

Application software is the key components section of driving simulator, real-time manage software and vehicle simulated model is the main section. Fig.3 shows you the software components of driving simulator. Real-time manage software is the whole system's manager, it controls the data exchange information and the simulation cycle which keeps the real-time simulation computer system work correctly and in accord. Vehicle simulated model computes the response of the vehicle as a result of the driver inputs for throttle displacement, brake pedal displacement, clutch engagement, Watergate and suspension etc.

Two fundamental requirements of vehicle dynamic simulation is that it executes faster than real time and that it provides sufficient fidelity to the actual vehicle to convince a simulator driver that they are driving actual vehicle[6]. Vehicle simulated model is a complex software, in order to rapidly and high efficiency develop the software, COTS (Commercial-Off-The-Shelf) software Matlab/Simulink[7] and Labview[8] GUI program and RCP technology was used. Fig.4 shows you the software diagram of vehicle simulated model Based on Matlab/Simulink.

COTS "Visual database generation" tools Multigen-Creator and Multigen-Vega Primer were used to create a comprehensive database for ocean training scene. Direct sound API is used to develop the audio simulation software.

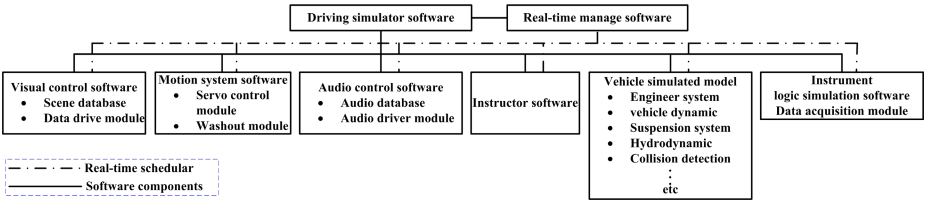

Fig. 3. Software components of driving simulator

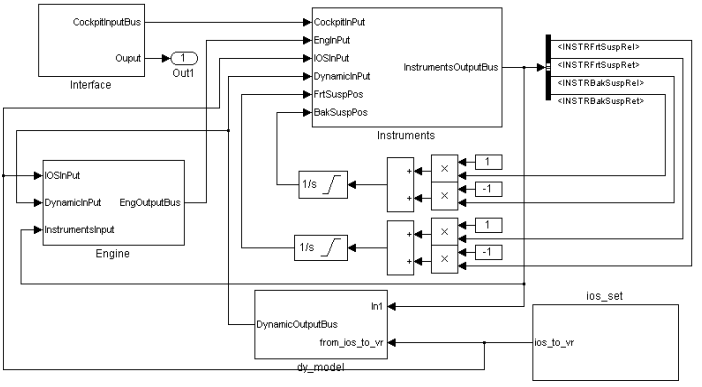

Fig. 4. Vehicle simulated model software diagram based on Matlab/Simulink

3 Experiments and Validation

Amphibious driving simulator were completed in Oct 2011 and functions well. More than five drivers operate the driving simulator and give the high fidelity simulation appraisement. Some experiments are done. Fig.5 and Fig.6 shows you the vehicle dynamic character amphibious and simulated dynamic character based on developed dynamic model in driving simulator. From the two diagrams, we can conclude that both are nearly same.

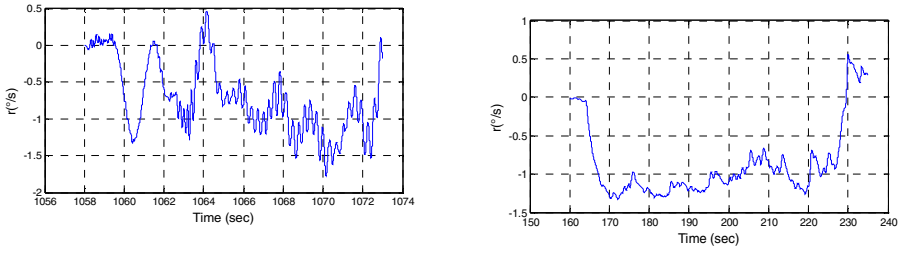

Fig. 5. Angle velocity curve actual and simulated on vehicle turn (left actual, right simulated)

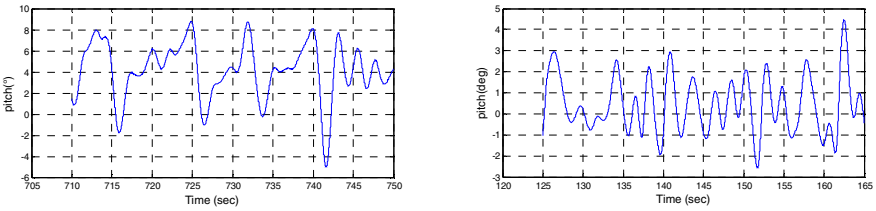

Fig. 6. Pitch-time curve actual and simulated on vehicle straight (left actual, right simulated)

Summary

With the development of computer and simulation technology, driving simulator has been used to design high performance vehicle and train driver's operation skill without actual vehicle. Amphibious driving simulator is used to training driver's operation skill in water. This paper shows the development and realization of an amphibious driving simulator. The driving simulator's hardware components, computer system structure and software structure were detailed given. In order to improve code quality and execute efficiency, COTS software Matlab/Simulink and RCP technology was used. The driving simulator was complete in Oct 2011. Experiments shows the development driving simulator can simulate the actual character of vehicle and short the training cycle of driver greatly.

References

1. Johansson, M., Nordin, J.: A survey of driving simulators and their suitability for testing Volvo cars, pp. 7–12. Chalmers university of technology, Sweden (2002)
2. Straus, S.H.: New, Improved, Comprehensive, and Automated Driver's License Test and Vision Screening System, pp. 67–86 (2005)
3. GJB524-88, Code for mooring and sea trials of high speed craft (planning craft) test for towage [GB], RPC military standard, pp. 1–4 (1988)
4. CB/Z 220-87, Method of assessing the hull resistance in still water for high speed craft [GB], china state Shipbuilding Corporation, pp.1–61 (1987)
5. Gruening, J., Bernard, J., Clover, C., Hoffmeister, K.: Driving simulation, SAE Special Publication. Vehicle Dynamics and Simulation 1361, 49–59 (1998) 980223
6. Heydinger, G.J., Salaani, M.K., Garrott, W.R., Grygier, P.A.: Vehicle dynamic modeling for the National Advanced Driving Simulator. In: Proceedings of the Institution of Mechanical Engineers, Part D: Journal of Automobile Engineering, pp. 307–318 (2002)
7. Mathworks, Matlab Using Simulink, The Math Works, Inc. (2004)
8. Travis, J., Kring, J.: Labview for every: Graphical programming made easy and fun, 3rd edn. (2006)

A Novel Bidirectional Onboard Charger for Electric Vehicle

Jiqing Dou[1], Bizhong Xia[1], and Weiwei Zheng[2]

[1] Graduate School at Shenzhen, Tsinghua University, Shenzhen 518055
[2] Sunwoda Electronics Co., LTD, Shenzhen 518108
doujiqing@126.com, xiabz@sz.tsinghua.edu.cn, zhww@sunwoda.com

Abstract. A novel bi-directional battery charger topology which consists of a full-bridge converter and a bidirectional DC-DC converter is proposed according to the special requirement of bidirectional battery charger for electric vehicle (EV),. This bidirectional charger can achieve two functions including battery charging and vehicle to grid (V2G), and its rated power is 2 kW. Experimental results verify the functions and performance of the charger.

Keywords: electric vehicle, converter, V2G (vehicle to grid).

1 Introduction

At present, we usually do not charge the batteries until the energy of electric and hybrid vehicles is about to run out. During the whole process of life, electric vehicles are parked in the vast majority of the time, so the battery self-discharge induces energy waste. With development of smart grid technology, it can not meet the requirements of future multi-functional applications of new energy vehicles.

For example, the batteries of new energy vehicles can be used as a generator. When the power shortage during the day and interruption of the civilian power grid, the car battery can be used as a power generator, not only alleviates the power shortage pressures but also increases the income of the car owner, which improves power supply reliability[1-2].

The bidirectional charging machine has two kinds of operating modes, it can get energy from the grid and transfer energy to the grid. Compared to the traditional battery charger, this novel structure is more efficient and safer.

2 System Overview

This system use TI company's TMS320F28335 as control core, through acquiring the battery voltage, current, bus voltage, power grid voltage and current sampling signals and outputting 8 roads PWM wave to control eight switch tubes, to realize charging and discharging. The system use phase shifting to control bidirectional DC/DC converter and SPWM to control voltage full-bridge AC/DC converter. The system structure is shown in Fig.1.

D. Jin and S. Lin (Eds.): Advances in Mechanical and Electronic Engineering, LNEE 176, pp. 521–527.
springerlink.com

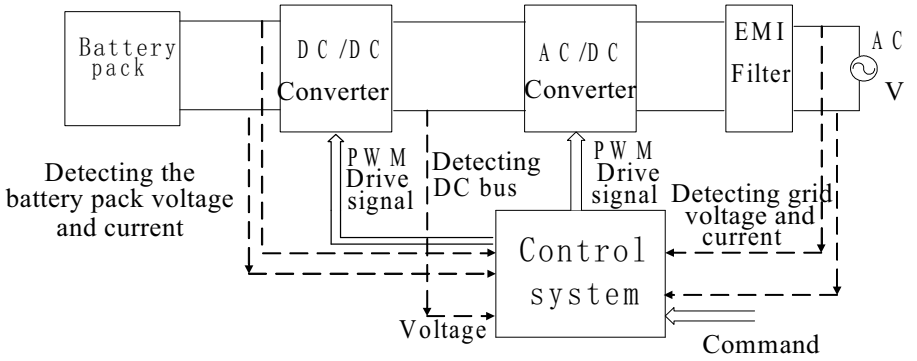

Fig. 1. System structure of the charger

2.1 Introduction Of Charger Topology Design

Fig.2 shows the topology of the new car charger presented in this paper. General topology of bidirectional car charger consists of the bidirectional DC/DC converter and AC/DC converter[3]. This new charger's topology also consists of two components: one is the bidirectional DC/DC converter in the battery side; the other is voltage full-bridge converter in the grid side.

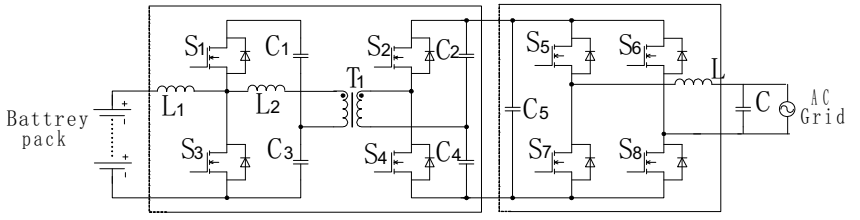

Fig. 2. The novel charger's topology

The dual active half-bridge bidirectional DC/DC converter what is transformer-isolated can realize energy two-way flow and improve the reliability and safety of the system at the same time. The voltage full-bridge converter in the grid side is mainly used to realize inverter and rectification.

2.2 Design The DC/DC Converter

Using a transformer to isolate the bidirectional DC/DC converter has the following advantages:

(1) If there is no transformer, when battery connects the voltage benchmark of the charger, the charger will not work.
(2) No DC current injection, avoiding the problems caused by distribution transformer saturation.

(3) No high-frequency leakage current, preventing emerging resonant circuit that consists of the parasitic capacitance between the battery terminals and ground and stray inductance among wires.

3 Bidirectional Charger Control

3.1 Bidirectional DC/DC Converter Control

Bidirectional DC/DC converter uses phase shifting control mode, duty cycle of the four switch tubes are all fixed at 50%, so the bidirectional DC/DC converter inductors C1, C2, C3 and C4 attain voltage equilibrium, transformer voltage is also symmetrical. By changing the phase angle θ between transformer primary and secondary side, it can achieve the adjustment of the output power. Specifically considered by the following formula:

achieve the adjustment of the output power. Specifically considered by the following formula:

$$P_0 = \frac{\int_0^{T_s} I_{r1} \bullet V_{r1} d_t}{T_s} = \frac{\theta \frac{1}{D}\left[4\pi(1-D) - \frac{1}{D}\theta\right]}{4\pi\omega L_s} \bullet V_b^{\,2} \tag{1}$$

Where: T_s is switch frequency cycle; I_{r1} is transformer primary side current; V_{r1} is transformer primary side voltage; θ is phase shift angle; ω is switch frequency; L_s is the sum of the transformer leaky inductance and external inductance; V_b is input voltage; D is duty cycle.

For this system, D=50%、f=20 kHz; then the above equation simplifies to:

$$P_0 = \frac{\theta(\pi - \theta)}{\pi\omega L_s} \bullet V_b^{\,2} \tag{2}$$

Bidirectional DC/DC converter has two operating modes:

(1) When the charger operating in the V2G condition, the converter works in positive boost mode, namely the four switch tubes operate in the same frequency, duty cycle is 50%, switch tubes on same bridge arm conduct in complementary mode, and the phase angle difference between the forward and backward bridge is θ. It adjusts the output power of the V2G mode by regulating and controlling the size of θ, at this time the main purpose is to keep stability of main bus voltage. The control process principle is shown in Fig.3 below.

(2) When the charger operating in charging condition, the converter works in negative boost work mode, similarly the four switch tubes operate in the same frequency, duty cycle is 50%. The phase angle difference between the backward and forward bridge is θ, and adjust the charging power by regulating and controlling the size of θ. At this time the main purpose is to keep stability of charging current and voltage. The control process principle is shown in figure 4 below.

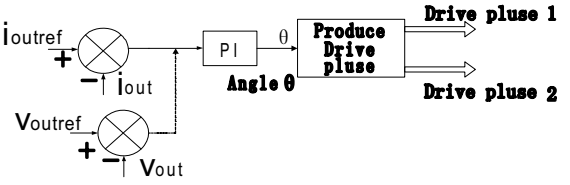

Fig. 3. Bidirectional DC/DC converter control schematic diagram in power generation mode

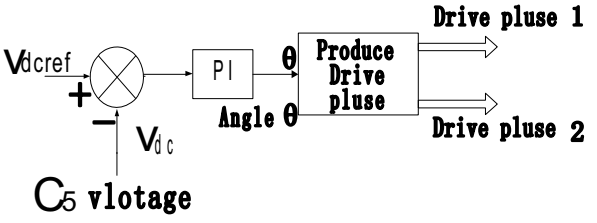

Fig. 4. Bidirectional DC/DC converter control schematic diagram in charging mode

3.2 The Voltage Full-Bridge AC/DC Converter Control

The full-bridge AC/DC converter has two operating modes:

(1) When the charger work in the V2G condition, the AC/DC converter operates in the forward inverse mode. At this time taking the safety of the battery into account, the AC/DC converter regulates and controls the stability of the output bus voltage, and through calculating the PWM and controlling switch tubes, so that current can match the grid voltage waveform.

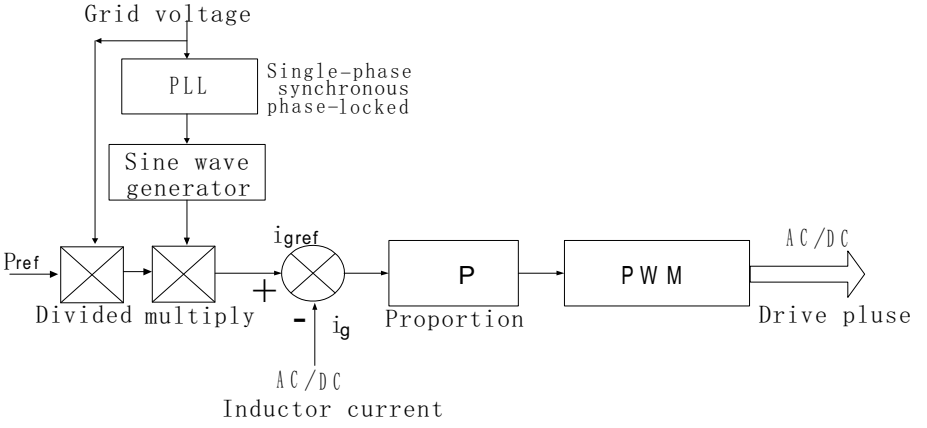

Fig. 5. Bidirectional AC/DC converter control schematic diagram in power generation mode

(2) When the charger works in charging condition, the AC/DC converter works in reverse rectifier mode, which adopts double closed loop control, namely the voltage outer loop and current inner loop. Voltage loop mainly stabilizes the DC bus voltage and current inner loop mainly control current according to the output of voltage outer loop, which not only realizes the power factor is equal to one but also improves the dynamic response of the system.

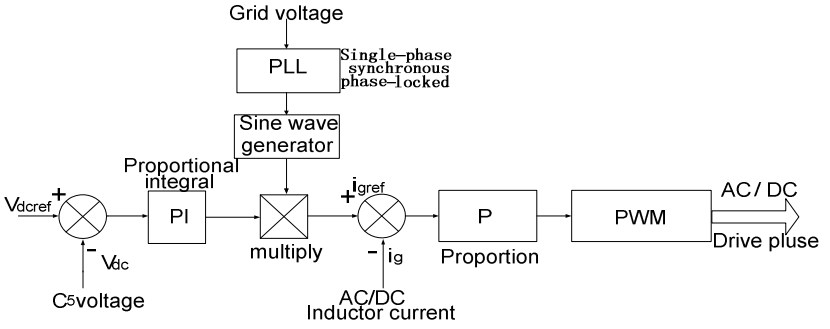

Fig. 6. bidirectional AC/DC converter control schematic diagram in charging mode

4 Main Circuit Parameters of the Bidirectional Charger

Bidirectional DC/DC converter and full-bridge AC/DC converter work in the same frequency (20 kHz). Charger's main circuit parameters include the boost capacitance of battery side, the DC bus capacitance and grid side filter capacitance.

4.1 Grid Side Filtering Inductance Design

In the full-bridge AC/DC converter main circuit design, the filter inductor value is very important; it determines the size of inductor's current ripple. It meet the following equation:

$$L \geq \frac{2U_d}{3\pi^2 f_c r_i \mathrm{I_m}}\left(1-\cos\frac{\sqrt{3}\pi}{4}\right) \tag{3}$$

Where: U_d is DC bus voltage; f_c is carrier frequency; r_i is current ripple coefficient; I_m is current peak. According to the practical system parameters, the calculation result is L = 1.8 mH.

4.2 DC Bus Capacitor Design

DC bus capacitance C_5 has the function of storing energy and stabilizing DC voltage. The prototype's parameters is 2kW/220V, DC bus voltage is 400V. According to stored energy to calculate and select the bus capacitor.

$$C_5 \geq \frac{2\sqrt{2}\,\mathrm{I_m}}{\pi^2 f_c \Delta U_d} \tag{4}$$

Where: ΔU_d is DC bus voltage ripple, its value is 5%.According to the practical system parameters, the calculation result is C5=400V/1000uF.

4.3 Design Battery Side's Inductors

Battery side's inductors include the boost inductor L1 and the transformer primary side's inductor L2:

(1) Design boost inductor L1
The boost inductor has to meet the conditions of critical continuous current and current ripple requirements.

According to the condition of critical continuous current, L1 should meet the following formula:

$$L_1 \geq \left(U_d - U_0\right)\frac{D}{r_i I_{om} f} \tag{5}$$

According to the condition of current ripple requirement, L1 should meet the following formula:

$$L_1 \geq \frac{{U_0}^2}{2 I_{om} f} D\left(1-D\right) \tag{6}$$

Where:U_0 is battery voltage;I_{om} is the maximum value of charge and discharge current. According to the practical system parameters, the calculation result is L1=600uH.
(2)Design transformer primary side's inductor L2
The battery pack voltage V_b is 64 V ~ 88 V, output voltage V_{DC} = 400 V, output power P_0 =2000 W, switch frequency f = 20 kHz, switch duty cycle D=50%:

$$L_2 = \frac{{V_b}^2}{2n^2 P_0} D^2\left(1-D\right)T/2 \tag{7}$$

According to the practical system parameters, the calculation result is L2=10uH.

5 Experimental Results

Based on the above analysis, the paper designs a bidirectional car charger, which uses DSP TMS320F28335 as control core, rated power is 2 kW. When it discharges to the grid, the voltage u_s, current i_s and DC bus voltage U_d are shown in fig.7.

Fig.7a shows the battery discharging voltage and current waveforms, the energy basically totally return to power grid, and the DC voltage is stable. Fig.7b shows transformer primary side voltage waveform, secondary side voltage waveform and inductor current waveform when the battery pack discharge.

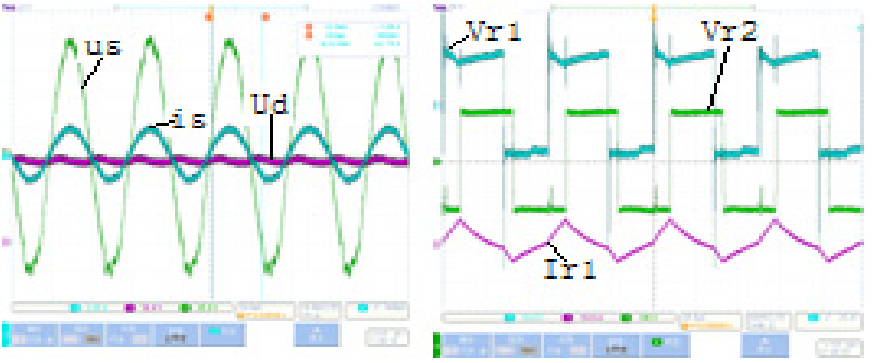

(a) output in V2G mode (b) transformer waveform

Fig. 7. Experimental results

6 Conclusions

This paper presents a new structure of the electric car bidirectional charger, using digital control, which guarantees the security, high power factor, small harmonic content, the perfect function. The experimental results show that the prototype complies with the design requirements and can be used in electric vehicles battery charging and energy feedback to the grid.

References

1. Clement, K., Haesen, E., Driesen, J.: Coordinated charging of multiple plug-in hybrid electric vehicles in residential distribution grids. In: IEEE Power Systems Conference and Exposition, pp. 1–7 (2009)
2. Kadurek, P., Loakimidis, C., Ferrao, P.: Electric Vehicles and their impact to the electric grid in isolated systems. In: IEEE Power Engineering International Conference on Energy and Electrical Drives, pp. 49–54 (2009)
3. Erb, D.C., Onar, O.C., Khaligh, A.: Bi-directional charging topologies for plug-in hybrid electric vehicles. In: IEEE Applied Power Electronics Conference and Exposition, pp. 2006–2072 (2010)
4. Zhou, X., Wang, G., Lukic, S., Bhattacharya, S., Huang, A.: Multi-function bi-directional battery charger for plug-in hybrid electric vehicle application. In: IEEE ECCE, pp. 3930–3936 (2009)

Bus Rapid Transit Signal Priority Using Advanced Detection

Min Yang[1], Bo Wang[2], and Gang Sun[3]

[1,3] School of Transportation, Southeast University
Nanjing, P.R. China
[2] Department of Civil Engineering Texas A&M University
1226 TAMU, College Station
yangmin@seu.edu.cn,
ggtywb@gmail.com,
rye_catcher1989@sina.com

Abstract. This research develops a Transit Signal Priority strategy to improve the bus efficiency significantly for Bus Rapid Transit (BRT) in China. The strategy detects one cycle before buses' arrival so that we can adapt a more flexible control algorithm to provide signal priority. And we use a microscopic traffic simulator VISSIM to analyze the proposed control strategies. The example is based on the BRT planning scheme on Sheng Li Avenue in Ying Tan City. The results show that this proposed strategy has remarkably improved the efficiency of public transit, compared with three other control strategies. It offers a case study for the management and control of BRT operation, and provides some practical insights about how to improve public transit efficiency.

Keywords: Transit signal priority, Advanced prediction, Example simulation.

1 Introduction

Bus Rapid Transit (BRT) is a high-quality bus-based transit system which requires lower initial capital investment, shorter implementation time, but larger capacity, better passenger facilities and more flexible routes. It also combines advantages such as the flexibility of conventional buses and the operational efficiency of rail transit [1]. However, priorities for BRT in China are mainly constrained in road portion, like exclusive bus lanes [2, 3], although some simple signal priority strategies may be adopted at intersection, bus efficiency has not been improved ideally. In order to provide more priority for the transit while minimizing impacts to automobiles, Wadjas and Furth proposed a strategy which was designed for light rail trains, using advanced detection [4]. Adaptive signal priority is a strategy that takes into consideration the trade-offs between the transit and traffic delay. However, currently, there is a lack of comprehensive documentation of the effectiveness of such transit priority measures over a wide range of traffic levels [5]. Therefore, on the basis of simulation model preparation of Ying Tan city in VISSIM, this study is to analyze the efficiency of public transit system under the aforementioned strategy (transit signal priority using advanced detection) integrated with BRT lanes.

D. Jin and S. Lin (Eds.): Advances in Mechanical and Electronic Engineering, LNEE 176, pp. 529–533.
springerlink.com

This paper includes following sections: First, it is a brief introduction of the city of Ying Tan and the model preparation of Sheng Li Avenue. Second, it explains the proposed signal control strategy. Third, it analyzes the evaluation results of the proposed running in VISSIM, compared with other three simple scenarios: base case, exclusive bus lane only and conventional active signal priority with bus lanes. Last, it summarizes this paper and recommends the proposed strategy from a practical aspect.

2 Data Resources and Simulation Preparation

In this study, a behavior based microscopic simulation software-VISSIM was used. And with this simulation software, we can model different scenarios and analyze their advantages and disadvantages with a set of indicators, which adopted here include two sets: one is the impacts on buses, the other is the impacts on automobiles [6, 7].

Ying Tan which is Located in the northeast of Jiangxi Province, is being through a rapid developing period, during which travel demand is increasing dramatically. To relieve traffic congestion, the local government has planned to provide priority to public transit and recently is about to install a BRT lane along Sheng li Avenue. With the help of data provided by the final report on urban transit planning of Ying Tan (2011-2020) [8], we modeled Sheng Li Avenue through the downtown area of Ying Tan in VISSIM. Sheng Li Avenue is a four lanes dual carriageway with three signalized intersections including Zhan Jiang, Jiao tong, Zheng Da, and each lane has a width of 3.5 meters. Eastbound bus volume during peak hour is 60 vehicles per hour, and passenger volume of maximum section is 3000 persons per hour.

Besides the implementation of BRT lane, the BRT system in Sheng li Avenue may have two differences from the traditional ones: First, bus stops installed in front of stop line of each intersection. Next, the objective of this proposed strategy is to provide red signal for buses to allow them have sufficient time to load and unload passengers and then drive through intersections during green signal.

3 Signal Priority Model

Suggested by the signal control priority strategy proposed by Wadjas[8], we develop a promoted signal control priority model to adjust the new bus system which differs from the normal BRT system in bus serving signal. The Brief process of this model will be introduced below.

For each intersection approach, transit corresponding detectors were located at a cycle time in front of the subject interaction stop line. There is no other intersection between the detector and its corresponding intersection, all buses are running on an exclusive bus lane which protects buses from the private traffic and bus stops are constructed right in front of the stop line. For these reasons forehead, the bus travel time is very reliable. So, bus travel time is just related to the distance between detectors and stop line and buses real-time travel speed when pass the detectors.

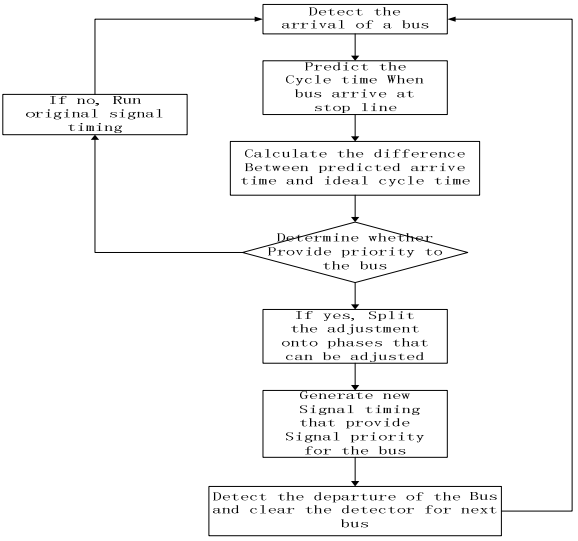

Fig. 1. Brief Algorithm of Active Signal Priority Using Advanced Detection

As mentioned above, the bus stops are installed in front of the stop line and the bus serving signal at intersections is red at intersections for buses to load and unload passengers. The desired (ideal) bus arrival time is 20-second red remaining time, which equals the minimum predicted dwell time. With the estimated the bus arrival time and compared it with the original signal timing, we can judge the arrival time is whether the desired one we wish.

After the judgment, if the bus arrival time is not the desired one, we will try to adjust the signal timing to make it satisfied. The adjusting method remains the same as the original. The difference between the predicted arrival time and the desired arrival time is the amount of adjustment. Because of the advanced detection, the amount of adjustment could be split to those phases among the advance. The adjustment methods include compression and extension. Take the compression situation as an example, the adjustable phases could be five phases (phases between the detect time and the desired arrival time), and we compress each phase with proportion of the original signal timing program. And the other one is similar, just to extent each adjustable phases.

4 Results Analysis

To analyze the efficiency of the proposed strategy in this study, we employed four simulation scenarios including: 1)base case; 2)adding exclusive bus lane; 3)conventional active transit signal priority; 4)transit signal priority using advanced detection, and modeled them in VISSIM respectively. The indicators used in this study include: delay and travel speed of buses and cars; reliability of buses.

Delay can be calculated as the time difference between the simulated travel time and the ideal travel time. Delays of buses and automobiles at three intersections and their average in four scenarios are listed below:

Table 1. Bus and Automobile Delays in Four Scenarios along Eastbound Shengli Road

Intersections	Simulation Scenarios							
	1		2		3		4	
	bus	auto	bus	auto	bus	auto	bus	auto
Zhan Jiang Road-Sheng Li Road	36.0	15.1	29.9	12.5	27.4	13.3	11.3	13.4
Jiao Tong Road-Sheng Li Road	47.0	18.2	41.8	13.3	30.8	15.5	11.4	14.2
Zheng Da Road-Sheng Li Road	56.0	17.4	36.8	12.6	27.2	16.1	11.2	15.1
average value	46.3	16.9	36.2	12.8	28.5	15.0	11.3	14.2

Table 2. Bus and Car average Speeds in Four Scenarios along Eastbound Shengli Road

Simulation Scenarios	1		2		3		4	
	bus	auto	bus	auto	bus	auto	bus	auto
Average speed	13.9	28.7	18.4	33.6	19.5	32.2	23.8	32.9

We can see above, scenario 2 leads to little delay and faster speed for buses and automobiles, which means that exclusive bus lanes can improve bus efficiency and private traffic operation conditions. When adding priority strategy, bus efficiency improvements can achieve a higher level, which demonstrates that exclusive bus lanes integrated with priority strategies can improve bus efficiency much more than merely implementing exclusive bus lanes. However, adding priority strategy will more or less negatively impact the private traffic. While what we need to know is that what priority strategy will cast the least impacts on private traffic. As we can see, private traffic operates most fluently in scenario 4, because advanced detection will provide more room for signal timing adjusting which leads to slight adjustment of each phase and impact least on private traffic.

Reliability of buses is a very important indicator which can reflect the reliable degree of bus travel time. This study uses the time that a bus needed to travel from the beginning of Sheng Li Avenue to the end as the bus reliability.

Table 3. Reliability of Bus Travel Time in Four Scenarios along Eastbound Shengli Road

Simulation Periods	Simulation Scenarios			
	1	2	3	4
10min-20min	410.6	303.1	292.5	238
20min-30min	429	292.9	297	234.7
30min-40min	383.4	298.3	281.7	232
40min-50min	373.3	326.1	290.2	234
50min-60min	401.2	301.1	288.6	230.3
Averages(s)	399.5	304.3	290	233.8
Stdev(s)	19.7	11.4	5.0	2.6

As we can see, the Scenario 4 shows more excellent than other three scenarios demonstrate, which means that bus travel time in these scenarios have no satisfactory consistency. Also, the data demonstrates that implementation of exclusive bus lanes and active signal priority contribute little to the improvement of bus reliability, on the other hand, buses have been much more reliable because of the proposed strategy.

5 Conclusion and Future Directions

In this study, we propose one priority strategy and integrate it with exclusive bus lane to see how it would impact public transport efficiency in the BRT system. And we used the microscopic simulation to analyze how this priority strategy will improve the public transit and private traffic. The results show the signal priority using advanced detection model has a positive influence on both buses and automobiles. Although this strategy performs well, it still has certain disadvantages to be deeply studied.

Acknowledgments. This research is supported by National Basic Research 973 Program (2012CB725402), National Natural Science Foundation of China (50908052, 51008061), the Fundamental Research Funds for the Central Universities and Foundation for Young Key Teachers of Southeast University.

References

1. Schramm, L.R., Watkins, K., Rutherford, S.: Features that Affect Variability of Travel Time on BRT Systems. Transportation Research Record (2143), 77–84 (2010)
2. Diaz, R.B.: Characteristics of Bus Rapid Transit for Decision-Making. Publication FTA-VA-26-7222-2004.1. FTA. U.S. Department of Transportation, McLean, VA (2004)
3. Wright, L., Hook, W.: Bus Rapid Transit Planning Guide, 3rd edn., New York. Institute for Transportation and Development Policy (2007)
4. Furth, P.G., Muller, T.H.J.: Conditional Bus Priority at Signalized Intersection: Better Service Quality with Less Traffic Disruption. Transportation Research Record (1731), 23–30 (2000)
5. Wadjas, Y., Furth, P.G.: Transit Signal Priority along an Arterial Using Advanced Detection. Transportation Research Record (1856), 220–230 (2003)
6. Jiang, S., Murga, M.: Linking Planning and Operations for BRT: A Microscopic Traffic Simulation Study for the Chicago Loop. Transportation Research Board (2010)
7. Balvanyos, T., Kourjanskaia, N., Misener, J.A., et al.: SmartBRT: A New Simulation Tool to Assess Bus Rapid Transit Systems. Transportation Research Board (2003)
8. Yang, M.: Final Report on Urban Transit Planning of Yingtan (2011-2020), p. 40. Southeast University (2011)

The Maximum Charge and Discharge Power Estimation in Hybrid Electric Vehicle Based on Artificial Neural Network

ZhiYong Li[1], KunYao Xu[2], RuiLin Xu[3], HongYu Long[4], and ChangHao Piao[1]

[1] Institution of Pattern Recognition and Application, Chongqing University of Posts and Communications, Chongqing, 400065, China
[2] Chongqing Electric Power Corporation, Chongqing 400014, China
[3] Chongqing Electric Power Research Institute, Chongqing 401123, China
[4] Postdoctoral Workstation of Chongqing Electric Power Corporation, Chongqing 400015, China
lizhiyong915@gmail.com, {xukunyao,xuruilin}@cqep.com.cn, h.y.long2008@hotmail.com, piaoch@cqupt.edu.cn

Abstract. In view of the hybrid electric vehicle's Ni-MH battery system, the paper predicts the maximum charge and discharge power through artificial neural network. The maximum discharge and charge power directly affect the efficiency operation of hybrid electric vehicle. It is one of the most important parameters of Ni-MH battery systems. The estimation can avoid Ni-MH battery systems overcharge and over discharge phenomenon and prolong the service life of battery system. It has important practical value and theoretical significance for reasonable use of Ni-MH battery systems. Firstly from the view of engineering application, check the matching table to get the target value's relation with the SOC (the rest charge value), voltage, temperature. Secondly select some of the voltage, temperature and the last moment of the predicted maximum charging and discharging power, to be the input variables of the network. Thirdly through the tests, design and optimization the artificial neural network model structure. Finally get the artificial neural network model which can successfully predict the target. As a result, its error is within 10% to meet the expected requirements.

Keywords: hybrid electric vehicle, battery, power, artificial neural network.

1 Introduction

The world's energy shortages, environmental pollution and other issues prompt many countries to research and develop the new energy, saving and environmental protection products. Transportation energy consumption accounts for 40% of the world total energy consumption, and the car 's energy consumption accounts for about 1/4. In the face of energy saving and environmental protection pressure, many countries in the world have been developed the new energy vehicles, including pure electric vehicle EV, fuel battery electric vehicle FC, and hybrid electric vehicle HEV. In contrast to its characteristics economic for gas station, for HEV the technical

D. Jin and S. Lin (Eds.): Advances in Mechanical and Electronic Engineering, LNEE 176, pp. 535–541.
springerlink.com

performance is relatively mature, with little pollution, low noise, simple operation, and low cost in three, compared with HEV at present the most energy saving and environmental protection advantages [1]. Therefore, hybrid electric industry independent research and development, becomes a hot chase, and people generally are optimistic about the prospect of its application.

In the hybrid vehicle, the maximum charge and discharge power is one of the most important parameters of the Ni-MH battery using of process. How to accurately predict the Ni-MH battery maximum discharge and charge power is always for domestic and foreign related researchers urgent attention and have devoted much energy to study. There are Several methods predicting the maximum allowable charging and discharging power, such as composite pulse method, based on the battery state of charge (State of charge, SOC) method, multi parameter constrained dynamic peak power estimation algorithm [2-3], artificial neural network method.

This paper presents an artificial neural network for the prediction of maximum discharge and charge power in the hybrid vehicle, with a strong prediction of the method of intelligence, and a strong learning ability, showing great flexibility and adaptability in handling a large number of rules or formulas that has been described the original data [4-5].

This article will introduce previous-time power of Ni-MH battery to the input variables, namely, selecting the current voltage, temperature, time of the previous-time power as input variables, and using proportion conjugate gradient algorithm to train the network. Repeated by a large number of training samples, neural networks are better able to learn and adapt to the dynamic characteristics of the unknown system, and this feature is stored in the hidden power of the connection within the network. Simulation results show that the proposed ANN algorithm can accurately predict hybrid vehicle Ni-MH battery maximum discharge and charge power, and the output results in a short time, with the average error of about 10%.

2 Training Algorithm

In artificial neural network predicting the maximum discharge and charge power, its input variables commonly are real-time detected variables, such as voltage, current, temperature and so on, and the output variables are also many. You can directly select the battery power as output, and the output can also be set to other methods for estimating its parameters, such as a battery model parameters or battery SOC [6-7].

In the experiment in order to avoid over-training network, use the alternating training and simulation approach. After the training sample have trained the network every time, maintain the network weights and thresholds remain unchanged, and then use the verified sample data as the network input, run the network forward, test the average error of the output. In the simulation, use the last time's simulation output as the next time's simulation input, that is,

$$P(i) = P'(i-1), \quad i > 1. \tag{1}$$

and is the integer. When the training cannot be reduced to an average error of the output of the network, we believe that the end of this round of network training.

BP algorithm is commonly used in long training time there, slow convergence and other shortcomings, this article uses the proportional conjugate gradient algorithm. Conjugate gradient algorithm requires linear in each training cycle to adjust the direction of the search network, and this linear way of search must be repeated each time, so a lot of time is consumed. The proportional conjugate gradient algorithm combine the model's value trust region algorithm and the conjugate gradient algorithm, effectively reduces the search time and improve the network training speed.

When given a training session of the BP network to provide a new memory model, the existed connection weights will be disrupted, leading to the memory learning mode's information disappears, and re-training of the new network needs to join the original learning model. Therefore, increasing the training sample, the original sample must be retained. If adding new training data, cannot train a network that is the average error on even smaller networks to illustrate the neural network has been close to the stability of the experimental wanted to get through the training of the neural network. BP used in this paper, neural network training process shows in Figure 1.

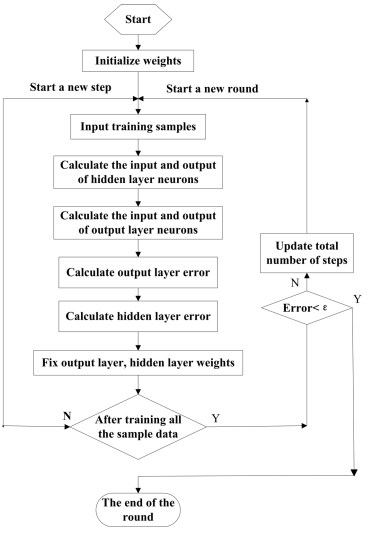

Fig. 1. Flow chart of neural network training

In Figure 1, the input training samples U, T are the data at the t time, and P is the data at the t-1(t>1) time, εis on behalf of the pre-set training end goals, that is not the smaller the better, because the network exists over-training problem. Update training step number is induced that doing the next round training without convergence. After training in the current round of experiments, also determine whether the average prediction error of neural network is smaller than the last round or not, if it is true, need to continue training the same way until no longer be reduced so far, otherwise increases samples to the new train.

3 Experimental Results and Analysis

According to the above designed ANN algorithm and the method of extracting the sample data, carry on the simulation by Matlab.

3.1 Experiment and Results

The first set of training data, is denoted by 1.mat (collect a data every 10ms, and put the continuous collected data about 60000 times into a group). 1.mat is trained to become a neural network model by the above designed neural network algorithm, denoted by net.1. Take 5 groups validated model (6.mat, 7.mat, 8.mat, 9.mat, 10.mat) respectively into the net.1 model, and work out the error between the net.1 model predictive power value and the respective own test data. In the same way, work out the error between the net.2, net3, net4, net5 model predictive power value and the respective own test data, the errors are as follows:

Table 1. Net.1, 2, 3, 4, 5 model average error

ANN model	Validation data	Error
Net.1	6.mat,7.mat,8.mat, 9.mat,10.mat	8.12%,11.5%,17.34% ,16.38%,17.04%
Net.2	6.mat,7.mat,8.mat, 9.mat,10.mat	14.05%,10.8%,2.16% ,0.77%,6.22%
Net.3	6.mat,7.mat,8.mat, 9.mat,10.mat	1.23%,10.9%,27.01% ,25.09%,7.37%
Net.4	6.mat,7.mat,8.mat, 9.mat,10.mat	19.1%,9.12%,59.22% ,60.68%,21.36%
Net.5	6.mat,7.mat,8.mat, 9.mat,10.mat	23.03%,7.49%,66.3% ,70%,40%

Combine 1.mat, 2.mat, 3.mat, 4.mat, 5.mat into a set of training data (then this group has collected about 6 * 50000 data), denoted by 12345.mat. According to the preceding method for training a neural network model, denoted by net.12345. Turn into 5 groups of validation data, the errors are as follows:

Table 2. Net.12345 model average error

ANN model	Validation data	Error
Net.12345	6.mat	0.17%
Net.12345	7.mat	9.4%
Net.12345	8.mat	7.2%
Net.12345	9.mat	5.38%
Net.12345	10.mat	2%

3.2 Analysis

We can see from Table 2, the maximum error of net.12345 for 5 groups validate data is only 9.4%, which error is less than 10%, and on the whole it is superior to that of

net1, net2, net3, net4, net5. The result shows that the network adaptive capacity is good, and the prediction is accurate. It predicts the maximum charge power value and testing data comparison chart in Figure 2. According to the same method, net12345 model predicts the maximum discharge power value and the corresponding testing data comparison chart in Figure 2.

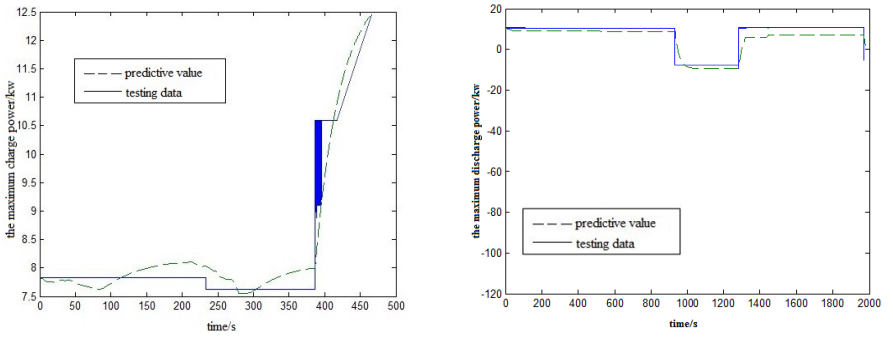

Fig. 2. Predictive value and testing data comparison chart

Through above training result analysis, the network is the good choice as a predictor of car batteries maximum discharge and charge power. Network architecture of the network shows in Figure 3, in which the hidden layer to output layer weights of the middle line in Figure 3, the data between the input layer to hidden layer weights shown in Table 3.

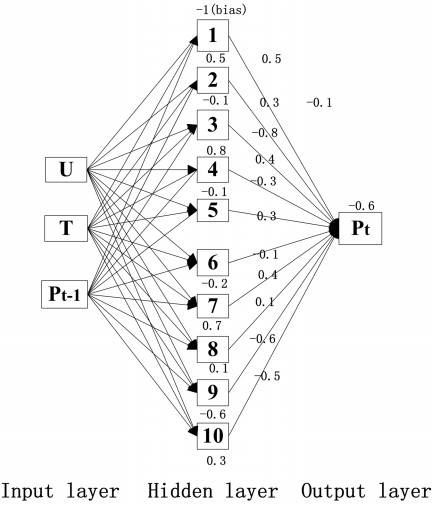

Fig. 3. Network architecture of ANN

Table 3. Input layer and hidden layer weights table

Input layer	Hidden layer	weights
U/v	1,2,3,4,5, 6,7,8,9,10	0.7,-0.3,0.1,0.02, 0.6, 0.5,0.2,0.9,0.7, 0.03
T/°C	1,2,3,4,5, 6,7,8,9,10	0.3,0.5,0.9,0.7,0.6, 0.2,0.9,0.8,0.2,0.7
P/w	1,2,3,4,5, 6,7,8,9,10	-0.8,-0.4,0.6,-1,0.7 0.6,0.5,0.2,0.5,0.6

3.3 Test and Verify

In order to verify this algorithm of artificial neural network to predict the maximum charging and discharging power of the nickel-hydrogen battery is feasible, we must introduce the most reliable method of current estimating the maximum charging and discharging power of nickel-hydrogen battery for comparing and analysis the prediction of outcome data.

The composite pulse method can real-time and accurate estimate the charge and discharge capacity of dynamic conditions, and its predictive value and the actual value is relatively close. Take this as to validate the algorithm of artificial neural network to predict the maximum charging and discharging power of nickel-hydrogen battery feasible.

Here is using artificial neural network model and composite pulse method to predict the maximum charge power value comparison curve, as shown in Figure 4. According to the same method, artificial neural network and composite pulse method to predict the maximum discharge power value comparison curve is shown in Figure 4.

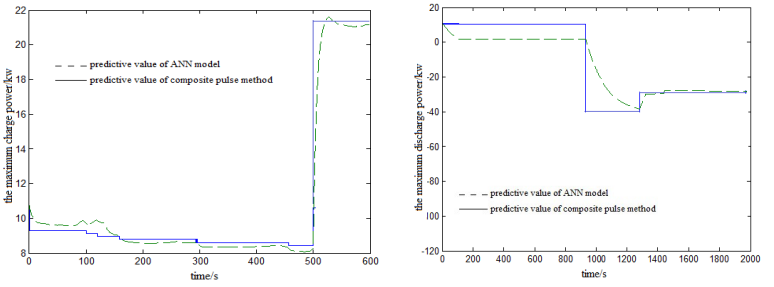

Fig. 4. ANN and composite pulse method comparison curve

In Figure 4, it can be seen from the figure of two different methods for the prediction of the effect of power is closer, and composite pulse method has proved very reliable, so the artificial neural network model to predict the power is more reliable, and it has certain feasibility.

4 Conclusion

To predict Ni-MH battery real-time power when the car is running, while maintaining good prediction accuracy and adaptability, this paper designs an artificial neural network that can be used to predict power of a Ni-MH battery, including 3 inputs, 10 neurons and 1 output. The neural network makes the last-time state of the battery power into the neural network prediction, which considers the impact from the last-time power to predicting the real-time power, and improve the adaptive ability of neural networks. During the training process of the neural network, proportional conjugate gradient algorithm is used, through alternating training simulation, continuous changing in a variety of network connection weights, finally coming out a fixed memory formation to predict the real-time power. At the same time, depending on the comparison of neural network simulation error, avoid over-training network. The simulation shows that the artificial neural network established by the sample in this experiment can accurately predict hybrid vehicle Ni-MH battery real-time power, and the adaptive capacity is good. These properties make the algorithm has a high application value.

References

1. Lu, S., Jie, B.X., Jie, Z.Y., Li, X.: Hybrid Technology and R & D Practice. Agricultural Equipment & Vehicle Engineering (2008)
2. Hunt, G.: Freedom CAR Battery Test Manual for Power-Assist Hybrid Electric Vehicles. In: DOE/ID-11069, Idaho National Engineering & Environmental Laboratory, USA (2003)
3. Plett, G.L.: High-Performance Battery-Pack Power Estimation Using a Dynamic Cell Model. IEEE Transactions on Vehicle Technology 53(5) (2004)
4. Salkind, A., Fennie, C., Singh, P., Atwater, T., Reisner, D.: Determination of State-of-Charge and State-of-Health of Batteries by Fuzzy Logic Methodology. Journal of Power Sources 80(2), 293–300 (1990)
5. Shen, W.X.: State of Available Capacity Estimation for Lead-Acid Batteries in Electric Vehicles Using Neural Network. Energy Conversion and Management 48(2), 433–442 (2007)
6. Piao, C.H., Yang, X.Y., Teng, C., Yang, H.Q.: An Improved Model Based on Artificial Neural Networks and Thevenin Model for Nickel Metal Hydride Power Battery. In: 2010 International Conference on Optics, Photonics and Energy Engineering. IEEE Press, China (2010)
7. Piao, C.H., Fu, W.L., Wang, J., Huang, Z.Y., Cho, C.: Estimation of the State of Charge of Ni-MH Battery Pack Based on Artificial Neural Network. In: International Telecommunications Energy Conference. IEEE Press, Korea (2009)

An Experiment System of Near-Minimal Energy-Optimal Trajectory Planning for the Car-Like Vehicle in a Changing Environment

Jian Yang[1], Mi Dong[1,*], and Yan Tang[2]

[1] School of Info. Science & Engineering, Central South University, Changsha, Hunan 410083, China
[2] Department of Mechanical Engineering, Embry-Riddle Aeronautical University, Daytona Beach, FL 32114, USA
dm1221@tom.com

Abstract. In this paper, we present a near-minimal energy-optimal method to determine the real-time collision-free path for a car-like vehicle moving in a changing environment. The proposed design is based on the polynomial parameterization of feasible trajectories by explicitly taking into account boundary conditions, kinematic constraints, and collision-avoidance criteria. The obtained optimal solution is analytical and suitable for practical applications which may require real-time trajectory planning and re-planning. Computer simulations have been conducted on the optimal solution we have addressed. The result verifies the advantage of the near-optimal solution. And an experiment system is setup to show the effectiveness of the algorithm, which offers a good platform for students.

Keywords: Trajectory Planning Experiment System, Car-Like Vehicle, Optimal Solution.

1 Introduction

Many modern applications involve mobile ground vehicles that are equipped with sensors of limited range but are required to move through a dynamically changing environment. It is becoming increasingly necessary to develop methods by which the mobile ground vehicles possess a higher degree of autonomy. Especially, finding trajectories in a dynamic environment by itself is a critically necessary. The trajectory should take motion constraints into consideration (including boundary condition, kinematic constraints and velocity bound), explicitly handle different type of static/moving objects and be obtained in realtime. It should be optimized in terms of some operational requirements.

A lot of research efforts have been directed toward motion planning in the presence of static obstacles, and many techniques have been proposed. Among them, the method of potential field pioneered in [1] is widely used. Also popular are the spline method [2]. To deal with kinematic constraints and the collision avoidance, some

* Corresponding author.

D. Jin and S. Lin (Eds.): Advances in Mechanical and Electronic Engineering, LNEE 176, pp. 543–548.
springerlink.com

other researchers use exhaustive search methods [3]. In this method, obstacle avoidance criterion and kinematic model are typically converted into a set of inequality and equality constrains. Methods to examine moving obstacles were developed in a few papers, Kant [4] decomposed the dynamic motion planning to a static trajectory planning problem and a velocity planning problem. However, these approaches suffer from the incomplete information and its solution is not guaranteed. To solve the real-time trajectory planning problem in a dynamic environment, a control-energy-related performance index [5] is defined in terms of the inputs of a chained system (a canonical form of the car-like vehicle); however, the physical meaning of a performance index in terms of the original inputs is hard to interpret.

This paper is organized into five sections. In section 2, the admissible trajectories are solved by polynomial parametrization and the feasible trajectories are defined,. In section 3, the near-minimal control energy solution is emphasized because it is analytical. This is a preferred property for real-time application. In section 4, simulation result is presented. In section 5, conclusions are drawn.

2 Problem Statement and Mathematical Formulation

In a changing environment shown as Fig. 1, a car-like vehicle moves in the presence of circular moving obstacles that are centered at O_i and of radius r_i. Range of the car-like vehicle's sensors is described by a circle centered at $O(t)$ and of radius R_s. In order to avoid the obstacles, the trajectory will be of distance at least $(r_0 + r_i)$ from the ith obstacle. Let T be the time for the car-like vehicle to complete its maneuver and T_s be the sampling period such that $\bar{k} = T / T_s$ is an integer, that centers of obstacles O_i are located at (x_i^k, y_i^k) at $t = t_0 + kT_s$, and that these objects are all moving with known constant velocities $v_i^k = [v_{i,x}^k, v_{i,y}^k]$ for $t \in [t_0 + kT_s, t_0 + (k+1)T_s)]$, where $k = 1, ..., \bar{k} - 1$. The family of trajectories of a mobile vechcle in the x-y plane from start to end can be solved by using polynomial parameterizations. That is, this family of trajectories is:

$$y = [1\ x\ x^2\ x^3\ x^4\ x^5](B)^{-1}(Y - Aa_6) + a_6 x^6 \tag{1}$$

where x and y are the coordinates of vehicle's guidepoint, and

$$Y^k = \begin{pmatrix} \left.\frac{\partial y}{\partial x}\right|_{x=x_k}^{y_k} \\ \left.\frac{\partial^2 y}{\partial x^2}\right|_{x=x_k} \\ \left.\frac{\partial y}{\partial x}\right|_{x=x_f}^{y_f} \\ \left.\frac{\partial^2 y}{\partial x^2}\right|_{x=x_f} \end{pmatrix} \quad A^k = \begin{pmatrix} (x_k)^6 \\ 6(x_k)^5 \\ 30(x_k)^4 \\ (x_f)^6 \\ 6(x_f)^5 \\ 30(x_f)^4 \end{pmatrix} \quad B = \begin{pmatrix} 1 & x_k & (x_k)^2 & (x_k)^3 & (x_k)^4 & (x_k)^5 \\ 0 & 1 & 2x_k & 3(x_k)^2 & 4(x_k)^3 & 5(x_k)^4 \\ 0 & 0 & 2 & 6x_k & 12(x_k)^2 & 20(x_k)^3 \\ 1 & x_f & (x_f)^2 & (x_f)^3 & (x_f)^4 & (x_f)^5 \\ 0 & 1 & 2x_f & 3(x_f)^2 & 4(x_f)^3 & 5(x_f)^4 \\ 0 & 0 & 2 & 6x_f & 12(x_f)^2 & 20(x_f)^3 \end{pmatrix}$$

The problem to find a trajectory with minimal control energy is stated as follows:

$$\min J_k^{E_1}\left(a_6^k\right)=\int_{t_k}^{t_f}\left(u_1^2+u_2^2\right)dt \qquad (2)$$
$$s.t.\quad \left(y-y_i^k-v_{i,y}^k\tau\right)^2+\left(x-x_i^k-v_{i,x}^k\tau\right)^2\geq\left(r_i+r_0\right)^2.$$

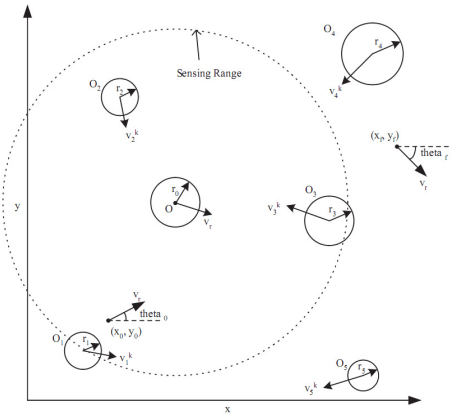

Fig. 1. A car-like vehicle in the presence of moving obstacles with limited sensing range

3 Near-Minimal Energy-Optimal Solution for Real-Time Trajectory Plan

For convenience, we let the horizontal speed of the vehicle be a constant *C*. If we substitute (1) into (2), the obstacle avoidance criterion of trajectories is

$$\min_{t\in[\underline{t}_i^*,\overline{t}_i^*]} G_i\left(t,\tau,a_6^k\right)=\min_{t\in[\underline{t}_i^*,\overline{t}_i^*]} g_2\left(x(t),k\right)\left(a_6^k\right)^2+g_{1,i}\left(x(t),k,\tau\right)a_6^k+g_{0,i}\left(x(t),k,\tau\right)\Big|_{\tau=t-t_0-kT_s}\geq 0 \qquad (3)$$

where $[\underline{t}_i^*,\overline{t}_i^*]\subset[t_0+kT_S,t_f]$ is the time interval (if exists) during $x_i^k\in[x(t)-v_{i,x}^k\tau-r_i-r_0,x(t)-v_{i,x}^k\tau+r_i+r_0]$ which collision maybe happen, and

$$g_2\left(x(t),k\right)=\left[\left(x(t)\right)^6-\underline{f}\left(x(t)\right)\left(B^k\right)^{-1}A^k\right]^2,$$
$$g_{1,i}\left(x(t),k,\tau\right)=2\left[\left(x(t)\right)^6-\underline{f}\left(x(t)\right)\left(B^k\right)^{-1}A^k\right]\cdot\left[\underline{f}\left(x(t)\right)\left(B^k\right)^{-1}Y^k-y_i^k-v_{i,y}^k\tau\right],$$
$$g_{0,i}\left(x(t),k,\tau\right)=2\left[\underline{f}\left(x(t)\right)\left(B^k\right)^{-1}Y^k-y_i^k-v_{i,y}^k\tau\right]^2+\left(x(t)-x_i^k-v_{i,x}^k\tau\right)^2-\left(r_i+r_0\right)^2.$$

where

$$\underline{f}\left(x(t)\right)=\begin{bmatrix}1 & x & x^2 & x^3 & x^4 & x^5\end{bmatrix} \qquad (4)$$

The problem (2) is rewritten as

$$\min J_k^{E_1}\left(a_6^k\right)=\int_{t_k}^{t_f}\left(u_1^2+u_2^2\right)dt \qquad s.t. \quad \min_{t\in[\underline{t}_i^*,\overline{t}_i^*]} G_i\left(t,\tau,a_6^k\right)\geq 0. \tag{5}$$

The expression of u_1 and u_2 is complicated, the optimization problem (5) can only be solved in a numerical method. This optimal approach is not applicable when the vehicle does not have a strong computation ability. Since the control energy used for steering only occupies a small part of the total energy, we can omit the steering energy to simplify the performance index and present the problem as a near-minimal control energy problem.

It is shown in the following theorem that an analytical solution to this optimization problem is obtained.

Theorem 1. *Suppose that the car-like vehicle operates in an environment with dynamically moving obstacles, and its trajectories are expressed in terms of an adjustable parameter* a_6^k. *Let* Ω *be the set of* a_6^k *avoiding obstacles, which is solved from inequalities (3). Let*

$$a_6^{k*}=\frac{11\left(\left.\frac{\partial^2 y}{\partial x^2}\right|_{x=x_k}+\left.\frac{\partial^2 y}{\partial x^2}\right|_{x=x_f}\right)}{12\left(x_k-x_f\right)^4}-\frac{22\left(\left.\frac{\partial y}{\partial x}\right|_{x=x_f}-\left.\frac{\partial y}{\partial x}\right|_{x=x_k}\right)}{3\left(x_f-x_k\right)^5}.$$

Choose a_6^k *from* Ω, *the* a_6^k *yielding* $\min|a_6^k-a_6^{k*}|$ *generates the optimal feasible trajectory with minimal cost* $J_k^{E_1}$. *It is marked as* $\tilde{a}_6^k$.

4 Simulation and Experiment

The sumulation is conducted on a car-like vehicle. The settings about the obstacles are as follows:

- Moving obstacles: $n_0=3$, $O_1(t_0)=[5,0]^T$, $O_2(t_0)=[9,4]^T$, $O_2(t_0)=[19,10]^T$ and $\tau_i=0.5$ for $i=1,2,3$
- Speeds of obstacles:

$$v_1^0=[0,0.4]^T, v_1^1=[0.5,0.2]^T, v_1^2=v_1^3=[0.2,0.2]^T,$$
$$v_2^0=[-0.5,0]^T, v_2^1=[0.6,0.1]^T, v_2^2=v_2^3=[0.6,0.1]^T,$$
$$v_3^0=[-0.2,-0.1]^T, v_3^1=[-0.2,0.1]^T, v_3^2=v_3^3=[-0.1,0.1]^T.$$

  Sampling period is adaptively chosen according to speed changes detected, and hence $T_s=10$ seconds.
- Sensor range $R_a=7$, implies that the vehicle has a limited sensor range so the vehicle detects the presence of objects 1, 2 and 3 intermittently.

The simulation result is shown in the Fig. 2. The position of the vehicle is marked by big circle and positions of three objects are marked by small circles which are drawn every 5 seconds.

From the figure 2, it is found that the near-minimal control energy solution decreases the consumed energy and the length path effectively. Also, an experiment system is setup in the lab. The experiment verifies the effectiveness of the algorithm. As shown in figure 3, the car-like vehicle (with red-circle) avoids the obstacles in the environment and keeps its control energy near-minimal. It offers a good platform for students in the lab to obtain instinct reorganization about trajectory planning and optimal control.

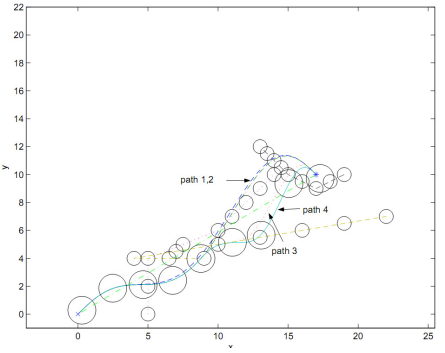

Fig. 2. The path of vehicle with near-minimal control energy and paths of obstacles

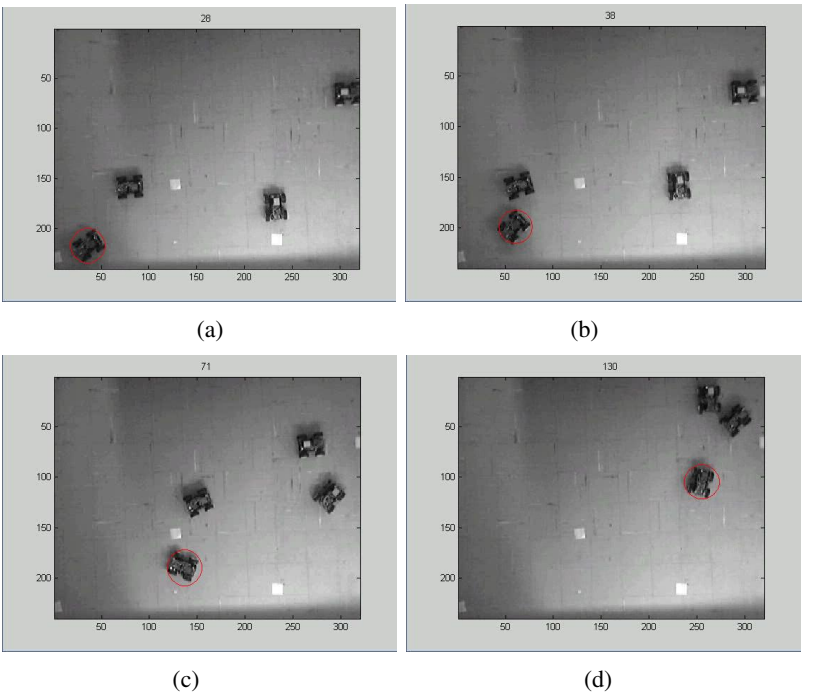

Fig. 3. The experiment result: path of vehicle with near-minimal control energy and paths of obstacles (the red circle shows the car-like vehicle, the others act as obstacles.)

5 Conclusion

In this paper, an optimal solution within the parameterized trajectory family to a car-like vehicle motion planning problem in the presence of moving obstacles are presented. Based on a piecewise polynomial parameterization of all feasible trajectories, the trajectory generation problem is formulated as a constrained parameter optimization problem subject to boundary conditions of the system and inequality constraints imposed by the obstacle avoidance criterion. The near-minimal control energy performance index give out an attractive solution. It is analytical and solved easily by using the symmetry property of parabola. This method is the preferred choice for real-time trajectory planning. When the proposed framework is applied to the car-like vehicle, simulation result has verified the effectiveness of the proposed method. And an experiment system is setup in the lab, which offers a good platform for students in the lab to learn the algorithm of control and trajectory planning.

Acknowledgments. This work was supported by the National Young Teacher Foundation under Grant 2011QNZT037.

References

1. Khatib, O.: Real-time obstacle avoidance for manipulator and mobile robots. Int. J. Robot. Res. 5, 90–98 (1986)
2. Lazaro, J., Gardel, A.: Adaptive workspace modeling, using regression methods, and path planning to the alternative guide of mobile robots in environments with obstacles. In: 7th IEEE International Conference on Emerging Technologies and Factory Automation, vol. 1, pp. 529–534 (October 1999)
3. Barraquand, J., Latombe, J.-C.: Nonholonomic multibody mobile robots: controllability and motion planning in the presence of obstacles. In: EEE Int. Confer. on Robotics and Automation, Sacramento, CA, pp. 2328–2335 (April 1991)
4. Kant, K., Zucker, S.W.: Planning collision free trajectories in time-varying environments: a two level hierarchy. In: IEEE International Conference on Robotics and Automation, Raleigh, NC, pp. 1644–1649 (1988)
5. Wang, J., Yang, J., Qu, Z.: An optimal solution to mobile robot trajectory generation in the presence of moving obstacles. In: Proc. 10th Int. Meeting Robot. Remote Syst., Gainesville, FL (March 2004)

Obstacle Detection for Unmanned Ground Vehicle in Cross-Country Environment

Yibing Zhao[1], Jining Li[2], Linhui Li[1], and Hai Wang[1]

[1] State Key Laboratory of Structural Analysis for Industrial Equipment, School of Automotive Engineering, Dalian University of Technology, 116024, Liaoning, China
zhaoyibing005@163.com
[2] Digital Arts Department, Dalian Neusoft Institute of Information, 116023, Liaoning, China
lijining@neusoft.edu.cn

Abstract. Reliable detection of non-traversable hazards is a key requirement and significant challenge to unmanned ground vehicle (UGV) autonomous cross-country navigation. DLUT is developing a daytime obstacle detection capability using UGV mounted sensors and has performed three obstacle detection algorithms. In this paper, we currently focus on the cues for obstacle detection color camera sensor provides. Color or monochrome images were collected from a general dynamics autonomous system and processed off-line with run-time passive perception software that includes: a water obstacle detector, a non-traversable tree trunk detector, a bush or shrub detector. A detailed description of each obstacle detection algorithm and their performance is presented in this paper.

Keywords: Unmanned Ground Vehicle, Cross-country environment, Obstacle detection, Non-traversable hazards.

1 Introduction

There are many types of non-traversable obstacles that UGV can encounter during autonomous navigation in cross-country environment [1]. The ability to detect and avoid hazard obstacle poses a current challenge to the acceptance and proliferation of tactical UGVs [2]. Note that there also are shrub or bush covers that could cause damage to the perception sensors in cross-country environment [3]. robust detection of those hazards is a critical perception requirement for UGV autonomous navigation. [4]. Brian Yamauchi et al have explored the use of ultra-wideband (UWB) radar, LIDAR, and stereo vision for all-weather navigation capabilities [5]. YAO et al proposes novel algorithm to detect water hazard [6]. JPL tried to detect water hazards by extracting and combining several features of water [7], Arturo Rankin models reflections of the sky for water by using water body intensity data to estimate the total reflection coefficient contribution [8]. Under the DARPA Perception for Off-Road Robots program JPL has designed a non-traversable tree trunk obstacle detector based on stereo range data [9]. Macedo et al observe that ladar beams will "penetrate" some distance into vegetation. [10]. Michael et al observe the point cloud images can be used to identify objects based on combined spatial and spectral features in three dimensions and at long standoff

D. Jin and S. Lin (Eds.): Advances in Mechanical and Electronic Engineering, LNEE 176, pp. 549–553.
springerlink.com

range [11]. Octavian et al observe the procedures based on the neural network solution allow the definition and the implementation of a computing algorithm [12]. This article is organized as follows. Section 1 presents introduction of object detection in cross-country environment. Section 2 is related to hardware description. Section 3, 4 and 5 describes water, tree trunk and bush or shrub detection respectively. Section 6 has the conclusions.

2 Hardware Description

The DLUT perception system consists of two AVT F-033B/C color cameras mounted to camera brackets, one real-time laser radar (SICK-221), and one American UNIQ USS-301 infrared camera and one ADVANTECH IPC-610H industrial PC. The camera brackets are equipped to the UGV's top mounting platform with shims that provided a 10º down tilt. Laser radar is mounted to the bumper with horizontal forward-looking scanning field of view. Figure 1 shows a picture of the UGV's perception system and other refitted systems mounted to the New Concept Vehicle of Cherry.

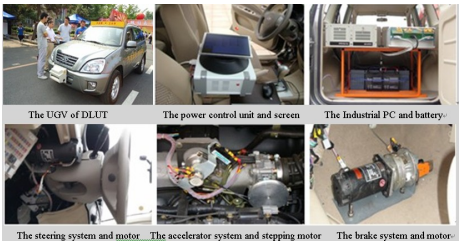

Fig. 1. The UGV's perception system and other refitted systems

3 Water Obstacle Detection

When a new image is input, the pixels are mapped into a smaller number of *k* "local" Gaussians using the EM algorithm *(k<n)*. These *k* local Gaussians are then merged into the memory of the learning algorithm. In detail, to update the memory, consider the *j-th* local Gaussian. The learning algorithm determines the closest Gaussian in the global memory, where closeness is determined through the Mahalanobis distance.

tribution is learned, which maintain a mixture of Gaussians. Each such mixture is a Gaussian defined in the *HSB* color space;

$$d(i, j) = (\mu_i - \mu_j)^T (\Sigma_i + \Sigma_j)^{-1} (\mu_i - \mu_j) \quad (1)$$

Let i be the index of the minimizing Gaussian in the memory. The remaining pixels are than classified using the learned mixture of Gaussian. Pixels whose *HSB* -value is near one or more of the learned Gaussians are recognized as water when the following judgement is satisfied:

$$d\ (i,\ j) \leq \phi \tag{2}$$

Where ϕ is an acceptance threshold. The parameters of this global Gaussian are set to the weighted mean:

$$\begin{aligned} \mu_i &\leftarrow \frac{m_i \mu_i}{m_i + m_j} + \frac{m_j \mu_j}{m_i + m_j} \\ \sum_i &\leftarrow \frac{m_i \sum_i}{m_i + m_j} + \frac{m_j \sum_j}{m_i + m_j} \\ m_i &\leftarrow m_i + m_j \end{aligned} \tag{3}$$

Here m_j is the number of pixels in the image that correspond to the *j-th* Gaussian. Figure 2 illustrates the detection of water hazard. White indicates where the color cue suggests water.

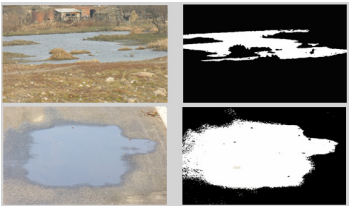

Fig. 2. A frame showing the water hazards (left) and water detection results on binary image (right)

4 Tree Trunk Obstacle Detection

We rely on the edge detector to recognize vertical structure with parallel line pairs that are leaning or curved. When the slope of the lines is almost equal, the obstacle is probably recognized as tree trunk under additional condition which satisfies the ratio F_k. Parallelogram factor is represented by the maximum of ratio F_k. Also we combine the ratio of width versus height to assist identifying tree trunk. In addition, we threshold the estimated range value of F_k and the angle of each tree trunk in the image plane to avoid detecting vertical objects that are lying on the ground (such as the road edge) in 3D world model.

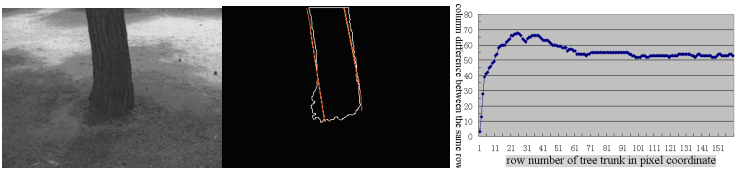

Fig. 3. A frame showing some tall vertical structure(left), a edge extraction image by using LOG operator and thinning algorithm, brown indicates the least squares line fit of edge points (middle), and tree trunk column difference between the same raw, which shows the slope of Least squares line fit (in brown) is almost equal (right)

5 Bush or Shrub Obstacle Detection

This paper puts forward new method to detect shrub or bush based on *edge-shape-factor* measured with edge's curvature. The first step is to segment monochrome image by using *Fisher Rule*, then to apply morphological dilation and region growing separately after noise removing. Secondly, LOG operator and thinning algorithm are employed to get single-pixel edge of obstacle, then to acquire the chain code and curvature of each obstacle pixel. The final step is to calculate *edge-shape-factor* by using formulas defined as follows:

$$e_i = \begin{cases} \left| c_{(k,i+k/8)} - c_{(k,i)} \right| & p_i \cdots not \quad signed \\ 0 & p_i \cdots \quad signed \end{cases} \tag{4}$$

$$edge - shape - factor = \frac{N_{e_i \in [3,13]}}{N_{e_i}} \tag{5}$$

The curvature of edge point is denoted by e_i . $c_{(k,i+k/8)} - c_{(k,i)}$ describes the difference of tangent angle measured from edge point p_i . $N_{e_i \in [3,13]}$ represents the number of e_i which lie between the minimum range of 3 and the maximum range of 13. Of course, N_{e_i} denotes the number of e_i .

Large amount of training samples illustrate that the edge-shape-factor of shrub or bush ranges from 0.0496 to 0.0762. Based on this shrub or bush is identified, which has good real-time ability and robustness.

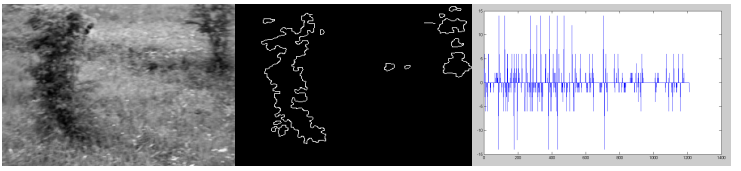

Fig. 4. Monochrome image of shrub is shown (left), LOG operator and thinning algorithm are employed to get single-pixel edge of obstacle (middle), then to acquire the chain code and curvature of each obstacle pixel, the number of single-pixel is 1201, the number of the curvature which lie between the minimum 3 and the maximum 13 is 79, and the edge-shape-factor is 0.0658 (right).

6 Results and Conclusions

We take multiple algorithm approaches to detect discrete objects with different dominant characteristics. The obstacle detection algorithms used on the Unmanned Ground Vehicle include water detector, tree trunk detect Digital images are processed at a resolution of 320x240. Test results show that most of the obstacles were detected and there were no false obstacle detections.

Acknowledgement. The Project Supported by China Academy of Space Technology (Grant No. WY-YY/M-200818JY001).

References

or and bush or shrub detector.

1. Rankin, A., Huertas, A., Matthies, L.H.: Stereo vision based terrain mapping for off-road autonomous navigation. In: Gerhart, G.R., Gage, D.W., Shoemaker, C.M. (eds.) Unmanned Systems Technology XI 2009. Proc. SPIE Int. Soc. Opt. Eng., vol. 7332, pp. 733210-1–733210-17. SPIE, Orlando (2009)
2. Mills, M.E.: Challenges to the Acceptance and Proliferation of Tactical UGVs. J. RUSI Defence Systems 10, 28–30 (2007)
3. Rankin, A., Bergh, C., Goldberg, S., Bellutta, P., Huertas, A., Matthies, L.: Passive Perception System for Day/Night Autonomous Off-Road Navigation. In: Unmanned Ground Vehicle Technology VI Conference 2005. Proc. SPIE Int. Soc. Opt. Eng., vol. 5804, pp. 343–358. SPIE, Orlando (2005)
4. Eric, K., Scott, F., Larry, J.: The DARPA PerceptOR evaluation experiments. J. Auton Robot. 22, 19–35 (2007)
5. Yamauchi, B.: Fusing ultra-wideband radar and lidar for small UGV navigation in all-weather conditions. In: Gerhart, G.R., Gage, D.W., Shoemaker, C.M. (eds.) Unmanned Systems Technology XII 2010. Proc. SPIE Int. Soc. Opt. Eng., vol. 7692, pp. 76920O-1–76920O-10. SPIE, Orlando (2010)
6. Yao, T.Z., Xiang, Z.Y., Liu, J.L.: Robust water hazard detection for autonomous off-road navigation. Journal of Zhejiang University 10, 786–793 (2009)
7. Rankin, A., Matthies, L., Huertas, A.: Daytime water detection by fusing multiple cues for autonomous off-road navigation. In: 24th Army Science Conference, pp. 177–184. IEEE Press, Piscataway (2006)
8. Rankin, A., Huertas, A., Matthies, L., Bajracharya, M., Assad, C., Sherwin, G.W., Brennan, S., Bellutta, P.: Unmanned ground vehicle perception using thermal infrared cameras. In: Gage, D.W., Shoemaker, C.M., Karlsen, R.E., Gerhart, G.R. (eds.) Unmanned Systems Technology XIII 2011. Proc. SPIE Int. Soc. Opt. Eng., vol. 8045, pp. 804503-1–804503-26. SPIE, Orlando (2011)
9. Huertas, A., Matthies, L., Rankin, A.: Stereo-Vision Based Tree Traversability Analysis for Autonomous Off-Road Navigation. In: Gerhart, G.R., Gage, D.W., Shoemaker, C.M. (eds.) Unmanned Systems Technology XI. Proc. SPIE Int. Soc. Opt. Eng., vol. 7332, pp. 733210-1–733210-17. SPIE, Orlando (2009)
10. Daniel, F.H., Martial, H.: Natural terrain classification using three-dimensional ladar data for ground robot mobility. Journal of Field Robotics 23(10), 839–861 (2006)
11. Powers, M.A., Davis, C.C.: Spectral LADAR as a UGV Navigation Sensor. In: Turner, M.D., Kamerman, G.W. (eds.) Proc. of SPIE 2011. Laser Radar Technology and Applications XVI, vol. 8037, p. 80371F-1– 80371F-15. SPIE, Bellingham (2011)
12. Octavian, G.M., Barbelian, M., Arhip, J., Jurba, M.: Intelligent Image Data Processing for Acquiring Target in a Multisensor Platform. In: 12th International Conference on Optimization of Electrical and Electronic Equipment, pp. 981–988. IEEE Press, Piscataway (2010)

Development of Knowledge-Based System for Bus Body Concept Design

Lingxia Kong[1], Chunning Jin[1], Qinghong Xu[2], Guofu Yang[3], and Dongbin Kan[1]

[1] School of Automotive Engineering, Dalian University of Technology, Dalian 116024, P.R.China
[2] The FAW-Wolkswagen Automotive Company LTD, Changchun 130042, P.R.China
[3] Geely Automobile Institute, Hangzhou 311228, P.R.China

Abstract. An intelligent system for bus body concept design, which implements integration of body frame geometry modeling, analysis and optimization is proposed based on the Knowledge Based Engineering technology. The system is guided by the design idea of analysis-driven design and developed by means of development tools, such as UG/KF, UG/Open API and UG/Wizard. It supports all phases of bus body concept design effectively. Parameterized body frame geometry model and finite element model are constructed rapidly and automatically in the system, and performance simulation is implemented before detailed design to afford the optimum plan for subsequent body design. Development process of the system is detailedly introduced in the paper. At last, the modal analysises are performed using the model built by both the system and traditional method. The comparison result shows the efficiency and rapidity of the bus body concept design system.

Keywords: knowledge based engineering, bus body, concept design, parameterized.

1 Introduction

Compared with car products, bus products are characterized by small batch and multi-type. This requires bus producers to shorten the design cycle and lower the development cost while ensuring the product quality [1]. However, in the traditional design method, the design of a new bus structure begins with the designers generating a fully detailed solid model, and they must do vast amount of geometry clean in preparation for meshing and analysis. Time consuming manual modification should be made according to the post processing results. In this way, the design and analysis stages are decoupled as they are undertaken by different experts utilizing different softwares. And a mass of time is spent during this process due to the manual operation manner [2].

An intelligent system for bus body concept design based on the Knowledge Based Engineering (KBE) technology is proposed. The purpose of the study is to develop a closed loop system that integrates geometry modeling, analysis and optimization in early stage of designing a new bus structure, and thus afford the optimum plan for subsequent body design [3,4]. Parameterized body concept geometry model and finite

D. Jin and S. Lin (Eds.): Advances in Mechanical and Electronic Engineering, LNEE 176, pp. 555–561.
springerlink.com

element model can be constructed rapidly and automatically in the system using UG/KF, UG/Open API, and UG/Wizard development tools. The development cost is reduced and the design efficiency is improved significantly because of automation.

2 System Workflow

The system is developed based on UG/NX 6.0 platform. As illustrated in Fig. 1, the procedure may be broken down into three phases: geometry modeling, finite element modeling and performance analysis.

First, a fully parameterized body frame geometry model is built using knowledge fusion (KF) langue. An assembly structure is adopted to represent the configuration of bus frame model tree. The part class is developed based on the basic class provided by UG/KF, and then these parts compose the component class, and finally the product class. Simultaneously structure parameters and geometric inputs are extracted.

Second, create finite element model for solver quickly and automatically based on UG/Open API secondary development tool.

Third, solve the solution by NX/Nastran solver, and the feedback of analysis results provides valuable information for better body architecture.

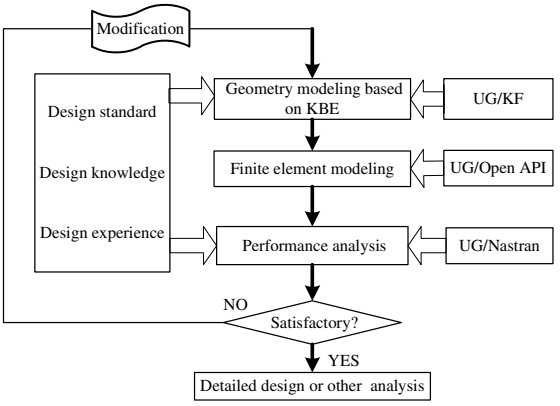

Fig. 1. System flowchart and corresponding development tools used in three phases

The three phases constitute a closed loop system, implementing CAD/CAE integrative virtual design in order to quicken the development process at concept design phase. The system is for variety design of body frame based on existing bus style. Fig. 2 shows the body surface adopted, subsequent frame model, FE model, as well as the whole process of bus body concept design. The system integrates design practices and engineering expertise, so even if a designer who is lack of experience can complete the whole process smoothly.

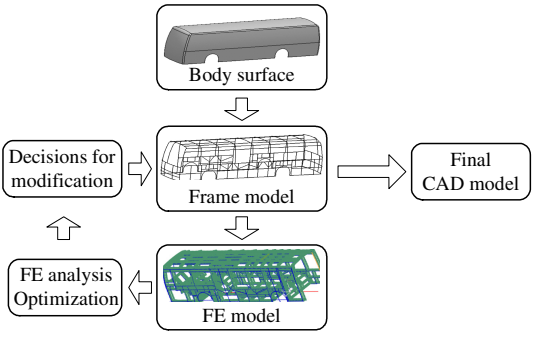

Fig. 2. The whole process of bus body concept design and related models

3 Bus Frame Geometry Modeling Based on KBE

Take the geometry elements of the body surface shown in Fig. 2 as basic inputs, extract design parameters, develop KF classes in different layers, and finally build a knowledge-based geometry model. Beam structures of the body frame are simplified to one-dimension lines in order to reduce design parameters and improve calculation speed. It is proved that the main performance of the bus body can be reflected by 1D beam, which is reasonable in early stage of design.

3.1 Bus Frame Assembly Structure

The whole bus body frame can be divided into five parts: Left side wall frame, Right side wall frame, Roof frame, Rear wall frame and Front wall frame [5]. And each part consists of many beams. According to the feature of these beams, this paper classifies them into the following six types: X beam, Y beam, Z beam, Skew beam, Symmetric beam and Boundary beam. Boundary beams are the beams that lie in the boundary of each wall. In the modeling process, Boundary beams will be created first, so the bus body frame will be divided into five parts clearly, and this will make the following model construction work more modularized. X, Y, Z beams are the beams along x-axis, y-axis, z-axis respectively accordingly. Skew beams are the diagonal braces which are used to enhance the structural rigidity. Symmetric beams are the beams that have symmetrical relationships which are defined through some functions in KF language. So if this kind of beam on one side wall was modified, the corresponding beam on the opposite side wall would change accordingly.

Based on the classification, the assembly structure of the body frame can be summarized three layers, as illustrated in Fig. 3, which shows the designing idea of top-to-bottom.

3.2 Bus Frame Class Development

The complicated frame structure is decomposed into individual beams by way of the assembly diagram. Then according to the hierarchical and assembly relationships

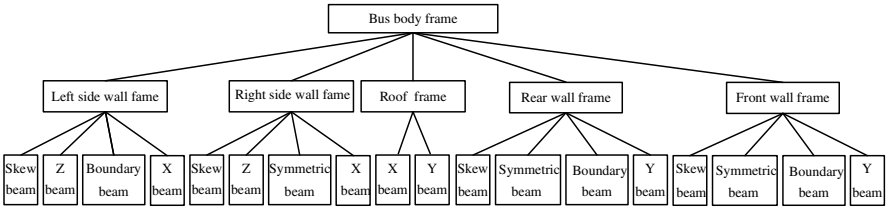

Fig. 3. The assembly structure diagram of the body frame of three layers

among different layers, self-defined classes in different layers are separately generated and stored into DFA files. Hierarchical relationships between parent classes and child classes are clearly shown in Fig. 4. The child class inherits the attributes of the parent class, and adds its own peculiar attributes [6].

The part classes describing the six types of the beams are developed based on the basic KF class through inheritance and parameterization. These part classes compose the component classes describing the five parts of the body frame. The classes also define non-geometry and connection relation information besides size and shape parameters, in preparation for the next analysis and optimization. And finally the part classes compose the product class, namely bus frame class.

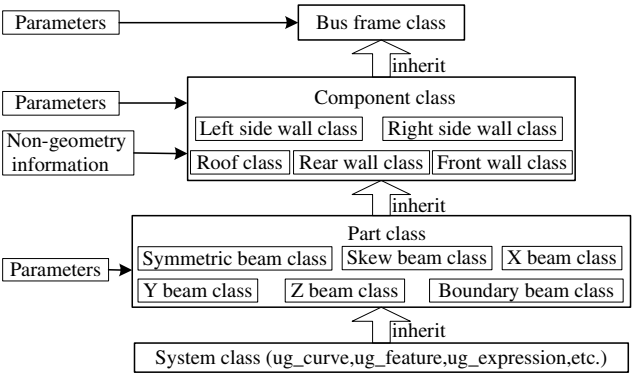

Fig. 4. Hierarchical relationships of KF classes

64 structure parameters and 18 basic geometric inputs are extracted, and 151 beams are created to describe the body frame model. Side wall frame needs the most structure parameters compared with other components, and it may influence subsequent design parameters. Hence we take left side wall frame for instance to show the extracted structure parameters. As shown in Fig. 5, Height of Waist rail (HW), Number of Window Pillar (NWP), Position of Window Pillar (PWP) and other various parameters are involved. The parameters are mutually related.

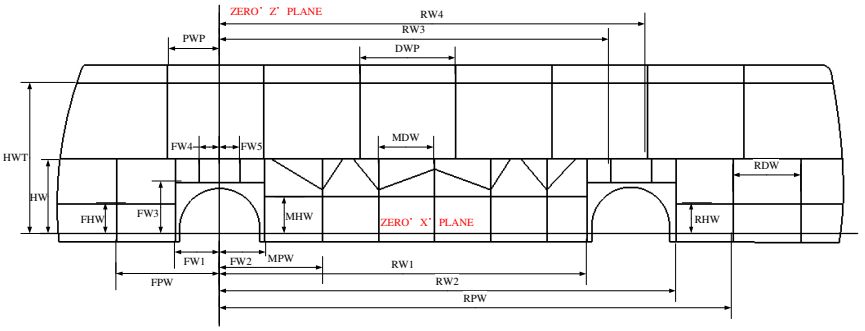

Fig. 5. Structure parameters about left side wall frame

3.3 Bus Frame Model Output and Editing

The output of the program is a complex bus frame assembly structure as shown in Fig. 2.

The wizard user interface is designed to realize interaction between program and customers. Customers just need select proper geometry elements and input reasonable parameters step by step according to the interface display, without searching for related standard and regulation about bus body design. Program interface design workflow is illustrated in Fig. 6.

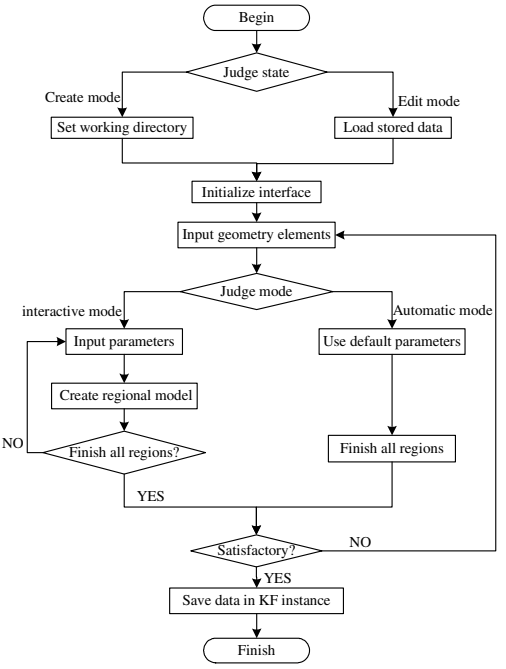

Fig. 6. Program interface design flowchart

The output of the design can be edited in three forms conveniently: editing parameters at the user interface, modifying the DFA files, and editing "Expression" by using the expression tool of UG. Moreover, deformation in design result in each layer of the bus body assembly structure can be made without changing beam structures or connection relationships.

4 Finite Element Modeling and System Verification

Finite element model shown in Fig. 2 is created rapidly and automatically based on UG/Open API secondary development tool. The process includes meshing the beams, assigning sectional and material properties, building connection, checking meshing, etc. Then the solution is solved by NX/Nastran solver. Analysis results will finally return to the CAD system in farther development, establishing a smooth workflow from CAD to CAE, then to CAD.

Modal analysis is carried out in the system, mode shapes charts are shown in Fig. 7.

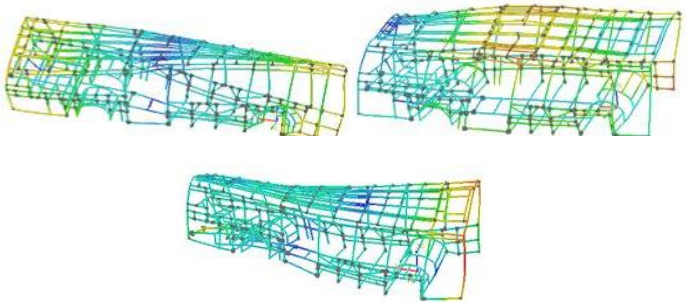

Fig. 7. The former three mode analyses results in order.

Meanwhile, modal analysis is carried out using detailed model and in manual method to verify efficiency and rapidity of the system. The result comparison between the two methods is shown in Table 1.

Table 1. Result comparison between concept design and detailed design

Parameter	Detailed model/HZ	Concept model/HZ	Error rate/%
First mode	8.11	8.45	4.19
Second mode	9.39	9.84	4.79
Third mode	11.15	11.76	5.47

As we can see from Table 1, the frequency values of the concept model are a little higher than those of the detailed model. The reason is that in the concept model the

connection between beams is simulated with rigid connection, and this enhances the rigidity of the bus body frame, leading to a higher frequency value.

Compared with the result of the detailed model, the error rate of the first step frequency of the concept model is 4.19%, the error rate of the second frequency is 4.79%, and that of the third frequency is 5.47%, so the difference is about 5%. This indicates that the concept design satisfies the precision requirement. By using this system, the time spending on the whole procedure from modeling to analysis will be cut to a few minutes, which may be a couple days if the work is done by the traditional method. So the system can shorten the cycle of product development greatly.

5 Conclusions

The system is guided by the design idea of analysis-driven design and knowledge-driven design. It supports the whole process of bus body concept design rapidly and automatically, and affords optimum parameters for subsequent detailed design. The modal analysises verify reliability and rapidity of the system.

Acknowledgments. This work was funded by the Fundamental Research Funds for the Central Universities (DUT11LK11). This support is gratefully acknowledged.

References

1. Xu, Z., Zhang, D.: Finite Elements Analysis and Optimization of Coach-body Frame. Journal of Hefei University of Technology (Natural Science) 32, 108–111 (2009)
2. Chapman, C.B., Pinfold, M.: The Application of A Knowledge Based Engineering Approach to the Rapid Design and Analysis of An Automotive Structure. Advances in Engineering Software 32(12), 903–912 (2001)
3. Hou, W., Zhang, H., Chi, R., Hu, P.: Development of Integrated System for Conceptual Design of Vehicle Body Structure. Computer Integrated Manufacturing Systems 15(2), 240–244 (2009)
4. Sui, H., Yang, S.: Problems in Analysis Driven Design Process and Practicable Solution. Journal of Taiyuan University of Technology 33(4), 459–461 (2002)
5. Tan, J., Zhang, D., Xiong, L., Xu, Z., Guo, Z.: Lightweight Design for Bus Body Frame. Automotive Engineering 28(4), 394–397+389 (2006)
6. Zhang, S., Liu, W., Ruan, F., Zhang, J.: Design of Mutual-inductor Mould Based on KEB Technology 25(8), 87–89 (2005)

Design of Controlling System in Multi-function Durability Testing Device for Vehicle Vacuum Booster with Brake Master Cylinder

Xianpeng Hao[1], Ranfeng Zhang[1], Xine Li[1], and Mengmeng Wang[2]

[1] Changchun Institute of Optics, Fine Mechanics and Physics, Chinese Academy of Sciences, Changchun, 130033, P.R. China
[2] School of Automotive Engineering Dalian University of Technology, Dalian, 116024, P.R. China
haoxp@ciomp.ac.cn, zhangranfengjlu@yahoo.com.cn, amylxe@sohu.com,835651169@qq.com

Abstract. The quality of vehicle vacuum booster with brake master cylinder is related to the safe of drivers and automobiles. The testing experiment must be executed strictly before leaving factory based on the national standards .The paper introduces the controlling system of multi-function durability testing device, which is designed for doing durable testing experiments and Anti-lock braking system (ABS) performance experiments. The structure and theory of device is presented. The controlling system is illuminated in detail. To test the dynamic property, this system was identified by a recursive BP neural network. According to the character of a great deal of sensors and actuators, the high precision, capabilities and reliability, the distributed control mode (DCS) including the computer and PLC by RS-485 bus is utilized. The four channels testing experiments are achieved at the same time. The test data is directly memorized into the computer. The results of general endurance and ABS endurance testing experiments are shown to demonstrate the excellent performance of the testing device.

Keywords: Vehicle Vacuum Booster, Brake Master Cylinder, Multi-function Durability Testing Device, DCS Mode.

1 Introduction

The brake master cylinder with vacuum booster is a crucial compoment of the vehicle brake, which performance impacts on the braking effect of vehicles and the vehicles' performance. It is directly related to the human safety at the same time. With the improvement of vehicles' technology and the velocity enhancement, higher brake performance is required. In order to examine each performance index of the brake master cylinder with the vacuum booster, a series of testing inspection equipments relating to the performance need to be developed. This equipment forms the manufacturing requirements of durability of the test bed on the basis of digesting the product test requirements of the United States, Germany, Japan, France, Italy and other countries of the famous auto manufacturers. The technical level and function

D. Jin and S. Lin (Eds.): Advances in Mechanical and Electronic Engineering, LNEE 176, pp. 563–568.
springerlink.com

integration of the equipment are very high, so its design and manufacturing are more difficult than existing testing platforms [1].

2 Basic Components of Multi-function Durability Testing Device

The multi-function durability testing device mainly consists of high and low temperature test chamber, electric/pneumatic thrust system, vacuum system, load simulation system, hydraulic system and electric control system. The basic composition is shown in Fig.1.The high and low temperature test chamber is divided into two working chambers, providing high and low temperature test environment for the experiments. Measured devices are installed in the first working chamber of the high and low temperature test box. The other working chamber is the intake working chamber of the vacuum booster. The temperatures of the two working chambers are controlled separately, according to the test requirements. The thrust mechanism is divided into electric thrust system and pneumatic thrust system. It is applied to thrust on the vacuum booster with the push rod system. The vacuum system is mainly used to provide vacuum environment for the vacuum booster testing experiment. Load simulation is divided into normal load and spring load. The former is used to adjust the initial volume of the hydraulic output system, so as to change the hydraulic output pressure or pneumatic thrust system of the stroke. The latter is mainly used to adjust the rigidity of the system, and accelerate the oil return of brake wheel cylinder during the push rod return at the same time. Hydraulic system mainly provides hydraulic environment for master cylinder, simulating the working environment of the measured devices. According to parameters set by test requirement, and coordinates among every systems, the electronic control system sends the instructions [2].

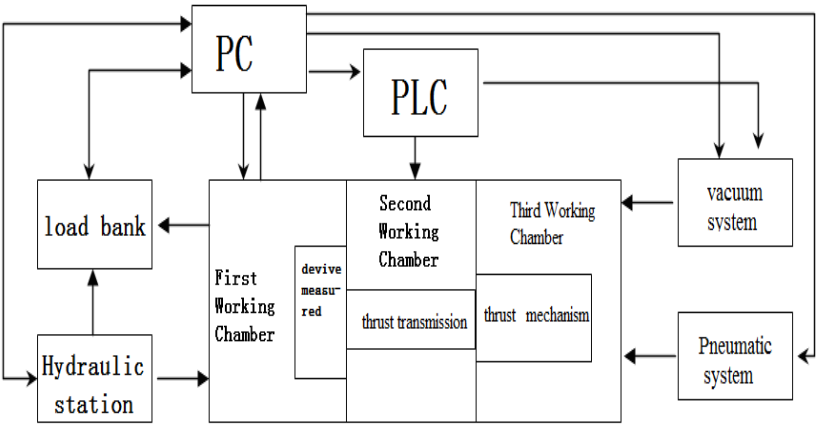

Fig. 1. The sketch map of basic component of multi-function durability testing device

3 Controlling System in Multi-function Durability Testing Device

According to t multi-function durability testing device, which has more sensors, more control units, more complex control links and higher reliability requirement, the controlling system is taked PC as upper computer and PLC as lower computer. The distributed control system (DCS) is establishes based on RS-485 bus communication mode. The whole system uses a approach of decentralized data collection and centralized control. There are some advantages, such as strong versatility, flexibility in system configuration, perfect control ability, facilitated data processing, centralized display operation, friendly interface, simple and standardized installation, convenient debug, safe and reliable operation, and so on[3].

3.1 Basic Components of the Controlling System

The controlling system in multi-function durability testing device consists of upper computer, lower computer, signal acquisition system, servo control system, power supply etc. The system is shown in Fig.2. Upper computer is the control center of the whole device. The testers set the working parameters by upper computer, control the testing process. Upper computer can display the real-time experimental data and reprocess the data. Lower computer controls the power and vacuum system using PLC with the high reliability, directly deals with the abnormal situation. The whole system communicates by the RS-485 bus between the upper and lower computer[4].

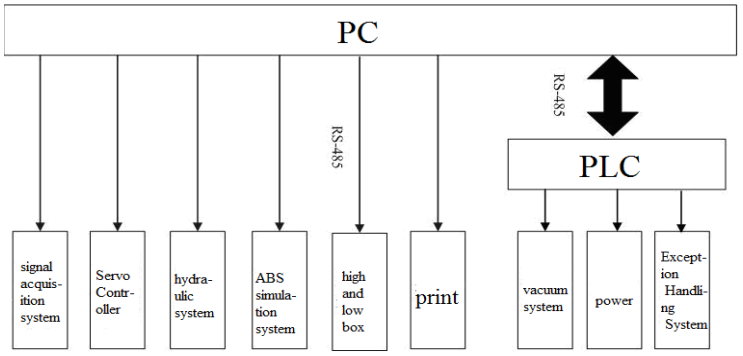

Fig. 2. The diagram of the Controlling System in multi-function Durability Testing Device

3.2 Software Structure

The software of the control system consists of upper computer software and lower computer software, which is shown in Fig.3. The upper computer software is programmed using Visual C++6.0 and mainly includes test module, data acquisition module, test curve display module, digital signal processing module, data post-processing module, main communication module etc. Test module is used to set various test parameters and send the control orders of high-low temperature test-box,

vacuum system, hydraulic system etc. Test curve display module displays the relevant sensor data obtained from the data acquisition module in accordance with the requirements in the testing process in order to observe the real-time condition of the test through the curve. Data processing module mainly completes the digital filtering and curve fitting for the collected data. The main communication module is used by upper computer to achieve the data communication between lower computer and high-low temperature test-box etc. Lower computer program mainly includes test control unit, vacuum system control unit, abnormal situation processing unit, communication unit of lower computer etc. According to the orders sent by upper computer, test control unit commands the test of each working-station. Vacuum system control unit is that lower computer controls the vacuum of each vacuum tank and working-station booster based on the parameters settings of upper computer and measure values of pressure sensors. Abnormal situations processing unit is that lower computer can automatically make the appropriate treatment to ensure the safety of operators and equipment when the abnormal conditions occurs.

Multi-function durability testing device has high requirements on the real-time, reliability and precision of the system. In order to ensure the real-time and reliability of the system, firstly, the quality of signals is ensured in hardware through the shielding, filtering etc. Secondly, communication protocol and communication mode are made some improvements. According to the characteristics of the system, the communication protocol is simplified, communication command words are given the priority. The synchronization point settings and synchronous response way are used in the protocol. Since the signals obtained in the experiment are often non-stationary signals, there may be many peaks or mutation parts, and the noise is also not stationary white noise. It is necessary to carry out noise reduction before analyzing

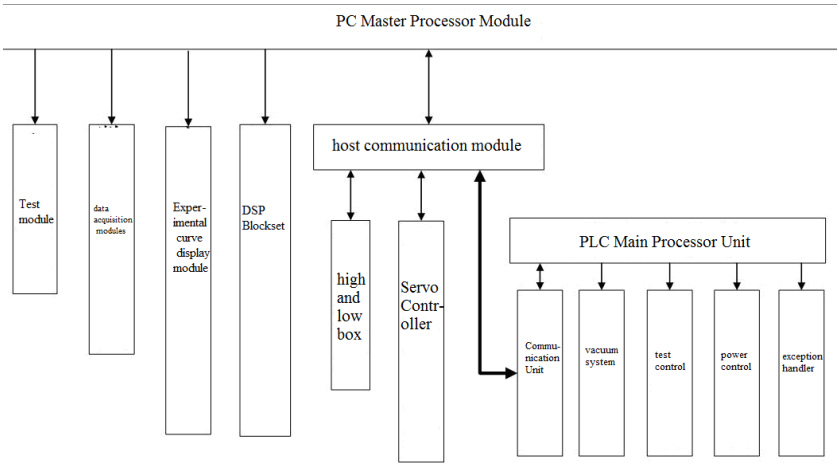

Fig. 3. The block diagram of the multi-function Durability Testing Platform

signals. It seems powerless if using the traditional Fourier transform analysis, because Fourier analyzes signals entirely in the frequency domain, which can not give the signal change at a certain time point, making any mutation of the signal on the time axis and affecting the entire spectrum of the signal. Wavelet Analysis can distinguish the mutations and noise of the signal effectively in different decomposition layers for analyzing the signal both in the time domain and frequency domain, so the signals are denoised well. It is impossible to establish the mathematical mode1 because of so many uncertain complex nonlinear systems. This system was identified by a recursive BP neural network. The fault diagnosis of software and redundancy design are also added to the upper computer and lower computer software design[5].

4 Testing Results

The durability tests of the brake master cylinder with the vacuum booster consist of high temperature, normal temperature, low temperature general endurance tests and high temperature, normal temperature, low temperature ABS endurance tests. As the space limitations, we only take the general endurance test and ABS endurance test at normal temperature for example.

4.1 The General Endurance Test at Normal Temperature

At normal temperature, the drive mode is pneumatic drive with one buck-boost period of 3.4s, a rise time of 0.3s, a holding time of 1.6s and a fall time of 0.2s. The testing curve is shown in Fig. 4.

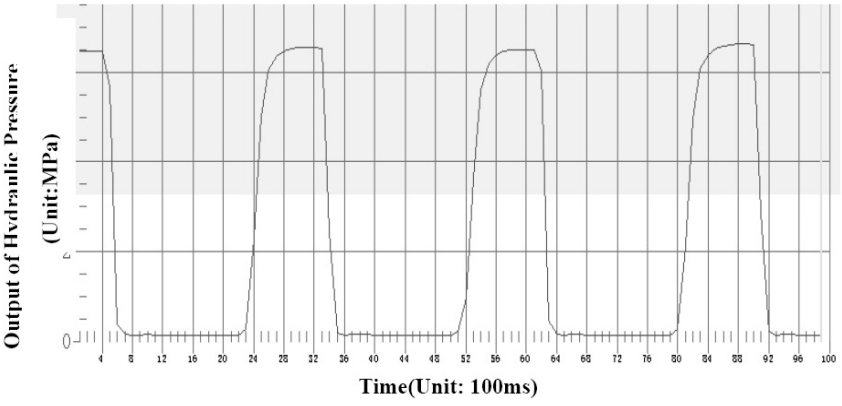

Fig. 4. The curve of the general endurance test at normal temperature

4.2 The ABS Endurance Test at Normal Temperature

There are three rise pulses and a fall pulse. The minimum input pressure is 4MPa at normal temperature. The rise input pulse pressures separately are 6MPa, 8MPa and 10MPa. Each period is 320ms, a single pulse time is 65ms. The testing curve is shown in Fig. 5.

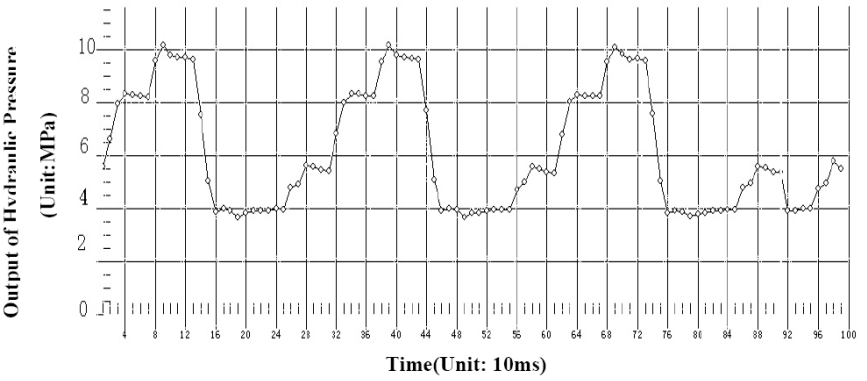

Fig. 5. The curve of the ABS endurance test at normal temperature

5 Conclusion

The multi-function durability testing device is a strong comprehensive integrated platform, so its studying and manufacturing process also has a greater challenge. At present, this device has been accomplished. The whole testing projects of vacuum booster with brake master cylinder has been done based on the national and user's standards. The results of testing experiment are shown to demonstrate the performance rationality of the testing device.

References

1. Li, Q., Wang, T., Zou, J.: Simulation Analysis of Automobile Test-bed Braking System. Science Technology and Engineering 10(18), 4562–4569 (2010)
2. Liu, X.: BC2005A durable multi-function test bed design. Graduate School of Chinese Academy of Sciences (2006)
3. Li, M., Shao, C.: Electric Controlling System Designing in Saloon Car Vacuum Aiding Force Implement Durability Testing Platform at Normal Temperature. Drive System Technique 17(1), 46–47 (2003)
4. Xu, B.: The communication protocol construction based on minitype distributed control system. Journal of Anhui University Natural Science Edition 30(3), 36–40 (2006)
5. Li, Z., et al.: System Identification for Fatigue Test System of Vacuum Booster with Brake Master Cylinder. Journal of System Simulation 19(16), 3724–3726 (2007)

The Design of an Embedded TCP/IP Protocol Stack of the Vehicle Detector

Bin Wu[1], Hongwen Jia[1], Wenji Yang[2], and Lanlan Li[1]

[1] Department of Information Engineering,
ChuZhou Vocational Technology College, Anhui Chuzhou, China
wubind2003@163.com
[2] ASUS Technology (Suzhou) Company Limited, Jiangsu Suzhou, China
saillimited@163.com

Abstract. This paper aims to develop a networking inductive loop vehicle detector, which comprises inductive loop vehicle detector and an embedded TCP/IP protocol stack of microcontroller connected to main controller in Intelligent Transportation System (ITS). The design is further described from two aspects. Firstly, it elaborates on the theory of inductive loop vehicle detector as a data collector. Secondly, it expounds how TCP/IP protocol stack uIP0. 9 is embedded in MCU, how the network chip RTL8019AS is controlled with the MCU and how a single inductive loop vehicle detector is networked with the intelligent signal controller in ITS.

Keywords: Inductive loop vehicle detector, ITS, Internet of Things, TCP/IP, MCU.

1 Introduction

Intelligent Transportation Systems (ITS) is an effective means to alleviate this problem without re-construction of roads. Vehicle detector is an important constituent of ITS. Commonly used in the world are induction loop detector, ultrasonic detectors, video detector etc[1]. Ultrasonic detectors are of long service life, portable, convenient to be erected, but easily affected by wind speed, with high mistake examining rate, high costs of video detector, poor constancy. And coil detectors, with high adaptability and cost-effectiveness, are currently the most widely used vehicle detector.

In modern era, Internet of Things gains ever-increasing popularity. It is vital to network a single coil vehicle detector with the ITS control module and plays a decisive role in laying the foundation for Internet of Things to develop in the future. This paper discusses how the control, usually by a MCU based on the principle of electromagnetic induction loop detector, is linked into the master control of the ITS by TCP / IP protocol module and how its software and hardware is designed.

2 Overview

A complete system is divided into two parts: hardware and software .The following Fig.1 describes the system block diagram of the overall hardware. Overall software block contains data collection software and networking software.

D. Jin and S. Lin (Eds.): Advances in Mechanical and Electronic Engineering, LNEE 176, pp. 569–574.
springerlink.com

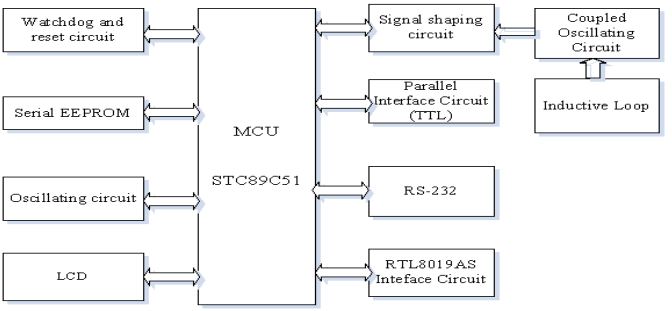

Fig. 1. Overall hardware block diagram

3 Inductive Loop Vehicle Detector

How it works: an induction loop vehicle detector comprises an oscillator circuit having a plurality of capacitors switchable in circuit with a road loop under the control of a microcomputer to determine the oscillator frequency. The microcomputer monitors the oscillator frequency and controls the switching of the capacitors to periodically return the frequency to a predetermined value. A counter counts a predetermined number of oscillator cycles and gates of clock into a second counter whereby the count of the counter represents the oscillator period. A "vehicle detected" output is given when the monitored frequency alters by more than a predetermined amount, representing a decrease in the inductance of the loop. On detecting an increase in the inductance above a predetermined threshold the detector is inhibited for a predetermined time, e.g. about 1 second, to avoid errors caused by magnetic effects.

Most Inductive loop vehicle detector work on the fact that metals in a magnetic field change the behavior of the field. There are two general approaches to detect these changes. In one approach, an alternating current is provided to a transmit coil. A receive coil is used to pick up the magnetic field generated by the transmitter. If a piece of metal comes inside the range of the magnetic field lines, the receive coil can detect a change in both amplitude and phase of the received signal. The amount of amplitude change and phase change is an indication for the size and distance of the metal, and can also be used to discriminate between ferrous and non-ferrous metals. In the other approach, current pulses are sent to the transmit coil. The magnetic field caused by these pulses start eddy currents in metals close to the coil. If the magnetic field is switched off fast enough, the eddy currents can be detected with the transmit coil, which then acts as a receiver. This design uses the latter detection method [1,2].

3.1 Hardware Design of the Detection and Identification System

Loop is a sensor coil buried in the traffic lane. The two ends of the loop wire are connected to the loop extension cable, which in turn connects to the vehicle detector. Loop acts as the coil inductance L in LC ring oscillator, when a metal object comes

near, its inductance changes, leading to oscillation frequency changes. On the frequency of detection and by comparison, it can be judged that vehicles enter or exit. The signal input circuit is formed by the LC oscillator circuit and the shaping circuit together, as shown in Fig.2.

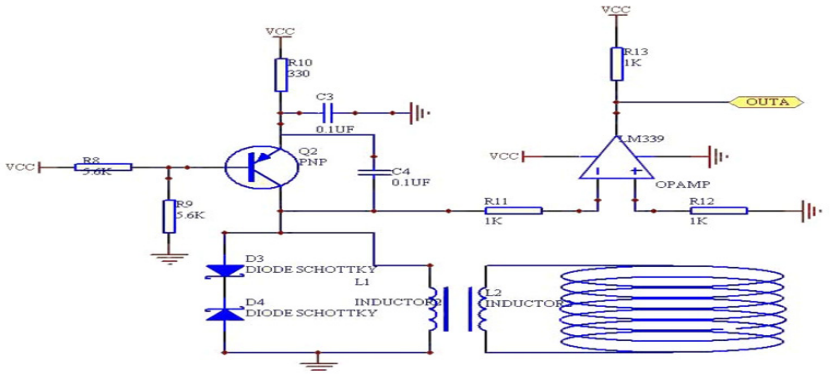

Fig. 2. Circular coil sensor

The coil and the movings are coupled through the electromagnetic field. When a vehicle passes through the circular coil at certain position, the eddy current caused in the body is definite, and the impact of eddy current on the circular coil is definite too, there is a certain ring coil mutual inductance between vehicle and coil. Thus, we consider the vehicle as a resistor R1, inductor L1 and short-circuit ring, which ring coil through mutual inductance M and the intersection of chains. Loop supply voltage is $U = U_m \sin \omega t$, provided by the oscillator circuit, inductance L2, a resistance R2. The equivalent inductance can be:

$$L = L_2 - \frac{(\omega M)^2 L_1}{R_1^2 + (\omega L_1)} \tag{1}$$

The first item of this changeable amplitude is related to L2 permeability of vehicles; the second item and eddy current effect are concerned. If working frequency is properly selected, when a vehicle passes through loop, change of the first equation is less than that of the second equation,, it means the equivalent inductance decreases. LC oscillators oscillation frequency is:

$$f = \frac{1}{2\pi\sqrt{LC}} \tag{2}$$

Obviously, when the vehicle passes through an annular coil, L becomes smaller, f larger, the microcontroller detection circuit measures its frequency changes, which can determine whether there is a vehicle passing through. Since the output of LC oscillator circuit is a sine wave with a burr, it is not suitable for microcontroller to do digital processing. Therefore, a single threshold voltage comparator LM339 is needed to turn them into square wave signal output. The result of the square wave is measured as shown in Fig.3.This design uses 51 core microcontroller P1.4 and P1.5

port count combined with timer interruption, Units of timer to collect 10MS oscillation circuit input the port of T0 with pulses, And set the current sensitivity requirements according to types of vehicle. Then compare with the reference frequency, to determine whether vehicle passes. Finally, send out output signal according to the procedures.

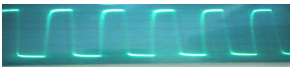

Fig. 3. Output square wave

3.2 Software Programming of Detection Recognition System

The Core technology of detection and identification system and its process are shown in Fig.4. The main program includes: 1602 LCD driver, the vehicle's fuzzy classification, measuring the vehicle's passing time and the pulse number in T0 within time unit.

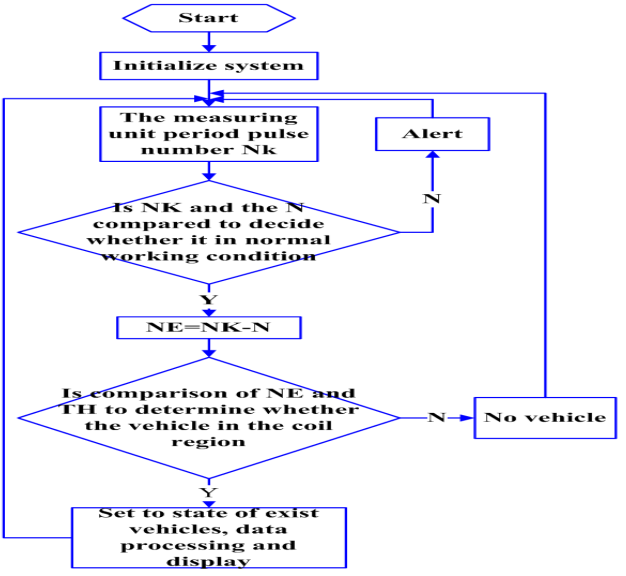

Fig. 4. Software diagram of detection part

4 Communication Part

In this design, the low-cost 51 MCU is used to control the network interface chip RTL8019AS and the simple free TCP / IP protocol stack uIP 0.9 is taken as a design core, to transmit data from loop detector to center controller of intelligent traffic signal controller.

4.1 RTL8019AS Ethernet Controller

RTL8019AS Ethernet controller produced by Taiwan Reahek, with its excellent performance and low price, occupies a large proportion in the market of 10Mbps nic.

a) Features[3]:
1) Compliant to Ethernet II and IEEE802.3 10Base5, 10Base2, 10BaseT;
2) Software compatible with NE2000 on both 8 and 16-bit slots;
3) Supports both jumper and jumperless modes;
4) Supports Full-Duplex Ethernet function to double channel bandwidth;

b) Internal Structure:
RTL8019AS internal can be divided into remote DMA interface, local DMA interface, MAC (Or qualitative access control) logic, data coding and decoding logic and other ports. Internal structure is shown in Fig. 5.

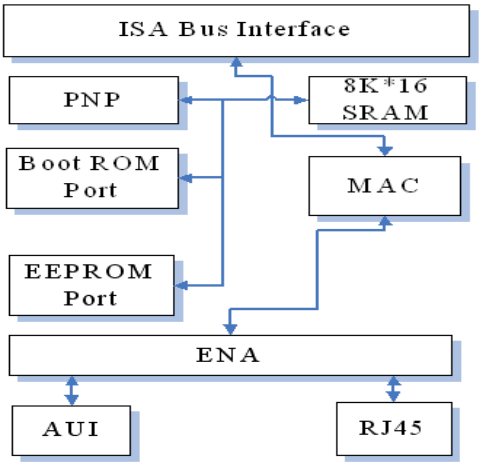

Fig. 5. RTL8019AS Internal Structure

Remote DMA interface is the internal RAM RTL8019AS microcontroller to read and write on the bus, ISA bus interface part. MCU transmit data by just the remote DMA operated. RTL8019AS local DMA interface is the connection with the network cable channel, controller and cables to complete the data exchange. Medium access control (MAC) logic to complete the following functions: when the microcontroller sends data to the net, a frame data is sent into the RTL8019AS buffer zone through remote DMA channel, then transmit command; When RTL8019AS completes sending the previous frame, it begins to send this frame. RTL8019AS data received through the MAC is stored in the buffer zone by FIFO after comparison, CRC check,; after over a collection notify the processor in the form of interruption or register flag . FIFO logic buffers sending and receiving data for 16 bytes to reduce the frequency of local DMA requests.

4.2 Software Part

uIP0.9 developed by Sweden's computer science research institute Adam Dunkels is special for 8/16-bit processor on the TCP/IP protocol stack [4]. Because uIP has notable features, 0.6 version has been transplanted into multiple processors, including MSP430, AVR and Z80 etc. This design will successfully transplant it to 51 microcontrollers.

uIP0.9 is in the middle level of network communication, the upper level protocol is called applications here, and lower level hardware or firmware is called network device drivers. Obviously, uIP0.9 is not only designed for Ethernet, with media irrelevance. In order to save resources occupation, and simplify application interface, uIP0.9 is specially treated in internalization.

Communication part is based on the hardware and software design described above, The loop vehicle detector hardware collects vehicle information, which is processed through testing software and sent to buffer and finally the data is transmitted to the main signal controller of ITS.

Acknowledgments. The authors would like to thank Anhui Provincial College Foundation for Young Talent (No.2012SQRL251) and the Nature Science Foundation of Anhui Provincial Colleges （No.KJ2012Z302） for financially supporting this research.

References

1. Liu, Z.Y.: Intelligent Traffic Control Theory and Its Application, pp. 3–5. Beijing Science Press (2003)
2. Lin, L., Han, X.B.: Miniature Inductive Loop Vehicle Sensor. Sensors and Actuators 19, 995–996 (2006)
3. RTL8019AS Realtek Full–Duplex Ethernet Controller with Plug and Play Function Specification, p. 3 (2002)
4. Dunkels, A.: uIP-A free Small TCP/IP Stack, p. 1 (2002)

Research on Intelligent Traffic Control System Based on Hybrid Genetic Algorithm

Tao Yang and Li Kang

Department of Electrical Engineering and Automation, Luoyang Institute of Science and Technology, Luoyang, 471023. Peoples R. China
{yangtao2012,kangli20112012}@163.com

Abstract. In view of the deficiency and inadequacy of existing urban traffic control systems, the paper introduces the hybrid genetic algorithm and establishes timing scheme with a delay model which realizes intelligent control and cost reduction and provides a new perspective for road traffic regulation and control. The simulation result shows us that hybrid genetic algorithm will effectively reduce the average waiting time of vehicles, have a very good application prospects in the complex and practical issues.

Keywords: Hybrid Genetic Algorithm, Intelligent Traffic Control System, Delay Model, Timing Scheme.

1 Introduction

With the rapid development of economy, city streets have more and more vehicles. Traffic congestion and jam phenomenon becomes more and more serious, because traffic accident frequency, the worsening environmental pollution and a series of problems, therefore, design a stable, flexible, convenient traffic signal intelligence control system has the necessity and reality [1].

The hybrid genetic algorithm is a reference to natural selection and natural biological genetic mechanism of random search algorithm, it can makes several good capability modified genetic algorithm for the proper combine, this can produce more superior performance of genetic algorithm [2]. The hybrid genetic algorithm is applied to the traffic signal control system, it must insist that the optimal control strategy to reduce the network traffic all the travel time based on the actual traffic flow, stream of concrete road traffic to design the traffic lights signal control plan [3], and even according to the traffic flow within the period of the speed in statistical scheme and optimization, ensure roads and maximize flow unit of time [4].

This article aim at urban traffic system's defects and insufficiency, the hybrid genetic algorithm is applied to intelligent traffic signal control system, establish the intelligent traffic signal control mathematical model, and the simulation realized based on hybrid genetic algorithm of intelligent traffic signal control system[5].

2 Modeling of Intelligent Traffic Control System

Intelligent traffic signal control system in order to solve the public infrastructure construction is slow and the vehicle grow is too fast offer a effective way , and in order

D. Jin and S. Lin (Eds.): Advances in Mechanical and Electronic Engineering, LNEE 176, pp. 575–580.
springerlink.com

to make intelligent traffic signal control system operation efficiently , need to build intelligent traffic signal control system mathematical model[6].

2.1 Modeling Issues

Assume that the vehicle arrived odd crossroad at random, and the arrival number of vehicles obey Poisson distribution and assume that to cross ports vehicles proportion for turn left, turn right and go straight is in certain. Considering the single phase four cross intersection with 4*3=12 lanes of the direction of vehicle control, because turn right vehicle without engagement of traffic signal restrictions. Therefore, only consider a single intersection eight lanes of the direction of vehicle traffic signal control. The below is establishing single traffic delay model.

Set a single crossover port place at the first t arrived within t seconds of the total number of vehicles is:

$$q_t = \begin{cases} m \\ 0 \end{cases} \tag{1}$$

Due to turn right is free from the traffic signal, so consider only turn left and go straight line of vehicles. A red light phase began the first t seconds left the vehicle queue length for $p_{t,l}$, and go straight vehicles queue length for $p_{t,d}$.

$$\begin{cases} p_{t,l} = p_{G,l} + \sum_{i=1}^{t} \alpha.q_i \\ p_{t,d} = p_{G,d} + \sum_{i=1}^{t} \beta.q_i \end{cases} \tag{2}$$

Type $p_{G,l}$ shows that the former green light is not clear to the left during the number of vehicles; $p_{G,d}$ shows that the former green light period did not clear to go straight during the number of vehicles. The red light vehicles during the queue waiting time is

$$D_{t,R} = \sum_{i=1}^{t} (p_{G,l} + p_{G,d} + \sum_{j=1}^{i} q_j) \tag{3}$$

If s is saturated flow, the green light phase began the first t (s), has been cleared of the left vehicle queue length is $S_{t,l}$ and go straight vehicle queue length $S_{t,d}$ is:

$$\begin{cases} S_{t,l} = \eta_l (p_{R,l} + \sum_{i=1}^{t} \alpha.q_i - \alpha.s.t) \\ S_{t,d} = \eta_d (p_{R,d} + \sum_{i=1}^{t} \beta.q_i - \beta.s.t) \end{cases} \tag{4}$$

$P_{R,l}$ is during previous red light for left turn lanes line up of the vehicle;$P_{R,d}$ is during previous red light for verticals lanes line up of the number of vehicles. Parameters η_l, η_d were the sign of cycle lanes and turn left lane vehicle whether have delay went. If the

number of the brackets is positive, the corresponding $\eta_i i=(l,d)$ take 1, otherwise $\eta_i i=(l,d)$ take 0,. The green light traffic during the waiting time is

$$D_{t,G} = \sum_{i=1}^{t} \eta_l .(p_{R,l} + \sum_{j=1}^{i} \alpha.q_j - \alpha.s.t) + \sum_{m=1}^{t} \eta_d .(p_{R,d} + \sum_{n=1}^{m} \beta.q_n - \beta.s.t) \tag{5}$$

Therefore, a cycle, the port of the total delay A_1 vehicles can be expressed as

$$D = D_{RR} + D_{GG} \tag{6}$$

$D_{RR,}$ D_{GG} show delay in effective red light time $R(s)$ and within effective green time G(s). For this, a cross in the port of each car for the average delay model is

$$d_m = \frac{D}{\sum_{l=1}^{R+G} (\alpha + \beta) q_i} \tag{7}$$

Similarly, it can get a cycle the intersection of every car average delay model.

In order to realize of the stream of real-time and then from the bottom of the model in a period of time for each car on an average delay of a model for planning, through the traffic lights for solutions, and once the light of the time to make the adjustment of eliminating the time, the average car is delay in the shortest.

2.2 Timing Scheme

Each intersection control scheme solving process is divided into the three steps.

The first step: assume that the number of vehicles at an intersection within 1s arrive at cross obey λ parameters for the Poisson distribution. According to the hypothesis test method can get traffic λ estimate, accordingly Poisson distribution function can calculate the traffic flow.

The second step: according to the current traffic to determine the next traffic signal timing cycle T

$$T = \frac{1.5.\sum_{i=1}^{I} (l_i + t_{zi}) + 5}{1 - \sum_{i=1}^{I} q_i / s_i} \tag{8}$$

In the type, phase I=4, assume that every phase the loss of time t_{zi}=2(s), the red time l_i= 2(s), the i believe size, the saturated flow of critical lane s_i=2700 (a/hours).

Step 3: toward each phase of the real-time timing scheme of code about binary system, transfer the corresponding hybrid genetic algorithms to planning to get an average delay time of the shortest phase timing scheme.

3 Intelligent Traffic Control System

Set the initial population size is M=50, the iterative algebra S_t= 100, also assume that vehicle left α=0.2 probability, the vehicles go straight probability β=0.5, vehicle turn right probability γ=0.3. In order to test the algorithm is strong adaptability, at the same time, in order to more practical, consider contains in the peak traffic distribution, the real-time timing formula establish problems, traffic in a period of time distribution of normal distribution, in the middle part of the emergence of a peak traffic. During peak hour traffic, each phase will appear intersection stranded vehicles.

After get the traffic information, take the cycle estimation methods of traffic lights that next cycle time. In the actual make sure cycle time T, should be based on the actual situation, the cycle of designation appropriate length. When traffic is very small, T value will be small; this means that each phase of the green time will be very short; this obviously on the traffic safety is unfavorable. Therefore, ought to set a shortest signal period limit value. Generally assume that can not less than P×l5s (P for phase digits). On the other hand, when the signal period length above a certain limits, the growth of the ability to pass will tend to be stagnant, and vehicle delay time increase sharply, therefore, also want to provisions the longest signal period limit. Here the shortest time set traffic light cycle is 80 seconds, the longest time is 200 seconds, according to (8) type for the calculation of the traffic lights change of long cycle accessory flow curve shown as shown in figure 1

Based on optimal retained the basic genetic algorithm and the hybrid genetic algorithm applies to the model at the same time, it is concluded that the contrast of the results are shown below:

Table 1. Scheme of different time distribution to compare

Project	Basic scheme	Fixed time scheme	Indefinite time scheme
The average delay time	26.88 (s)	25.40 (s)	22.31 (s)
Algebra of basic genetic	101	106	110
Algebra of hybrid genetic	18	24	29

The fixed timing scheme adopts the experimental data of a cycle timing formula, this time the four phase setting time for 20s, 37s, 20s, and 37s. As can be seen in the traffic flow change, fixed timing formula average delay time is the largest, uncertain period when the average scheme with real time delay is the shortest, not fixed cycle with real time timing dial and fixed cycle real time timing dial scheme fixed timing scheme compare the effect of the scheme increased by 6.51% and 17.93%.

From table 1 of the comparison method can be concluded that: as for the optimization model, based on the most optimized reserved basic genetic algorithms also can converge to the optimal solution, but the hybrid genetic algorithm convergence speed is faster than the basic algorithm, the basic genetic algorithm to realize the real-time control, the hybrid genetic algorithm for the fast convergence of the traffic control real-time realize offer possible.

The most optimized reserved basic genetic algorithm and the hybrid genetic algorithm in uncertain period timing scheme solving process is the convergence speed in table 2 and figure 2 shows

Table 2. Constringency speed of two algorithms to compare

Time	10 Generation	20Generation	30Generation
Results of basic genetic algorithm	26.64(s)	24.55(s)	21.87(s)
Results of hybrid genetic algorithm	24.41(s)	23.03(s)	21.22(s)

From table 2 we can see, the same genetic algebra, the hybrid genetic algorithm is superior to the results basal optimal save basic genetic algorithms, figure 2 shows, basic genetic algorithm convergence algebra is 112 generation, and elite adaptive hybrid genetic algorithm of the average convergence algebra is 28 generation, accelerate the algorithm convergence speed.

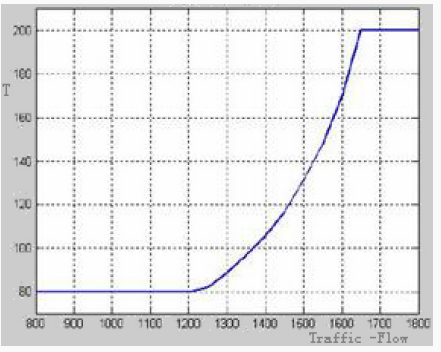

Fig. 1. Curve of cycle length with traffic-flow

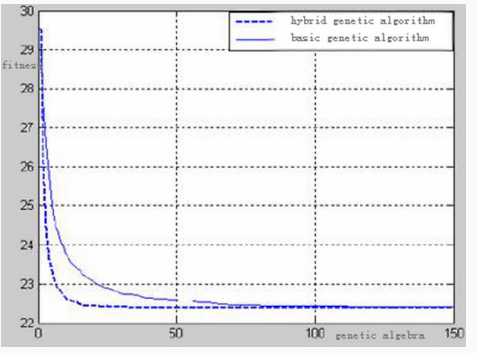

Fig. 2. Comparison of convergence speed

From the above we can see, the genetic algorithm in these large complex problems is in a fit place, and basic genetic algorithm convergence speed is slow, spend more operation cost, and can't meet in real-time require, but improved the hybrid genetic algorithm convergence speed is fast, not only it's capability choiceness, but also can satisfy the requirements of practical application.

4 Conclusion

For real-time traffic control such complicated practical problems, traditional optimization methods is hard to obtain satisfactory effect, the hybrid genetic algorithm in this place play out huge application potential. The hybrid genetic algorithm based on the intelligent traffic signal control system can simply and effectively relieves traffic; improve the traffic capacity of intersection.

References

1. Hinojosa, Y., Kalcsics, J., Nickel, S., et al.: Dynamic supply chain design with inventory. Computers and Operations Research, 118–120 (2008)
2. Galvao, R.D., Santibanez, G.A.: Lagrangean heuristic for the pk-median dynamic location problem. European Journal of Operational Research (23), 11–14 (1992)
3. Hinojosa, Y., Puerto Fernandez, J.F.R.: A multiperiod two-echelon multicommodity capacitated plant location problem. European Journal of Operational Research (2000)
4. Gen Machine R. Genetic Algorithms and Engineering Optimization 30(8), 18–21 (2000)
5. Wang, H.F., Wu, K.Y.: Hybrid genetic algorithm for optimization problems with permutation property 18(3), 211–215 (2004)
6. Albareda-Sambola, M., Fernandez, E., Hinojosa, Y., et al.: The multi-period incremental service facility location problem. European Journal of Operational Research 20(10), 45–49 (2009)

An Experiment System of Multi-objective Control Design for Autonomous Vehicles

Mi Dong[1], Jian Yang[1,*], Jingrong Yu[1], Jiangmin Chunyu[2], and Yan Tang[3]

[1] School of Info. Sci. & Eng., Central South University, Changsha, Hunan 410083, China
[2] Delta Tau Data Systems, Inc., Chatsworth, CA 91311, USA
[3] Dep. of ME, Embry-Riddle Aeronautical University, Daytona Beach, FL 32114, USA
fish2bear@gmail.com

Abstract. In this paper, a nonlinear control design is proposed for a team of wheeled mobile robots to cooperate in a dynamically evolving environment to track their virtual leader(s), while avoiding static and dynamic obstacles. Then, an experiment system of multi-objective control problem is formulated, and the control is synthesized by generating a potential field force for each objective and combining them through analysis and design. The results are illustrated by several experiments including cooperative motion of a team of vehicles moving through urban settings with static and moving obstacles, as well as narrow passages.

Keywords: experiment system of cooperative motion, tracking of virtual leader, obstacle avoidance, oscillation suppression.

1 Introduction

Many future missions such as cooperative robot reconnaissance [1], marine minesweeping [2], and formation flight control [3] will be implemented with distributed autonomous systems, which require formation movement capability. Most existing methods dealing with formation movement control use one of three strategies: behavior based, virtual structure, or leader-follower.

In the behavior based approach [4], a series of primitive goal oriented behaviors are proposed to each robot. The disadvantage is that it is difficult to formalize and analyze the group dynamics mathematically, consequently it is difficult to study the convergence of the formation to a desired geometric configuration. The virtual structure approach [5] is inspired by the rigid body motion of a physical object with all points in the object maintaining a fixed geometric relationship via a system of physical constraints. The disadvantage is that the virtual structure's position is controlled by the positions of the robots, which makes the formation itself, be the centralized control. In the leader-follower approach [6], some robots are designed as leaders moving along predefined reference trajectories. The remaining robots are followers and are required to maintain a desired posture (distance and orientation)

* Corresponding author.

D. Jin and S. Lin (Eds.): Advances in Mechanical and Electronic Engineering, LNEE 176, pp. 581–586.
springerlink.com

relative to their own leader. The disadvantage is that the formation does not tolerate leader faults, since the leader's predefined trajectory is independent of the motion of each associated follower.

To handle the formation movement effectively, cooperative formation control with collision avoidance is addressed in this paper. Instead of directly extending the single agent controls to the multi-agents case, we incorporated it with the cooperative control design. The proposed decentralized control is reactive, considers the formation feedback, and allows topological changes in the sensing and communication networks. Since the proposed control is based on a potential field method, its inherent oscillation problem is also addressed to improve group transient performance.

2 Problem Formulation

Consider a collection of point-mass agents whose dynamics are given by

$$\dot{q}_{r\mu} = v_{r\mu}, \dot{v}_{r\mu} = u_{r\mu}, (\mu = 1, \cdots, m) \tag{1}$$

where $q = [x, y]^T$ denotes the center position, $v = [x, y]^T$ represents the velocity, and uis the control input. Thus we can define the states $S(t) = (q(t), v(t))$. Subscripts r, g and o indicate the vehicle, goal and obstacle respectively.

Given the initial configurations $S_{r\mu}(t_0) = (q_{r\mu}(t_0), v_{r\mu}(t_0))$, as shown in Figure1, the objective of this paper can be summarized as follows:

i). tracking the specified virtual leader $S_{g\mu}(t_0) = (q_{g\mu}(t_0), v_{g\mu}(t_0))$;

ii). avoiding the n obstacles $S_{oi} = (q_{oi}(t), v_{oi}(t))(i = 1, 2, \cdots n)$;

iii). avoiding the remaining m–1 agents $S_{rj} = (q_{rj}(t), v_{rj}(t))$, $(j = 1, 2, \cdots, \mu - 1, \mu + 1, \cdots, m)$;

iv). suppressing the oscillation of the system trajectory.

To solve the problem, one can make the following choices without loss of generality:

i). The μth agent under consideration is represented by a 2-D circle with the center at $q_{r\mu}(t)$ and of radius *R*. The range of its sensors is also described by a circle centered at $q_{r\mu}(t)$ and of radius R_s.

ii). The ith static/moving obstacle will be represented by a convex object of any shape (such as circle, ellipse, or polygon).

3 Cooperative Formation Control of Networked Agents with Collision Avoidance

Consider a group of networked dynamic systems given by the following canonical Form

$$\dot{X}_i = A_i X_i + B_i U_i, Y_i = C_i X_i, \dot{\eta}_i = g_i(\eta_i, X_i) \tag{2}$$

where $i=1,\cdots,q,l_i\geq 1$ is an integer, $X_i\in\Re^{l_i m}$, $\eta_i\in\Re^{n_i-l_i m}$, $I_{m\times m}$ is the m dimensional identity matrix, $\otimes$ denotes the Kronecker product, J_k is the kth order Jordan canonical form given by

$$J_k=\begin{bmatrix}-1 & 1 & 0 & \cdots & 0 & 0\\ 0 & -1 & 1 & \ddots & 0 & 0\\ \vdots & \ddots & \ddots & \ddots & \ddots & \vdots\\ 0 & 0 & \cdots & -1 & 1 & 0\\ 0 & 0 & 0 & \cdots & -1 & 1\\ 0 & 0 & 0 & \cdots & 0 & -1\end{bmatrix}\in\Re^{k\times k} \tag{3}$$

where $A_i=J_{l_i}\otimes I_{m\times m}\in\Re^{(l_i m)\times(l_i m)}$ $B_i=\begin{bmatrix}0\\ I_{m\times m}\end{bmatrix}\in\Re^{(l_i m)\times m}$ $C_i=[I_{m\times m}\quad 0]\in\Re^{m\times(l_i m)}$, $Y_i\in\Re^m$ is the output $U_i\in\Re^m$ is the cooperative control law to be designed, and subsystem $\dot{\eta}_i=g_i(\eta_i,X_i)$ is input-to-state stable.

We consider the general case where exchange of output information among the vehicles occurs only intermittently and locally. To capture this information flow, let us define the following sensing/communication matrix and its corresponding time sequence $\{t_k^s:k=0,1,...\}$

$$S(t)=\begin{bmatrix}S_1(t)\\ S_2(t)\\ \vdots\\ S_p(t)\end{bmatrix}=\begin{bmatrix}s_{11}(t) & s_{12}(t) & \cdots & s_{1p}(t)\\ s_{21}(t) & s_{22}(t) & \cdots & s_{2p}(t)\\ \vdots & \vdots & \vdots & \vdots\\ s_{p1}(t) & s_{p2}(t) & \cdots & s_{pp}(t)\end{bmatrix},\begin{cases}S(t)=S(t_k),\forall t\in[t_k,t_{k+1})\\ S(k)=S(t_k)\end{cases} \tag{4}$$

where $s_{ii}(t)\equiv 1$; $s_{ij}(t)\equiv 1$ if the jth vehicle is known to the ith vehicle at time t, and $s_{ij}(t)\equiv 0$ otherwise, and. Time sequence $\{t_{sk}\}$ and the corresponding changes in the row $s_i(t)$ of matrix $s(t)$ are detectable instantaneously and locally at the ith vehicle, but they are not predictable, prescribed or known a priori or modeled in any way.

Cooperative controls proposed in this paper are in the class of linear, piecewise constant, local feedback controls with feedback gain matrices $G_i(t)=[G_{i1}(t),...,G_{iq}(t)]$, where $i=1,...,q$,

$$G_{ij}(t)=G_{ij}(t_k^s),\quad \forall t\in[t_k^s,t_{k+1}^s);\ G_{ij}(k)=G_{ij}(t_k^s)=\frac{s_{ij}(t_k^s)}{\sum_{\eta=1}^{p}s_{i\eta}(t_k^s)}K_c,\quad j=1,...,q; \tag{5}$$

where $s_{ij}(t)$ are piecewise-constants as defined in (4) and $K_C\in\Re^{(l_i m)\times(l_i m)}$ is a constant, nonnegative, and row stochastic matrix. That is, cooperative controls are of form

$$U_i=\sum_{j=1}^{q}G_{ij}(t)[s_{ij}(t)y_j]=G_i(t)Y \tag{6}$$

where $Y = [Y_1^T, \cdots Y_q^T]^T$. Although $S(t)$ is not known a *priori* nor can it be modeled, $S(t)$ is piecewise constant, diagonally positive and binary, and the value of row $s_i(t)$ is known at time t to the ith vehicle. The above choice of the feedback gain matrix block $G_{ij}(t)$ in terms of $s_{ij}(t)$ ensures that matrices $G_i(t)$ are row stochastic and that control is always local and implementable with only available information.

Theorem 1: Consider dynamics system in (2) and under cooperative control (6). Then systems of (2) exhibit a single cooperative behavior as,

$$X_{ss} = l_{N_q} cX(t_0) = c_0 l_{N_q}, \text{, and } Y_{ss} = c_0 l_m, \ c \in R^{l \times N_q}, c_0 = R, \tag{7}$$

provided that
i) Gain matrix K_c is chosen to be irreducible and row stochastic.
ii) Systems in (2) have a sequentially complete sensing/communication.

Through state transformations, the formation control problem for (1) can be recast as the cooperative control design problem (2). Let the transformation be

$$X_\mu = O_\mu(t) - O_\mu^d(t), \tag{8}$$

Then we introduce the canonical model with $X_\mu = [X_{\mu 1}, X_{\mu 2}, X_{\mu 3},]^T \in R^3$, $U_\mu = R^3$, and $Y_\mu = R^3$.

$$\dot{X}_\mu = \lambda * (A_\mu X_\mu + B_\mu U_\mu), Y_\mu = C_\mu X_\mu. \tag{9}$$

where A_μ, B_μ and C_μ are given by

$$A_\mu = \begin{pmatrix} -1 & 0 & 0 \\ 0 & -1 & 0 \\ 0 & 0 & -1 \end{pmatrix}, B_\mu = \begin{pmatrix} 1 & 0 & 0 \\ 0 & 1 & 0 \\ 0 & 0 & 1 \end{pmatrix}, C_\mu = \begin{pmatrix} 1 & 0 & 0 \\ 0 & 1 & 0 \\ 0 & 0 & 1 \end{pmatrix}.$$

To this end, if we can design the cooperative control U_μ such that states X_μ for all μ converge to the same steady state X_{ss}, then

$$O_\mu \to X_{ss} + O_\mu^d(t) \ ,$$

from which it can be seen that the desired formation is achieved for the whole group, while the agents move along the desired trajectory shape.

Considering the dynamic system, where we aim to make $\| X_i - X_j \| \to 0$ while at the same time ensure that $\| O_i - O_j \|^2 \geq \rho_s$ for some positive constant ρ_s. The following condition is then imposed:

$$\| O_i^d(t) - O_j^d(t) \|^2 \geq \rho_s.$$

To address the collision avoidance problem, let us consider the control to be given by

$$\begin{aligned} U_\mu^* = U_\mu + \sum_{j=1, j\neq\mu}^{q} & [-\nabla P_r(O_{r\mu} - O_{rj}) - \dot{\eta}(O_{r\mu} - O_{rj}) \| v_{g\mu} - v_{rj} \|^2 \\ & + f_d(O_{r\mu} - O_{rj})T - \eta(O_{r\mu} - O_{rj})(v_{g\mu} - v_{rj})^T (v_{g\mu} - v_{rj})] \\ & + \sum_{l=1}^{n} [-\nabla P_r(O_{r\mu} - O_{ol}) - \dot{\eta}(O_{r\mu} - O_{ol}) \| v_{g\mu} - v_{ol} \|^2 \\ & + f_d(O_{r\mu} - O_{ol})T - \eta(O_{r\mu} - O_{ol})(v_{g\mu} - v_{ol})^T (v_{g\mu} - v_{ol})] \end{aligned} \tag{10}$$

4 Experiment

Three agents are required to execute the formation movement with the desired triangular formation. The initial location of the virtual leader is (1850,-1000) with the following waypoints: (1800, 3000), (1900, 11000), and (1850, 15000). The initial location of the above three agents are: (1850,-960), (1930,-1040), and (1770,-1040). In the workspace, there are six rectangular static obstacles, (700, 3000, 2000, 6000), (700, 11000, 2000, 6000), (3000, 3000, 2000, 6000), (3000, 11000, 2000, 6000), (1850, 7000, 60, 150), and (1752.5, 13700, 60, 150). In addition, one circular moving obstacle of radius being 10 is also considered. The experiment result considering all obstacles, static and moving is shown in Figure 1.

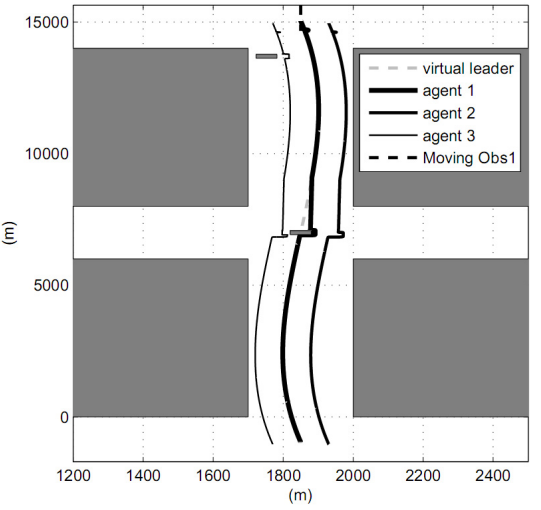

Fig. 1. Cooperative formation movement with avoiding static obstacles

5 Conclusion

In this paper, we proposed a systematic approach to accommodate and achieve multiple objectives. Rigorous proof of incorporation of the proposed control for the single agent with the cooperative formation control is still needed. The effectiveness of the incorporation has been validated by the experiment system.

Acknowledgments. This work was supported by the National Young Teacher Foundation under Grant 2011QNZT037.

References

1. Balch, T., Arkin, R.C.: Behavior-based formation control for multi-robot team. IEEE Transactions on Robotics and Automation 14(6), 926–939 (1998)
2. Edwards, D.B., Bean, T., Odell, D., Anderson, M.J.: A Leader-Follower Algorithm for Multiple AUV Formations. In: Proceedings of 2004 IEEE/OES Autonomous Underwater Vehicles, June 17-18, Sebasco Estates, Maine (2004)
3. Ren, W., Beard, R.W.: Virtual Structure based Spacecraft Formation Control with Formation Feedback. In: AIAA Guidance and Control Conference, Monterey, CA (August 2002); AIAA Paper no. 4963
4. Lewis, M.A., Tan, K.H.: High Precision Formation Control of Mobile Robots Using Virtual Structures. Autonomous Robots 4(4), 387–403 (1997)
5. Lawton, J., Beard, R., Young, B.: A Decentralized Approach To Formation Maneuvers. IEEE Transactions on Robotics and Automation 19(6), 933–941 (2003)
6. Tanner, H.G., Pappas, G.J., Kumar, V.: Leader-to-Formation Stability. IEEE Transactions on Robotics and Automation 20(3), 433–455 (2004)

A Design of Bike Sharing System Based on GPS

Aizhang Guo* and Guoling Liu

School of Information, Shandong Polytechnical University, Jinan, China
{gaz,liugl}@spu.edu.cn

Abstract. This paper explores the problem for bike sharing system. Whatever we think is whether environment protection, personal life quality or urban traffic management, it is time for the implement of bike sharing. In this paper a new level design of bike sharing system model is proposed. The new system model applies network technology, RFID technology, database technology and GPS technology. It can provide optimized route navigation and record the user's riding route by GPS receiver configured in bikes. This paper also describes the leasing station' s configuration, planning and scientific deployment. All the technologies that applied in this bike sharing system could guard against theft and vandalism availably.

Keywords: Bike Sharing System, GPS, Route Navigation.

1 Introduction

Bike sharing systems (also known as: public bikes, or free bikes) are increasingly popular and diverse. A number of bicycles are made available for shared use by individuals who do not own the bicycles. Public bicycles are a mobility service, mainly useful in urban environment for proximity travels. It is able to remove three difficulties of daily cycling use: home parking, theft and maintenance of your private bicycle.

Bike-share programs have existed in Paris, Copenhagen, Vancouver, Barcelona and Milan, but only a few American cities, including Washington, D.C., have tried it[1]. Bike sharing has spread to many other European cities and is currently enjoying surging popularity in North America. Two of more prominent launches have been a small program started in Washington D.C. [2], and a much larger program, called Bixi, launched in Montreal in the spring of 2009.

Bike sharing has also become popular in China. Hangzhou's bike sharing system has 50,000 bikes, surpassing Paris' Velib program which offers over 20,000 bikes. Bike sharing stations can be found in Hangzhou every 100 meters compared to the 300 meters in Paris. The reasons for implementing bicycle sharing systems are as numerous as the forms the systems take. Maybe theft and vandalism emerge as problems. But bike-sharing can seem to shake its reputation for being a culture magnet. In this paper, we propose a new level design of bike sharing system with GPS

* **Biographies:** Aizhang Guo, born in 1964, female, Jinan people of Shandong Province, professor, Master's degree, research field in information management and information system.

D. Jin and S. Lin (Eds.): Advances in Mechanical and Electronic Engineering, LNEE 176, pp. 587–592.
springerlink.com

navigation. The customers can get the optimal route guidance by GPS receiver in bike. The GPS receiver also can record the customer's riding route. In addition, this paper gives a design of unattended rent station.

1.1 Environment Protection

As part of urban transportation, bicycle rental does not bring atmosphere and noise pollution, and provides a convenient green travel mode for residents and tourists. According to the European estimation methods, average emission of carbon dioxide is about 160g per kilometer for motor vehicle travel. Under this standard, calculation the number of using bicing system in year and trip distance in capita showed that in the first year the system, the carbon dioxide emissions of city reduced by about 4176 tons [5]. There are 20,600 public bicycles in all in Verlib system and the annual average riding mileage is about 1 million kilometers. According to the same standards, the excess carbon dioxide emissions would be nearly 33,000 tons in Paris every year if all the trips were completed by cars. Also, more than 1,000 tons of carbon dioxide emissions may be reduced in Lyon by verlo' v 6.4 million km riding mileage per year.

1.2 Personal Life Quality

Bike riding is conducive to keeping fit. Bicycle riding has many advantages. When riding a bicycle you notice the sights and sounds that you, almost always, miss when driving or riding in a car and you get a whole new perspective on your environment. It gives you a chance to leave the rat race behind and lets you stop and smell the roses. Cycling can help you shed unwanted pounds. A 150 pound rider can burn up over 400 calories an hour riding at about 12 mph.

The physical exercise gained from cycling is generally linked with increased health and well-being. According to the World Health Organization, physical inactivity is second only to tobacco smoking as a health risk in developed countries, and this is associated with many tens of billions of dollars of healthcare costs [6]. The WHO' s report suggests that increasing physical activity is a public health ' best buy' , and that cycling is a highly suitable activity for this purpose.

1.3 Urban Traffic Management

Compared with buses, bicycles with a small volume, flexible operation, accessibility, drink and less investment, can be used as complementary tools to rail transport links and consumedly promote the rational use of various traffic resource. They meet residents' transport needs of multi-level short-distance travel and different travel purposes, so as to distribute of passenger flow conveniently and efficiently and improve the overall efficiency of urban traffic.

In Jinan, China, cycle lanes are laid to encourage people to leave their cars at home, get fit, and cut energy use.

1.4 Urban Digital Management

The digital urban management planning is set of information tools with number of applications designed to manage urban areas efficiently.

The key technologies necessary for digital city include: super large-capacity and high-speed computers, scientific computing technology, virtual reality technology, satellite image analysis and 3S (Remote Sensing RS, Geographical information System GIS, Global Positioning System GPS) technology, broadband satellite communications technology, ATM (asynchronous transfer mode), network technology, interoperable system, and metadata, etc.As an advanced measurement tools and new productivity with all-weather, high-precision measurement and automatic features, GPS technology has been integrated into the national economic construction, national defense and social development in various applications. So, we can employ GPS technology in bike sharing system to provide better visualized service and advance the city digital process.

2 Design of Bike Sharing System

Bike sharing system includes not only application software but also hardware. Hardware includes locking devices, centralized controller and backend servers and switches, etc. Application software includes database management software, user management software and terminal applications, etc.

2.1 System Architecture

Bicycle sharing system consists of the centre management system, the terminal data collection system and network communications system. In advantage of the back-end server, centralized controller and locking device the system implements efficient, accurate, timely, and unattended automated management through automatic control technology, CAN bus technology, RFID card technology. System architecture is shown as Fig. 1.

Terminal Data Collection System. Terminal data collection system is mainly used for individual service bicycle to collect and rough process circulation information. It mainly consists of terminal equipment allocated in various leasing station, including the lock device, screen, concentrated controller device, the customer enquires terminals, etc. The lock device is installed in each service to fix bicycle vehicles It is a interaction medium of the user and centralized controller information. Centralized controller is the customer terminal allocated by public bicycle information management system in the service station. Through the lock it can collect basic information such as bicycle identity information and circulation information, bicycle dynamic allowance in formation in service station and user RFID card. Through the transmitting end it can send such basic information to the backend server.

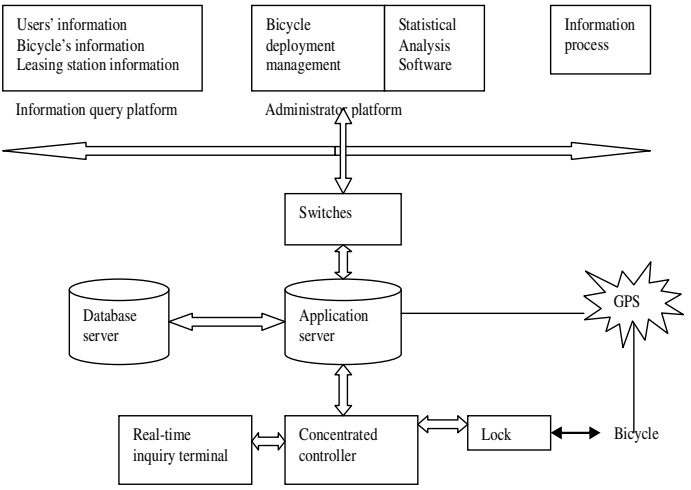

Fig. 1. Bicycle sharing system architecture

Centre Management System. Centre management system is the core of the whole bike sharing management information system, mainly responsible for the entire area public bicycle users' information management, and various leasing station bicycle information management. Through the backend server it can in real-time monitor the bicycles' loadable state and rental situation in various leasing station, so as to carry out controlling and coordinating of various leasing station together with optimization of the resources allocation.

Network Communications System. The communication between the equipments in public bicycle management information system is mainly through the network. As the existing major telecommunication operators' network infrastructure has been lay out widely, network communication can implement in advantage of the existing communications operators' broadband network which is easy to use, extensibility, saving investment, etc.

2.2 Leasing Station Planning

Displayed equations or formulas are centered and set on a separate line (with an extra line or halfline space above and below). Displayed expressions should be numbered for reference. The numbers should be consecutive within each section or within the contribution, with numbers enclosed in parentheses and set on the right margin.

Reasonable choice of leasing stations is one of the key factors of the whole system successful implementation. The following are some principles for leasing stations planning.

Leasing stations are allocated scattered as much as possible and with the demand growing leasing stations' number and storage scale increases gradually. In the early period, leasing stations can be allocated around crowd hubs such as rail transit station and bus station hub, residential areas' service centre, business centre, foreign transport hub, scenic spots.

Leasing stations have clear signs and guide lines so as to ensure that users can find the leasing station easily and quickly.

Leasing stations parking number should be appropriately more than the storage number as reserved space for future's expansion.

Leasing stations set up special locks or lock frame. Locking (or unlocking) must be convenient and theft proof. Users first identify by RFID card on the bike's lock. Users' information is acquired and sent to the backend server with the bike's id. After the centre management information system recognizes the operation is borrowing or returning it sends operation instruction to the bike's lock.

2.3 Scientific Deployment

Leasing stations at different locations have different usage requirements. Around the subway station, the transfer requirement in bicycle and subway is two-way so the bicycles' circulation can level off basically. In some one-way passenger leasing stations, such as the vicinity of residential areas, it is necessary to monitor remaining bicycles in leasing stations in real-time through the computer statistics software station by professional, and ensure that the peak use needs are met timely.

Mobile operators and bicycle sharing business can jointly develop query system by which users can simply send the user' s location (such as Science park) to the information desk, thenceforth, the query system would automatically reply to the nearest bicycle leasing station' s location and its corresponding number of bicycles for rent. When the users encountered some wrong and need call for help, their locations could be found through GPS by control centre.

2.4 Advanced GPS Route Navigation

An important success factor of this bike sharing system is its convenience, which is reflected in three aspects.

First the user can easily rent and return the bicycle. The system is smart and intelligent. It can identify the users' operation and basic information. It can automatically communicate with data centre.

Second the users can at any time inquires their required information. All the leasing stations are connected with control centers through the network so they could return the borrowed bicycle at any leasing station. Users can also get real-time information through the web page, telephone and leasing station terminal. These are based on advanced mature information technology.

Third every bicycle is configured with GPS receiver which can provide optimized route navigation and record the user's riding route. The Global Positioning System (GPS) is a space-based global navigation satellite system (GNSS) that provides reliable location and time information in all weather and at all times and anywhere on or near the Earth when and where there is an unobstructed line of sight to four or more GPS satellites. It is maintained by the United States government and is freely accessible by anyone with a GPS receiver.

GPS was created and realized by the U.S. Department of Defense (USDOD) and was originally run with 24 satellites. It was established in 1973 to overcome the limitations of previous navigation systems [7].

In addition to GPS other systems are in use or under development.

3 Conclusions

Recently and most notably, many municipal governments worldwide have promoted bike sharing for intermodal transport, allowing people to shift easily from other transport to bicycles and back again.

Such a system can reduce the carbon footprint of commuting as well as enable residents to become healthier through exercise. We think these bikes to become icons of a city just like blue buses and yellow taxis. We think it would be proud of the city, giving every residential an opportunity to use the cleanest, greenest form of transport and an chance to keep fit..

In this paper, we propose a new level design of bike sharing system which applies network technology, RFID technology, database technology and GPS technology. We also describe the leasing station' s configuration and planning. In future research, we would explore the system security in internet environment deeply.

References

1. Furness, Z.: One Less Car: Bicycling and the Politics of Automobility, pp. 55–59. Temple University Press, Philadelphia (2010)
2. Chan, S.: City Will Explore Bike-Sharing Program. The New York Times, http://cityroom.blogs.nytimes.com/2008/07/09 city-will-explore-bike-sharing-program/?hp
3. Erb, C.: Sneak peak of a Bixi bike, http://spacingmontreal.ca/2009/01/31/ sneak-peak-of-a-bixi-bike/
4. http://www.treehugger.com/files/2008/11/ montreal-bike-share-gets-new-name.php
5. Wang, Z.-G., Kong, Z., Xie, J.-H., Yin, L.-E.: The 3rd Generation of Bike Sharing Systems in Europe: Programs and Implications. Urban Transport of China 7(4), 7–12 (2009)
6. Hillman, M., Morgan, D.: Cycling: Towards Health and Safety. Oxford University Press (1992)
7. National Research Council (U.S.) Committee on the Future of the Global Positioning System; National Academy of Public Administration (1995). The global positioning system: a shared national asset: recommendations for technical improvements and enhancements, p. 16. National Academies Press (1995)

Lane Mark Detection Based on Improved Hough Transformation for Vehicle Electronic Technology

Lizhuang Liu[1,2], Jianzhu Cui[2], and Jing Li[3]

[1] School of Communication and Information Engineering, Shanghai University, China
[2] Shanghai Advanced Research Institute (SARI), Chinese Academy of Sciences
[3] College of Information Technology, Shanghai Ocean University, Shanghai, China
liulz@sari.ac.cn, cuijianlou@163.com, j_li@shou.edu.cn

Abstract. A lane mark detection is used in various driver assist systems for vehicle electronic technology. One of the subjects for the vision system is improvement of robustness. Various methods have been tried to achieve it. In this work, we tried to improve the approach for the robustness. Our main idea is the noise reduction based on narrowing a width of search area. The proposed method uses the road model based on the generalized hough transformation. We use the gradient direction to reduce the number of votes and the method is Kernel-based Hough transform. It is shown that the method can achieve better detection result.

Keywords: vehicle electronic technology, hough transform, Kernel-based, generalized.

1 Introduction

The Hough transform is a feature extraction technique used in image analysis, computer vision, and digital image processing.[1] The purpose of the technique is to find imperfect instances of objects within a certain class of shapes by a voting procedure. This voting procedure is carried out in a parameter space, from which object candidates are obtained as local maxima in a so-called accumulator space that is explicitly constructed by the algorithm for computing the Hough transform.

The classical Hough transform was concerned with the identification of lines in the image, but later the Hough transform has been extended to identifying positions of arbitrary shapes, most commonly circles or ellipses. The Hough transform as it is universally used today was invented by Richard Duda and Peter Hart in 1972, after the related 1962 patent of Paul Hough.[3] The transform was popularized in the computer vision community by Dana H. Ballard through a 1981 journal article titled "Generalizing the Hough transform to detect arbitrary shapes".

In automated analysis of digital images, a subproblem often arises of detecting simple shapes, such as straight lines, circles or ellipses. In many cases an edge can be used as a pre-processing stage to obtain image points or image pixels that are on the desired curve in the image space. Due to imperfections in either the image data or the edge detector, however, there may be missing points or pixels on the desired curves as well as spatial deviations between the ideal line/circle/ellipse and the noisy edge points as they are obtained from the edge detector. For these reasons, it is often non-trivial to

D. Jin and S. Lin (Eds.): Advances in Mechanical and Electronic Engineering, LNEE 176, pp. 593–598.
springerlink.com

group the extracted edge features to an appropriate set of lines, circles or ellipses. The purpose of the Hough transform is to address this problem by making it possible to perform groupings of edge points into object candidates by performing an explicit voting procedure over a set of parameterized image objects[2].

Lack of attention by the driver is identified as the cause for 91% of driver related accidents. This places Forward Collision Warning (FCW) high on the list of solutions that can contribute significantly to reduction of the number and the severity of driving accidents. Forward collision warning system can detect immediate forward collision danger. With this functionality the system provides a timely warning for the most common causes of accidents in nowadays traffic. Lane detection is part of aces Forward Collision Warning (FCW) system for vehicle electronic technology.

2 System Overview

The input to the system is a sequence of images captured by the camera installed inside the vehicle. A SONY DCR-DVD805 camera has been used to acquire the video sequences. The input interface records the images delivered by the camera, and performs the necessary operations to accommodate them to the format expected by the video processing module, i.e., decompresses, rotates and de-interlaces the image, and rescales it to a 760x320 format.

The system is composed of two blocks, as shown in Fig.1 and Fig.2. The contribution of this paper is: we propose a robust lane marking detection system. lane marking detection system is based on generalized and Kernel-based hough transformation. Obstacle classification is based on fuzzy neural network. The rest of the paper is organized as follows: Section 2 gives a brief description of obstacle detection and classification system. Then in Section 3, we describe the algorithm in detail. Section 4 is experiment.

3 Lane Mark Detection

The simplest case of Hough transform is the linear transform for detecting straight lines. In the image space, the straight line can be described as $y = mx + b$ and can be graphically plotted for each pair of image points (x, y). In the Hough transform, a main idea is to consider the characteristics of the straight line not as image points (x1,y1), (x2, y2), etc., but instead, in terms of its parameters, i.e., the slope parameter m and the intercept parameter b. Based on that fact, the straight line $y = mx + b$ can be represented as a point (b, m) in the parameter space. However, one faces the problem that vertical lines give rise to unbounded values of the parameters m and b. For computational reasons, it is therefore better to use a different pair of parameters, denoted r and θ (theta), for the lines in the Hough transform. These are the Polar Coordinates.

The parameter r represents the distance between the line and the origin, while θ is the angle of the vector from the origin to this closest point. Using this parameterization, the equation of the line can be written as[4].

$$y = (-\frac{\cos\theta}{\sin\theta})x + (\frac{r}{\sin\theta}) \quad (1)$$

The (r,θ) plane is sometimes referred to as Hough space for the set of straight lines in two dimensions. This representation makes the Hough transform conceptually very close to the two-dimensional Radon transform. (They can be seen as different ways of looking at the same transform.[5]).

For an arbitrary point on the image plane with coordinates, e.g., (x0, y0), the lines that go through it are

$$r(\theta) = x_0 * \cos\theta + y_0 * \sin\theta \quad (2)$$

where r (the distance between the line and the origin) is determined by θ. This corresponds to a sinusoidal curve in the (r,θ) plane, which is unique to that point. If the curves corresponding to two points are superimposed, the location (in the Hough space) where they cross corresponds to a line (in the original image space) that passes through both points. More generally, a set of points that form a straight line will produce sinusoids which cross at the parameters for that line. Thus, the problem of detecting collinear points can be converted to the problem of finding concurrent curves.[6]

The Hough transform algorithm uses an array, called an accumulator, to detect the existence of a line y = mx + b. The dimension of the accumulator is equal to the number of unknown parameters of the Hough transform problem. For example, the linear Hough transform problem has two unknown parameters: m and b. The two dimensions of the accumulator array would correspond to quantized values for m and b. For each pixel and its neighbourhood, the Hough transform algorithm determines if there is enough evidence of an edge at that pixel. If so, it will calculate the parameters of that line, and then look for the accumulator's bin that the parameters fall into, and increase the value of that bin. By finding the bins with the highest values, typically by looking for local maxima in the accumulator space, the most likely lines can be extracted, and their (approximate) geometric definitions read off. [4]The simplest way of finding these peaks is by applying some form of threshold, but different techniques may yield better results in different circumstances - determining which lines are found as well as how many. Since the lines returned do not contain any length information, it is often next necessary to find which parts of the image match up with which lines. Moreover, due to imperfection errors in the edge detection step, there will usually be errors in the accumulator space, which may make it non-trivial to find the appropriate peaks, and thus the appropriate lines.

The result of the Hough transform is stored in a matrix that often called an accumulator. One dimension of this matrix is the θ (theta) values (angles) and the other dimension is the ρ (rho) values (distances), and each element has a value telling how many points/pixel that lie on the line with the parameters (ρ, θ). So the element with the highest value tells what line that is most represented in the input image.[7]

Using the gradient direction to reduce the number of votes.

An improvement suggested by O'Gorman and Clowes can be used to detect lines if one takes into account that the local gradient of the image intensity will necessarily be orthogonal to the edge. Since edge detection generally involves computing the intensity gradient magnitude, the gradient direction is often found as a side effect. If a given

point of coordinates (x,y) happens to indeed be on a line, then the local direction of the gradient gives the θ parameter corresponding to said line, and the r parameter is then immediately obtained. (Shapiro and Stockman, 305) The gradient direction can be estimated to within 20°, which shortens the sinusoid trace from the full 180° to roughly 45°. This reduces the computation time and has the interesting effect of reducing the number of useless votes, thus enhancing the visibility of the spikes corresponding to real lines in the image.

Kernel-based Hough transform:

Once one has computed the variances and covariance associated with r and thota, the votes are cast using a bi-variated Gaussian distribution given by

$$G_k(\rho_j, \theta_j) = \frac{1}{2\Pi\sigma_\rho\sigma_\theta\sqrt{1-r^2}} e^{-\frac{z}{2(1-r^2)}} \tag{3}$$

We suggested an improved voting scheme for the Hough transform that allows a software implementation to achieve real-time performance even on relatively large images (e.g., 1280×960). The Kernel-based Hough transform uses the same (r, θ) parameterization proposed by Duda and Hart but operates on clusters of approximately collinear pixels. For each cluster, votes are cast using an oriented elliptical-Gaussian kernel that models the uncertainty associated with the best-fitting line with respect to the corresponding cluster. The approach not only significantly improves the performance of the voting scheme, but also produces a much cleaner accumulator and makes the transform more robust to the detection of spurious lines.

Generalised Hough transform:

Although the version of the transform described above applies only to finding straight lines, a similar transform can be used for finding any shape which can be represented by a set of parameters. A circle, for instance, can be transformed into a set of three parameters, representing its center and radius, so that the Hough space becomes three dimensional. Arbitrary ellipses and curves can also be found this way, as can any shape easily expressed as a set of parameters. For more complicated shapes, the Generalised Hough transform is used, which allows a feature to vote for a particular position, orientation and/or scaling of the shape using a predefined look-up table.

4 Experiment

Carefully chosen parameter space: A high-dimensional parameter space for the Hough Transform is not only slow, but if implemented without forethought can easily overrun the available memory. Even if the programming environment allows the allocation of an array larger than the available memory space through virtual memory, the number of page swaps required for this will be very demanding because the accumulator array is used in a randomly accessed fashion, rarely stopping in contiguous memory as it skips from index to index.

Consider the task of finding ellipses in an 800x600 image. Assuming that the radii of the ellipses are oriented along principal axes, the parameter space is four-dimensional. (x,y) defines the center of the ellipse, and a and b denote the two radii. Allowing the center to be anywhere in the image, adds the constraint 0<x<800 and 0<y<600. If the radii are given the same values as constraints, what is left is a sparsely filled accumulator array of more than 230 billion values. Matlab has functions aimed specifically for sparse matrices, but they only handle two dimensional matrices, not four dimensional.

A program thus conceived is unlikely to be allowed to allocate sufficient memory. This doesn't mean that the problem can't be solved, but only that new ways to constrain the size of the accumulator array are to be found, which makes it feasible.

Fig3 show our algorithm can work in complex environment. Tests have been made on images belonging to video sequences captured from cameras inside a car. The proposed strategy has been efficiently implemented in a general purpose PC, working in real time for different frame rates according to the size of the images: 15 fps. Overall, an average detection rate of above 92% is obtained for a set of scenarios, including different illumination, weather and traffic conditions.

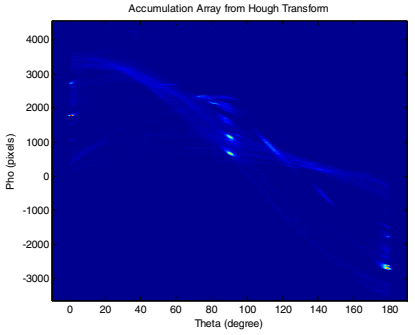

Fig. 1. Result of accumulation space

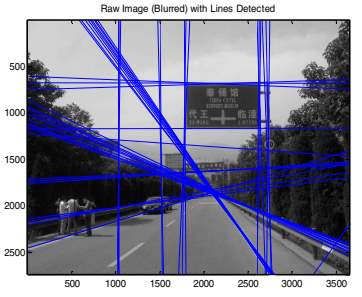

Fig. 2. Result of all lines

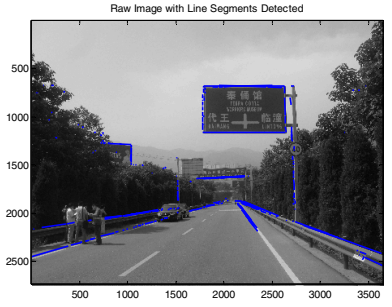

Fig. 3. Result of some useful lines

Fig. 4. Lane markings

Limitations: The Hough Transform is only efficient if a high number of votes fall in the right bin, so that the bin can be easily detected amid the background noise. This means that the bin must not be too small, or else some votes will fall in the neighboring

bins, thus reducing the visibility of the main bin.[10] Also, when the number of parameters is large (that is, when we are using the Hough Transform with typically more than three parameters), the average number of votes cast in a single bin is very low, and those bins corresponding to a real figure in the image do not necessarily appear to have a much higher number of votes than their neighbors. The complexity increases at a rate of with each additional parameter, where A is the image space and mis the number of parameters. (Shapiro and Stockman, 310) Thus, the Hough Transform must be used with great care to detect anything other than lines or circles.

Finally, much of the efficiency of the Hough Transform is dependent on the quality of the input data: the edges must be detected well for the Hough Transform to be efficient. Use of the Hough Transform on noisy images is a very delicate matter and generally, a denoising stage must be used before. In the case where the image is corrupted by speckle, as is the case in radar images, the Radon transform is sometimes preferred to detect lines, because it attenuates the noise through summation.

References

1. Shapiro, L., Stockman, G.: Computer Vision. Prentice-Hall, Inc. (2001)
2. Duda, R.O., Hart, P.E.: Use of the Hough Transformation to Detect Lines and Curves in Pictures. Comm. ACM 15, 11–15 (1972)
3. Hough, P.V.C.: Machine Analysis of Bubble Chamber Pictures. In: Proc. Int. Conf. High Energy Accelerators and Instrumentation (1959)
4. Jensen, J.: Hough Transform for Straight Lines (retrieved December 16, 2011)
5. Fernandes, L.A.F., Oliveira, M.M.: Real-time line detection through an improved Hough transform voting scheme. Pattern Recognition 41(1), 299–314 (2008)
6. Vosselman, G., Dijkman, S.: 3D Building Model Reconstruction from Point Clouds and Ground Plans. In: International Archives of the Photogrammetry, Remote Sensing and Spatial Information Sciences, Annapolis, MA, USA, October 22-24, vol. 34, part 3/W4, pp. 37–44 (2001)
7. Rabbani, T.: Automatic reconstruction of industrial installations - Using point clouds and images. Publications on Geodesy 62, Delft, 43–44 (2006), ISBN 978 90 6132 297 9, http://www.ncg.knaw.nl/Publicaties/Geodesy/62Rabbani.html
8. Achtert, E., Böhm, C., David, J., Kröger, P., Zimek, A.: Global Correlation Clustering Based on the Hough Transform. Statistical Analysis and Data Mining 1(3), 111–127 (2008), http://dx.doi.org/10.1002/sam.10012
9. Rabbani, T., van den Heuvel, F.: Efficient hough transform for automatic detection of cylinders in point clouds. In: Proceedings of the 11th Annual Conference of the Advanced School for Computing and Imaging (ASCI 2005), The Netherlands (June 2005)
10. Xie, Y., Ji, Q.: A new efficient ellipse detection method 2, 957 (2002), doi:10.1109/ICPR.2002.1048464

Object Detection Based on Reinforcement Learning and Gabor Feature for Image Electronic Technology

Lizhuang Liu[1,2], Jianzhu Cui[2], and Jing Li[3]

[1] School of Communication and Information Engineering, Shanghai University, China
[2] Shanghai Advanced Research Institute (SARI), Chinese Academy of Sciences
[3] College of Information Technology, Shanghai Ocean University, Shanghai, China
liulz@sari.ac.cn, cuijianlou@163.com, j_li@shou.edu.cn

Abstract. Detection is the first and foremost step in any automated recognition system in image electronic technology. Its reliability greatly affects the performance and usability of the whole system. In this paper, the processing is done as follows: Step one is feature extraction. Gabor feature functions that can transform a small patch of image into a vector. This function is the feature extraction function and should extract features in a wise manner, followed by normalization. Step two is the Classifier training. Detection system needs a classifier that looks at your vector and decides if it is the deal or not. Detection System uses Neural Network as its classifier. Given a single image or a video frame, the detector should have the ability to locate all the present objects inside that image, regardless of their position, gestures, variations in scale and orientation. Furthermore it should be robust against variation in illumination, skin color or background.

Keywords: image electronic technology, gabor feature, artificial neural network, reinforcement learning.

1 Introduction

Object detection is the first and foremost step in any automated recognition system in image electronic technology. Its reliability greatly affects the performance and usability of the whole system. Given a single image or a video frame, an ideal object detector should have the ability to locate all the present objects inside that image, regardless of their position, facial gestures, variations in scale and orientation. Furthermore it should be robust against variation in illumination, skin color or background.

Several clues may facilitate the detection process. Shape is one that often can be used. Motion (for detecting objects in video) is another well-known clue that can be estimated by analyzing several video frames in a row. But the hardest kind of detection is object detector in grey-level still images, in which there is no cue of any type such as color or motion.

In image processing, a Gabor filter, named after Dennis Gabor, is a linear filter used for edge detection. Frequency and orientation representations of Gabor filters are similar to those of the human visual system, and they have been found to be particularly appropriate for texture representation and discrimination. In the spatial domain, a 2D

D. Jin and S. Lin (Eds.): Advances in Mechanical and Electronic Engineering, LNEE 176, pp. 599–604.
springerlink.com

Gabor filter is a Gaussian kernel function modulated by a sinusoidal plane wave. The Gabor filters are self-similar: all filters can be generated from one mother wavelet by dilation and rotation. J. G. Daugman discovered that simple cells in the visual cortex of mammalian brains can be modeled by Gabor functions.[1] Thus, image analysis by the Gabor functions is similar to perception in the human visual system.

2 System Overview

In this paper, the processing is done as follows: Step one is feature extraction. Gabor feature functions that can transform a small patch of image into a vector. This function is the feature extraction function and should extract features in a wise manner, followed by normalization. Step two is the Classifier training. Detection system needs a classifier that looks at your vector and decides if it is the deal or not. Detection System uses Neural Network as its classifier. Given a single image or a video frame, the detector should have the ability to locate all the present objects inside that image, regardless of their position, gestures, variations in scale and orientation. Furthermore it should be robust against variation in illumination, skin color or background.

3 Detection System

3. 1 Feature Extraction

The response of gabor feature is defined by a harmonic function multiplied by a Gaussian function[4]. Because of the multiplication-convolution property (Convolution theorem), the Fourier transform of a Gabor filter's impulse response is the convolution of the Fourier transform of the harmonic function and the Fourier transform of the Gaussian function. The filter has a real and an imaginary component representing orthogonal directions[2]. The two components may be formed into a complex number or used individually ($\varphi = \theta_f$).

$$f(x,y)=\frac{1}{2\pi\sigma_x\sigma_y}\exp\left[-\left(\frac{x'^2}{2\sigma_x^2}+\frac{y'^2}{2\sigma_y^2}\right)+j2\pi(\omega_{xf}x+\omega_{yf}y)\right] \tag{1}$$

$$\begin{cases} x'=x\cos\theta_f+y\sin\theta_f \\ y'=-x\sin\theta_f+y\cos\theta_f \end{cases} \tag{2}$$

$$\omega_f=\sqrt{\omega_{xf}^2+\omega_{yf}^2}\ , \quad \varphi=\tan^{-1}\left(\omega_{yf}\Big/\omega_{xf}\right) \quad \varphi=\theta_f \tag{3}$$

$$f(x,y)=\frac{1}{2\pi\sigma_x\sigma_y}\exp\left[-\left(\frac{x'^2}{2\sigma_x^2}+\frac{y'^2}{2\sigma_y^2}\right)+j2\pi\omega_f x'\right] \tag{4}$$

Fourier transform of $f(x, y)$ is :

$$F(\omega_x, \omega_y) = \frac{1}{2}\exp\left\{-2\pi^2\left[\sigma_x^2(\omega_x - \omega_f)^2 + \sigma_y^2\omega_y^2\right]\right\} \tag{5}$$

$$\begin{cases} \omega'_x = \omega_x \cos\theta_f + \omega_y \sin\theta_f \\ \omega'_y = -\omega_x \sin\theta_f + \omega_y \cos\theta_f \end{cases} \tag{6}$$

In this equation, ω represents the wavelength of the sinusoidal factor, θ represents the orientation of the normal to the parallel stripes of a Gabor function, σ is the sigma of the Gaussian envelope. A set of Gabor filters with different frequencies and orientations may be helpful for extracting useful features from an image.

3. 2 Train the Classifier

Detection system needs a classifier that looks at your vector and decides if it is the deal or not. In case of face detection, the classifier looks for faces. The main issues are to choose your classifier and set the parameters in a way that you get reasonable results. This detection System uses Neural Network as its classifier.

In the artificial intelligence field, artificial neural networks have been applied successfully to speech recognition, image analysis and adaptive control, in order to construct software agents (in computer and video games) or autonomous robots. Most of the currently employed artificial neural networks for artificial intelligence are based on statistical estimations, classification optimization and control theory. A neural network (NN) [5], in the case of artificial neurons called artificial neural network (ANN) or simulated neural network (SNN), is an interconnected group of natural or artificial neurons that uses a mathematical or computational model for information processing based on a connectionistic approach to computation. In most cases an ANN is an adaptive system that changes its structure based on external or internal information that flows through the network.

The utility of artificial neural network models lies in the fact that they can be used to infer a function from observations and also to use it. Unsupervised neural networks can also be used to learn representations of the input that capture the salient characteristics of the input distribution, e.g., see the Boltzmann machine (1983) [6], and more recently, deep learning algorithms, which can implicitly learn the distribution function of the observed data. Learning in neural networks is particularly useful in applications where the complexity of the data or task makes the design of such functions by hand impractical.

The tasks to which artificial neural networks are applied tend to fall within the following broad categories:

Function approximation, or regression analysis, including time series prediction and modeling.

Classification, including pattern and sequence recognition, novelty detection and sequential decision making.

Data processing, including filtering, clustering, blind signal separation and compression.

An artificial neural network (ANN), usually called neural network (NN), is a mathematical model or computational model that is inspired by the structure and/or functional aspects of biological neural networks[7]. A neural network consists of an interconnected group of artificial neurons, and it processes information using a connectionist approach to computation. In most cases an ANN is an adaptive system that changes its structure based on external or internal information that flows through the network during the learning phase. Modern neural networks are non-linear statistical data modeling tools. They are usually used to model complex relationships between inputs and outputs or to find patterns in data.

Neural network models in artificial intelligence are usually referred to as artificial neural networks (ANNs); these are essentially simple mathematical models defining a function $f: x \longrightarrow y$ or a distribution[8] over both x and y, but sometimes models are also intimately associated with a particular learning algorithm or learning rule.

An ANN is typically defined by three types of parameters:

The interconnection pattern between different layers of neurons
The learning process for updating the weights of the interconnections
The activation function that converts a neuron's weighted input to its output activation.

Mathematically, a neuron's network function $f(x)$ is defined as a composition of other functions $g_i(x)$, which can further be defined as a composition of other functions. This can be conveniently represented as a network structure, with arrows depicting the dependencies between variables. A widely used type of composition is the nonlinear weighted sum, where $f(x) = K(\sum_i w_i g_i(x))$, where K (commonly referred to as the activation function[1]) is some predefined function, such as the hyperbolic tangent. It will be convenient for the following to refer to a collection of functions g_i as simply a vector $g = (g1, g2, ..., gn)$. What has attracted the most interest in neural networks is the possibility of learning. Given a specific task to solve, and a class of functions F, learning means using a set of observations to find $f^* \in F$ which solves the task in some optimal sense. This entails defining a cost function $C : F \to R$ such that, for the optimal solution f^*, $C(f^*) \leq C(f) \forall f \in F$ (i.e., no solution has a cost less than the cost of the optimal solution).

The cost function C is an important concept in learning, as it is a measure of how far away a particular solution is from an optimal solution to the problem to be solved. Learning algorithms search through the solution space to find a function that has the smallest possible cost. For applications where the solution is dependent on some data, the cost must necessarily be a function of the observations; otherwise we would not be modelling anything related to the data. It is frequently defined as a statistic to which

only approximations can be made. As a simple example, consider the problem of finding the model f, which minimizes $C = E[(f(x) - y)^2]$, for data pairs (x, y) drawn from some distribution D. In practical situations we would only have N samples from D and thus, for the above example, we would only minimize $\hat{C} = \frac{1}{N}\sum_{i=1}^{N}(f(x_i) - y_i)^2$. Thus, the cost is minimized over a sample of the data rather than the entire data set.

While it is possible to define some arbitrary, ad hoc cost function, frequently a particular cost will be used, either because it has desirable properties (such as convexity) or because it arises naturally from a particular formulation of the problem (e.g., in a probabilistic formulation the posterior probability of the model can be used as an inverse cost). Ultimately, the cost function will depend on the desired task. [9]

In reinforcement learning, data x are usually not given, but generated by an agent's interactions with the environment. At each point in time t, the agent performs an action yt and the environment generates an observation xt and an instantaneous cost ct , according to some (usually unknown) dynamics. The aim is to discover a policy for selecting actions that minimizes some measure of a long-term cost; i.e., the expected cumulative cost. The environment's dynamics and the long-term cost for each policy are usually unknown, but can be estimated.

More formally, the environment is modeled as a Markov decision process (MDP) with states $s_1,...,s_n \in S$ and actions $a_1,...,a_m \in A$ with the following probability distributions: the instantaneous cost distribution $P(c_t \mid s_t)$, the observation distribution $P(x_t \mid s_t)$ and the transition $P(s_{t+1} \mid s_t, a_t)$, while a policy is defined as conditional distribution over actions given the observations. Taken together, the two define a Markov chain (MC). The aim is to discover the policy that minimizes the cost; i.e., the MC for which the cost is minimal.

ANNs are frequently used in reinforcement learning as part of the overall algorithm. Dynamic programming has been coupled with ANNs (Neuro dynamic programming) by Bertsekas and Tsitsiklis[2] and applied to multi-dimensional nonlinear problems such as those involved in vehicle routing or natural resources management because of the ability of ANNs to mitigate losses of accuracy even when reducing the discretization grid density for numerically approximating the solution of the original control problems. Tasks that fall within the paradigm of reinforcement learning are control problems, games and other sequential decision making tasks.

4 Experiment

Fig 1 show our algorithm can work in complex environment. The proposed strategy has been efficiently implemented in a general purpose PC, working in real time for different frame rates according to the size of the images: 15 fps. Overall, an average detection rate of above 90% is obtained for a set of scenarios, including different illumination, weather and traffic conditions.

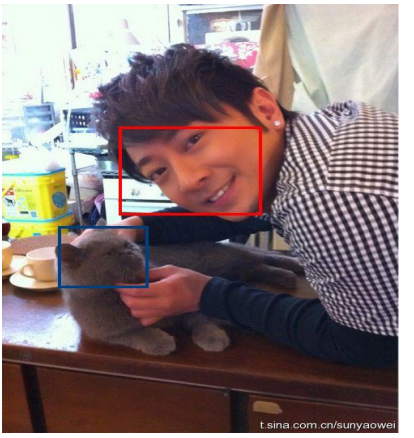

Fig. 1. Detection result

References

1. Dagan, E., Mano, O., Stein, G.P., Shashua, A.: Forward Collision Warning with a Single Camera. In: IEEE Intelligent vehicles Symposium (IV 2004), Parma, Italy, pp. 201–205 (June 2004)
2. Henriksen, J.J.: 3D surface tracking and approximation using Gabor filters. South Denmark University (March 28, 2007)
3. Daugman, J.G.: Two-dimensional spectral analysis of cortical receptive field profiles. Vision Res. 20(10), 847–856 (1980)
4. Jones, J.P., Palmer, L.A.: An evaluation of the two-dimensional gabor filter model of simple receptive fields in cat striate cortex. J. Neurophysiol. 58(6), 1233–1258 (1987)
5. Feichtinger, H.G., Strohmer, T.: Gabor Analysis and Algorithms. Birkhäuser (1998) ISBN 0817639594
6. Feichtinger, H.G., Strohmer, T.: Advances in Gabor Analysis. Birkhäuser (2003) ISBN 0817642390
7. Gröchenig, K.: Foundations of Time-Frequency Analysis. Birkhäuser (2001) ISBN 0817640223
8. Bertsekas, D.P., Tsitsiklis, J.N.: Neuro-dynamic programming. Athena Scientific, 512 (1996) ISBN 1-886529-10-8
9. de Rigo, D., Castelletti, A., Rizzoli, A.E., Soncini-Sessa, R., Weber, E.: A selective improvement technique for fastening Neuro-Dynamic Programming in Water Resources Network Management. In: Zítek, P. (ed.) Proceedings of the 16th IFAC World Congress - IFAC-Papers On Line (January 2005)

A Strategy to Solve the Local Minima Problem for Autonomous Mechanical Vehicles

Jian Yang[1], Jingrong Yu[1,*], Mi Dong[1], Jiangmin Chunyu[2]

[1] School of Info. Sci. & Eng., Central South University, Changsha, Hunan 410083, China
[2] Delta Tau Data Systems, Inc., Chatsworth, CA 91311, USA
jingrong_yu@126.com

Abstract. In this paper, we address the local minima problem (LMP) inherent in potential field methods (PFMs). The related potential fields are built from electronic image processing of autonomous mechanical vehicles. The LMP is formulated and its existence is analyzed. A switching control strategy is then proposed to tackle this mechanical engineering problem. When trapped into local minima, the autonomous mechanical vehicle can escape from local minima by following the planned goal. The proposed control law also takes into account the presence of possible mechanical saturation constraints. Simulation results of escaping from classical local minima scenarios are provided to show the validity and effectiveness.

Keywords: Autonomous mechanical vehicles, local minima, potential field methods (PFMs).

1 Introduction

In mechanical engineering, potential field methods are widely used for autonomous mechanical vehicle navigation due to its simplicity, elegance and high efficiency [1]. However, as pointed out in [2], one critical drawback often associated with PFMs is the problem of local minima. Most existing methods dealing with LMP use one of these two strategies: eliminating local minima and escaping from local minima.

In the eliminating local minima approach, very special functions are proposed which exhibit a few or even no local minima. For instance, the navigation function method does not render local minima [3]. However, they are generally computationally intensive and therefore may not be practical for real-time navigation in partially known or unknown environments. The total potential field poses no local minima in most cases.

In the escaping the local minima approach, the motivation is to attract the autonomous mechanical vehicle away from local minima when a trap-situation occurs. Random walk-like techniques have been used to help potential field based motion planning techniques to escape from local minimum configurations [4]. Virtual obstacles are placed around local minima to repel an autonomous mechanical vehicle from local minima [5]. Many of these proposed methods are heuristic and the lack of analytical design guidelines can be problematic in applications.

* Corresponding author.

D. Jin and S. Lin (Eds.): Advances in Mechanical and Electronic Engineering, LNEE 176, pp. 605–610.
springerlink.com

In this paper, we propose a switching control to solve the local minima problem which originates in PFMs based navigation through unknown environments with complex shape obstacles. By using a simple switching strategy, goal convergence and obstacle avoidance are achieved at the same time.

2 Preliminaries and Problem Formulation

Consider an autonomous mechanical vehicle whose dynamics are given by

$$\dot{q}_\tau = v_\tau, \qquad \dot{v}_\tau = u_1. \tag{1}$$

where $q = [x, y, z]^T \in \Re^3$ denotes the center position, $v = \left[v_x, v_y, v_z \right]^T \in \Re^3$ represents the velocity, and $u_1 \in \Re^3$ is the control input. Subscripts *r*, *g* and *o* indicate the robot, goal and obstacle, respectively.

Let a compact set $\Omega_{oi} \subset \Re^3$, which are typically built from electronic image processing of autonomous mechanical vehicles, represent the 3-dimensional shape of the *i*th obstacle, we thereby introduce the pairwise repelling set

$$\overline{\Omega}_{oi} = \left\{ q_\tau \in \Re^3 \mid d_i(q_\tau, \Omega_{oi}) < D_i \right\}$$

where $d_i(q_\tau, \Omega_{oi})$ is the minimum distance between q_r and the *i*th obstacle. And $D_i > 0$ indicates the region size of $\overline{\Omega}_{oi} \setminus \Omega_{oi}$.

Then the overall avoidance region Ω_o is given by $\Omega_o = \bigcup_{i \in N} \Omega_{oi}$, and the overall repelling region $\overline{\Omega}_o$ is given by $\overline{\Omega}_o = \bigcup_{i \in N} \overline{\Omega}_{oi}$,where *N* is the total number of obstacles.

Regarding the basic idea of potential field methods, the so-called attractor and repeller are created based on the geometry of the goal and obstacles, and the obstacles' shape which are specified by environmental conditions.

In order to have a well-defined problem, we assume the following throughout the paper:

Assumption 1. The autonomous mechanical vehicle is represented by a 3-D sphere with the center at $q_\tau(t)$ and of radius R. The range of its sensors is also described by a sphere centered at $q_\tau(t)$ and of radius R_S.

Assumption 2. The autonomous mechanical vehicle has the following two saturation constraints:

1. Velocity bound, i.e. $\|u_1(t)\| \le \bar{v}_\tau$; 2. Control input saturation, i.e. $\|u_1(t)\| \le \bar{a}_\tau$.

Assumption 3. $\Omega_i (i = 1, \cdots N)$ are convex on $\Re^3$.

The control objectives and main contributions of this paper can be summarized as follows:

i. Goal convergence, i.e. using PFMs, $\lim_{t\to\infty} q_\tau(t) \to q_g$ provided that goal q_g is τ reachable; ii. Obstacle avoidance, i.e. $q_\tau(t) \notin \Omega_o, \forall t \geq t_0$ provided that $q_\tau(t_0) \notin \Omega_o$

3 Switching Control Design

In the unknown environment, local minima cannot be identified a priori, upon which we propose a two-stage switching control scheme with state and control magnitude constraints being addressed as well. Afterwards, goal convergence and obstacle avoidance of this switching control system are analyzed using the Lyapunov theory. The detailed design and proofs are explored as follows.

We introduce a planned goal $q_p(t)$. When the autonomous mechanical vehicle is trapped into local minima q^*, the planned goal is designed to instantaneously switch from q_g to q^* and then move along the equipotential surface $S_r(P_r(q^*))$ until $P_a(q_p(t)) < P_a(q^*)$. Meanwhile, the robot is required to track $q_p(t)$ and ensure the tracking error is uniformly bounded for the purpose of obstacle avoidance.

Before proceeding to the control law, we first introduce the following definition:

Definition 3.1. $q_r(t)$ is said to be trapped into local minima if and only if the following conditions hold: 1. $q_r(t) \in \bar{\Omega}_0 \backslash \Omega_0$; 2. $\|v_r(t)\| \leq \sigma$ and $\|u_1\| \leq \sigma$; where $\sigma > 0$ is a very small number.

We begin with the following augmented system dynamical model given by

$$\dot{q}_r = v_r, \quad \dot{v}_r = u_1, \quad \dot{q}_p = u_2 \tag{2}$$

The two-stages witching control is given as follows:

- **Stage A**: Normal mode to track goal and avoid obstacles

$$u_1 = -\nabla P_a(q_r) - \nabla P_r(q_r) - \xi(.)v_r, \quad q_p(t_s^{B\to A}) = q_g \quad \text{and} \quad u_2 = 0,$$

where $t_s^{B\to A}$ is the switching time from stage B to A.

- **Stage B**: escape from local minima

$$u_1 = -k_a(q_r - q_p) - \xi v_r, \tag{3}$$

and

$$q_p(t_s^{A\to B}) = q_r(t_s^{A\to B}), \quad u_2 = \frac{\delta^2 \cdot \dfrac{\nabla P_r^{\perp}(q_p)}{\| \nabla P_r^{\perp}(q_p) \|} \min(\xi - \gamma, k_a\gamma)}{(\gamma(1+\xi) + k_a)(\| v_r \| + \| q_r - q_p \| + 1)}, \tag{4}$$

where $t_s^{A\to B}$ is t he switching time from stage A to stage B. Gains $\gamma > 0$, $k_a > 0$ and the nonlinear damping function $\xi(\cdot) > \gamma$.

- **Design of** $\nabla P_r^{\perp}(q_p)$

At the point $q_p(t_s^{A\to B})$, let T be tangent vector lying in the tangent plane of $S_r(P_r(q_p(t_s^{A\to B})))$ such that

$$\left\langle T, \nabla P_r(q_p(t_s^{A\to B}))\right\rangle = 0.$$

Then using the right hand rule, the direction of $\nabla P_r^{\perp}(q_p)$ is determined by $\nabla P_r(q_p)\times T$ .And also

$$\| \nabla P_r^{\perp}(q_p) \| = \| \nabla P_r(q_p) \|.$$

In particular, for the 2-D case, T can be either $[0,0,1]^T$ or $[0,0,-1]^T$.

- **Switching strategies**

(1) When $t = t_0$, choose control design for stage A. Then we continue to (2);

(2) Choose control design for stage A. I f $q_r(t)$ is trapped into local minima, then we switch to (3);

(3) Choose control design for stage B. And we switch back to (2) at time $t_s^{B\to A}$ only when $V(t_s^{B\to A}) < V(t_s^{A\to B})$.

Choose a Lyapunov function as $V = P_a(q_r) + P_r(q_r) + \frac{\| v_r \|^2}{2}$ .The proposed two stages witching control is proved to ensure that V is decreasing over time, which implies goal convergence and obstacle avoidance as shown the following theorem.

Theorem 1. Suppose assumptions 1 and 3 hold. If $q_r(t_0) \notin \Omega_0$ and the initial conditions $q_r(t_0)$ and $v_r(t_0)$ are bounded. Consider system (1) under controls in stage A and B , as long as q_g is τ reach able and D_i is sufficiently small, then we can draw the following conclusions

1. $\lim_{t\to+\infty} \| q_r(t) - q_g \| = 0$; 2. $q_r(t) \notin \Omega_0$, $\forall t \geq t_0$.

4 Simulation

To show the effectiveness of the proposed control in Sections 3, this section describes the simulation results as follows. The nonlinear damping function $\xi(\cdot)$ is simply chosen to be a constant function. The parameters used for these simulations are: $R = 0.5m$, $R_S = 2m$, $\gamma = 1$, $k_a = 6$, $\sigma = 0.01$, $\xi(\cdot) = 3.16$, $k_1 = 1$, $k_2 = 100$ and $D_i = 1.5$. And the bound on the linear velocity is 2 m/s.

There are some rectangular, circular and even concave obstacles scattered in a 45m×45m workspace. We set the conditions of three mechanical vehicles (robots) be: $q_{r1}(t_0)=(1,1)^T, q_{r2}(t_0)=(25,5)^T, q_{r3}(t_0)=(7,36)^T$ and $v_{r1}(t_0)=v_{r2}(t_0)=v_{r3}(t_0)=(0,0)^T$. The goal q_g is located at $(27.5,28)^T$. In this simulation, we do not consider the collision avoidance among three robots.

Under the standard PFMs, three robots are trapped into their local minima, which are illustrated in Fig. 1. By applying the proposed control, three mechanical vehicles successfully escape from their local minima, which are shown in Fig. 2.

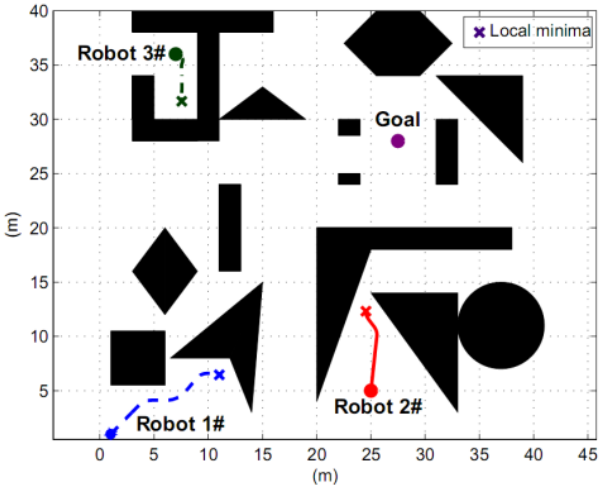

Fig. 1. Illustration of trapping situations due to local minima

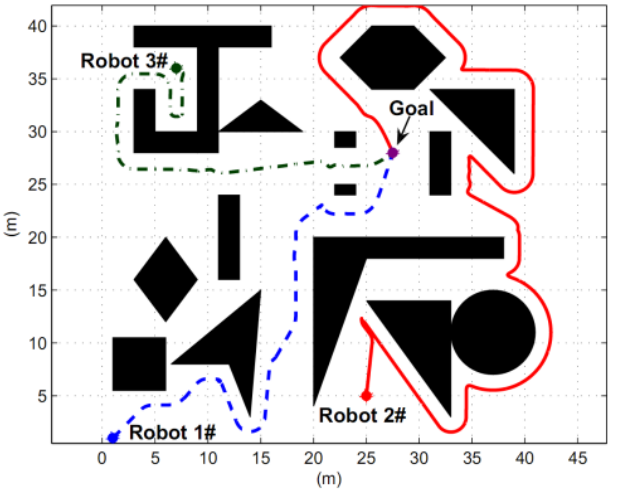

Fig. 2. Illustration of escaping from the local minima

5 Conclusion

In this paper, we proposed a systematic approach to solve the local minima problem of mechanical engineering, which is naturally arising from PFMs mechanical saturation of state and control input.

Examples through simulations confirm the effectiveness of two-stage switching control for the point-mass autonomous mechanical vehicles proposed in Section 4. Future research will consider more complex dynamic mechanical models to accommodate a larger class of autonomous mechanical vehicles.

Acknowledgments. This work was supported by the Fundamental Research Funds for the Central Universities of Central South University, under the grant 2011QNZT037, Hunan Science Department Tech Plan Foundation under Grant 2011FJ3221 and Hunan Science Foundation under Grant 11JJ5035.

References

1. Khatib, O.: Real-time obstacle avoidance for manipulator and mobile robots. Int. J. Robot. Res. 5, 90–98 (1986)
2. Koren, Y., Borenstein, J.: Potential field methods and their inherent limitations for mobile robot navigation. In: Proceeding of the IEEE International Conference on Robotics and Automation, pp. 1398–1404 (1991)
3. Rimon, E., Koditschek, D.: Exact robot navigation using artificial potential functions. IEEE Transactions on Robotics and Automation 8, 283–294 (1992)
4. Chang, H.: A new technique to handle local minimum for imperfect potential field based motion planning. In: Proceeding of the IEEE International Conference on Robotics and Automation, pp. 108–112 (1996)
5. Lee, M.C., Park, M.G.: Artificial potential field based path planning for mobile robots using a virtual obstacle concept. In: IEEE/ASME International Conference on Advanced Intelligent Mechatronics, vol. 2, pp. 735–740 (2003)

Application of Neuro-fuzzy Inference in Longitudinal Vehicle Control and Warning Systems

Gang Liu, Mei-jiao Liu, and Yong-jin Liu

School of Science, Shenyang Aerospace University,
110136 Shenyang, China
liugangljlp@126.com

Abstract. In this paper, a novel soft computing modeling of adaptive neuro-fuzzy inference system in longitudinal vehicle control and warning systems is investigated. Fuzzy inference system on the outputs of neuro-fuzzy classifiers is proposed, making decision of whether the current activity is normal or intrusive. Finally, a genetic algorithm which optimizes the structure of the fuzzy decision engine is constructed. A simulation is undertaken to performance of the proposed method and results are shown promising.

Keywords: Ambiguity function, Neuron-fuzzy inference, acquisition of range of image, genetic algorithms, vehicle control and warning system.

1 Introduction

A new mathematical approach known as soft computing (SC) is emerging that shows promise in dealing with the inherent complexity of modeling network intrusion. SC is a discipline situated at the combination of several relatively new and distinct mathematical techniques: fuzzy logic (FL), neural networks (NN) and probabilistic reasoning (PR) which include genetic algorithmsand learning theory.The guiding principle of soft computing is: the tolerance for imprecision, uncertainty and partial truth to achieve tractability, robustness and low solution cost. What is important to consider is that SC is not an uncoordinated combination of FL, NN and PR. Rather, it is a partnership in which each contributes usually at different organizational levels providing a hybrid system. In this perspective, the principal contributions of FL, NN and PR are complementary rather than competitive.

One hybrid system that is the most visible today is neuro-fuzzy systems which applies a combination of artificial neural networks (ANN) and fuzzy systems. ANN's have been employed in several applications ranging from target recognition to financial forecasting.They are particularly powerful in clustering the solution space identifying important features. Fuzzy logic was founded by Lofti A. Zadeh [1].The combination of ANN and fuzzy sets offers a powerful method to model human behavior. The ANN is used to define the clustering in the solution space which result in creation of the fuzzy sets. The ANN learns these clusters based on actual human behavior test data. A further advantage is that the solution space rather than being represented point by point as some expert systems clumps the space as described by Kosko [2,3]. This results in fewer rules and lower computer resources.

D. Jin and S. Lin (Eds.): Advances in Mechanical and Electronic Engineering, LNEE 176, pp. 611–616.
springerlink.com

2 Main Methods and Analyzing Process

2.1 Soft Computing

The realization that modeling of highly complex systems, that require intelligent systems, must combine knowledge, mathematical techniques and methodologies from several sources. It seems reasonable that it would be advantageous to use several mathematical techniques together to form a hybrid system that leverages off the advantages of various modeling techniques. SC is the development of these hybrid systems that are also known as neuro-fuzzy computing [4,5,6]. This technique uses the power of artificial neural networks that classify patterns in data and adapt that classification with highly dynamic environments.

The key to SC is the ability to deal with uncertainty and learn to adapt to unknown and highly dynamic environments to improve performance. Furthermore, two of these techniques (neural nets and genetic algorithms) a are biologically inspired techniques.

2.2 Neuro-fuzzy System

Neural networks exhibit the ability to learn patterns of static or dynamical systems. In the following neuro-fuzzy approach[7], the learning and pattern recognition of NN are exploited in two stages: first, to learn static response curves of a given system; and second, to learn the real-time dynamical changes in a system to serve as a reference model. The adaptive capability of the fuzzy controller is manifested in a rule generation mechanism and automatic adjustment of scaling factors or shapes of membership functions. The NN functions as a classifier of the system's temporal responses. A multi-layer perceptron NN is used to classify the tem-poral response of the system into different patterns. Depending on the type of pattern such as 'Vesponse with overshoot", "damped response", "oscillating response" etc. the scaling factor of the input and output membership functions are adjusted to make the system respond in a desired manner.

The rule generation mechanism also utilizes the temporal response of the system to evaluate new fuzzy rules. The non-redundant rules are appended to the existing rule base during the tuning cycles. This controller architecture is used in real-time to control a direct drive motor. Figure 1 illustrate the architecture of the Neuro-fuzzy controller where the two NNs and the fuzzy control architecture are integrated for adaptive control of nonlinear systems PI .

2.3 Fuzzy Inference Systems

Fuzzy inference systems[8] use IF THEN ELSE rules as do conventional AI techniques. Imprecise and incomplete sensory data provided by human sensory modalities to the brain is effectively processed into a perception of the world. With classical set theory the concept of a crisp set is used where there is a distinct and precise boundary. Fuzzy sets have boundaries that are not precise in that the transition from non-membership to membership is gradual rather than abrupt. This gradual change is defined by a membership grade function μ_A

$$\mu_A : X \rightarrow [0,1] \tag{1}$$

Where X is the universal crisp set that is being considered and A is the label of fuzzy set defined. The value of the membership grade is between 0 and 1 thus defining the compatibility to the set in question. The basic feature of fuzzy sets is the lack of sharp distinctions, the ability to capture the vagueness of natural language and measurement uncertainty.

The necessary steps in defining a fuzzy system include selection of input and output variables, selection of the linguistic states for each variable, selection of linguistic fuzzy inference rules, initial definition of membership grade functions for all linguistic states, initial selection of operations for inference rules and selection of a defuzzification methodology. The key part in developing a fuzzy system is to define the fuzzy functions (shape and linguistic label) based on practical experience or the examination of test data.

3 The Adaptive Neuro-fuzzy Inference System

The proposed system is discussed in details in this section. First, the system are explained. Data resource selected from KDD[9,10]for training the system, are introduced. Afterwards, layers of proposed framework are presented in more tails.

3.1 The Neuro-fuzzy Classifiers

The subtractive clustering method has been used to partition the training sets and generate and adaption of membership functions, training sets were used for training ANFIS. Each ANFIS trains at 50 epochs of learning and final FIS that is associated with the minimum checking error has been chosen. All the MFs of the input fuzzy sets were selected in the form of Gaussian functions with two parameters.

3.2 The Fuzzy Decision Module

The fuzzy inference module has five inputs, obtained from output values of each ANFIS classifiers. The fuzzy inference module, based on these inputs, determines whether the current connection record is an attack or not.

A five-input, single-output of Mamdani fuzzy inference system with centroid of area defuzzfication strategy was used for this purpose. Each input fuzzy set includes two MFs and all MFs are Gaussian functions which are specified by four parameters. The proposed fuzzy inference module uses the rules shown in the fuzzy associative memory in Table 1. The output of the fuzzy inference engine, which varies between-1 and 1, specifies how intrusive the current record is, 1 to show completely intrusive and -1 for completely normal. Records with positive intrusive values are selected as intrusive patterns. After an attack is detected, its class is selected based on the ANFIS module class which returns the highest value.

Table 1. Fuzzy associative memory for the proposed fuzzy inference rules

Normal	PROBE	DoS	U2R	R2L	Output
High	-	-	-	-	Normal
-	¬High	¬High	¬High	¬High	Normal
-	High	-	-	-	Attack
-	-	High	-	-	Attack
-	-	-	High	-	Attack
-	-	-	-	High	Attack
Low	-	-	-	-	Attack
-	Low	Low	Low	Low	Normal

3.3 Genetic Algorithm Module

The genetic algorithm repeatedly modifies a population by a set of genetic operators including mutation, crossover, and selection. It selects individuals evolving toward an optimal solution from the current population and uses them to produce children of the next generation. The algorithm stops when the stopping criterion is met. In the proposed system, each individual has genes codifying parameters the MFs of the input fuzzy set of the fuzzy decision engine. A chromosome consists of 320 bits of binary data. Each 8 bits of a chromosome determines one parameter out of the four parameters of an MF. Figure 1 illustrates the decoding process of each individual chromosome .

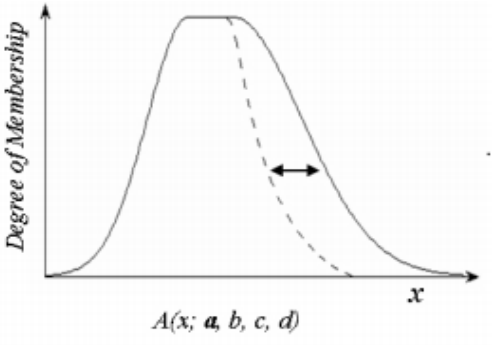

Fig. 1. Schematic decoding process of the individual chromosome

The genetic algorithm , which is used here to optimize the input MFs of the fuzzy decision-making module, uses a subset selected from 10% of KDD dataset for the optimization process. The distribution of samples for this subset is shown in Table 2.

Table 2. The sample distributions on the selected subset of 10% data for KDD dataset for the optimization process

	Normal	Probe	DoS	U2R	R2L
Number of Samples	200	104	200	52	104

For the purpose of classifier algorithm evaluation, another comparative measure is defined which is "Cost per Example"(CPE).

CPE is calculated using the following formula:

$$CPE = \frac{1}{N}\sum_{i=1}^{m}\sum_{j=1}^{m} CM(i,j) * C(i,j) \tag{2}$$

Where CM and C are function matrix and cost matrix, respectively, and N represents the total number of test instances, m is the number of the classes in classification. A confusion matrix is a square matrix in which each column corresponds to the predicted class, while rows correpond to the actual classes. An entry at row i and column $j, CM(i,j)$, represents the number of misclassified instances that originally belong to class i, although incorrectly identified as a member of class j. The entries of the primary diagonal, $CM(i,i)$, stand for the number of properly detected instances.

4 Conclusions

A new kind of soft computing approach for longitudinal vehicle control and warning systems is introduced and successfully demonstrated its usefulness on the training and testing subset of KDD cup 99 dataset. Fuzzy decision-making system is developed to make the system more powerful for attack detection, using the fuzzy inference approach. Finally, this paper proposes to use genetic algorithms to optimize the fuzzy decision-making engine. Experiment results show that the proposed method is effective in detecting various intrusions in vehicle control and warning systems .

Acknowledgments. This research is supported in part by the Young Teacher's Foundation of Shenyang Aerospace University (201109Y), China. We also thank the anonymous referees for useful suggestions on the earlier draft of the manuscript.

References

1. Zadeh, L.A.: Fuzzy Sets. Information and Control 8, 65–70 (1965)
2. Song, D., Heywood, M.I., Zincir-Heywood, A.N.: Training Genetic Programming on Half a Million Patterns, An Example from Anomaly Detection. IEEE Transactions on Evolutionary Computation 9(3), 225–239 (2005)
3. Gomez, J., Dasgupta, D.: Evolving Fuzzy Classifiers for Intrusion Detection. In: Proceeding of 2002 IEEE Workshop on Information Assurance, pp. 68–75. United States Military Academy, West Point (2001)
4. Shah, K., Dave, N.S., Chavan, S., Mukherjee, S., Abraham, A., Sanyal, S.: Adaptive Neuro-Fuzzy Intrusion Detection System. In: Proceeding of IEEE International Conference on Information Technology: Coding and Computing (ITCC 2004), April 5-7, vol. 1, pp. 70–74. IEEE Computer Society, USA (2004)
5. Abadeh, M.S., Habibi, J., Lucas, C.: Intrusion detection using a fuzzy genetics-based learning algorithm. Journal of Network and Computer Applications, 323–330 (2005)
6. Jang, J.-S.R.: ANFIS: Adaptive-Network-based Fuzzy Inference Systems. IEEE Transactions on Systems, Man, and Cybernetics 23(3), 665–685 (1993)
7. Agarwal, R., Joshi, M.V.: PNrule: A New Framework for Learning classifier Models in Data Mining. Department of Computer Science, University of Minnesota, Report No. RC-21719 (2000)
8. Yeung, D.Y., Chow, C.: Parzen-window Network Intrusion Detectors. In: Proceeding of 16th International Conference on Pattern Recognition, vol. 4, pp. 385–388. IEEE Computer Society (August 2002)
9. Jang, J., Sun, C., Mizutani, E.: Neuro-Fuzzy and Soft Computing. Prentice Hall (1997)
10. Kumbla, K.K.: Adaptive Neuro-Fuzzy controller for Passive Nonlinear systems. Ph.D. Dissertation, University of New Mexico (April 1997)

Author Index